ANTIMYCOBACTERIAL 2-AMINOQUINAZOLINONES AND BENZOXAZOLE-BASED OXIMES: SYNTHESIS, BIOLOGICAL EVALUATION, PHYSICOCHEMICAL PROFILING AND SUPRAMOLECULAR DERIVATIZATION

Paul M. Njaria

Supervisor:
Prof. Kelly Chibale
Department of Chemistry, University of Cape Town

Co-supervisor:
Prof. Mino R. Caira
Department of Chemistry, University of Cape Town

Thesis Presented for the Degree of

DOCTOR OF PHILOSOPHY

In the Department of Chemistry

UNIVERSITY OF CAPE TOWN

October 2017

DECLARATION

I, **Paul Magutu Njaria**, hereby:

a) grant the University of Cape Town free license to reproduce the thesis, in whole or in part, for the purpose of research;

b) declare that this thesis is my own unaided work, both in concept and execution, and that apart from the normal guidance of my supervisors; I have received no assistance apart from that acknowledged; and that neither the substance nor any part of the thesis has been submitted in the past, or is to be submitted for a Degree at this University or any other University.

Signed: Signed by candidate Date: 30th October 2017

DEDICATION

To

My beloved wife, Jane Wangari, and my adoring son, Reagan Njaria, as an expression of my cordial gratitude

For your blissful love, personal sacrifice, sheer patience, endless support, constant encouragement and prayers throughout my PhD journey.

ACKNOWLEDGEMENTS

First and most important, I would like to pay special thanks to my Almighty God for the gift of life and health, without which this work would have been futile.

I would like to gratefully acknowledge my supervisor, Prof. Kelly Chibale, for the opportunity to work in your laboratory. Your endless support, steady guidance and constant encouragement made my PhD journey bearable. Thank you for being an exceptional inspiration and extraordinary role model. I sum it up by saying, *ahsante sana* for helping me unravel my potential.

To my co-supervisor, Prof. Mino Caira, I sincerely acknowledge your determination, unwavering encouragement, patience and limitless confidence you had in me. Your many hours and manpower in teaching me crystallographic principles are highly appreciated.

I wish to extend my warm gratitude to Ms. Elaine Rutherfoord-Jones for her excellent administrative tasks in our research group. Thank you for your endless support.

I give special thanks to the current and former members of the KC Medicinal Chemistry and H3D research groups, who played a crucial role in shaping my research work. Thank you all for the friendship and comradeship; your constructive criticism and feedback during our group meetings are appreciated. Many thanks to Dr. Nicholas Njuguna and Dr. Aloysius Nchinda for the orientation and helping me settle in the synthesis laboratories. Special thanks also go to Dr. Rudolf Mueller for his medicinal chemistry tips and tricks as well as all the efforts he put in ensuring that some aspects of this work were accomplished efficiently.

I wish to acknowledge Mrs. Ronnett Seldon for the technical assistance in performing antimycobacterial assays. Many thanks also go to Pete Roberts for honouring all my requests for NMR spectroscopy experiments. My

heartfelt gratitude is extended to Terence Noonan and Dr. Hong Su for the technical assistance on the crystallographic aspects of this thesis work.

I would also like to sincerely acknowledge all our collaborators whose input was critical in getting the overall proof-of-concept for this work: Prof. Anne Lenaerts and Dr. Gregory Robertson (Mycobacteria Research Laboratories, Department of Microbiology, Immunology and Pathology, Colorado State University); Prof. Digby Warner and Dr. Atica Moosa (Molecular Mycobacteriology Research Unit, Division of Medical Microbiology, University of Cape Town); Dr. Thomas R. Ioerger (Department of Computer Science and Engineering, Texas A&M University (TAMU)).

I also wish to pay special thanks to Novartis Pharma AG for the opportunity and sponsorship to participate in the unique 2016 Novartis Next Generation Scientist (NGS) Program in Basel, Switzerland. My heartfelt thanks go to the NGS core mentors: Drs. Colin Pillai, Marcello Gutierrez, Henri-Michelle Yere and Sandra Felix and Ms. Akiko Keller. Similarly, my NGS project mentors are appreciated: Dan Akschuti and Dr. Michael Keller for imparting new skills on formulation of therapeutic peptides and oligonucleotides.

It is also my pleasure to acknowledge my long-time mentor, Prof. Grace Thoithi, for her constant encouragement and limitless confidence in my abilities.

To all my family members, thank you for your support, patience and understanding why I did this work away from home.

Last but not least, I would like to wholeheartedly extend my thanks to the South African Medical Research Council, South African National Research Foundation (NRF), Novartis Research Foundation and the Department of Chemistry for their generous financial assistance, without which this work would not have been possible.

ABSTRACT

Tuberculosis (TB) is a life-threatening infectious disease caused by *Mycobacterium tuberculosis* (*Mtb*). Globally, TB is a major public health burden with an estimated 10.4 million new cases and 1.8 million deaths reported in 2015. Although TB is curable, the treatment options currently available are beset by numerous shortcomings such as lengthy and complex treatment regimens, drug-drug interactions, drug toxicities, as well as emergence of widespread multi-drug resistance. Therefore, there is an urgent and compelling need to develop new, more effective, safer drugs with novel mechanisms of action, and which are capable of shortening treatment duration.

This study focused on hit-to-lead optimization of two new classes of compounds with potential anti-TB properties: 2-aminoquinazolinones (AQZs) and benzoxazole-based oximes (BZOs). A hit compound for each of these classes with low micromolar antimycobacterial activity had previously been identified through phenotypic whole-cell *in vitro* screening.

With respect to the 2-aminoquinazolinones, the hit compound **2** (**Figure 1**) was structurally modified at two points (**SAR 1** and **SAR 2**), while keeping the 2-aminoquinazolinone core constant, in an effort to explore the structure-activity relationships (SAR) associated with this class of compounds. In this regard, 43 analogues were synthesized, fully characterized, and evaluated *in vitro* for their antimycobacterial activity against the drug-susceptible *Mtb* $H_{37}Rv$ strain cultured in GAST-Fe and 7H9/ADC media. Of these, 17 compounds exhibited potent antimycobacterial activity ($MIC_{99} \leq 10$ µM) and clear SAR trends. Furthermore, selected active compounds manifested low cytotoxicity ($IC_{50} > 25$ µM) when tested *in vitro* against the Chinese Hamster Ovarian (CHO) cells and the human hepatic cells, HepG2. Besides, potent compounds displayed high microsomal metabolic stability in mouse liver microsomes (MLM). At this juncture, the frontrunner compound **3** [the

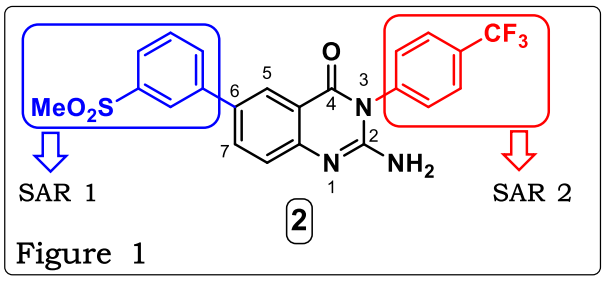

Figure 1

sulfoxide variant of **2**] was subjected to *in vivo* pharmacokinetics studies in mice where it was found to be extensively metabolised to the equally active sulfone-based **2**. Both the parent compound and its active metabolite exhibited good plasma exposure, favorable half-life, moderate volume of distribution, low rate of clearance, and were well tolerated in mice at the maximum administered oral dose of 300 mg/kg. However, when compound **3** was evaluated for *in vivo* efficacy in an acute TB infection mouse model (BALB/c) at 100 and 200 mg/kg oral doses, it lacked activity. Further studies revealed that the 2-aminoquinazolinones killed *Mtb in vitro* via a glycerol-dependent mechanism of action, hence lacking *in vivo* efficacy in mice. These findings correlated well with the results of the studies on generation of spontaneous resistant mutants, wherein the strains resistant to **3** manifested mutations mapping to the glycerol metabolism genes that encode for glycerol kinase (*glpK*; Rv3696c) and glycerol-3-phosphate dehydrogenase (*glpD2*; Rv3302c).

Benzoxazole-based oxime analogues were designed from the hit compound **46** (**Figure 2**) by making structural modifications at three points of diversity (**SAR 1**, **SAR 2**, and **SAR 3**). As a result, 38 structural variants were synthesized and evaluated *in vitro* for their antimycobacterial activity against the drug-susceptible *Mtb* $H_{37}Rv$ strain. Unlike the 2-aminoquinazolinones, benzoxazole-based oximes exhibited a tight SAR, with only **SAR 2** modifications being tolerated. As such, all attempts to introduce changes at the **SAR 1** and **SAR 3** positions yielded inactive compounds (MIC_{99} > 125 µM). Moreover, even though **SAR 2** analogues were active, they exhibited flat SAR, which was informed by the display of similar antimycobacterial activities for analogues with different substituents at varying positions on the phenyl ring. Subsequently, most of the active compounds exhibited low *in vitro* cytotoxicity against the CHO cells. To this end, low microsomal metabolic stability [7.3% remaining after 30 minutes in MLM for **46**] posed a major hurdle to the advancement of

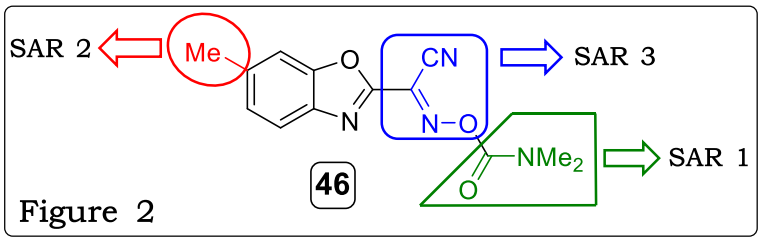

Figure 2

benzoxazole-based oximes to other studies as planned. The low metabolic stability was most likely due to the metabolically labile dimethyl carbamate moiety; however, all attempts to remove it by forming free oximes as well as oxime ethers resulted in complete loss of antimycobacterial activity.

All target compounds were subjected to physicochemical profiling and aqueous solubility studies, wherein the turbidimetric method was applied. The solubility values obtained were then correlated with melting points, HPLC retention times (t_R), TLC retardation factors (R_f), and cLogP, in order to establish structure-property relationships (SPR) across the two compound sets. Accordingly, correlations were deduced, and t_R [R^2 = 0.49 for AQZs and 0.65 for BZOs] and R_f [R^2 = 0.64 for AQZs and 0.57 for BZOs] were found to be the most strongly correlated factors, albeit moderate.

Further, compound **3** was selected for supramolecular derivatization studies in an effort to enhance its aqueous solubility, which involved formation of cocrystals, salts, and cyclodextrin inclusion complexes. The crystal structure of **3** was elucidated. This revealed the molecular geometry and the main intermolecular interactions in **3**, which facilitated the selection of potential co-formers for co-crystallization. However, all attempts to synthesize cocrystals were unsuccessful, as salts were formed instead. All the new solid states of **3** were characterized by X-ray diffraction, thermal analysis, NMR spectroscopy, and thereafter subjected to solubility assessment by HPLC. In effect, only a moderate increase in solubility was observed in the salts of **3**, whereby **3** mesylate exhibited the most improved solubility in the range of 2-fold increase (38 µM).

Largely, this thesis work identifies the opportunities and challenges associated with the two classes of compounds from the drug discovery perspective, as potential novel antituberculosis agents. Indeed, the importance of utilizing *in vitro* antimycobacterial phenotypic screening conditions in the early stages of drug discovery, which are reflective of the *in vivo* biological conditions during an active TB infection, is highlighted.

LIST OF ABBREVIATIONS AND SYMBOLS

Å	Angström
ºC	Degrees Celsius
µL	Microlitre
µM	Micromolar
µm	Micrometer
ACP	Acyl Carrier Protein
ADMET	Absorption, Distribution, Metabolism, Excretion and Toxicology
AIDS	Acquired Immune Deficiency Syndrome
AQZ	2-Aminoquinazolinone
ART	Antiretroviral Therapy
ARV	Antiretroviral
ASU	Asymmetric Unit
ATP	Adenosine-5'-triphosphate
AUC	Area Under the Curve
BCG	Bacillus Calmette-Guérin
BCS	Biopharmaceutical Classification System
BZO	Benzoxazole-Based Oxime
CD	Cyclodextrin
$CDCl_3$	Deuterated Chloroform
CFU	Colony Forming Unit
CHO	Chinese Hamster Ovarian (Cells)
Cl	Clearance
cLogP	Calculated Logarithm of n-octanol/water Partition Coefficient
CNS	Central Nervous System
CYP	Cytochrome P450
DC	Drug Candidate
DCG	Dry Co-Grinding
DCM	Dichloromethane
DIPEA	*N,N*-Diisopropylethylamine
DMF	*N,N*-Dimethylformamide
DMPK	Drug Metabolism and Pharmacokinetics

DMSO	Dimethylsulfoxide
DNA	Deoxyribonucleic Acid
DR	Drug Resistant
DS	Drug Susceptible/Sensitive
DSC	Differential Scanning Calorimetry
DST	Drug Sensitivity Test
EDCI	1-Ethyl-3-(3-Dimethylaminopropyl)Carbodiimide
EMB	Ethambutol
ESI	Electro-Spray Ionisation
EtOH	Ethanol
FDA	(United States) Food and Drug Administration
GAST-Fe	Glycerol-Alanine-Salts supplemented with Tween 80 and Iron
GFP	Green Fluorescent Protein
GRAS	Generally Regarded As Safe
HBA	Hydrogen Bond Acceptor
HBD	Hydrogen Bond Donor
hERG	Human Ether-à-*go-go*-Related Gene
HIV	Human Immunodeficiency Virus
HLM	Human Liver Microsomes
HPLC	High Performance Liquid Chromatography
HSM	Hot-Stage Microscopy
Hz	Hertz
IFN-γ	Gamma Interferon
IGRA	Interferon-Gamma Release Assay
INH	Isoniazid
IV	Intravenous
LAG	Liquid-Assisted Grinding
LC-MS	Liquid Chromatography coupled to Mass Spectrometry
LOD	Limit of Detection
LTBI	Latent Tuberculosis Infection
m.p.	Melting Point
m/z	Mass-to-Charge ratio
M:F	Male:Female ratio

MABA	Microplate Alamar Blue Assay
MDR	Multidrug Resistant
mg	Milligram
MHz	Megahertz
MIC	Minimum Inhibitory Concentration
Min	Minute
mL	Milliliter
MLM	Mouse Liver Microsomes
mM	Millimolar
Mtb	*Mycobacterium Tuberculosis*
MTC	*Mycobacterium Tuberculosis* Complex
MW	Microwave
Mwt	Molecular Weight
NAD	Nicotinamide-Adenine Dinucleotide
NADP	Nicotinamide-Adenine Dinucleotide Phosphate
NADPH	Nicotinamide-Adenine Dinucleotide Phosphate (reduced form)
NCE	New Chemical Entity
NIAID	National Institute for Allergy and Infectious Disease
NIH	National Institutes of Health
NITD	Novartis Institute for Tropical Diseases
NK	Natural Killer
NMR	Nuclear Magnetic Resonance (spectroscopy)
PBS	Phosphate-Buffered Saline
PI	Protease Inhibitor
PK	Pharmacokinetics
po	Per Oral (orally)
POA	Pyrazinoic Acid
PPB	Plasma Protein Binding
PXRD	Powder X-Ray Diffraction
PZA	Pyrazinamide
QD	Once Per Day
RB	Rotatable Bond
R_f	Retardation Factor

RIF	Rifampicin
RLM	Rat Liver Microsomes
RO5	Rule Of Five
RR	Rifampicin Resistant
SAR	Structure-Activity Relationship
SCXRD	Single Crystal X-Ray Diffraction
SDG	Sustainable Development Goal
SMILES	Simplified Molecular Input Line Entry System
S_NAr	Nucleophilic Aromatic Substitution
SPR	Structure-Property Relationship
STM	Streptomycin
TB	Tuberculosis
TB.D	Anti-Tuberculosis Drug
TDR	Total Drug Resistant
TEA	Triethylamine
TFA	Trifluoroacetic Acid
TGA	Thermogravimetric Analysis
TLC	Thin Layer Chromatography
TNF-α	Tumor Necrotic Factor-Alpha
tPSA	Topological Polar Surface Area
t_R	Retention Time
TST	Tuberculin Skin Test
Vd	Volume of Distribution
WGS	Whole Genome Sequencing
WHO	World Health Organization
XDR	Extensively Drug Resistant
XRD	X-Ray Diffraction

TABLE OF CONTENTS

LIST OF FIGURES

Page

LIST OF SCHEMES

Page

LIST OF TABLES

PUBLICATIONS, CONFERENCES AND TRAINING COURSES

Paul M. Njaria, John Okombo, Nicholas M. Njuguna and Kelly Chibale. Chloroquine-containing compounds: a patent review (2010 – 2014). *Expert Opinion on Therapeutic Patents*. **2015**, 25(9): 1003–1024.

Novartis Next Generation Scientist Program (NGS) (1st June – 31st August 2016). Novartis Pharma AG, Basel, Switzerland. Next Generation Scientist Research Day, 29th August 2016. Poster Presentation: *Quality by Design (QbD) Strategies in Formulation Development*.

The 3rd H3D Symposium (15th – 18th November 2016) held at Goudini Spa, Cape Town, South Africa. Poster Presentation: *Structure-Antimycobacterial Activity Studies of 2-Aminoquinazolinones*.

Tuberculosis Drug Discovery and Development: Gordon Research Seminar (GRS) (24th – 25th June 2017) and Gordon Research Conference (GRC) (25th – 30th June 2017). Renaissance Tuscany Il Ciocco, Lucca (Barga), Italy. Poster Presentation: *Antimycobacterial 2-Aminoquinazolinones: Synthesis and Biological Evaluation*.

CHAPTER 1

INTRODUCTION AND LITERATURE REVIEW

1.1 Chapter Overview

In this chapter, a brief overview of tuberculosis (TB) and its treatment is provided. TB is highlighted with respect to etiology, epidemiology and pathogenesis; prevention, control and treatment; challenges in treating TB and their mitigation; as well as advances made in anti-TB drug discovery and development. In addition, attrition of drug candidates and the importance of optimizing physicochemical properties of compounds in the early stages of drug discovery are examined. Importantly, aqueous solubility of drug candidates is emphasized, and therefore its importance and strategies to improving the same are brought to the fore. Also, benzoheterocyclic structural motifs that form the basis of this thesis work as potential scaffolds for new anti-TB agents are reviewed and discussed. To sum up the chapter, a research program is examined, whereby study justifications, hypothesis, along with study objectives are briefly mentioned.

1.2 Etiology of TB

TB, a contagious airborne disease, is caused by the bacterium *Mycobacterium tuberculosis* (*Mtb*). *Mtb* is an oblong, rod-shaped, bacillus-type, non-motile, non-sporulating, acid-fast, slow-growing, and aerobic bacterium that measures about 1–4 µm in length and 0.3–0.6 µm wide (**Figure 1.1**).[1,2]

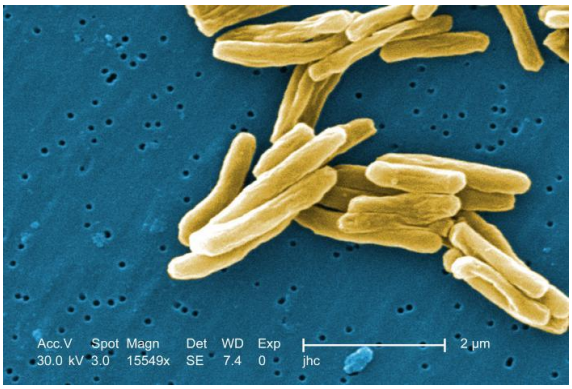

Figure 1.1: Scanning electron micrograph of *Mycobacterium tuberculosis*.[2]

On March 24, 1882, a German scientist, Robert Koch, announced the discovery of *Mtb* as the causative agent of TB.[3,4] *Mtb* is a member of the *Mycobacterium tuberculosis* complex (MTC), which is characterized by extensive conservation of the 16S ribosomal deoxyribonucleic acid (rDNA) sequence, 99.9% similarity at the nucleotide level, as well as high DNA-DNA relatedness across the member species.[5] Other members of the MTC include *Mycobacterium africanum* and *Mycobacterium canettii*, which are also human pathogens; *Mycobacterium microti*, a rodent pathogen; and *Mycobacterium bovis*, which is a pathogen with a wide spectrum of hosts.[6] For a long time, *Mtb* was believed to have evolved from the present-day *M. bovis*; however, genomic studies have provided compelling evidence against this hypothesis. Indeed, it has been shown that the two species could have independently evolved from an *Mtb*-like common ancestral species, more than 15 000 years ago.[6–8] Furthermore, the availability of complete *Mtb* genome sequence, as well as the technological advances in the field of genomics, have provided invaluable insights into the evolution and biology of *Mtb*.[9] *M. bovis* causes zoonotic TB in humans mainly through consumption of unpasteurized dairy products. Consequently, in 2015, there were an estimated 149 000 cases of zoonotic TB globally.[10] Also, there are no known animal or environmental reservoirs for *Mtb*, making it an obligate human pathogen.[11]

Mtb is characterized by vast virulence factors that are incorporated in proteins and cell wall components. The *Mtb* cell wall is a distinctive, highly evolved, lipid-, protein-, and carbohydrate-based structure essential for its survival. It is composed of peptidoglycans linked to mycolic acids via covalent attachments to linear galactofurans and several strands of highly branched arabinofuran.[12] In addition, arabinogalactan and lipoarabinomannan are abundantly present in the *Mtb* cell wall. Indeed, their presence has been reported by Lee and colleagues in a study involving high-resolution magic-angle spinning (HR-MAS) nuclear magnetic resonance (NMR) on live mycobacterial cells.[13] The waxy nature of the cell wall is due to mycolic acids, which are critical in *Mtb* survival by conferring properties such as acid-fastness, hydrophobicity, resistance to changes in pH, and

immunostimulatory attributes.[12,14]

1.3 Epidemiology of TB

Although curable, TB continues to be a weighty public health scourge of epidemic proportions with high morbidity and mortality globally, particularly in low- and middle-income countries. Even in recent times, TB has failed to relinquish its grip on mankind, and it can still be considered a "Captain Among these Men of Death", an epithet it earned in the early 19th century.[4] It is a social disease roughly estimated to have infected a third of the world's population, with majority having latent TB infection (LTBI). In the absence of treatment, approximately 50% of individuals who develop active TB disease will succumb to it.[15] One of the goals of the United Nations' Sustainable Development Goals (SDGs) for 2030 is to end the global TB epidemic. As a result, the World Health Organization (WHO) End TB Strategy (2016–2035) targets reducing TB deaths and incidence by 90% and 80%, respectively, by the year 2030, compared to 2015.[16] For these goals to be achieved, a 4–5% annual worldwide decline in TB incidence is targeted by the year 2020. This comprehensive approach is anchored on three pillars: patient-centered TB care and prevention; bold policies and supportive systems; and intensified research and innovation.[16]

The WHO global TB report, 2016, provides figures that demonstrate the global burden of TB in terms of incidence, prevalence, and mortality. The data is derived from comprehensive reports received from 202 countries and territories that account for > 99% of the world's population and TB cases. In 2015, the incidence of TB was estimated to be 10.4 million cases worldwide, signifying a 1.5% decline from that reported for 2014.[10] Of these cases, 60% occurred in six countries: India, Indonesia, China, Nigeria, Pakistan, and South Africa, listed in the order of decreasing incidence (**Figure 1.2**). Overall, adults contributed to 90% of new cases while 10% were children, and the male:female (M:F) ratio was 1.6:1. In addition, an estimated 11% of incident TB cases in 2015 were Human Immunodeficiency Virus (HIV)-linked, a proportion that was highest in Africa, and exceeded 50% in some

parts of southern Africa. It is also estimated that there were 1.4 million TB deaths in 2015 (**Figure 1.3**), and an additional 0.4 million deaths resulting from TB disease among HIV/AIDS (Acquired Immune Deficiency Syndrome) patients.[10] These sobering statistics suggest that in 2015, about three human lives were exterminated every minute by TB.

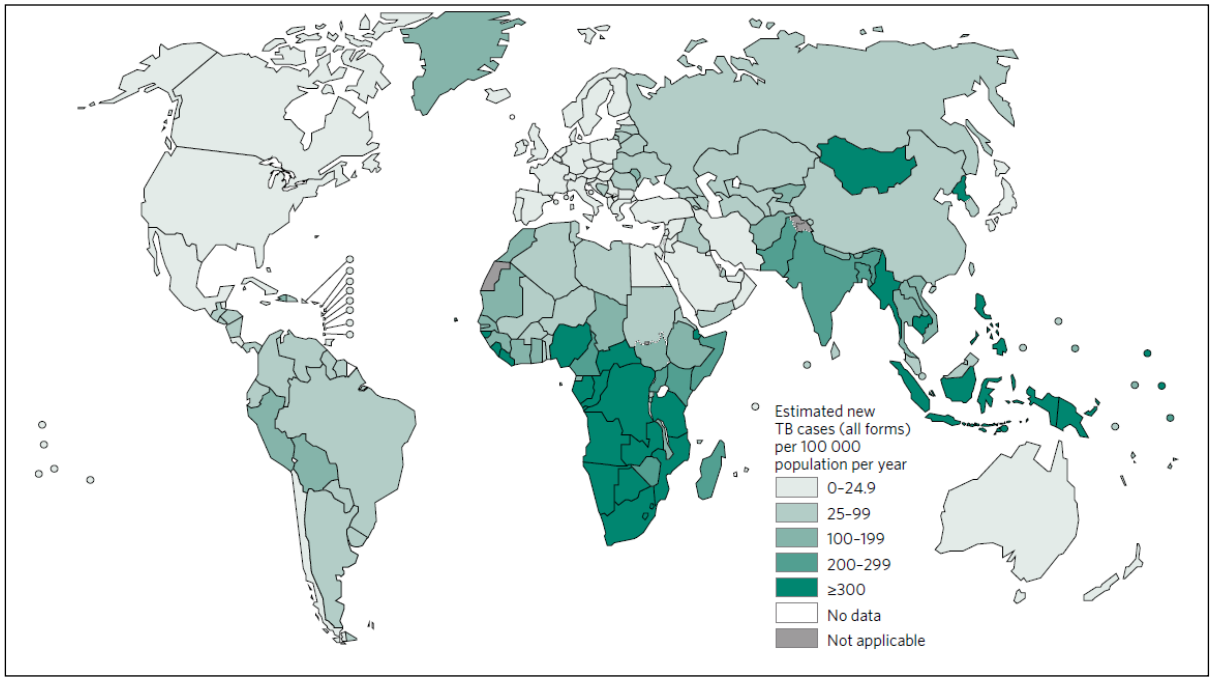

Figure 1.2: Estimated global TB incidence rates in 2015.[10]

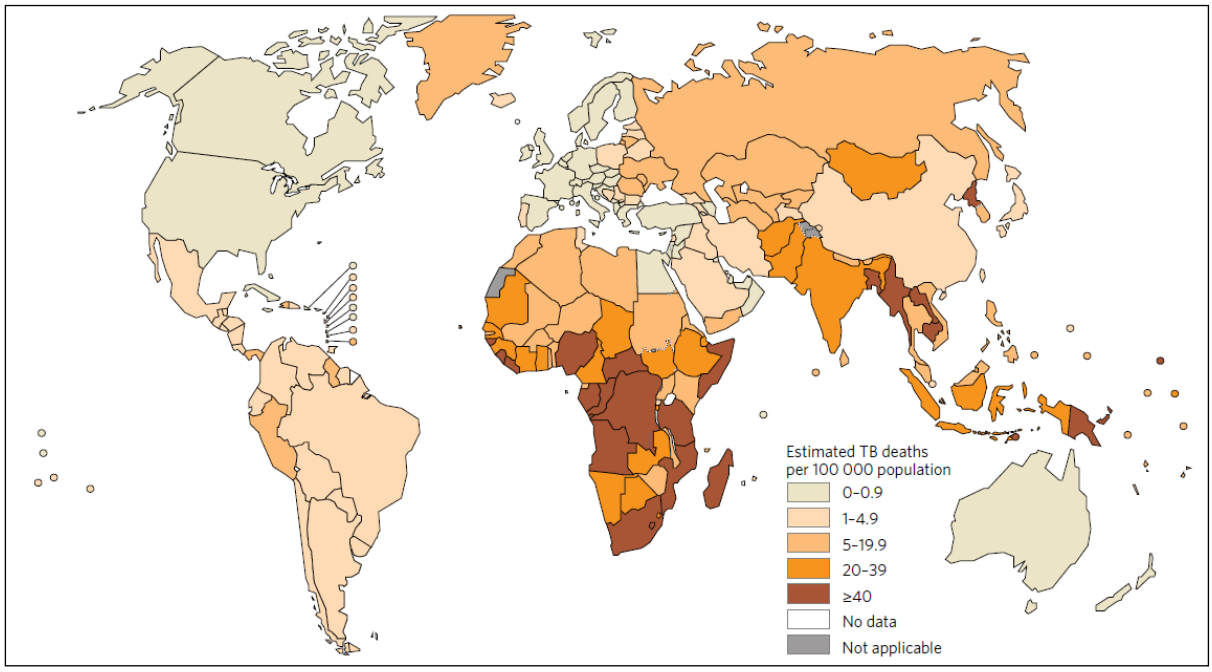

Figure 1.3: Estimated TB mortality rates in HIV-negative people in 2015.[10]

Globally, HIV is a major risk factor for TB infection, mainly due to a compromised body immunity. HIV not only increases the risk of reactivating LTBI, but also readily accelerates progression to active disease soon after primary infection or reinfection with *Mtb*.[17,18] Equally important, as a co-epidemic, TB is a major cause of mortality and morbidity among HIV-positive patients, and therefore poses a risk throughout the course of HIV/AIDS.[19] Indeed, the estimated TB deaths in 2015 were 0.20 million among HIV-positive men, 0.14 million among HIV-positive women, and 0.04 million among HIV-positive children.[10] 75% of these deaths occurred in Africa, with a M:F ratio close to 1. Globally, 15% of TB patients with a HIV test result were HIV-positive. Overall, the percentage of TB patients testing HIV-positive has been falling globally since 2008.[10]

Considering the fact that HIV-infected people make up only 0.5% of the world's population, then other endogenous and exogenous risk factors for TB infection come into play.[20] These include other diseases, socioeconomic factors, as well as behavioral determinants. For instance, diabetes mellitus,[21] malnutrition, excessive alcohol use,[22] tobacco smoking,[23] air pollution, and use of immunosuppressive drugs. Moreover, increased household crowding, poor nutrition, and homelessness brought about by poverty, greatly accentuate the incidence and transmission of TB.[20]

Worldwide, drug-resistant TB (DR-TB) is a major drawback in the treatment of TB. In 2015, there were an estimated 480 000 new cases of multidrug-resistant TB (MDR-TB) and an additional 100 000 people with rifampicin-resistant TB (RR-TB), globally. India, China, and the Russian Federation accounted for 45% of these cases. Of the estimated 580 000 people newly eligible for MDR-TB treatment, only 125 000 (20%) were enrolled. The average proportion of MDR-TB cases with extensively drug-resistant TB (XDR-TB) was 9.5%. Globally, the latest treatment outcome data show a treatment success rate of 83% for TB (2014), 52% for MDR-TB (2013) and 28% for XDR-TB (2013). There were about 250 000 deaths from MDR/RR-TB in 2015.[10]

1.4 Transmission, Pathogenesis and Clinical Presentation of TB

TB most commonly affects the respiratory system, a condition referred to as pulmonary or lung TB. Pulmonary TB is acquired through inhalation of airborne, aerosolized *Mtb*-containing droplet nuclei, which are expectorated from an infected individual with active pulmonary or laryngeal TB through coughing, spitting, or sneezing.[24] *Mtb* in aerosols are airborne and viable for several hours in the atmosphere, and the infectious dose is estimated to be a single bacterium.[7,25] Additionally, there are cases of extrapulmonary TB that can cause disease in other body organs, for instance the central nervous system (CNS), genitourinary tract, bones, joints, as well as disseminated or miliary TB that affects many organs.[26,27]

Pulmonary TB exists in a dynamic spectrum: an active, symptomatic disease; or an asymptomatic, non-transmissible LTBI, in which *Mtb* are contained by persistent immune responses.[28,29] After inhalation, a cascade of events follows in a bid to clear *Mtb* from the host's airways. In this regard, the mucociliary system in the upper respiratory tract offers the initial physical defense, whereby the *Mtb* bacilli are trapped by mucus, which is then driven up the airways by cilia.[26] The pathogens that survive this barrier translocate down the airways to the alveoli. Afterwards, a local infection might set up, followed by propagation to draining lymphatics, as well as hematogenous spread throughout the body. Biochemical products of *Mtb* such as the mannosylated lipoarabinomannan, trehalose dimycolate, and N-glycolylmuramyl dipeptide, facilitate recognition of *Mtb* by the alveolar macrophages – the main phagocytic cells infected by *Mtb*.[30] Consequently, *Mtb* are engulfed by the alveolar macrophages via receptor-mediated phagocytosis, triggering a sequence of innate host-pathogen immune responses. This has been studied using small mammals, such as mice, guinea pigs and rabbits, as well as non-human primates that have substantially helped to experimentally identify the momentousness of the early immunopathological phenomena during TB infection.[31]

The host's immune response serves to limit multiplication and spread of the

tubercle bacilli, as well as to provide an opportunity for the body to destroy the invading mycobacteria and prevent infection. Nonetheless, to ensure its survival, *Mtb* employs diverse evasion strategies including blocking the fusion of phagosome with lysosome, delaying phagosome maturation, detoxifying reactive oxygen and nitrogen radicals, and releasing potent bioactive cell wall contents.[32,33] The innate immune responses lead to elimination or persistence of the pathogen.

Phagocytosis by the alveolar macrophages induce a localized proinflammatory response, leading to recruitment of immune cells such as neutrophils, natural killer (NK) T cells, $CD4^+$ T cells, and $CD8^+$ T cells. This process is influenced by the inflammatory cytokines and chemokines produced by the infected macrophages. Tumour necrosis factor (TNF)-α is the dominant cytokine, while chemokines include CCL2, CXCL10, CCL3, 4, 5, and CXCL9. In addition, the inflammatory process is regulated and quietened by gamma interferon (IFN-γ). At this stage, the immunopathogenesis culminates in the formation of a structure consisting of infected macrophages, foamy macrophages, mononuclear phagocytes, lymphocytes, and a fibrous cuff of collagen (**Figure 1.4**).[1,7,26,31,34] This mass of cellular debris is known as the granuloma, the hallmark of TB, which leads to remodeling of the infection site and containment of *Mtb* in a quiescent and latent state. Granuloma formation is valuable to both the host, for control of infection, and the bacilli, as a place to hide.[35]

Primary infection is uncommon, but may occur in neonates. Globally, reactivation and disease progression causes majority of TB infections, with 5–10% of individuals with LTBI developing symptomatic, clinical TB infection in their lifetime.[36] Conditions such as old age, malnutrition, stress, or co-infection with HIV, which reduce the number and impair the function of $CD4^+$ T cells, disrupt the containment of *Mtb* in LTBI. Such a change in immune status causes necrosis and caseation of the granulomas, followed by their rupture and spillage of thousands of infectious bacilli into the airways, and a productive cough ensues. The cough facilitates the spread and transmission of *Mtb* via aerosolized droplet nuclei. A summary of the

Mtb transmission and immunopathogenetic continuum of pulmonary TB is depicted in **Figure 1.4** below.

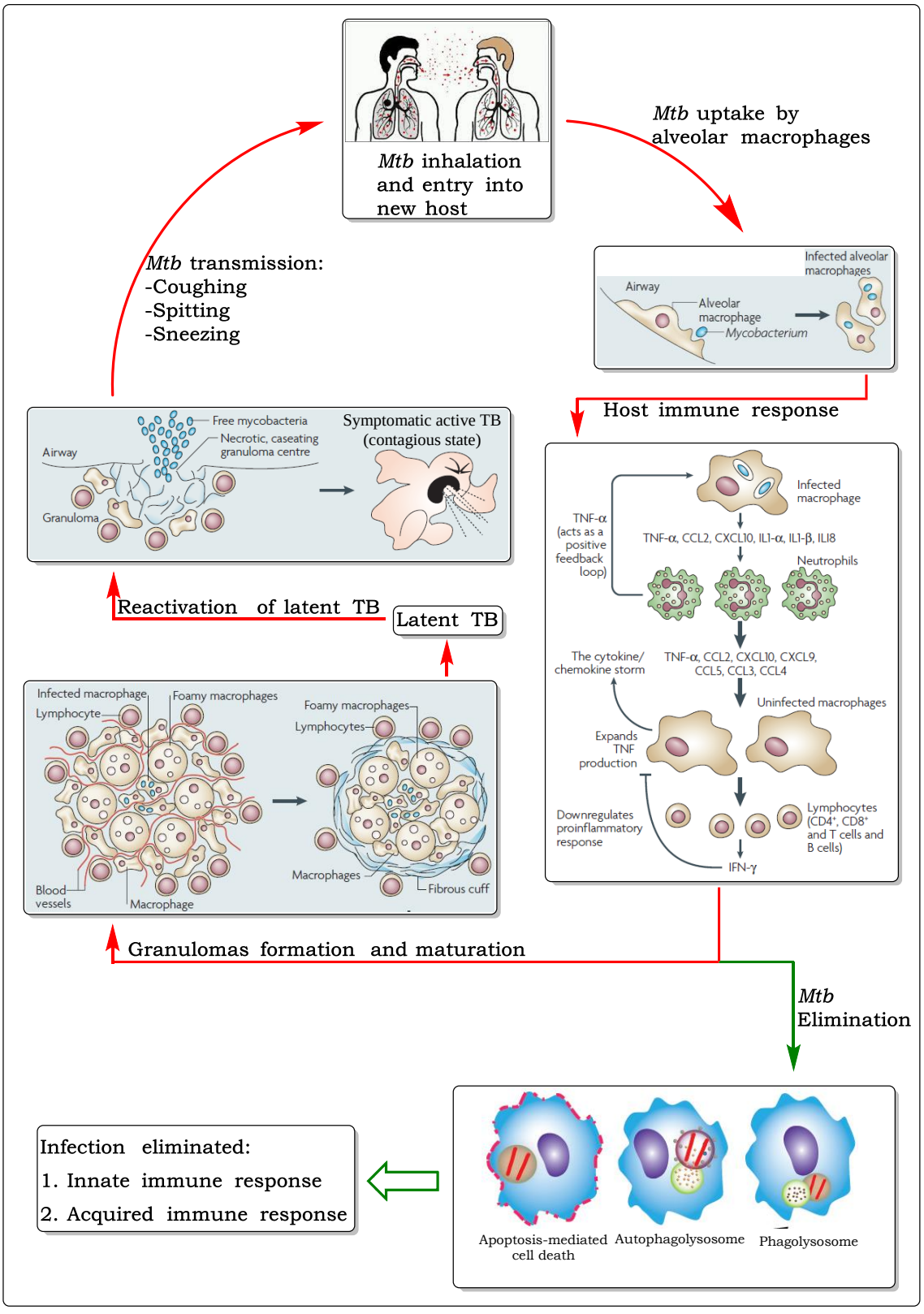

Figure 1.4: Diagrammatic representation of the transmission and immunopathogenetic continuum of pulmonary TB.[7,33,34]

Individuals with active TB present with symptoms such as fever, night sweats, chills, weight loss, persistent cough, and hemoptysis. However, some patients with active, culture-positive TB may be asymptomatic, and are principally reported as having subclinical TB.[29] People who have LTBI neither feel sick, nor have any symptoms, and cannot spread TB to others. Symptoms of extrapulmonary TB vary considerably depending on the site of infection.[27]

Diagnosis of active pulmonary TB can be culture-based or molecular-based. Accurate diagnosis of latent and active TB, as well as detection of drug resistance are highly important in the effective management and prevention of TB. Diagnosis involves clinical assessment, sputum smear microscopy, TB cultures, and chest X-ray radiography. Additionally, the Tuberculin Skin Test (TST) is the gold standard for diagnosis of LTBI. However, these diagnostic techniques have limited capabilities, and hence technological advances in newer diagnostic methods have been ongoing. For instance, Nucleic Acid Amplification (NAA) for diagnosis of active TB, and T-Cell-based *in vitro* assays that detect IFN-γ for diagnosis of LTBI, have been developed.[37]

1.5 Prevention, Control and Treatment of TB

1.5.1 Prevention of TB

Prevention of TB entails pivotal strategies aimed at stopping the spread of *Mtb*. For example identifying and treating the infected;[38] preventing reactivation of LTBI by early diagnosis and chemoprophylaxis, particularly in individuals at high risk of disease progression; reducing the spread of DR-TB;[39] tracing of contacts for screening, treatment and monitoring;[40,41] isolating and treating patients with active TB until such a time they become noninfectious;[42] efficient management of outbreaks; as well as educating the general public on TB in efforts to reduce stigma and improve treatment compliance.[43] Furthermore, control, management, and minimization of risk factors for TB infection such as HIV, are essential in the overall TB prevention strategy.[44–46] It is also advisable for health care workers to use personal protective equipment.[47,48] Also, pasteurization of milk and proper

cooking of beef are important in preventing zoonotic TB in humans.[49,50]

Vaccination plays a key role in protecting infants and children below 16 years against TB infection.[51] The only TB vaccine currently available is the Bacillus Calmette-Guérin (BCG). In 2015, 163 countries reported providing BCG vaccination as a standard part of childhood immunization programmes.[10] This vaccine is critical in preventing fatal meningitis TB in infants and schoolchildren. However, its efficacy against pulmonary TB in children is estimated to be about 50%.[52,53] Nonetheless, at least 13 vaccine candidates are currently in clinical development. A tremendous effort is being made to design new vaccines in such a way that they are effective in adolescents and adults, because pulmonary TB is mostly spread by these age groups.[33,54]

1.5.2 TB Chemotherapy

1.5.2.1 Treatment of Drug-Susceptible TB (DS-TB)

It is estimated that 80% of all patients diagnosed with active TB disease are infected with fully drug-susceptible (DS) *Mtb* strains while the remaining 20% are infected with drug-resistant strains.[55] According to the TB treatment guidelines published by the WHO, drugs for treatment of DS-TB are classified as first-line, based on their efficacy, experience of use, safety and pharmacological class. They were previously categorized as Group 1 category in the old 5-group system. However, this classification has been reviewed, and it classifies only the second-line drugs used in the treatment of DR-TB.[56,57] First-line oral anti-TB agents include isoniazid (INH), rifampicin (RIF), ethambutol (EMB), pyrazinamide (PZA), rifabutin (RFB), and rifapentine (RPT). **Figure 1.5** shows the chemical structures of the above-mentioned drugs.

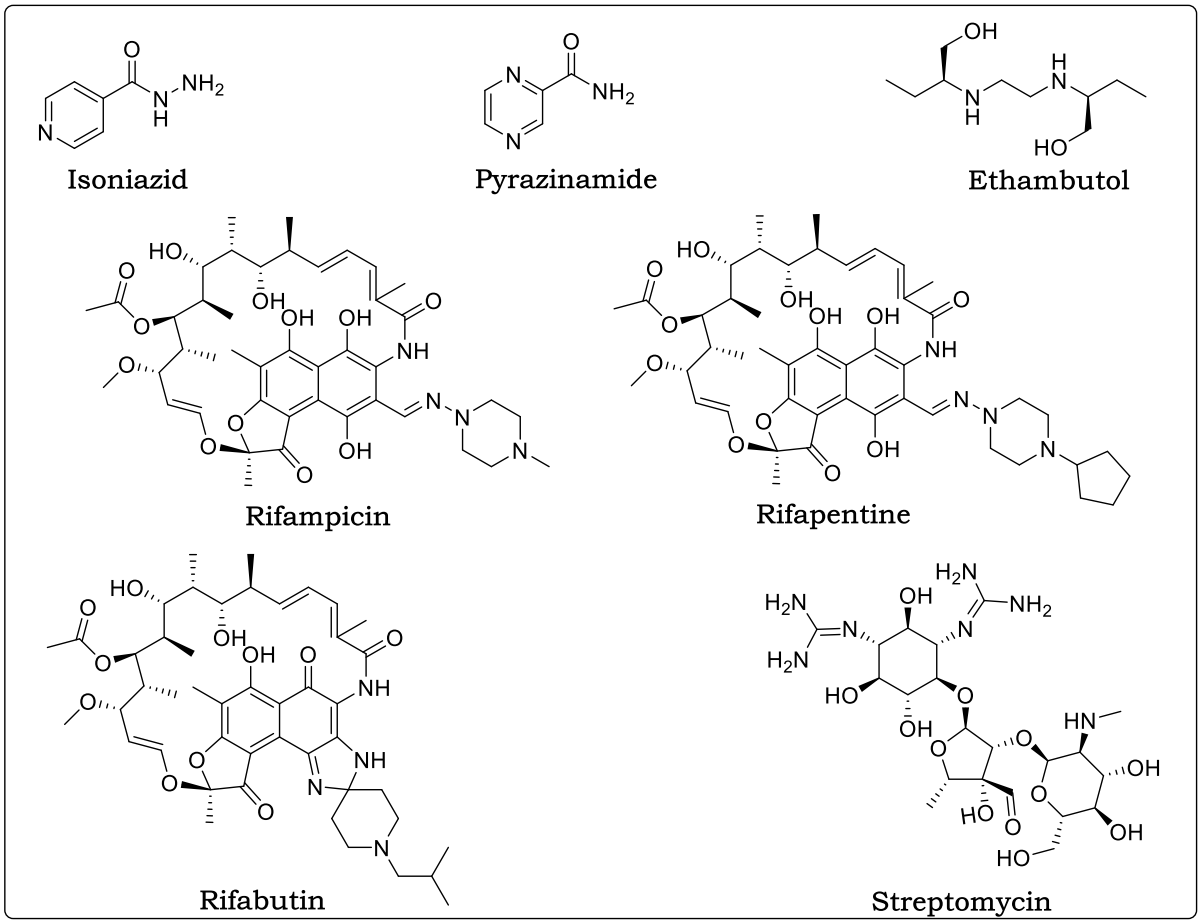

Figure 1.5: Chemical structures of the first-line anti-TB drugs.

Streptomycin (STM) is administered parenterally, and is considered a first-line agent due to high rates (> 50% in some countries) of streptomycin resistance in strains of MDR-TB.[56] Although the first-line drugs have been shown to be the most potent and well tolerated, it is strongly recommended that their clinical use be based on laboratory and clinical evidence of their effectiveness, especially through drug-sensitivity tests (DST).[58]

Optimal treatment of DS-TB and prevention of drug resistance involve the use of anti-TB drugs in combinations, which are based on regimen guidelines provided by the WHO. For example, new patients with active pulmonary TB are treated with a standard therapy containing rifampicin for a minimum of 6 months: 2 months intensive phase with INH, RIF, PZA, and EMB, followed by a 4 months continuation phase of INH and RIF. The treatment guidelines also prescribe the dosages and frequency of administration, preferably through the directly observed therapy-short

course (DOTS) – a strategy endorsed by the WHO to promote optimal adherence and treatment success.[59,60] In addition, it is recommended that the drugs be formulated as fixed dose combinations (FDCs) to reduce the pill burden and therefore promote compliance.[61–64] Also, a significant proportion of patients have been reported to develop toxicity to these drugs, ranging from mild to severe adverse events. Thus, it is important to monitor patients for adverse events such as severe hepatitis, immune thrombocytopaenia, agranulocytosis, haemolysis, renal failure, optic neuritis, and ototoxicity, which may cause severe morbidity and compromise TB therapy.[65–68] Equally important, as a follow-up support, repeat sputum smears, cultures and chest X-rays are recommended and used as indicators of treatment efficacy and progress. Where possible and cost notwithstanding, therapeutic drug monitoring (TDM) should be conducted to provide information that may facilitate dosing decisions.[69]

Isoniazid was first synthesized in 1912 and later introduced as an anti-TB drug in 1952.[70] It is a prodrug with a complex mode of action that is believed to proceed via production of various highly reactive compounds targeting multiple *Mtb* enzymes. Indeed, several studies have revealed that mutations in about 117 *Mtb* enzymes, which influence metabolic pathways and cell wall biosynthesis, could be associated with INH resistance.[71] INH is activated by the catalase-peroxidase (KatG) and $MnCl_2$ to form an isonicotinoyl radical or anion, which then reacts with nicotinamide-adenine dinucleotide (NAD^+) and nicotinamide-adenine dinucleotide phosphate ($NADP^+$), to generate INH-NAD(P) adducts. The INH-NAD complex inhibits the enoyl-acyl carrier protein (ACP)-reductase enzyme (inhA), while INH-NADP is an inhibitor of dihydrofolate reductase (dfrA) and 3-oxoacyl-ACP reductase.[72–77] INH mainly kills the actively replicating *Mtb*. Strains of *Mtb* resistant to INH have been reported, and the genes responsible for their resistance identified. Most INH-resistant strains have mutations in *katG* and *inhA* genes. In this regard, S315T is a specific *katG* variant found in 94% of INH-resistant clinical isolates.[78] Moreover, there are many other genes associated with INH resistance. For instance, in a study conducted by

Shekar *et al.*, 60 genes responsible for INH resistance were identified, including *katG*, *inhA*, *ahpC*, *kasA*, and *NDH*. Equally important, their functions were pinpointed to functions in the *Mtb*'s cell wall, metabolism, and respiration.[79]

Rifampicin is a rifamycin derivative that was introduced for TB treatment in 1972.[80] It strongly binds and selectively inhibits bacterial DNA-dependent ribonucleic acid (RNA) polymerase, thus interfering with DNA transcription.[81] *Mtb* resistance to RIF is mainly mediated by mutations in the *rpoB* gene, which lead to changes in the structure of the RNA polymerase β-subunit.[82–84] Rifabutin and rifapentine are rifamycins with similar chemistry and microbiological profiles as rifampicin. Rifabutin is routinely used in the treatment of active TB in HIV-positive patients receiving protease inhibitors, whereas rifapentine is a long-acting rifamycin used in some countries for treatment of LTBI and active TB.[56] There have been reports of *Mtb* cross-resistance across rifamycins.[85]

Pyrazinamide was introduced in the early 1950's as an important sterilizing prodrug, which contributes to TB treatment shortening due to its high efficacy on the persister *Mtb* bacilli.[86] The exact mechanism of action for PZA remains unknown. It has previously been reported that PZA requires acidic conditions for its activation, whereby nicotinamidase/pyrazinamidase converts pyrazinamide into its active form, pyrazinoic acid (POA), which disrupts membrane energetics leading to inhibition of membrane transport.[86] Also, it has been reported that POA binds to the ribosomal protein S1 (RpsA) leading to inhibition of protein translation, as well as the ribosome-sparing process of trans-translation, a mechanism that could explain the sterilizing action of PZA.[87] However, both mechanisms of action have since been debunked, further complicating the understanding of the PZA mode of action.[88–89] Pyrazinamide-resistant *Mtb* strains lose pyrazinamidase activity due to mutations in the *pncA* gene.[90–91]

Ethambutol was introduced for treatment of TB in 1966. Its site of action is on the cell wall where it inhibits the biosynthesis and polymerization of

arabinan by targeting the arabinosyltransferase enzyme. This leads to accumulation of mycolic acids with eventual *Mtb* cell death.[92–94] Resistance of *Mtb* to EMB is mainly attributed to mutations in the *embB* gene.[95]

Streptomycin is a natural product discovered in 1944, and was the first antibiotic to be used successfully to treat TB.[96] It is an aminoglycoside that inhibits protein synthesis by binding the ribosomal 30S subunit at the ribosomal protein S12 and the 16S rRNA.[97] Resistance to streptomycin occurs due to mutations on this target as well as by enzymatic inactivation of the drug. Indeed, 60–70% of streptomycin-resistant *Mtb* strains have mutations in the *rpsL* and *rrs* genes, which encode for the S12 and 16S rRNA, respectively.[98]

The regimen of the first-line drugs used to treat DS pulmonary TB is also applicable for treating majority of the extrapulmonary TB cases, except TB of the central nervous system, bone, and joint, where longer therapy regimens are recommended.[59,99] For example, the treatment of TB meningitis lasts 9–12 months due to the high risk of disability, while treating TB of the bones takes a minimum of 9 months due to difficulties in monitoring treatment success.

The WHO recommends that all HIV-positive individuals with active TB disease, irrespective of their $CD4^+$ T cell count, should start antiretroviral therapy (ART) within the first 2 months of TB treatment. Nonetheless, there are two main challenges experienced when initiating ART during TB treatment: drug-drug interactions and immune reconstitution inflammatory syndrome (IRIS). Consequently, the scientific debate has been about when is the best time to start ART: early or delayed initiation? There is strong evidence from various studies, systematic reviews, and meta-analyses that ART initiation ought to be based on $CD4^+$ T cell count. The general recommendation is to delay ART in HIV-positive patients who have $CD4^+$ T cell counts > 220 per µL until after 6 months of TB treatment. Conversely, it has been found beneficial to initiate ART early enough during TB treatment of HIV-positive patients with $CD4^+$ T cell counts < 50 per µL.[100–104]

1.5.2.2 Treatment of Latent Tuberculosis Infection (LTBI)

LTBI is defined as an asymptomatic state of persistent cellular immune responses, particularly mycobacteria-specific T-cell responses to stimulation by the *Mtb* antigens without clinical evidence of active TB.[105] Individuals with LTBI are at a significant risk of developing active TB, and therefore, treatment should be initiated in high risk individuals to prevent its reactivation and progression. In 2015, the WHO published guidelines for testing and treating LTBI, with an emphasis on evidence-based practices. It is highly recommended to initiate testing and treatment of LTBI in high risk individuals such as HIV-positive patients, contacts of pulmonary TB cases, patients initiating anti-TNF treatment, patients on dialysis, patients preparing for transplantation, and patients with silicosis. Additionally, prisoners, health care workers, immigrants from high TB burden countries, homeless persons, and illicit drug users, may be considered for LTBI testing and treatment.[106]

The WHO prescribes either the interferon-gamma release assays (IGRA) or the Mantoux TST for LTBI testing. Although the IGRA test can distinguish between BCG-induced and *Mtb* infection-induced positive TST results,[107] the WHO recommends that IGRA should not replace TST in low-income countries. Both tests are hampered by the lack of ability to accurately distinguish between either LTBI and active TB, or new infections and re-infections; low predictive values for disease progression; as well as low sensitivity, especially in immunocompromised populations.[108]

The regimen options recommended for the treatment of LTBI are: 6–9 months of isoniazid, or 3 months of weekly rifapentine plus isoniazid, or 3–4 months of isoniazid plus rifampicin, or 3–4 months of rifampicin alone.[106,109] Although the 9 months INH therapy has > 90% efficacy, it is unfortunately seriously hampered by adverse events, including hepatotoxicity.[110] Consequently, it is important that patients are regularly monitored, and the risks and benefits of treatment carefully balanced for each individual.[111]

1.5.2.3 Treatment of Drug-Resistant TB (DR-TB)

First-line drugs have been instrumental in the successful treatment and prevention of TB over the years they have been in existence. However, this success has been under far-reaching threat by the emergence of DR-TB. Cases of DR-TB can be classified into categories that are not mutually exclusive: 1. Mono-resistant TB is resistant to one first-line anti-TB drug only; 2. Poly-resistant TB is resistant to more than one first-line anti-TB drug, other than both isoniazid and rifampicin; 3. MDR-TB is resistant to at least both isoniazid and rifampicin; 4. XDR-TB causes more severe disease manifestation and is defined as MDR-TB with additional resistance to any fluoroquinolone, and at least one of the three second-line injectable drugs (capreomycin, kanamycin, and amikacin); 4. Rifampicin resistant TB (RR-TB) is resistant to rifampicin, with or without resistance to other anti-TB drugs;[56] 5. Totally drug-resistant TB (TDR-TB) or extremely drug resistant TB is resistant to all first- and second-line anti-TB drugs.[112] For example, in a recent study conducted by Dheda and colleagues at the University of Cape Town regarding the programmatically incurable TB patients, 56% of isolates from patients with treatment failure were resistant to eight or more drugs.[113]

Phenotypic, culture- and molecular-based methods are available for detection of DR-TB. Importantly, increased rollout and use of Xpert® MTB/RIF in many settings as a diagnostic tool for active TB has led to an upsurge in detection of MDR-TB, as well as improving the universal drug-susceptibility testing.[114–116] This nucleic acid amplification-based tool produces results in less than 2 hours leading to greatly enhanced efficiency in initiation of treatment.[117,118] Other diagnostic methods recommended by the WHO include loop-mediated isothermal amplification (TB-LAMP) and molecular line probe assays for rapid screening of patients at risk of MDR-TB.[119,120] Moreover, several new diagnostic tools are in the development pipeline, with priority being to develop a rapid, low-cost, non-sputum-based test for use at the primary health care level.[121]

Because developing new anti-TB drugs is a lengthy, expensive, and an

uncertain process, treatment of DR-TB is achieved by applying strategies such as the use of existing anti-TB drugs that were previously not widely prescribed; repurposing of existing drugs; as well as the use of current anti-TB drugs in high doses. Consequently, the WHO in its 2016 update on the DR-TB treatment guidelines, approved a hierarchical classification of second-line anti-TB drugs into four groups as shown in **Table 1.1**. The role of this classification is to guide clinicians when deciding and designing treatment regimens for MDR-TB and XDR-TB. Compared to the first-line anti-TB drugs, these agents are usually less effective, more expensive, and more often associated with toxicity risks, therefore calling for close monitoring of key adverse events during their use.[57,122]

Table 1.1: Classification of medicines recommended for the treatment of DR-TB.[33,57,122]

Group	Drugs	Mechanism of Action	Key Adverse Events
Group A (Fluoroquinolones)	Levofloxacin (Lfx) Moxifloxacin (Mfx) Gatifloxacin (Gfx)	Inhibition of DNA gyrase	• QT interval prolongation (Cardiotoxicity)
Group B (Second-line injectable agents)	Amikacin (Am) Capreomycin (Cm) Kanamycin (Km) Streptomycin (STM)[a]	Inhibition of protein synthesis	• Nephrotoxicity • Ototoxicity • Electrolyte derangement
Group C (Other core second-line agents)	Ethionamide (Eto) Prothionamide (Pto) Cycloserine (Cs) Terizidone (Trd) Linezolid (Lzd) Clofazimine (Cfz)	• Inhibition of cell wall synthesis (Eto & Pto) • Inhibition of protein synthesis (All others)	• Nausea and vomiting (all) • Hypothyroidism (all) • CNS effects, including psychosis, confusion and depression (terizidone and cycloserine) • Peripheral neuropathy (linezolid) • Myelosuppression (linezolid) • Ocular toxicity (linezolid) • QT interval prolongation (clofazimine) • Skin and conjunctival pigmentation (clofazimine)
Group D1 (Add-on agents (not part of the core MDR-TB regimen)	Pyrazinamide (PZA) Ethambutol (EMB) High-dose isoniazid (INH^h)	• Disruption of plasma membranes (PZA) • Inhibition of cell wall synthesis (EMB) • Inhibition of mycolic acid synthesis (INH)	• Hepatotoxicity (PZA) • Gout (PZA) • Ocular toxicity (EMB) • Hepatotoxicity (INH) • Peripheral neuropathy (INH) • CNS toxicity (INH)

Table 1.1: Classification of medicines recommended for the treatment of DR-TB.[33,57,122]

Group	Drugs	Mechanism of Action	Key Adverse Events
Group D2	Bedaquiline (Bdq) Delamanid (Dlm)	• Inhibition of mitochondrial ATP synthase (Bdq) • Inhibition of mycolic acid synthesis (Dlm)	<u>Bdq</u> • QT interval prolongation • Arthralgia • Hepatitis • Headache <u>Dlm</u> • Nausea • Vomiting • Dizziness • QT interval prolongation
Group D3	• Para (*p*)-aminosalicylic acid (PAS) • Imipenem–cilastatin (Ipm) • Meropenem (Mpm) • Amoxicillin-clavulanate (Amx-Clv) • Thioacetazone (T)[b]	• Inhibition of DNA precursor Synthesis (PAS) • Inhibition of peptidoglycan synthesis (Ipm, Mpm, or Amx-Clv) • Inhibition of mycolic acid synthesis (T)	<u>PAS</u> • Gastrointestinal toxicity <u>Ipm, Mpm, or Amx-Clv</u> • Seizures <u>T</u> • Severe skin reactions (for example, Stevens–Johnson syndrome and toxic epidermal necrolysis), especially in HIV-positive patients

[a]Streptomycin can be used when the isolate is susceptible and none of the other injectable drugs are available.
[b]Thioacetazone should not be used in HIV-positive patients due to severe skin reactions.

Treatment regimens for DR-TB are less well defined than those of DS-TB. Nevertheless, in patients with MDR-TB, at least five effective medicines are recommended during the intensive phase of therapy whereby pyrazinamide and four core second-line drugs, one chosen from Group A, one from Group B, and at least two from Group C, are used. Alternatively, an agent from Group D2 and other agents from Group D3 may be added to bring the total to five. This regimen can further be strengthened with high-dose isoniazid and/or ethambutol.[57] The treatment duration is usually at least 20 months, but a 9–12 month regimen may be adequate in selected patients after careful consideration of previous treatment and resistance profiles.[57]

Fluoroquinolones were introduced into clinical practice in the 1980s and are widely used for treating diverse bacterial infections such as those of the respiratory, gastrointestinal, and urinary tracts.[123] Only later-generation fluoroquinolones such as levofloxacin, moxifloxacin, and gatifloxacin are indicated for use in the treatment of MDR-TB. Indeed, it is recommended that ofloxacin and ciprofloxacin be phased out from the MDR-TB regimens.[57] Fluoroquinolones are administered orally, can penetrate macrophages, have a bactericidal effect,[124] and act by antagonizing the bacterial DNA gyrase thereby disrupting DNA replication.[125] Generally, they have favourable safety profiles but carry the risk of cardiotoxicity due to QT interval [beginning of the Q wave to the end of the T wave in the heart's electrical cycle] prolongation,[126] which is a concern especially when used in combination with drugs with a similar risk such as bedaquiline, delamanid, and clofazimine.

Members of Group B are injectable drugs namely kanamycin (Km), amikacin (Am), and capreomycin (Cm). Although they are usually intramuscularly injected, the drugs may also be administered by slow intravenous injection. Kanamycin and amikacin are aminoglycosides, which inhibit protein synthesis by altering the 16S rRNA.[97] On the other hand, capreomycin is a cyclic peptide antibiotic that inhibits protein synthesis by binding to the 23S rRNA.[127] Close monitoring of patients taking these drugs is recommended because they are associated with severe adverse events such as hearing loss

and nephrotoxicity.[57] Chemical structures of group A, B, and C drugs are shown below in **Figure 1.6**.

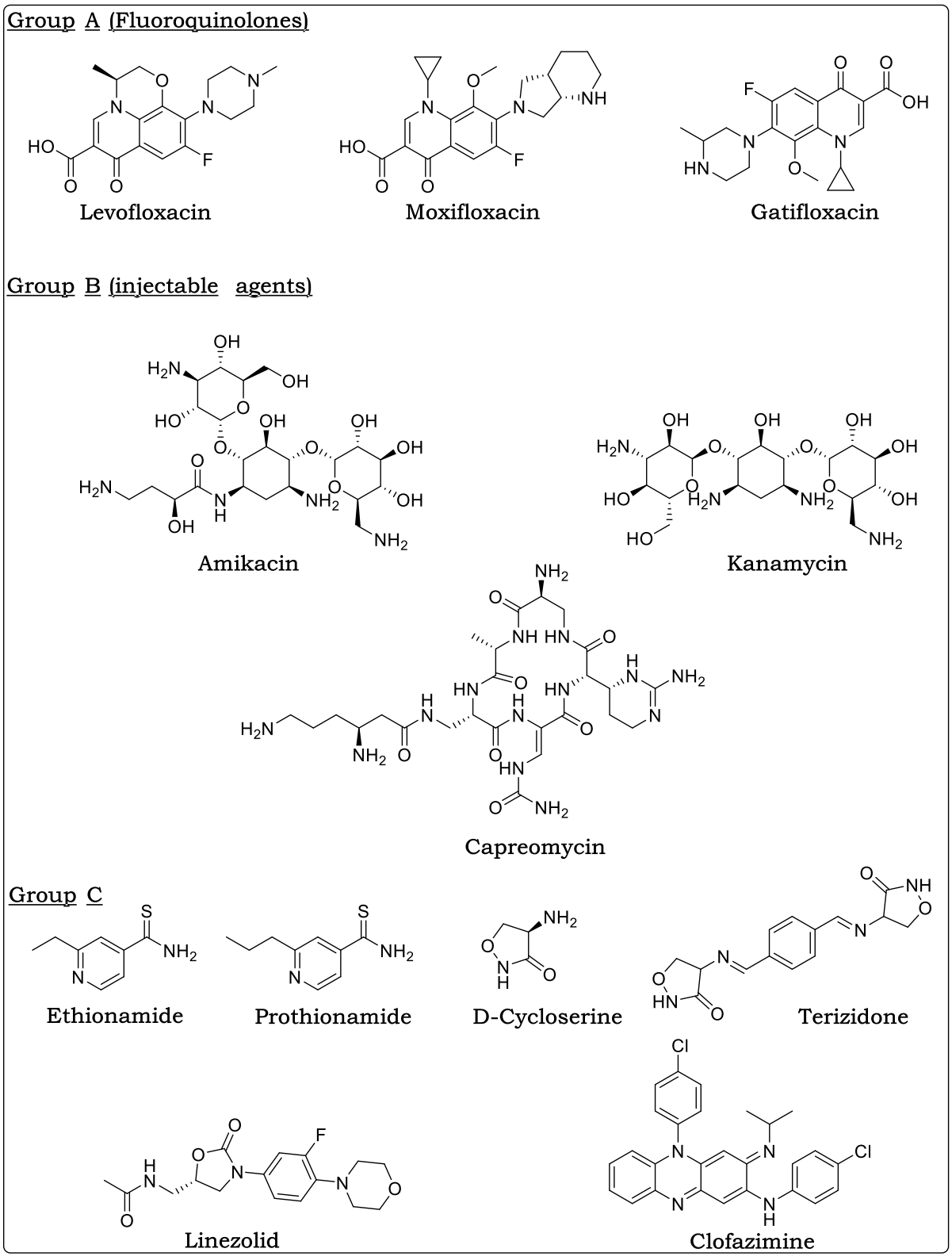

Figure 1.6: Chemical structures of the second-line anti-TB drugs.

Other core second-line drugs include pharmacologically diverse agents that are classified as Group C. Two or more of these agents are to be included in an MDR-TB treatment regimen to bring the total number of effective second-line TB drugs to at least four in the intensive phase: ethionamide (or prothionamide), cycloserine (or terizidone), linezolid, and clofazimine.

Linezolid is a repurposed drug belonging to the oxazolidinone class of antibiotics, which exert their effects by inhibiting bacterial protein synthesis through binding to the 23S rRNA.[128,129]

Clofazimine is a riminophenazine dye that is applied worldwide for the treatment of leprosy. It is believed to serve a sterilizing function in MDR-TB regimens where pyrazinamide is ineffective. Although several studies have reported favorable outcomes on MDR-TB patients put on clofazimine-containing regimens, majority of them suffer from skin discoloration and ichthyosis that may cause distress in some patients, which could result in treatment noncompliance.[130,131]

Group D1 consists of first-line anti-TB drugs namely pyrazinamide, ethambutol, and high-dose isoniazid. They are usually added to the core second-line drugs, unless confirmed resistance, pill burden, intolerance, or drug–drug interactions outweigh their potential benefits.

Group D2 drugs are bedaquiline and delamanid. Bedaquiline (TMC-207) was the first new anti-TB drug to be approved after more than 40 years with no new discoveries.[132] It is a diarylquinoline that received conditional regulatory approval due to limited evidence on its safety and efficacy by the Food and Drug Administration (FDA) in late 2012 and by the European Commission in 2014, for the treatment of pulmonary MDR-TB in adults.[133] It is strongly bactericidal and exerts a sterilizing effect. On the other hand, delamanid is a dihydro-nitroimidazole prodrug, which received accelerated conditional approval by the European Medicines Agency (EMA) in November 2013.[134,135] Both drugs are orally administered and exert their effects through novel mechanisms whereby bedaquiline inhibits adenosine-5'-triphosphate (ATP) synthase,[136,137] while delamanid inhibits the synthesis of the mycobacterial

cell wall components such as methoxy mycolic acid and ketomycolic acid. In addition, both drugs have not exhibited cross-resistance to the other anti-TB drugs; have good sterilizing properties, which may result in shorter treatment regimens; and their addition to treatment regimens, particularly bedaquiline, has resulted in low health care costs.[138–140]

Group D3 drugs include *p*-aminosalicylic acid (PAS), carbapenems (imipenem–cilastatin and meropenem), clavulanate (available as amoxicillin-clavulanate), and thioacetazone. They are the lowest ranked in terms of safety and efficacy, and therefore they should only be used when a regimen with at least five effective drugs in the intensive phase cannot otherwise be composed. It is recommended that in order to reduce their metabolism, carbapenems should be combined with amoxicillin-clavulanate, whenever used in a regimen.[57] **Figure 1.7** shows the chemical structures of group D2 and D3 drugs.

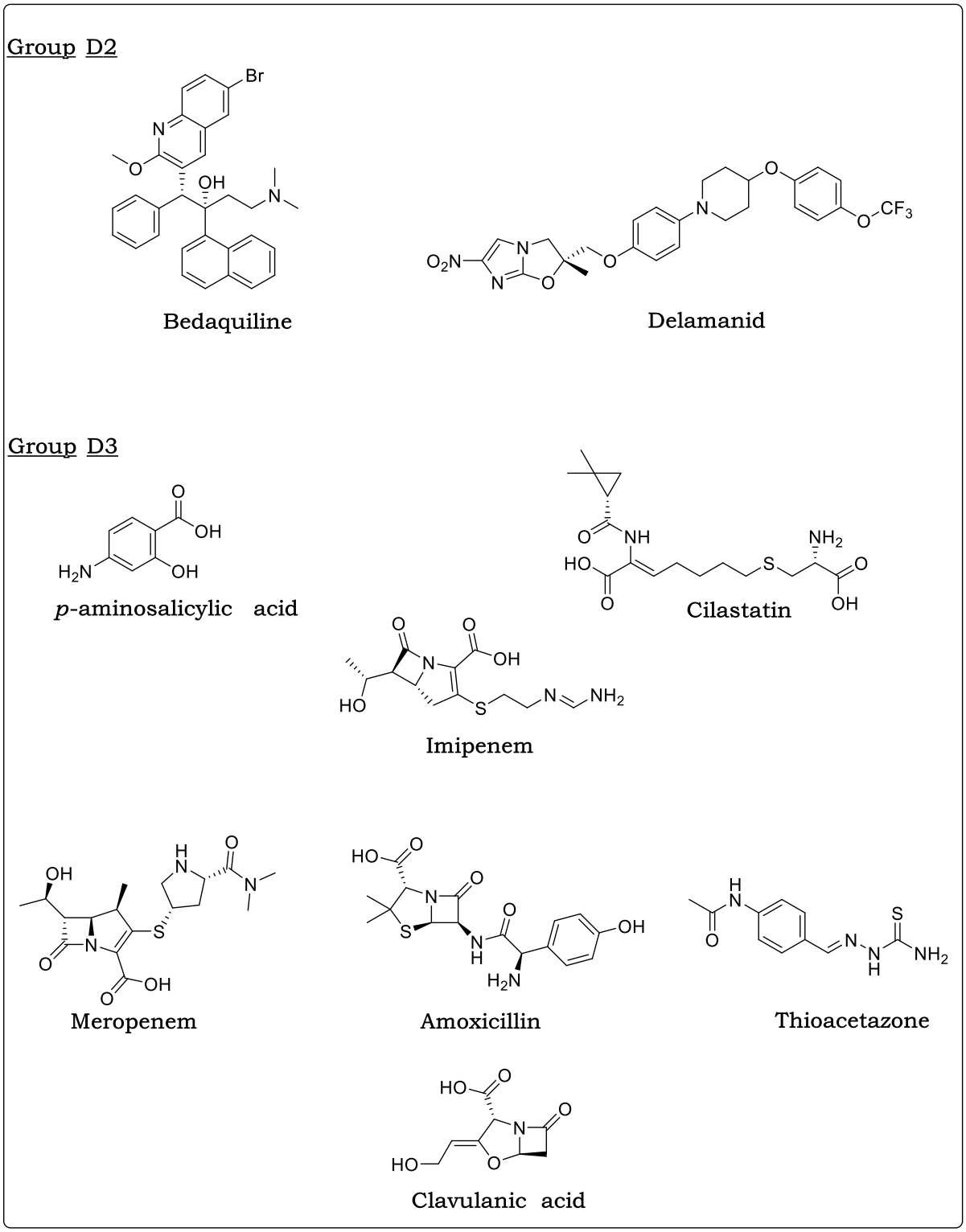

Figure 1.7: Chemical structures of group D second-line anti-TB drugs.

1.5.3 Unmet medical needs in TB and challenges associated with the current TB chemotherapy

Unmet medical needs in TB along with various shortcomings faced by the current therapeutic regimens, lead to unfavorable treatment outcomes. For instance, treatment protocols for both LTBI and active TB disease are lengthy and complex mainly due to the physiological heterogeneity of TB. As a consequence, clinicians experience prescribing challenges and patients suffer from adverse events, which may lead to noncompliance. This more often leads to treatment failures, relapses, deaths, as well as emergence of drug-resistance. Furthermore, DR-TB requires an even longer duration of treatment with drugs that are often of low availability especially in low-income countries, less efficacious, more toxic, and much more expensive than the first-line drugs.[141]

Also, drug-drug interactions are a stumbling block in the optimal treatment of TB patients suffering from other co-infections, particularly the treatment of HIV and TB co-infected individuals. In this regard, cytochrome P450 (CYP) 3A4 interactions with rifampicin and antiretrovirals (ARVs) such as non-nucleoside reverse transcriptase inhibitors (NNRTIs) and protease inhibitors (PIs) are a significant impediment in the management of TB patients co-infected with HIV. For instance, rifampicin induces CYP 3A4 leading to increased metabolism of PIs, and hence reducing their blood concentration and effectiveness.[142–145] Equally important, both ARVs and isoniazid can cause shared toxicities such as peripheral neuropathy and hepatitis, hence exacerbating the adverse events during co-treatment.[146] Besides drug-drug interactions, co-infections and other underlying non-communicable co-morbidities like diabetes mellitus pose other obstacles such as pill burden, toxicities, and acceleration of the TB disease, further complicating TB treatment.[147]

Even after successful treatment completion and cure, some patients still suffer from permanent lung injury and functional impairment, which is characterized by chronic cough and breathlessness. Treatments for

prevention of lung injury are still not available and therefore presenting another unmet medical need in the management of TB.[148]

Also, there is a pressing need for improved biomarkers to guide and monitor treatment as well as to speed up the process of drug development.[148]

The constraints experienced with the current anti-TB drugs, as well as the enormous global burden of TB, have stimulated renewed interest by the pharmaceutical industry and research institutions in recent decades to develop new anti-TB medicines, albeit with low market incentives. The major goals driving research into new and improved TB therapy include: shortening and simplifying treatment of DS-TB; improving and shortening treatment of DR-TB, particularly by use of new, affordable, better-tolerated, and more effective agents with novel mechanisms of action; simultaneous treatment of TB and HIV/AIDS by developing new anti-TB drugs that can be co-administered with ARVs; shortening the duration of treating LTBI to replace the currently recommended protocol of 9 months of isoniazid.[149]

Consequently, various new anti-TB agents, repurposed drugs, and new treatment regimens are currently in various stages of development.

1.5.4 Development pipeline for new anti-TB drugs and regimens

Worldwide, there are a total of about eighteen new anti-TB agents and regimens currently undergoing clinical development and ten new compounds in preclinical evaluation. This is according to the data on new anti-TB drugs development pipeline compiled and updated by the STOP TB Partnership Working Group on New TB Drugs as shown in **Figure 1.8**.

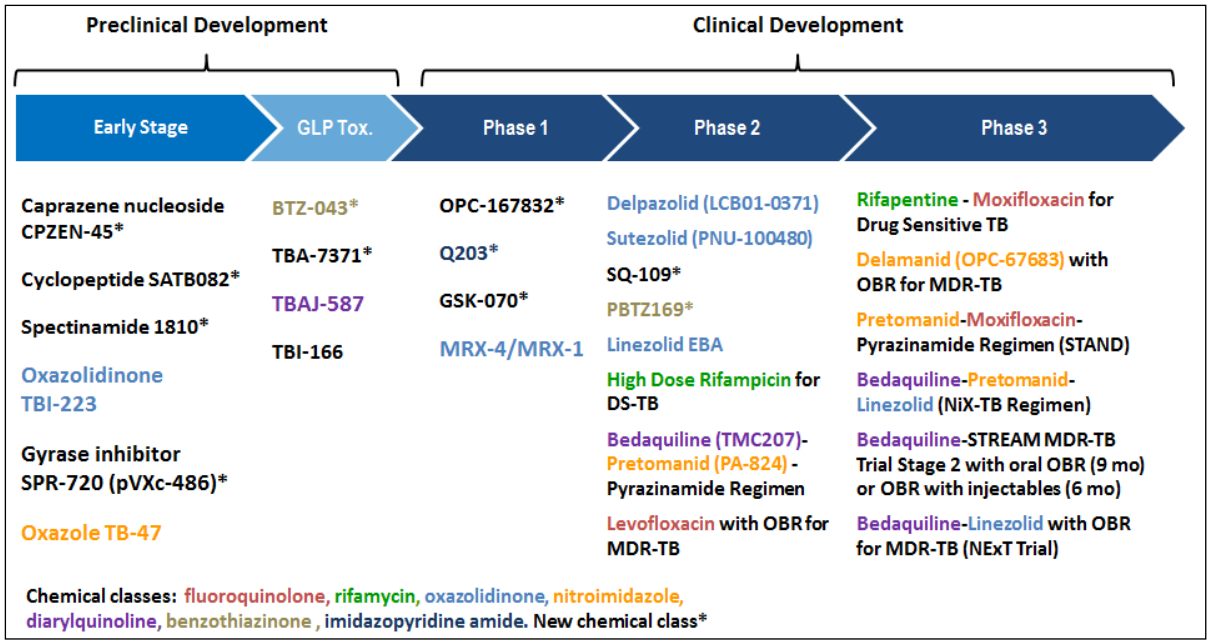

Figure 1.8: Current global drug pipeline for new anti-TB agents and regimens in preclinical and clinical development (*Updated: July 2017*).[150]

Bedaquiline and delamanid are currently in the confirmatory phase III clinical studies,[151] having previously been granted accelerated approval for the management of pulmonary MDR-TB in adults. During a multicenter phase II clinical study (TMC207-C208), addition of bedaquiline to a five-drug regimen resulted in faster and higher rate of sputum-culture conversion at 24 weeks. However, the study did not conclusively assess whether bedaquiline simplifies and/or shortens TB treatment. In addition, there were more deaths observed in the bedaquiline group compared to those on placebo (10 vs 2, p = 0.02).[152] Although the exact causes of deaths were unclear, bedaquiline is beset by long term safety concerns particularly because it causes QT interval prolongation and distributes considerably in peripheral tissues. These concerns, as well as assessment of treatment

shortening are expected to be addressed to a greater extent when the current phase III clinical studies publish their reports sometime in 2019 and 2021.[153] Examples of the current clinical studies include the New Investigational Drugs for XDR-TB (NiX-TB) regimen (clinical trial: NCT02333799) comprised of 6 months of bedaquiline-pretomanid-linezolid (6Bdq-Pa-Lzd). The assessment is being conducted in South Africa to evaluate Bdq-Pa-Lzd as a salvage therapy for XDR-TB and is expected to conclude in 2021. Other bedaquiline studies include the NExT trials (NCT02454205), also in South Africa, involving 6–9 months of bedaquiline-levofloxacin-linezolid-ethionamide-pyrazinamide/isoniazid/terizidone; Evaluation of a Standard Treatment Regimen of Anti-tuberculosis Drugs for Patients with MDR-TB (STREAM) Stage 2 trials (NCT024092290) being carried out in Vietnam to investigate 9 months of bedaquiline-levofloxacin-clofazimine-pyrazinamide-high dose isoniazid-prothionamide regimen, and in South Africa to assess a 6 months regimen of bedaquiline-kanamycin-levofloxacin-clofazimine-pyrazinamide.[150,151,153]

A definitive phase III, multicentered, randomized, double-blinded, placebo-controlled, parallel group clinical trial is currently underway to evaluate the safety and efficacy of delamanid. The trial seeks to assess delamanid when administered orally at a dose of 100 mg twice daily for 2 months followed by 200 mg once daily for 4 months in combination with an optimized background regimen (OBR) versus a placebo. Due to its impressive non-interaction with ARVs, delamanid is also being studied in a select number of HIV-positive individuals who are on ARVs to give a clear perspective on drug-drug interactions.[150] In addition, some studies have demonstrated delamanid's promising potential for use in children, and for this reason two clinical trials are currently planned or underway to evaluate its safety, efficacy, and optimal dosing in pediatric populations.[154]

Pretomanid (PA-824), like delamanid, is a nitroimidazole that is currently in phase III clinical trials. Pretomanid is bactericidal and active against both replicating and hypoxic, non-replicating *Mtb*. It is a prodrug that undergoes intracellular metabolic activation by a deazaflavin (cofactor F_{420})-dependent

nitroreductase (Ddn or Rv3547). The active metabolites kill *Mtb* by a dual mechanism: aerobic disruption of formation of mycolic acid, as well as by releasing nitric oxide to create a toxic environment that leads to respiratory poisoning of *Mtb* in anaerobic conditions.[155–157] In an open-label, partly randomized phase IIb clinical trial, a combination of pretomanid, moxifloxacin, and pyrazinamide was found to be safe, well tolerated, and with superior bactericidal activity during the 8 weeks of treatment.[158] This regimen is currently in phase III Shortening Treatments by Advancing New Drugs (STAND) trial (NCT02342886) to assess its treatment-shortening and simplifying capabilities.[151]

Sutezolid (PNU-100480), like linezolid, belongs to oxazolidinone class of antibiotics. It exerts its anti-TB actions by binding to the 23S ribosomal subunit, thereby disrupting protein synthesis. At a daily dose of 1200 mg, sutezolid is reported to be better tolerated and more efficacious than linezolid. Furthermore, it is neither associated with inhibition nor induction of CYP enzymes, thus expected to exhibit low risk of drug-drug interactions. It is currently undergoing phase II clinical assessment.[159]

Another drug in phase II clinical trials is SQ109, an adamantane-based 1,2-ethylenediamine (ethambutol analogue) with a novel mechanism of action that is different from that of ethambutol. Indeed, it has been reported to be active against ethambutol-resistant strains of *Mtb*.[160] It works by inhibiting MmpL3, a transmembrane trehalose monomycolate transporter that is essential for incorporation of mycolic acid into the *Mtb* cell wall, and therefore hinders cell wall assembly.[160–162] It has also been shown to act via depleting the transmembrane electrochemical proton gradient.[163]

Two new agents are currently in phase I clinical trials: Q203 and PBTZ169. The compound Q203 belongs to the imidazopyridine amide class and is reported to affect energy metabolism in *Mtb* by targeting cytochrome b subunit (QcrB) of the respiratory cytochrome *bc*1 complex electron transport chain, and accordingly inhibits the synthesis of ATP.[164,165] Benzothiazinones PBTZ169 and BTZ043 (in advanced preclinical development) kill *Mtb* by

binding to the essential flavo-enzyme, decaprenylphosphoryl-*β*-D-ribose-2-epimerase (DprE1), leading to its inhibition and irreversible inactivation. DprE1 catalyzes epimerization of decaprenylphosporyl ribose to decaprenylphosporyl arabinose during the synthesis of arabinans, which are essential parts of the *Mtb* cell wall.[166] Studies in zebrafish and mouse models of TB suggest that PBTZ169 is a more efficacious and safer compound compared to BTZ043.[167]

There are several compounds in the stage of preclinical development.[150,168] BTZ043 and TBA7371 (1,4-azaindole)[169,170] are DprE1 inhibitors while GSK-070 is a Leucyl-tRNA synthetase inhibitor.[150] TBI-166 is a riminophenazine analogue that is less lipophilic than clofazimine, therefore less accumulated in tissues and poses a lower risk of skin discoloration.[171,172] CPZEN-45, a caprazamycin derivative, inhibits *Mtb*'s decaprenyl-phosphate-GlcNAc-1-phosphate transferase (WecA), which is responsible for initiation of cell wall biosynthesis.[173] Spectinamide 1810 is a structurally modified spectinomycin to improve target affinity and prevent efflux. It disrupts protein synthesis by binding to the 16S bacterial ribosomal subunit, thereby blocking ribosome translocation.[174] SATB-082, a cyclopeptide derivative (cyclohexylgriselimycin), prevents DNA replication by binding to DNA β-sliding clamp, coded by *DnaN* gene, hence inhibiting DNA polymerase III.[175] The chemical structures of the above-mentioned anti-TB drug candidates are shown in **Figure 1.9** below.

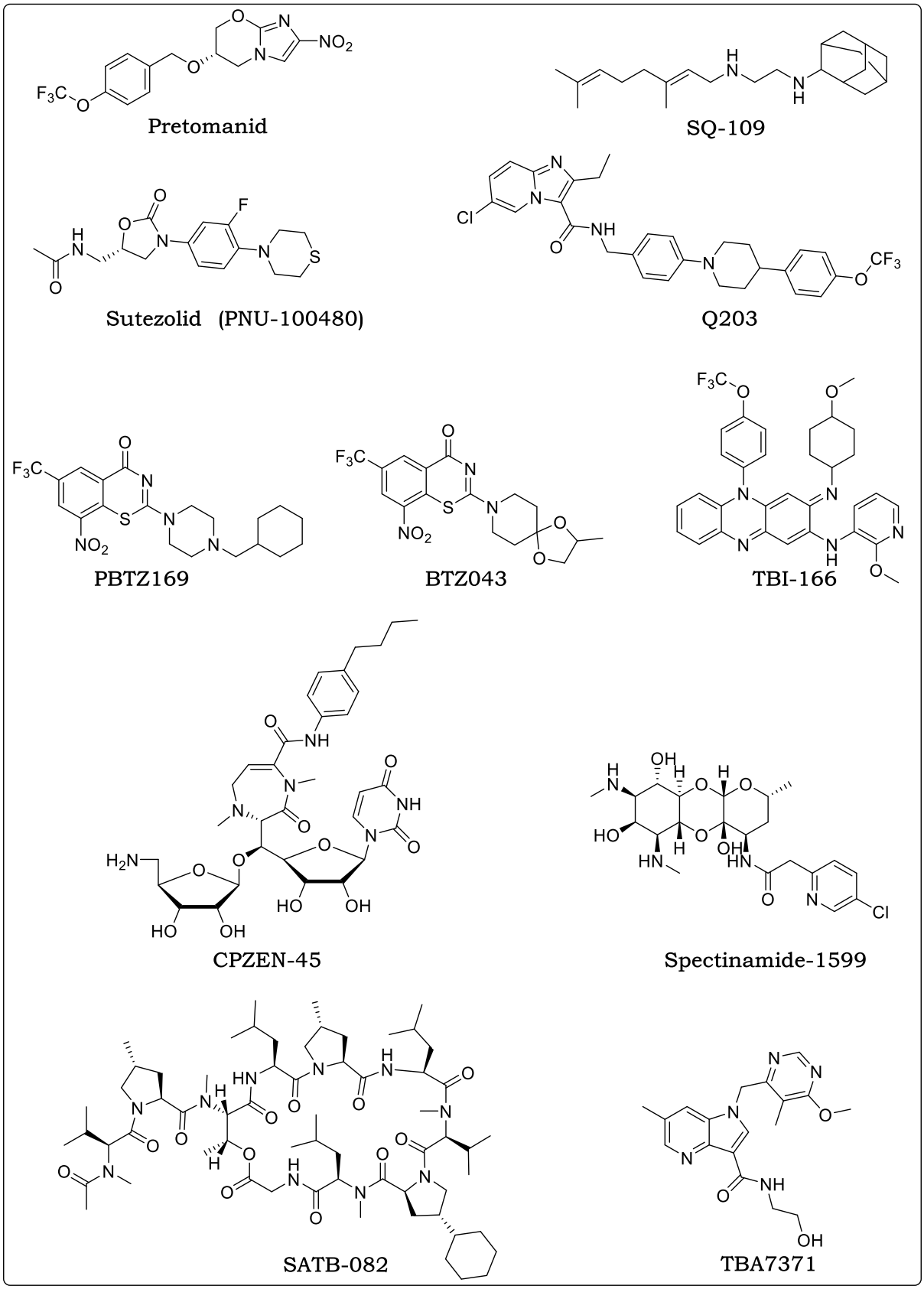

Figure 1.9: Chemical structures of preclinical and clinical anti-TB drug candidates.

To summarize and further illustrate the intensified research in the recent past towards delivering novel anti-TB medicines, **Figure 1.10** shows a pipeline of currently ongoing projects in multifarious early stages of drug discovery. Some projects involve discovery of new agents for novel targets, whereas others are based on the already established targets as well as phenotypic whole-cell screening approaches.

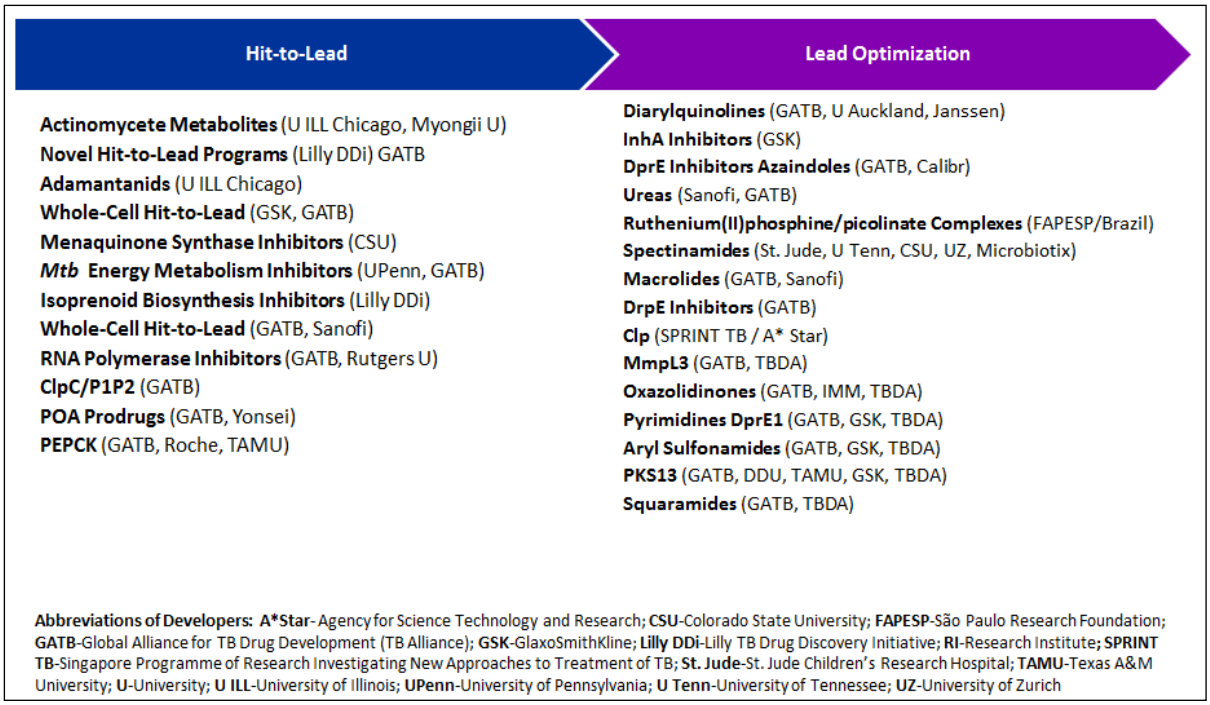

Figure 1.10: Global TB drug discovery pipeline (*Updated: July 2017*).[150]

1.6 Attrition of Drug Candidates

From the foregoing discussion, it is observable that there are more projects in the early drug discovery phase compared to those in the preclinical and clinical development. This is most likely ascribable to not only attrition of drug candidates along the development pipeline, but also a reflection of a period of about five decades of near inactivity in developing new anti-TB drugs.[70] For instance, the development of AZD5847, an oxazolidinone, by AstraZeneca was terminated due to lack of efficacy, while the development of TBA-354, a nitroimidazole, was discontinued due to toxicity in a Phase I clinical trial.[10]

Generally, it is estimated that attrition rate is about 80% in the discovery

phase and 90% during the development stage. Overall, close to 99% of nominated drug candidates fail at some stage in development, suggesting that only about 1 in 50 projects make it through the arduous drug discovery and development process.[176–178] A 2015 analysis by Waring and colleagues on progression status of 812 oral small-molecule drug candidates from four major pharmaceutical companies (AstraZeneca, Eli Lilly and Company, GlaxoSmithKline (GSK) and Pfizer) in the period 2000–2010, gives a clear illustration of the general attrition trend in drug development as depicted in **Figure 1.11**.[179]

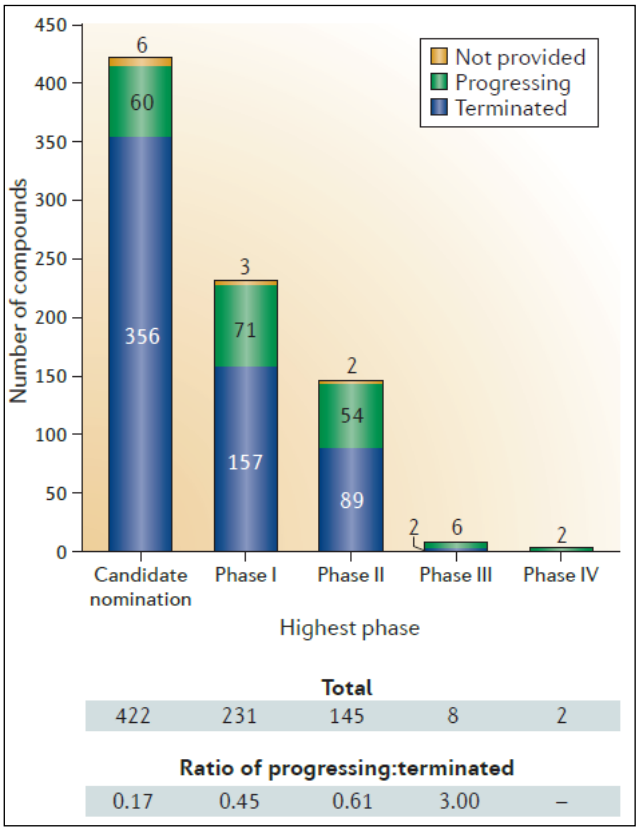

Figure 1.11: Progression of drug candidates during discovery and development phases.[179]

Causes of attrition of drug candidates are multiple and can be categorized into three major classes: compound-related, biology-related, and organization-related. Compound-related failures are associated with unfavorable drug metabolism and pharmacokinetics (DMPK), safety, formulation, and synthesis. Biology-related attrition arises from failures in target-disease linkage, clinical efficacy, as well as target-based toxicity (exaggerated pharmacology), while the organization-related terminations are

associated with companies' portfolio rationalization, disease priorities, and costs.[176,179–181] **Table 1.2**, obtained from the work of Waring *et al.*, is a summary of the causes and their associated percentage contribution to the attrition of drug candidates that were studied.[179] In summary, these results demonstrate and suggest that the major reasons for termination are non-clinical toxicology (59%) for the preclinical phase; clinical safety (25%) for phase I; lack of efficacy (35%) and clinical safety (25%) for phase II; and rationalization of company portfolio, which was generally constant for the three phases at 20%. Moreover, it was noted that there was an overall decrease in the drug candidates' failure between compounds developed in the period 2000–2005 compared to those developed in 2006–2010, a likely indication of some success in efforts towards curbing attrition.[179]

Table 1.2: Primary causes of failure for terminated compounds.[179]

Termination reason	Overall	Period		Phase		
		2000–2005	2006–2010	Candidate nomination	Phase I	Phase II
Clinical safety	68 (11%)	48 (13%)	20 (8%)	5 (1%)	40 (25%)	22 (25%)
Commercial	40 (7%)	23 (6%)	17 (7%)	26 (7%)	10 (6%)	4 (4%)
Efficacy	55 (9%)	45 (11%)	10 (4%)	10 (3%)	14 (9%)	31 (35%)
Formulation	9 (1%)	4 (1%)	5 (2%)	8 (2%)	1 (0.6%)	0
Non-clinical toxicology	240 (40%)	144 (40%)	96 (40%)	211 (59%)	21 (13%)	7 (8%)
Patent issue	1 (0.2%)	0	1 (0.4%)	1 (0.3%)	0	0
Pharmacokinetics or bioavailability	29 (5%)	19 (5%)	10 (4%)	3 (0.8%)	25 (16%)	1 (1%)
Rationalization of company portfolio	124 (21%)	46 (13%)	78 (32%)	75 (21%)	29 (18%)	19 (21%)
Regulatory	2 (0.3%)	2 (0.6%)	0	1 (0.3%)	1 (0.6%)	0
Scientific	33 (5%)	28 (8%)	5 (2%)	13 (4%)	15 (10%)	5 (6%)
Technical	3 (1%)	3 (1%)	0	2 (0.6%)	1 (0.6%)	0
Other	1 (0.2%)	0	1 (0.4%)	1 (0.3%)	0	0
Total	605	362	243	356	157	89

Furthermore, the analysis by Waring *et al.* reaffirms the existence of a relationship between compounds' physicochemical properties and clinical failures. In this regard, most pharmacologically active compounds fail to progress to drugs mainly because they have less than optimal

physicochemical properties, which place them in a chemical space devoid of drug-likeness. Such suboptimal properties result in pharmacokinetics-, safety-, and efficacy-related failures due to poor and unfavorable absorption, distribution, metabolism, elimination, and toxicology (ADMET) profiles.[180,182–185] Aqueous solubility, size, lipophilicity, and polarity are fundamental physicochemical properties, which influence the drug-likeness of candidate molecules.

Previous studies have led to the establishment of a set of acceptable cut-off values for calculated molecular descriptors, which are paramount in predicting optimal physicochemical properties for an oral drug-like space. Examples of these parameters include those of the Lipinski's rule of five (RO5), which states that good oral absorption and permeation are more likely when a compound's calculated logarithm of n-octanol/water partition coefficient (cLogP) is ≤ 5; molecular weight (Mwt) is ≤ 500 Daltons (Da); the number of hydrogen-bond donors (OH plus NH count) is ≤ 5; and the number of hydrogen-bond acceptors (O plus N atoms) is ≤ 10.[186–188] Also, Veber and co-workers, in a 2002 study of oral bioavailability of about 1100 drug candidates in rats, observed and suggested that compounds, which have 10 or fewer rotatable bonds and total polar surface area (tPSA) ≤ 140 $Å^2$ (or total number of both H-bond donors and acceptors ≤ 12) have an increased chance of achieving acceptable oral bioavailability.[189,190]

Caveats and challenges notwithstanding,[191] these rules and guidelines are invaluable tools applicable during potential drug candidate design and optimization campaigns in efforts to achieve drug-likeness. Thus, it is highly beneficial to optimize physicochemical properties such as aqueous solubility in the early stages of drug discovery since this serves to ensure that sufficient screening out of suboptimal compounds takes place at the earliest opportunity. Consequently, there is an element of cost-saving where such compounds fail earlier (fast) rather than later.

1.7 Strategies to improve aqueous solubility of drug candidates

Solubility of a compound in a solvent is the maximum amount of the most stable crystalline form that can remain in solution in a given volume of solvent at a given temperature and pressure under equilibrium conditions.[192] Aqueous solubility, dissolution rate, gastrointestinal tract permeability, first-pass metabolism, and susceptibility to efflux are key factors affecting the overall bioavailability of orally administered drugs. Water solubility is an important drug property that not only affects the rate and extent of drug absorption but also the success of pharmaceutical formulation processes. In addition, high water solubility is essential for drugs designed for parenteral administration.[193] For drugs to have sufficient oral bioavailability, optimal aqueous solubility and gastrointestinal tract (GIT) permeability are fundamental. These two parameters form the basis of the Biopharmaceutical Classification System (BCS), which classifies drugs into four classes as proposed by Amidon and colleagues in 1995: class I are high solubility-high permeability; class II are low solubility-high permeability; class III are high solubility-low permeability; while class IV are Low solubility-low permeability compounds.[194]

It is estimated that about 40% of marketed drugs and up to 75% of new chemical entities (NCE) are poorly water-soluble and the problems associated with low water solubility seem to be increasing.[195] Multiple factors have contributed to discovery of compounds with poor aqueous solubility, including the use of parallel and combinatorial chemistry to generate chemical libraries; high-throughput screening methods often performed in non-aqueous solvents such as dimethyl sulfoxide (DMSO);[196] focus on increased potency; quest to explore novel drug targets, some of which are associated with highly lipophilic endogenous ligands; as well as increased application of *in vitro* target-based drug discovery approaches, whereby target binding is partially mediated by hydrophobic interactions.[195] Low-solubility compounds are plagued by numerous negative effects such as poor and inconsistent oral absorption and bioavailability; insufficient solubility for intravenous dosing; artificially low activity values and

decreased test sensitivity in bioassays due to precipitation of compounds in assay media; erratic and inconsistent assay results; drug development challenges leading to expensive formulations and increased development time and costs; and burden on patients due to the frequent high-dose administrations because poorly soluble drugs often require high doses in order to reach the desired therapeutic plasma concentrations, and this may be associated with adverse events and noncompliance.[197,198]

Low oral bioavailability of drugs due to poor aqueous solubility is a concern for BCS classes II and IV compounds. There are several medicinal chemistry approaches involving chemical structural modification of compounds to address solubility insufficiencies. These include introduction of polar and ionizable groups, salt formation, reduction of lipophilicity (Log P), addition of hydrogen-bonding moieties, disruption of molecular planarity and symmetry, reduction of aromaticity, lowering of molecular weight, design of chiral non-flat compounds, as well as construction of prodrugs. Modification of a compound's chemical structure affects physicochemical properties such as lipophilicity (determined by van der Waals, dipolar, hydrogen bonds, ionic interactions), size (molecular weight and shape), acid-base dissociation constant (p*K*a) (determined by functional group ionizability), and crystal lattice energy that is determined by crystal stacking and melting point.[197] However, for some targets, reducing lipophilicity and increasing water solubility by modification of a compound's structure may result in an unacceptable reduction or loss of potency. Thus, a number of formulation strategies are designed to address a compound's poor solubility without affecting their parent chemical structures. Such approaches include the use of cosolvents, surfactants, cyclodextrins, particle size reduction, co-crystals, polymorphs, complexation, and amorphous solid dispersions.[195,197–201]

1.7.1 Chemical structural modification strategies

1.7.1.1 Addition of ionizable groups and salt formation

It is estimated that about 70% of drugs are ionizable with a majority being basic.[201] Introducing an ionizable group in the structure of a compound is a

common and effective technique applied to enhance water solubility. For example, introduction of a side chain with a basic amine or a carboxylic acid enhances aqueous solubility, particularly in pH buffers where such groups exist in their ionized forms, due to improved interactions with water molecules. These groups influence the p*K*a of a compound and are thus important groups in salt formation, another technique with widespread application to improve aqueous solubility.[202]

Indeed, salt formation is the most preferred approach for the development of parenteral formulations.[203] For example artemisinin derivatives containing an amino group or a carboxylic acid and their corresponding salts are more water soluble than the parent artemisinin.[204] Salt formation by acidic or basic drugs and their dissociation back into their free forms depends on factors such as intrinsic solubility, pH, p*K*a, solubility product (*K*sp), and pH of maximum solubility.[205] It is therefore necessary to carefully analyze the interrelationship between these factors for successful selection of appropriate counterions to prepare salts. Examples of counterions for the formation of salts of basic drugs include hydrochloride, methanesulfonate (mesylate) hydrobromide/bromide, acetate, fumarate, sulfate/bisulfate, succinate, citrate, phosphate, maleate, nitrate, tartrate, benzoate, carbonate, and pamoate. On the other hand, for acidic drugs, the most commonly used counterions are sodium, calcium, potassium, and tromethamine.[205]

In addition to improving solubility, salts also modify other physicochemical properties such as dissolution rate, crystallinity, hygroscopicity, and mechanical properties (hardness, elasticity). These properties greatly impact on a compound's bioavailability, stability, and manufacturability.[197]

1.7.1.2 Lowering of Log P and Molecular Weight

Structural modifications aimed at reducing log P can be achieved by introducing hydrophilic groups, replacement of phenyl groups with heterocycles such as pyridyl and pyrimidinyl, as well as reducing the size of

a molecule. Hydrophilic groups increase the polarity of a compound and enhance solubility as discussed in the next subsection.[197]

1.7.1.3 Introduction of polar groups and use of prodrugs

Introduction of hydrogen bond donors such as hydroxyl and amino groups and acceptors such as carbonyl groups into a molecule enhances solubility by facilitating hydrogen bonding interaction between water molecules and solutes.[206,207] These polar and sometimes charged groups form the basis of construction of prodrugs that have higher solubility than the parent compounds. Ester, carbonate, amide, carbamate, oxime, and amino acid-conjugated prodrugs are common, highly soluble, bioreversible derivatives designed to undergo enzymatic hydrolysis *in vivo* to release the active parent drug.[208–210] For example, fosphenytoin, a prodrug of phenytoin with an added phosphate, has a greatly increased solubility, and undergoes enzymatic hydrolysis in the intestines to release phenytoin for absorption.[197]

1.7.1.4 Disruption of Crystal-stacking

Solubility of a compound is a function of its log P and melting point as depicted by the general solubility equation (GSE): log [solubility (M)] = 0.5-(log P)-0.01[melting point (ºC)-25].[211,212] Melting point is related to crystal lattice and crystal packing energies. Crystallinity affects the interaction of a compound with water molecules and thus amorphous compounds have better solubilities than crystalline ones. Therefore, strategies that reduce crystallinity or disrupt crystal packing generally increase aqueous solubility. Examples of these approaches include reduction of aromaticity by increasing the fraction of sp^3-hybridized carbons (escape from flatland), which results in decreased melting points.[213] Also, increasing the dihedral angle of biaryl compounds reduces the molecular planarity, and thus disruption of the crystal-stacking efficiency. This, for example, is achieved by adding *ortho*-substituents such as methyl and fluoro groups on biaryl compounds.[212] **Figure 1.12** depicts examples of strategies to improve water solubility by various structural modifications.

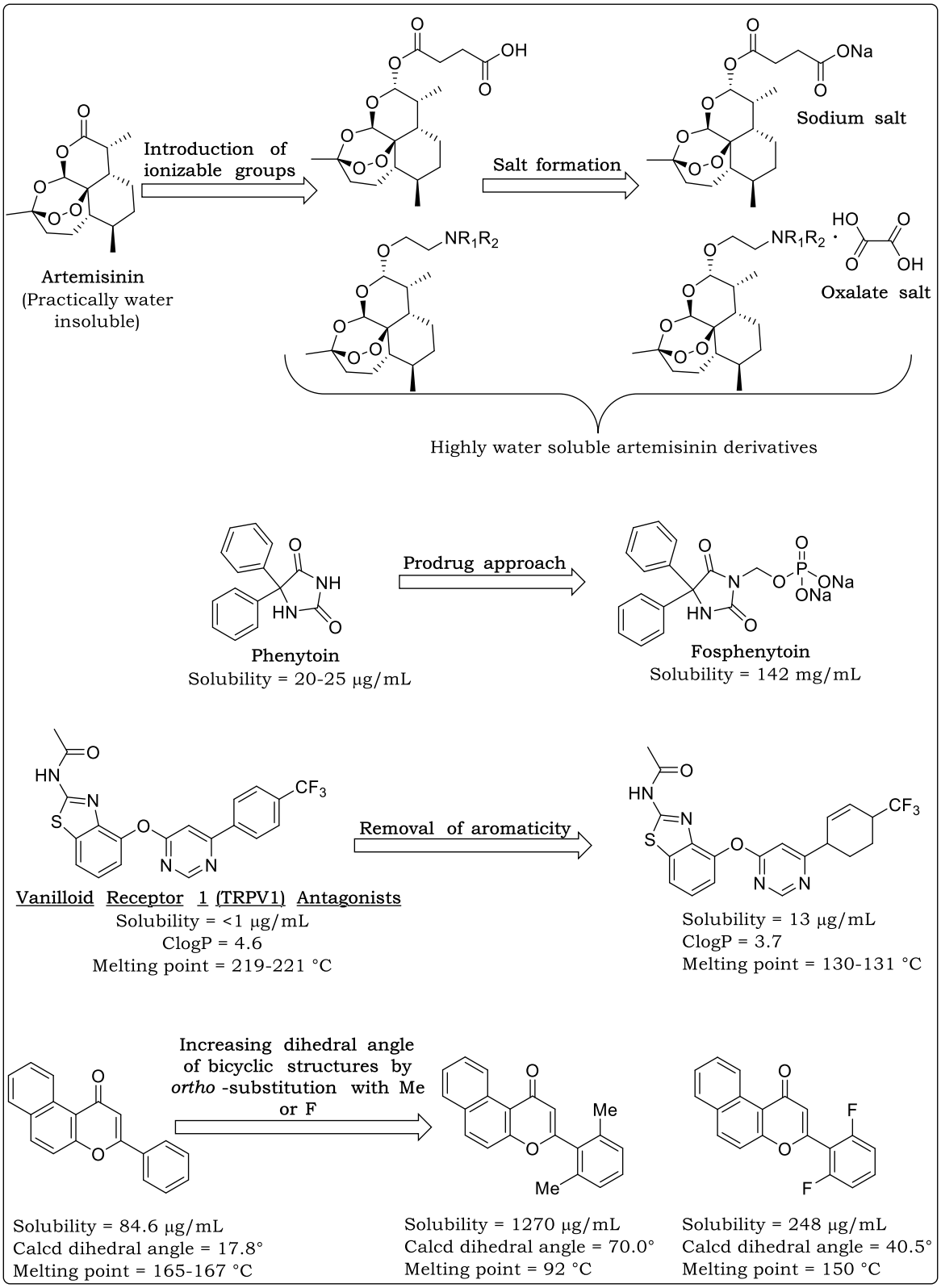

Figure 1.12: Examples of chemical modifications for enhancement of aqueous solubility.[197,212]

1.7.2 Physical Modification Strategies

1.7.2.1 Use of Cosolvents

Cosolvents are water-miscible organic solvents that are less polar than water. They are believed to enhance aqueous solubility of poorly soluble drugs by disrupting the intermolecular hydrogen bonding networks that are present in aqueous systems, thus lowering the polarity of the bulk solvent to a level that is almost similar to that of the drug.[214] Examples of widely used cosolvents in drugs include ethanol, propylene glycol, polyethylene glycol (PEG) 300/400, glycerol, DMSO, and dimethyl acetamide (DMA). Cosolvents have been used at concentrations above 50% v/v and are reported to solubilize 10–15% of FDA-approved parenteral products, both neutral and ionizable compounds.[195,215]

1.7.2.2 Surfactants

Surfactants are surface active agents that reduce the surface tension between two liquids or between a liquid and a solid. Due to their amphiphilic nature, surfactants self-associate in aqueous environments to form micelles that improve wetting of hydrophobic materials. Micelle formation takes place at a surfactant concentration above the critical micelle concentration (CMC). Poorly soluble drugs are solubilized by incorporation into the hydrophobic micelle core as well as via favourable interaction and orientation into the polar/nonpolar water-micelle interface. Both drug hydrophobicity and surfactant charge influence the location of solubilization. Examples used in drug formulations include tween 20/80, cremophor RH 40/60, cremophor EL, and solutol HS-15, typically used at final concentrations of 5–10% v/v.[195] Despite their increased use in drug formulation, surfactants may be poorly tolerated in chronic use and may pose a significant threat of drug precipitation on dilution.[216]

Additionally, surfactants have been reported to possess the potential to enhance drug bioavailability through their inhibitory effects on metabolic and anti-transport processes such as cellular efflux where they demonstrate a transporter-specific interaction. These effects might be expected to

increase the bioavailability of drugs, particularly where intestinal efflux transporters such as P-glycoproteins limit absorption, as well as enhance drug access to cells such as those of the CNS.[217]

1.7.2.3 Particle Size Reduction

Particle size reduction enhances solubility and dissolution rate by increasing the surface area available for solvation. This technique is achieved through either top-down or bottom-up processes.[195] In the top-down processes, commonly referred to as micronization, larger particles are fragmented into smaller particles of micron sizes by dry-impact techniques, which utilize mills such as hammer, ball, and air-jet mills. On the other hand, the bottom-up processes involve harvesting of small particles after recrystallization of a drug from a supersaturated solution. Similarly, nano-sized particles are achieved by using nanomilling technologies and stabilization systems.[218] Nonetheless, due to their highly cohesive nature, nanoparticles are beset by shortcomings associated with aggregation. Also, nanoparticles have the propensity to undergo polymorphic transition during manufacturing or storage.[219] Furthermore, not all drugs have the necessary physicochemical properties to withstand effective size reduction.

1.7.2.4 Solid Dispersions

A solid dispersion contains a poorly soluble drug dispersed within an inert, more hydrophilic carrier matrix such as water soluble sugars, polymers, or surface active emulsifiers. Solid dispersions increase drug dissolution through reduced effective particle size, improved wetting, enhanced solubilization, and stabilization of a drug in the more soluble amorphous state.[195,220]

1.7.2.5 Supramolecular Derivatization

1.7.2.5.1 Crystal Habit Engineering

Examples of crystal engineering techniques for enhancement of aqueous solubility include utilization of polymorphism and formation of cocrystals. Different polymorphs (different crystalline forms of a compound) or the

amorphous form have different aqueous solubilities. Where low aqueous solubility is a significant limitation to absorption, it is important to select the most soluble polymorph or polymorphic mixture, whether anhydrous or solvate/hydrate forms.[221]

A pharmaceutical cocrystal is a single crystalline solid that incorporates two molecules, one being an active pharmaceutical ingredient (API) and the other a cocrystal former (co-former), in the same crystal lattice.[222,223] Favourable geometries of cocrystals lead to self-assembled supramolecular networks. The cocrystal former may be an excipient or another drug whose main purpose is to improve the drug's physicochemical properties such as solubility, dissolution rate, stability, hygroscopicity, and compressibility. It is important to select co-formers from the FDA-approved generally regarded as safe (GRAS) additives to ensure non-toxicity.[224] Unlike salts, which are formed only with ionizable compounds, cocrystals are advantageous because they can be applied on both ionizable and neutral compounds, since no proton exchange is required. Hydrogen bonding is critical in cocrystal formation, and arrangements are mainly based on synthons of strong and weak hydrogen bonds as shown in **Figure 1.13**.[225,226]

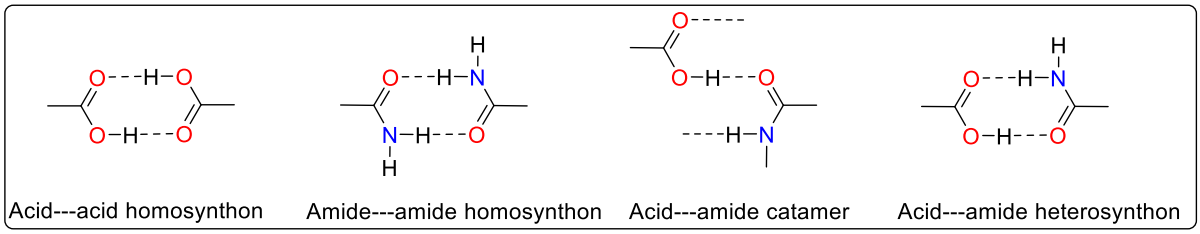

Figure 1.13: Examples of synthons for cocrystal formation.[225]

1.7.2.5.2 Cyclodextrin Complexes

Cyclodextrins (CDs) are macrocyclic oligosaccharides with a hydrophilic exterior and a hydrophobic inner core. They are classified as α, β, or γ depending on their size, number of monosaccharides, and physicochemical properties, as illustrated in **Figure 1.14**.

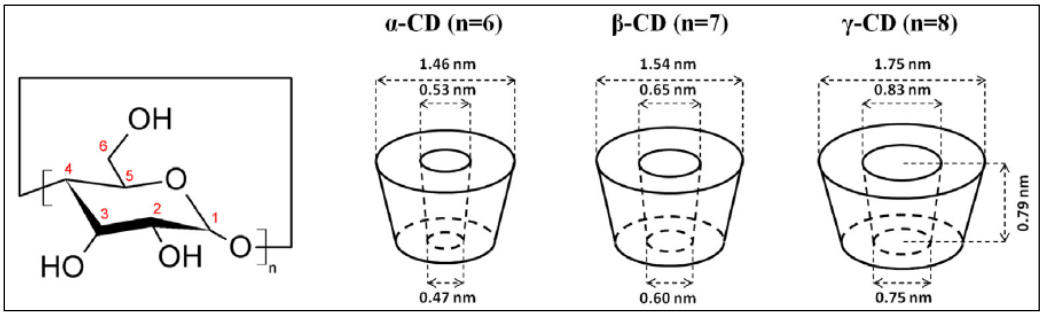

Figure 1.14: Classification of cyclodextrins.[227]

CDs form inclusion complexes whereby lipophilic portions of drug molecules are taken into the lipophilic central cavities of CDs to form complexes, which may self-assemble to supramolecular structures that act as drug carriers (**Figure 1.15**).[227,228] CD absorption into cells is limited by the high molecular weight, high hydrophilicity, and the large number of H-bond donors and acceptors. They improve physicochemical properties of drugs such as aqueous solubility and dissolution rates. In addition, they have been shown to reduce gastrointestinal and ocular irritation, eliminate unpleasant odours or taste, and in some instances prevent drug-additive interactions.[229] Although bulkiness is a challenge for use of cyclodextrins in solid formulations, increasing complexation efficiency has been shown to mitigate this setback.[230]

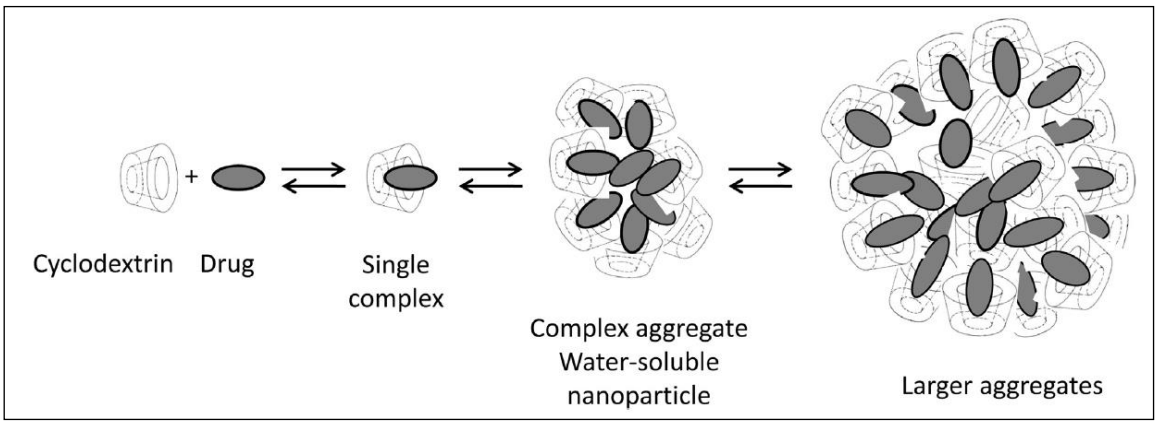

Figure 1.15: Cyclodextrin-drug inclusion complexes in aqueous solution.[227]

In conclusion, both chemical and physical strategies of improving aqueous solubility of some benzoheterocyclic compounds were explored in this thesis work, particularly the introduction of polar and ionizable substituents, formation of salts, cocrystals, and cyclodextrin inclusion complexes.

1.8 Benzoheterocyclic Chemotypes

Benzoheterocyclic structural motifs are composed of a benzene ring fused to oxygen-, sulfur-, or in most cases nitrogen-containing rings. Examples include benzoxazole, benzothiazole, benzofuran, indole, benzothiophene, benzimidazole, quinoline, quinaxaline, and quinazoline. They form privileged, unique, versatile, readily accessible, chemically tractable, and biologically important scaffolds with widespread applications in the design of organic compounds such as drugs, food flavors, biocides, and other industrial chemicals.[231] In addition, heterocycles are immensely interwoven in many natural products such as nucleic acids, amino acids, carbohydrates, vitamins, and alkaloids. Thus, they are important in drug discovery programs because therapeutic effects of many drugs are mainly mediated by mechanisms that mimic or inhibit actions of naturally occurring biochemical compounds.[232] Moreover, in the pharmaceutical industry, heterocycles play key roles in drug design because they are easily modified and derivatized to modulate physicochemical properties such as lipophilicity, polarity, hydrogen bonding, and solubility, all aimed at achieving favourable pharmacological, pharmacokinetic, and toxicological profiles of drug candidates and ultimately drugs.[232]

In this thesis work, quinazolinone and benzoxazole motifs were the benzoheterocyclic skeletons (**Figure 1.16**) that were appropriately derivatized to a range of novel compounds, which were then subjected to various biological and pharmacological studies with the aim of investigating their antimycobacterial structure-activity relationship (SAR) profiles. An attendant aim was to explore structure-property relationship (SPR) for the target compounds, and supramolecular derivatization of selected analogues.

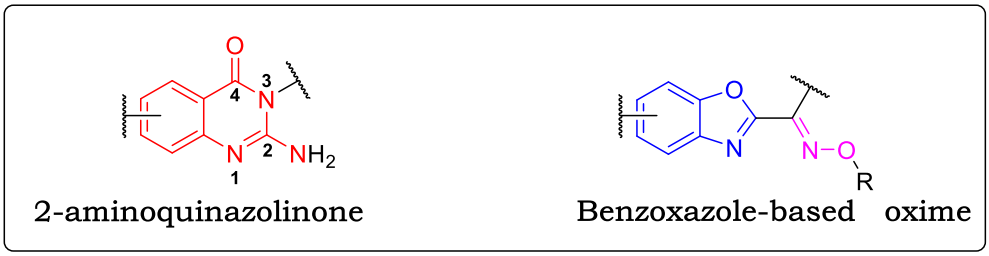

Figure 1.16: Scaffolds of 2-aminoquinazolinone and benzoxazole-based oxime.

1.8.1 2-Aminoquinazolinones

2-Aminoquinazolinone is an invaluable heterocyclic moiety derived from the 4-quinazolinone ring system. This structural motif is synthetically versatile, chemically stable, and possesses immense biological and medicinal significance. There is a large array of quinazolinone-based pharmacologically active compounds, including approved drugs, which exhibit diverse spectrum of biological activities[233,234] such as antiviral;[235] antibacterial;[236] antimalarial;[237] antifungal;[238] anticancer;[239] anti-inflammatory/analgesic;[240] sedative-hypnotic;[241] antitubercular;[242–244] anticoccidiosis in poultry;[245] antihypertensive and diuretic;[246] antiallergy;[247] antidepressant;[248] and anticonvulsant.[249,250] It is also estimated that the quinazolinone moiety forms a core element in over 150 natural products, particularly alkaloids.[233]

Despite the immense studies carried out on quinazolinone-based compounds, literature review on biologically active 2-aminoquinazolinone-containing compounds, including approved drugs, reveals that 2-aminoquinazolinones are the least exploited in drug discovery programs, particularly compounds with a primary amine at position 2. Nevertheless, more quinazolinone compounds with secondary or tertiary amines at position 2 have been studied and reported. Examples of these compounds are shown in **Figure 1.17**.

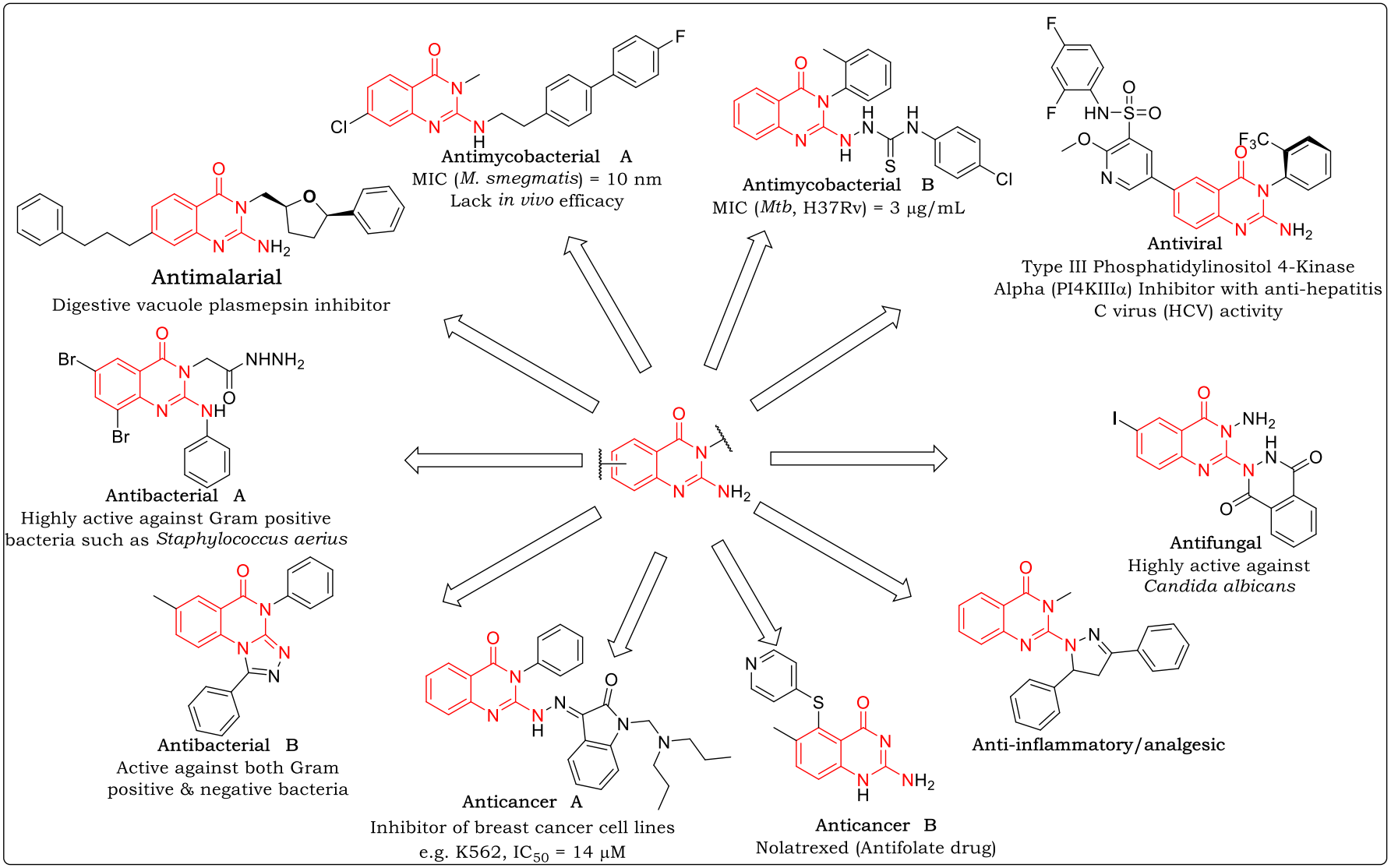

Figure 1.17: Examples of 2-aminoquinazolinones: antimycobacterial A,[251] antimycobacterial B,[252] antimalarial,[237,253] antiviral,[254,255] antibacterial A,[236] antibacterial B,[256] anticancer A,[257] anticancer B,[239] antifungal,[258] analgesic.[259]

Comparatively, there are fewer 2-aminoquinazolinone-containing compounds that have been studied for their bioactivities against *Mtb*. Indeed, to the best of our knowledge, there are no published patents on anti-TB compounds containing the 2-aminoquinazolinone skeleton. On the other hand, recent studies conducted by Couturier and colleagues in 2016, revealed quinazolinone-based compounds (antimycobacterial **A** in **Figure 1.17**) with high *in vitro* activity against *Mycobacterium smegmatis* (MIC = 10 nm) but lacking *in vivo* efficacy in mice.[251] Poor aqueous solubility, non-proportional oral mice PK, and overall poor drug-likeness were cited as the probable causes of the lack of *in vivo* efficacy.[251]

In summary, owing to the large number of quinazolinone-based drug candidates and approved drugs with versatile bioactivities, the quinazolinone moiety may be termed as a privileged scaffold, which is a building block with many sites of modification to yield drug-like compounds. Therefore, there is a high probability of delivering novel anti-TB quinazolinone-based compounds by appropriate chemical functionalization and early optimization of physicochemical properties. Nonetheless, the diverse bioactivities displayed by quinazolinones may also be an indication of their promiscuity and therefore could probably be plagued by unwanted side effects.

1.8.2 Benzoxazole-Based Oximes

Benzoxazole-based oximes have been reported to exhibit antimicrobial activities[260] as well as act as emitters of blue light.[261] Although literature on them is scarce, a lot more has been reported about benzoxazole- or oxime-containing compounds in an independent manner.

Benzoxazole, like quinazolinone, has widespread applications and forms part of many compounds with biological activities such as antibacterial, anti-inflammatory, anticonvulsant, analgesic, anticancer, as well as herbicidal.[262–265]

Similarly, compounds with oxime functionalities have a wide spectrum of pharmacological activities such as antibacterial,[266] antifungal,[267]

antimycobacterial,[268–270] as well as antidotes such as obidoxime, which is used in the treatment of organophosphate (nerve agents) poisoning.[271] Examples of benzoxazole- and/or oxime-containing drugs are shown in **Figure 1.18**.

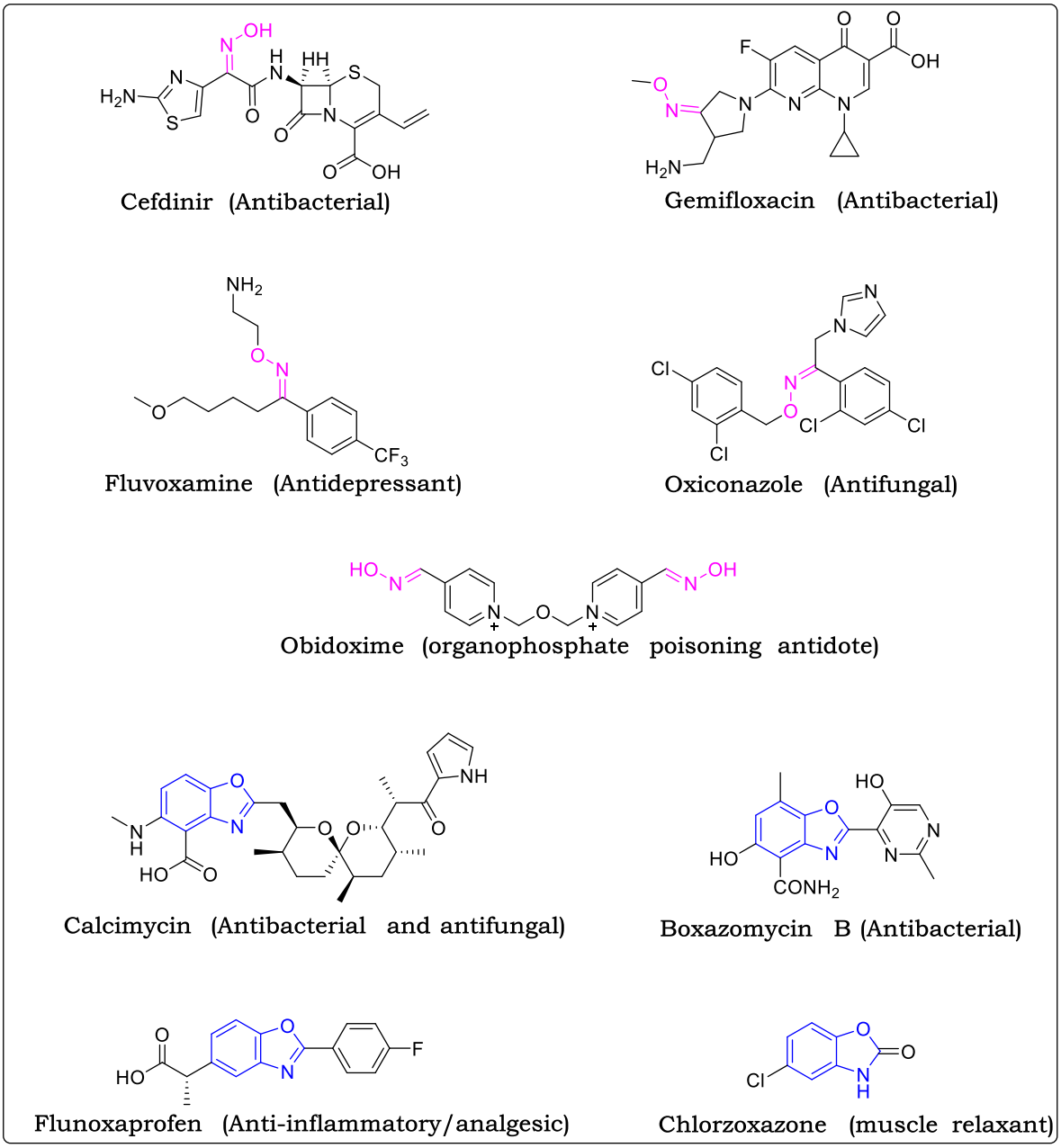

Figure 1.18: Chemical structures of oxime- or benzoxazole-containing drugs.

By and large, we were encouraged by the diverse bioactivities as well as drug-likeness exhibited by benzoxazole- and/or oxime-based compounds to further pursue and investigate benzoxazole-based oximes as potential anti-TB agents.

1.9 Research Program

1.9.1 Study Justification

Research gaps, which formed the foundation of this thesis work, were identified. Firstly, there is an urgent need to develop new anti-TB drugs to alleviate the setbacks hampering the current therapeutic agents. Indeed, the WHO global tuberculosis report 2015 states that "without new TB drugs and regimens, it will be very difficult to improve treatment outcomes in the near future."[272] Development of new anti-TB agents is driven by objectives such as to improve and simplify the current treatment by shortening the treatment duration; improve on the MDR-TB treatment by developing well tolerated drugs with novel mechanisms of action; reduce drug-drug interactions, especially for TB treatment in patients taking ARVs; and to provide more effective LTBI treatment. Furthermore, intensified research and innovation is the third pillar of the End TB Strategy 2015, which advocates for discovery, development, and rapid uptake of new tools, interventions, and strategies to combat TB.

Secondly, attrition of drug candidates is a challenge to successful development of new drugs, and has been identified as a probable cause of gaps in the anti-TB drug discovery pipeline. It is thus imperative to continually replenish the reservoir of new drug candidates in the discovery pipeline to effectively cover for failures. Attrition is partially attributed to suboptimal physicochemical properties of drug candidates, which have links to several causes of failures including unfavorable DMPK profiles, toxicity, lack of efficacy, and formulation difficulties. It is therefore important to optimize physicochemical properties early enough to promote success of drug discovery and development projects. This will go a long way towards successful and hastened delivery of new anti-TB agents.

Also, to overcome the problem of drug resistance, new, affordable, better-tolerated, and more effective agents with novel mechanisms of action are needed. In this thesis work, we investigated two classes of benzoheterocyclic chemotypes as potential anti-TB agents: the 2-aminoquinazolinones, and

the benzoxazole-based oximes. A literature search based on these privileged structural motifs revealed that compounds containing them have widespread industrial applications, including drugs. This is encouraging because of the high probability of drug-likeness associated with these scaffolds. Equally important, there is limited application of these benzoheterocycles, both as anti-TB drugs or potential anti-TB agents. Indeed, none of the approved anti-TB drugs and drug candidates contains these skeletons, further augmenting the chances of novel mechanisms of action. Moreover, the literature review has revealed adequate intellectual property space to study and investigate 2-aminoquinazolinones and benzoxazole-based oximes as potential anti-TB drug leads.

1.9.2 Hypothesis

2-Aminoquinazolinones and benzoxazole-based oximes are potential novel antituberculosis drug leads with favorable potency, pharmacokinetics and physicochemical properties.

1.9.3 Objective

The overall objective was to optimize previously identified antimycobacterial 2-aminoquinazolinones and benzoxazole-based oximes by investigating their antimycobacterial structure-activity relationship (SAR) profiles. An attendant aim was to explore structure-property relationships (SPR) for the target compounds and perform supramolecular derivatization of selected analogues.

1.9.4 Specific Aims

- To synthesize 2-aminoquinazolinones and benzoxazole-based analogues as potential antituberculosis agents (Chapter 2).
- To biologically evaluate the synthesized target compounds for antimycobacterial potency, cytotoxicity, and DMPK profiles (Chapter 3).
- To profile all final target compounds with respect to physicochemical properties, including aqueous solubility; deduce structure-property relationships (SPR); and carry out supramolecular derivatization of

selected potent compounds (Chapter 4).

The workflow or screening cascade that was followed towards achieving the above-mentioned objectives is illustrated in **Figure 1.19** below.

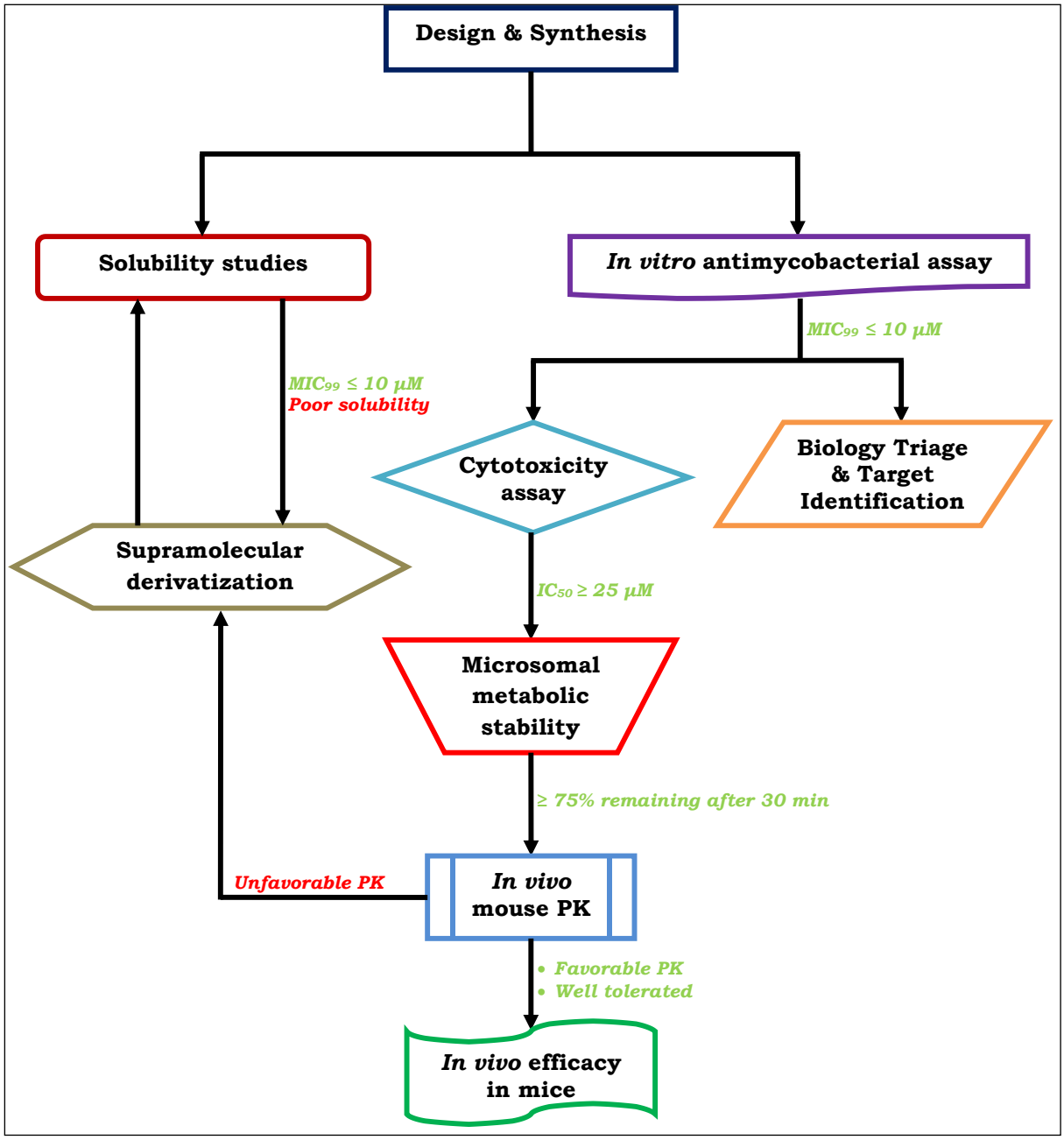

Figure 1.19: Screening cascade summarizing the workflow and criteria for progression to various studies.

References

(1) Sakamoto, K. The Pathology of *Mycobacterium tuberculosis* Infection. *Vet. Pathol.* **2012**, *49*, 423–439.

(2) Scanning electron micrograph of *Mycobacterium tuberculosis* https://phil.cdc.gov/phil/details.asp?pid=9997 (accessed Aug 19, 2017)

(3) Barnes, D. S. Historical Perspectives on the Etiology of Tuberculosis. *Microbes Infect.* **2000**, *2*, 431–440.

(4) Daniel, T. M. The History of Tuberculosis. *Respir. Med.* **2006**, *100*, 1862–1870.

(5) Frothingham, R.; Hills, H. G.; Wilson, K. H. Extensive DNA Sequence Conservation throughout the *Mycobacterium tuberculosis* Complex. *J Clin Microbiol* **1994**, *32*, 1639–1643.

(6) Brosch, R.; Gordon, S. V.; Marmiesse, M.; Brodin, P.; Buchrieser, C.; Eiglmeier, K.; Garnier, T.; Gutierrez, C.; Hewinson, G.; Kremer, K.; Parsons, L. M.; Pym, A. S.; Samper, S.; van Soolingen, D.; Cole, S. T. A New Evolutionary Scenario for the *Mycobacterium tuberculosis* Complex. *Proc. Natl. Acad. Sci.* **2002**, *99*, 3684–3689.

(7) Russell, D. G. Who Puts the Tubercle in Tuberculosis? *Nat. Rev. Microbiol.* **2007**, *5*, 39–47.

(8) Mostowy, S.; Cousins, D.; Brinkman, J.; Aranaz, A.; Behr, M. A. Genomic Deletions Suggest a Phylogeny for the *Mycobacterium tuberculosis* Complex. *J. Infect. Dis.* **2002**, *186*, 74–80.

(9) Cole, S. T.; Brosch, R.; Parkhill, J.; Garnier, T.; Churcher, C.; Harris, D.; Gordon, S. V.; Eiglmeier, K.; Gas, S.; Barry, C. E.; Tekaia, F.; Badcock, K.; Basham, D.; Brown, D.; Chillingworth, T.; Connor, R.; Davies, R.; Devlin, K.; Feltwell, T.; Gentles, S.; Hamlin, N.; Holroyd, S.; Hornsby, T.; Jagels, K.; Krogh, A.; McLean, J.; Moule, S.; Murphy, L.; Oliver, K.; Osborne, J.; Quail, M. A.; Rajandream, M. A.; Rogers, J.; Rutter, S.; Seeger, K.; Skelton, J.; Squares, R.; Squares, S.; Sulston, J. E.; Taylor, K.; Whitehead, S.; Barrell, B. G. Deciphering the Biology of *Mycobacterium tuberculosis* from the Complete Genome Sequence. *Nature* **1998**, *393*, 537–544.

(10) World Health Organization. *Global Tuberculosis Report*; Geneva, 2016.

(11) Comas, I.; Coscolla, M.; Luo, T.; Borrell, S.; Holt, K. E.; Kato-Maeda, M.; Parkhill, J.; Malla, B.; Berg, S.; Thwaites, G.; Yeboah-Manu, D.; Bothamley, G.; Mei, J.; Wei, L.; Bentley, S.; Harris, S. R.; Niemann, S.; Diel, R.; Aseffa, A.; Gao, Q.; Young, D.; Gagneux, S. Out-of-Africa

Migration and Neolithic Coexpansion of *Mycobacterium tuberculosis* with Modern Humans. *Nat. Genet.* **2013**, *45*, 1176–1182.

(12) Barry, C. E.; Lee, R. E.; Mdluli, K.; Sampson, A. E.; Schroeder, B. G.; Slayden, R. A.; Yuan, Y. Mycolic Acids: Structure, Biosynthesis and Physiological Functions. *Prog. Lipid Res.* **1998**, *37*, 143–179.

(13) Lee, R. E. B.; Li, W.; Chatterjee, D.; Lee, R. E. Rapid Structural Characterization of the Arabinogalactan and Lipoarabinomannan in Live Mycobacterial Cells Using 2D and 3D HR-MAS NMR: Structural Changes in the Arabinan due to Ethambutol Treatment and Gene Mutation Are Observed. *Glycobiology* **2005**, *15*, 139–151.

(14) Brennan, P. J. Structure, Function, and Biogenesis of the Cell Wall of *Mycobacterium tuberculosis*. *Tuberculosis* **2003**, *83*, 91–97.

(15) Tiemersma, E. W.; van der Werf, M. J.; Borgdorff, M. W.; Williams, B. G.; Nagelkerke, N. J. D. Natural History of Tuberculosis: Duration and Fatality of Untreated Pulmonary Tuberculosis in HIV Negative Patients: A Systematic Review. *PLoS One* **2011**, *6*, e17601, 1–13.

(16) World Health Organization. *The End TB Strategy*; Geneva, 2015.

(17) Corbett, E. L.; Watt, C. J.; Walker, N.; Maher, D.; Williams, B. G.; Raviglione, M. C.; Dye, C. The Growing Burden of Tuberculosis. *Arch. Intern. Med.* **2003**, *163*, 1009–1021.

(18) Daley, C. L.; Small, P. M.; Schecter, G. F.; Schoolnik, G. K.; McAdam, R. A.; Jacobs, W. R.; Hopewell, P. C. An Outbreak of Tuberculosis with Accelerated Progression among Persons Infected with the Human Immunodeficiency Virus. *N. Engl. J. Med.* **1992**, *326*, 231–235.

(19) Havlir, D. V; Getahun, H.; Sanne, I. Opportunities and Challenges for HIV Care. *J. Am. Med. Assoc.* **2008**, *300*, 423–430.

(20) Narasimhan, P.; Wood, J.; Macintyre, C. R.; Mathai, D. Risk Factors for Tuberculosis. *Pulm. Med.* **2013**, *2013*, 1–12.

(21) Jeon, C. Y.; Murray, M. B. Diabetes Mellitus Increases the Risk of Active Tuberculosis: A Systematic Review of 13 Observational Studies. *PLoS Med.* **2008**, *5*, 1091–1101.

(22) Rehm, J.; Samokhvalov, A. V; Neuman, M. G.; Room, R.; Parry, C.; Lönnroth, K.; Patra, J.; Poznyak, V.; Popova, S. The Association between Alcohol Use, Alcohol Use Disorders and Tuberculosis (TB). A Systematic Review. *BMC Public Health* **2009**, *9*, 450.

(23) Bates, M. N. Risk of Tuberculosis From Exposure to Tobacco Smoke. *Arch. Intern. Med.* **2007**, *167*, 335.

(24) Sepkowitz, K. A. How Contagious Is Tuberculosis? *Clin. Infect. Dis.* **1996**, *23*, 954–962.

(25) Klein, K.; Yang, Z. Comparison of Ambient Air Survival of *Mycobacterium tuberculosis* Clinical Strains Associated with Different Epidemiological Phenotypes. *Int. J. Mycobacteriology* **2014**, *3*, 211–213.

(26) Knechel, N. A. Tuberculosis: Pathophysiology, Clinical Features, and Diagnosis. *Crit. Care Nurse* **2009**, *29*, 34–43.

(27) Quast, T.M.; Browning, R. F. Pathogenesis and Clinical Manifestations of Pulmonary Tuberculosis. *Disease-a-Month* **2006**, *52*, 413–419.

(28) Barry, C. E.; Boshoff, H. I.; Dartois, V.; Dick, T.; Ehrt, S.; Flynn, J.; Schnappinger, D.; Wilkinson, R. J.; Young, D. The Spectrum of Latent Tuberculosis: Rethinking the Biology and Intervention Strategies. *Nat. Rev. Microbiol.* **2009**, *7*, 845–855.

(29) Esmail, H.; Barry, C. E.; Young, D. B.; Wilkinson, R. J. The Ongoing Challenge of Latent Tuberculosis. *Philos. Trans. R. Soc. Lond. B. Biol. Sci.* **2014**, *369*, 20130437.

(30) Lawn, S. D.; Zumla, A. I. Tuberculosis. *Lancet* **2011**, *378*, 57–72.

(31) Orme, I. M.; Robinson, R. T.; Cooper, A. M. The Balance between Protective and Pathogenic Immune Responses in the TB-Infected Lung. *Nat. Immunol.* **2014**, *16*, 57–63.

(32) Russell, D. G. *Mycobacterium tuberculosis* and the Intimate Discourse of a Chronic Infection. *Immunol. Rev.* **2011**, *240*, 252–268.

(33) Pai, M.; Behr, M. A.; Dowdy, D.; Dheda, K.; Divangahi, M.; Boehme, C. C.; Ginsberg, A.; Swaminathan, S.; Spigelman, M.; Getahun, H.; Menzies, D.; Raviglione, *M. tuberculosis*. *Nat. Rev. Dis. Prim.* **2016**, *2*, 1–23.

(34) Yuk, J.-M.; Jo, E.-K. Host Immune Responses to Mycobacterial Antigens and Their Implications for the Development of a Vaccine to Control Tuberculosis. *Clin. Exp. Vaccine Res.* **2014**, *3*, 155–167.

(35) Flynn, J. L.; Chan, J. What's Good for the Host Is Good for the Bug. *Trends Microbiol.* **2005**, *13*, 98–102.

(36) Harries, A. D.; Dye, C. Tuberculosis. *Ann. Trop. Med. Parasitol.* **2006**, *100*, 415–431.

(37) Nahid, P.; Pai, M.; Hopewell, P. C. Advances in the Diagnosis and Treatment of Tuberculosis. *Proc. Am. Thorac. Soc.* **2006**, *3*, 103–110.

(38) Abouda, M.; Yangui, F.; Triki, M.; Kammoun, H.; Khouani, H.; Charfi,

M. R. Prévention de La Tuberculose. *Rev. Pneumol. Clin.* **2015**, *71*, 159–167.

(39) Shah, N. S.; Auld, S. C.; Brust, J. C. M.; Mathema, B.; Ismail, N.; Moodley, P.; Mlisana, K.; Allana, S.; Campbell, A.; Mthiyane, T.; Morris, N.; Mpangase, P.; van der Meulen, H.; Omar, S. V.; Brown, T. S.; Narechania, A.; Shaskina, E.; Kapwata, T.; Kreiswirth, B.; Gandhi, N. R. Transmission of Extensively Drug-Resistant Tuberculosis in South Africa. *N. Engl. J. Med.* **2017**, *376*, 243–253.

(40) Coprada, L.; Yoshimatsu, S.; Querri, A.; Lopez, E.; Agujo, P.; Paulino, M. R.; Medina, A.; Garfin, A. M. C.; Ohkado, A. A Review of Tuberculosis Contact Investigations in the Poor Urban Areas of Manila, The Philippines. *Public Heal. Action* **2016**, *6*, 220–225.

(41) Egere, U.; Sillah, A.; Togun, T.; Kandeh, S.; Cole, F.; Jallow, A.; Able-Thomas, A.; Hoelscher, M.; Heinrich, N.; Hill, P. C.; Kampmann, B. Isoniazid Preventive Treatment among Child Contacts of Adults with Smear-Positive Tuberculosis in The Gambia. *Public Heal. Action* **2016**, *6*, 226–231.

(42) Mitruka, K.; Volkmann, T.; Pratt, R. H.; Kammerer, J. S. Disparities in Tuberculosis Treatment Completion by Incarceration Status, U.S., 1999–2011. *Am. J. Prev. Med.* **2017**, *52*, 483–490.

(43) Landry, J. S.; Menzies, D. Tuberculosis Prevention. In *International Encyclopedia of Public Health*; Elsevier, 2008; pp. 391–397.

(44) González-Martín, J.; García-García, J. M.; Anibarro, L.; Vidal, R.; Esteban, J.; Blanquer, R.; Moreno, S.; Ruiz-Manzano, J. [Consensus Document on the Diagnosis, Treatment and Prevention of Tuberculosis]. *Arch. Bronconeumol.* **2010**, *46*, 255–274.

(45) Pathmanathan, I.; Pevzner, E.; Cavanaugh, J.; Nelson, L. Addressing Tuberculosis in Differentiated Care Provision for People Living with HIV. *Bull. World Health Organ.* **2017**, *95*, 3–3.

(46) Briggs, M. A.; Emerson, C.; Modi, S.; Taylor, N. K.; Date, A. Use of Isoniazid Preventive Therapy for Tuberculosis Prophylaxis among People Living with HIV/AIDS: A Review of the Literature. *J. Acquir. Immune Defic. Syndr.* **2015**, *68 Suppl 3*, S297-305.

(47) Kanabus, A. Information about Tuberculosis http://www.tbfacts.org/tb-prevention/ (accessed Aug 19, 2017).

(48) Jo, K.-W. Preventing the Transmission of Tuberculosis in Health Care Settings: Administrative Control. *Tuberc. Respir. Dis. (Seoul).* **2017**, *80*, 21.

(49) Kaneene, J. B.; Miller, R.; Steele, J. H.; Thoen, C. O. Preventing and Controlling Zoonotic Tuberculosis: A One Health Approach. *Vet. Ital.* **2014**, *50*, 7–22.

(50) Thoen, C. O.; Kaplan, B.; Thoen, T. C.; Gilsdorf, M. J.; Shere, J. A. Zoonotic Tuberculosis. A Comprehensive ONE HEALTH Approach. *Medicina (B. Aires).* **2016**, *76*, 159–165.

(51) Franco-Paredes, C.; Rouphael, N.; del Rio, C.; Santos-Preciado, J. I. Vaccination Strategies to Prevent Tuberculosis in the New Millennium: From BCG to New Vaccine Candidates. *Int. J. Infect. Dis.* **2006**, *10*, 93–102.

(52) Brewer, T. F. Preventing Tuberculosis with Bacillus Calmette-Guérin Vaccine: A Meta-Analysis of the Literature. *Clin. Infect. Dis.* **2000**, *31 Suppl 3*, S64-7.

(53) Chawla, S.; Garg, D.; Jain, R. B.; Khanna, P.; Choudhary, S.; Sahoo, S.; Singh, I. Tuberculosis Vaccine: Time to Look into Future. *Hum. Vaccin. Immunother.* **2014**, *10*, 420–422.

(54) Hatherill, M.; Tait, D.; McShane, H. Clinical Testing of Tuberculosis Vaccine Candidates. *Microbiol. Spectr.* **2016**, *4*, 1–18.

(55) World Health Organization. *Drug-Resistant TB Surveillance and Response. Supplement to Global TB Report 2014*; Geneva, 2014.

(56) World Health Organization. *Companion Handbook*; Geneva, 2014.

(57) World Health Organization. *WHO Treatment Guidelines for Drug-Resistant Tuberculosis*; Geneva, 2016.

(58) API Consensus Expert Committee. API TB Consensus Guidelines 2006: Management of Pulmonary Tuberculosis, Extra-Pulmonary Tuberculosis and Tuberculosis in Special Situations. *J. Assoc. Physicians India* **2006**, *54*, 219–234.

(59) Nahid, P.; Dorman, S. E.; Alipanah, N.; Barry, P. M.; Brozek, J. L.; Cattamanchi, A.; Chaisson, L. H.; Chaisson, R. E.; Daley, C. L.; Grzemska, M.; Higashi, J. M.; Ho, C. S.; Hopewell, P. C.; Keshavjee, S. A.; Lienhardt, C.; Menzies, R.; Merrifield, C.; Narita, M.; O'Brien, R.; Peloquin, C. A.; Raftery, A.; Saukkonen, J.; Schaaf, H. S.; Sotgiu, G.; Starke, J. R.; Migliori, G. B.; Vernon, A. Official American Thoracic Society/Centers for Disease Control and Prevention/Infectious Diseases Society of America Clinical Practice Guidelines: Treatment of Drug-Susceptible Tuberculosis. *Clin. Infect. Dis.* **2016**, *63*, 853–867.

(60) Karumbi, J.; Garner, P. Directly Observed Therapy for Treating Tuberculosis. In *Cochrane Database of Systematic Reviews*; Karumbi,

J., Ed.; John Wiley & Sons, Ltd: Chichester, UK, 2015.

(61) Toujani, S.; Ben Safta, B.; Ben Salah, N.; Mjid, M.; Ouahchi, Y.; Louzir, B.; Daghfous, J.; Cherif, J.; Mehiri, N.; Beji, M. Contribution of Fixed-Dose Combinations in the Treatment of Tuberculosis. *Tunis. Med.* **2016**, *94*, 401–405.

(62) Gallardo, C. R.; Rigau Comas, D.; Valderrama Rodríguez, A.; Roqué i Figuls, M.; Parker, L. A.; Caylà, J.; Bonfill Cosp, X. Fixed-Dose Combinations of Drugs versus Single-Drug Formulations for Treating Pulmonary Tuberculosis. In *Cochrane Database of Systematic Reviews*; Gallardo, C. R., Ed.; John Wiley & Sons, Ltd: Chichester, UK, 2016.

(63) Lienhardt, C.; Cook, S. V; Burgos, M.; Yorke-Edwards, V.; Rigouts, L.; Anyo, G.; Kim, S.-J.; Jindani, A.; Enarson, D. A.; Nunn, A. J.; Study C Trial Group. Efficacy and Safety of a 4-Drug Fixed-Dose Combination Regimen Compared with Separate Drugs for Treatment of Pulmonary Tuberculosis: The Study C Randomized Controlled Trial. *JAMA* **2011**, *305*, 1415–1423.

(64) Zuur, M. A.; Akkerman, O. W.; Davies Forsman, L.; Hu, Y.; Zheng, R.; Bruchfeld, J.; Tiberi, S.; Migliori, G. B.; Alffenaar, J.-W. C. Fixed-Dose Combination and Therapeutic Drug Monitoring in Tuberculosis: Friend or Foe? *Eur. Respir. J.* **2016**, *48*, 1230–1233.

(65) Yee, D.; Valiquette, C.; Pelletier, M.; Parisien, I.; Rocher, I.; Menzies, D. Incidence of Serious Side Effects from First-Line Antituberculosis Drugs among Patients Treated for Active Tuberculosis. *Am. J. Respir. Crit. Care Med.* **2003**, *167*, 1472–1477.

(66) van Hest, R.; Baars, H.; Kik, S.; van Gerven, P.; Trompenaars, M.-C.; Kalisvaart, N.; Keizer, S.; Borgdorff, M.; Mensen, M.; Cobelens, F. Hepatotoxicity of Rifampin-Pyrazinamide and Isoniazid Preventive Therapy and Tuberculosis Treatment. *Clin. Infect. Dis.* **2004**, *39*, 488–496.

(67) Cojutti, P.; Duranti, S.; Isola, M.; Baraldo, M.; Viale, P.; Bassetti, M.; Pea, F. Might Isoniazid Plasma Exposure Be a Valuable Predictor of Drug-Related Hepatotoxicity Risk among Adult Patients with TB? *J. Antimicrob. Chemother.* **2016**, *71*, 1323–1329.

(68) Li, Y.; Zhu, Y.; Zhong, Q.; Zhang, X.; Shu, M.; Wan, C. Serious Adverse Reactions from Anti-Tuberculosis Drugs Among 599 Children Hospitalized for Tuberculosis. *Pediatr. Infect. Dis. J.* **2017**, *36*, 720–725.

(69) Peloquin, C. The Role of Therapeutic Drug Monitoring in

Mycobacterial Infections. *Microbiol. Spectr.* **2017**, *5*, 1–8.

(70) Zumla, A.; Nahid, P.; Cole, S. T. Advances in the Development of New Tuberculosis Drugs and Treatment Regimens. *Nat. Rev. Drug Discov.* **2013**, *12*, 388–404.

(71) Jena, L.; Nayak, T.; Deshmukh, S.; Wankhade, G.; Waghmare, P.; Harinath, B. C. Isoniazid with Multiple Mode of Action on Various Mycobacterial Enzymes Resulting in Drug Resistance. *J. Infect. Dis. Ther.* **2016**, *4*, 1–8.

(72) Nguyen, M.; Claparols, C.; Bernadou, J.; Meunier, B. A Fast and Efficient Metal-Mediated Oxidation of Isoniazid and Identification of Isoniazid-NAD(H) Adducts. *Chembiochem* **2001**, *2*, 877–883.

(73) Zhao, X.; Yu, H.; Yu, S.; Wang, F.; Sacchettini, J. C.; Magliozzo, R. S. Hydrogen Peroxide-Mediated Isoniazid Activation Catalyzed by *Mycobacterium tuberculosis* Catalase−Peroxidase (KatG) and Its S315T Mutant. *Biochemistry* **2006**, *45*, 4131–4140.

(74) Argyrou, A.; Jin, L.; Siconilfi-Baez, L.; Angeletti, R. H.; Blanchard, J. S. Proteome-Wide Profiling of Isoniazid Targets in *Mycobacterium tuberculosis*. *Biochemistry* **2006**, *45*, 13947–13953.

(75) Timmins, G. S.; Deretic, V. Mechanisms of Action of Isoniazid. *Mol. Microbiol.* **2006**, *62*, 1220–1227.

(76) Sandy, J. Binding of the Anti-Tubercular Drug Isoniazid to the Arylamine N-Acetyltransferase Protein from Mycobacterium Smegmatis. *Protein Sci.* **2005**, *14*, 775–782.

(77) Rawat, R.; Whitty, A.; Tonge, P. J. The Isoniazid-NAD Adduct Is a Slow, Tight-Binding Inhibitor of InhA, the *Mycobacterium tuberculosis* Enoyl Reductase: Adduct Affinity and Drug Resistance. *Proc. Natl. Acad. Sci.* **2003**, *100*, 13881–13886.

(78) Vilchèze, C.; Jacobs, W. R. Resistance to Isoniazid and Ethionamide in *Mycobacterium tuberculosis*: Genes, Mutations, and Causalities. *Microbiol. Spectr.* **2014**, *2*, MGM2-0014-2013.

(79) Shekar, S.; Yeo, Z. X.; Wong, J. C. L.; Chan, M. K. L.; Ong, D. C. T.; Tongyoo, P.; Wong, S.-Y.; Lee, A. S. G. Detecting Novel Genetic Variants Associated with Isoniazid-Resistant *Mycobacterium tuberculosis*. *PLoS One* **2014**, *9*, e102383.

(80) Lester, W. Rifampin: A Semisynthetic Derivative of Rifamycin-A Prototype for the Future. *Annu. Rev. Microbiol.* **1972**, *26*, 85–102.

(81) Floss, H. G.; Yu, T.-W. Rifamycin Mode of Action, Resistance, and Biosynthesis. *Chem. Rev.* **2005**, *105*, 621–632.

(82) Wehrli, W. Rifampin: Mechanisms of Action and Resistance. *Rev. Infect. Dis.* **1983**, *5 Suppl 3*, S407-11.

(83) De La Iglesia, A. I.; Morbidoni, H. R. Mechanisms of Action of and Resistance to Rifampicin and Isoniazid in *Mycobacterium tuberculosis*: New Information on Old Friends. *Rev. Argent. Microbiol.* **2006**, *38*, 97–109.

(84) Somoskovi, A.; Parsons, L. M.; Salfinger, M. The Molecular Basis of Resistance to Isoniazid, Rifampin, and Pyrazinamide in *Mycobacterium tuberculosis*. *Respir. Res.* **2001**, *2*, 164–168.

(85) Palomino, J.; Martin, A. Drug Resistance Mechanisms in *Mycobacterium tuberculosis*. *Antibiotics* **2014**, *3*, 317–340.

(86) Zhang, Y.; Mitchison, D. The Curious Characteristics of Pyrazinamide: A Review. *Int. J. Tuberc. Lung Dis.* **2003**, *7*, 6–21.

(87) Shi, W.; Zhang, X.; Jiang, X.; Yuan, H.; Lee, J. S.; Barry, C. E.; Wang, H.; Zhang, W.; Zhang, Y. Pyrazinamide Inhibits Trans-Translation in *Mycobacterium tuberculosis*. *Science* **2011**, *333*, 1630–1632.

(88) Peterson ND, Rosen BC, Dillon NA, Baughn AD. Uncoupling environmental pH and intrabacterial acidification from pyrazinamide susceptibility in *Mycobacterium tuberculosis*. *Antimicrob. Agents. Chemother.* **2015**, *59*, 7320–7326

(89) Dillon, N. A.; Peterson, N. D.; Feaga, H. A.; Keiler, K. C.; Baughn, A. D. Anti-Tubercular Activity of Pyrazinamide Is Independent of Trans-Translation and RpsA. *Sci. Rep.* **2017**, *7*, 6135.

(90) Sun, Z.; Zhang, Y. Reduced Pyrazinamidase Activity and the Natural Resistance of Mycobacterium Kansasii to the Antituberculosis Drug Pyrazinamide. *Antimicrob. Agents Chemother.* **1999**, *43*, 537–542.

(91) Sheen, P.; Lozano, K.; Gilman, R. H.; Valencia, H. J.; Loli, S.; Fuentes, P.; Grandjean, L.; Zimic, M. pncA Gene Expression and Prediction Factors on Pyrazinamide Resistance in *Mycobacterium tuberculosis*. *Tuberculosis (Edinb).* **2013**, *93*, 515–522.

(92) Mikusová, K.; Slayden, R. A.; Besra, G. S.; Brennan, P. J. Biogenesis of the Mycobacterial Cell Wall and the Site of Action of Ethambutol . Biogenesis of the Mycobacterial Cell Wall and the Site of Action of Ethambutol. *Antimicrob. Agents Chemother.* **1995**, *39*, 2484–2489.

(93) Ramaswamy, S. V; Amin, A. G.; Göksel, S.; Stager, C. E.; Dou, S. J.; El Sahly, H.; Moghazeh, S. L.; Kreiswirth, B. N.; Musser, J. M. Molecular Genetic Analysis of Nucleotide Polymorphisms Associated with Ethambutol Resistance in Human Isolates of *Mycobacterium*

tuberculosis. *Antimicrob. Agents Chemother.* **2000**, *44*, 326–336.

(94) Radmacher, E.; Stansen, K. C.; Besra, G. S.; Alderwick, L. J.; Maughan, W. N.; Hollweg, G.; Sahm, H.; Wendisch, V. F.; Eggeling, L. Ethambutol, a Cell Wall Inhibitor of *Mycobacterium tuberculosis*, Elicits L-Glutamate Efflux of Corynebacterium Glutamicum. *Microbiology* **2005**, *151*, 1359–1368.

(95) Telenti, A.; Philipp, W. J.; Sreevatsan, S.; Bernasconi, C.; Stockbauer, K. E.; Wieles, B.; Musser, J. M.; Jacobs, W. R. The Emb Operon, a Gene Cluster of *Mycobacterium tuberculosis* Involved in Resistance to Ethambutol. *Nat. Med.* **1997**, *3*, 567–570.

(96) Grosset, J. H.; Singer, T. Streptomycin. In *Brenner's Encyclopedia of Genetics*; Elsevier, 2013; pp. 568–569.

(97) Kotra, L. P.; Haddad, J.; Mobashery, S. Aminoglycosides: Perspectives on Mechanisms of Action and Resistance and Strategies to Counter Resistance. *Antimicrob. Agents Chemother.* **2000**, *44*, 3249–3256.

(98) Gillespie, S. H. Evolution of Drug Resistance in *Mycobacterium tuberculosis*: Clinical and Molecular Perspective. *Antimicrob. Agents Chemother.* **2002**, *46*, 267–274.

(99) World Health Organization. *Treatment of Tuberculosis Guidelines*; Geneva, 2010.

(100) Uthman, O. A.; Okwundu, C.; Gbenga, K.; Volmink, J.; Dowdy, D.; Zumla, A.; Nachega, J. B. Optimal Timing of Antiretroviral Therapy Initiation for HIV-Infected Adults With Newly Diagnosed Pulmonary Tuberculosis: A Systematic Review and Meta-Analysis. *Ann. Intern. Med.* **2015**, *163*, 32–39.

(101) Mfinanga, S. G.; Kirenga, B. J.; Chanda, D. M.; Mutayoba, B.; Mthiyane, T.; Yimer, G.; Ezechi, O.; Connolly, C.; Kapotwe, V.; Muwonge, C.; Massaga, J.; Sinkala, E.; Kohi, W.; Lyantumba, L.; Nyakoojo, G.; Luwaga, H.; Doulla, B.; Mzyece, J.; Kapata, N.; Vahedi, M.; Mwaba, P.; Egwaga, S.; Adatu, F.; Pym, A.; Joloba, M.; Rustomjee, R.; Zumla, A.; Onyebujoh, P. Early versus Delayed Initiation of Highly Active Antiretroviral Therapy for HIV-Positive Adults with Newly Diagnosed Pulmonary Tuberculosis (TB-HAART): A Prospective, International, Randomised, Placebo-Controlled Trial. *Lancet. Infect. Dis.* **2014**, *14*, 563–571.

(102) Odone, A.; Amadasi, S.; White, R. G.; Cohen, T.; Grant, A. D.; Houben, R. M. G. J. The Impact of Antiretroviral Therapy on Mortality in HIV Positive People during Tuberculosis Treatment: A Systematic Review and Meta-Analysis. *PLoS One* **2014**, *9*, e112017.

(103) Naidoo, K.; Yende-Zuma, N.; Padayatchi, N.; Naidoo, K.; Jithoo, N.; Nair, G.; Bamber, S.; Gengiah, S.; El-Sadr, W. M.; Friedland, G.; Abdool Karim, S. The Immune Reconstitution Inflammatory Syndrome after Antiretroviral Therapy Initiation in Patients with Tuberculosis: Findings from the SAPiT Trial. *Ann. Intern. Med.* **2012**, *157*, 313–324.

(104) Laureillard, D.; Marcy, O.; Madec, Y.; Chea, S.; Chan, S.; Borand, L.; Fernandez, M.; Prak, N.; Kim, C.; Dim, B.; Nerrienet, E.; Sok, T.; Delfraissy, J.-F.; Goldfeld, A. E.; Blanc, F.-X.; CAMELIA (ANRS 1295 – CIPRA KH001) Study Team. Paradoxical Tuberculosis-Associated Immune Reconstitution Inflammatory Syndrome after Early Initiation of Antiretroviral Therapy in a Randomized Clinical Trial. *AIDS* **2013**, *27*, 2577–2586.

(105) Mack, U.; Migliori, G. B.; Sester, M.; Rieder, H. L.; Ehlers, S.; Goletti, D.; Bossink, A.; Magdorf, K.; Holscher, C.; Kampmann, B.; Arend, S. M.; Detjen, A.; Bothamley, G.; Zellweger, J. P.; Milburn, H.; Diel, R.; Ravn, P.; Cobelens, F.; Cardona, P. J.; Kan, B.; Solovic, I.; Duarte, R.; Cirillo, D. M. LTBI: Latent Tuberculosis Infection or Lasting Immune Responses to M. Tuberculosis? A TBNET Consensus Statement. *Eur. Respir. J.* **2009**, *33*, 956–973.

(106) World Health Organization. *Guidelines on the Management of Latent Tuberculosis Infection*; Geneva, 2015.

(107) Pai, M.; Denkinger, C. M.; Kik, S. V.; Rangaka, M. X.; Zwerling, A.; Oxlade, O.; Metcalfe, J. Z.; Cattamanchi, A.; Dowdy, D. W.; Dheda, K.; Banaei, N. Gamma Interferon Release Assays for Detection of *Mycobacterium tuberculosis* Infection. *Clin. Microbiol. Rev.* **2014**, *27*, 3–20.

(108) Pai, M.; Behr, M. Latent *Mycobacterium tuberculosis* Infection and Interferon-Gamma Release Assays. *Microbiol. Spectr.* **2016**, *4*.

(109) Sharma, S. K.; Sharma, A.; Kadhiravan, T.; Tharyan, P. Rifamycins (Rifampicin, Rifabutin and Rifapentine) Compared to Isoniazid for Preventing Tuberculosis in HIV-Negative People at Risk of Active TB. In *Cochrane Database of Systematic Reviews*; Sharma, S. K., Ed.; John Wiley & Sons, Ltd: Chichester, UK, 2013; p. CD007545.

(110) Lobue, P.; Menzies, D. Treatment of Latent Tuberculosis Infection: An Update. *Respirology* **2010**, *15*, 603–622.

(111) Fox, G. J.; Dobler, C. C.; Marais, B. J.; Denholm, J. T. Preventive Therapy for Latent Tuberculosis Infection-the Promise and the Challenges. *Int. J. Infect. Dis.* **2017**, *56*, 68–76.

(112) Velayati, A. A.; Farnia, P.; Farahbod, A. M. Overview of Drug-Resistant

Tuberculosis Worldwide. *Int. J. Mycobacteriology* **2016**, *5*, S161.

(113) Dheda, K.; Limberis, J. D.; Pietersen, E.; Phelan, J.; Esmail, A.; Lesosky, M.; Fennelly, K. P.; Te Riele, J.; Mastrapa, B.; Streicher, E. M.; Dolby, T.; Abdallah, A. M.; Ben-Rached, F.; Simpson, J.; Smith, L.; Gumbo, T.; van Helden, P.; Sirgel, F. A.; McNerney, R.; Theron, G.; Pain, A.; Clark, T. G.; Warren, R. M. Outcomes, Infectiousness, and Transmission Dynamics of Patients with Extensively Drug-Resistant Tuberculosis and Home-Discharged Patients with Programmatically Incurable Tuberculosis: A Prospective Cohort Study. *Lancet. Respir. Med.* **2017**, *5*, 269–281.

(114) Detjen, A. K.; DiNardo, A. R.; Leyden, J.; Steingart, K. R.; Menzies, D.; Schiller, I.; Dendukuri, N.; Mandalakas, A. M. Xpert MTB/RIF Assay for the Diagnosis of Pulmonary Tuberculosis in Children: A Systematic Review and Meta-Analysis. *Lancet Respir. Med.* **2015**, *3*, 451–461.

(115) Raizada, N.; Sachdeva, K. S.; Nair, S. A.; Kulsange, S.; Gupta, R. S.; Thakur, R.; Parmar, M.; Gray, C.; Ramachandran, R.; Vadera, B.; Ekka, S.; Dhawan, S.; Babre, A.; Ghedia, M.; Alavadi, U.; Dewan, P.; Khetrapal, M.; Khanna, A.; Boehme, C.; Paramsivan, C. N. Enhancing TB Case Detection: Experience in Offering Upfront Xpert MTB/RIF Testing to Pediatric Presumptive TB and DR TB Cases for Early Rapid Diagnosis of Drug Sensitive and Drug Resistant TB. *PLoS One* **2014**, *9*, e105346.

(116) Steingart, K. R.; Schiller, I.; Horne, D. J.; Pai, M.; Boehme, C. C.; Dendukuri, N. Xpert® MTB/RIF Assay for Pulmonary Tuberculosis and Rifampicin Resistance in Adults. In *Cochrane Database of Systematic Reviews*; Steingart, K. R., Ed.; John Wiley & Sons, Ltd: Chichester, UK, 2014.

(117) Blakemore, R.; Story, E.; Helb, D.; Kop, J.; Banada, P.; Owens, M. R.; Chakravorty, S.; Jones, M.; Alland, D. Evaluation of the Analytical Performance of the Xpert MTB/RIF Assay. *J. Clin. Microbiol.* **2010**, *48*, 2495–2501.

(118) Iruedo, J.; O'Mahony, D.; Mabunda, S.; Wright, G.; Cawe, B. The Effect of the Xpert MTB/RIF Test on the Time to MDR-TB Treatment Initiation in a Rural Setting: A Cohort Study in South Africa's Eastern Cape Province. *BMC Infect. Dis.* **2017**, *17*, 1–9.

(119) World Health Organization. *The Use of Loop-Mediated Isothermal Amplification (TB-LAMP) for the Diagnosis of Pulmonary Tuberculosis*; Geneva, 2016.

(120) World Health Organization. *Molecular Line Probe Assays for Rapid*

Screening of Patients at Risk of Multidrug-Resistant Tuberculosis; Geneva, 2008.

(121) World Health Organization. *Tuberculosis Diagnostics Technology and Market Landscape*; Geneva, 2014.

(122) Tiberi, S.; Scardigli, A.; Centis, R.; D'Ambrosio, L.; Muñoz-Torrico, M.; Salazar-Lezama, M. Á.; Spanevello, A.; Visca, D.; Zumla, A.; Migliori, G. B.; Caminero Luna, J. A. Classifying New Anti-Tuberculosis Drugs: Rationale and Future Perspectives. *Int. J. Infect. Dis.* **2017**, *56*, 181–184.

(123) Walker, R. C. The Fluoroquinolones. *Mayo Clin. Proc.* **1999**, *74*, 1030–1037.

(124) Ginsburg, A. S.; Grosset, J. H.; Bishai, W. R. Fluoroquinolones, Tuberculosis, and Resistance. *Lancet Infect. Dis.* **2003**, *3*, 432–442.

(125) Hooper, D. C. Mechanisms of Action and Resistance of Older and Newer Fluoroquinolones. *Clin. Infect. Dis.* **2000**, *31 Suppl 2*, S24-8.

(126) Briasoulis, A.; Agarwal, V.; Pierce, W. J. QT Prolongation and Torsade de Pointes Induced by Fluoroquinolones: Infrequent Side Effects from Commonly Used Medications. *Cardiology* **2011**, *120*, 103–110.

(127) Akbergenov, R.; Shcherbakov, D.; Matt, T.; Duscha, S.; Meyer, M.; Wilson, D. N.; Bottger, E. C. Molecular Basis for the Selectivity of Antituberculosis Compounds Capreomycin and Viomycin. *Antimicrob. Agents Chemother.* **2011**, *55*, 4712–4717.

(128) Lee, M.; Lee, J.; Carroll, M. W.; Choi, H.; Min, S.; Song, T.; Via, L. E.; Goldfeder, L. C.; Kang, E.; Jin, B.; Park, H.; Kwak, H.; Kim, H.; Jeon, H.-S.; Jeong, I.; Joh, J. S.; Chen, R. Y.; Olivier, K. N.; Shaw, P. A.; Follmann, D.; Song, S. D.; Lee, J.-K.; Lee, D.; Kim, C. T.; Dartois, V.; Park, S.-K.; Cho, S.-N.; Barry, C. E. Linezolid for Treatment of Chronic Extensively Drug-Resistant Tuberculosis. *N. Engl. J. Med.* **2012**, *367*, 1508–1518.

(129) Rose, P. C.; Hallbauer, U. M.; Seddon, J. A.; Hesseling, A. C.; Schaaf, H. S. Linezolid-Containing Regimens for the Treatment of Drug-Resistant Tuberculosis in South African Children. *Int. J. Tuberc. Lung Dis.* **2012**, *16*, 1588–1593.

(130) Gopal, M.; Padayatchi, N.; Metcalfe, J. Z.; O'Donnell, M. R. Systematic Review of Clofazimine for the Treatment of Drug-Resistant Tuberculosis [Review Article]. *Int. J. Tuberc. Lung Dis.* **2013**, *17*, 1001–1007.

(131) Tang, S.; Yao, L.; Hao, X.; Liu, Y.; Zeng, L.; Liu, G.; Li, M.; Li, F.; Wu,

M.; Zhu, Y.; Sun, H.; Gu, J.; Wang, X.; Zhang, Z. Clofazimine for the Treatment of Multidrug-Resistant Tuberculosis: Prospective, Multicenter, Randomized Controlled Study in China. *Clin. Infect. Dis.* **2015**, *60*, 1361–1367.

(132) Goel, D. Bedaquiline: A Novel Drug to Combat Multiple Drug-Resistant Tuberculosis. *J. Pharmacol. Pharmacother.* **2014**, *5*, 76–8.

(133) Cox, E.; Laessig, K. FDA Approval of Bedaquiline — The Benefit–Risk Balance for Drug-Resistant Tuberculosis. *N. Engl. J. Med.* **2014**, *371*, 689–691.

(134) Xavier, A.; Lakshmanan, M. Delamanid: A New Armor in Combating Drug-Resistant Tuberculosis. *J. Pharmacol. Pharmacother.* **2014**, *5*, 222–224.

(135) Lewis, J. M.; Sloan, D. J. The Role of Delamanid in the Treatment of Drug-Resistant Tuberculosis. *Ther. Clin. Risk Manag.* **2015**, *11*, 779–791.

(136) Andries, K.; Verhasselt, P.; Guillemont, J.; Göhlmann, H. W. H.; Neefs, J.-M.; Winkler, H.; van Gestel, J.; Timmerman, P.; Zhu, M.; Lee, E.; Williams, P.; de Chaffoy, D.; Huitric, E.; Hoffner, S.; Cambau, E.; Truffot-Pernot, C.; Lounis, N.; Jarlier, V. A Diarylquinoline Drug Active on the ATP Synthase of *Mycobacterium tuberculosis*. *Science* **2005**, *307*, 223–227.

(137) Gualano, G.; Capone, S.; Matteelli, A.; Palmieri, F. New Antituberculosis Drugs: From Clinical Trial to Programmatic Use. *Infect. Dis. Rep.* **2016**, *8*, 43–49.

(138) Lu, X.; Smare, C.; Kambili, C.; El Khoury, A. C.; Wolfson, L. J. Health Outcomes of Bedaquiline in the Treatment of Multidrug-Resistant Tuberculosis in Selected High Burden Countries. *BMC Health Serv. Res.* **2017**, *17*, 87–98.

(139) Wolfson, L. J.; Walker, A.; Hettle, R.; Lu, X.; Kambili, C.; Murungi, A.; Knerer, G. Cost-Effectiveness of Adding Bedaquiline to Drug Regimens for the Treatment of Multidrug-Resistant Tuberculosis in the UK. *PLoS One* **2015**, *10*, e0120763.

(140) Matsumoto, M.; Hashizume, H.; Tomishige, T.; Kawasaki, M.; Tsubouchi, H.; Sasaki, H.; Shimokawa, Y.; Komatsu, M. OPC-67683, a Nitro-Dihydro-Imidazooxazole Derivative with Promising Action against Tuberculosis *in vitro* and in Mice. *PLoS Med.* **2006**, *3*, e466.

(141) Laurenzi, M.; Ginsberg, A.; Spigelman, M. Challenges Associated with Current and Future TB Treatment. *Infect. Disord. Drug Targets* **2007**,

7, 105–119.

(142) Burman, W. J.; Jones, B. E. Treatment of HIV-Related Tuberculosis in the Era of Effective Antiretroviral Therapy. *Am. J. Respir. Crit. Care Med.* **2001**, *164*, 7–12.

(143) Burman, W. J.; Gallicano, K.; Peloquin, C. Therapeutic Implications of Drug Interactions in the Treatment of Human Immunodeficiency Virus-Related Tuberculosis. *Clin. Infect. Dis.* **1999**, *28*, 419–429.

(144) Dean, G. L.; Edwards, S. G.; Ives, N. J.; Matthews, G.; Fox, E. F.; Navaratne, L.; Fisher, M.; Taylor, G. P.; Miller, R.; Taylor, C. B.; de Ruiter, A.; Pozniak, A. L. Treatment of Tuberculosis in HIV-Infected Persons in the Era of Highly Active Antiretroviral Therapy. *AIDS* **2002**, *16*, 75–83.

(145) Flanigan, T. P.; Carter, E. J.; Kwara, A. Highly Active Antiretroviral Therapy (HAART) in Adults with Tuberculosis: Current Status. *Int. J. Tuberc. Lung Dis.* **2005**, *9*, 248–257.

(146) Rangaka, M. X.; Wilkinson, R. J.; Boulle, A.; Glynn, J. R.; Fielding, K.; van Cutsem, G.; Wilkinson, K. A.; Goliath, R.; Mathee, S.; Goemaere, E.; Maartens, G. Isoniazid plus Antiretroviral Therapy to Prevent Tuberculosis: A Randomised Double-Blind, Placebo-Controlled Trial. *Lancet* **2014**, *384*, 682–690.

(147) Baghaei, P.; Marjani, M.; Javanmard, P.; Tabarsi, P.; Masjedi, M. Diabetes Mellitus and Tuberculosis Facts and Controversies. *J. Diabetes Metab. Disord.* **2013**, *12*, 58.

(148) Wallis, R. S.; Maeurer, M.; Mwaba, P.; Chakaya, J.; Rustomjee, R.; Migliori, G. B.; Marais, B.; Schito, M.; Churchyard, G.; Swaminathan, S.; Hoelscher, M.; Zumla, A. Tuberculosis-Advances in Development of New Drugs, Treatment Regimens, Host-Directed Therapies, and Biomarkers. *Lancet Infect. Dis.* **2016**, *16*, e34–e46.

(149) Ginsberg, A. M.; Spigelman, M. Challenges in Tuberculosis Drug Research and Development. *Nat. Med.* **2007**, *13*, 290–294.

(150) TB drug pipeline http://www.newtbdrugs.org/ (accessed Aug 19, 2017).

(151) Clinical trials https://www.clinicaltrials.gov/ (accessed Aug 19, 2017).

(152) Diacon, A. H.; Pym, A.; Grobusch, M. P.; de los Rios, J. M.; Gotuzzo, E.; Vasilyeva, I.; Leimane, V.; Andries, K.; Bakare, N.; De Marez, T.; Haxaire-Theeuwes, M.; Lounis, N.; Meyvisch, P.; De Paepe, E.; van Heeswijk, R. P. G.; Dannemann, B. Multidrug-Resistant Tuberculosis and Culture Conversion with Bedaquiline. *N. Engl. J. Med.* **2014**, *371*,

723–732.

(153) Sloan, D. J.; Lewis, J. M. Management of Multidrug-Resistant TB: Novel Treatments and Their Expansion to Low Resource Settings. *Trans. R. Soc. Trop. Med. Hyg.* **2016**, *110*, 163–172.

(154) Rustomjee, R.; Zumla, A. Delamanid Expanded Access Novel Treatment of Drug Resistant Tuberculosis. *Infect. Drug Resist.* **2015**, *8*, 359–366.

(155) Stover, C. K.; Warrener, P.; VanDevanter, D. R.; Sherman, D. R.; Arain, T. M.; Langhorne, M. H.; Anderson, S. W.; Towell, J. A.; Yuan, Y.; McMurray, D. N.; Kreiswirth, B. N.; Barry, C. E.; Baker, W. R. A Small-Molecule Nitroimidazopyran Drug Candidate for the Treatment of Tuberculosis. *Nature* **2000**, *405*, 962–966.

(156) Haver, H. L.; Chua, A.; Ghode, P.; Lakshminarayana, S. B.; Singhal, A.; Mathema, B.; Wintjens, R.; Bifani, P. Mutations in Genes for the F 420 Biosynthetic Pathway and a Nitroreductase Enzyme Are the Primary Resistance Determinants in Spontaneous *In vitro* -Selected PA-824-Resistant Mutants of *Mycobacterium tuberculosis*. *Antimicrob. Agents Chemother.* **2015**, *59*, 5316–5323.

(157) Singh, R.; Manjunatha, U.; Boshoff, H. I. M.; Ha, Y. H.; Niyomrattanakit, P.; Ledwidge, R.; Dowd, C. S.; Lee, I. Y.; Kim, P.; Zhang, L.; Kang, S.; Keller, T. H.; Jiricek, J.; Barry, C. E. PA-824 Kills Nonreplicating *Mycobacterium tuberculosis* by Intracellular NO Release. *Science (80-.).* **2008**, *322*, 1392–1395.

(158) Dawson, R.; Diacon, A. H.; Everitt, D.; van Niekerk, C.; Donald, P. R.; Burger, D. A.; Schall, R.; Spigelman, M.; Conradie, A.; Eisenach, K.; Venter, A.; Ive, P.; Page-Shipp, L.; Variava, E.; Reither, K.; Ntinginya, N. E.; Pym, A.; von Groote-Bidlingmaier, F.; Mendel, C. M. Efficiency and Safety of the Combination of Moxifloxacin, Pretomanid (PA-824), and Pyrazinamide during the First 8 Weeks of Antituberculosis Treatment: A Phase 2b, Open-Label, Partly Randomised Trial in Patients with Drug-Susceptible or Drug-Resistant Pul. *Lancet* **2015**, *385*, 1738–1747.

(159) Wallis, R. S.; Dawson, R.; Friedrich, S. O.; Venter, A.; Paige, D.; Zhu, T.; Silvia, A.; Gobey, J.; Ellery, C.; Zhang, Y.; Eisenach, K.; Miller, P.; Diacon, A. H. Mycobactericidal Activity of Sutezolid (PNU-100480) in Sputum (EBA) and Blood (WBA) of Patients with Pulmonary Tuberculosis. *PLoS One* **2014**, *9*, e94462.

(160) Sacksteder, K. A.; Protopopova, M.; Barry, C. E.; Andries, K.; Nacy, C. A. Discovery and Development of SQ109: A New Antitubercular Drug

with a Novel Mechanism of Action. *Future Microbiol.* **2012**, *7*, 823–837.

(161) Tahlan, K.; Wilson, R.; Kastrinsky, D. B.; Arora, K.; Nair, V.; Fischer, E.; Barnes, S. W.; Walker, J. R.; Alland, D.; Barry, C. E.; Boshoff, H. I. SQ109 Targets MmpL3, a Membrane Transporter of Trehalose Monomycolate Involved in Mycolic Acid Donation to the Cell Wall Core of *Mycobacterium tuberculosis*. *Antimicrob. Agents Chemother.* **2012**, *56*, 1797–1809.

(162) Protopopova, M. Identification of a New Antitubercular Drug Candidate, SQ109, from a Combinatorial Library of 1,2-Ethylenediamines. *J. Antimicrob. Chemother.* **2005**, *56*, 968–974.

(163) Li, W.; Upadhyay, A.; Fontes, F. L.; North, E. J.; Wang, Y.; Crans, D. C.; Grzegorzewicz, A. E.; Jones, V.; Franzblau, S. G.; Lee, R. E.; Crick, D. C.; Jackson, M. Novel Insights into the Mechanism of Inhibition of MmpL3, a Target of Multiple Pharmacophores in *Mycobacterium tuberculosis*. *Antimicrob. Agents Chemother.* **2014**, *58*, 6413–6423.

(164) Pethe, K.; Bifani, P.; Jang, J.; Kang, S.; Park, S.; Ahn, S.; Jiricek, J.; Jung, J.; Jeon, H. K.; Cechetto, J.; Christophe, T.; Lee, H.; Kempf, M.; Jackson, M.; Lenaerts, A. J.; Pham, H.; Jones, V.; Seo, M. J.; Kim, Y. M.; Seo, M.; Seo, J. J.; Park, D.; Ko, Y.; Choi, I.; Kim, R.; Kim, S. Y.; Lim, S.; Yim, S.-A.; Nam, J.; Kang, H.; Kwon, H.; Oh, C.-T.; Cho, Y.; Jang, Y.; Kim, J.; Chua, A.; Tan, B. H.; Nanjundappa, M. B.; Rao, S. P. S.; Barnes, W. S.; Wintjens, R.; Walker, J. R.; Alonso, S.; Lee, S.; Kim, J.; Oh, S.; Oh, T.; Nehrbass, U.; Han, S.-J.; No, Z.; Lee, J.; Brodin, P.; Cho, S.-N.; Nam, K.; Kim, J. Discovery of Q203, a Potent Clinical Candidate for the Treatment of Tuberculosis. *Nat. Med.* **2013**, *19*, 1157–1160.

(165) Kang, S.; Kim, R. Y.; Seo, M. J.; Lee, S.; Kim, Y. M.; Seo, M.; Seo, J. J.; Ko, Y.; Choi, I.; Jang, J.; Nam, J.; Park, S.; Kang, H.; Kim, H. J.; Kim, J.; Ahn, S.; Pethe, K.; Nam, K.; No, Z.; Kim, J. Lead Optimization of a Novel Series of Imidazo[1,2- a]Pyridine Amides Leading to a Clinical Candidate (Q203) as a Multi- and Extensively-Drug-Resistant Anti-Tuberculosis Agent. *J. Med. Chem.* **2014**, *57*, 5293–5305.

(166) Bhutani, I.; Loharch, S.; Gupta, P.; Madathil, R.; Parkesh, R. Structure, Dynamics, and Interaction of *Mycobacterium tuberculosis* (Mtb) DprE1 and DprE2 Examined by Molecular Modeling, Simulation, and Electrostatic Studies. *PLoS One* **2015**, *10*, e0119771.

(167) Makarov, V.; Lechartier, B.; Zhang, M.; Neres, J.; van der Sar, A. M.; Raadsen, S. A.; Hartkoorn, R. C.; Ryabova, O. B.; Vocat, A.; Decosterd, L. A.; Widmer, N.; Buclin, T.; Bitter, W.; Andries, K.; Pojer,

F.; Dyson, P. J.; Cole, S. T. Towards a New Combination Therapy for Tuberculosis with next Generation Benzothiazinones. *EMBO Mol. Med.* **2014**, *6*, 372–383.

(168) da Silva, P. B.; Campos, D. L.; Ribeiro, C. M.; da Silva, I. C.; Pavan, F. R. New Antimycobacterial Agents in the Pre-Clinical Phase or beyond: Recent Advances in Patent Literature (2001–2016). *Expert Opin. Ther. Pat.* **2017**, *27*, 269–282.

(169) Shirude, P. S.; Shandil, R. K.; Manjunatha, M. R.; Sadler, C.; Panda, M.; Panduga, V.; Reddy, J.; Saralaya, R.; Nanduri, R.; Ambady, A.; Ravishankar, S.; Sambandamurthy, V. K.; Humnabadkar, V.; Jena, L. K.; Suresh, R. S.; Srivastava, A.; Prabhakar, K. R.; Whiteaker, J.; McLaughlin, R. E.; Sharma, S.; Cooper, C. B.; Mdluli, K.; Butler, S.; Iyer, P. S.; Narayanan, S.; Chatterji, M. Lead Optimization of 1,4-Azaindoles as Antimycobacterial Agents. *J. Med. Chem.* **2014**, *57*, 5728–5737.

(170) Chatterji, M.; Shandil, R.; Manjunatha, M. R.; Solapure, S.; Ramachandran, V.; Kumar, N.; Saralaya, R.; Panduga, V.; Reddy, J.; KR, P.; Sharma, S.; Sadler, C.; Cooper, C. B.; Mdluli, K.; Iyer, P. S.; Narayanan, S.; Shirude, P. S. 1,4-Azaindole, a Potential Drug Candidate for Treatment of Tuberculosis. *Antimicrob. Agents Chemother.* **2014**, *58*, 5325–5331.

(171) Lu, Y.; Zheng, M.; Wang, B.; Fu, L.; Zhao, W.; Li, P.; Xu, J.; Zhu, H.; Jin, H.; Yin, D.; Huang, H.; Upton, A. M.; Ma, Z. Clofazimine Analogs with Efficacy against Experimental Tuberculosis and Reduced Potential for Accumulation. *Antimicrob. Agents Chemother.* **2011**, *55*, 5185–5193.

(172) Zhang, D.; Lu, Y.; Liu, K.; Liu, B.; Wang, J.; Zhang, G.; Zhang, H.; Liu, Y.; Wang, B.; Zheng, M.; Fu, L.; Hou, Y.; Gong, N.; Lv, Y.; Li, C.; Cooper, C. B.; Upton, A. M.; Yin, D.; Ma, Z.; Huang, H. Identification of Less Lipophilic Riminophenazine Derivatives for the Treatment of Drug-Resistant Tuberculosis. *J. Med. Chem.* **2012**, *55*, 8409–8417.

(173) Ishizaki, Y.; Hayashi, C.; Inoue, K.; Igarashi, M.; Takahashi, Y.; Pujari, V.; Crick, D. C.; Brennan, P. J.; Nomoto, A. Inhibition of the First Step in Synthesis of the Mycobacterial Cell Wall Core, Catalyzed by the GlcNAc-1-Phosphate Transferase WecA, by the Novel Caprazamycin Derivative CPZEN-45. *J. Biol. Chem.* **2013**, *288*, 30309–30319.

(174) Lee, R. E.; Hurdle, J. G.; Liu, J.; Bruhn, D. F.; Matt, T.; Scherman, M. S.; Vaddady, P. K.; Zheng, Z.; Qi, J.; Akbergenov, R.; Das, S.; Madhura, D. B.; Rathi, C.; Trivedi, A.; Villellas, C.; Lee, R. B.; Rakesh;

Waidyarachchi, S. L.; Sun, D.; McNeil, M. R.; Ainsa, J. A.; Boshoff, H. I.; Gonzalez-Juarrero, M.; Meibohm, B.; Böttger, E. C.; Lenaerts, A. J. Spectinamides: A New Class of Semisynthetic Antituberculosis Agents That Overcome Native Drug Efflux. *Nat. Med.* **2014**, *20*, 152–158.

(175) Kling, A.; Lukat, P.; Almeida, D. V.; Bauer, A.; Fontaine, E.; Sordello, S.; Zaburannyi, N.; Herrmann, J.; Wenzel, S. C.; Konig, C.; Ammerman, N. C.; Barrio, M. B.; Borchers, K.; Bordon-Pallier, F.; Bronstrup, M.; Courtemanche, G.; Gerlitz, M.; Geslin, M.; Hammann, P.; Heinz, D. W.; Hoffmann, H.; Klieber, S.; Kohlmann, M.; Kurz, M.; Lair, C.; Matter, H.; Nuermberger, E.; Tyagi, S.; Fraisse, L.; Grosset, J. H.; Lagrange, S.; Muller, R. Targeting DnaN for Tuberculosis Therapy Using Novel Griselimycins. *Science (80-.).* **2015**, *348*, 1106–1112.

(176) Kola, I.; Landis, J. Opinion: Can the Pharmaceutical Industry Reduce Attrition Rates? *Nat. Rev. Drug Discov.* **2004**, *3*, 711–716.

(177) Vasaikar, S.; Bhatia, P.; Bhatia, P.; Chu Yaiw, K. Complementary Approaches to Existing Target Based Drug Discovery for Identifying Novel Drug Targets. *Biomedicines* **2016**, *4*, 27.

(178) Brown, D.; Superti-Furga, G. Rediscovering the Sweet Spot in Drug Discovery. *Drug Discov. Today* **2003**, *8*, 1067–1077.

(179) Waring, M. J.; Arrowsmith, J.; Leach, A. R.; Leeson, P. D.; Mandrell, S.; Owen, R. M.; Pairaudeau, G.; Pennie, W. D.; Pickett, S. D.; Wang, J.; Wallace, O.; Weir, A. An Analysis of the Attrition of Drug Candidates from Four Major Pharmaceutical Companies. *Nat. Rev. Drug Discov.* **2015**, *14*, 475–486.

(180) Schuster, D.; Laggner, C.; Langer, T. Why Drugs Fail: A Study on Side Effects in New Chemical Entities. *Curr. Pharm. Des.* **2005**, *11*, 3545–3559.

(181) Kramer, J. A.; Sagartz, J. E.; Morris, D. L. The Application of Discovery Toxicology and Pathology towards the Design of Safer Pharmaceutical Lead Candidates. *Nat. Rev. Drug Discov.* **2007**, *6*, 636–649.

(182) Waring, M. J. Lipophilicity in Drug Discovery. *Expert Opin. Drug Discov.* **2010**, *5*, 235–248.

(183) Gleeson, P.; Bravi, G.; Modi, S.; Lowe, D. ADMET Rules of Thumb II: A Comparison of the Effects of Common Substituents on a Range of ADMET Parameters. *Bioorg. Med. Chem.* **2009**, *17*, 5906–5919.

(184) Hughes, J. D.; Blagg, J.; Price, D. A.; Bailey, S.; Decrescenzo, G. A.; Devraj, R. V; Ellsworth, E.; Fobian, Y. M.; Gibbs, M. E.; Gilles, R. W.;

Greene, N.; Huang, E.; Krieger-Burke, T.; Loesel, J.; Wager, T.; Whiteley, L.; Zhang, Y. Physiochemical Drug Properties Associated with in Vivo Toxicological Outcomes. *Bioorg. Med. Chem. Lett.* **2008**, *18*, 4872–4875.

(185) Beaumont, K.; Smith, D. A. Does Human Pharmacokinetic Prediction Add Significant Value to Compound Selection in Drug Discovery Research? *Curr. Opin. Drug Discov. Devel.* **2009**, *12*, 61–71.

(186) Leeson, P. Drug Discovery: Chemical Beauty Contest. *Nature* **2012**, *481*, 455–456.

(187) Lipinski, C. A.; Lombardo, F.; Dominy, B. W.; Feeney, P. J. Experimental and Computational Approaches to Estimate Solubility and Permeability in Drug Discovery and Development settings. PII of Original Article: S0169-409X(96)00423-1. The Article Was Originally Published in Advanced Drug Delivery Reviews 23 (1997) 3. *Adv. Drug Deliv. Rev.* **2001**, *46*, 3–26.

(188) Leeson, P. D.; Springthorpe, B. The Influence of Drug-like Concepts on Decision-Making in Medicinal Chemistry. *Nat. Rev. Drug Discov.* **2007**, *6*, 881–890.

(189) Veber, D. F.; Johnson, S. R.; Cheng, H.-Y.; Smith, B. R.; Ward, K. W.; Kopple, K. D. Molecular Properties That Influence the Oral Bioavailability of Drug Candidates. *J. Med. Chem.* **2002**, *45*, 2615–2623.

(190) Clark, D. E. Rapid Calculation of Polar Molecular Surface Area and Its Application to the Prediction of Transport Phenomena. 2. Prediction of Blood-Brain Barrier Penetration. *J. Pharm. Sci.* **1999**, *88*, 815–821.

(191) Leeson, P. D.; Springthorpe, B. The Influence of Drug-like Concepts on Decision-Making in Medicinal Chemistry. *Nat. Rev. Drug Discov.* **2007**, *6*, 881–890.

(192) Bhattachar, S. N.; Deschenes, L. A.; Wesley, J. A. Solubility: It's Not Just for Physical Chemists. *Drug Discov. Today* **2006**, *11*, 1012–1018.

(193) Khadka, P.; Ro, J.; Kim, H.; Kim, I.; Kim, J. T.; Kim, H.; Cho, J. M.; Yun, G.; Lee, J. Pharmaceutical Particle Technologies: An Approach to Improve Drug Solubility, Dissolution and Bioavailability. *Asian J. Pharm. Sci.* **2014**, *9*, 304–316.

(194) Amidon, G. L.; Lennernäs, H.; Shah, V. P.; Crison, J. R. A Theoretical Basis for a Biopharmaceutic Drug Classification: The Correlation of *in vitro* Drug Product Dissolution and in Vivo Bioavailability. *Pharm. Res.* **1995**, *12*, 413–420.

(195) Williams, H. D.; Trevaskis, N. L.; Charman, S. A.; Shanker, R. M.; Charman, W. N.; Pouton, C. W.; Porter, C. J. H. Strategies to Address Low Drug Solubility in Discovery and Development. *Pharmacol. Rev.* **2013**, *65*, 315–499.

(196) Keserü, G. M.; Makara, G. M. The Influence of Lead Discovery Strategies on the Properties of Drug Candidates. *Nat. Rev. Drug Discov.* **2009**, *8*, 203–212.

(197) Edward H. Kerns and Li Di. *Drug-like Properties: Concepts, Structure Design and Methods*; 1st Ed.; Elsevier Inc, 2008.

(198) Savjani, K. T.; Gajjar, A. K.; Savjani, J. K. Drug Solubility: Importance and Enhancement Techniques. *ISRN Pharm.* **2012**, *2012*, 1–10.

(199) Jain, S.; Patel, N.; Lin, S. Solubility and Dissolution Enhancement Strategies: Current Understanding and Recent Trends. *Drug Dev. Ind. Pharm.* **2015**, *41*, 875–887.

(200) Singh, A.; Worku, Z. A.; Van den Mooter, G. Oral Formulation Strategies to Improve Solubility of Poorly Water-Soluble Drugs. *Expert Opin. Drug Deliv.* **2011**, *8*, 1361–1378.

(201) Kalepu, S.; Nekkanti, V. Insoluble Drug Delivery Strategies: Review of Recent Advances and Business Prospects. *Acta Pharm. Sin. B* **2015**, *5*, 442–453.

(202) Manallack, D. The pKa Distribution of Drugs: Application to Drug Discovery. In *Dyes and Drugs*; Apple Academic Press, 2011; pp. 80–102.

(203) Sweetana, S.; Akers, M. J. Solubility Principles and Practices for Parenteral Drug Dosage Form Development. *PDA J. Pharm. Sci. Technol. 50*, 330–342.

(204) Li, Y.; Zhu, Y. M.; Jiang, H. J.; Pan, J. P.; Wu, G. S.; Wu, J. M.; Shi, Y. L.; Yang, J. D.; Wu, B. A. Synthesis and Antimalarial Activity of Artemisinin Derivatives Containing an Amino Group. *J. Med. Chem.* **2000**, *43*, 1635–1640.

(205) Serajuddin, A. T. M. Salt Formation to Improve Drug Solubility. *Adv. Drug Deliv. Rev.* **2007**, *59*, 603–616.

(206) Le Manach, C.; Nchinda, A. T.; Paquet, T.; Gonzàlez Cabrera, D.; Younis, Y.; Han, Z.; Bashyam, S.; Zabiulla, M.; Taylor, D.; Lawrence, N.; White, K. L.; Charman, S. A.; Waterson, D.; Witty, M. J.; Wittlin, S.; Botha, M. E.; Nondaba, S. H.; Reader, J.; Birkholtz, L.-M.; Jiménez-Díaz, M. B.; Martínez, M. S.; Ferrer, S.; Angulo-Barturen, I.; Meister, S.; Antonova-Koch, Y.; Winzeler, E. A.; Street, L. J.; Chibale,

K. Identification of a Potential Antimalarial Drug Candidate from a Series of 2-Aminopyrazines by Optimization of Aqueous Solubility and Potency across the Parasite Life Cycle. *J. Med. Chem.* **2016**, *59*, 9890–9905.

(207) Le Manach, C.; Paquet, T.; Gonzàlez Cabrera, D.; Younis, Y.; Taylor, D.; Wiesner, L.; Lawrence, N.; Schwager, S.; Waterson, D.; Witty, M. J.; Wittlin, S.; Street, L. J.; Chibale, K. Medicinal Chemistry Optimization of Antiplasmodial Imidazopyridazine Hits from High Throughput Screening of a SoftFocus Kinase Library: Part 2. *J. Med. Chem.* **2014**, *57*, 8839–8848.

(208) Stella, V. J.; Nti-Addae, K. W. Prodrug Strategies to Overcome Poor Water Solubility. *Adv. Drug Deliv. Rev.* **2007**, *59*, 677–694.

(209) Jornada, D.; dos Santos Fernandes, G.; Chiba, D.; de Melo, T.; dos Santos, J.; Chung, M. The Prodrug Approach: A Successful Tool for Improving Drug Solubility. *Molecules* **2015**, *21*, 42.

(210) Rautio, J.; Kumpulainen, H.; Heimbach, T.; Oliyai, R.; Oh, D.; Järvinen, T.; Savolainen, J. Prodrugs: Design and Clinical Applications. *Nat. Rev. Drug Discov.* **2008**, *7*, 255–270.

(211) Jain, N.; Yalkowsky, S. H. Estimation of the Aqueous Solubility I: Application to Organic Nonelectrolytes. *J. Pharm. Sci.* **2001**, *90*, 234–252.

(212) Ishikawa, M.; Hashimoto, Y. Improvement in Aqueous Solubility in Small Molecule Drug Discovery Programs by Disruption of Molecular Planarity and Symmetry. *J. Med. Chem.* **2011**, *54*, 1539–1554.

(213) Lovering, F.; Bikker, J.; Humblet, C. Escape from Flatland: Increasing Saturation as an Approach to Improving Clinical Success. *J. Med. Chem.* **2009**, *52*, 6752–6756.

(214) Miyako, Y.; Khalef, N.; Matsuzaki, K.; Pinal, R. Solubility Enhancement of Hydrophobic Compounds by Cosolvents: Role of Solute Hydrophobicity on the Solubilization Effect. *Int. J. Pharm.* **2010**, *393*, 48–54.

(215) Nema, S.; Washkuhn, R. J.; Brendel, R. J. Excipients and Their Use in Injectable Products. *PDA J. Pharm. Sci. Technol.* **1997**, *51*, 166–171.

(216) Pouton, C. W. Formulation of Poorly Water-Soluble Drugs for Oral Administration: Physicochemical and Physiological Issues and the Lipid Formulation Classification System. *Eur. J. Pharm. Sci.* **2006**, *29*, 278–287.

(217) Bogman, K.; Erne-Brand, F.; Alsenz, J.; Drewe, J. The Role of

Surfactants in the Reversal of Active Transport Mediated by Multidrug Resistance Proteins. *J. Pharm. Sci.* **2003**, *92*, 1250–1261.

(218) Kumar, A.; Chen, F.; Mozhi, A.; Zhang, X.; Zhao, Y.; Xue, X.; Hao, Y.; Zhang, X.; Wang, P. C.; Liang, X.-J. Innovative Pharmaceutical Development Based on Unique Properties of Nanoscale Delivery Formulation. *Nanoscale* **2013**, *5*, 8307.

(219) Van Eerdenbrugh, B.; Van den Mooter, G.; Augustijns, P. Top-down Production of Drug Nanocrystals: Nanosuspension Stabilization, Miniaturization and Transformation into Solid Products. *Int. J. Pharm.* **2008**, *364*, 64–75.

(220) Vasconcelos, T.; Sarmento, B.; Costa, P. Solid Dispersions as Strategy to Improve Oral Bioavailability of Poor Water Soluble Drugs. *Drug Discov. Today* **2007**, *12*, 1068–1075.

(221) Censi, R.; Di Martino, P. Polymorph Impact on the Bioavailability and Stability of Poorly Soluble Drugs. *Molecules* **2015**, *20*, 18759–18776.

(222) Steed, J. W. The Role of Co-Crystals in Pharmaceutical Design. *Trends Pharmacol. Sci.* **2013**, *34*, 185–193.

(223) Stahly, G. P. A Survey of Cocrystals Reported Prior to 2000. *Cryst. Growth Des.* **2009**, *9*, 4212–4229.

(224) Gadade, D. D.; Pekamwar, S. S. Pharmaceutical Cocrystals: Regulatory and Strategic Aspects, Design and Development. *Adv. Pharm. Bull.* **2016**, *6*, 479–494.

(225) Chandramouli, Y.; Gandhimathi, R.; Rubia, B.; Vikram, A.; Mahitha, B.; Imroz, S. M. Review on Cocrystal As an Approach With Newer Implications in Pharmaceutical Field. *Int. J. Med. Chem. Anal.* **2012**, *2*, 91–100.

(226) Caira, M. R.; Bourne, S. A.; Samsodien, H.; Engel, E.; Liebenberg, W.; Stieger, N.; Aucamp, M. Co-Crystals of the Antiretroviral Nevirapine: Crystal Structures, Thermal Analysis and Dissolution Behaviour. *CrystEngComm* **2012**, *14*, 2541–2551.

(227) Ryzhakov, A.; Do Thi, T.; Stappaerts, J.; Bertoletti, L.; Kimpe, K.; Sá Couto, A. R.; Saokham, P.; Van den Mooter, G.; Augustijns, P.; Somsen, G. W.; Kurkov, S.; Inghelbrecht, S.; Arien, A.; Jimidar, M. I.; Schrijnemakers, K.; Loftsson, T. Self-Assembly of Cyclodextrins and Their Complexes in Aqueous Solutions. *J. Pharm. Sci.* **2016**, *105*, 2556–2569.

(228) Loftsson, T.; Brewster, M. E. Pharmaceutical Applications of Cyclodextrins: Basic Science and Product Development. *J. Pharm.*

Pharmacol. **2010**, *62*, 1607–1621.

(229) García, A.; Leonardi, D.; Salazar, M. O.; Lamas, M. C. Modified β-Cyclodextrin Inclusion Complex to Improve the Physicochemical Properties of Albendazole. Complete *In vitro* Evaluation and Characterization. *PLoS One* **2014**, *9*, e88234.

(230) Loftsson, T.; Brewster, M. E. Cyclodextrins as Functional Excipients: Methods to Enhance Complexation Efficiency. *J. Pharm. Sci.* **2012**, *101*, 3019–3032.

(231) Bakthadoss, M.; Selvakumar, R.; Srinivasan, J. An Efficient Protocol for the Synthesis of Benzoheterocyclic Compounds via Solid-State Melt Reaction (SSMR). *Tetrahedron Lett.* **2014**, *55*, 5808–5812.

(232) Gomtsyan, A. Heterocycles in Drugs and Drug Discovery. *Chem. Heterocycl. Compd.* **2012**, *48*, 7–10.

(233) Rashmi, A.; Ashish, K.; Gill, N.; Rana, A. Quinazolinone: An Overview. *Int. Res. J. Pharm.* **2011**, *2*, 22–28.

(234) Khan, I.; Zaib, S.; Batool, S.; Abbas, N.; Ashraf, Z.; Iqbal, J.; Saeed, A. Quinazolines and Quinazolinones as Ubiquitous Structural Fragments in Medicinal Chemistry: An Update on the Development of Synthetic Methods and Pharmacological Diversification. *Bioorg. Med. Chem.* **2016**, *24*, 2361–2381.

(235) Hwu, J. R.; Kapoor, M.; Tsay, S.-C.; Lin, C.-C.; Hwang, K. C.; Horng, J.-C.; Chen, I.-C.; Shieh, F.-K.; Leyssen, P.; Neyts, J. Benzouracil–coumarin–arene Conjugates as Inhibiting Agents for Chikungunya Virus. *Antiviral Res.* **2015**, *118*, 103–109.

(236) Azab, M. E.; Kassab, E. A.; El-Hashash, M. A.; Ali, R. S. Synthesis and Antibacterial Activity of Some New 4(3H)Quinazolin-4-One Derivatives. *Phosphorus. Sulfur. Silicon Relat. Elem.* **2009**, *184*, 610–625.

(237) Rasina, D.; Otikovs, M.; Leitans, J.; Recacha, R.; Borysov, O. V.; Kanepe-Lapsa, I.; Domraceva, I.; Pantelejevs, T.; Tars, K.; Blackman, M. J.; Jaudzems, K.; Jirgensons, A. Fragment-Based Discovery of 2-Aminoquinazolin-4(3 H)-Ones As Novel Class Nonpeptidomimetic Inhibitors of the Plasmepsins I, II, and IV. *J. Med. Chem.* **2016**, *59*, 374–387.

(238) Taboada, J.; Grooters, A. M. Systemic Antifungal Therapy. In *Small Animal Clinical Pharmacology*; Elsevier, 2008; pp. 186–197.

(239) Hughes, A. N.; Rafi, I.; Griffin, M. J.; Calvert, A. H.; Newell, D. R.; Calvete, J. A.; Johnston, A.; Clendeninn, N.; Boddy, A. V. Phase I Studies with the Nonclassical Antifolate Nolatrexed Dihydrochloride

(AG337, THYMITAQ) Administered Orally for 5 Days. *Clin. Cancer Res.* **1999**, *5*, 111–118.

(240) Haanaes, H. R.; Benterud, U. J.; Skoglund, L. A. RF 46-790 versus Paracetamol: Effect on Post-Operative Pain. *Int. J. Clin. Pharmacol. Ther. Toxicol.* **1986**, *24*, 598–601.

(241) Ochiai, T.; Ishida, R. Pharmacological Studies on 6-Amino-2-fluoromethyl-3-(O-tolyl)-4(3*H*)-quinazolinone (Afloqualone), a New Centrally Acting Muscle Relaxant. (II) Effects on the Spinal Reflex Potential and the Rigidity. *Jpn. J. Pharmacol.* **1982**, *32*, 427–438.

(242) Patel, M. B.; Kumar, S. P.; Valand, N. N.; Jasrai, Y. T.; Menon, S. K. Synthesis and Biological Evaluation of Cationic Fullerene Quinazolinone Conjugates and Their Binding Mode with Modeled *Mycobacterium tuberculosis* Hypoxanthine-Guanine Phosphoribosyltransferase Enzyme. *J. Mol. Model.* **2013**, *19*, 3201–3217.

(243) Al-deeb, A. O.; Alafeefy, A. M. Synthesis of Some New 3*H*-Quinazolin-4-one Derivatives as Potential Antitubercular Agents. *Appl. Sci.* **2008**, *5*, 94–99.

(244) Pattan, S. R.; Reddy, V. V. K.; Manvi, F. V.; Desai, B. G.; Bhat, A. R. Synthesis of N-3[4-(4-chlorophenyl) thiazole-2-yl]-2-(aminomethyl)quinazoline-4(3*H*)-one and Their Derivatives for Antitubercular Activity. *Indian J. Chem.* **2006**, *45B*, 1778–1781.

(245) Pines, M.; Nagler, A. Halofuginone: A Novel Antifibrotic Therapy. *Gen. Pharmacol. Vasc. Syst.* **1998**, *30*, 445–450.

(246) Cohen, E.; Klarberg, B.; Vaughan, J. R. Quinazolinone Sulfonamides. A New Class of Diuretic Agents 1. *J. Am. Chem. Soc.* **1960**, *82*, 2731–2735.

(247) Czarnetzki, B. M.; Brechtel, B.; Braun-Falco, O.; Christophers, E.; Schöpf, E.; Reckers-Czaschka, R.; Baudin, M.; Dupuy, P. Topical Tiacrilast, a Potent Mast Cell Degranulation Inhibitor, Does Not Improve Adult Atopic Eczema. *Dermatology* **1993**, *187*, 112–114.

(248) Zhang, H.-J.; Wang, S.-B.; Quan, Z.-S. Synthesis and Antidepressant Activities of 4-(Substituted-phenyl)tetrazolo[1,5-a]quinazolin-5(4*H*)-ones and Their Derivatives. *Mol. Divers.* **2015**, *19*, 817–828.

(249) Zhang, H.-J.; Jin, P.; Wang, S.-B.; Li, F.-N.; Guan, L.-P.; Quan, Z.-S. Synthesis and Anticonvulsant Activity Evaluation of 4-Phenyl-[1,2,4]triazolo[4,3-a]quinazolin-5(4*H*)-one and Its Derivatives. *Arch. Pharm. (Weinheim).* **2015**, *348*, 564–574.

(250) Abdel Gawad, N. M.; Georgey, H. H.; Youssef, R. M.; El Sayed, N. A. Design, Synthesis, and Anticonvulsant Activity of Novel Quinazolinone Analogues. *Med. Chem. Res.* **2011**, *20*, 1280–1286.

(251) Couturier, C.; Lair, C.; Pellet, A.; Upton, A.; Kaneko, T.; Perron, C.; Cogo, E.; Menegotto, J.; Bauer, A.; Scheiper, B.; Lagrange, S.; Bacqué, E. Identification and Optimization of a New Series of Anti-Tubercular Quinazolinones. *Bioorg. Med. Chem. Lett.* **2016**, *26*, 5290–5299.

(252) Alagarsamy, V.; Anjana, G. V.; Sulthana, M. T.; Parthiban, P.; Solomon, V. R. Antimicrobial Activities of Some Synthesized 1-(3-(2-methylphenyl)-4-oxo-3*H*-quinazolin-2-yl-4-(substituted) thiosemicarbazide Derivatives. *Russ. J. Bioorganic Chem.* **2016**, *42*, 332–339.

(253) Jirgensons, A.; Domraceva, I.; Kanepelapsa, I.; Rasina, D.; Jaudzems, K.; Otikovs, M. Novel Substituted 2-Aminoquinazolin-4(3*H*)-one Derivatives as Malarial Aspartic Protease Inhibitors. WO 2015/063544 A1, 2015.

(254) Leivers, A. L.; Tallant, M.; Shotwell, J. B.; Dickerson, S.; Leivers, M. R.; McDonald, O. B.; Gobel, J.; Creech, K. L.; Strum, S. L.; Mathis, A.; Rogers, S.; Moore, C. B.; Botyanszki, J. Discovery of Selective Small Molecule Type III Phosphatidylinositol 4-Kinase Alpha (PI4KIIIα) Inhibitors as Anti Hepatitis C (HCV) Agents. *J. Med. Chem.* **2014**, *57*, 2091–2106.

(255) Lindsey, B. A.; Janos, B.; Maosheng, D.; Robert, L. M.; Bradford, S. J.; David, T. M.; Howard, D. S.; W-F, T. V.; Blount, M. R.; Maria, R. A.; Jianjun, Y.; Xiofei, L.; Maria, G. D.; George, C. J.; George, A. Quinazolinone Derivatives As Antiviral Agents. WO2012087938 (A1), 2012.

(256) Alanazi, A. M.; Abdel-Aziz, A. A.-M.; Shawer, T. Z.; Ayyad, R. R.; Al-Obaid, A. M.; Al-Agamy, M. H. M.; Maarouf, A. R.; El-Azab, A. S. Synthesis, Antitumor and Antimicrobial Activity of Some New 6-Methyl-3-phenyl-4(3*H*)-quinazolinone Analogues: In Silico Studies. *J. Enzyme Inhib. Med. Chem.* **2015**, 1–15.

(257) Radwan, A.; Alanazi, F.; Al-Dhfyan, A. Synthesis, and Docking Studies of Some Fused-Quinazolines and Quinazolines Carrying Biological Active Isatin Moiety as Cell-Cycle Inhibitors of Breast Cancer Cell Lines. *Drug Res. (Stuttg).* **2013**, *63*, 129–136.

(258) El-Hashash, M. A.; Elshahawi, M. M.; Ragab, E. A.; Nagdy, S. Synthesis and Antifungal Activity of Novel Quinazolin-4(3*H*)-one Derivatives. *Synth. Commun.* **2015**, *45*, 2240–2250.

(259) Yeşilada, A.; Koyunoğlu, S.; Saygılıa, N.; Kupeli, E.; Yeşilada, E.; Bedir, E.; Khanc, I. Synthesis, Anti-Inflammatory and Analgesic Synthesis, Anti-Inflammatory and Analgesic New 4(3*H*)-quinazolinone Derivatives. *Arch. Pharm. (Weinheim).* **2004**, *337*, 96–104.

(260) Nikolay, G.; Andrzej, G. Light Insensitive Silver(I) Cyanoximates As Antimicrobial Agents For Indwelling Medical Devices. US2013096098 (A1), 2013.

(261) Ilkun, O. T.; Archibald, S. J.; Barnes, C. L.; Gerasimchuk, N.; Biagioni, R.; Silchenko, S.; Gerasimchuk, O. A.; Nemykin, V. N. Benz(2-Heteroaryl)cyanoximes and Their Tl(i) Complexes: New Room Temperature Blue Emitters. *Dalt. Trans.* **2008**, 5715.

(262) Kaur, A.; Wakode, S.; Pathak, D. P. Benzoxazole: The Molecule of Diverse Pharmacological Importance. *Int. J. Pharm. Pharm. Sci. Vol 7, Issue 1, 2015* **2015**, *7*, 16–23.

(263) Gautam, M. K.; Sonal; Sharma, N. K.; Priyanka; Jha, K. K. Pharmacological Profile and Pharmaceutical Importance of Substituted Benzoxazoles: A Comprehensive Review. *Int. J. ChemTech Res.* **2012**, *4*, 640–650.

(264) Rana, D. N.; Chhabria, M. T.; Shah, N. K.; Brahmkshatriya, P. S. Discovery of New Antitubercular Agents by Combining Pyrazoline and Benzoxazole Pharmacophores: Design, Synthesis and Insights into the Binding Interactions. *Med. Chem. Res.* **2014**, *23*, 2218–2228.

(265) Imramovsky, A.; Kozic, J.; Pesko, M.; Stolarikova, J.; Vinsova, J.; Kralova, K.; Jampilek, J. Synthesis and Antimycobacterial and Photosynthesis-Inhibiting Evaluation of 2-[(*E*)-2-Substituted-Ethenyl]-1,3-Benzoxazoles. *Sci. World J.* **2014**, *2014*, 1–11.

(266) Kamachi, H.; Narita, Y.; Okita, T.; Abe, Y.; Iimura, S.; Tomatsu, K.; Yamasaki, T.; Okumura, J.; Naito, T.; Oki, T.; Kawaguchi, H. Synthesis and Biological Activity of a New Cephalosporin, BMY-28232 and Its Prodrug-Type Esters for Oral Use. *J. Antibiot. (Tokyo).* **1988**, *41*, 1602–1616.

(267) Ayati, A.; Falahati, M.; Irannejad, H.; Emami, S. Synthesis, *in vitro* Antifungal Evaluation and in Silico Study of 3-Azolyl-4-Chromanone Phenylhydrazones. *DARU J. Pharm. Sci.* **2012**, *20*, 46.

(268) Zhang, R.; Lv, K.; Wang, B.; Li, L.; Wang, B.; Liu, M.; Guo, H.; Wang, A.; Lu, Y. Design, Synthesis and Antitubercular Evaluation of Benzothiazinones Containing an Oximido or Amino Nitrogen Heterocycle Moiety. *RSC Adv.* **2017**, *7*, 1480–1483.

(269) Huang, J.; Wang, M.; Wang, B.; Wu, Z.; Liu, M.; Feng, L.; Zhang, J.; Li, X.; Yang, Y.; Lu, Y. Synthesis, Antimycobacterial and Antibacterial Activity of 1-(6-Amino-3,5-difluoropyridin-2-yl)fluoroquinolone Derivatives Containing an Oxime Functional Moiety. *Bioorg. Med. Chem. Lett.* **2016**, *26*, 2262–2267.

(270) Wei, Z.; Wang, J.; Liu, M.; Li, S.; Sun, L.; Guo, H.; Wang, B.; Lu, Y. Synthesis, *in vitro* Antimycobacterial and Antibacterial Evaluation of IMB-070593 Derivatives Containing a Substituted Benzyloxime Moiety. *Molecules* **2013**, *18*, 3872–3893.

(271) Jokanovic, M.; Prostran, M. Pyridinium Oximes as Cholinesterase Reactivators. Structure-Activity Relationship and Efficacy in the Treatment of Poisoning with Organophosphorus Compounds. *Curr. Med. Chem.* **2009**, *16*, 2177–2188.

(272) World Health Organization. *Global Tuberculosis Report 2015*; Geneva, 2015.

CHAPTER 2

DESIGN, SYNTHESIS AND CHARACTERIZATION OF BENZOHETEROCYCLES

2.1 Chapter Overview

Chapter 2 provides a discussion of the studies, and the results thereof, which were carried out in order to address the first specific aim of this thesis work, which was: To synthesize 2-aminoquinazolinones and benzoxazole-based oximes as potential antituberculosis agents.

This chapter begins with a brief introduction to the sources of drug leads, particularly the process of identifying hits in drug discovery programs. Thereafter, the chapter is divided into two broad sections; one covers the 2-aminoquinazolinones, while the other one highlights the benzoxazole-based oximes. Accordingly, each section describes the genesis, design, synthesis, and characterization of target analogues.

2.2 Identification of Hit Compounds

Drug discovery mainly begins with the identification of hit molecules, and/or biological targets for a particular disease state. A hit, in this context, is a biologically active and chemically tractable small molecule, which is amenable to medicinal chemistry-based modifications associated with hit-to-lead optimization campaigns. Generally, hits are identified from either natural products or chemically synthesized compounds. Natural products are generally identified as unmodified compounds, or used as starting points and/or building blocks for chemical synthesis of more complex molecules. They have the benefit of structural and biological diversity and complexity, which are sometimes lacking in chemically synthesized compounds.[1–5] In some instances, diverse natural products are organized into libraries from which screening can be undertaken for purposes of hit identification.[6]

Chemical synthesis, on the other hand, particularly combinatorial chemistry, has been instrumental in accelerated generation of vast numbers, running into millions, of new chemical entities.[7] These, in most

cases, are then collated into chemical libraries and databases from which drug hits can be discovered through screening.[8,9]

Predominantly, compound screening is carried out either biologically, or through the use of computer-based (virtual or *in silico*) techniques. Automation of screening protocols has resulted in simplification, miniaturization, and speeding up of screening assays. In this regard, high-throughput screening promotes screening of large numbers of diverse compounds in relatively short periods of time, along with tremendous information harvest.[10,11] Furthermore, screening can either be target-based, or phenotypic whole-cell-based; two opposing, but nevertheless complimentary approaches towards hit discovery.

Phenotypic whole-cell screening more often leads to the identification of molecules that modify a particular disease phenotype by influencing an undescribed target, or by acting simultaneously on more than one target at the cellular level, and without target bias. Thus, one of the benefits of whole-cell screens is that the identified hits are endowed with the appropriate physicochemical properties to reach their destined molecular target(s) in the biologically robust cellular environment. In addition, this holistic, target-naive approach allows for testing of hit compounds against complex, multifaceted biological systems and disease states where the exact disease mechanism(s) may not be fully understood. The downside, however, is that the subsequent mechanistic deconvolution studies towards the identification of the relevant molecular target(s) as well as the process of elucidating the mechanism(s) of action, are often slow, or in worst cases impossible. Furthermore, these screens are less feasible for large chemical libraries, and reproducibility of results may sometimes be hampered by multiple physiological variables.[12,13]

On the other hand, advances in molecular biology, genomics, and proteomics have led to a surge in target-based screens, which are believed to relatively accelerate the drug discovery process, particularly in structure-based rational drug design. In that case, with a known, fully characterized, and validated biological target, screening can be performed biologically or

virtually. Virtual screening is generally practicable in cases where crystal structures of biological targets are available.[14] Indeed, virtual screening has proved to be indispensable in the identification of drug hits,[15–17] some of which have contributed to the discovery of hitherto approved drugs.[18] Target-based screens are highly amenable to high-throughput screening; however, they may not be effective where more than one target is involved in a particular disease phenotype or where biological compensation comes into play.[12] Also, target druggability is sometimes difficult to predict, and this has intermittently been implicated in challenges associated with translating *in vitro* activity to *in vivo* efficacy. This, for instance, is due to physiological differences between biological systems and isolated targets.[19]

Moreover, approaches whereby pre-existing drugs are tested for new disease indications have become a common practice. In this case, where a pre-existing drug is used for new indications without any structural modification, the process is referred to as drug repurposing. Conversely, drug repositioning is a term used whenever the chemical structure of a pre-existing drug is modified, for instance, to make it suitable for the new disease indication. The major benefits derived from these approaches are, for example, the pharmacokinetics and the safety profiles of the approved drugs are already known, which in turn leads to substantial cost and time saving compared to the *de novo* drug discovery and development process.[20–22]

Within the context of this thesis work, the hits for the two series of benzoheterocycles were identified through the phenotypic whole-cell screening approach.

2.3 2-Aminoquinazolinones

2.3.1 General Introduction

The research work on 2-aminoquinazolinones as antimycobacterial agents has its origins in studies involving the exploration of 2-aminopyridines as antimalarial agents. This work was conducted by researchers at the University of Cape Town, Drug Discovery and Development Centre (H3D).

Figure 2.1 below summarizes the process that led to the identification of antimycobacterial 2-aminoquinazolinones.

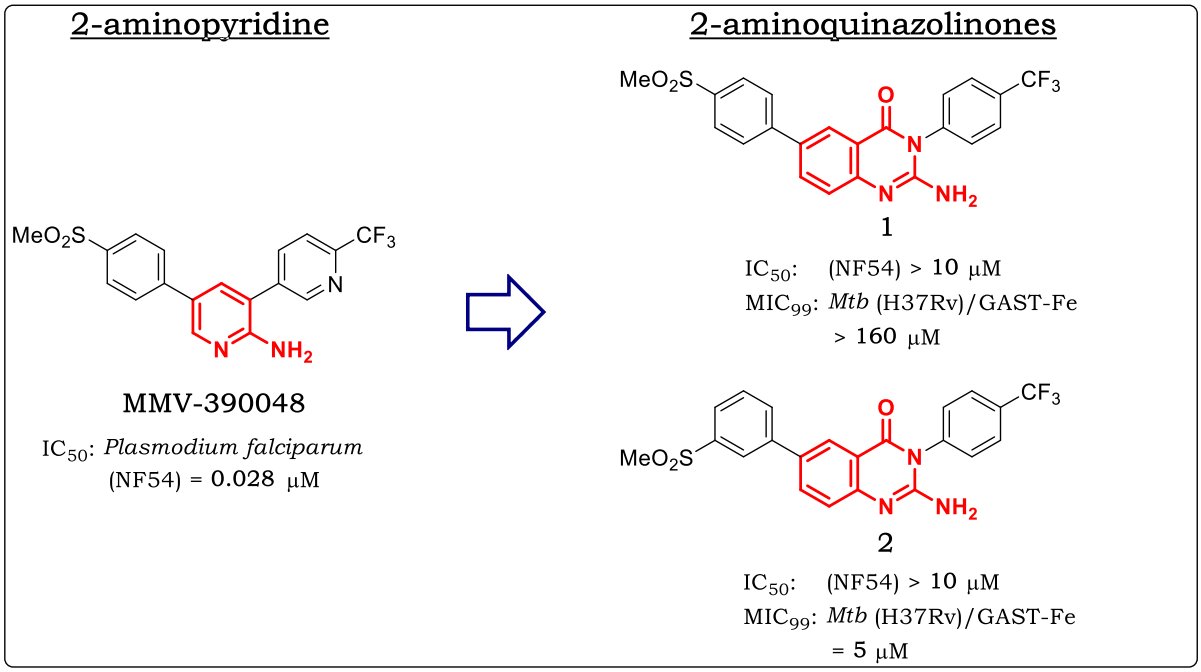

Figure 2.1: Identification of 2-aminoquinazolinones as antimycobacterial compounds.

In earlier studies, the 2-aminopyridines were identified as highly potent antiplasmodial compounds from phenotypic whole-cell high-throughput screening of a commercially available SoftFocus kinase library. Subsequent medicinal chemistry explorations and preclinical assessment of this series led to the selection of **MMV-390048** (**Figure 2.1** above) as a potential clinical candidate.[23] Further SAR exploration around the 2-aminopyridine core[24,25] resulted in the identification of the 2-aminoquinazolinones. To this effect, the pyridine ring was replaced with the 4-quinazolinone ring system. Consequently, compounds **1** and **2**, shown in **Figure 2.1** above, were synthesized and evaluated *in vitro* for their antiplasmodial activity against the drug-susceptible NF54 *Plasmodium falciparum* strain, and cross-screened for their antimycobacterial activity against the H37Rv *Mtb* strain, in phenotypic whole-cell assays. In this case, the replacement of the 2-aminopyridine core with the 2-aminoquinazolinone core led to loss of antiplasmodial activity. Compound **2**, on the other hand, exhibited potent *in vitro* antimycobacterial activity (MIC_{99} = 5 µM), and was therefore identified as the hit compound for the 2-aminoquinazolinone series. Notably,

compound **1** was inactive against *Mtb* despite the fact that it only differs from compound **2** at the position of the methylsulfonyl substituent relative to the quinazolinone core [*para*-position (4−SO_2MePh) for **1** and *meta*-position (3−SO_2MePh) for **2**]. Interestingly, these results suggested that the 2-aminoquinazolinone-based compounds could have selectivity and specificity towards yet unknown *Mtb* biological target(s), such that minor structural changes would yield compounds exhibiting varying antimycobacterial activities.

Encouraged by the above mentioned preliminary results, this thesis work was aimed at conducting further medicinal chemistry exploratory studies with respect to hit-to-lead optimization. This entailed synthesis, biological assessment, as well as SAR and SPR analyses, in efforts to explore the opportunities and liabilities associated with the 2-aminoquinazolinone class of compounds as potential anti-TB agents.

2.3.2 Design

In designing analogues of compound **2**, it was postulated that making structural modifications around the 2-aminoquinazolinone core would be essential in exploring the preliminary SAR around this series of compounds. Consequently, two points of diversity, **SAR 1** and **SAR 2** as shown in **Figure 2.2** below, were selected, while the 2-aminoquinazolinone core was kept constant.

Initially, both the **SAR 2** moiety at position 3 [the 4-trifluoromethyl phenyl group (4−CF_3Ph)], on the right-hand side and the 2-aminoquinazolinone core were kept constant while structural changes were made around the **SAR 1** moiety at position 6 [the methylsulfonyl phenyl group (3-SO_2MePh)] on the left-hand side.

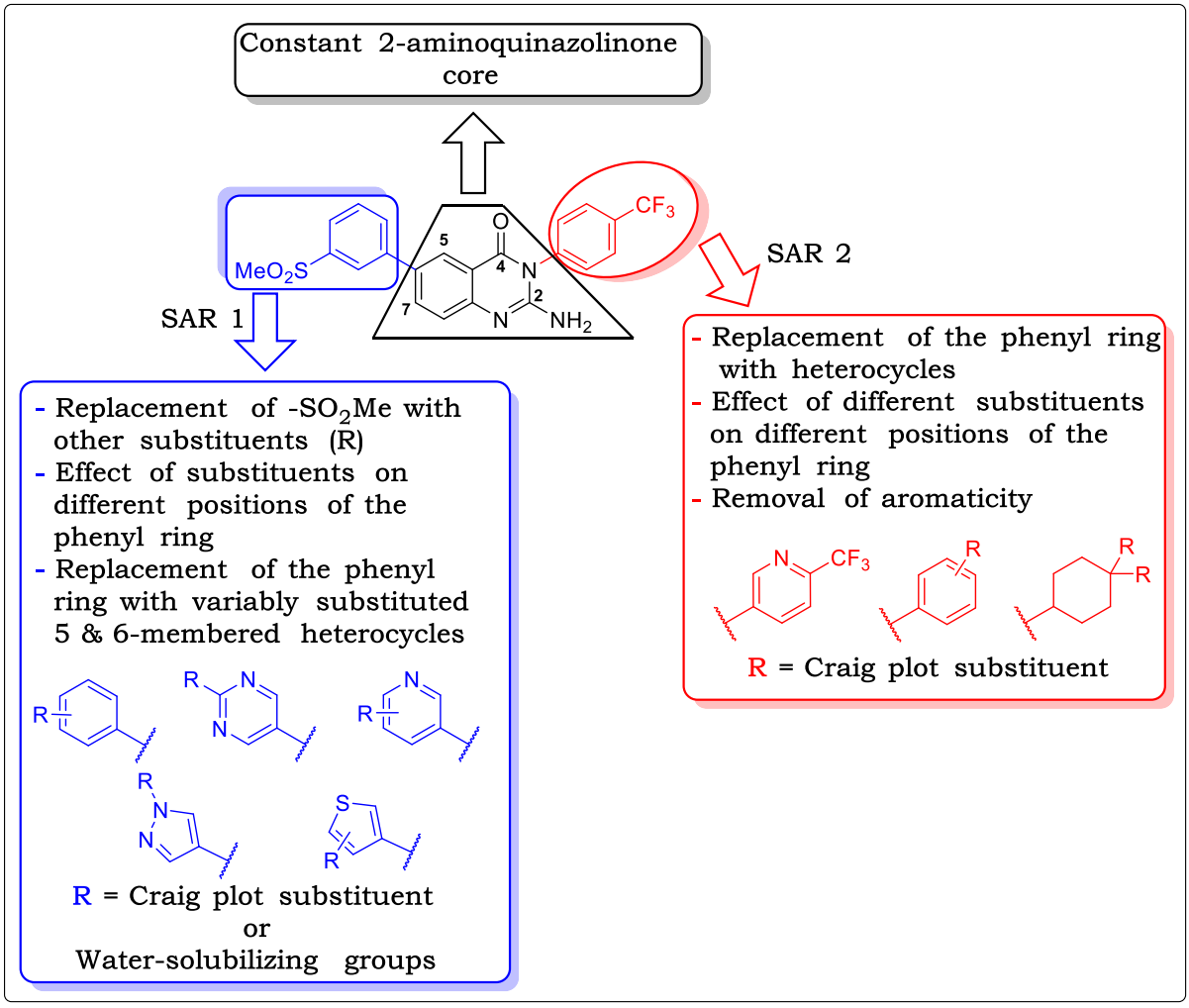

Figure 2.2: Design of 2-aminoquinazolinone analogues.

In order to introduce structural diversity, and explore different chemical spaces, **SAR 1** groups were selected from appropriately substituted ring structures, which ranged from phenyl to 5- and 6-membered heterocycles. Based on medicinal chemistry practices, substituents **R** were chosen in such a manner as to bring variety in terms of electronic, steric, and hydrophobicity effects on the target compounds. Thus, the Craig Plot (**Figure 2.3** below) played a key role in guiding the selection of various substituents, whereby all its four quadrants were appropriately considered and represented.[26,27] In addition, water-solubilizing groups, such as morpholinyl and piperazinyl, which are not part of the Craig Plot but capable of enhancing intermolecular hydrogen-bonding, were selected as substituents in attempts to improve the aqueous solubility. The choice of **SAR 1** groups was also informed by the commercial availability of the

relevant synthetic starting materials and reagents, though not central to the design strategy.

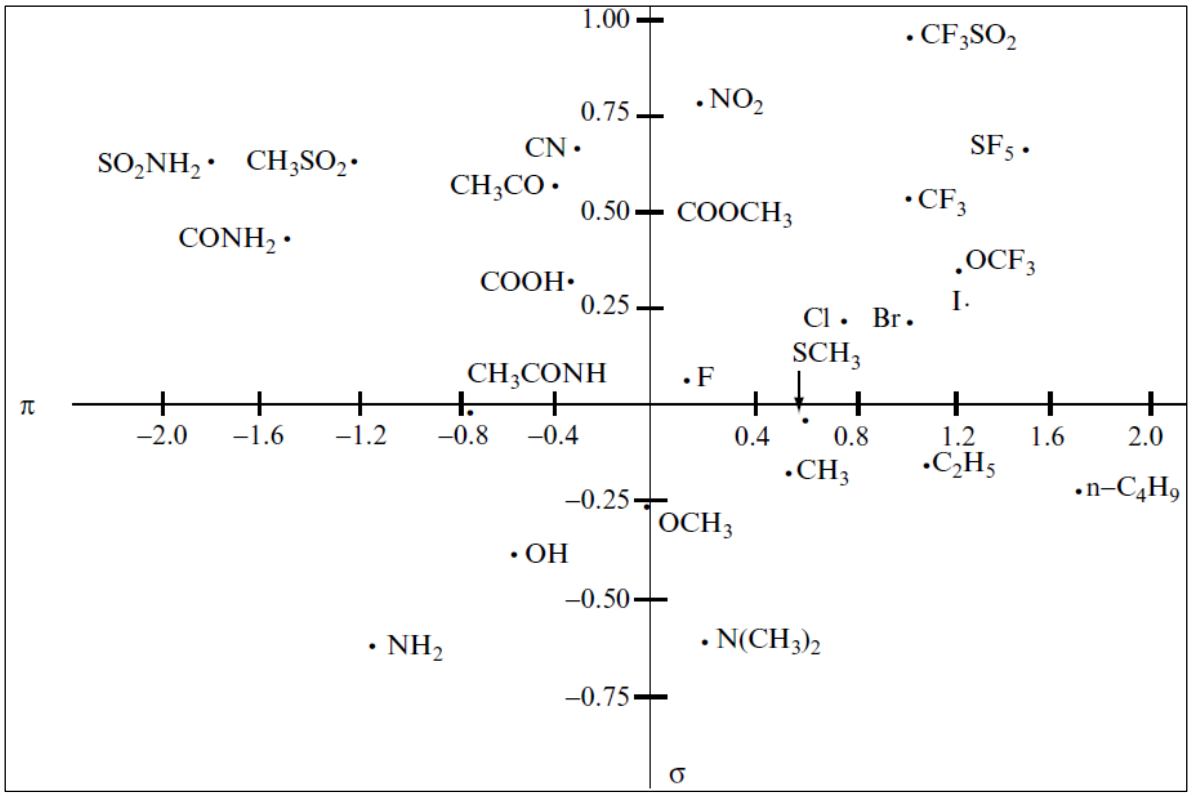

Figure 2.3: Craig Plot of Hammett constants (σ) [electronic effects] against hydrophobicity (π) values.[27]

Based on the antimycobacterial activities of compound **1** and **2** [Figure 2.1 above], the preferred position of the phenyl substitution by these diverse groups was the *meta*-position. Other phenyl positions, however, were explored, including di-substitution in some of the target analogues. In addition, substitution patterns were partially guided by the Topliss decision tree.[27]

The design of **SAR 2** analogues followed the same rationale as that of **SAR 1**. This was after fixing the **SAR 1** (left-hand side) moiety as 3-methylsulfinyl phenyl (3-SOMePh). This sulfoxide analogue of **2** had the best balance of aqueous solubility and potency. In addition, it was found to be an active 'prodrug' that underwent biotransformation *in vivo* to yield the parent sulfone-based compound **2**. The overall design strategy was to then combine the best structural features from **SAR 1** with those from **SAR 2** in the subsequent hit-to-lead optimization steps.

2.3.3 Chemistry

2.3.3.1 Synthesis of SAR 1 Analogues

The quinazolinone motif is one of the most established and extensively studied ring systems. Thus, there are a multitude of protocols, which have been published and reported for the synthesis of quinazolinone-based compounds.[28–31] However, publications describing the synthesis of the 2,3-disubstituted quinazolinones are scarce, particularly the literature on the 2-aminoquinazolinones. The synthesis of 2-aminoquinazolinones studied in this thesis work is mainly based on the work of Leivers and coworkers who recently published results of a study on various type III phosphatidylinositol 4-kinase alpha (PI4KIIIα) 2-aminoquinazolinone inhibitors with antihepatitis C virus (HCV) activity.[32] As such, all the **SAR 1** target compounds were obtained following a five-step synthetic procedure as shown in **Scheme 2.1** below, and their yields are listed in **Table 2.1**.

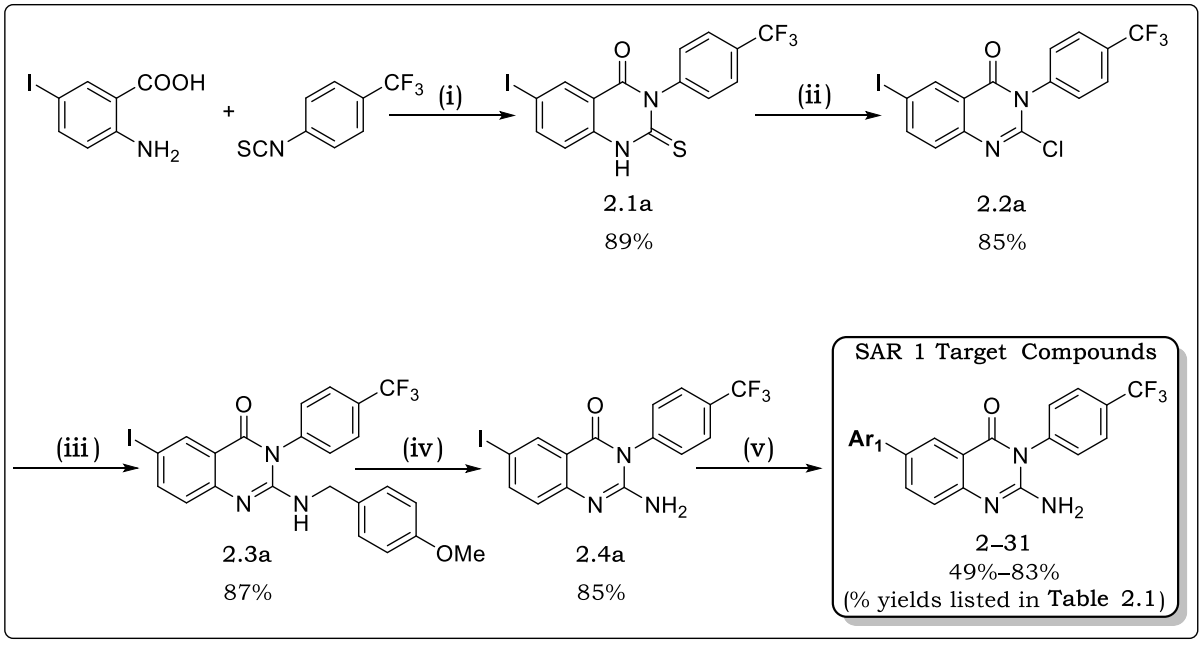

Scheme 2.1: Synthetic protocol towards **SAR 1** 2-aminoquinazolinone target compounds **2–31**. *Reagents and conditions*: (**i**) Dioxane, TEA, reflux (110 °C), 6 h; (**ii**) $POCl_3$, PCl_5, 110 °C, 12–15 h; (**iii**) DMF, 4-methoxybenzylamine, DIPEA, 80 °C, 4 h; (**iv**) TFA, reflux, 48 h or MW, 110 °C, 20 min; (**v**) Dioxane-water solvent mixture, appropriate arylboronic acid ($Ar_1B(OH)_2$) or ester, Pd(dppf)Cl_2-DCM, Cs_2CO_3, 80 °C, 1–3 h.

Table 2.1: Isolated yields for **SAR 1** 2-aminoquinazolinone target analogues.

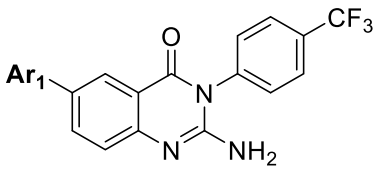

Compound	Ar_1	Yield (%)
2	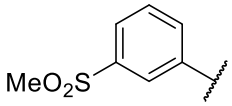	77
3	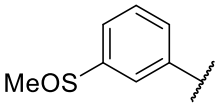	57
4	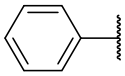	55
5	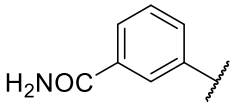	56
6	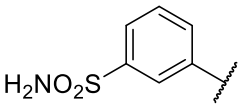	71
7	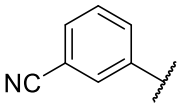	58
8	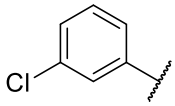	67
9	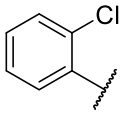	79
10	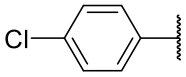	66
11	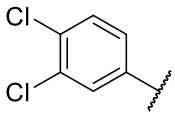	58
12	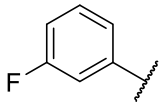	56
13	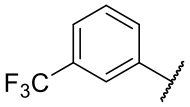	55
14	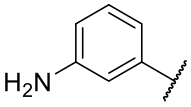	66
15	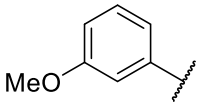	66

Table 2.1: Isolated yields for **SAR 1** 2-aminoquinazolinone target analogues.

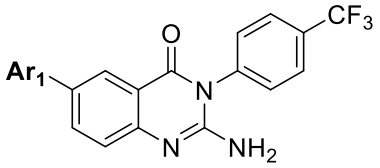

Compound	Ar_1	Yield (%)
16	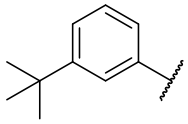	49
17	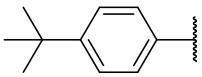	61
18	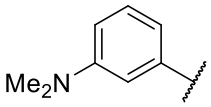	55
19	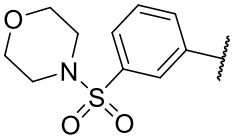	78
20	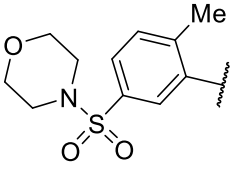	81
21	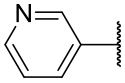	74
22	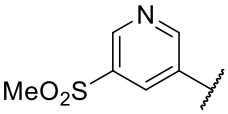	70
23	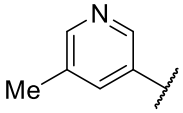	61
24	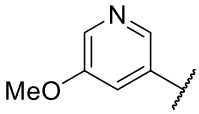	82
25	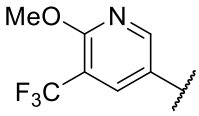	76
26	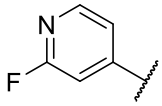	54
27	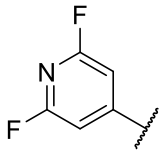	60

Table 2.1: Isolated yields for **SAR 1** 2-aminoquinazolinone target analogues.

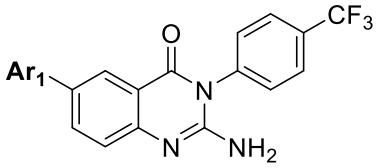

Compound	Ar_1	Yield (%)
28	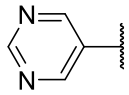	83
29	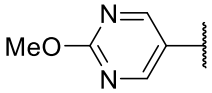	81
30	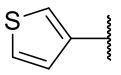	64
31	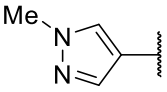	78

The synthesis started with the dehydrative cyclocondensation of the commercially available 2-amino-5-iodobenzoic acid with 4-(trifluoromethyl) phenyl isothiocyanate. This was achieved by refluxing the mixture in dioxane under the mediation of triethylamine (TEA) to afford the 2-thioxoquinazolinone intermediate **2.1a** in high yields.

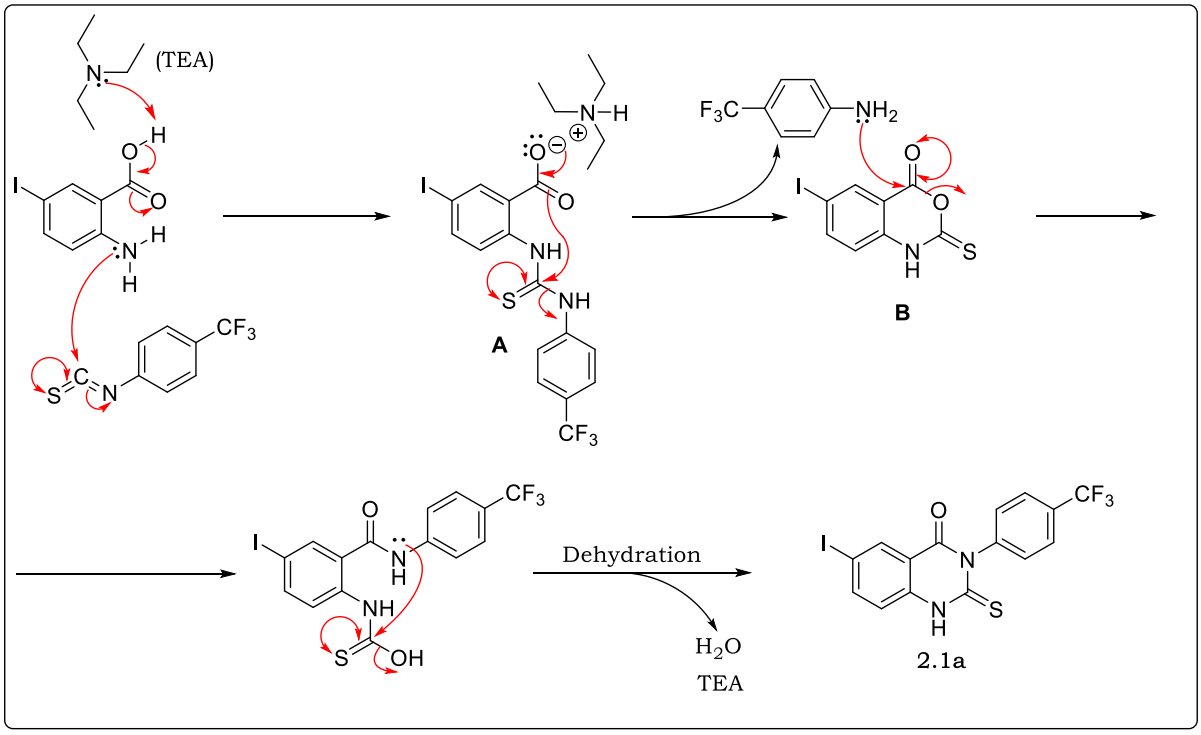

Scheme 2.2: Proposed reaction mechanism for the formation of the 2-thioxoquinazolinone intermediate.

In this case, as schematically represented in **Scheme 2.2** above, the nucleophilic amino nitrogen of the 2-amino-5-iodobenzoic acid attacks the electrophilic isothiocyanate carbon to form the thiourea intermediate **A**. Triethylamine (TEA) then abstracts a proton from the carboxylic acid leading to its preferential existence as a nucleophilic carboxylate ion. The attack of the electron-deficient thiourea **A** carbon by the nucleophilic carboxylate group leads to loss of aniline affording a thiono-isatoic anhydride intermediate **B**, which then undergoes a nucleophilic attack by the liberated aniline. This is followed by dehydrative cyclization to yield the 2-thioxoquinazolinone intermediate **2.1a**.[33]

The next step was a chlorination reaction, which was accomplished by heating the intermediate **2.1a** in phosphorus oxychloride ($POCl_3$) in the presence of phosphorus pentachloride (PCl_5) to furnish the 2-chloroquinazolinone intermediate **2.2a**. The chlorination reaction mechanism is believed to occur via a 2-dichlorophosphoryl thioquinazolinone intermediate resulting from preferential nucleophilic attack of the phosphorus in $POCl_3$ by the sulfur atom followed by elimination of a chloride ion. Then, attack on the electron-deficient sulfur-bearing carbon by the chloride ion results in the elimination of phosphenothioic chloride and hydrochloric acid to yield the 2-chloroquinazolinone intermediate **2.2a**. The regioselectivity for chlorination of the thiocarbonyl at position 2 versus the carbonyl at position 4 is due to the chemoselectivity of phosphorous (V) for sulphur versus oxygen caused by the substantially better orbital overlap between their 3p orbitals. Both $POCl_3$ and PCl_5 are believed to take part in the chlorination process through a similar mechanism, which is depicted in **Scheme 2.3** below.[34]

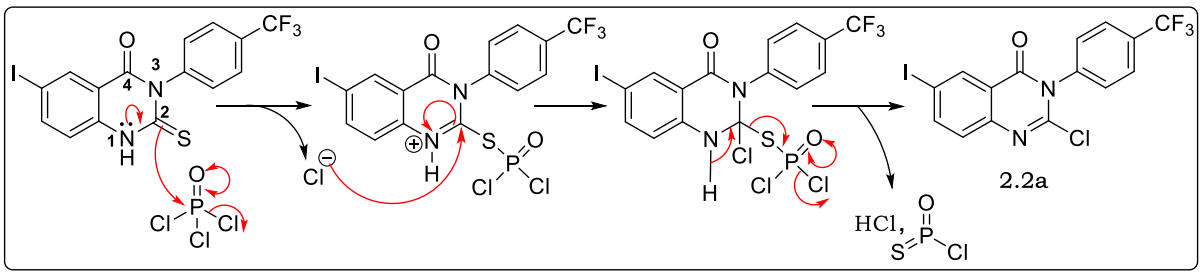

Scheme 2.3: Proposed chlorination reaction mechanism.

The step that followed was the introduction of the 2-amino group through the substitution of the chloro substituent with 4-methoxybenzylamine. In this case, the reaction was executed by heating a mixture of **2.2a** and 4-methoxybenzylamine in *N*,*N*-dimethylformamide (DMF), and in the presence of diisopropylethylamine (DIPEA) to yield the intermediate **2.3a**. The reaction mechanism involved is the addition-elimination nucleophilic aromatic substitution (S_NAr). The S_NAr reaction, in this instance, regioselectively takes place at the choro-bearing carbon (C-2) due to its more enhanced electron deficiency than the iodo-bearing carbon. This is attributable to the fact that C-2 is attached to two electron-withdrawing nitrogen atoms, which exhibit an *ortho*-directing effect, as well as acting as electron sinks. The electron deficiency of C-2 is further promoted by the inductive electron-withdrawing chloro group. In addition, the aromaticity of the quinazolinone ring system leads to resonance stabilization while the carbonyl oxygen at position 4 acts as an anion-stabilizing group. These factors act in concert to make the chloro an excellent leaving group while the iodo serves to further activate the quinazolinone ring system through its inductive electron-withdrawing effect. Generally, the first step involves the nucleophilic amino nitrogen of the 4-methoxybenzylamine attacking the chloro-bearing carbon to form an intermediate with disrupted aromaticity. This is the rate-limiting addition step. In the second step, there is regeneration of the aromatic quinazolinone ring system followed by the elimination of the chloride ion. Finally, the chloride ion abstracts a proton to form HCl, which is then mopped up by DIPEA as a hydrochloride salt. The proposed S_NAr reaction mechanism is summarized in **Scheme 2.4** below.[34]

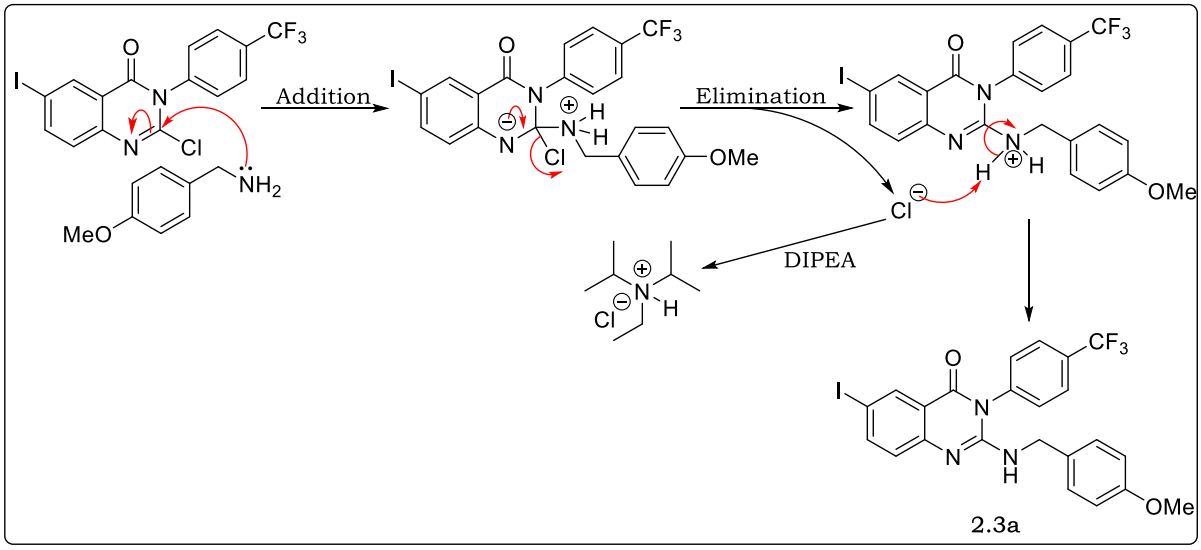

Scheme 2.4: Proposed S_NAr reaction mechanism.

Thereafter, an acid-catalysed cleavage of the 4-methoxybenzyl moiety was attained by heating compound **2.3a** in trifluoroacetic acid (TFA) under reflux or microwave (MW) conditions to afford the penultimate intermediate **2.4a**. Firstly, the benzyl nitrogen atom is protonated, and then the breaking of the C–N bond is facilitated by the push of electrons through the benzyl ring system from the methoxyl oxygen, as indicated in **Scheme 2.5** below. The free primary amine was then obtained by acid-base exchange using Amberlyst® A21 free base resin.

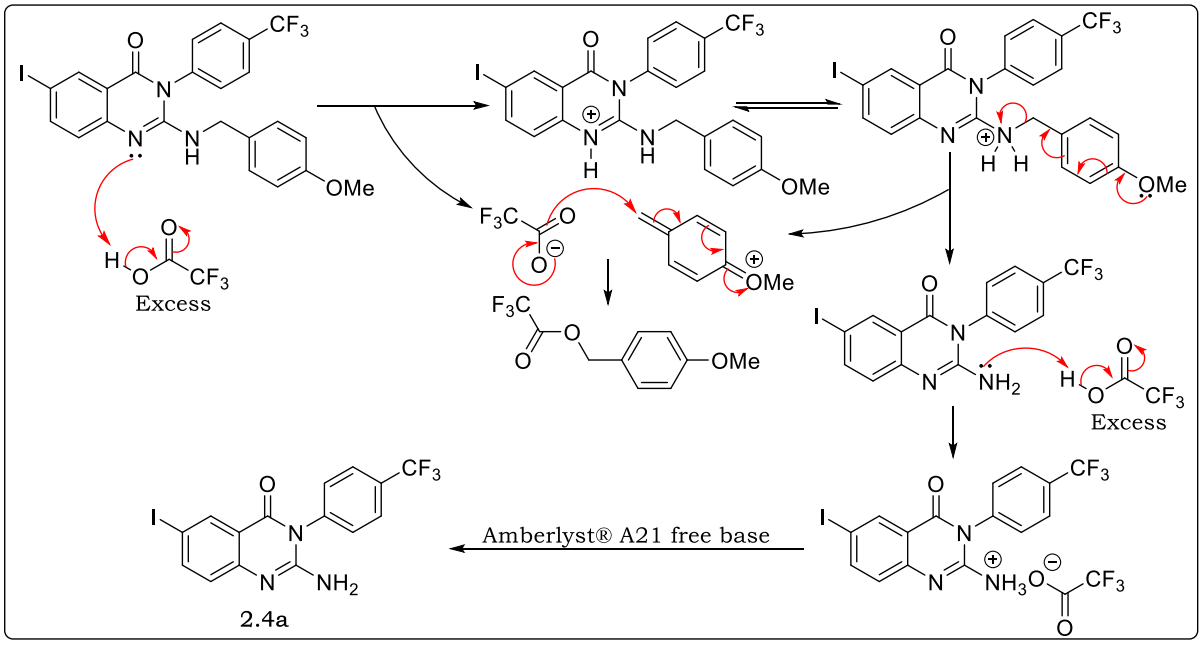

Scheme 2.5: Proposed mechanism of acid-catalysed cleavage of the 4-methoxybenzyl moiety.

Finally, the Suzuki-Miyaura cross-coupling reaction of **2.4a** with the appropriate arylboronic acids was undertaken to yield the desired target compounds **2**–**31** in good yields. The catalyst employed in this reaction was [1,1′-bis(diphenylphosphino)ferrocene]dichloropalladium(II) complexed with dichloromethane (Pd(dppf)Cl_2-DCM), while cesium carbonate (Cs_2CO_3) was the base used. The Suzuki-Miyaura cross-coupling is a versatile reaction with many advantages such as the commercial availability of large numbers of diverse boronic acids; the stability of key reagents to heat, air and moisture; and the ease of separation of reaction products.[35,36] This reaction, on the other hand, may be plagued by impediments such as unwanted byproducts as a result of self-coupling and coupling of phosphine-bound aryls, which could result in decreased isolated yields.[37]

The Suzuki-Miyaura cross-coupling reaction proceeds via a catalytic cycle as shown in **Scheme 2.6** below. Three major steps are involved: oxidative addition, transmetallation, and reductive elimination. Oxidative addition of the arylhalide to the palladium (0) complex (Pd^0L_2) affords a stable trans-σ-palladium (II) complex. This is the rate-determining step, which is followed by displacement of the halide ion by a base to yield a more reactive organopalladium hydroxide. This then undergoes transmetallation with the organoboronic acid or ester. The base accelerates the transmetallation step, presumably through a more nucleophilic complex. This step yields a complex from which the desired product is expelled by reductive elimination, and regeneration of the ligand-bound Pd^0 catalyst ensues.[34,38–40]

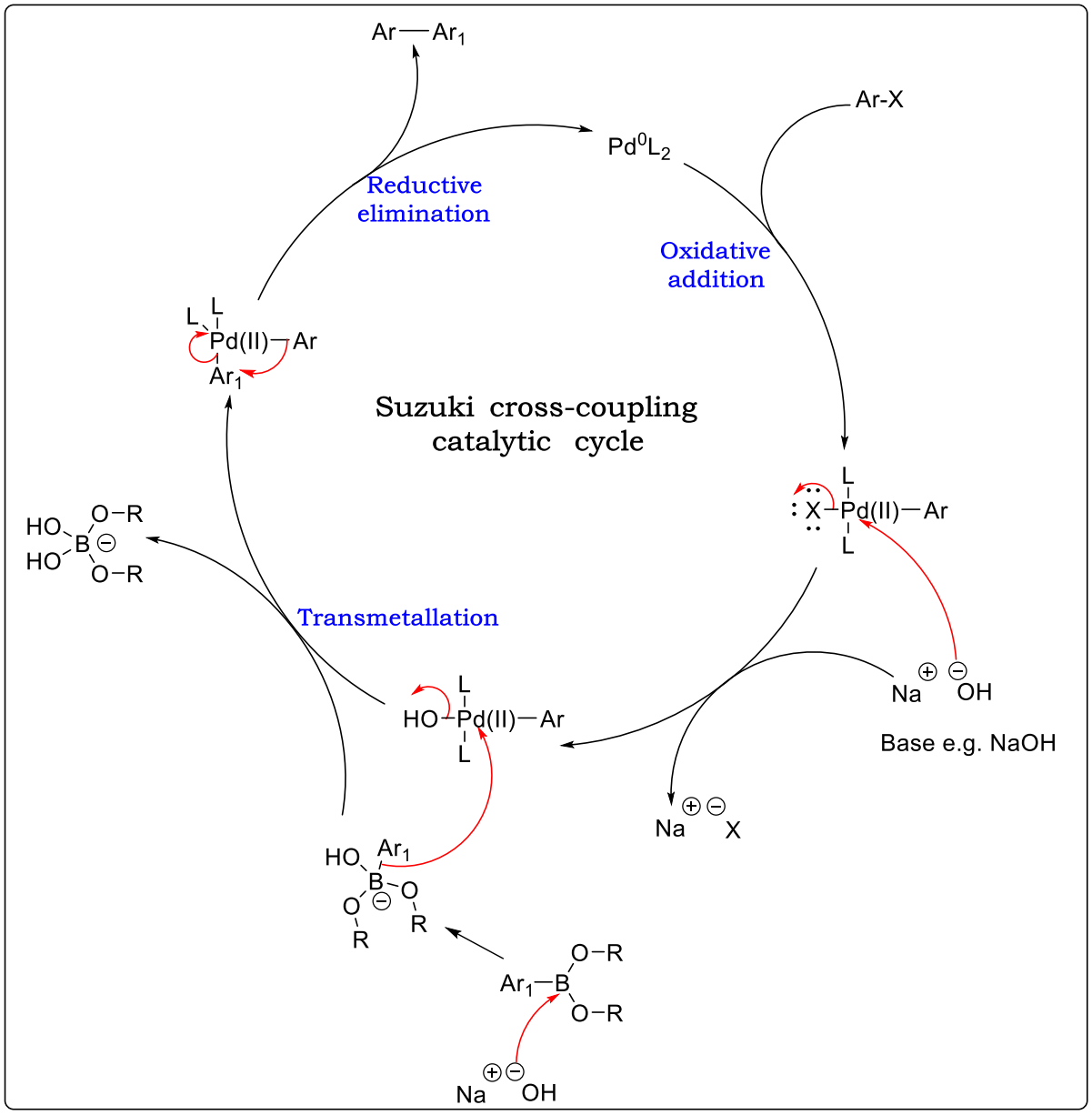

Scheme 2.6: Catalytic cycle for Pd-catalysed Suzuki-Miyaura cross-coupling reaction.

2.3.3.2 Synthesis of SAR 2 Analogues

Some of the **SAR 2** analogues were accessed through the same synthetic approach as that described in the foregoing discussion regarding the synthesis of **SAR 1** target compounds. In this case, structural modifications were made on the right-hand side of the quinazolinone core. However, due to the scarcity of commercially available arylisothiocyanates, it was not possible to create adequate structural heterogeneity by adapting the **SAR 1** synthetic protocol described in **Scheme 2.1** above. As such, synthesis of some arylisothiocyanates from commercially available anilines was

attempted.[41–43] Despite the potential associated with this approach, the use of highly toxic reagents such as carbon disulfide, coupled with low product yields, and the chemical instability of some isothiocyanates discouraged further exploration of this option.

Consequently, other synthetic protocols were investigated, particularly those involving the use of diverse and readily available primary anilines, as this would allow the creation of diversity in **SAR 2** analogues. In this regard, the work of Lecoutey and colleagues was adapted. These researchers previously reported a one-pot procedure for the synthesis of 2-amino-3-aryl-quinazolin-4(3*H*)-ones.[44] In this particular study, several methyl 2-aminobenzoates were used as key starting materials, which were reacted with ethoxycarbonyl isothiocyanate and primary amines in a one-pot reaction mediated by 1-ethyl-3-(3-dimethylaminopropyl)carbodiimide (EDCI), to yield the desired quinazolinone-based products. However, our attempts to use methyl 2-amino-5-bromobenzoate in the one-pot synthetic protocol failed. Nonetheless, in search of a solution, investigations were carried out into this protocol based on the chemistry and the reaction mechanisms involved. To our delight, it became discernible that one of the synthetic intermediates was precipitating out of solution, and thus hindering further reaction progress. The procedure was therefore modified to a four-step protocol as shown in **Scheme 2.7** below. Interestingly, the compound that was crushing out of solution was identified as the versatile intermediate **2.5**, which was isolated in quantitative yields. In addition, although ethoxycarbonyl isothiocyanate is commercially available, it was successfully generated *in situ* from relatively inexpensive and readily available ethyl chloroformate and potassium thiocyanate.[45]

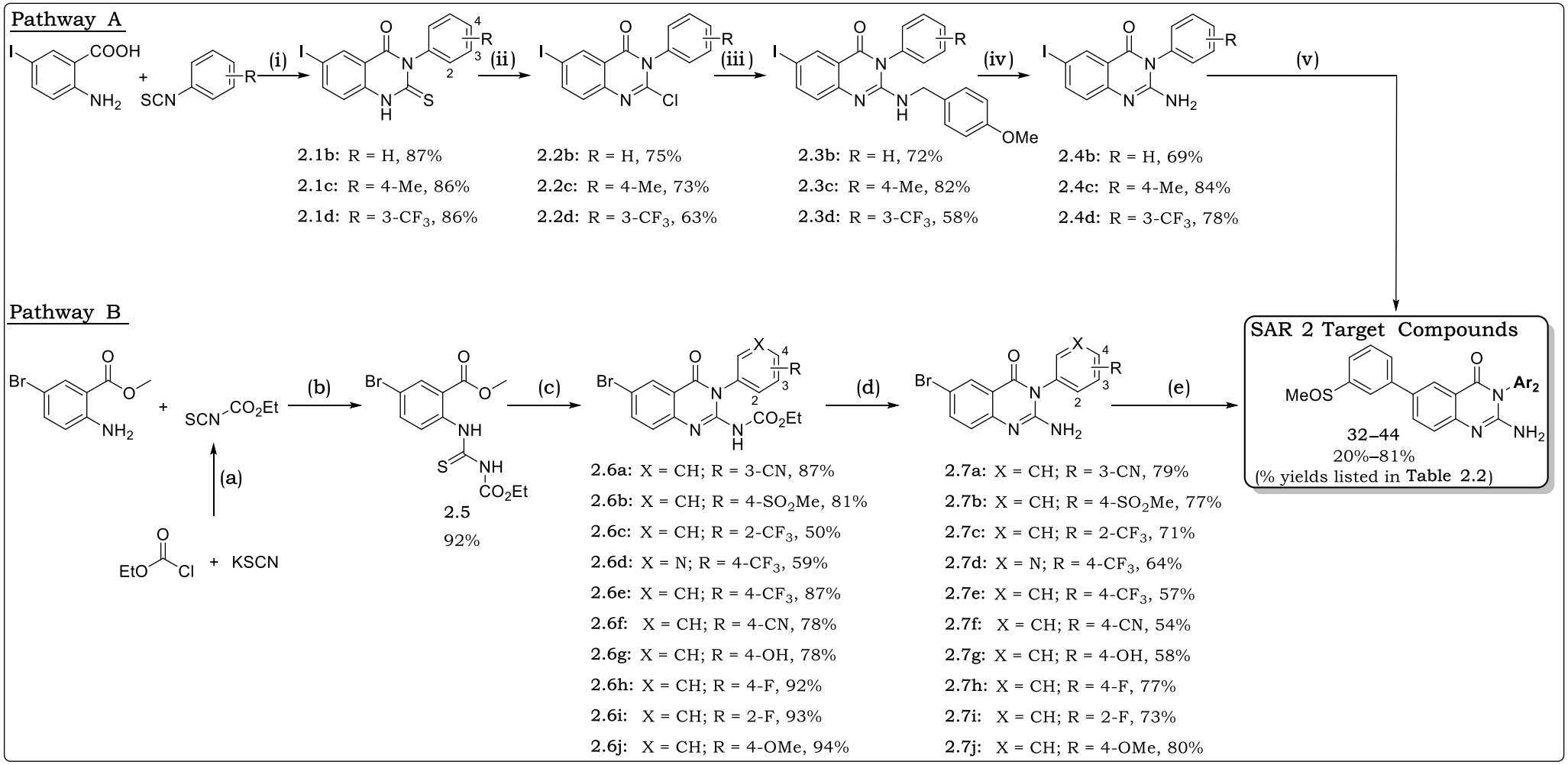

Scheme 2.7: Synthetic protocol towards **SAR 2** 2-aminoquinazolinone target compounds **32**–**44**. *Reagents and conditions*: **Pathway A** (same as **Scheme 2.1**): (**i**) Dioxane, TEA, reflux (110 °C), 6 h; (**ii**) $POCl_3$, PCl_5, 110 °C, 12–15 h; (**iii**) DMF, 4-methoxybenzylamine, DIPEA, 80 °C, 4 h; (**iv**) TFA, reflux, 48 h or MW, 110 °C, 20 min; (**v**) Dioxane/water, appropriate boronic acid ($Ar_1B(OH)_2$) or ester, $PdCl_2$(dppf)-DCM, Cs_2CO_3, 80 °C, 1–3 h. **Pathway B:** (**a**) MeCN, 25 °C, 2 h; (**b**) MeCN, 0 °C, 30 min; (**c**) DCM, appropriate primary aromatic amine (Ar_2NH_2), EDCI, 25 °C, 6–29 h; (**d**) TFA, MW, 110 °C, 20 min; (**e**) DMF, appropriate arylboronic acid, $Pd(PPh_3)_2Cl_2$, K_2CO_3, 100 °C, 1–4 h.

Table 2.2: Isolated yields for **SAR 2** target analogues.

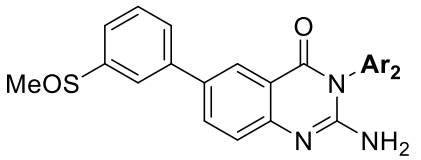

Compound	Ar_2	Yield (%)
32	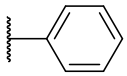	55
33	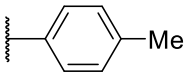	32
34	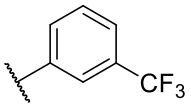	55
35	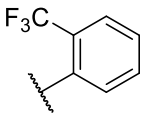	33
36	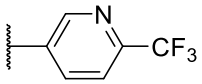	56
37	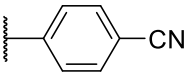	32
38	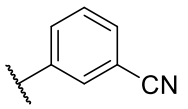	38
39	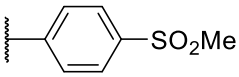	20
40	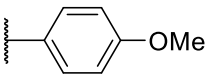	81
41	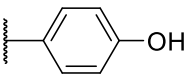	40
42	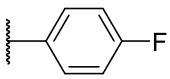	71
43	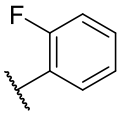	66
44*	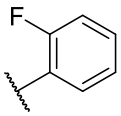	76

***Same as **43** but with a –SO_2Me instead of –SOMe on the left-hand side.

The reaction of methyl 2-amino-5-bromobenzoate with ethoxycarbonyl isothiocyanate was accomplished by stirring a mixture of the two in acetonitrile (MeCN) at 25 °C to afford the thiourea intermediate **2.5** in high yields.

The step that followed was the coupling and cyclization of this intermediate with the appropriate primary amine. This was attained by stirring at 25 °C a mixture of **2.5**, the appropriate aniline, and EDCI in dichloromethane (DCM) to generate the desired 2-carbamate quinazolinone-based intermediates **2.6a**–**2.6j**. This reaction is believed to proceed through the mechanism depicted in **Scheme 2.8** below. Accordingly, the relatively more electron-deficient carbon atom of the EDCI is nucleophilically attacked by the thiourea sulfur atom, making it a better leaving group while increasing the electrophilicity of the thiourea carbon. The nucleophilic nitrogen atom of the amine then attacks the thiourea carbon followed by loss of EDCI as a stable, water-soluble thiourea byproduct. The resulting intermediate then cyclizes when the more nucleophilic nitrogen atom attacks the carbonyl carbon of the methyl ester to form the desired compound via loss of methanol.[46]

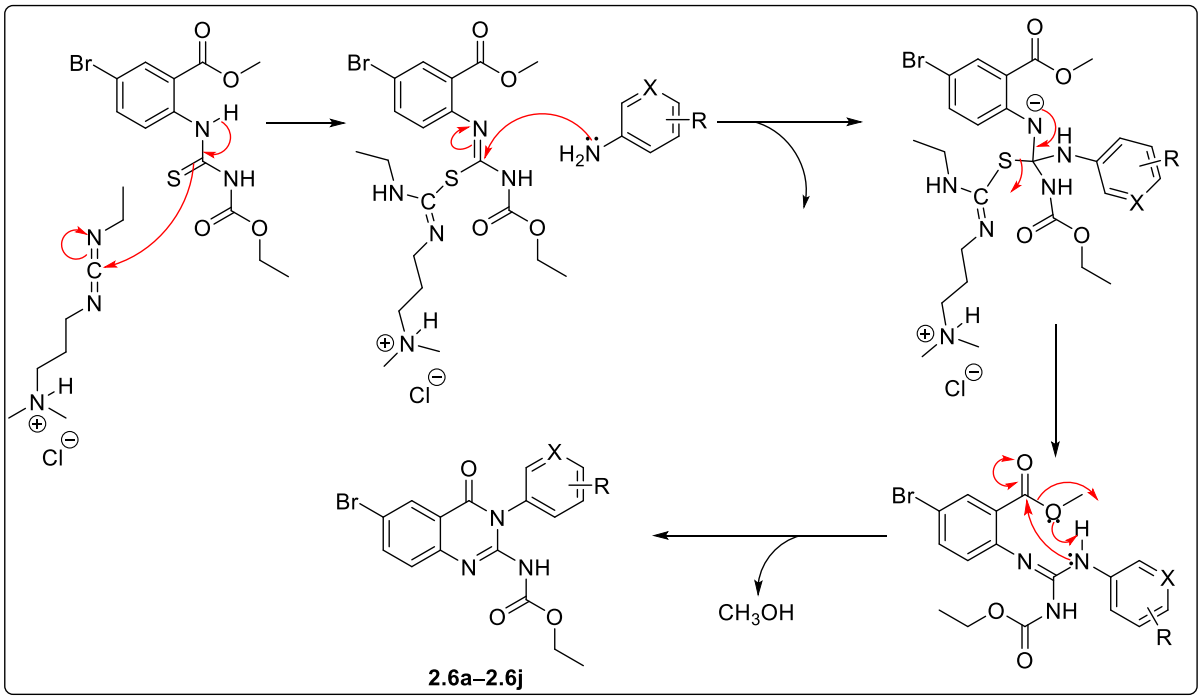

Scheme 2.8: Reaction mechanism for the formation of 2-carbamate quinazolinone intermediates.

Then, the acid-catalysed cleavage of the carbamate amide bond followed. This was accomplished by heating the appropriate starting material in trifluoroacetic acid under microwave energy to furnish the corresponding primary amine intermediates **2.7a**–**2.7j**. This reaction proceeds via a mechanism depicted in **Scheme 2.9** below, whereby the ester portion is lost

as ethyltrifluoroacetate and carbon dioxide. Acid-base exchange using Amberlyst® A21 free base resin then affords the desired products as neutral primary amines.

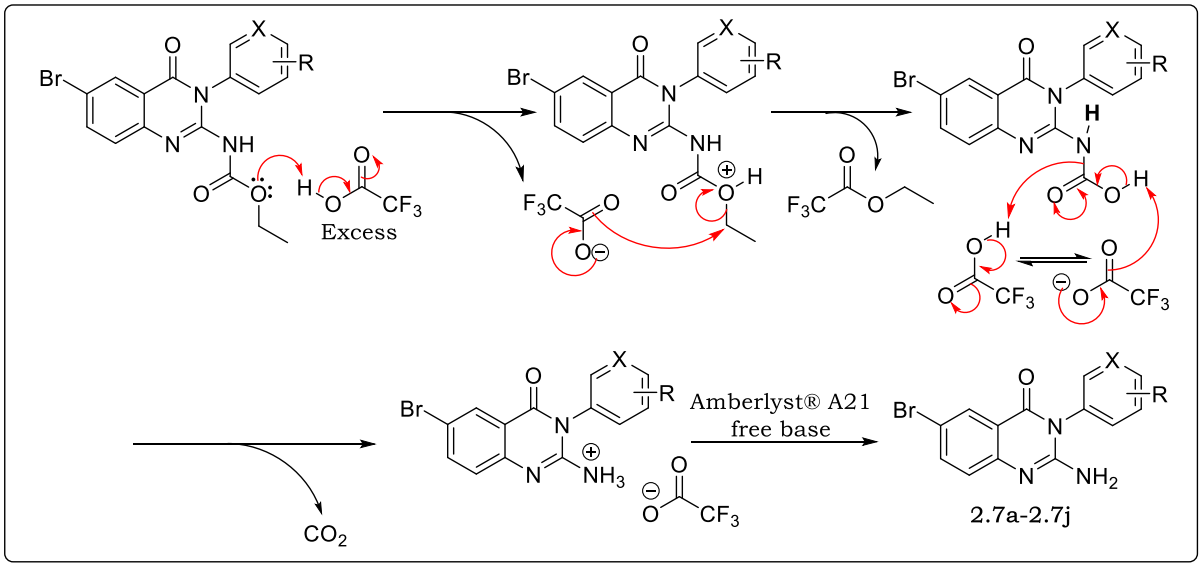

Scheme 2.9: Proposed reaction mechanism for the acid-catalysed deprotection.

The 2-aminoquinazolinone penultimate intermediates were then subjected to a Suzuki-Miyaura cross-coupling reaction with 3-methylsulfinylphenyl boronic acid to afford the desired **SAR 2** target compounds in yields ranging from low to high, as shown in **Table 2.2** above. The bromo-containing penultimate intermediates were poorly soluble in the dioxane-water solvent mixture, which was successfully used with the iodo-containing counterparts. Thus, the solvent was changed to DMF while the Pd(dppf)Cl_2-DCM catalyst was replaced by the more soluble catalyst, bis(triphenylphosphine)palladium(II) dichloride ($Pd(PPh_3)_2Cl_2$).

2.3.4 Spectroscopic and Chromatographic Characterization

All the synthesized intermediates and final target compounds were subjected to various spectroscopic and chromatographic techniques for purposes of monitoring reactions; purification and purity determination; as well as elucidation and confirmation of chemical structures. To this effect, thin layer chromatography (TLC), and reversed phase high performance liquid chromatography coupled to mass spectrometry (LC-MS) were applied to monitor the progress of all the reactions. LC-MS played a vital role in determining the chromatographic purities, which were calculated as percentage peak areas. Also, LC-MS was applied in confirming molecular formulas of compounds by using parameters such as the pseudo-molecular ions $(M+H)^+$, and fragmentation patterns derived from the LC mass spectra. Another important piece of information obtained from the LC-MS was the ultraviolet/visible electromagnetic radiation (UV-VIS) scan, which was facilitated by the use of diode array HPLC detector (DAD). This was instrumental in determining the wavelength of maximum absorption (λ_{max}) at which eluates were monitored and collected during the chromatographic purification of most compounds using the Biotage Isolera One® flash chromatograph.

Proton (^{1}H) NMR spectroscopy, and carbon-13 (^{13}C) NMR spectroscopy, on the other hand, were important in the elucidation and confirmation of chemical structures for all the synthesized compounds.

The characterization of compound **2**, as an example, is discussed herein, including that of the associated synthetic intermediates **2.1a**–**2.4a**. **Figure 2.4** below shows the stacked one-dimensional (1D) ^{1}H NMR spectra for these intermediates. All the spectra were consistent with the chemical structures of the corresponding compounds. As such, the spectrum corresponding to compound **2.1a** showed a highly deshielded quinazolinone NH proton (**H-7**) resonating most downfield at chemical shift (δ) 13.15 as a broad singlet (br, s). Proton **H-1** produced a doublet (d) signal at δ 8.18 and exhibited a long-range coupling (^4J = 2.0 Hz) with proton **H-2**. As a result, proton **H-2** yielded

a doublet of doublets (dd, ^{3}J = 8.6 and ^{4}J = 2.0 Hz) signal at δ 8.08 due to the second coupling with proton **H-3** (d, ^{3}J = 8.6 Hz).

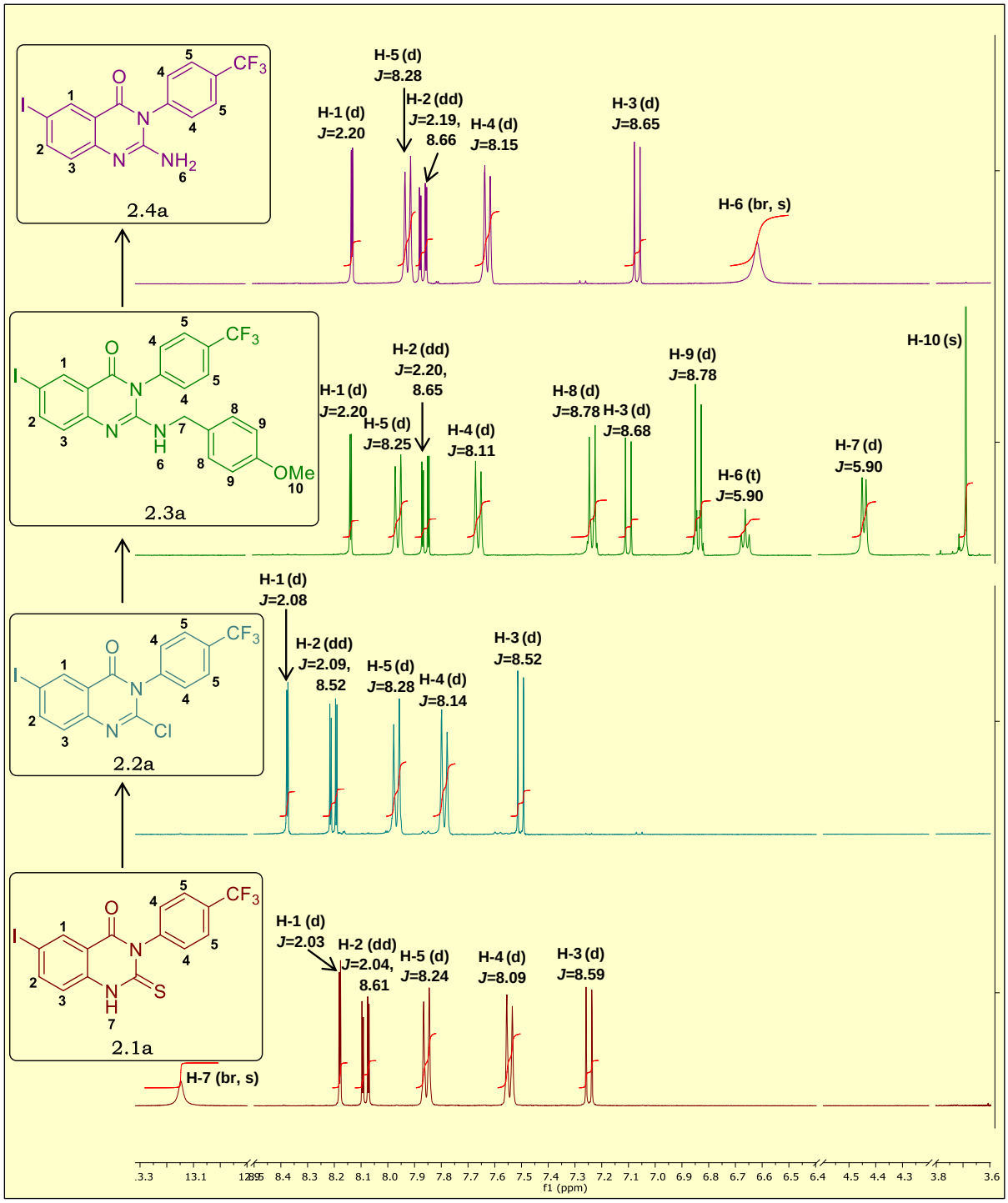

Figure 2.4: Stacked 1D ^{1}H NMR spectra for the synthetic intermediates **2.1a**–**2.4a** in DMSO-d_6 at 400 MHz.

The presence the iodo group makes protons **H-1** and **H-2** the most deshielded aromatic protons due to its inductive electron-withdrawing effect. Proton **H-3** was the most shielded aromatic proton (δ 7.25) due to the

delocalization of the ring electrons making the carbon bearing it negatively charged in one of the resonance structures. The two pairs of chemical shift-equivalent phenyl protons **H-4** and **H-5** couple with each other, and therefore yielded two doublets with each integrating for two protons, and with similar coupling constants (J = 8.2 Hz). As expected, protons **H-5** were more deshielded (δ 7.86) than the **H-4** protons (δ 7.54) due to the electron-withdrawing effect of the trifluoromethyl (-CF_3) group.

Since the quinazolinone and the 4-CF_3Ph groups were constant in the subsequent compounds, the ^{1}H NMR signals corresponding to the protons described in the foregoing discussion were generally expected to remain the same.

The diagnostic features for the successful chlorination reaction leading to compound **2.2a** were the loss of proton **H-1**, and the more downfield resonance for all the other protons due to the inductive electron-withdrawing effect of the chloro group.

The ^{1}H NMR spectrum corresponding to the S_NAr reaction product **2.3a** showed additional protons characteristic of the added 4-methoxybenzylamine group: the three methoxyl protons **H-10** yielded a singlet at δ 3.69; the two methylene protons **H-7** gave a doublet (J = 5.9 Hz) at δ 4.42 due to its coupling with the **H-6** NH proton, which afforded a broad triplet (J = 5.9 Hz) at δ 6.65; and the aromatic benzyl protons **H-8** and **H-9** yielded two doublet (J = 8.8 Hz) signals, each integrating for two protons at δ 7.22 and δ 6.83, respectively. Protons **H-9** are more shielded than **H-8** due to the electron-donating effect of the methoxy group, and therefore resonate more upfield.

Likewise, the ^{1}H NMR spectrum of the deprotection product **2.4a** showed a diagnostic broad singlet signal at δ 6.61, attributable to the free primary amine. In addition, another diagnostic feature in this spectrum was the loss of all the signals corresponding to the 4-methoxybenzyl group.

The synthetic step that followed was the Suzuki coupling to yield the final target compound **2**. As shown in **Figure 2.5** below, there were additional

signals compared to the spectrum for the penultimate intermediate **2.4a**. After the analysis of the spectrum, the signals were consistent with the chemical structure of compound **2**.

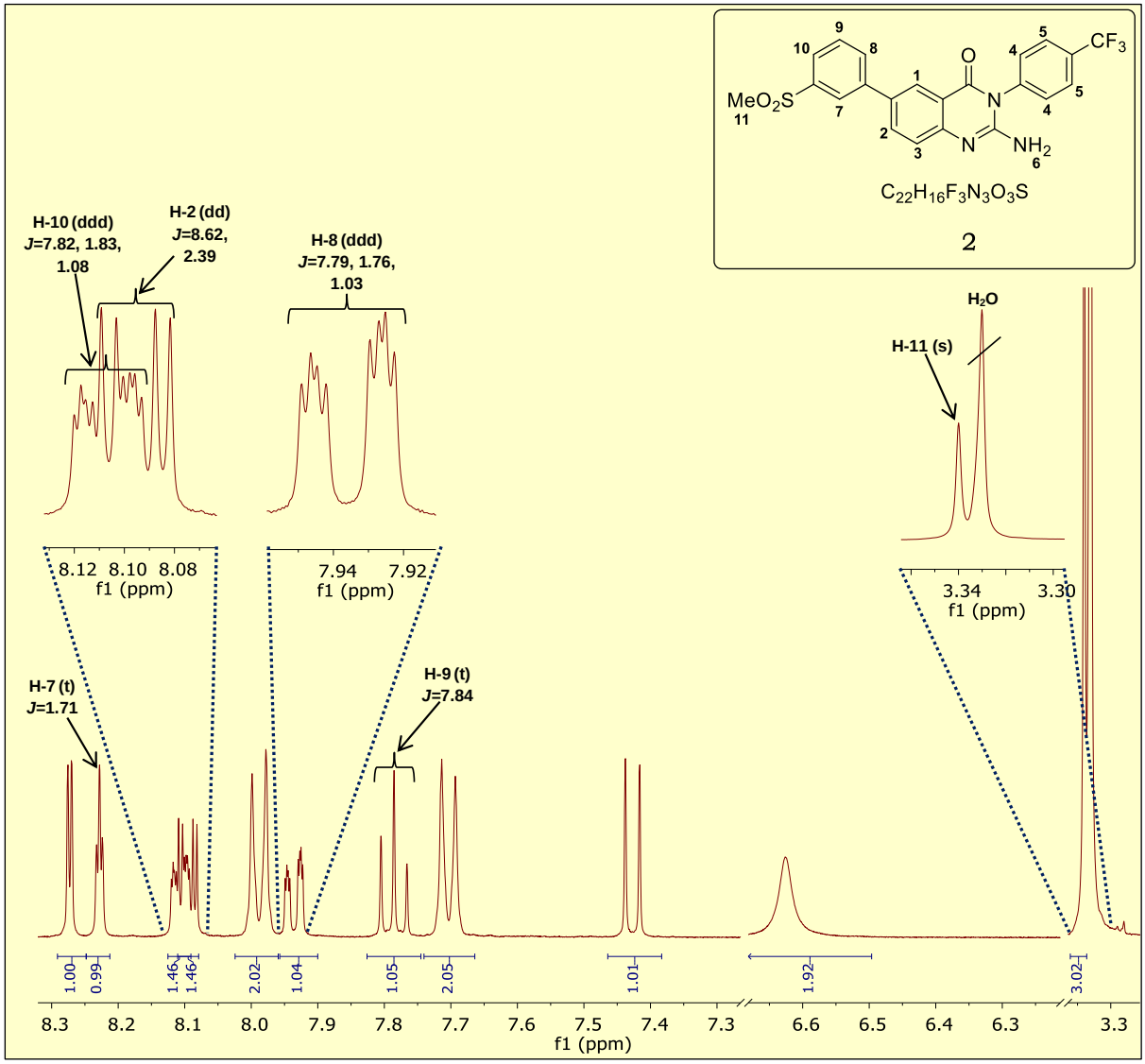

Figure 2.5: ^{1}H NMR spectrum of **2** in DMSO-d_6 at 400 MHz.

Briefly, the singlet at δ 3.34, which integrated for three protons, was assigned to the methyl protons **H-11**. The downfield triplet signal at δ 8.23 corresponded to proton **H-7**, which experienced two equal long-range couplings (^{4}J = 1.7 Hz) from protons **H-8** and **H-10**. In this case, protons **H-8** and **H-10** each experienced a short-range coupling with proton **H-9**, a long-range coupling with **H-7**, and a long-range coupling with each other. Consequently, the signals that split into doublet of doublet of doublets (ddd) were assigned to **H-8** (ddd, J = 7.8, 1.8, 1.0 Hz) at δ 7.94, and **H-10** (ddd, J =

7.8, 1.8, 1.0 Hz) at δ 8.11. **H-10** is more deshielded, and thus resonated more downfield than **H-8** due to its close proximity to the electron-withdrawing *ortho*-methylsulfonyl group. Although the **H-10** signal coincidentally overlapped with the **H-2** dd signal, independent manual integration of the two signals enabled assignment of the two protons, which otherwise yielded a multiplet (m) integrating for two protons. The triplet signal at δ 7.79 was assigned to proton **H-9**, which experienced two equal couplings (t, *J* = 7.8 Hz) from **H-8** and **H-10**. The other signals in this spectrum were characteristically consistent with the rest of the chemical structure for compound **2** as described for the penultimate intermediate **2.4a** in **Figure 2.4**.

In addition, ^{13}C NMR spectroscopy was used to provide further evidence to support the chemical structure of compound **2**. As depicted in **Figure 2.6** below, although 20 distinct signals were obtained, the chemical shift-equivalent pairs of carbons in the trifluoromethylphenyl moiety resonated at the same chemical shifts, and therefore all the 22 carbons were accounted for. The diagnostic signals were those due to the most deshielded carbonyl carbon (**C-12**) resonating most downfield at δ 161.87, and the most shielded methyl carbon (**C-17**) resonating most upfield at δ 43.57. Also, the relatively more downfield and shorter signals were assigned to the quaternary carbons bearing electronegative atoms like nitrogen and sulfur, besides oxygen. In this case, **C-13**, **C-14**, **C-15**, and **C-16** resonated at δ 151.80, 150.51, 141.85, and 140.59, respectively.

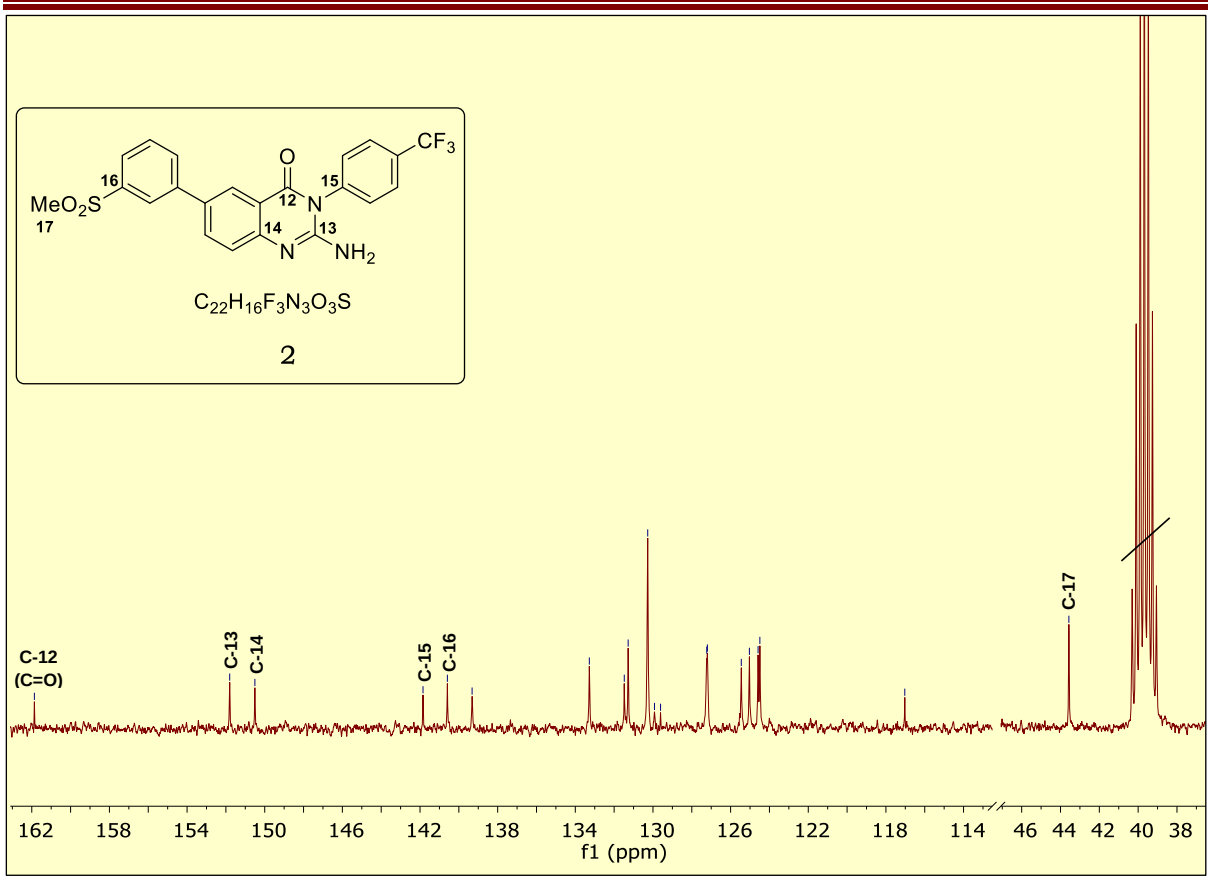

Figure 2.6: ^{13}C NMR spectrum of compound **2** in DMSO-d_6 at 400 MHz.

Data obtained from the LC-MS, as shown in **Figure 2.7** below, provided more information on the structural characteristics of compound **2**. This information was three-fold: The LC chromatogram provided the purity as > 99%, based on the percentage peak area; the mass spectrum exhibited a pseudo-molecular ion [$(M+H)^+$] of 460.1 as the base peak (100%), corresponding to the calculated one for $C_{22}H_{16}F_3N_3O_3S$; the UV-VIS spectrum displayed two peaks depicting the λ_{max} as 240 and 300 nm.

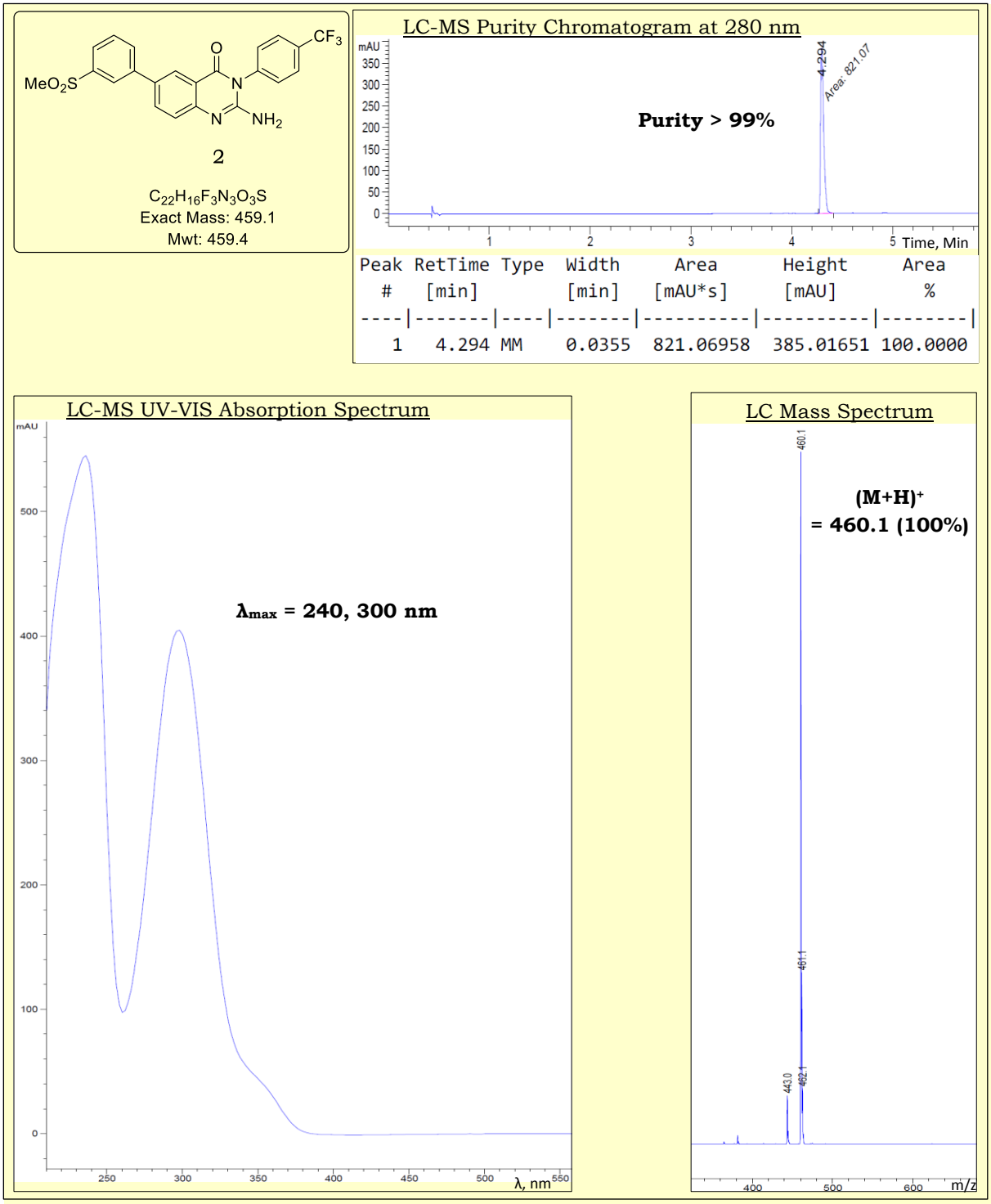

Figure 2.7: LC-MS readout for compound **2**.

The Experimental chapter (Chapter 6) describes the full characterization data for each of the synthesized compounds.

2.4 Benzoxazole-Based Oximes

2.4.1 General Introduction

The Novartis Institute for Tropical Diseases (NITD) carried out antimycobacterial phenotypic whole-cell high-throughput screening of a library of about 6000 compounds comprising of small polar compounds. The profiles of the compounds, which formed the selection criteria, included Mwt = 150–350, cLogP = -1–3, rotatable bonds ≤ 5, tPSA < 140 $Å^2$, non-reactive with no toxicophores, and MIC_{99} ≤ 20 µM. From this exercise, nine hit series of compounds were selected and designated NITD **S1**–**S9**. The nine series of NCEs were transferred to H3D as part of a collaborative agreement between NITD and H3D. The main objective was to initiate hit-to-lead and lead optimization campaigns on these series, as well as to conduct studies on target identification.

The NITD **S6** and **S7** series formed part of this thesis work. The representative **S6** hit is benzothiazole-based while the representative **S7** hit is benzoxazole-based, and both contain a dimethyl carbamate-functionalized oxime moiety. **Figure 2.8** below summarizes the genesis of this thesis work on benzoxazole-based oximes. Also, the figure shows unpublished preliminary SAR and biological evaluation studies conducted at H3D, along with the general liabilities associated with the **S6** and **S7** series of compounds. In summary, the compounds exhibited clear SAR trends whereby the benzoxazole- and benzothiazole-based compounds were found to be equipotent, while benzimidazoles had very weak antimycobacterial activities. A dimethyl carbamate group on the oxime moiety was found to be essential for activity for all nitrile-containing compounds, while their free oxime counterparts were inactive. However, the dimethyl carbamate moiety was associated with low microsomal metabolic stability exhibited by these agents. Besides, the replacement of the nitrile group with groups such as thiazole resulted in compounds that were active as free oximes. Additionally, replacement of the benzothiazole phenyl ring with a pyridyl led to loss of antimycobacterial activity.

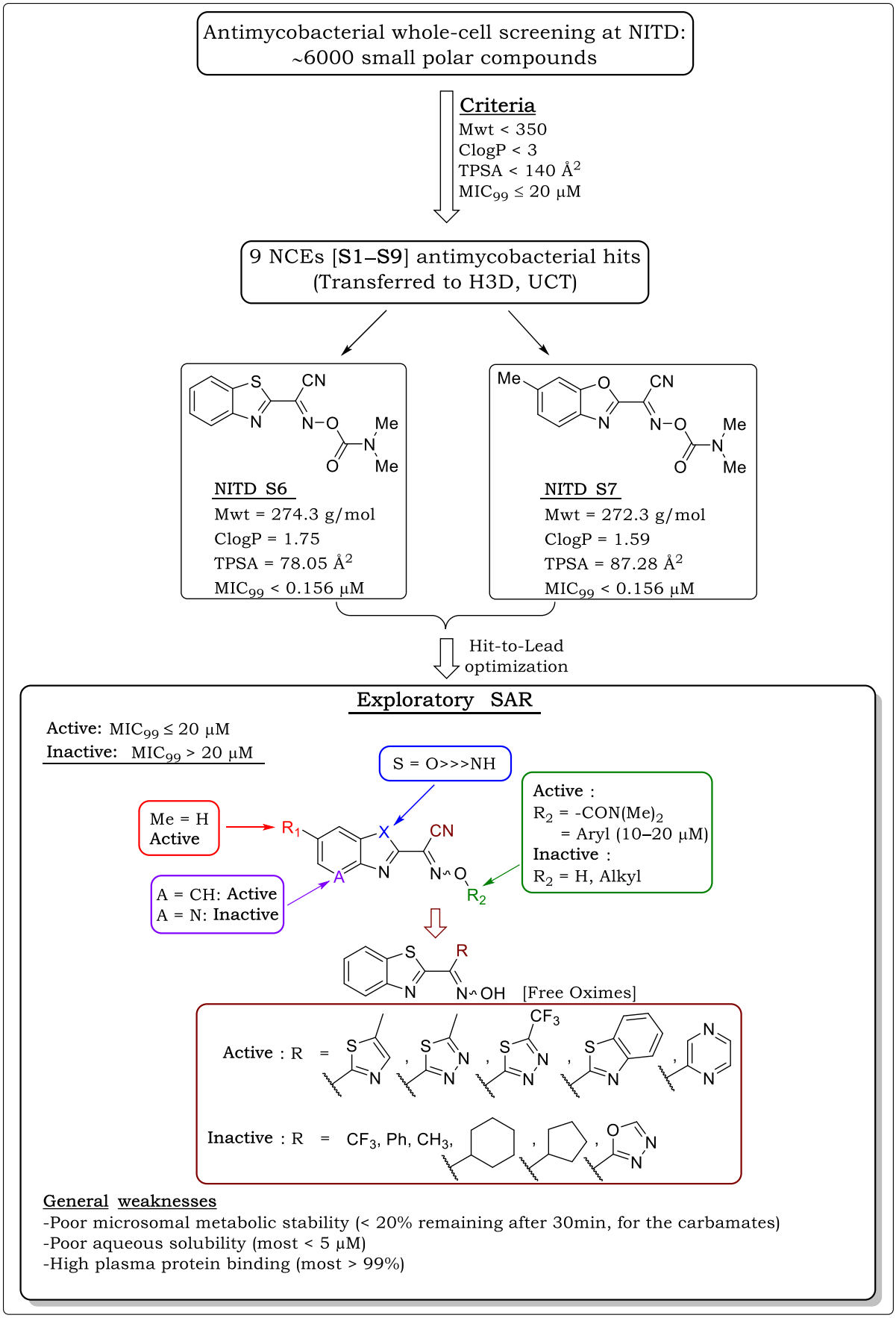

Figure 2.8: Identification and preliminary SAR for the oxime-based NITD **S6** and **S7** series.

This thesis work aimed to design and synthesize compounds in such a manner as to mitigate some of the reported liabilities such as low metabolic stability and poor aqueous solubility, along with expanding the SAR studies particularly on the benzoxazole-based compounds (NITD **S7**), which were least explored in the preliminary studies.

2.4.2 Design

Three positions were identified for structural modifications while the benzoxazole motif was maintained constant. Accordingly, these medicinal chemistry plans were designated **SAR 1**, **SAR 2**, and **SAR 3** as shown in **Figure 2.9** below.

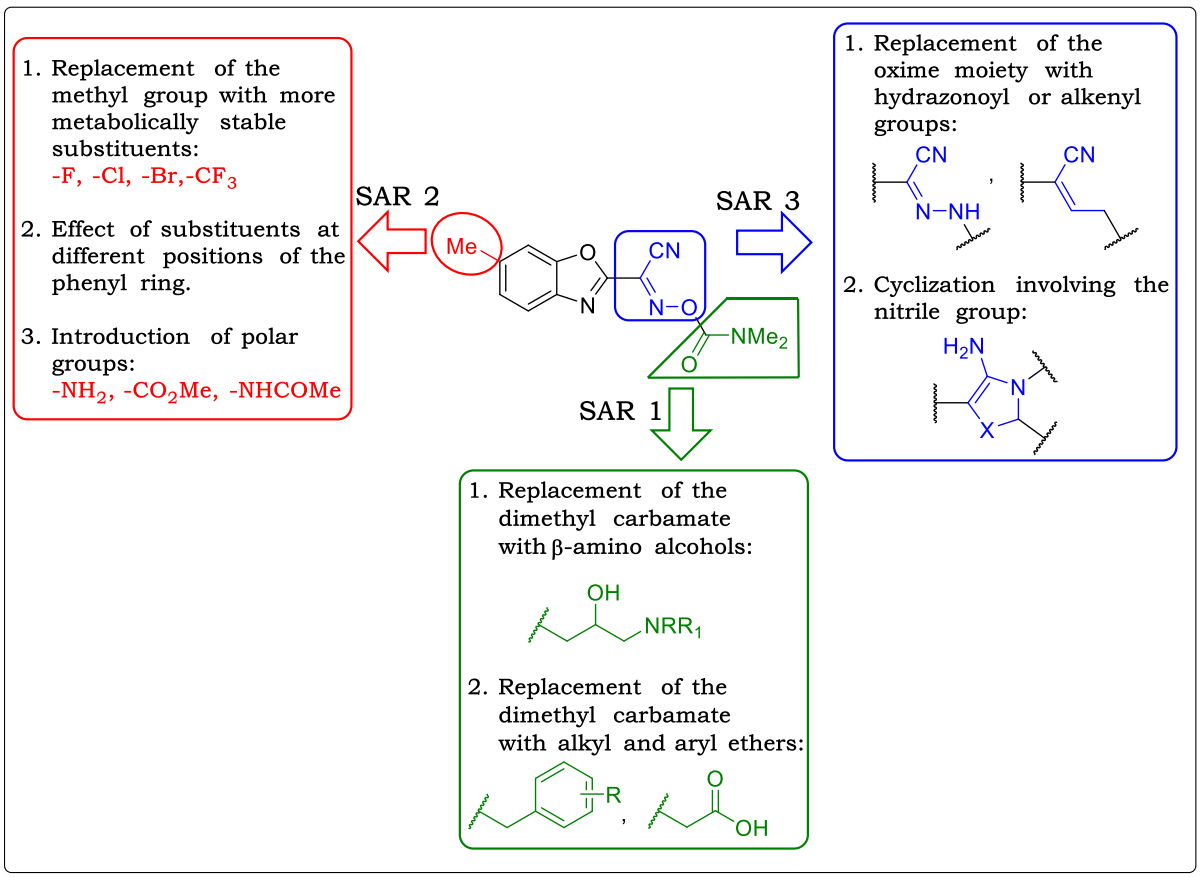

Figure 2.9: Design of benzoxazole-based oxime analogues.

With regard to **SAR 1** analogues, it was hypothesized that replacing the metabolically labile dimethyl carbamate with β-amino alcohols, linked to the oxime via an ether linkage, would produce compounds with enhanced metabolic stability. The choice of β-amino alcohols was also informed by the fact that they would introduce hydrophilic amino and hydroxyl groups,

which generally would enhance both intermolecular and intramolecular hydrogen bonding, along with improved aqueous solubility. In addition, the introduced chirality would reduce the flatness of these compounds, hence affecting their crystallinity, and in turn have the overall effect of improving aqueous solubility. Moreover, there are some known anti-TB drugs that contain the β-amino alcohol substructure, for instance ethambutol and mefloquine, whose chemical structures are depicted in **Figure 2.10** below. In effect, β-amino alcohols would further impart drug-likeness to this class of compounds.

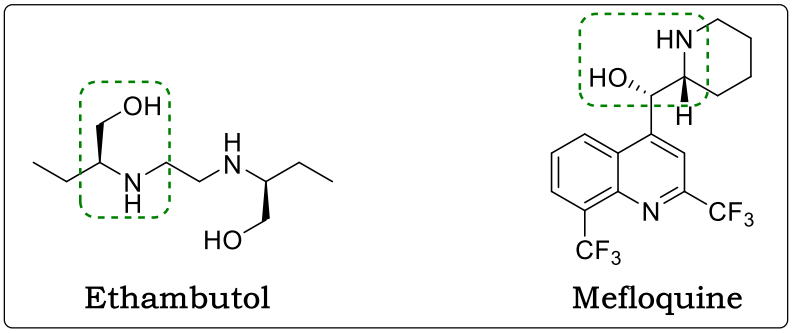

Figure 2.10: Chemical structures of β-amino alcohol-containing drugs.

Other **SAR 1** analogues were also designed to replace the oxime-ester linkage with an oxime-ether linkage in order to improve metabolic stability, and potentially permeability. The choice of the groups such as benzyl and alkyl ethers was inspired by some approved drugs containing various functionalized oxime-ether moieties, for example oxiconazole and cefixime, as shown in **Figure 2.11** below.

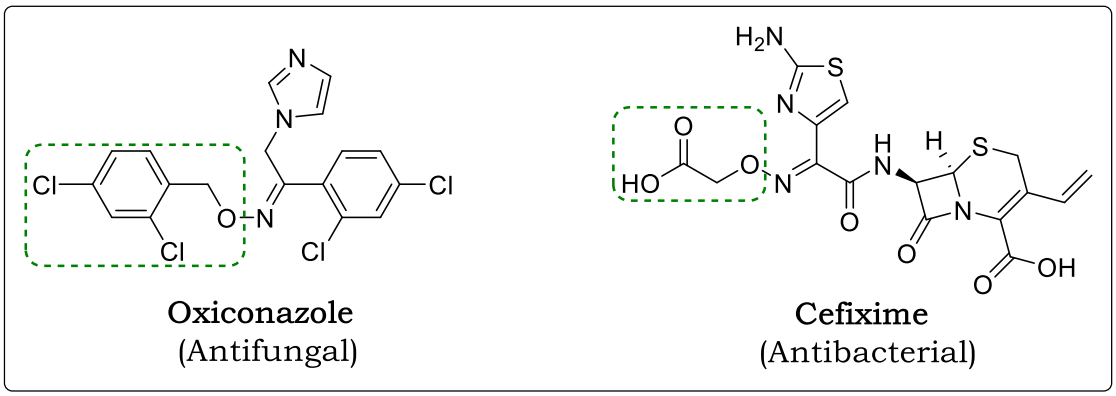

Figure 2.11: Chemical structures of drugs containing an oxime-ether linkage.

SAR 2 analogues were designed in such a manner as to replace the metabolically labile methyl group with the relatively more metabolically stable substituents such as the halogens. The halogens, being good leaving groups, would also serve as points of further derivatizations through nucleophilic substitution, Buchwald-Hartwig amination, or Suzuki-Miyaura cross-coupling reactions. Also, the effect of different substituents at different positions on the phenyl group was explored. In addition, plans were made to introduce polar groups such as amino, ester, and amide, all geared towards improving the aqueous solubility. These changes would further serve to expand the SAR exploration for this series of compounds.

As shown in **Figure 2.9** above, **SAR 3** analogues were designed to evaluate the effect of replacing the oxime with hydrazonoyl- or alkenyl-based moieties. The decision was informed by the fact that the 2-benzoxazolyl acetonitrile is a versatile intermediate for such modifications. Indeed, in 2005, Rida and colleagues synthesized novel benzoxazole-based compounds from 2-benzoxazolyl acetonitrile, which were evaluated for their anti-HIV, anticancer, and antibacterial activities.[47] In addition, the effect of various modifications based on cyclizations involving the nitrile group were investigated.

2.4.3 Chemistry

2.4.3.1 Synthesis of SAR 1 and SAR 2 Analogues

The benzoxazole-based oxime analogues, designated under **SAR 1** and **SAR 2**, were obtained following a common synthetic pathway. This pathway was successfully conceived through the retrosynthetic analysis of the final targeted compounds, as well as by following literature protocols. The retrosynthetic scheme is illustrated in **Figure 2.12** below, with the disconnection of carbon-heteroatom bonds taking center stage. As such, the disconnection of the group attached to the oxime oxygen atom would yield a free oxime. Thus, during synthesis, the introduction of this group would form the last step, and this was envisaged to be achieved, in the case of oxime esters, through reactions involving the nucleophilic oxime hydroxyl group with a carboxylic acid, acyl chloride, or an acid anhydride. Similarly, the synthesis of oxime ethers would follow the same protocol while using appropriate alkyl halides. The formation of the oxime substructure was then planned to be accessed through reactions between the methylene carbon and nitrous acid. The last two disconnections revealed that the commercially available and appropriately substituted 2-aminophenols, as well as malononitrile, would serve as key starting materials for the synthesis of all benzoxazole-based oximes through the 2-benzoxazolyl acetonitrile-based intermediates.

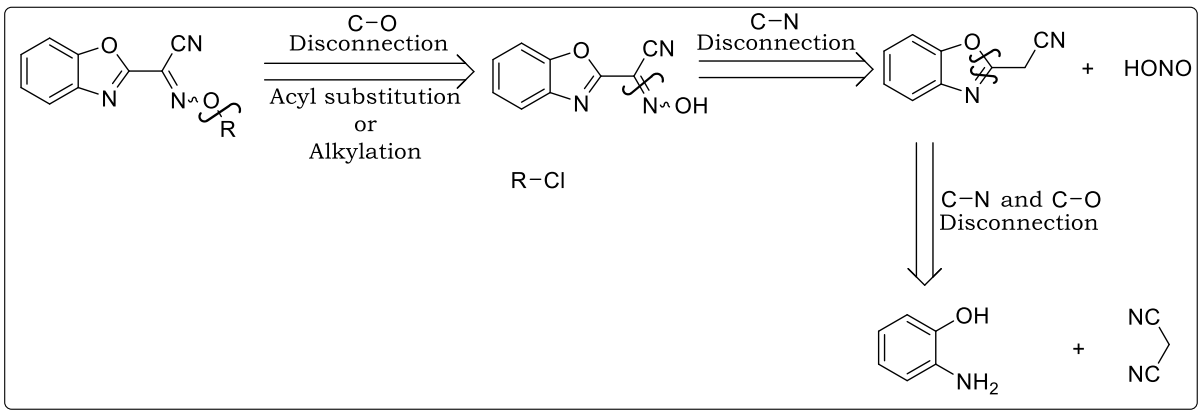

Figure 2.12: Retrosynthetic analysis of benzoxazole-based oximes.

The synthesis of **SAR 1** and **SAR 2** target compounds followed the protocols outlined in **Scheme 2.10** and **Scheme 2.13** below.

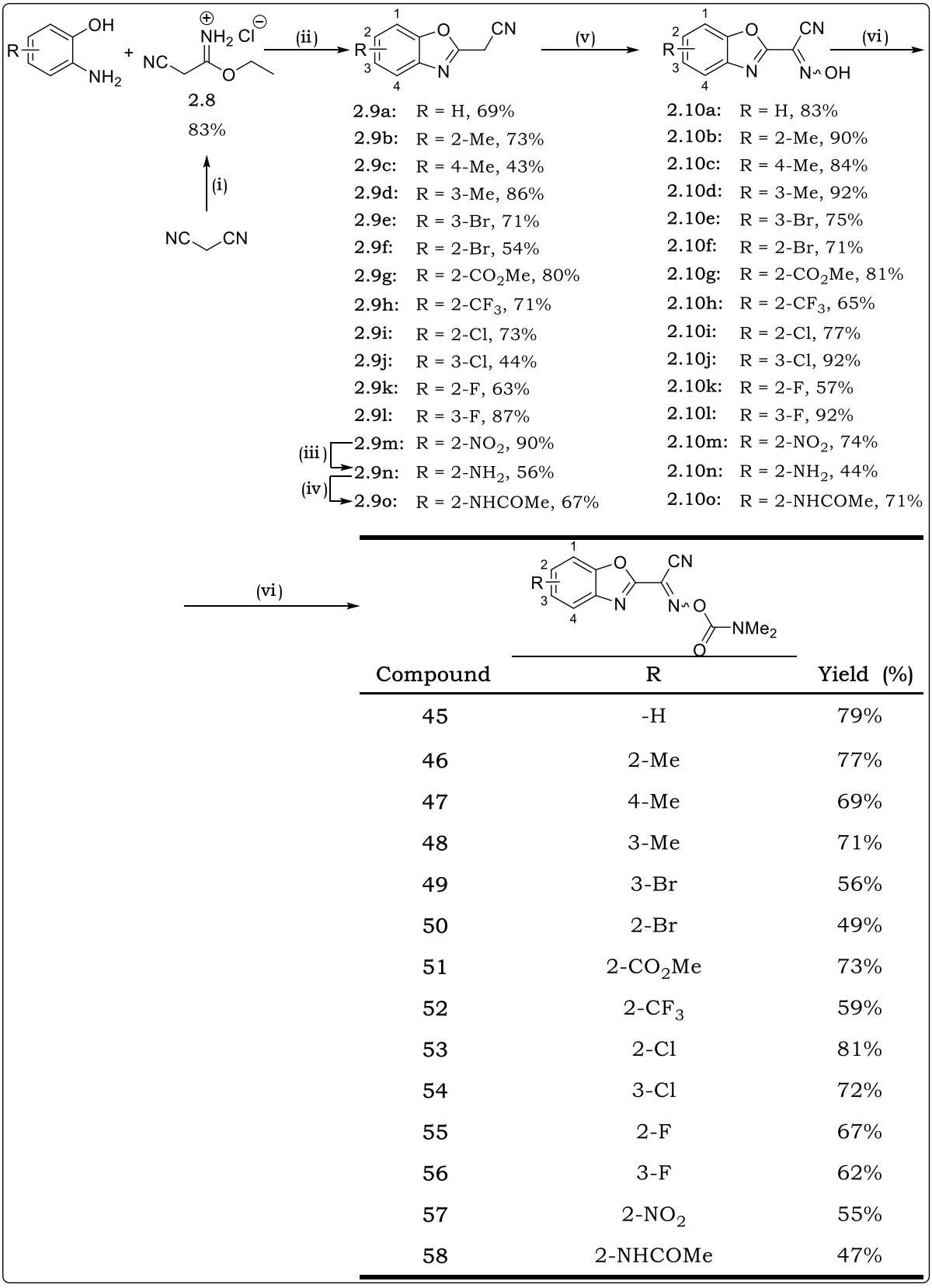

Compound	R	Yield (%)
45	-H	79%
46	2-Me	77%
47	4-Me	69%
48	3-Me	71%
49	3-Br	56%
50	2-Br	49%
51	2-CO_2Me	73%
52	2-CF_3	59%
53	2-Cl	81%
54	3-Cl	72%
55	2-F	67%
56	3-F	62%
57	2-NO_2	55%
58	2-NHCOMe	47%

Scheme 2.10: Synthetic protocol towards **SAR 2** benzoxazole-based target compounds. *Reagents and conditions*: (**i**) EtOH, TMSCl, 0 °C, 17 h; (**ii**) DCM, appropriately substituted 2-aminophenol, 25 °C, 10 min then 50 °C, 20 h; (**iii**) H_2, Pd/C, 15 h; (**iv**) MeCN, K_2CO_3, acetyl chloride, 40 °C, 0.5 h (**v**) AcOH, $NaNO_2$, 0 °C–25 °C, 12 h; (**vi**) DCM, dimethylcarbamoyl chloride, TEA, 50 °C, 15 h or MeCN, K_2CO_3, dimethylcarbamoyl chloride, 90 °C, 1 h.

Although **SAR 1** compounds were the first to be synthesized and biologically evaluated, for purposes of logical flow herein, the synthesis of **SAR 2** analogues is reported first. In addition, due to the loss of antimycobacterial activity following all attempts to replace the dimethyl carbamate moiety in **SAR 1** analogues, all **SAR 2** target final compounds bear the oxime functionalized with the dimethyl carbamate moiety.

Attempts were made to synthesize the 2-benzoxazolyl acetonitrile intermediate **2.9a** by reacting 2-aminophenol with malononitrile as reported by Das and colleagues.[48] However, the yields obtained were in the range of 20%. After several attempts with different reagents and conditions in an effort to increase the yields, a different protocol was adapted, which involved the activation of malononitrile before reacting it with the appropriately substituted 2-aminophenols. This protocol was published by Ammar and colleagues in 2003, and the yield of 2-benzoxazolyl acetonitrile increased significantly to about 69%.[49] Thus, in the synthesis of all target compounds, the starting point was the activation of malononitrile with absolute ethanol in the presence of chlorotrimethylsilane (TMSCl) to give a more reactive 2-cyanoacetimidic acid ethyl ester hydrochloride intermediate **2.8** in high yields. The appropriately substituted 2-aminophenols were then reacted with **2.8** by refluxing the mixture in dichloromethane (DCM) for about 20 hours to give the corresponding 2-benzoxazolyl acetonitrile-based intermediates **2.9a**–**2.9o** in moderate to high yields.[49] This reaction is believed to proceed via the reaction mechanism shown in **Scheme 2.11** below. Briefly, the primary amine nitrogen atom attacks the electron deficient carbon of the ester resulting in loss of ethanol and formation of a stable carbocation, which is then attacked by the nucleophilic phenoxyl oxygen atom to form a 5-membered ring. The aromatic benzoxazole ring system is then formed after a proton abstraction from the benzoxazolyl nitrogen atom by the chloride ions, and the subsequent loss of ammonia as ammonium chloride.

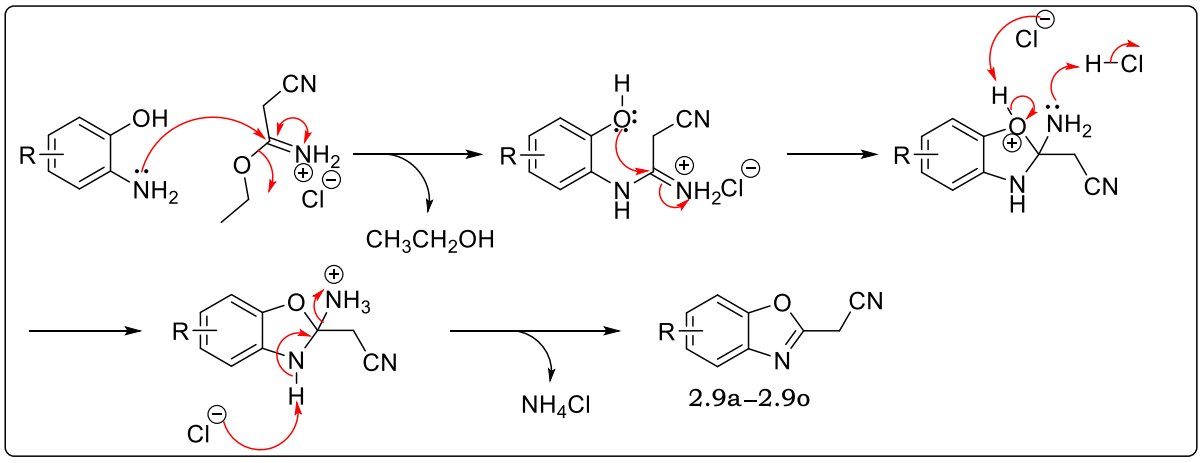

Scheme 2.11: Proposed reaction mechanism for the formation of 2-benzoxazolyl acetonitrile-based intermediates.

Oxime formation at the methylene carbon was achieved by a nitrosation reaction, following a literature protocol.[50] In this case, a frozen solution of the appropriate 2-benzoxazolyl acetonitrile-based intermediate in glacial acetic acid (AcOH) was slowly treated with sodium nitrite. The reaction mechanism involved in this step is proposed to proceed as shown in **Scheme 2.12** below.[34]

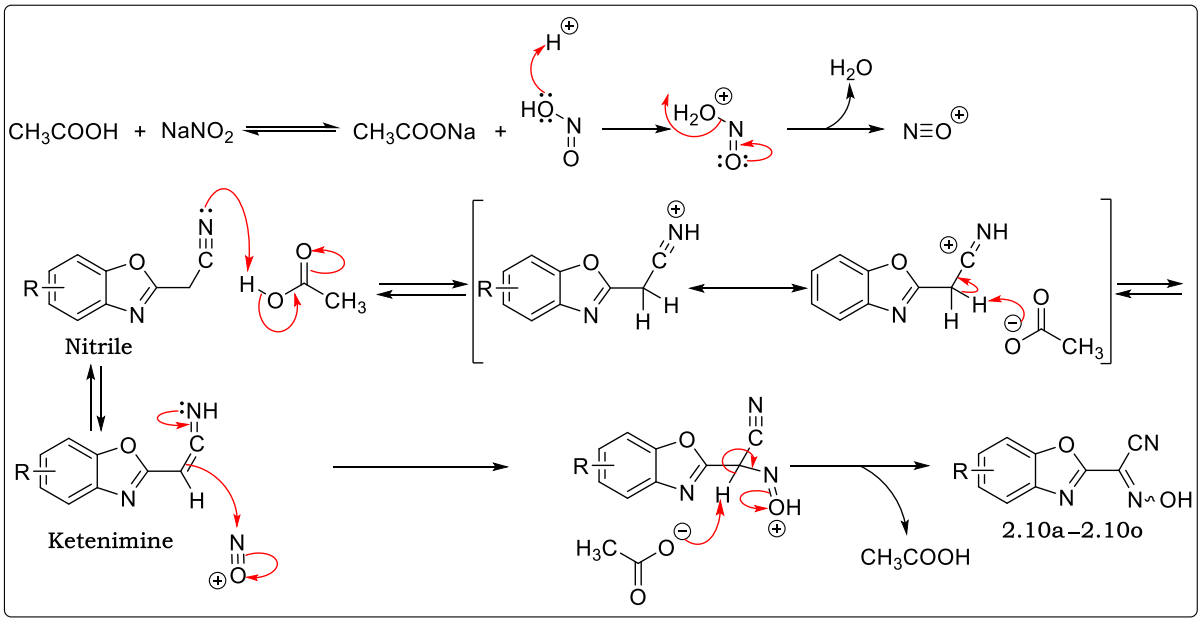

Scheme 2.12: Proposed reaction mechanism for the oxime formation.

Initially, the electron-deficient nitrosonium ion (NO) is formed from the nitrous acid (HONO) generated *in situ*. At the same time, the acid-catalysed nitrile-ketenimine tautomerism is believed to occur when glacial acetic acid

protonates the nitrile nitrogen atom to yield a cation, which can be represented by two resonance structures, as shown in **Scheme 2.12**.[51] This process activates the α-protons leading to the abstraction of one of them by the acetate ions [conjugate base] yielding the ketenimine intermediate, as well as regenerating the acetic acid. The resulting ketenimine C=C double bond provides electrons for the nucleophilic attack by the α-carbon on the electron-deficient nitrosonium ion. This in turn is followed by loss of a proton to furnish the free oxime intermediate, generally as a mixture of *E*- and *Z*-isomers. Literature reports indicate that the *E*-isomer is predominantly formed (~90%).[50] For all the **SAR 2** analogues, the oxime intermediates were functionalized to yield dimethyl carbamate oxime esters as the final target compounds. This was executed by reacting the oximes with dimethyl carbamoyl chloride in a reaction mediated by triethylamine or anhydrous potassium carbonate.

The β-amino alcohol-based target compounds for **SAR 1** were accessed through the epoxide intermediates **59** and **60** as shown in **Scheme 2.13** below. Epoxide **60**, with a chloro substituent, was preferred over the methyl-bearing **59** because of its expected higher metabolic stability. Both epoxides were synthesized by heating a mixture of the free oxime and epichlorohydrin in acetonitrile under mediation of anhydrous potassium carbonate.[52] Several attempts to apply literature procedures, where the use of sodium hydride as the base is prescribed, were unsuccessful.[53–55] The proposed reaction mechanism for the epoxide formation is illustrated in **Scheme 2.14** below. Briefly, K_2CO_3 abstracts a proton from the oxime hydroxyl group, thus enhancing its nucleophilicity, which then attacks the electron deficient carbon of epichlorohydrin to form a transition intermediate. An attack on the more electron-deficient chloro-bearing carbon by the oxygen atom leads to the formation of the epoxide along with elimination of KCl.

Synthesis of aryl and alkyl ethers **70**–**74** utilized similar reaction conditions and reagents as the epoxidation reaction. In this case, in place of epichlorohydrin, an appropriately substituted aryl halide was used, for instance benzyl chloride.

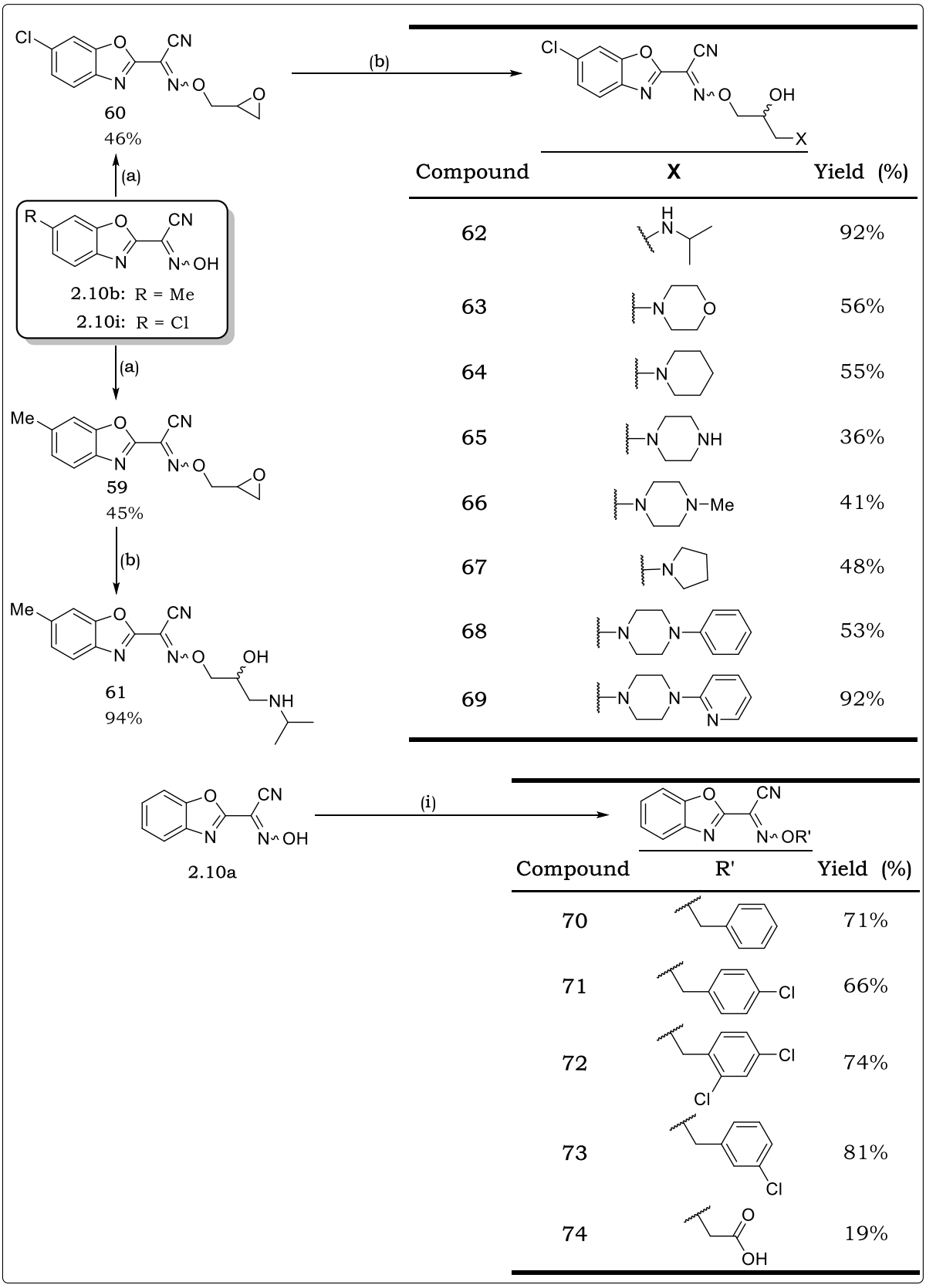

Compound	X	Yield (%)
62		92%
63		56%
64		55%
65		36%
66		41%
67		48%
68		53%
69		92%

Compound	R'	Yield (%)
70		71%
71		66%
72		74%
73		81%
74		19%

Scheme 2.13: Synthetic protocol towards **SAR 1** benzoxazole-based target compounds. *Reagents and conditions*: (**a**) MeCN, K_2CO_3, epichlorohydrin, 90 °C, 18 h; (**b**) MeCN, appropriate amine, lithium perchlorate, 25 °C, 2–24 h; (**i**) MeCN, K_2CO_3, appropriate alkyl halide, 90 °C, 1–2 h.

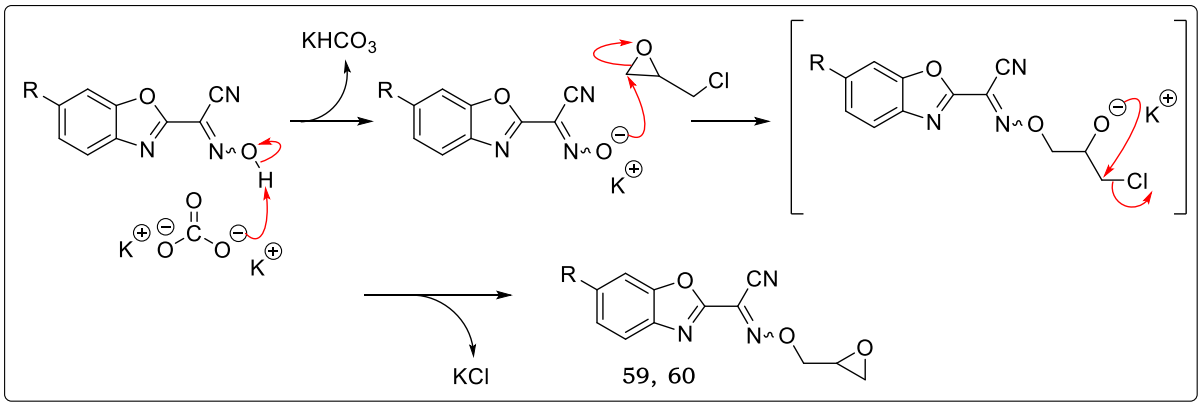

Scheme 2.14: Proposed reaction mechanism for epoxide formation.

The β-amino alcohol-based final target compounds were obtained in moderate to high yields through the opening of the epoxide intermediates by the appropriate primary or secondary amines. This reaction took place at room temperature in acetonitrile under mediation of lithium perchlorate as a catalyst.[55,56] Previous attempts to react the epoxide and amines by heating the mixtures in toluene in the absence of a catalyst, as reported in some literature protocols, were unsuccessful.[53,57] This reaction is believed to proceed through the mechanism illustrated in **Scheme 2.15** below. In summary, lithium ions coordinate between the epoxide oxygen and the oxime oxygen resulting in enhanced electron withdrawal from the two epoxide carbons. This enhances regioselectivity whereby amines nucleophilically attack the less substituted epoxide carbon resulting in ring opening. Subsequent proton-lithium exchange with the generated perchloric acid affords the desired β-amino alcohol-based target compound as a racemate or an enantiomeric mixture, coupled with the regeneration of lithium perchlorate.

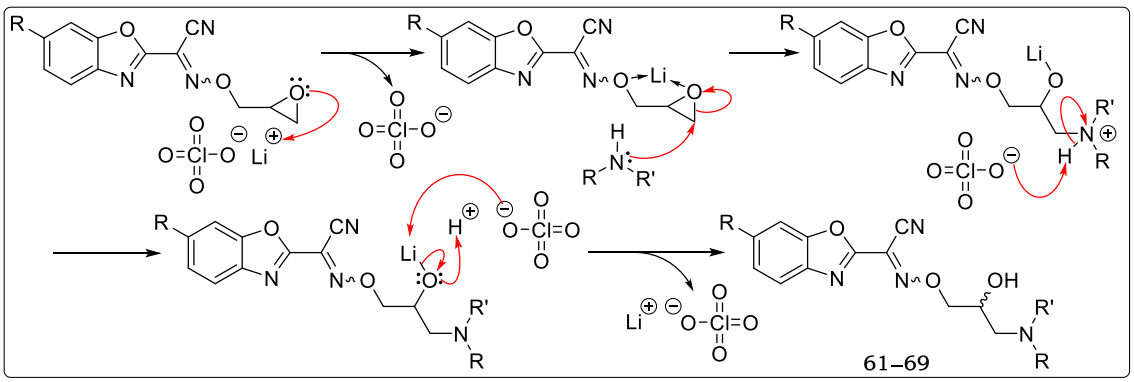

Scheme 2.15: Proposed reaction mechanism for nucleophilic epoxide ring opening by amines.

2.4.3.2 Synthesis of SAR 3 Analogues

In order to investigate the effect of replacing the oxime moiety, the versatile 2-benzoxazolyl acetonitrile (**2.9a**) was derivatized to a number of small and polar oxime-free target compounds. To achieve this, the work of Rida and colleagues was adapted.[47] They previously reported some novel benzoxazole-based compounds with potential anti-HIV, anticancer, and antibacterial properties.[47] The procedures, which were followed in the synthesis of **SAR 3** analogues, are outlined in **Scheme 2.16** below.

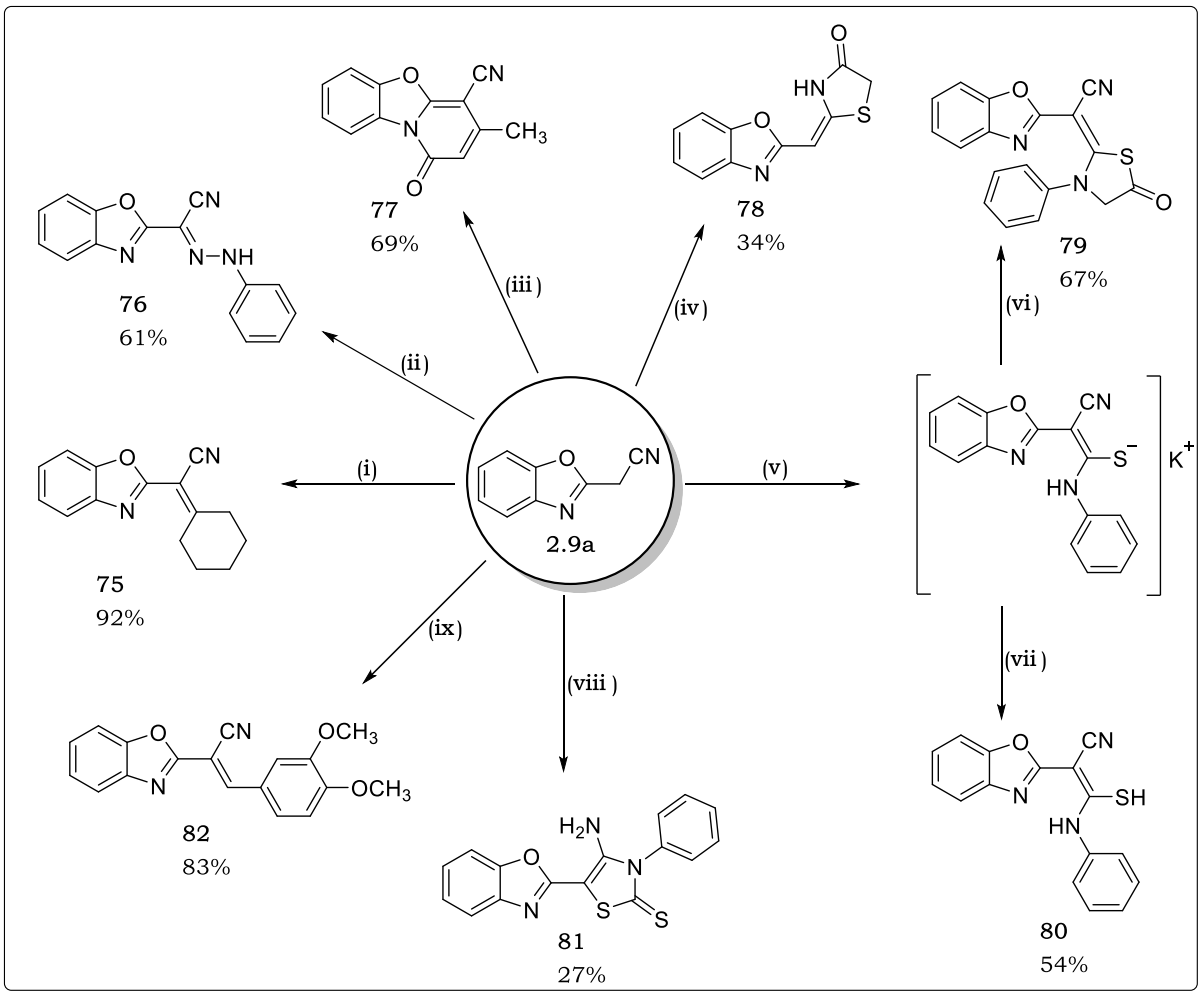

Scheme 2.16: Synthetic protocols towards **SAR 3** benzoxazole-based target compounds. *Reagents and conditions*: (**i**) EtOH, cyclohexanone, ammonium acetate, 25 °C, 1 h; (**ii**) AcOH, freshly prepared benzenediazonium acetate, 25 °C, 30 min; (**iii**) EtOH, ethyl acetoacetate, ammonium acetate, reflux (90 °C), 7 h; (**iv**) EtOH, thioglycolic acid, reflux (90 °C), 7 h; (**v**) DMF, KOH, phenyl isothiocyanate, 0–25 °C, 3 h; (**vi**) DMF, Chloroacetyl chloride, 0–25 °C, 6 h; (**vii**) 0.1 N HCl to pH 3–4; (**viii**) EtOH, finely divided sulfur, TEA, 25 °C, 30 min, then phenyl isothiocyanate, 25 °C, 1 h; (**ix**) EtOH, 3,4-dimethoxybenzaldehyde, TEA, 25 °C, 2 h.

As shown in **Scheme 2.16**, 2-benzoxazolyl-2-cyclohexylideneacetonitrile **75** was prepared by reacting **2.9a** with cyclohexanone in ethanol using ammonium acetate as a catalyst. Similarly, treating a solution of **2.9a** in ethanol with 3,4-dimethoxybenzaldehyde in the presence of a catalytic amount of triethylamine (TEA), delivered compound **82** in high yields. As earlier discussed in **Scheme 2.12**, the same reaction mechanism is believed to be involved, except that in this case a base-catalysed tautomerism occurs. The ketenimine facilitates the nucleophilic reaction with the electron-deficient carbonyl carbon of ketones or aldehydes. Likewise, the reactions leading to all the other compounds listed in **Scheme 2.16** follow related mechanisms, with the main mechanism being nucleophilic attack on a selected electron-deficient atom of the appropriate reactant by the ketenimine α-carbon of **2.9a**.

The benzenediazonium acetate used in procedure **ii** was freshly prepared by treating aniline with an equimolar aqueous solution of sodium nitrite at 0 °C. It was then mixed with a solution of **2.9a** in glacial acetic acid to yield the hydrazonoyl benzoxazole **76** in good yield.

Refluxing **2.9a** with an equivalent amount of ethyl acetoacetate or thioglycolic acid in ethanol yielded **77** or **78**, respectively.

Synthesis of compounds **79** and **80** proceeded through the formation of a common thiocarbamoyl potassium salt intermediate. This was achieved by treating **2.9a** with phenyl isothiocyanate in dimethylformamide (DMF) under mediation of potassium hydroxide. Cyclization of the potassium salt intermediate with chloro acetylchloride in DMF yielded **79** in moderate yield. On the other hand, acidification of the potassium salt intermediate using HCl furnished **80** in good yield.[58]

Treating a mixture of **2.9a**, sulfur, and TEA in absolute ethanol with phenyl isothiocyanate furnished benzoxazolyl aminothiazole **81** in low yield.[59]

2.4.4 Spectroscopic and Chromatographic Characterization

As described for the 2-aminoquinazolinones in section **2.3.4**, all the synthesized benzoxazole-based compounds were fully characterized by subjecting them to various spectroscopic and chromatographic techniques.

The NMR spectra, for example, which were used to confirm the chemical structure of the β-amino alcohol-based compound **63**, along with all the associated intermediates, will herein be used to represent how the characterization of compounds was carried out. In this case, the 6-chloro-2-benzoxazolyl acetonitrile **2.9i** was the first intermediate to be synthesized and its structure was confirmed using the ^{1}H NMR spectrum shown in **Figure 2.13** below. The signal corresponding to the two diagnostic methylene protons (**H-4**) appeared as a singlet (s) resonating at δ 4.12, while all the three aromatic protons were accounted for. As such, proton **H-1** yielded a doublet signal at δ 7.59 with a small coupling constant (^{4}J = 1.7) due to a long-range coupling with proton **H-2**. In this case, proton **H-2** and proton **H-3** produced a doublet of doublets and a doublet, respectively.

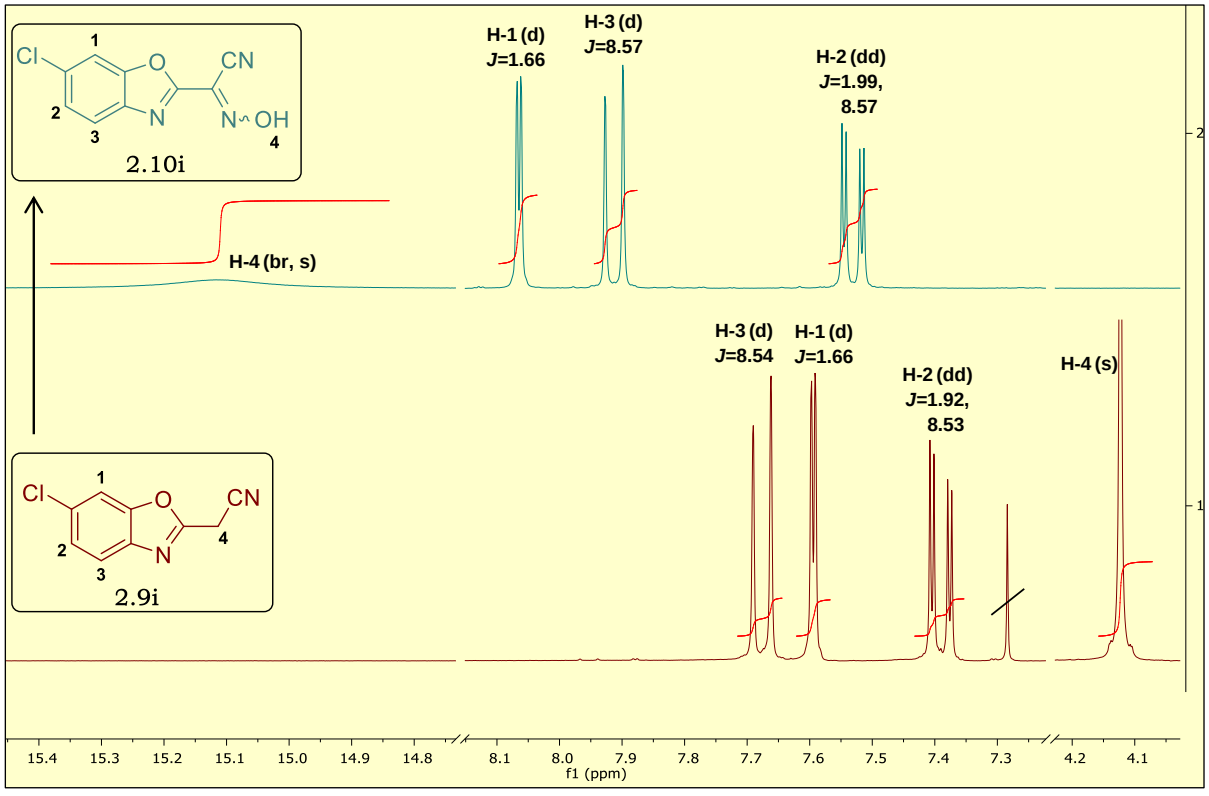

Figure 2.13: ^{1}H NMR spectra of **2.9i** in $CDCl_3$ at 300 MHz and **2.10i** in DMSO-d_6 at 300 MHz.

The ^{1}H NMR spectrum of the oxime intermediate **2.10i** is also shown in **Figure 2.13**. The characteristic features include the appearance of a broad singlet signal at δ 15.10 due to the oxime proton **H-4**, and the absence of the signal due to the methylene protons in the aliphatic region. Also, all the aromatic protons appeared relatively more deshielded, and therefore resonated more downfield compared to those of **2.9i**. This is most likely due to withdrawal of electrons from the benzoxazole nucleus by the oxime moiety.

The synthetic step that followed was the formation of the epoxide intermediate **60**. As shown in **Figure 2.14** below, there were five diagnostic signals in the aliphatic region of the ^{1}H NMR spectrum attributable to the diastereotopic methyloxiranyl protons [**H-4** (×2), and **H-6** (×2)] and proton **H-5** on the chiral center. The diastereotopicity arises from the stereogenic influence of the chiral center, which results in no symmetry element, and therefore the methylene protons **H-4** and **H-6** are diastereotopic.

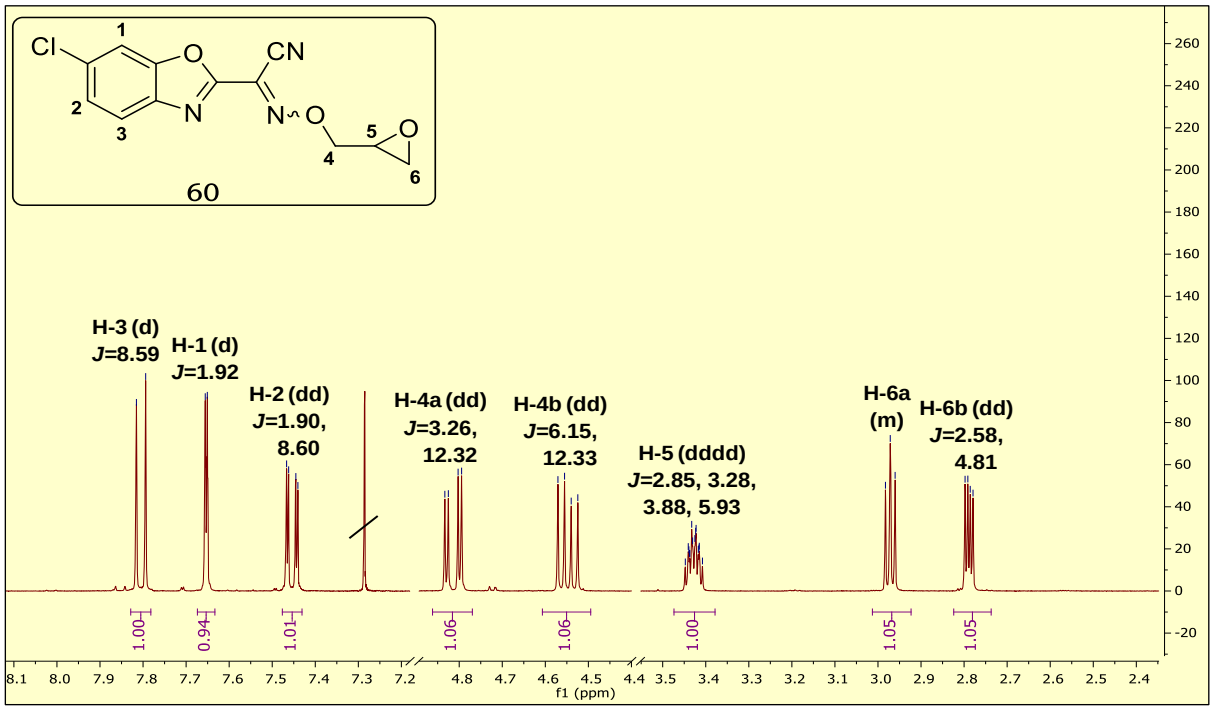

Figure 2.14: ^{1}H NMR spectrum of **60** in $CDCl_3$ at 400 MHz.

The signals due to protons **H-4**, for instance, exhibited a pair of finely resolved doublet of doublets: one at δ 4.62 (**H-4a**) with coupling constants *J* = 12.3 Hz and 3.3 Hz, and the second at δ 4.51 (**H-4b**) with *J* = 12.3 Hz and

6.2 Hz. The larger coupling constant is attributable to geminal coupling between the pair, while the other two are due to vicinal coupling of the respective proton to proton **H-5** on the chiral center. Consequently, proton **H-5** yielded a doublet of doublet of doublet of doublets (dddd) due to four unequal couplings from the diastereotopes **H-4** and **H-6**, as shown in **Figure 2.14** above.

Figure 2.15 below is a ^{1}H NMR spectrum for the target compound **63.** The opening of the epoxide by morpholine was confirmed by the appearance of a doublet signal in the aliphatic region (δ 5.04) due to the hydroxyl proton **H-7** coupling with proton **H-5**. In addition, extra signals in the spectrum corresponding to the morpholinyl protons **H-8** and **H-9** were observed. Notably, the equivalent two pairs of aliphatic protons **H-9** yielded a triplet (^{3}J = 4.7 Hz) due to coupling with protons **H-8**, and integrated for four protons at δ 3.58.

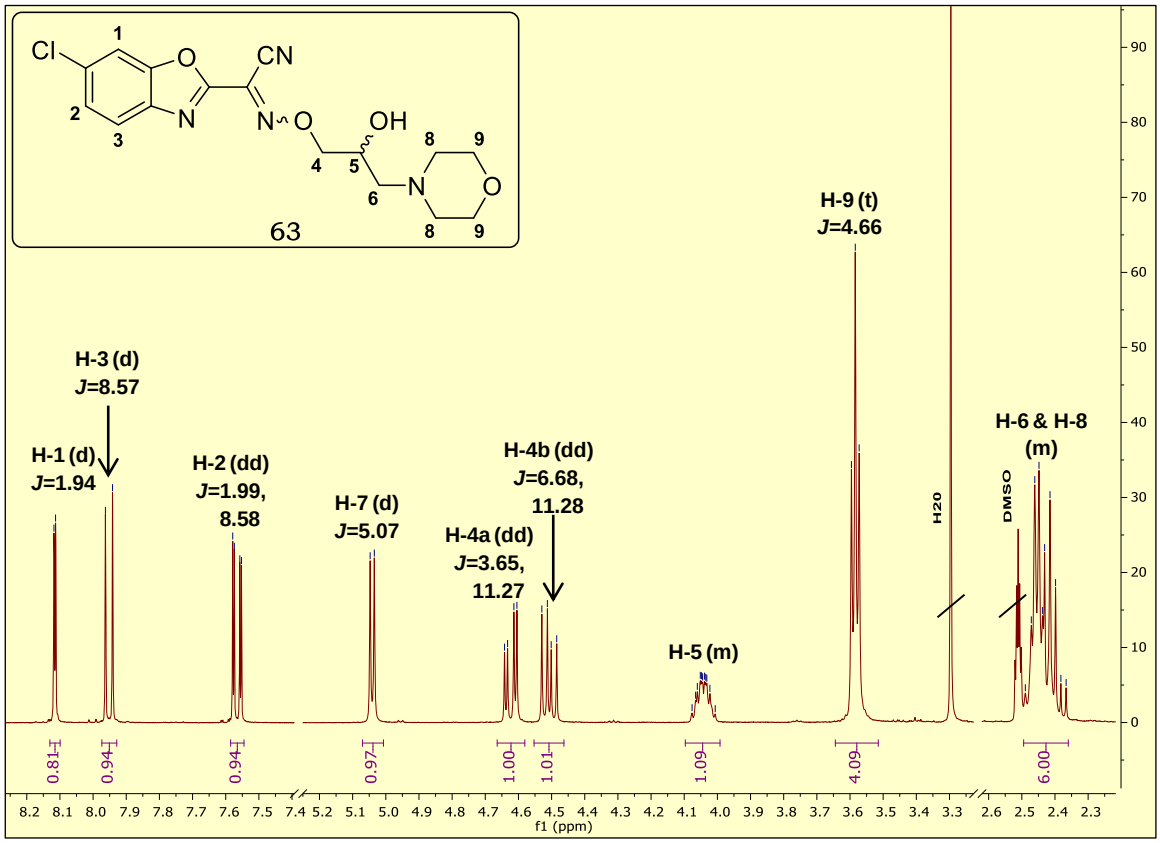

Figure 2.15: ^{1}H NMR spectrum of the target compound **63** in DMSO-d_6 at 400 MHz.

^{13}C NMR spectroscopy also played an important role in confirming the chemical structures of new synthetic intermediates and all final target

compounds. For example, with respect to compound **63**, there were 14 distinct signals in its ^{13}C NMR spectrum attributable to the 16 carbons of the compound, as shown in **Figure 2.16** below. In all cases, the aromatic benzoxazolyl carbons resonated most downfield whereby the carbons attached to the relatively more electronegative oxygen and/or nitrogen atoms were the most deshielded. **C-13**, for instance, is the most downfield-resonating carbon (δ 155.61) because of the neighbouring oxygen and nitrogen atoms, which act as electron sinks, and therefore highly deshielding. Signals due to the morpholinyl carbons, on the other hand, appeared upfield, and had greater intensities compared to others because each signal arose from two chemical shift-equivalent carbons **C-8** or **C-9**. In addition, carbons **C-9** (δ 66.72) by virtue of being attached to the morpholinyl oxygen atom, were more deshielded than carbons **C-8** (δ 54.49), and therefore resonated more downfield. All the other signals were successfully assigned to their corresponding carbons by taking into consideration their electronic environments, and the carbon type (aromatic, aliphatic, quaternary, or proton-bearing).

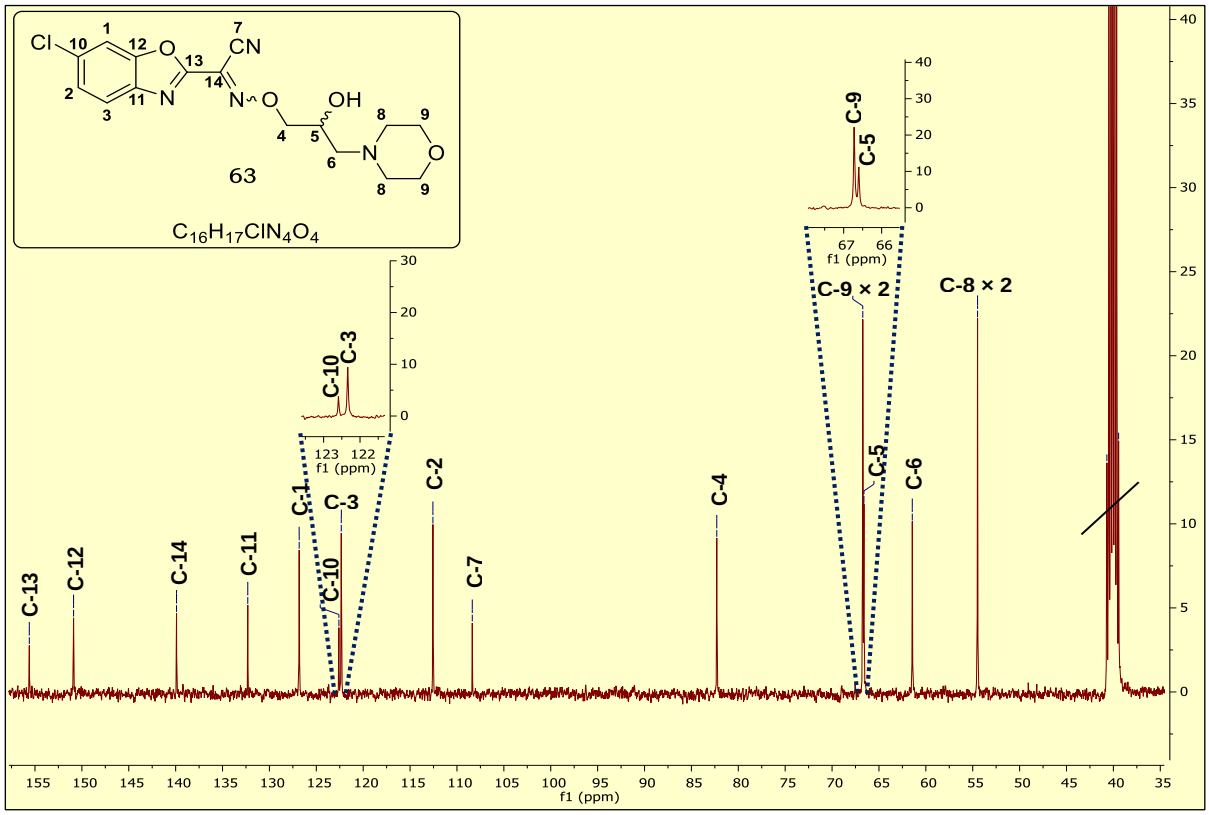

Figure 2.16: ^{13}C NMR spectrum of **63** in DMSO-d_6 at 400 MHz.

As shown in **Figure 2.17** below, a single run on the LC-MS provided more characteristic information about compound **63**.

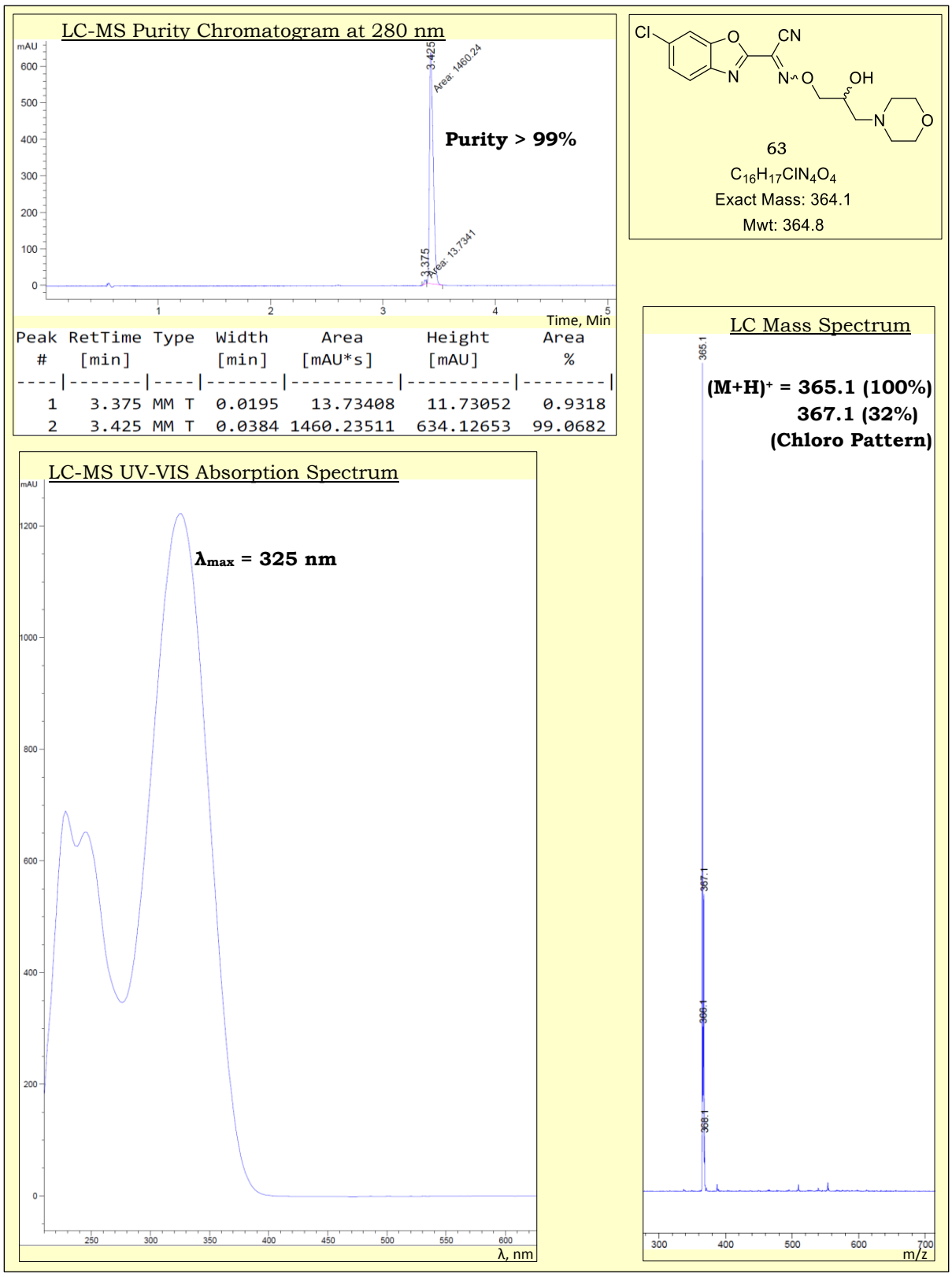

Figure 2.17: LC-MS readout for compound **63**.

In this regard, the chromatogram was used to determine the purity of **63** as > 99%, which was based on the percentage peak area. The mass spectrum, on the other hand, afforded pseudo-molecular ions $(M+H)^+$ at m/z = 365.1 (100%), and 367.1 (32%), which were similar to the calculated ones for $C_{16}H_{17}ClN_4O_4$. In this case, the mass spectrum exhibited a pattern characteristic of a compound containing a chloro group, due to the two isotopes of chlorine. In addition, the UV-VIS spectrum revealed the wavelength of maximum absorption for compound **63** as 325 nm.

In brief, the ^{1}H NMR spectra for the dimethyl carbamate-containing target compounds exhibited two diagnostic upfield singlets, each integrating for three protons, and therefore attributable to the two sets of methyl protons. Similarly, the corresponding ^{13}C NMR spectra manifested the two methyl carbons as two distinct signals. The restricted rotation about the N–CO bond makes the two methyl groups different. This is due to significant double-bond character of the amide bond, which is linked to conjugation, whereby the lone pair of electrons on the nitrogen is delocalized into the carbonyl group. The aforementioned rationale is illustrated in **Figure 2.18** below.

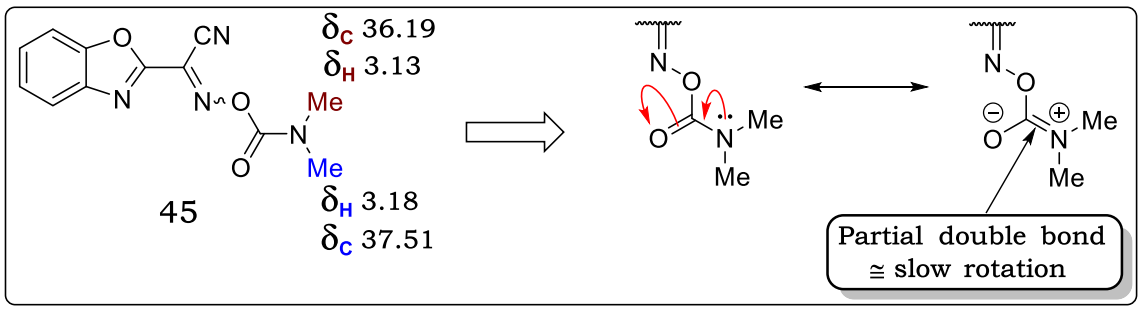

Figure 2.18: Effect of N–CO partial double bond on NMR spectra.

In conclusion, two-dimensional correlation NMR spectroscopic techniques (2D NMR) were paramount in the assignment of signals to their contributing protons. This was necessary, for instance, where multiplicity ambiguities, as well as coincidental overlaps of signals, were encountered in the 1D ^{1}H NMR spectra. These, for example, included the through-bond correlation methods such as the homonuclear correlation spectroscopy (COSY) and the heteronuclear single-quantum correlation spectroscopy (HSQC).

2.5 Conclusion

This chapter described the synthesis and characterization of compounds belonging to the two classes of benzoheterocycles studied in this thesis work: the 2-aminoquinazolinones and the benzoxazole-based oximes. The compounds were designed by employing rational medicinal chemistry principles, and thereafter successfully synthesized in accordance with protocols adapted from published synthetic methods. All the synthesized compounds were fully characterized using spectroscopic techniques such as NMR spectroscopy; chromatographic methods, including TLC and HPLC-MS; along with physical attributes such as melting points and appearance.

The final target compounds, as well as some selected intermediates, were subjected to biological evaluation and physicochemical profiling. The chapter, which follows [that is, Chapter 3], discusses the results of biological studies, while Chapter 4 discusses the analyses of the relevant physicochemical properties. In addition, the data relating to the characterization of each of the synthesized compounds is fully described in the experimental chapter (Chapter 6).

References

(1) Demain, A. L.; Sanchez, S. Microbial Drug Discovery: 80 Years of Progress. *J. Antibiot. (Tokyo).* **2009**, *62*, 5–16.

(2) Njuguna, N. M.; Masimirembwa, C.; Chibale, K. Identification and Characterization of Reactive Metabolites in Natural Products-Driven Drug Discovery. *J. Nat. Prod.* **2012**, *75*, 507–513.

(3) Newman, D. J.; Cragg, G. M. Natural Products as Sources of New Drugs from 1981 to 2014. *J. Nat. Prod.* **2016**, *79*, 629–661.

(4) Cheuka, P.; Mayoka, G.; Mutai, P.; Chibale, K. The Role of Natural Products in Drug Discovery and Development against Neglected Tropical Diseases. *Molecules* **2016**, *22*, 1–41.

(5) Lahlou, M. The Success of Natural Products in Drug Discovery. *Pharmacol. Pharm.* **2013**, *4*, 17–31.

(6) Gu, J.; Gui, Y.; Chen, L.; Yuan, G.; Lu, H.-Z.; Xu, X. Use of Natural Products as Chemical Library for Drug Discovery and Network Pharmacology. *PLoS One* **2013**, *8*, e62839.

(7) Czarnik, A. W.; Keene, J. D. Combinatorial Chemistry. *Curr. Biol.* **1998**, *8*, R705–R707.

(8) Villar, H. O.; Hansen, M. R. Design of Chemical Libraries for Screening. *Expert Opin. Drug Discov.* **2009**, *4*, 1215–1220.

(9) Dolle, R. E. Historical Overview of Chemical Library Design. *Methods Mol. Biol.* **2011**, *685*, 3–25.

(10) Szymański, P.; Markowicz, M.; Mikiciuk-Olasik, E. Adaptation of High-Throughput Screening in Drug Discovery—Toxicological Screening Tests. *Int. J. Mol. Sci.* **2011**, *13*, 427–452.

(11) Liu, B.; Li, S.; Hu, J. Technological Advances in High-Throughput Screening. *Am. J. Pharmacogenomics* **2004**, *4*, 263–276.

(12) Kotz, J. Phenotypic Screening, Take Two. *Sci. Exch.* **2012**, *5*, 1–3.

(13) Butera, J. A. Phenotypic Screening as a Strategic Component of Drug Discovery Programs Targeting Novel Antiparasitic and Antimycobacterial Agents: An Editorial. *J. Med. Chem.* **2013**, *56*, 7715–7718.

(14) Shoichet, B. K. Virtual Screening of Chemical Libraries. *Nature* **2004**, *432*, 862–865.

(15) Njogu, P. M.; Guantai, E. M.; Pavadai, E.; Chibale, K. Computer-Aided Drug Discovery Approaches against the Tropical Infectious Diseases Malaria, Tuberculosis, Trypanosomiasis, and Leishmaniasis. *ACS*

Infect. Dis. **2016**, *2*, 8–31.

(16) Pavadai, E.; El Mazouni, F.; Wittlin, S.; de Kock, C.; Phillips, M. A.; Chibale, K. Identification of New Human Malaria Parasite *Plasmodium falciparum* Dihydroorotate Dehydrogenase Inhibitors by Pharmacophore and Structure-Based Virtual Screening. *J. Chem. Inf. Model.* **2016**, *56*, 548–562.

(17) Sliwoski, G.; Kothiwale, S.; Meiler, J.; Lowe, E. W. Computational Methods in Drug Discovery. *Pharmacol. Rev.* **2013**, *66*, 334–395.

(18) Talele, T. T.; Khedkar, S. A.; Rigby, A. C. Successful Applications of Computer Aided Drug Discovery: Moving Drugs from Concept to the Clinic. *Curr. Top. Med. Chem.* **2010**, *10*, 127–141.

(19) Swinney, D. C. Phenotypic vs. Target-Based Drug Discovery for First-in-Class Medicines. *Clin. Pharmacol. Ther.* **2013**, *93*, 299–301.

(20) Langedijk, J.; Mantel-Teeuwisse, A. K.; Slijkerman, D. S.; Schutjens, M.-H. D. B. Drug Repositioning and Repurposing: Terminology and Definitions in Literature. *Drug Discov. Today* **2015**, *20*, 1027–1034.

(21) Novac, N. Challenges and Opportunities of Drug Repositioning. *Trends Pharmacol. Sci.* **2013**, *34*, 267–272.

(22) Ashburn, T. T.; Thor, K. B. Drug Repositioning: Identifying and Developing New Uses for Existing Drugs. *Nat. Rev. Drug Discov.* **2004**, *3*, 673–683.

(23) Younis, Y.; Douelle, F.; Feng, T.-S.; Cabrera, D. G.; Manach, C. Le; Nchinda, A. T.; Duffy, S.; White, K. L.; Shackleford, D. M.; Morizzi, J.; Mannila, J.; Katneni, K.; Bhamidipati, R.; Zabiulla, K. M.; Joseph, J. T.; Bashyam, S.; Waterson, D.; Witty, M. J.; Hardick, D.; Wittlin, S.; Avery, V.; Charman, S. A.; Chibale, K. 3,5-Diaryl-2-Aminopyridines as a Novel Class of Orally Active Antimalarials Demonstrating Single Dose Cure in Mice and Clinical Candidate Potential. *J. Med. Chem.* **2012**, *55*, 3479–3487.

(24) González Cabrera, D.; Douelle, F.; Younis, Y.; Feng, T.-S.; Le Manach, C.; Nchinda, A. T.; Street, L. J.; Scheurer, C.; Kamber, J.; White, K. L.; Montagnat, O. D.; Ryan, E.; Katneni, K.; Zabiulla, K. M.; Joseph, J. T.; Bashyam, S.; Waterson, D.; Witty, M. J.; Charman, S. A.; Wittlin, S.; Chibale, K. Structure–Activity Relationship Studies of Orally Active Antimalarial 3,5-Substituted 2-Aminopyridines. *J. Med. Chem.* **2012**, *55*, 11022–11030.

(25) Younis, Y.; Douelle, F.; González Cabrera, D.; Le Manach, C.; Nchinda, A. T.; Paquet, T.; Street, L. J.; White, K. L.; Zabiulla, K. M.; Joseph, J. T.; Bashyam, S.; Waterson, D.; Witty, M. J.; Wittlin, S.; Charman, S.

A.; Chibale, K. Structure–Activity-Relationship Studies around the 2-Amino Group and Pyridine Core of Antimalarial 3,5-Diarylaminopyridines Lead to a Novel Series of Pyrazine Analogues with Oral in Vivo Activity. *J. Med. Chem.* **2013**, *56*, 8860–8871.

(26) Craig, P. N. Interdependence between Physical Parameters and Selection of Substituent Groups for Correlation Studies. *J. Med. Chem.* **1971**, *14*, 680–684.

(27) Thomas, G. *Fundamentals of Medicinal Chemistry*; 1st Ed.; John Wiley & Sons Ltd: London, 2003.

(28) Connolly, D. J.; Cusack, D.; O'Sullivan, T. P.; Guiry, P. J. Synthesis of Quinazolinones and Quinazolines. *Tetrahedron* **2005**, *61*, 10153–10202.

(29) Asif, M. Chemical Characteristics, Synthetic Methods, and Biological Potential of Quinazoline and Quinazolinone Derivatives. *Int. J. Med. Chem.* **2014**, *2014*, 1–27.

(30) Vijayakumar, B.; Prasanthi, P.; Teja, K. M.; Reddy, K. M. K.; Nishanthi, P.; Nishanthi, M. Quinazoline Derivatives & Pharmacological Activities: A Review. *Med. Chem. Anal.* **2013**, *3*, 10–21.

(31) He, L.; Li, H.; Chen, J.; Wu, X.-F. Recent Advances in 4(3*H*)-Quinazolinone Syntheses. *RSC Adv.* **2014**, *4*, 12065–12077.

(32) Leivers, A. L.; Tallant, M.; Shotwell, J. B.; Dickerson, S.; Leivers, M. R.; McDonald, O. B.; Gobel, J.; Creech, K. L.; Strum, S. L.; Mathis, A.; Rogers, S.; Moore, C. B.; Botyanszki, J. Discovery of Selective Small Molecule Type III Phosphatidylinositol 4-Kinase Alpha (PI4KIIIα) Inhibitors as Anti Hepatitis C (HCV) Agents. *J. Med. Chem.* **2014**, *57*, 2091–2106.

(33) R. Mahmoud, M.; Abou-Elmagd, W. S. I.; Abdelwahab, S. S.; A. Soliman, E.-S. Synthesis and Spectral Characterization of Novel 2, 3-Disubstituted Quinazolin-4(3*H*) One Derivatives. *Am. J. Org. Chem.* **2012**, *2*, 1–8.

(34) Clayden, J.; Greeves, N.; Warren, S. *Organic Chemistry*; 2nd Ed.; Oxford University Press Inc.: New York, 2012.

(35) Dreher, S. D.; Lim, S.-E.; Sandrock, D. L.; Molander, G. A. Suzuki−Miyaura Cross-Coupling Reactions of Primary Alkyltrifluoroborates with Aryl Chlorides. *J. Org. Chem.* **2009**, *74*, 3626–3631.

(36) Parry, P. R.; Wang, C.; Batsanov, A. S.; Bryce, M. R.; Tarbit, B. Functionalized Pyridylboronic Acids and Their Suzuki Cross-Coupling Reactions To Yield Novel Heteroarylpyridines. *J. Org. Chem.* **2002**, *67*,

7541–7543.

(37) Kotha, S.; Lahiri, K.; Kashinath, D. Recent Applications of the Suzuki–Miyaura Cross-Coupling Reaction in Organic Synthesis. *Tetrahedron* **2002**, *58*, 9633–9695.

(38) Miyaura, N.; Suzuki, A. Palladium-Catalyzed Cross-Coupling Reactions of Organoboron Compounds. *Chem. Rev.* **1995**, *95*, 2457–2483.

(39) Suzuki, A. Recent Advances in the Cross-Coupling Reactions of Organoboron Derivatives with Organic Electrophiles, 1995–1998. *J. Organomet. Chem.* **1999**, *576*, 147–168.

(40) Littke, A. F.; Fu, G. C. Palladium-Catalyzed Coupling Reactions of Aryl Chlorides. *Angew. Chemie Int. Ed.* **2002**, *41*, 4176–4211.

(41) Zhang, Z.; Wu, H.-H.; Tan, Y.-J. A Simple and Straightforward Synthesis of Phenyl Isothiocyanates, Symmetrical and Unsymmetrical Thioureas under Ball Milling. *RSC Adv.* **2013**, *3*, 16940–16944.

(42) Majetich, G.; Irvin, T. C.; Thompson, S. B. One-Pot Dehydrations Using Phenyl Isothiocyanate. *Tetrahedron Lett.* **2015**, *56*, 3326–3329.

(43) Bello, A. M.; Wei, L.; Majchrzak-Kita, B.; Salum, N.; Purohit, M. K.; Fish, E. N.; Kotra, L. P. Small Molecule Mimetics of an Interferon-α Receptor Interacting Domain. *Bioorg. Med. Chem.* **2014**, *22*, 978–985.

(44) Lecoutey, C.; Fossey, C.; Rault, S.; Fabis, F. Efficient Room-Temperature One-Pot Synthesis of 2-Amino-3-alkyl(3-aryl)quinazolin-4(3*H*)-ones. *European J. Org. Chem.* **2011**, *2011*, 2785–2788.

(45) Ishimoto, K.; Fukuda, N.; Nagata, T.; Sawai, Y.; Ikemoto, T. Development of a Scalable Synthesis of a Vascular Endothelial Growth Factor Receptor-2 Kinase Inhibitor: Efficient Construction of a 6-Etherified [1,2,4]triazolo[1,5-a]pyridine-2-amine Core. *Org. Process Res. Dev.* **2014**, *18*, 122–134.

(46) Montalbetti, C. A. G. N.; Falque, V. Amide Bond Formation and Peptide Coupling. *Tetrahedron* **2005**, *61*, 10827–10852.

(47) Rida, S.; Ashour, F.; Elhawash, S.; Elsemary, M.; Badr, M.; Shalaby, M. Synthesis of Some Novel Benzoxazole Derivatives as Anticancer, Anti-HIV-1 and Antimicrobial Agents. *Eur. J. Med. Chem.* **2005**, *40*, 949–959.

(48) Das, J.; Rao, C. V. L.; Sastry, T. V. R. S.; Roshaiah, M.; Sankar, P. G.; Khadeer, A.; Kumar, M. S.; Mallik, A.; Selvakumar, N.; Iqbal, J.; Trehan, S. Effects of Positional and Geometrical Isomerism on the Biological Activity of Some Novel Oxazolidinones. *Bioorg. Med. Chem. Lett.* **2005**, *15*, 337–343.

(49) Ammar, H. Ben; Kaddachi, M. T.; Kahn, P. H. Conversion of Malononitrile into 2-Cyanomethyl Compounds. *Phys. Chem. News* **2003**, *9*, 137–139.

(50) Ilkun, O. T.; Archibald, S. J.; Barnes, C. L.; Gerasimchuk, N.; Biagioni, R.; Silchenko, S.; Gerasimchuk, O. A.; Nemykin, V. N. Benz(2-Heteroaryl)cyanoximes and Their Tl(i) Complexes: New Room Temperature Blue Emitters. *Dalton Trans.* **2008**, 5715–5729.

(51) Saraví Cisneros, H.; Laurella, S.; Ruiz, D. L.; Ponzinibbio, A.; Allegretti, P. E.; Furlong, J. J. P. Spectrometric Study of the Nitrile-Ketenimine Tautomerism. *Int. J. Spectrosc.* **2009**, *2009*, 1–18.

(52) Tseng, C.-H.; Tzeng, C.-C.; Chiu, C.-C.; Yang, C.-L.; Lu, P.-J.; Chou, C.-K.; Liu, C.-Y.; Chen, Y.-L. Synthesis and Antiproliferative Evaluation of 9-Methoxy-6-(piperazin-1-yl)-11*H*-indeno[1,2-c]quinoline-11-one Derivatives. Part 4. *Medchemcomm* **2014**, *5*, 937–948.

(53) Ghabbour, H.; El-Bendary, E.; El-Ashmawy, M.; El-Kerdawy, M. Synthesis, Docking Study and β-Adrenoceptor Activity of Some New Oxime Ether Derivatives. *Molecules* **2014**, *19*, 3417–3435.

(54) Bouzoubaa, M.; Leclerc, G.; Decker, N.; Schwartz, J.; Andermann, G. Synthesis and Beta-Adrenergic Blocking Activity of New Aliphatic and Alicyclic Oxime Ethers. *J. Med. Chem.* **1984**, *27*, 1291–1294.

(55) Saccomanni, G.; Badawneh, M.; Adinolfi, B.; Calderone, V.; Cavallini, T.; Ferrarini, P. L.; Greco, R.; Manera, C.; Testai, L. Synthesis and β-Blocking Activity of (R,S)-(*E*)-Oximeethers of 2,3-Dihydro-1,8-Naphthyridine and 2,3-dihydrothiopyrano[2,3-b]pyridine: Identification of β3-Antagonists. *Bioorg. Med. Chem.* **2003**, *11*, 4921–4931.

(56) Ferrarini, P. L.; Mori, C.; Badawneh, M.; Calderone, V.; Greco, R.; Manera, C.; Martinelli, A.; Nieri, P.; Saccomanni, G. Synthesis and Beta-Blocking Activity of (R,S)-(*E*)-Oximeethers of 2, 3-Dihydro-1,8-Naphthyridine and 2,3-dihydrothiopyrano[2,3-b]pyridine:potential Antihypertensive Agents - Part IX. *Eur. J. Med. Chem.* **2000**, *35*, 815–826.

(57) Angelone, T.; Caruso, A.; Rochais, C.; Caputo, A. M.; Cerra, M. C.; Dallemagne, P.; Filice, E.; Genest, D.; Pasqua, T.; Puoci, F.; Saturnino, C.; Sinicropi, M. S.; El-Kashef, H. Indenopyrazole Oxime Ethers: Synthesis and β1-Adrenergic Blocking Activity. *Eur. J. Med. Chem.* **2015**, *92*, 672–681.

(58) Gouda, M. A.; Abu-Hashem, A. A. Synthesis, Characterization, Antioxidant and Antitumor Evaluation of Some New Thiazolidine and Thiazolidinone Derivatives. *Arch. Pharm. (Weinheim).* **2011**, *344*, 170–

177.

(59) Badawey, E. A. M.; Hazzaa, A. A.; Rida, S. M.; Fahmy, H. T. Y. Assessment of Anti-HIV Activity of Some Benzimidazolylthiazoles. *Arch. Pharm. (Weinheim).* **1992**, *325*, 565–567.

CHAPTER 3

BIOLOGICAL EVALUATION

3.1 Chapter Overview

Chapter 3 describes the biological studies that were conducted in order to address the second specific aim of this thesis work, which was: To biologically evaluate the synthesized target compounds for antimycobacterial potency, cytotoxicity, and DMPK profiles.

Sequentially, these studies followed a well-defined screening cascade as illustrated in **Figure 3.1** below, which also depicts the criteria [cut-off values] that informed the advancement of compounds to various biological studies. The cut-off values, adapted from the H3D, played a major role in the prioritization of compounds for various assays.

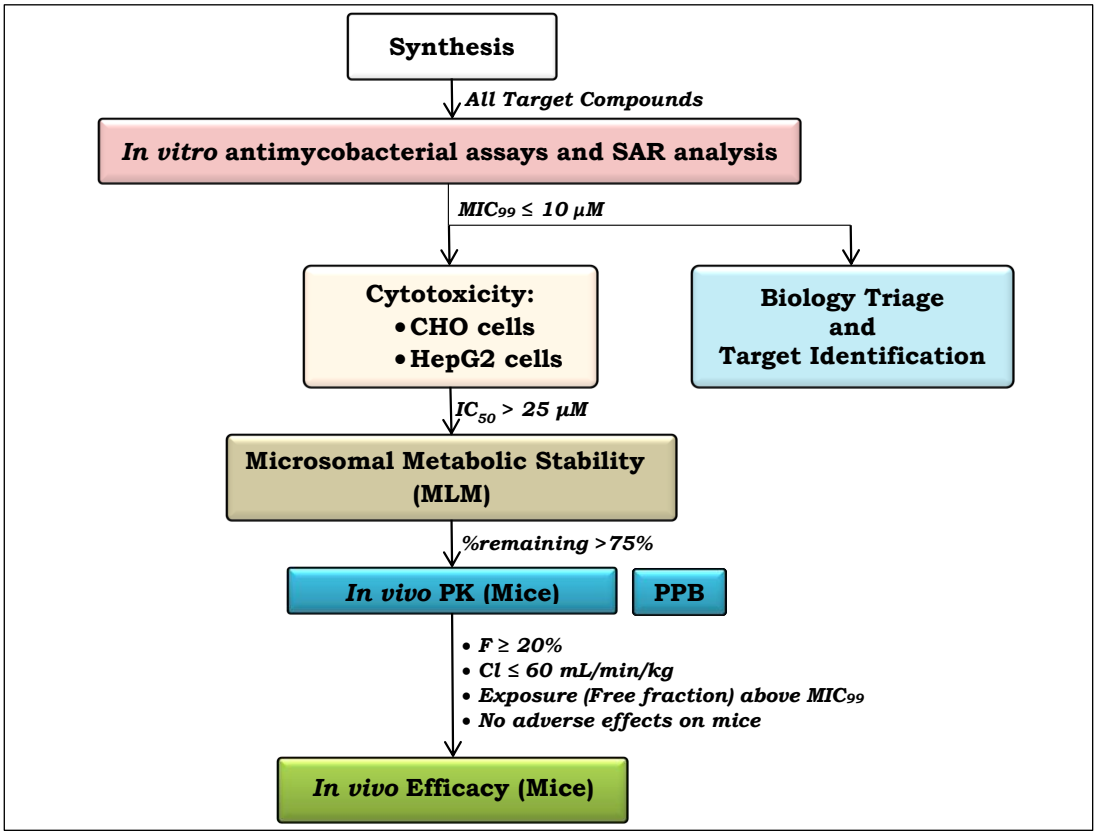

Figure 3.1: The screening cascade adapted in the biological evaluation of target compounds. CHO: Chinese Hamster Ovarian cells; HepG2: Human hepatic cells; Biology Triage: counter-screen against *Mtb*Δ*cyd* mutant, bioluminescence reporter (LUX) assays [P*recA*-LUX and P*ini*-LUX]; Target identification: spontaneous mutant generation studies; MLM: Mouse liver microsomes; PPB: Plasma protein binding; F: Oral bioavailability; Cl: Rate of clearance of an intravenous dose.

In summary, this chapter principally highlights the hit-to-lead optimization screens. It begins with a discussion on *in vitro* antimycobacterial assays, the associated SAR analysis as well as various counter-screen assays, which were carried out on selected potent analogues. What follows is a discussion on *in vitro* cytotoxicity assays and the subsequent *in vitro* microsomal metabolic stability studies. With respect to the 2-aminoquinazolinones, Chapter 3 also provides an overview of the *in vivo* pharmacokinetics and efficacy studies in mice, which were conducted on the frontrunner compounds. In addition, a brief description of the preliminary target identification studies is provided, which involved generation of spontaneous resistant mutants.

3.2 2-Aminoquinazolinones

3.2.1 *In vitro* Antimycobacterial Activity

Once synthesized, all target compounds were evaluated *in vitro* for their antimycobacterial activity against the drug-susceptible *Mtb* $H_{37}Rv$ strain, under replicating conditions. These assays were conducted by Mrs. Ronnett Seldon at the Institute of Infectious Disease and Molecular Medicine, University of Cape Town, South Africa. In all cases, two types of culture media were employed in an effort to create diversity in the *in vitro* assay conditions: GAST-Fe (Glycerol-Alanine-Salts supplemented with Tween 80 and Iron), and 7H9/ADC (Middlebrook 7H9 broth enriched with Albumin-Dextrose Complex, glycerol, and tween 80). Generally, literature protocols were adapted, wherein broth microdilution in a 96-well microplate was utilized.[1–3] Briefly, a 12.8 mM stock solution of a test compound was prepared in DMSO and then diluted with the desired growth medium to a concentration of 640 µM. This was followed by stepwise two-fold serial dilutions up to a concentration of 0.3125 µM. Afterwards, a 1:100 diluted culture of *Mtb* $H_{37}Rv$ at an optical density of 0.6–0.7 at 600 nm (OD_{600}) was added into the wells except those in row 1 [the contamination controls] and incubated at 37 °C. Finally, the lowest concentration of the test compound that inhibited the growth of more than 99% of *Mtb* population [Minimum Inhibitory Concentration (MIC_{99})] was scored visually at day 7 and day 14

post-inoculation. MIC_{99} scoring was facilitated by the use of Alamar blue dye in a technique commonly referred to as the Microplate Alamar Blue Assay (MABA), which is paramount in the visual or fluorimetric cell-growth reading. In some instances, however, the green fluorescent protein (GFP)-tagged *Mtb* $H_{37}Rv$ (pMSP12::GFP) was used in the assays. In this case, the MICs were determined using a dose-response curve analysis of the relative fluorescence [excitation wavelength at 485 nm and emission wavelength at 520 nm] measured on a FLUOstar OPTIMA® microplate reader.

3.2.1.1 Phase I Structure-Activity Relationship (SAR 1) Analysis

The antimycobacterial SAR of the 2-aminoquinazolinones was evaluated by introducing structural variations at position 6 [**SAR 1**] and position 3 [**SAR 2**] of the quinazolin-4(3*H*)-one core, and then screening the final target compounds for their *in vitro* activity against *Mtb*. **Figure 3.2** below is a recapitulation of the general structure of the target analogues of compound **2**, as earlier described in Chapter 2.

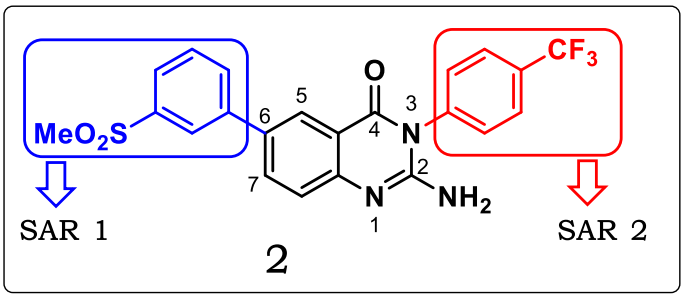

Figure 3.2: The positions of the structural modifications of **2** to yield **SAR 1** and **SAR 2** 2-aminoquinazolinone analogues.

The *in vitro* antimycobacterial activities (MIC_{99} values) displayed by the **SAR 1** target compounds are outlined in **Table 3.1** below.

Table 3.1: *In vitro* antimycobacterial activities of **SAR 1** 2-aminoquinazolinones.

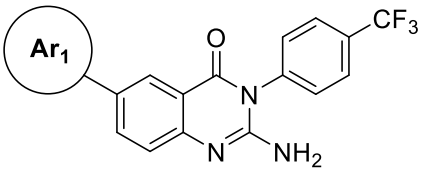

			***In vitro* antimycobacterial activity^ against *Mtb* $H_{37}Rv$; MIC_{99} (µM) [Day 14]**	
Ar_1	**R_1**	**Code**	**GAST-Fe**	**7H9/ADC**
	4–SO_2Me	**1**	>160	>160
	3–SO_2Me	**2**	0.625	1.25
	3–SOMe	**3**	1.25	1.25
	H	**4**	>160	>160
	3–$CONH_2$	**5**	0.625	1.25
	3–SO_2NH_2	**6**	>125*	>125*
	3–CN	**7**	>160	>160
	3–Cl	**8**	0.675	2.31
	2–Cl	**9**	>160	>160
	4–Cl	**10**	>160	>160
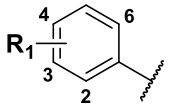	3,4–Cl_2	**11**	>160	>160
	3–F	**12**	>160	>160
	3–CF_3	**13**	0.31	1.25
	3–NH_2	**14**	40	80
	3–OMe	**15**	10	>160
	3–*t*-butyl	**16**	20	80
	4–*t*-butyl	**17**	>160	>160
	3–$N(Me)_2$	**18**	2.5	6.25
	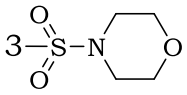	**19**	>125*	>125*
	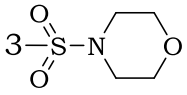 6–Me	**20**	>125*	>125*

Table 3.1: *In vitro* antimycobacterial activities of **SAR 1** 2-aminoquinazolinones.

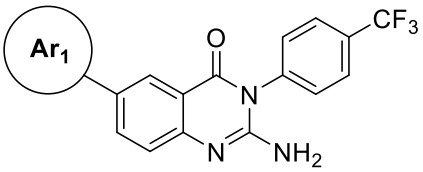

			***In vitro* antimycobacterial activity^ against *Mtb* $H_{37}Rv$; MIC_{99} (µM) [Day 14]**	
Ar_1	**R_1**	**Code**	**GAST-Fe**	**7H9/ADC**
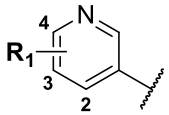	H	**21**	0.625	5
	3–SO_2Me	**22**	>160	>160
	3–Me	**23**	2.5	10
	3–OMe	**24**	10	10
	4–OMe 3–CF_3	**25**	>160	>160
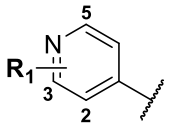	3–F	**26**	>160	>160
	3,5–F_2	**27**	>160	>160
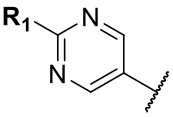	H	**28**	10	80
	OMe	**29**	>160	>160
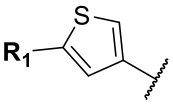	H	**30**	>160	>160
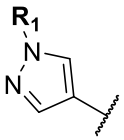	Me	**31**	>160	>160
Controls	Rifampicin		0.0039	0.0039
	Kanamycin		1.562	3.125
	Fusidic acid		0.156	2.5

^Activity determined using the Microplate Alamar Blue Assay (MABA) method; *****Activity determined by GFP-based fluorimetric assay method; $H_{37}RV$: Drug-susceptible *Mtb* strain; GAST-Fe: Glycerol-Alanine-Salts supplemented with Tween 80 and Iron; 7H9/ADC: Middlebrook 7H9 broth enriched with Albumin-Dextrose Complex, Glycerol, and Tween 80.

As shown in **Table 3.1** above, a general trend of relatively higher MIC_{99} values from the 7H9/ADC medium compared to those recorded in the GAST-Fe medium was observed. This is most likely attributable to protein binding of the test compounds by the albumin in the 7H9/ADC medium.

Based on their MIC_{99} values, the test compounds were stratified into four categories, chiefly for purposes of SAR analysis: all compounds with $MIC_{99} \leq 10$ µM were regarded as active; those with MIC_{99} ranging from 10–20 µM had moderate activity; MIC_{99} = 20–125 µM denoted poor activity; whereas compounds exhibiting $MIC_{99} > 125$ µM were categorized as inactive.

For compounds bearing a phenyl group as the **Ar_1** moiety, substitution at the *meta*-position, relative to the quinazolinone ring system, was found to be essential for antimycobacterial activity. Generally, the activity was independent of the electronic properties as well as the degree of hydrophobicity imparted by various substituents. This was augmented by the observation that substituents expected to introduce similar properties to a molecule, in some cases, yielded compounds with varying antimycobacterial potencies. As such, various substituents from each of the four Craig Plot quadrants yielded both active and inactive compounds. For instance, compound **2** [3−SO_2Me-bearing] was active (MIC_{99} = 0.625 µM), whereas, in stark contrast, analogue **6** [3−SO_2NH_2-bearing] was inactive ($MIC_{99} > 125$ µM), despite the two substituents having similar electron withdrawing and hydrophobicity properties. Comparatively, the more active compounds mainly gravitated towards having an electron withdrawing substituent at the *meta*-position. Accordingly, the −CF_3-, −SO_2Me-, −SOMe-, −$CONH_2$-, and −Cl-bearing compounds **13**, **2**, **3**, **5**, and **8** respectively, were the most active and exhibited MIC_{99} values ranging from 0.31 to 1.25 µM. Conversely, all attempts to introduce substituents on the other phenyl positions resulted in loss of activity. For example, *ortho*-substitution (2−Cl, **9**), *para*-substitution (4−SO_2Me, **1**; 4−*t*-butyl, **17**; and 4−Cl, **10**), as well as di-substitution (3,4−Cl_2, **11**) yielded inactive compounds with $MIC_{99} > 160$ µM. In contrast, compounds containing these same substituents at the *meta*-position were all active; an observation that revealed the right pharmacophore responsible for specificity in target interactions. Besides, lack of a substituent on the phenyl ring led to loss of activity (analogue **4**).

Like the phenyl-based analogues, heterocycles as the **Ar_1** moiety delivered compounds with varying antimycobacterial activities. In an intriguing

observation, the pyridyl-based compounds **21** and **22** exhibited contrasting activities compared to their phenyl-based counterparts **4** and **2**, respectively. As such, the unsubstituted pyridyl-based **21** was active (MIC_{99} = 0.625 µM) while the phenyl-based **4** was inactive. Likewise, the 3-methylsulfonylphenyl-based **2** was active (MIC_{99} = 0.625 µM) whereas the 3-methylsulphonylpyridyl-containing **22** was not. In addition, the position of the pyridyl nitrogen atom was found to be critical for activity: compounds bearing the pyridyl nitrogen atom at the *para*-position [**26** and **27**] were inactive, whereas distinctly, the active pyridyl-based compounds [**21**, **23**, and **24**; MIC_{99} = 0.625, 2.5, and 10 µM respectively] bear the pyridyl nitrogen atom at the *meta*-position.

Moreover, the unsubstituted pyrimidinyl-based compound **28** was active (MIC_{99} = 10 µM) while its methoxy-substituted counterpart (**29**) lacked antimycobacterial activity. Also, the 5-membered heterocycles, thiophene and pyrazole (in analogues **30** and **31** respectively) were not tolerated, and therefore both compounds lacked antimycobacterial activity.

In conclusion, the **SAR 1** analogues exhibit clear *in vitro* antimycobacterial SAR trends, which are informed by the diverse potencies manifested by different compounds, some having relatively minor structural differences. This is most likely due to specific interactions between the compounds and the relevant *Mtb* molecular target(s), such that changes in the pharmacophore result in varying levels of potencies. At this juncture, inactive compounds were deprioritized, and were therefore not advanced to other biological studies in the screening cascade.

Subsequently, having fixed the $\mathbf{Ar_1}$ moiety as 3-SOMePh [borne by compound **3**] that manifested the best balance of potency and aqueous solubility, further expansion of the 2-aminoquinazolinone chemical space was undertaken by exploring the right-hand side in the proposed Phase II medicinal chemistry studies [**SAR 2**].

3.2.1.2 Phase II Structure-Activity Relationship (SAR 2) Analysis

All **SAR 2** target compounds were evaluated *in vitro* for their antimycobacterial activities against the GFP-expressing *Mtb* $H_{37}Rv$ strain, in which both GAST-Fe and 7H9/ADC were employed as the culture media. The results obtained are listed in **Table 3.2** below as MIC_{99} values obtained after 14 days of incubation.

Table 3.2: *In vitro* antimycobacterial activities for **SAR 2** target compounds.

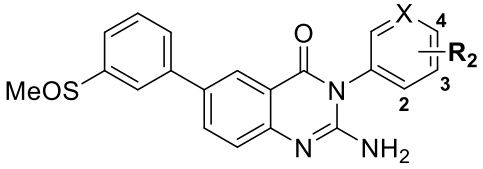

X = CH, for all except 36: X = N

Code	R_2	***In vitro* antimycobacterial activity* against *Mtb* $H_{37}Rv$; MIC_{99} (µM) [Day 14]**	
		GAST-Fe	**7H9/ADC**
32	H	33.4	13.0
33	4−Me	3.09	2.28
34	3−CF_3	14.8	5.21
35	2−CF_3	>125	>125
36	4−CF_3	0.922	0.769
37	4−CN	9.28	7.36
38	3−CN	43	23.1
39	4−SO_2Me	>125	>125
40	4−OMe	6.75	9.34
41	4−OH	>125	>125
42	4−F	4.84	5.32
43	2−F	67	90.3
44	2−F, but R_1 = 3−SO_2Me	>125	>125

*Activity determined by GFP-based fluorimetric assay method; $H_{37}RV$: Drug-susceptible *Mtb* strain (GFP-expressing); GAST-Fe: Glycerol-Alanine-Salts supplemented with Tween 80 and Iron; 7H9/ADC: Middlebrook 7H9 broth enriched with Albumin-Dextrose Complex, Glycerol, and Tween 80.

The compounds studied in phase II plans exhibited relatively comprehensible SAR trends, which were mainly driven by the type of substituent as well as the position of substitution on the phenyl ring. In this case, the MIC_{99} values obtained with the GAST-Fe medium are used for purposes of describing the SAR. Overall, substitution at the *para*-position (4) of the phenyl ring appeared to be the optimal position for antimycobacterial activity. As a result, shifting the position of the $-CF_3$ moiety from the *para*-position [analogue **3**; MIC_{99} = 1.25 µM] to the *meta*-position [analogue **34**; MIC_{99} = 14.8 µM] led to an approximately 12-fold reduction in activity, whereas a shift to the *ortho*-position [analogue **35**; MIC_{99} > 125 µM] led to complete loss of activity. A similar trend was observed with the nitrile and fluoro substituents. In this case, the 4−CN-bearing analogue **37** (MIC_{99} = 9.28 µM) and the 4−F-bearing analogue **42** (MIC_{99} = 4.84 µM) exhibited significantly higher activity compared to their *ortho*-substituted peers **38** (MIC_{99} = 43 µM) and **43** (MIC_{99} = 67 µM) respectively, which displayed poor activity. In a peculiar case where a 2-FPh as the **Ar_2** moiety was combined with a 3-SO_2MePh as the **Ar1** moiety [analogue **44**; MIC_{99} > 125 µM], antimycobacterial activity was severely affected.

Comparatively, replacement of the $4-CF_3$ group with other substituents generally led to reduction in activity. For instance, although active, the 4−Me, 4−CN, 4−OMe, and 4−F substituents in analogues **33** (MIC_{99} = 3.09 µM), **37** (MIC_{99} = 9.28 µM), **40** (MIC_{99} = 6.75 µM), and **42** (MIC_{99} = 4.84 µM) respectively, resulted in a slight decrease in activity compared to the $4-CF_3$-based analogue **3** (MIC_{99} = 1.25 µM). Likewise, the unsubstituted phenyl-based analogue **32** exhibited moderate antimycobacterial activity (MIC_{99} = 33.4 µM). On the other hand, the replacement of the $4-CF_3$ moiety with groups such as $4-SO_2Me$ [**39**; MIC_{99} > 125 µM], and 4−OH [**41**; MIC_{99} > 125 µM] led to complete loss of activity.

Furthermore, replacing the phenyl ring with a pyridyl, while maintaining the $4-CF_3$ substituent, yielded analogue **36** with markedly enhanced antimycobacterial activity (MIC_{99} = 0.922 µM). It suffices, therefore, at this juncture to conclude that a pyridyl bearing a $4-CF_3$ group is the optimal **Ar_2**

moiety for antimycobacterial activity. **Figure 3.3** below provides a graphical representation of the foregoing **SAR 2** analysis, displaying the effect on antimycobacterial activity by various substituents at different aromatic ring positions. In order to promote visualization of potencies, MIC_{99} were converted to $pMIC_{99}$, and therefore manifest a direct proportionality between the $pMIC_{99}$ values and the antimycobacterial activity.

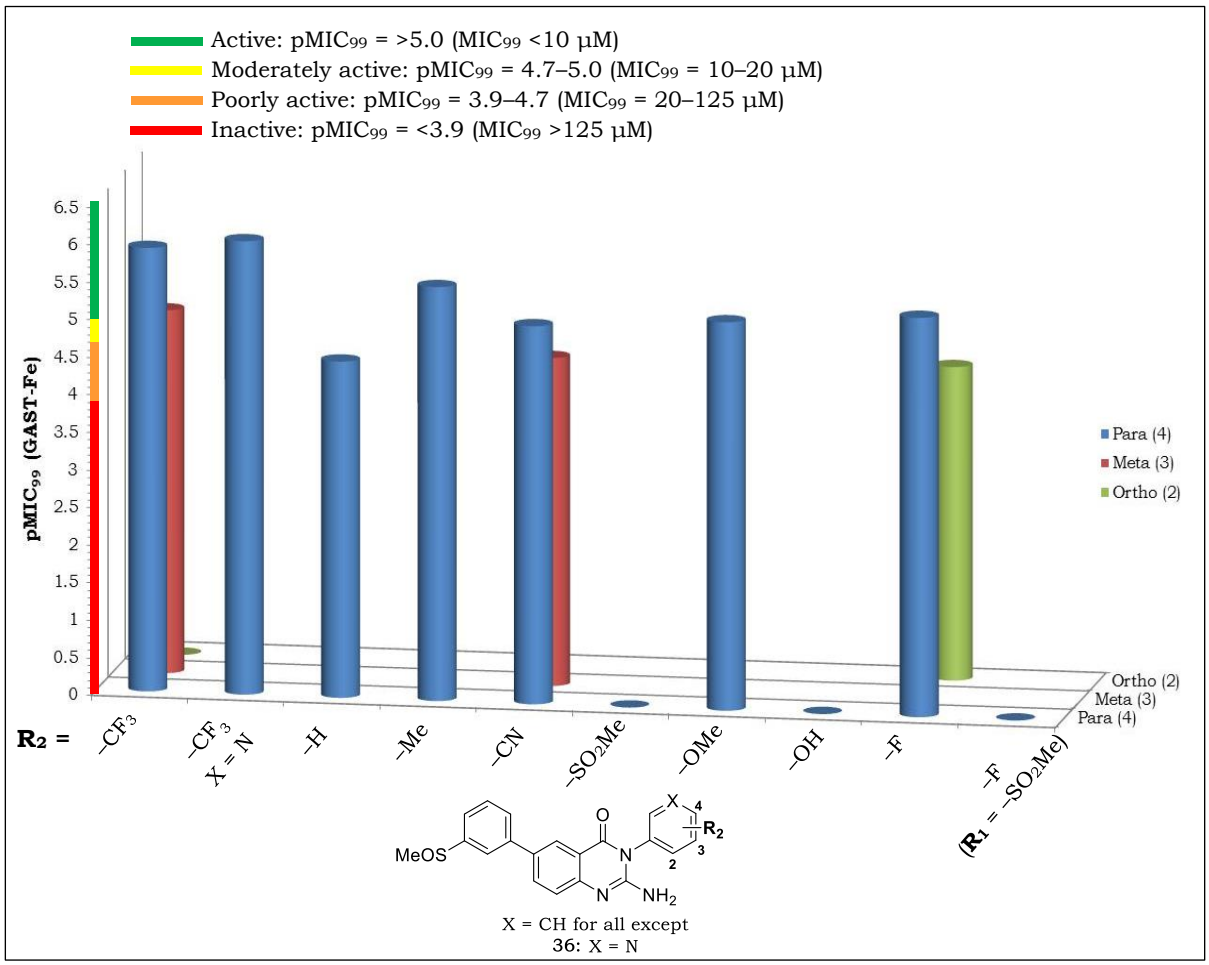

Figure 3.3: Three-dimensional graphical representation of **SAR 2** analysis.

After determining the *in vitro* antimycobacterial activities of 2-aminoquinazolinones, potent compounds were selected and subjected to other biological screens, principally aimed at rapidly assessing the provisional mechanism(s) of action for triage purposes in an effort to facilitate further ranking and prioritization. Although these assays do not furnish definitive mechanism(s) of action, they nonetheless provide a convenient insight into the cellular processes involved in the displayed activity. Therefore, there are two main reasons for carrying out biology triage

studies: Firstly, to provide information about whether or not active compounds exert their activity through known mechanism(s) of action; and secondly, to deprioritize compounds whose tentative biochemical targets are known to be promiscuous (unselective). These assays, for instance, include the counter-screen assay against the *Mtb*Δ*cyd* [cytochrome bd oxidase knockout] mutant, as well as the luminescence-based (LUX) assays described in the following subsections. These biology triage (Tier 1) assays were conducted in Associate Professor Digby Warner's laboratory, Molecular Mycobacteriology Research Unit, Division of Medical Microbiology, University of Cape Town, South Africa.

3.2.2 *In vitro* Antimycobacterial Counter-screen Assay against *Mtb*Δ*cyd*

A representative batch of compounds, which demonstrated potent whole-cell activity [that is, $MIC_{99} \leq 10$ μM] against the GFP-expressing *Mtb* $H_{37}Rv$ strain, was counter-screened against the *Mtb*Δ*cyd* mutant. This mutant lacks a functional cytochrome *bd* oxidase, and therefore it is entirely dependent on the cytochrome *bc*1 complex for oxidative phosphorylation-driven respiration. Consequently, the mutant is hypersusceptible to compounds that inhibit the QcrB-containing cytochrome *bc*1 complex. QcrB is a putative ubiquinol [a form of coenzyme Q_{10}] cytochrome c reductase, subunit b, which is an integral member of the *bc*1 complex of the respiratory electron transport chain.[4] From a drug discovery perspective, QcrB is a biochemical target to a significantly high number of structurally diverse compounds, and therefore it is considered a promiscuous target. In addition, the oxidative phosphorylation pathway is largely conserved between prokaryotes and eukaryotes. Therefore, in some cases, unselective inhibition of the QcrB leads to unwanted target-based toxicity. This notwithstanding, it is a promising novel target pathway, particularly in instances where there is compelling evidence of selective inhibition of *Mtb* oxidative phosphorylation while sparing the homologous energy metabolism pathway in humans. For instance, bedaquiline interferes with *Mtb* energy metabolism via selective inhibition of ATP synthase, while Q203 and lansoprazole are potential anti-TB drugs that selectively inhibit the cytochrome *bc*1 complex.[5–9]

Accordingly, this counter-screen assay was performed for two reasons: Firstly, to identify compounds that might be targeting the QcrB, as this is considered a "red flag" in TB drug discovery programs due to possible target-based toxicities in humans. Secondly, to establish whether active compounds also display activity against a non-GFP expressing *Mtb* strain, hence confirming that indeed the inferred *in vitro* inhibitory activity is real, and not a function of interrupted GFP production. The *in vitro* antimycobacterial activities of the selected 2-aminoquinazolinone analogues against the *Mtb*Δ*cyd* mutant are shown in **Table 3.3** below.

Table 3.3: *In vitro* antimycobacterial activity against the *Mtb*Δ*cyd*.

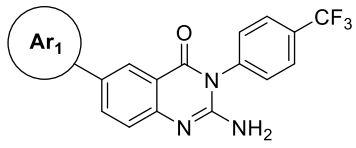			***In vitro* antimycobacterial activity against *Mtb* $H_{37}Rv$; MIC_{99} (µM) [Day 14]**		***In vitro* antimycobacterial activity against *Mtb*Δ*cyd*; MIC_{99} (µM) [Day 14]**	
Ar_1	**R_1**	**Code**	**GAST-Fe**	**7H9/ADC**	**GAST-Fe**	**7H9/ADC**
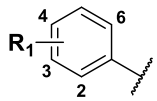	3–SO_2Me	**2**	0.625	1.25	ND	ND
	3–SOMe	**3**	1.25	1.25	2.5	2.5
	3–$CONH_2$	**5**	0.625	1.25	5	2.5
	3–Cl	**8**	0.675	2.31	ND	ND
	3–CF_3	**13**	0.31	1.25	5	2.5
	3–$N(Me)_2$	**18**	2.5	6.25	5	10
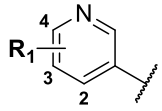	H	**21**	0.625	5	1.25	5
	3–Me	**23**	2.5	10	1.25	>10
	3–OMe	**24**	10	10	10	>10
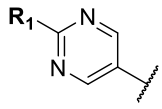	H	**28**	10	80	>10	>10

$H_{37}RV$: Drug-susceptible *Mtb* strain; *Mtb*Δ*cyd*: *Mtb* mutant with cytochrome *bd* oxidase knockout; GAST-Fe: Glycerol-Alanine-Salts supplemented with Tween 80 and Iron; 7H9/ADC: Middlebrook 7H9 broth enriched with Albumin-Dextrose Complex, Glycerol, and Tween 80.

These results depict comparable activity trends of the tested compounds against the two *Mtb* strains, with no observed decrease in MIC_{99} against the

*Mtb*Δ*cyd*. Therefore, QcrB was excluded as a possible target for the 2-aminoquinazolinones.

3.2.3 Luminescence-Based (LUX) Assays

LUX assays are designed to provide preliminary insights into mechanism of action through a rapid, first-pass detection of compounds that disrupt two macromolecular cellular pathways: the *Mtb* cell wall biosynthesis and homeostasis, and the maintenance of DNA integrity. These assays are based on luminescence signals generated by mycobacterial luciferase (*luxAB*) operons, whose expression is driven by gene promoters, which are induced by either cell wall or DNA damage. In this regard, the three-gene *iniBAC* operon is known to be stimulated in response to many agents that disrupt the *Mtb* cell wall homeostasis, including the frontline anti-TB drug, isoniazid, as well as inhibitors of peptidoglycan, arabinogalactan, mycolic acids, and fatty acids biosynthesis.[10] Accordingly, this response is referred to as P*iniB*-LUX. On the other hand, *recA* and *radA* promoters are known to be upregulated in response to genotoxic agents as part of mycobacterial DNA damage (SOS response). These responses, therefore, are denoted as either P*recA*-LUX or P*radA*-LUX.[11]

Three representative 2-aminoquinazolinone analogues [**3**, **5**, and **13**] were evaluated for their ability to induce either a cell wall (P*iniB*-LUX) or a DNA damage (P*recA*-LUX) response. In this assay, two-fold serial dilutions of each test compound were prepared in 96-well microplates containing the reporter *Mtb* H_{37}Rv strain [transformants of *lux* plasmids], followed by incubation at 37°C for 12 days. Luminescence, recorded as relative luminescence units [RLU], was measured every 24 hours. Isoniazid and ciprofloxacin served as the maximum luminescence controls for P*iniB*-LUX and P*recA*-LUX assays, respectively.[11] All the three compounds yielded negative results for both LUX assays. Therefore, it was highly likely that the apparent *in vitro* inhibitory activities displayed by the 2-aminoquinazolinone analogues were not through mechanisms associated with the disruption of the *Mtb* cell wall or DNA integrity.

3.2.4 Carbon Starvation Assay

In most cases, a significant subpopulation of *Mtb* exists in a non-replicating state during the active TB disease. These *Mtb* bacilli are refractory to some anti-TB drugs, and therefore contribute to the need for prolonged antibiotic therapy. As such, development of drugs capable of sterilizing the non-replicating *Mtb* will significantly contribute to the shortening of TB therapy. In this regard, *in vitro* carbon (nutrient) starvation (tolerance) assays are used to evaluate compounds for their ability to inhibit non-replicating *Mtb*.[12] In effect, the media for nutrient starvation, such as Middlebrook 7H9 enriched with 0.05% Tyloxapol, should ideally contain essential cofactors and trace elements to maintain live bacilli, but not sufficient carbon to support growth.

Four 2-aminoquinazolinone analogues, which exhibited high potency against the replicating *Mtb* $H_{37}Rv$ strain, were selected and submitted for carbon starvation assays at the Centre of Excellence for Biomedical TB Research, National Health Laboratory Service, University of Witwatersrand, South Africa. The results are shown in **Table 3.4** below.

Under starvation conditions, there was a general increase in *Mtb* tolerance for the tested analogues, with majority of the compounds exhibiting >16-fold increase in MIC_{99} compared to the replicating conditions, except analogue **13**, which yielded a two-fold increase in MIC_{99}. This assay, therefore, generally indicates that the 2-aminoquinazolinones most likely do not inhibit the non-replicating *Mtb*, although a bigger sample size would be required to draw a clear-cut conclusion about this series. Alternatively; the differences in the displayed MIC_{99} values could as well be attributed to differences in the growth media employed. Notably, rifampicin and isoniazid assay controls yielded the expected results.

Table 3.4: Carbon starvation assay results.

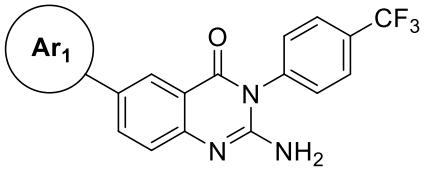

Code	Ar_1	7H9/ADC-Fe Day 14 MIC_{99} (µM)	Starvation (Tolerance); 7H9/Tyloxapol Day 14 MIC_{99} (µM)
2	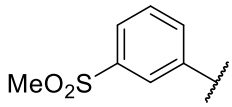	0.625	160
3	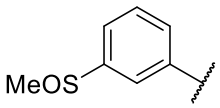	1.25	20
5	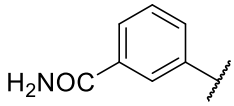	0.625	10
13	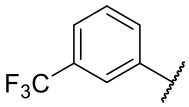	1.25	2.5
	Rifampicin	32-fold increase in MIC_{99}	
	Isoniazid	4-fold increase in MIC_{99}	

7H9/ADC-Fe: Middlebrook 7H9 broth enriched with Albumin-Dextrose Complex, Glycerol, Tween 80, and iron.

3.2.5 Cytotoxicity Studies

In an effort to determine the selectivity of 2-aminoquinazolinones for *Mtb*, and in essence provide the predictive evidence of their safety profile, *in vitro* cytotoxicity studies were performed on selected potent analogues against two cell lines. Accordingly, cytotoxicity studies against the Chinese Hamster Ovarian (CHO) cells were conducted at the Division of Clinical Pharmacology, University of Cape Town, while studies against the human hepatic cell line, HepG2, were carried out at the Tuberculosis Research Section, Laboratory of Clinical Infectious Diseases, National Institute for Allergy and Infectious Disease (NIAID), National Institutes of Health (NIH), United States of America.

Cytotoxicity assays against the CHO cells were conducted using 3-(4,5-dimethylthiazol-2-yl)-2,5-diphenyltetrazolium bromide(MTT),which facilitates the measurement of cell proliferation and chemosensitivity. Emetine was used as the positive control while DMSO was the negative control.

The assay against HepG2 cells was carried out in both glucose- and galactose-containing media. This was to facilitate the detection of drug-induced mitochondrial dysfunction; that is, HepG2 cells are forced to rely on mitochondrial oxidative phosphorylation rather than glycolysis when galactose is substituted for glucose in growth media. Consequently, oxygen consumption increases in the galactose-grown HepG2 cells, and therefore their susceptibility to mitochondrial toxicants increases.[13] In all cases, the CellTiter-Glo® luminescent cell viability/proliferation assay protocol was adapted. Cytotoxicity data for the representative 2-aminoquinazolinone analogues are listed in **Table 3.5** below.

Table 3.5: *In vitro* cytotoxicity assay results for selected analogues.

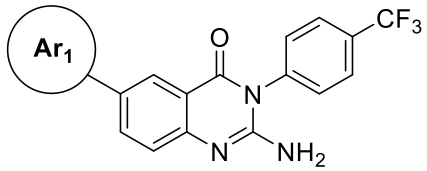

			Cytotoxicity IC_{50} (µM)		
Ar_1	**R_1**	**Code**	**CHO**	**HepG2 (Galactose)**	**HepG2 (Glucose)**
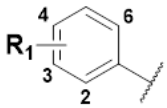	3–SO_2Me	**2**	190±2	>50	>50
	3–SOMe	**3**	>226±ND	26.7	>50
	3–$CONH_2$	**5**	>236±ND	37.7	>50
	3–Cl	**8**	>241±ND	>50	>50
	3–CF_3	**13**	>223±ND	>50	>50
	3–$N(Me)_2$	**18**	>236±ND	>50	>50
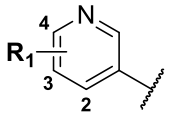	H	**21**	>262±ND	>50	>50
	3–Me	**23**	177±27.2	>50	>50
	3–OMe	**24**	>243±ND	>50	>50
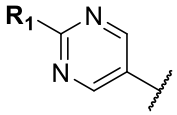	H	**28**	>261±ND	>50	>50
Emetine			0.319±0.09	ND	ND

ND: Not determined; CHO: Chinese Hamster Ovarian cells; HepG2: human hepatic cell line.

The cytotoxicity results from these two assays were expressed as 50% inhibitory concentration (IC_{50}), which was obtained from the analysis of the

dose-response curves. On the other hand, the *in vitro* antimycobacterial activities were expressed as MIC_{99}, and therefore it would be inaccurate to calculate selectivity indices based on the two inhibitory concentrations. As such, the acceptable level of cytotoxicity was set at a cut-off value of IC_{50} > 25 µM.

The tested compounds exhibited low cytotoxicity (IC_{50} > 25 µM) against the two cell lines. Of particular interest, analogues **2** and **5** exhibited higher cytotoxicity [IC_{50} = 26.7 and 37.7 µM, respectively] against the HepG2 cells grown in the galactose-containing medium compared to those in the glucose-containing medium [IC_{50} > 50 µM for both analogues]. In view of this, although the cytotoxicity level was within the acceptable range, the two compounds could be considered as potential mitochondrial toxicants. However, the differences could also have resulted from possible higher solubility of these compounds in the galactose-containing medium.

Within the context of cytotoxicity and selectivity, selected active compounds with low cytotoxicity were further evaluated for their potential to inhibit the cardiac potassium ion channel as described below.

3.2.6 HERG Electrophysiological Patch Clamp Assay

The human Ether-à-*go*-*go*-Related Gene (hERG) encodes for the alpha subunit of a voltage-dependent cardiac potassium ion channel (usually denoted as hERG), which contributes to the electrical activity of the heart, and thus coordinates the heart's rhythmic beating. A loss of function or a drug-related inhibition of this channel in humans more often leads to a fatal heart disorder known as the long QT syndrome or Torsades de Pointes (TdP) ventricular tachycardia, which is associated with cardiac arrhythmia that usually leads to sudden death.[14] It is for this reason that it is essential to screen compounds for their potential to inhibit the hERG channel during the early stages of drug discovery. In cases where significant hERG blockade is revealed, appropriate medicinal chemistry approaches are triggered to address this liability at the earliest.[15,16] Electrophysiology-based assay methods as well as virtual predictions are available for hERG screening.[17–20]

Four representative 2-aminoqunazolinone analogues were selected and submitted for *in vitro* hERG inhibition assay at the Ion Channel Discovery Services, Essen Bioscience, United Kingdom. The IonWorks patch clamp electrophysiology protocol was applied. Briefly, electrophysiological recordings were made from a Chinese Hamster Lung cell line, which stably expresses the full length hERG channel. In effect, 8-point concentration-response curves were generated using 3-fold serial dilutions from the maximum final assay concentration equivalent to 33 µM. These curves plot the log of molar concentration of a test compound against its effect on the hERG current, which is expressed as a percentage of the pre-compound signal. The results are shown in **Table 3.6** below.

Table 3.6: HERG inhibition assay results.

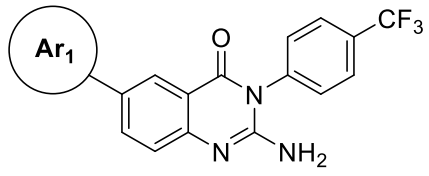

Code	Ar_1	IC_{50} (µM)[a]	95% CI	Comments[b]
2	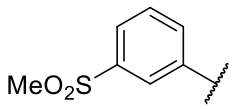	>3.7	-	-20 ± 17% inhibition at 3.7 µM, solubility issues at 11 and 33 µM
3	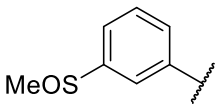	4.8	3.1–7.3	solubility issues at 33 µM
5	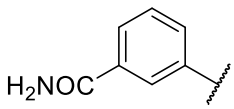	>3.7	-	5 ± 13% inhibition at 3.7 µM, solubility issues at 11 and 33 µM
13	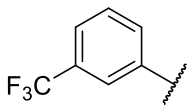	>1.2	-	19 ± 36% inhibition at 1.2 µM, solubility issues at 3.7, 11, and 33 µM
Quinidine		1.6	0.8–3.1	-

CI = Confidence interval; [a]Denotes values were obtained from a 4-parameter logistic fit of the concentration-response data; [b]Denotes maximal percentage inhibition where the IC_{50} values could not be determined.

For most compounds (those with > values), the inhibition potency could not be fully resolved mainly due to limited concentration range, particularly

because of poor solubility. Analogue **3**, however, did not have solubility issues at low concentration, and therefore its IC_{50} value was considered more accurate. According to a general potency ranking system used to indicate the potency of test compounds in inhibiting the hERG channel, though not absolute cut-offs [low, IC_{50} > 10 µM; moderate, 1 µM ≤ IC_{50} ≤ 10 µM; high, IC_{50} < 1 µM],[21] it can be concluded that compound **3** has a moderate inhibition of the hERG channel. Moreover, these results highlight the poor aqueous solubility associated with this 2-aminoquinazolinone series.

3.2.7 Metabolic Stability Assay

The most potent (MIC_{99} ≤ 10 µM) and less cytotoxic (IC_{50} > 25 µM versus CHO and HepG2) analogues were selected for evaluation of their *in vitro* metabolic stability. This study was conducted by Dr. Mathew Njoroge at the Division of Clinical Pharmacology, University of Cape Town, South Africa.

In summary, hepatic metabolism is the primary elimination mechanism for most exogenous compounds, which influences the bioavailability, clearance, and elimination half-life of a xenobiotic. Thus, it is important to screen compounds for the extent of hepatic metabolism, usually in an *in vitro* assay that utilizes liver microsomes. Three types of liver microsomes are commonly employed, which to a large extent are composed of membrane-bound enzymes such as the CYP450 [Phase I metabolism]: the human liver microsomes (HLM), the rat liver microsomes (RLM), and the mouse liver microsomes (MLM); in order to determine any interspecies differences.[22] Alternatively, metabolic stability can be assessed using the S9 fraction, which has more Phase I and Phase II drug metabolizing enzymes compared to microsomes. In addition, cytosol, which is mainly composed of soluble Phase II enzymes, can be employed. In this thesis study, however, MLM were prioritized over the other options because it was anticipated that the *in vivo* pharmacokinetics and efficacy studies would be conducted in mice models.

A single time-point [30 minutes] assay protocol was applied. Briefly, the test compounds were appropriately diluted to 0.1 µM using a phosphate buffer pH 7.4 in a 96-well microtiter plate. The MLM (0.4 mg/mL) were then added

into the wells along with NADPH, which served as an enzyme cofactor for initiation of the enzymatic reactions involved. This mixture was then incubated at 37 °C for 30 minutes, while shaking the microplates. Subsequently, the reaction was stopped by adding ice cold acetonitrile. The mixture was then centrifuged to remove proteins as sediments, while the supernatant was analyzed using liquid chromatography tandem mass spectrometry (LC-MS/MS).[23] The LC-MS/MS readout was then used to determine the percentage amount of intact compound remaining after 30 minutes of incubation in the MLM, as shown in **Table 3.7** below.

Table 3.7: *In vitro* microsomal metabolic stability in the mouse liver microsomes.

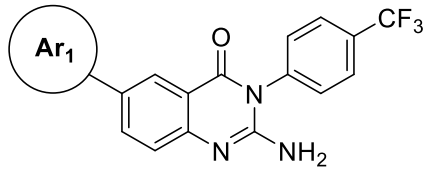		**Compound Code**	**% Remaining after 30 min in MLM**	**Preliminary Main Metabolite Identity**
Ar_1	**R_1**			
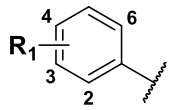	3–SO_2Me	**2**	97	ND
	3–SOMe	**3**	73	Oxidation to sulfone-based **2**
	3–$CONH_2$	**5**	88	ND
	3–Cl	**8**	88	Hydroxylation
	3–CF_3	**13**	97	ND
	3–$N(Me)_2$	**18**	37	N-demethylation (mono- and di-)
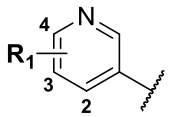	H	**21**	68	Hydroxylation
	3–Me	**23**	87	ND
	3–OMe	**24**	72	O-demethylation
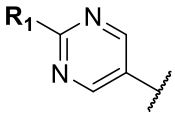	H	**28**	94	ND
References		Midazolam	<5	-
		MMV390048	>99	-

ND: Not determined; MLM: Mouse Liver Microsomes.

The MLM-unstable midazolam as well as the metabolically stable MMV390048 were used as controls in this assay. A value ≥ 75% remaining after 30 minutes is generally an acceptable measure of microsomal

metabolic stability that can be translated to indicate favourable *in vivo* half-life ($t_{1/2}$).

All the tested compounds, except **18**, displayed high microsomal metabolic stability. The low metabolic stability (37% remaining) of **18** was most likely due to the metabolically labile *N*,*N*-dimethyl moiety, which undergoes rapid mono- and di-demethylation by the microsomal enzymes.

In instances where the analytical sensitivity as well as the extent of metabolism permitted, preliminary metabolite identification was carried out. Notably, the sulfoxide-based analogue **3** was mainly metabolised to the more metabolically stable sulfone-based **2**. This, therefore, allowed advancing of analogue **3** to other studies in the screening cascade, although its microsomal metabolic stability was 73%, which was outside the set criteria of ≥ 75% remaining after 30 minutes.

At this juncture, it was apparent that analogue **3** was the most favourable candidate for *in vivo* pharmacokinetic (PK) studies due to its favourable profile with respect to *in vitro* potency (MIC_{99} = 1.25 µM), aqueous solubility (80 µM), cytotoxicity (IC_{50} > 25 µM), and metabolic stability (73% remaining). The choice of **3** as the lead compound was further augmented by its 'prodrug' predisposition, whereby it was postulated that it would facilitate the *in vivo* delivery of the active (MIC_{99} = 0.625 µM), more metabolically stable (97% remaining) analogue **2**, which, on the other hand, was beset by poor aqueous solubility (10 µM).

3.2.8 Plasma Protein Binding

Plasma protein binding (PPB) is an important parameter that modulates the effective drug concentration at a particular pharmacological target site, and is known to significantly influence the rate of drug diffusion between plasma and tissues. This, for instance, affects the clearance (Cl) and the volume of distribution (Vd) of xenobiotics.[24] In the early stages of drug discovery, PPB values are paramount in adjusting the pharmacokinetics parameters such as exposure, which are then considered when establishing the dose levels for *in vivo* efficacy studies. This is influenced by the fact that it is the unbound

fraction of a particular compound that is responsible for its efficacy and toxicity.

Analogues **3** and **13** were selected for plasma protein binding assay, which was conducted at the Centre for Drug Candidate Optimisation (CDCO), Australia. In summary, aliquots of mouse plasma were spiked with DMSO/acetonitrile/water solutions of each test compound individually to a nominal concentration of 1000 ng/mL. Following ultracentrifugation, an aliquot of protein-free supernatant was taken from each of the ultracentrifuge tubes for determination of the unbound compound concentration by LC-MS.

The PPB data, as shown in **Table 3.8** below, revealed that the tested compounds were highly bound to mouse plasma proteins (> 95% bound). These results were thereafter used to correct the *in vivo* PK indices for purposes of dose evaluation in preparation for *in vivo* efficacy studies in mice.

Table 3.8: Mouse plasma protein binding.

Compound Code	Structure	Fraction unbound (% Bound)
3	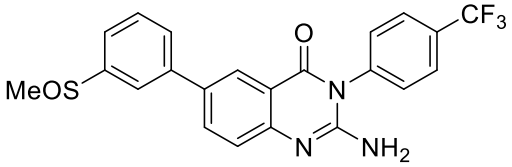	0.045 ± 0.0051 (95.5% Bound)
13	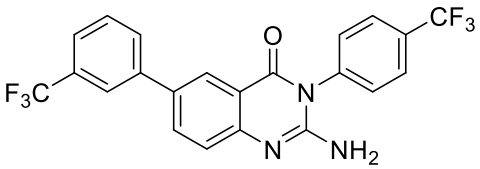	0.038 ± 0.0070 (96.2% Bound)

3.2.9 *In vivo* Pharmacokinetics Study

The sulfoxide-based analogue **3** was selected as the candidate for *in vivo* pharmacokinetics assessment in mice. This study was performed by Dr. Dale Taylor at the Division of Clinical Pharmacology, University of Cape Town, South Africa.

Initially, snapshot 24-hour PK experiments were conducted on compounds **2** and **3**. This was chiefly to establish whether the sulfone-based analogue **2** would significantly be generated *in vivo* from **3**. In addition, these experiments were essential in comparing the PK profile of the orally administered **2** versus **2** as a metabolite of **3**. Each compound was administered orally [per oral (po)] as a suspension in hydroxypropyl methylcellulose (HPMC) in phosphate-buffered saline (PBS), pH 7.4, and at dose levels of 25 × 2, 100, and 200 mg/kg, with three mice (n = 3) at each dose level.

As hypothesized, the sulfoxide-based **3** was significantly metabolised to the sulfone-based **2** as shown in plots **C** in **Figure 3.4** below. These PK profiles depicted the mean circulating plasma concentrations of the active metabolite **2** increasing steadily as the concentration of **3** decreased. This pattern was replicated for the three dose levels. Although the conversion of **3** was extensive, it did not go to completion within 24 hours. Furthermore, the metabolism of **3** was fast, with metabolite **2** being detected immediately after administration of the parent compound **3**, even at the lowest dose level.

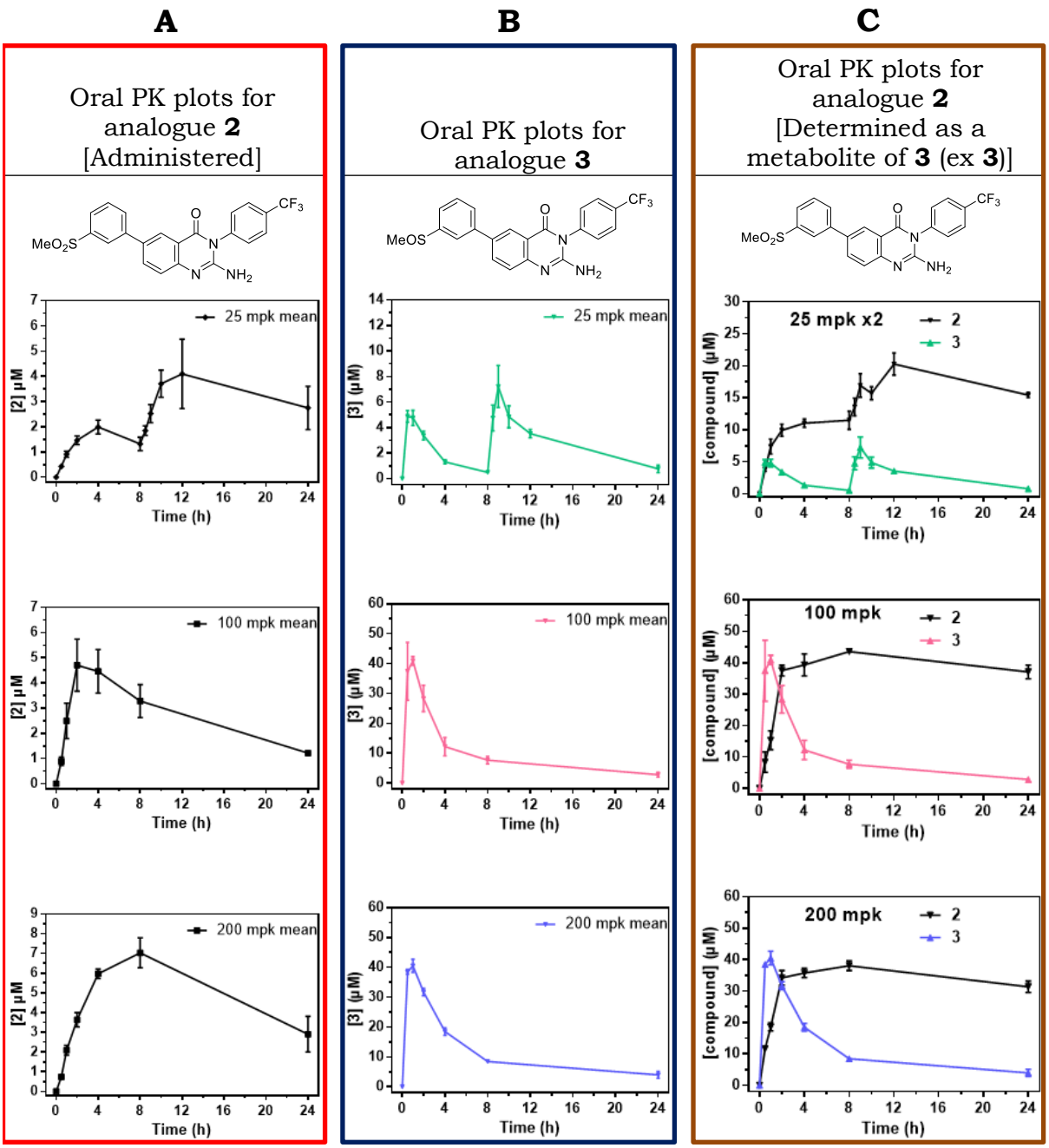

Figure 3.4: Concentration-time (rising dose) profiles (mean of n = 3 mice at each dose level) for the orally administered **2** [Plots **A**], **3** [Plots **B**], and **2** as a metabolite of **3** [Plots **C**], at 25 × 2 (second dose after 8 hours), 100, and 200 mg/kg (mpk) dose levels.

The average half-life ($t_{1/2}$) of **3** was estimated to be 7.2 hours (plots **B**). Comparatively, although not conclusively determined, the active metabolite **2** exhibited longer $t_{1/2}$ [~33–251 hours; that is, the metabolite appeared far from elimination after 24 hours as shown in plots **C**]. Moreover, the exposure of metabolite **2** was greater than that of the parent compound **3** as demonstrated by the area under the curve (AUC) equivalent to 810.1

h.µmol/L for **2** versus 269.1 h.µmol/L for **3** at 200 mg/kg. Also, the oral administration of **2** yielded lower plasma concentrations [maximum concentration (C_{max}) of 4.1, 4.7, and 7.0 µM at 25 × 2, 100, and 200 mg/kg respectively – plots **A**] compared to its peak plasma concentrations as a metabolite of **3** [C_{max} = 20.0, 40.9, and 39.0 µM – plots **C**]. This was most likely attributable to solubility-limited absorption of **2**. However, on the upside, higher exposure of **2** could be achieved by orally administering the more soluble analogue **3**. Accordingly, it was considered more desirable and advantageous to administer analogue **3** for subsequent *in vivo* experiments.

The kinetics of compound **3** were fairly linear up to 100 mg/kg before some measure of saturation occurred. At all doses, the exposure of the metabolite exceeded that of the parent compound; however, exposure maximized at the intermediate dose of 100 mg/kg [C_{max} = 40.9 µM], and not at the highest dose of 200 mg/kg [C_{max} = 40.5 µM], most likely suggesting a limited absorption of **3** from the gut at the highest dose.

Subsequently, the full mouse rising dose (single) PK and tolerability assessment of compound **3** was performed over 48 hours at 50, 100, and 200 mg/kg po; and 5 mg/kg intravenous (IV) dose. The compound was administered orally as a suspension in 0.5% w/v carboxymethylcellulose (CMC) solution, while the IV solution was made in *N*,*N*-dimethylacetamide (DMA): polyethylene glycol (PEG400): 5% dextrose (D5W) [15:50:35; v/v/v] mixture. Circulating plasma concentrations of both the parent compound (**3**) and the active metabolite (**2**) were quantified, and their PK profiles are shown in **Figure 3.5** below.

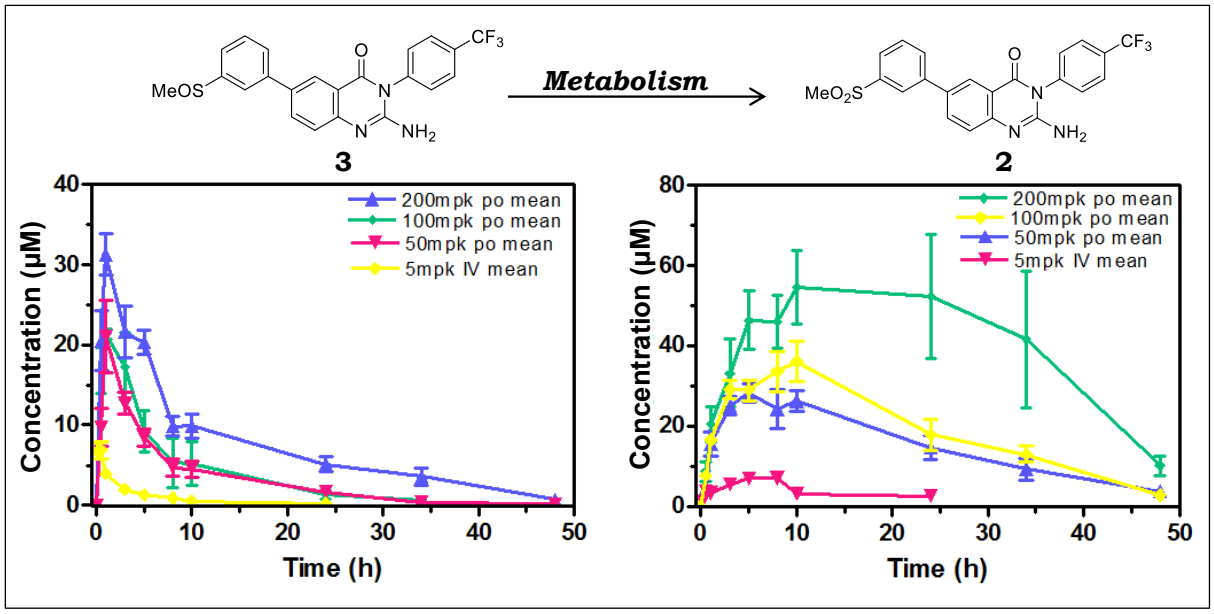

Figure 3.5: Concentration-time profiles (mean of n = 3 mice) for compound **3** [graph on the left-hand side], and its active metabolite **2** at 50, 100, and 200 mg/kg (mpk) oral doses (po); and 5 mg/kg (mpk) intravenous (IV) dose.

The PK profiles obtained were similar to those of the aforementioned snapshot 24-hour PK studies. The calculated PK properties for both the parent compound and the active metabolite are presented in **Table 3.9** below. Compound **3**, complemented by its active metabolite **2**, exhibited favourable PK properties that satisfied the criteria for progression to *in vivo* efficacy studies.

Table 3.9: Pharmacokinetics parameters of analogue **3** and its active metabolite **2**.

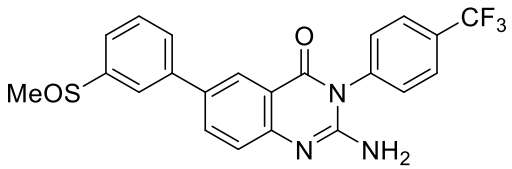

3

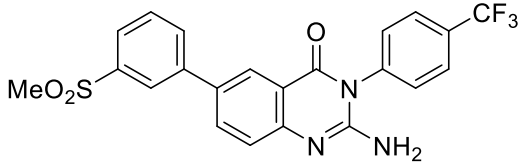

2 (metabolite of **3**)

	Oral dose (mg/kg)			**IV dose**	**Oral dose of 3 (mg/kg)**			**IV dose (3)**
PK Parameter (units)	**50**	**100**	**200**	**5 mg/kg**	**50**	**100**	**200**	**5 mg/kg**
$t_{1/2}$ (h)	6.2	7.3	8.0	7.1	13.4	8.7	12.2	14.0
t_{max} (h)	1.0	1.0	1.0	0.4	3.6	10.0	10.0	8.0
C_{max} (µM)	21.1	21.1	31.3	8.1	29.0	36.0	56.7	7.1
Vd (L/kg)	-	-	-	4.5	-	-	-	-
Cl_{tot} (mL/min/kg)	-	-	-	7.2	-	-	-	-
$AUC_{0\text{-}inf}$ (min.µmol/L)	9012	10273	21781	1572	48430	57149	128342	9347
F (%)	57	33	35	-	-	-	-	-

Abbreviations: $t_{1/2}$ (h) = Half-life in hours; t_{max} = Time taken to reach the maximum concentration; C_{max} = Maximum (peak) plasma concentration; $AUC_{0\text{-}inf}$ = Area under the concentration-time curve extrapolated to infinity; Vd = Volume of distribution; Cl_{tot} = Total rate of clearance of an IV dose; F = Bioavailability expressed as a percentage.

Moreover, absorption of **3** was fast, resulting in significantly high C_{max} of 21.1 µM at 50 and 100 mg/kg oral dose, and 31.3 µM at 200 mg/kg within one hour. Likewise, the metabolism was fast, which resulted in metabolite **2** being detected immediately after both the oral and the IV administration of **3**. Both compounds exhibited long half-lives [$t_{1/2}$ > 6 hours], with **3** displaying a moderate volume of distribution (Vd) [4.5 L/kg], low rate of clearance (Cl_{tot}) [7.2 mL/min/kg], and oral bioavailability (% F) ranging from 33–57%. In addition, there was a linear dose-response relationship between the 100 and 200 mg/kg regimen; that is, as the dose doubled, the response (AUC) also doubled. This was unlike the preliminary 24-hour experiments that revealed some degree of saturation at 100 mg/kg dose, most likely due to differences in the vehicles used to make the oral suspensions.

By factoring in the PPB of 95.5%, the adjusted concentration-time profile (**Figure 3.6**) with respect to the free fraction at 100 and 200 mg/kg oral doses revealed favourable free fraction exposure of the active metabolite (**2**), which was above the highest recorded MIC_{99} of 1.5 µM. Furthermore, both compounds were well tolerated by the mice throughout the exposure at the three dose levels, wherein neither death nor acute toxic effects were observed. Accordingly, compound **3** was selected for *in vivo* efficacy studies in mice at oral doses of 100 and 200 mg/kg.

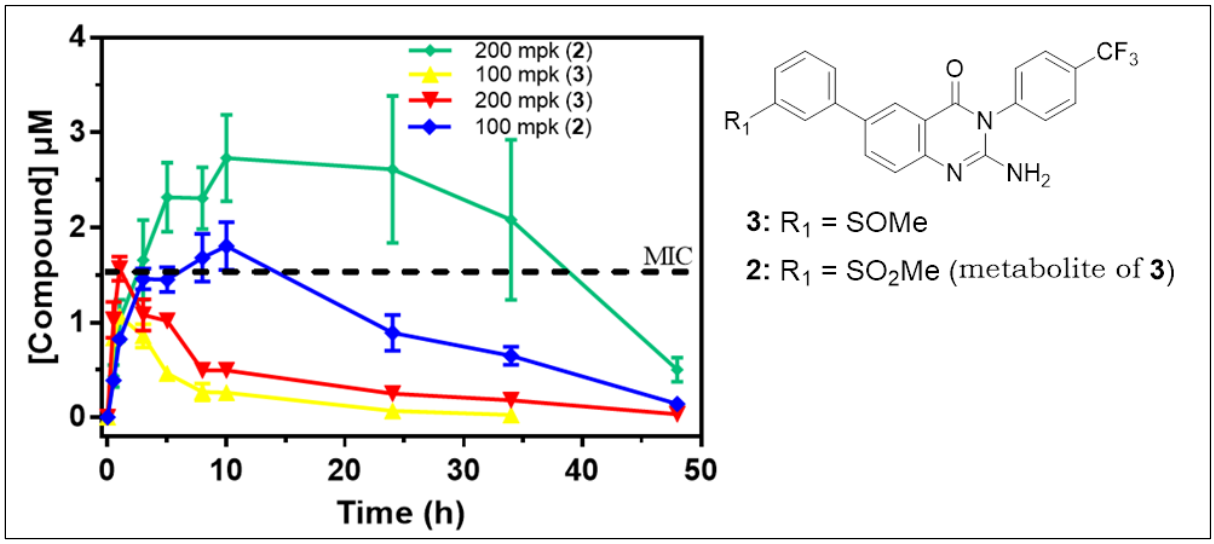

Figure 3.6: Concentration-time profiles (mean of n = 3) for the free fractions of **2** and **3** at 100 and 200 mg/kg po.

3.2.10 *In vivo* Efficacy Study

The *in vivo* proof-of-concept efficacy assessment of compound **3** was conducted by Prof. Anne Lenaerts and Dr. Gregory Robertson, at the Mycobacteria Research Laboratories, Department of Microbiology, Immunology and Pathology, Colorado State University, USA.

This study was performed in an acute infection BALB/c mouse model. Although these mice do not develop and recapitulate the necrotizing lesions and granulomas observed in humans, they are essential and efficient for initial, fast *in vivo* efficacy screening of compounds against *Mtb*, with minimal compound requirements during the early stages of drug discovery.[25–27]

Initially, compound **3** was screened for tolerability in mice by administering it by oral gavage at 100, 200, and 300 mg/kg once per day (QD) for 3 consecutive days, followed by seven days of observation. Three mice were employed for each dose level. The compound was well tolerated by all the mice at the administered doses and no acute toxic effects were observed at the end of the ten days; therefore permitting initiation of efficacy studies. In summary, 6–8 weeks old female BALB/c mice were infected with low dose aerosol (LDA) of the *Mtb* Erdman-Lux (luciferase-expressing) strain (~50–100 bacilli/mouse) in an aerosol infection chamber. Thereafter, treatment with the appropriate control drugs as well as **3** was initiated in groups of 5–6 mice per compound on day 7 post-infection for twelve consecutive days [day 7 to day 18]. In this case, compound **3** was administered by oral gavage at 100 and 200 mg/kg QD. Samples for in-study PK profiling in the infected mice were obtained by bleeding the compound **3**-treated mice during the last week of dosing at 1 and 24 hours post-administration. On day 21 post-infection [that is, 72 h after the last dose – the drug washout period], all treatment and vehicle control groups were sacrificed. Then, the bioburden analysis was carried out by enumerating the colony forming units (CFU) following 3–4 weeks of incubation of homogenates of the aseptically harvested lung tissues.[28]

Unexpectedly, no reduction in the lung mycobacterial burdens was observed following 12 consecutive days of treatment with **3** at 100 and 200 mg/kg oral daily doses. All controls, on the other hand, yielded the expected responses; wherein bedaquiline (25 mg/kg), isoniazid (25 mg/kg) and moxifloxacin (100 mg/kg) all promoted significant reductions in lung burdens, and in most cases to levels at or near the limit of detection. Linezolid (100 mg/kg), PA-824 (50 mg/kg), and ethambutol (100 mg/kg) all displayed intermediate activity, while rifampicin (10 mg/kg) and pyrazinamide (150 mg/kg) were found to be largely static in this model. These results are presented graphically in **Figure 3.7** below.

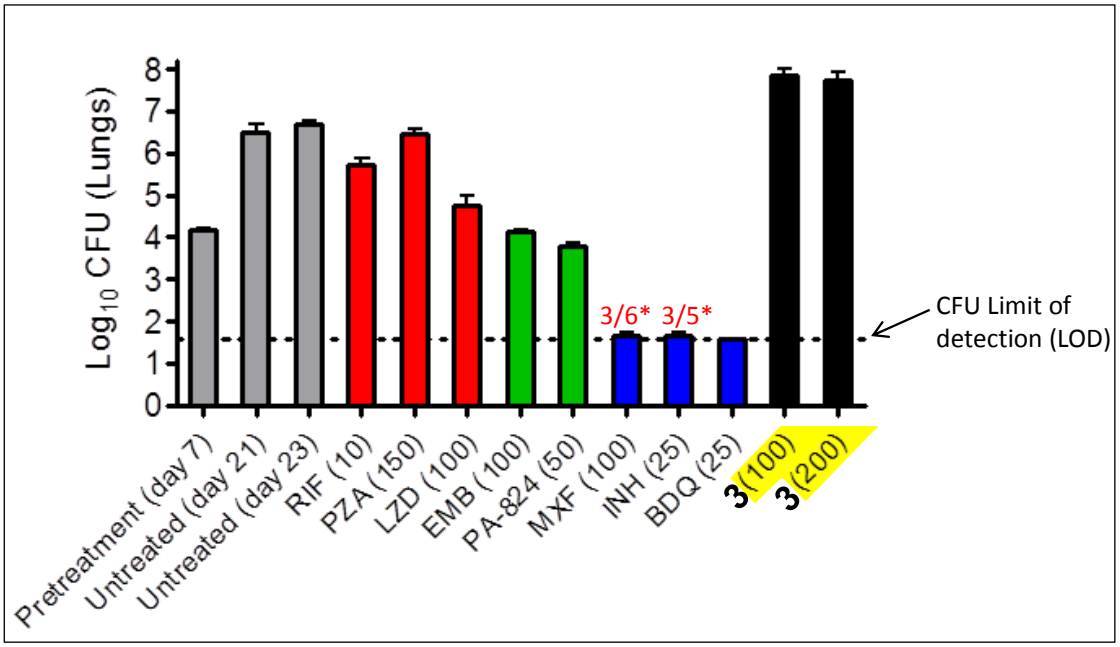

Figure 3.7: Bar graph representing the lung *Mtb* bioburdens [colony forming units (CFU)] following 12 consecutive days of oral dosing with **3** and the appropriate drug controls. *Denotes the number of mice with CFU below the LOD. The drug washout period for the bedaquiline (BDQ) group and the corresponding untreated control group was 5 days.

Further investigative studies were initiated in an attempt to decipher the disconnect between the apparent good *in vitro* inhibitory activity and the lack of *in vivo* efficacy displayed by **3**. Firstly, the PK properties of **3** and its metabolite **2** in the infected mice were analyzed. Of particular interest were the circulating plasma concentrations as a measure of the exposure of **3** during treatment. This was carried out in order to establish whether any PK differences between the healthy mice and the infected mice could be the cause of *in vivo* inactivity.

Table 3.10: Circulating plasma concentrations of **3** and its active metabolite **2**.

Dose of 3 (mg/kg)	Time Point (post dose)	Concentration of 3 (µM)		Concentration of 2 [metabolite] (µM)	
		CSU (infected)	UCT (healthy)	CSU (infected)	UCT (healthy)
100	1 hour	21	21	33	16
	24 hour	2.5	1.3	32	18
200	1 hour	34	31	55	20
	24 hour	5.8	5.1	50	52

CSU denotes concentration determined at the Colorado State University; UCT denotes concentration determined at the University of Cape Town.

As shown in **Table 3.10** above, favourable plasma concentrations of both compounds in the infected [in-study] mice were recorded. These concentrations were similar to the historical values recorded with the single dose PK studies conducted on the healthy mice at UCT. Furthermore, the circulating plasma levels of metabolite **2** in the infected mice were higher at the steady state compared to those after single dose in the healthy mice; most likely reflecting the long half-life of metabolite **2** after daily dosing with **3**. Therefore, it was concluded that lack of exposure was unlikely to account for the lack of *in vivo* efficacy by **3** in mice.

The step that followed was to test compound **3** *in vitro* using different *Mtb* strains cultured in different media. These assays were carried out at the Mycobacteria Research Laboratories, Department of Microbiology, Immunology and Pathology, Colorado State University, USA. As shown in **Table 3.11** below, analogue **3** was active against both $H_{37}Rv$ and Erdman *Mtb* strains [MIC_{99} = 1 and 0.5 mg/L, respectively] when grown in media containing glycerol as the carbon source. In stark contrast, **3** lost activity [MIC_{99} > 16 mg/L] against the two *Mtb* strains when cultured in the 7H12 glycerol-free medium.

Table 3.11: *In vitro* antimycobacterial activity of analogue **3** in different assay conditions.

Strain	Media	MIC_{99} (mg/L):		
		3	**RIF**	**INH**
Erdman	7H9 + glycerol + ADC	1	0.03	0.016
$H_{37}Rv$	7H9 + glycerol + ADC	0.5	0.016	0.016
Erdman	7H12 + casitone + palmitic acid + BSA + catalase + Tween-80	>16	<0.008	0.016
$H_{37}Rv$	7H12 + casitone + palmitic acid + BSA + catalase + Tween-80	>16	<0.008	0.016

Erdman and $H_{37}Rv$ = Virulent strains of *Mtb*; ADC = Albumin-dextrose complex; BSA = Bovine serum albumin; MIC = Minimum inhibitory concentration; RIF = Rifampicin; INH = Isoniazid.

Further independent *in vitro* antimycobacterial testing performed at the National Institute of Allergy and Infectious Diseases (NIAID), National Institutes of Health (NIH), USA, revealed that **3** was only active in media where glycerol was the sole carbon source. These assays at the NIAID were expanded to include 15 additional 2-aminoquinazolinone actives, including three compounds studied in this thesis work. The results revealed that the 2-aminoquinazolinones only exhibited antimycobacterial activity in glycerol-containing media, hence linking their activity to the *Mtb*'s ability to metabolize glycerol. The results are shown in **Table 3.12** below. Moreover, the glycerol-dependent activity was independently confirmed by the *in vitro* spontaneous resistant mutant generation studies.

Table 3.12: *In vitro* antimycobacterial activity of 2-aminoquinazolinones in diverse media.

Medium	MIC$_{99}$ (µM) [14 days] against $H_{37}Rv$		
	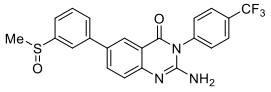	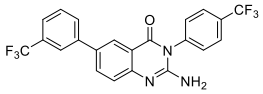	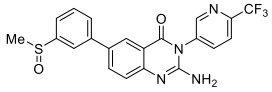
	3	**13**	**36**
GAST-Fe [NIH]	1.2	3.13	4.7
7H9/ADC [NIH]	9.4	12.5	9.4
GAST-Fe [UCT]	1.25	0.31	0.922
7H9/ADC [UCT]	1.25	1.25	0.769
7H9/glucose/ BSA/tyloxapol [NIH]	>50	>50	>50
7H9/glucose/ casitone/tyloxapol [NIH]	>50	>50	>50

$H_{37}RV$ = Drug-susceptible *Mtb* strain; GAST-Fe = Glycerol-Alanine-Salts supplemented with Tween 80 and Iron; 7H9/ADC = Middlebrook 7H9 broth enriched with Albumin-Dextrose Complex, Glycerol, and Tween 80; BSA = Bovine serum albumin; NIH = National Institutes of Health; UCT = University of Cape Town.

3.2.11 Spontaneous Resistant Mutant Generation Study

The spontaneous resistant mutant generation experiments were performed by Dr. Atica Moosa in Associate Professor Digby Warner's laboratory, Molecular Mycobacteriology Research Unit, Division of Medical Microbiology, University of Cape Town. The whole genome sequencing (WGS) analysis was conducted by Dr. Thomas R. Ioerger at the Department of Computer Science and Engineering, Texas A&M University (TAMU), USA.

This study independently and unambiguously substantiated the glycerol-dependent mechanism of action of **3**. In this case, six resistant mutants were generated and the WGS analysis revealed that all had mutations mapping exclusively to glycerol metabolism genes, which encode for glycerol kinase (*glpK*; Rv3696c) and glycerol-3-phosphate dehydrogenase (*glpD2*; Rv3302c). Three of these mutants had polymorphism in *glpK* resulting from substitution of threonine (T) residue 69 for a methionine (M) [T69M] in one

mutant, and cytosine (C) insertion in codons 189 and 517 in the other two mutants. Likewise, polymorphism in *glpD2* was observed in three mutants, wherein substitution of the phenylalanine (F) residue 122 for valine (V) [F122V] was observed in one mutant, while substitution of F for leucine (L) at the same position [F122L] occurred in the other two mutants. The roles of *glpK* and *glpD2* in glycerol metabolism by *Mtb* are illustrated in **Figure 3.8** below.

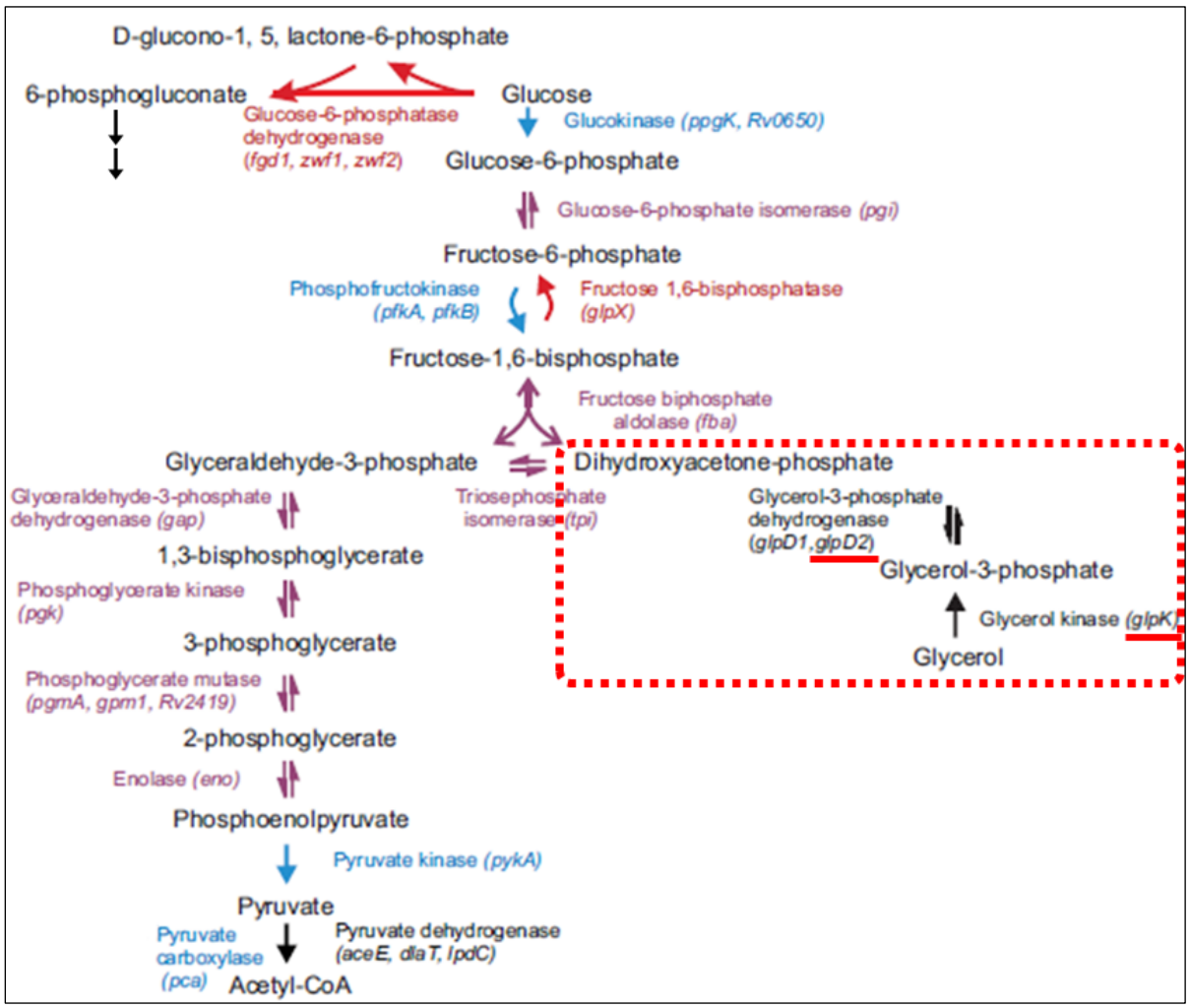

Figure 3.8: Schematic representation of part of the *Mtb* Central Carbon Metabolism network depicting the roles of glycerol kinase and glycerol-3-phosphate dehydrogenase in glycerol metabolism.[29]

Although the resistant mutants depicted the *Mtb* mechanism of resistance to **3**; taken together with the glycerol-dependent *in vitro* activity of 2-aminoquinazolinones, along with the lack of *in vivo* efficacy, these results highly suggested that the mechanism of action of 2-aminoquinazolinones is associated with glycerol dissimilation. In addition, the mutations revealed

that glycerol kinase [the first committing enzyme for glycerol metabolism] and glycerol-3-phosphate dehydrogenase enzymes are most likely the molecular targets of 2-aminoquinazolinone analogues. Consequently, the fact that glycerol is not the primary sole source of carbon utilized *in vivo* by *Mtb*, clearly explains the lack of *in vivo* efficacy as well as the *in vitro* inactivity in glycerol-free media by compounds targeting the glycerol metabolism pathway. Thus, glycerol metabolizing enzymes are futile as drug targets.

The carbon source-dependent disconnect between *in vitro* activity and lack of *in vivo* efficacy has previously been reported by other researchers.[30–34] For instance, in 2010, Pethe and coworkers identified novel, *in vitro*-potent antimycobacterial pyrimidine–imidazoles (PIs) devoid of *in vivo* efficacy.[30] In this case, the researchers carried out the mechanism of action studies using a chemical genetic screen, which linked the activity of PIs to glycerol metabolism. The killing mechanism was found to be due to the induction of *Mtb* self-poisoning arising from the accumulation of glycerol-3-phosphate as well as rapid depletion of the intracellular ATP pool. Moreover, the killing mechanism of PIs has been associated with the interference of methyl glyoxal [a reactive cytotoxic metabolite] detoxification pathway, leading to its accumulation to levels that are toxic to *Mtb*.[33]

In conclusion, the biological evaluation of 2-aminoquinazolinones highlights the importance of developing and applying *in vitro* antimycobacterial screening conditions as well as animal models that highly reflect the *in vivo* biology at play during an active TB infection in humans. This, therefore, will increase the chances of translating *in vitro* activity to *in vivo* efficacy. Although the current practice is to screen compounds in more than one media [that is, utilization of different carbon sources such as glycerol, glucose, cholesterol, lipids, and fatty acids], the challenge still remains that the assay conditions may not adequately mimic the *in vivo* TB infection. This appears to be reinforced by the lack of clear consensus within the TB community on the *in vitro* phenotypic assay conditions as well as animal models that best mirror the *in vivo* TB infection in humans.

3.3 Benzoxazole-Based Oximes

3.3.1 *In vitro* Antimycobacterial Activity

The *in vitro* antimycobacterial assays on benzoxazole-based oximes were conducted under conditions similar to those employed in the screening of 2-aminoquinazolinones, except that in this case, the Middlebrook 7H9 broth was supplemented with glucose instead of glycerol. Antimycobacterial activities were determined using the GFP-based fluorimetric assay method. The MIC_{99} values are presented in **Table 3.13** [**SAR 1** and **SAR 2** analogues] and **Table 3.14** [**SAR 3** analogues] below. In this regard, the target analogues are based on the general structure depicted in **Figure 3.9**.

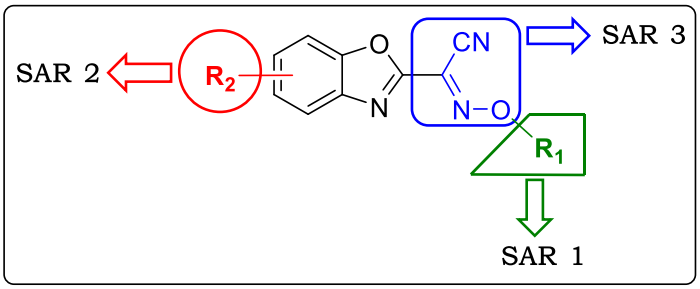

Figure 3.9: General structure of benzoxazole-based oxime analogues depicting the three positions of structural variation.

Table 3.13: *In vitro* antimycobacterial activities of **SAR 1** and **SAR 2** benzoxazole-based oxime target compounds.

	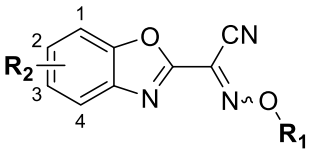		***In vitro* antimycobacterial activity* against *Mtb* $H_{37}Rv$; MIC_{99} (µM) [Day 14]**	
Code	**R_1**	**R_2**	**GAST-Fe**	**7H9-GLU-ADC**
45	$-CONMe_2$	H	<0.244	1.37
46	$-CONMe_2$	2–Me	<0.244	<0.244
47	$-CONMe_2$	4–Me	<0.244	0.598
48	$-CONMe_2$	3–Me	<0.244	7.82
49	$-CONMe_2$	3–Br	<0.244	2.13

Table 3.13: *In vitro* antimycobacterial activities of **SAR 1** and **SAR 2** benzoxazole-based oxime target compounds.

	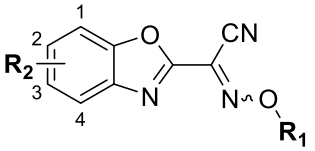		***In vitro* antimycobacterial activity* against *Mtb* $H_{37}Rv$; MIC_{99} (µM) [Day 14]**	
Code	**R_1**	**R_2**	**GAST-Fe**	**7H9-GLU-ADC**
50	$-CONMe_2$	2–Br	<0.244	6.14
51	$-CONMe_2$	$2-CO_2Me$	<0.244	37.60
52	$-CONMe_2$	$2-CF_3$	<0.244	12.60
53	$-CONMe_2$	2–Cl	<0.244	7.82
54	$-CONMe_2$	3–Cl	<0.244	1.31
55	$-CONMe_2$	2–F	<0.244	1.73
56	$-CONMe_2$	3–F	<0.244	2.13
57	$-CONMe_2$	$2-NO_2$	<0.244	5.04
58	$-CONMe_2$	2–NHCOMe	5.20	23.10
59	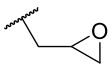	2–Me	23.20	>125
60	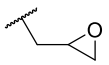	2–Cl	22.40	>125
61	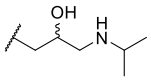	2–Me	>125	>125
62	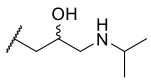	2–Cl	>125	>125
63	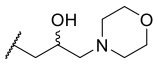	2–Cl	>125	>125
64	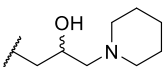	2–Cl	>125	>125
65	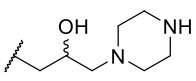	2–Cl	>125	>125

Table 3.13: *In vitro* antimycobacterial activities of **SAR 1** and **SAR 2** benzoxazole-based oxime target compounds.

	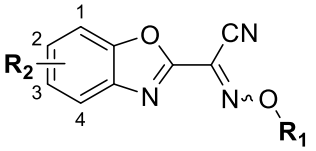		***In vitro* antimycobacterial activity* against *Mtb* $H_{37}Rv$; MIC_{99} (µM) [Day 14]**	
Code	**R_1**	**R_2**	**GAST-Fe**	**7H9-GLU-ADC**
66	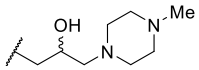	2−Cl	>125	>125
67	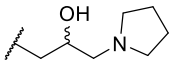	2−Cl	>125	>125
68	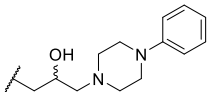	2−Cl	>125	>125
69	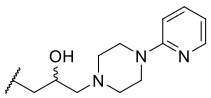	2−Cl	>125	>125
70	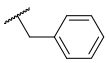	H	>125	>125
71	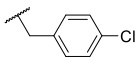	H	>125	>125
72	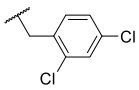	H	>125	>125
73	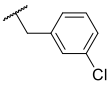	H	>125	>125
74		H	>125	>125
	Rifampicin		0.00318	0.00681

*Activity determined by GFP-based fluorimetric assay method; $H_{37}RV$: Drug-susceptible *Mtb* strain; GAST-Fe: Glycerol-Alanine-Salts supplemented with Tween 80 and Iron; 7H9-GLU-ADC: Middlebrook 7H9 broth enriched with Albumin-Dextrose Complex, Glucose, and Tween 80.

Table 3.14: *In vitro* antimycobacterial activities of **SAR 3** benzoxazole-based target compounds.

Code	Structure	***In vitro* antimycobacterial activity* against *Mtb* $H_{37}Rv$; MIC_{99} (µM) [Day 14]**	
		GAST-Fe	**7H9-GLU-ADC**
75	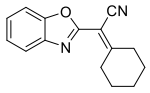	>125	>125
76	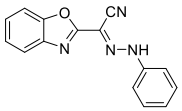	>125	>125
77	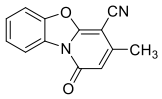	>125	>125
78	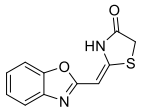	>125	110
79	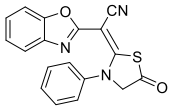	>125	>125
80	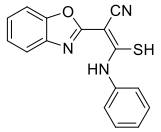	>125	>125
81	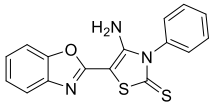	>125	>125
82	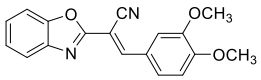	>125	>125
	Rifampicin	0.00318	0.00681

*Activity determined by GFP-based fluorimetric assay method; $H_{37}RV$: Drug-susceptible *Mtb* strain; GAST-Fe: Glycerol-Alanine-Salts supplemented with Tween 80 and Iron; 7H9-GLU-ADC: Middlebrook 7H9 broth enriched with Albumin-Dextrose Complex, Glucose, and Tween 80.

Unlike the 2-aminoquinazolinones, benzoxazole-based oximes exhibited a tight SAR, with only **SAR 2** modifications being tolerated. As such, all attempts to introduce changes at the **SAR 1** and **SAR 3** positions yielded inactive compounds [most compounds had MIC_{99} > 125 µM]. For instance,

all the oxime ether-based **SAR 1** analogues were inactive except the epoxide-bearing analogues **59** and **60**, which displayed moderate activity in GAST-Fe medium (MIC_{99} = 23.2 and 22.4 µM, respectively), although they were inactive in the 7H9-GLU-ADC medium. These findings imply that only the dimethyl carbamate moiety is tolerated at the oxime oxygen atom. Similarly, all attempts to replace the oxime moiety with other groups such as the hydrazonoyl, alkenyl, or ring systems [**SAR 3**] resulted in complete loss of antimycobacterial activity in both media.

Despite being active, **SAR 2** analogues exhibited a flat SAR, which was informed by the display of similar antimycobacterial activities for analogues with different substituents at varying positions on the phenyl ring. For instance, all **SAR 2** compounds exhibited MIC_{99} < 0.244 µM when tested in GAST-Fe medium, except the amide-bearing (2–NHCOMe) compound **58**, which had an MIC_{99} = 5.2 µM. Conversely, these compounds manifested relatively higher MICs in the 7H9-GLU-ADC medium, most likely due to significant compound-binding effect of albumin contained in this medium. Nonetheless, the MIC shifts were generally not conclusive to suspect a glycerol-dependent mechanism of action because most compounds retained potent activity [MIC_{99} < 10 µM] in both media. Accordingly, the SAR trends associated with **SAR 2** analogues could be deduced from the results obtained with the 7H9-GLU-ADC medium. In this regard, the hit compound **46**, bearing a methyl group at position 2, was the most active compound [R_2 = 2–Me; MIC_{99} < 0.244 µM]. Shifting the methyl group to position 3 led to a significant decline in activity [**48**; MIC_{99} = 7.82 µM], whereas a methyl group at position 4 resulted in a very slight reduction in activity [**47**; MIC_{99} = 0.598 µM]. Overall, the replacement of the methyl group with other moities had diverse impact on activity. Notably, some groups led to greater than a 100-fold reduction in activity; for instance, compound **51** (2–CO_2Me) exhibited an MIC_{99} value of 37.6 µM, while the MIC_{99} of **58** (2–NHCOMe) was 23.1 µM.

In summary, two intriguing observations were made from the aforementioned SAR: firstly, all active compounds bear an acyl group (*N,N*-dimethyl carbamate moiety; –$CONMe_2$) on the oxime oxygen atom,

irrespective of the nature of the group on the **SAR 2** position. The acyl group had previously been implicated in the low microsomal metabolic stability observed in these analogues. Considering the high antimycobacterial activity, along with the low metabolic stability, it can thus be hypothesized that the acyl-functionalized oxime compounds act as prodrugs. As such, it can be postulated that the dimethyl carbamate moiety affords the appropriate physicochemical properties necessary for the compounds to penetrate the lipid-rich *Mtb* cell wall. Therefore, once in the cytoplasm, the acyl group is cleaved by the *Mtb* esterases and amidases to yield a free oxime, which is highly believed to be the active entity. This hypothesis is further supported by the observation that the oxime ethers lack activity, perhaps because they are not substrates of the *Mtb* esterases and amidases, and therefore do not yield an active free oxime-bearing compound. Overall, it is postulated that the free oxime-based compounds bearing a nitrile group do not penetrate the *Mtb* cell wall, and therefore lack antimycobacterial activity. This hypothesis is illustrated in **Figure 3.10** below.

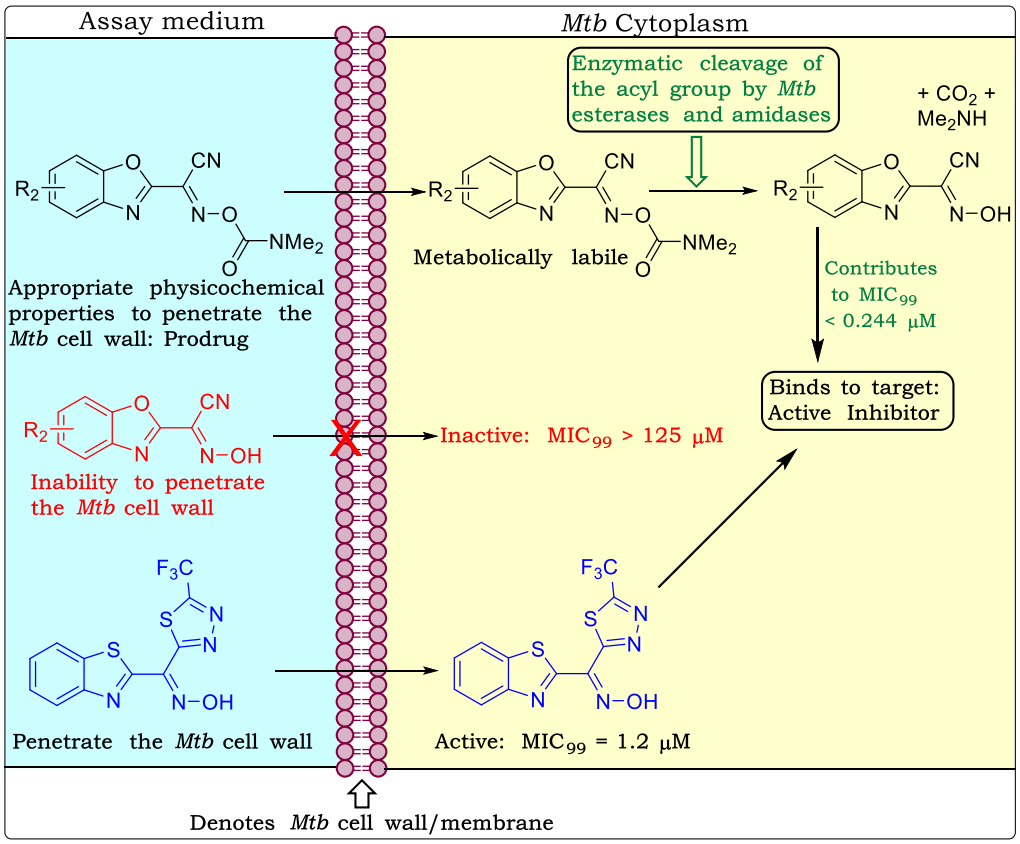

Figure 3.10: Hypothetical description of a probable prodrug-based activity of acyl-functionalized oxime compounds.

On the other hand, replacement of the nitrile group with more lipophilic groups such as substituted thiadiazole (**Figure 3.10**), yields active free oxime-based compounds [benzothiazole-based free oximes], suggesting that a lipophilicity-driven mode of action could be involved. Thus, this hypothesis could be tested by designing experiments that measure the degree of permeability of these compounds into the *Mtb* cell. If the hypothesis is indeed true, the challenge of *in vivo* activation of the prodrugs by the circulating esterases as well as hepatic hydrolysis, before reaching the *Mtb*, could prevent further development of the acyl-functionalized oximes.

The second observation is that intramolecular hydrogen bonding between the oxime hydroxyl hydrogen and a heteroatom appears to contribute to the exhibited activity. This is informed by the observation that the replacement of the nitrile group with lipophilic groups lacking a heteroatom, for instance a phenyl group (**Figure 3.11** below), leads to loss of antimycobacterial activity. Therefore, most likely the intramolecular hydrogen bonding contributes to permeability as well as compound-target interactions.

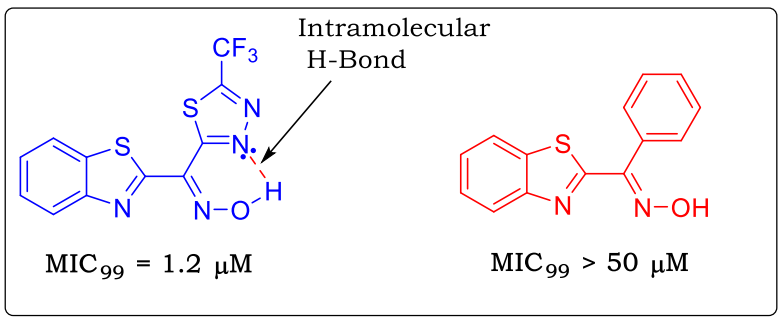

Figure 3.11: Oxime-based compounds depicting intramolecular hydrogen bonding.

3.3.2 Cytotoxicity Studies

Selected active compounds were subsequently evaluated for their cytotoxicity against the CHO cells in a study conducted at the Division of Clinical Pharmacology, University of Cape Town. The cytotoxicity values obtained are shown in **Table 3.15** below.

Table 3.15: *In vitro* cytotoxicity assay results.

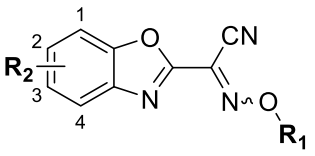

Code	R_1	R_2	Cytotoxicity against CHO cells	
			IC_{50} (µM)	**Std Dev**
45	$-CONMe_2$	H	>387	ND
46	$-CONMe_2$	2–Me	339	9.90
47	$-CONMe_2$	4–Me	286	17.8
48	$-CONMe_2$	3–Me	175	12.6
50	$-CONMe_2$	2–Br	158	13.6
51	$-CONMe_2$	$2-CO_2Me$	7.05	0.78
52	$-CONMe_2$	$2-CF_3$	46.3	4.91
53	$-CONMe_2$	2–Cl	182	33.7
54	$-CONMe_2$	3–Cl	131	29.5
55	$-CONMe_2$	2–F	162	54.1
57	$-CONMe_2$	$2-NO_2$	46.8	11.1
58	$-CONMe_2$	2–NHCOMe	>317	ND

CHO = Chinese Hamster Ovarian; Std Dev = Standard Deviation.

All compounds exhibited favourably low cytotoxicity levels except the methyl ester-bearing **51**, which yielded an IC_{50} of 7.05 ± 0.78 µM.

To this end, the low microsomal metabolic stability exhibited by the representative compound (**46**) [7.3, 26.0, and 7.3% remaining after 30 minutes of incubation in HLM, RLM, and MLM respectively] posed a major hurdle against advancement of the active benzoxazole-based oximes [functionalized with the dimethyl carbamate moiety] to the other proposed studies in the screening cascade. Accordingly, other studies such as determination of the permeability of these compounds into macrophages and *Mtb* cells [intracellular antimycobacterial assays], as well as stability in plasma would be essential at this juncture.

3.4 Conclusion

This chapter described the various hit-to-lead biological investigations performed on the final target compounds. Briefly, the 2-aminoquinazolinone analogues manifested clear SAR trends following *in vitro* evaluation of their antimycobacterial activity against the drug-susceptible *Mtb* $H_{37}Rv$ strain cultured in GAST-Fe and 7H9/ADC. In addition, the selected potent compounds exhibited low cytotoxicity against the CHO and HepG2 cell lines, along with high microsomal metabolic stability in MLM. Besides, the proposed hypothesis behind the design of the sulfoxide-based analogue **3** was supported by experimental findings. The empirical evidence behind this was provided by the extensive *in vivo* biotransformation of **3** in mice to the active sulfone-based analogue **2**. Both compounds exhibited favourable pharmacokinetic properties and were well tolerated at the highest administered dose of 300 mg/kg. Despite the good pharmacological profiles exhibited by the 2-aminoquinazolinones, the frontrunner analogue **3** was devoid of *in vivo* efficacy in an acute TB infection mouse model [BALB/c] at 100 and 200 mg/kg doses. Further studies, including the use of different *in vitro* assay conditions such as glycerol-free media, revealed that the 2-aminoquinazolinones killed *Mtb in vitro* via a glycerol-dependent mechanism of action, hence lacking *in vivo* efficacy. These findings correlated well with the results of studies on generation of spontaneous resistant mutants, whereby all strains resistant to **3** had mutations mapping to the glycerol metabolism genes, which encode for glycerol kinase (*glpK*) and glycerol-3-phosphate dehydrogenase (*glpD2*). Overall, these biological studies highlight the importance of developing and applying *in vitro* antimycobacterial phenotypic screening conditions, in early drug discovery, which are reflective of the *in vivo* biological conditions during TB infection.

The intermediates synthesized towards delivering **SAR 2** target analogues were all evaluated for their antimycobacterial activity against the *Mtb* $H_{37}Rv$ strain. All were inactive (MIC_{99} > 125 µM) except intermediate **2.6g** (**Figure 3.12**), which had interesting results in that its *in vitro* antimycobacterial activity was independent of the media used in the assays. However, SAR

exploration studies revealed that **2.6g** exhibited an idiosyncratic antimycobacterial activity, wherein any modification on the chemical structure led to complete loss of activity (Jessica Akester, MSc Dissertation 2017, UCT). This includes the subsequent intermediate **2.7g** (primary amine at position 2) and the final target compound **41** studied in this thesis work, which had MIC_{99} > 125 µM.

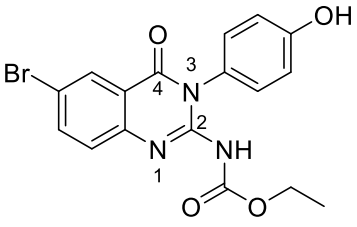

2.6g

GAST & 7H9/ADC: MIC_{99} < 0.244 µM
7H9/Glucose/BSA/Tyloxapol: MIC_{99} = 3.13 µM
7H9/Glucose/Casitone/Tyloxapol: MIC_{99} = 4.7 µM

Figure 3.12: Chemical structure of the active intermediate **2.6g**.

Benzoxazole-based oximes, on the other hand, exhibited a tight SAR, with only **SAR 2** modifications being tolerated. As such, all attempts to introduce changes at **SAR 1** and **SAR 3** yielded inactive compounds. To this end, although the active compounds exhibited low *in vitro* cytotoxicity against the CHO cells, the low microsomal metabolic stability exhibited by the representative compound (**46**) [7.3% remaining after 30 minutes in MLM] was the major impediment to advancing the active benzoxazole-based oximes to the other studies in the screening cascade.

All target compounds, regardless of their activity, were evaluated for their aqueous solubility, which was thereafter correlated with selected physicochemical factors in an attempt to deduce structure-property relationships (SPR). These studies, along with the supramolecular derivatization studies, are discussed in the next chapter: Chapter 4.

References

(1) Collins, L.; Franzblau, S. G. Microplate Alamar Blue Assay versus BACTEC 460 System for High-Throughput Screening of Compounds against *Mycobacterium tuberculosis* and *Mycobacterium avium*. *Antimicrob. Agents Chemother.* **1997**, *41*, 1004–1009.

(2) Collins, L.; Torrero, M. N.; Franzblau, S. G. Green Fluorescent Protein Reporter Microplate Assay for High-Throughput Screening of Compounds against *Mycobacterium tuberculosis*. *Antimicrob. Agents Chemother.* **1998**, *42*, 344–347.

(3) Franzblau, S. G.; DeGroote, M. A.; Cho, S. H.; Andries, K.; Nuermberger, E.; Orme, I. M.; Mdluli, K.; Angulo-Barturen, I.; Dick, T.; Dartois, V.; Lenaerts, A. J. Comprehensive Analysis of Methods Used for the Evaluation of Compounds against *Mycobacterium tuberculosis*. *Tuberculosis* **2012**, *92*, 453–488.

(4) Abrahams, K. A.; Cox, J. A. G.; Spivey, V. L.; Loman, N. J.; Pallen, M. J.; Constantinidou, C.; Fernández, R.; Alemparte, C.; Remuiñán, M. J.; Barros, D.; Ballell, L.; Besra, G. S. Identification of Novel Imidazo[1,2-a]pyridine Inhibitors Targeting *M. tuberculosis* QcrB. *PLoS One* **2012**, *7*, e52951.

(5) Bald, D.; Villellas, C.; Lu, P.; Koul, A. Targeting Energy Metabolism in *Mycobacterium tuberculosis*, a New Paradigm in Antimycobacterial Drug Discovery. *MBio* **2017**, *8*, e00272-17.

(6) Arora, K.; Ochoa-Montano, B.; Tsang, P. S.; Blundell, T. L.; Dawes, S. S.; Mizrahi, V.; Bayliss, T.; Mackenzie, C. J.; Cleghorn, L. A. T.; Ray, P. C.; Wyatt, P. G.; Uh, E.; Lee, J.; Barry, C. E.; Boshoff, H. I. Respiratory Flexibility in Response to Inhibition of Cytochrome C Oxidase in *Mycobacterium tuberculosis*. *Antimicrob. Agents Chemother.* **2014**, *58*, 6962–6965.

(7) Lu, P.; Heineke, M. H.; Koul, A.; Andries, K.; Cook, G. M.; Lill, H.; van Spanning, R.; Bald, D. The Cytochrome *bd*-type Quinol Oxidase Is Important for Survival of *Mycobacterium smegmatis* under Peroxide and Antibiotic-Induced Stress. *Sci. Rep.* **2015**, *5*, 10333.

(8) Berney, M.; Hartman, T. E.; Jacobs, W. R. A *Mycobacterium tuberculosis* Cytochrome *bd* Oxidase Mutant Is Hypersensitive to Bedaquiline. *MBio* **2014**, *5*, e01275-14-e01275-14.

(9) Rybniker, J.; Vocat, A.; Sala, C.; Busso, P.; Pojer, F.; Benjak, A.; Cole, S. T. Lansoprazole Is an Antituberculous Prodrug Targeting Cytochrome *bc*1. *Nat. Commun.* **2015**, *6*, 7659.

(10) Alland, D.; Steyn, A. J.; Weisbrod, T.; Aldrich, K.; Jacobs, W. R.

Characterization of the *Mycobacterium tuberculosis iniBAC* Promoter, a Promoter That Responds to Cell Wall Biosynthesis Inhibition. *J. Bacteriol.* **2000**, *182*, 1802–1811.

(11) Naran, K.; Moosa, A.; Barry, C. E.; Boshoff, H. I. M.; Mizrahi, V.; Warner, D. F. Bioluminescent Reporters for Rapid Mechanism of Action Assessment in Tuberculosis Drug Discovery. *Antimicrob. Agents Chemother.* **2016**, *60*, 6748–6757.

(12) Grant, S. S.; Kawate, T.; Nag, P. P.; Silvis, M. R.; Gordon, K.; Stanley, S. A.; Kazyanskaya, E.; Nietupski, R.; Golas, A.; Fitzgerald, M.; Cho, S.; Franzblau, S. G.; Hung, D. T. Identification of Novel Inhibitors of Nonreplicating *Mycobacterium tuberculosis* Using a Carbon Starvation Model. *ACS Chem. Biol.* **2013**, *8*, 2224–2234.

(13) Marroquin, L. D.; Hynes, J.; Dykens, J. A.; Jamieson, J. D.; Will, Y. Circumventing the Crabtree Effect: Replacing Media Glucose with Galactose Increases Susceptibility of HepG2 Cells to Mitochondrial Toxicants. *Toxicol. Sci.* **2007**, *97*, 539–547.

(14) Redfern, W. S.; Carlsson, L.; Davis, A. S.; Lynch, W. G.; MacKenzie, I.; Palethorpe, S.; Siegl, P. K. S.; Strang, I.; Sullivan, A. T.; Wallis, R.; Camm, A. J.; Hammond, T. G. Relationships between Preclinical Cardiac Electrophysiology, Clinical QT Interval Prolongation and Torsade de Pointes for a Broad Range of Drugs: Evidence for a Provisional Safety Margin in Drug Development. *Cardiovasc. Res.* **2003**, *58*, 32–45.

(15) Jamieson, C.; Moir, E. M.; Rankovic, Z.; Wishart, G. Medicinal Chemistry of hERG Optimizations: Highlights and Hang-Ups. *J. Med. Chem.* **2006**, *49*, 5029–5046.

(16) Pollard, C.; Abi Gerges, N.; Bridgland-Taylor, M.; Easter, A.; Hammond, T.; Valentin, J.-P. An Introduction to QT Interval Prolongation and Non-Clinical Approaches to Assessing and Reducing Risk. *Br. J. Pharmacol.* **2010**, *159*, 12–21.

(17) Roche, O.; Trube, G.; Zuegge, J.; Pflimlin, P.; Alanine, A.; Schneider, G. A Virtual Screening Method for Prediction of the hERG Potassium Channel Liability of Compound Libraries. *Chembiochem* **2002**, *3*, 455–459.

(18) Danker, T.; Möller, C. Early Identification of hERG Liability in Drug Discovery Programs by Automated Patch Clamp. *Front. Pharmacol.* **2014**, *5*, 1–11.

(19) Schyman, P.; Liu, R.; Wallqvist, A. General Purpose 2D and 3D Similarity Approach to Identify hERG Blockers. *J. Chem. Inf. Model.*

2016, *56*, 213–222.

(20) Guth, B.; Rast, G. Dealing with hERG Liabilities Early: Diverse Approaches to an Important Goal in Drug Development. *Br. J. Pharmacol.* **2010**, *159*, 22–24.

(21) Yu, H.; Zou, B.; Wang, X.; Li, M. Investigation of Miscellaneous hERG Inhibition in Large Diverse Compound Collection Using Automated Patch-Clamp Assay. *Acta Pharmacol. Sin.* **2016**, *37*, 111–123.

(22) Masimirembwa, C. M.; Bredberg, U.; Andersson, T. B. Metabolic Stability for Drug Discovery and Development: Pharmacokinetic and Biochemical Challenges. *Clin. Pharmacokinet.* **2003**, *42*, 515–528.

(23) Knights, K. M.; Stresser, D. M.; Miners, J. O.; Crespi, C. L. *In vitro* Drug Metabolism Using Liver Microsomes. In *Current Protocols in Pharmacology*; John Wiley & Sons, Inc.: Hoboken, NJ, USA, 2016; p. 7.8.1-7.8.24.

(24) Bohnert, T.; Gan, L.-S. Plasma Protein Binding: From Discovery to Development. *J. Pharm. Sci.* **2013**, *102*, 2953–2994.

(25) Kramnik, I.; Beamer, G. Mouse Models of Human TB Pathology: Roles in the Analysis of Necrosis and the Development of Host-Directed Therapies. *Semin. Immunopathol.* **2016**, *38*, 221–237.

(26) Orme, I. M. The Mouse as a Useful Model of Tuberculosis. *Tuberculosis* **2003**, *83*, 112–115.

(27) De Groote, M. A.; Gilliland, J. C.; Wells, C. L.; Brooks, E. J.; Woolhiser, L. K.; Gruppo, V.; Peloquin, C. A.; Orme, I. M.; Lenaerts, A. J. Comparative Studies Evaluating Mouse Models Used for Efficacy Testing of Experimental Drugs against *Mycobacterium tuberculosis*. *Antimicrob. Agents Chemother.* **2011**, *55*, 1237–1247.

(28) Gao, W.; Kim, J.-Y.; Anderson, J. R.; Akopian, T.; Hong, S.; Jin, Y.-Y.; Kandror, O.; Kim, J.-W.; Lee, I.-A.; Lee, S.-Y.; McAlpine, J. B.; Mulugeta, S.; Sunoqrot, S.; Wang, Y.; Yang, S.-H.; Yoon, T.-M.; Goldberg, A. L.; Pauli, G. F.; Suh, J.-W.; Franzblau, S. G.; Cho, S. The Cyclic Peptide Ecumicin Targeting ClpC1 Is Active against *Mycobacterium tuberculosis In vivo*. *Antimicrob. Agents Chemother.* **2015**, *59*, 880–889.

(29) Baughn, A. D.; Rhee, K. Y. Metabolomics of Central Carbon Metabolism in *Mycobacterium tuberculosis*. *Microbiol. Spectr.* **2014**, *2*, 1–16.

(30) Pethe, K.; Sequeira, P. C.; Agarwalla, S.; Rhee, K.; Kuhen, K.; Phong, W. Y.; Patel, V.; Beer, D.; Walker, J. R.; Duraiswamy, J.; Jiricek, J.; Keller, T. H.; Chatterjee, A.; Tan, M. P.; Ujjini, M.; Rao, S. P. S.;

Camacho, L.; Bifani, P.; Mak, P. A.; Ma, I.; Barnes, S. W.; Chen, Z.; Plouffe, D.; Thayalan, P.; Ng, S. H.; Au, M.; Lee, B. H.; Tan, B. H.; Ravindran, S.; Nanjundappa, M.; Lin, X.; Goh, A.; Lakshminarayana, S. B.; Shoen, C.; Cynamon, M.; Kreiswirth, B.; Dartois, V.; Peters, E. C.; Glynne, R.; Brenner, S.; Dick, T. A Chemical Genetic Screen in *Mycobacterium tuberculosis* Identifies Carbon-Source-Dependent Growth Inhibitors Devoid of *in vivo* Efficacy. *Nat. Commun.* **2010**, *1*, 1–8.

(31) Shi, L.; Sohaskey, C. D.; Pfeiffer, C.; Datta, P.; Parks, M.; McFadden, J.; North, R. J.; Gennaro, M. L. Carbon Flux Rerouting during *Mycobacterium tuberculosis* Growth Arrest. *Mol. Microbiol.* **2010**, *78*, 1199–1215.

(32) Stanley, S. A.; Grant, S. S.; Kawate, T.; Iwase, N.; Shimizu, M.; Wivagg, C.; Silvis, M.; Kazyanskaya, E.; Aquadro, J.; Golas, A.; Fitzgerald, M.; Dai, H.; Zhang, L.; Hung, D. T. Identification of Novel Inhibitors of *M. tuberculosis* Growth Using Whole Cell Based High-Throughput Screening. *ACS Chem. Biol.* **2012**, *7*, 1377–1384.

(33) Manjunatha, U. H.; Smith, P. W. Perspective: Challenges and Opportunities in TB Drug Discovery from Phenotypic Screening. *Bioorg. Med. Chem.* **2015**, *23*, 5087–5097.

(34) Keating, L. A.; Wheeler, P. R.; Mansoor, H.; Inwald, J. K.; Dale, J.; Hewinson, R. G.; Gordon, S. V. The Pyruvate Requirement of Some Members of the *Mycobacterium tuberculosis* Complex is due to an Inactive Pyruvate Kinase: Implications for *in vivo* Growth. *Mol. Microbiol.* **2005**, *56*, 163–174.

CHAPTER 4

PHYSICOCHEMICAL PROFILING AND SUPRAMOLECULAR DERIVATIZATION

4.1 Chapter Overview

Chapter 4 provides a discussion of the studies that were performed towards addressing the third specific aim of this thesis work, which was: To profile all final target compounds with respect to physicochemical properties, including aqueous solubility; deduce structure-property relationships (SPR); and carry out supramolecular derivatization of selected potent compounds.

The chapter begins with an outline of the *in silico* and experimental physicochemical properties of the synthesized final target compounds. These properties were then subjected to statistical analyses in order to establish their distribution profiles across each compound dataset. In addition, statistical evaluation and comparison of various compound datasets is explored, including conventional anti-TB drugs (TB.Ds) and drug candidates (DCs) in clinical development, in an effort to establish the chemical space occupied by each cluster. Then, correlation and SPR studies aimed at unravelling the main factors responsible for the observed aqueous solubility are highlighted. The chapter ends with a discussion of supramolecular derivatization studies conducted on compound **3**.

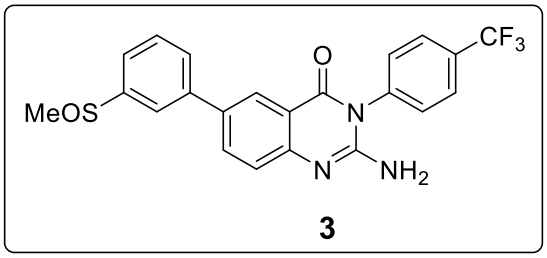

3

Figure 4.1: The chemical structure of compound **3**.

4.2 General Introduction

Physicochemical properties make a considerable contribution to the *in vitro* potency and *in vivo* efficacy exhibited by compounds. More often, unfavourable ADMET profiles and formulation challenges are mainly attributable to poor physicochemical properties, particularly aqueous solubility.[1–4]

Several studies have revealed relationships between physicochemical properties and drug-likeness. This has led to the establishment of a set of acceptable cut-off values for the calculated surrogate molecular descriptors, which are paramount in predicting optimal physicochemical properties for an oral drug-like space. For instance, the Lipinski's rule of five (RO5) postulates that good oral absorption and permeation of a compound are more likely when cLogP ≤ 5; molecular weight (Mwt) ≤ 500 Daltons (Da); the number of hydrogen-bond donors (HBD) ≤ 5; and the number of hydrogen-bond acceptors (HBA) ≤ 10.[5,6] Furthermore, Veber and colleagues suggested that compounds with 10 or fewer rotatable bonds (RB) [measure of molecular flexibility] and topological polar surface area (tPSA) ≤ 140 $Å^2$ (or total number of both HBD and HBA ≤ 12) have an increased chance of achieving acceptable oral bioavailability.[7]

4.3 Evaluation of Physicochemical Properties

The aforementioned molecular descriptors [Mwt, cLogP, tPSA, HBD, and HBA] relating to the synthesized 2-aminoquinazolinones (AQZs) and benzoxazole-based oximes (BZOs) were predicted using StarDrop® 6.4 Software. The main aim was to establish whether these compounds fall within the chemical space prescribed by the Lipinski's RO5 and Veber *et al.*, in order to predict good oral bioavailability during hit-to-lead optimization. In addition, on account of these compounds exhibiting antimycobacterial activity, a statistical comparison of their predicted physicochemical properties versus those of conventional anti-TB drugs and drug candidates currently in clinical development [described in Chapter 1] was performed. This was mainly to establish the significance of any differences or similarities between the pairs, which would in turn partially explain the

observed activity as well as inform the design of analogues with 'drug-like' properties close to those of anti-TB drugs. For each compound, therefore, a Simplified Molecular-Input Line-Entry System (SMILES) was generated using ChemBioDraw Ultra 16.0 and used as the primary format of data entry into StarDrop® 6.4 for property prediction. All statistical analyses were performed using Microsoft® Office Excel 2010, supplemented by XLSTAT 2017 add-in.

Aqueous solubility, permeability, and metabolic stability considerably influence the oral bioavailability of drugs. Of these factors, this thesis work focused mainly on strategies of improving aqueous solubility as well as analyzing the structural factors responsible for improved solubility. Accordingly, kinetic solubility of all the synthesized target compounds was determined using the turbidimetric assay method.[8] Briefly, the procedure involved serial dilution of a 10 mM stock solution in DMSO using phosphate-buffered saline (PBS) at pH 7.4 to obtain triplicate final concentrations of 0.0, 5.0, 10.0, 20.0, 40.0, 80.0, 160.0, and 200 µM in clear, flat-bottomed 96-well microtiter plates. The concentration of DMSO in the assay solutions was 2% v/v. The plates were then left to equilibrate for two hours at ambient temperature. After incubation, UV-VIS absorbance readings were measured at 620 nm using a SpectraMax 340PC[384] spectrophotometer. Absorbance readings were then plotted against concentration, and the point at which absorbance rose from the baseline was taken as the limit of solubility in PBS pH 7.4. Therefore, compared to HPLC methods, turbidimetric solubility is far less accurate, mainly because solubility values can only be of the order of the aforementioned concentrations as opposed to the exact compound concentration in solution. Also, non-specificity is a pitfall of the turbidimetric method because observed values only depend on turbidity. Nonetheless, the turbidimetric method is simpler, less costly, and time-saving, particularly when handling large sample sizes.

The recorded solubility values were then statistically correlated with the experimentally determined factors such as melting point, HPLC retention

time (t_R), and TLC retardation factor (R_f). Each of these factors was used as a measure of a particular inherent compound characteristic, which in turn influences aqueous solubility. For example, melting point was used as a measure of crystal packing energy; t_R and R_f as a measure of polarity; while cLogP was indicative of lipophilicity. In this regard, similar HPLC and TLC methods were applied for all compounds in each of the two classes of compounds studied in this thesis work, in order to have comparable data among the compounds.

4.3.1 Results and Discussion

The calculated and experimentally determined physicochemical properties of the 2-aminoquinazolinones and the benzoxazole-based oximes are listed in **Tables 4.1**–**4.4** below.

Table 4.1: Physicochemical properties of the **SAR 1** 2-aminoquinazolinones.

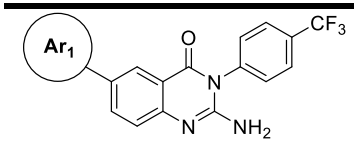

			Calculated Physicochemical Properties†					Experimental Physicochemical Properties			
Ar_1	**R_1**	**Code**	**Mwt ($g.mol^{-1}$)**	**cLogP**	**tPSA ($Å^2$)**	**HBD**	**HBA**	**R_f[a]**	**t_R[b] (Min)**	**m.p.[c] (°C)**	**Sol.[d] (µM)**
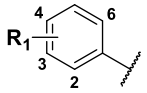	3–SO_2Me	**2**	459.4	3.727	95.05	1	6	0.33	4.29	253	10
	3–SOMe	**3**	443.4	4.101	77.98	1	5	0.19	4.28	174	80
	H	**4**	381.4	4.316	60.91	1	4	0.41	4.68	298	5
	3–$CONH_2$	**5**	424.4	3.230	104.00	2	6	0.12	4.25	300	40
	3–SO_2NH_2	**6**	460.4	3.281	121.1	2	7	0.20	4.18	311	80
	3–CN	**7**	406.4	4.495	84.7	1	5	0.33	4.48	303	40
	3–Cl	**8**	415.8	4.818	60.91	1	4	0.43	4.89	278	5
	2–Cl	**9**	415.8	4.818	60.91	1	4	0.43	4.73	250	5
	4–Cl	**10**	415.8	4.818	60.91	1	4	0.43	4.89	306	5
	3,4–Cl_2	**11**	450.2	5.302	60.91	1	4	0.38	5.17	273	5
	3–F	**12**	399.3	4.421	60.91	1	4	0.38	4.70	289	10
	3–CF_3	**13**	449.4	5.014	60.91	1	4	0.35	4.85	244	10
	3–NH_2	**14**	396.4	3.762	86.93	2	5	0.26	4.30	283	160
	3–OMe	**15**	411.4	4.192	70.14	1	5	0.37	4.65	276	5
	3–*t*-butyl	**16**	437.5	5.781	60.91	1	4	0.44	5.27	258	5
	4–*t*-butyl	**17**	437.5	5.781	60.91	1	4	0.42	5.33	270	10
	3–$N(Me)_2$	**18**	424.4	4.281	64.15	1	5	0.33	4.73	240	10
		**19**	530.5	3.321	107.5	1	8	0.36	4.08	279	20
	 6–Me	**20**	544.5	3.627	107.5	1	8	0.31	4.13	222	10

Table 4.1: Physicochemical properties of the **SAR 1** 2-aminoquinazolinones.

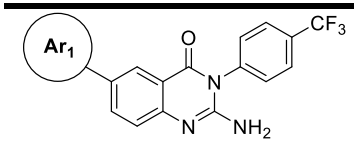

			Calculated Physicochemical Properties†					Experimental Physicochemical Properties			
Ar_1	**R_1**	**Code**	**Mwt ($g.mol^{-1}$)**	**cLogP**	**tPSA ($Å^2$)**	**HBD**	**HBA**	**R_f[a]**	**t_R[b] (Min)**	**m.p.[c] (°C)**	**Sol.[d] (µM)**
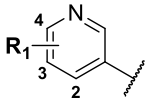	H	**21**	382.3	3.406	73.8	1	5	0.18	4.28	288	20
	3–SO_2Me	**22**	460.4	2.804	107.9	1	7	0.21	4.16	326	10
	3–Me	**23**	396.4	3.785	73.8	1	5	0.22	4.41	274	5
	3–OMe	**24**	412.4	3.313	83.03	1	6	0.24	4.39	255	40
	4–OMe 3–CF_3	**25**	480.4	4.085	83.03	1	6	0.41	4.83	257	10
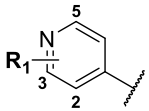	3–F	**26**	400.3	3.532	73.8	1	5	0.33	4.41	350	20
	3,5–F_2	**27**	418.3	3.646	73.8	1	5	0.39	4.57	365	20
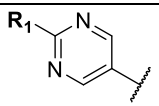	H	**28**	383.3	3.526	86.69	1	6	0.18	4.18	327	40
	OMe	**29**	413.4	3.673	95.92	1	7	0.28	4.33	287	10
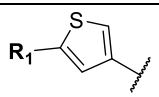	H	**30**	387.4	4.333	60.91	1	4	0.40	4.57	311	5
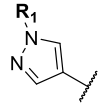	Me	**31**	385.3	3.412	78.73	1	6	0.24	4.20	271	20

Abbreviations: Mwt = Molecular weight; cLogP = Calculated logarithm of n-octanol/water partition coefficient; tPSA = Topological polar surface area; HBD = Hydrogen bond donors; HBA = Hydrogen bond acceptors; R_f = Retardation factor (TLC); t_R = Retention time (HPLC); m.p. = Melting point; Sol. = Aqueous solubility at pH 7.4.

†Denotes properties predicted using StarDrop® 6.4; [a]Analytical TLC with 5% methanol in dichloromethane as the mobile phase; [b]HPLC method described in Chapter 6; [c]Average of the melting range; [d]Turbidimetric solubility.

Table 4.2: Physicochemical properties of the **SAR 2** 2-aminoquinazolinones.

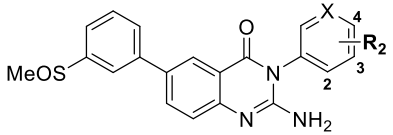

X = CH, for all except 36: X = N

Code	R_2	Calculated Physicochemical Properties†					Experimental Physicochemical Properties			
		Mwt ($g.mol^{-1}$)	cLogP	tPSA ($Å^2$)	HBD	HBA	R_f[a]	t_R[b] (Min)	m.p.[c] (°C)	Sol.[d] (µM)
32	H	375.4	2.802	77.98	1	5	0.17	3.78	231	20
33	4−Me	389.5	3.216	77.98	1	5	0.19	3.42	247	20
34	3−CF_3	443.4	4.101	77.98	1	5	0.18	3.72	153	40
35	2−CF_3	443.4	4.101	77.98	1	5	0.15	3.35	137	80
36	4−CF_3	444.4	3.199	90.87	1	6	0.11	3.38	154	80
37	4−CN	400.5	2.883	101.8	1	6	0.13	2.94	333	40
38	3−CN	400.5	2.883	101.8	1	6	0.16	2.88	258	40
39	4−SO_2Me	453.5	1.984	112.1	1	7	0.13	2.67	300	40
40	4−OMe	405.5	2.696	87.21	1	6	0.14	3.16	240	40
41	4−OH	391.4	2.290	98.21	2	6	0.08	2.66	297	160
42	4−F	393.4	2.953	77.98	1	5	0.12	3.05	235	40
43	2−F	393.4	2.953	77.98	1	5	0.12	3.08	266	80
44*	2−F	409.4	2.501	95.05	1	6	0.24	3.04	272	20

Abbreviations: Mwt = Molecular weight; cLogP = Calculated logarithm of n-octanol/water partition coefficient; tPSA = Topological polar surface area; HBD = Hydrogen bond donors; HBA = Hydrogen bond acceptors; R_f = Retardation factor (TLC); t_R = Retention time (HPLC); m.p. = Melting point; Sol. = Aqueous solubility at pH 7.4.

†Denotes properties predicted using StarDrop® 6.4; [a]Analytical TLC with 5% methanol in dichloromethane as the mobile phase; [b]HPLC method described in Chapter 6; [c]Average of the melting range; [d]Turbidimetric solubility; *R_1 = 3−SO_2Me.

Table 4.3: Physicochemical properties of the **SAR 1** and **SAR 2** benzoxazole-based oximes.

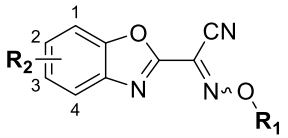

Code	R_1	R_2	Calculated Physicochemical Properties†					Experimental Physicochemical Properties			
			Mwt ($g.mol^{-1}$)	cLogP	tPSA ($Å^2$)	HBD	HBA	R_f[a]	t_R[b] (Min)	m.p.[c] (°C)	Sol.[d] (µM)
45	$-CONMe_2$	H	258.2	1.750	91.72	0	7	0.75	3.97	219	40
46	$-CONMe_2$	2−Me	272.3	2.154	91.72	0	7	0.75	4.43	206	20
47	$-CONMe_2$	4−Me	272.3	2.154	91.72	0	7	0.74	4.39	186	40
48	$-CONMe_2$	3−Me	272.3	2.154	91.72	0	7	0.74	4.33	196	40
49	$-CONMe_2$	3−Br	337.1	2.406	91.72	0	7	0.81	4.45	232	ND
50	$-CONMe_2$	2−Br	337.1	2.406	91.72	0	7	0.81	4.46	235	20
51	$-CONMe_2$	$2-CO_2Me$	316.3	1.764	118.0	0	9	0.76	4.19	235	40
52	$-CONMe_2$	$2-CF_3$	326.2	2.570	91.72	0	7	0.81	4.51	191	10
53	$-CONMe_2$	2−Cl	292.7	2.345	91.72	0	7	0.80	4.38	229	20
54	$-CONMe_2$	3−Cl	292.7	2.345	91.72	0	7	0.80	4.38	192	5
55	$-CONMe_2$	2−F	276.2	1.887	91.72	0	7	0.78	4.07	204	10
56	$-CONMe_2$	3−F	276.2	1.887	91.72	0	7	0.76	4.14	197	ND
57	$-CONMe_2$	$2-NO_2$	303.2	1.691	137.5	0	10	0.78	4.37	212	20
58	$-CONMe_2$	2−NHCOMe	315.3	1.298	120.8	1	9	0.30	3.09	242	80
59		2−Me	257.2	2.244	83.94	0	6	0.77	4.32	117	20
60		2−Cl	277.7	2.488	83.94	0	6	0.79	4.54	145	10

Table 4.3: Physicochemical properties of the **SAR 1** and **SAR 2** benzoxazole-based oximes.

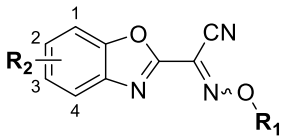

Code	R_1	R_2	Calculated Physicochemical Properties†					Experimental Physicochemical Properties			
			Mwt ($g.mol^{-1}$)	cLogP	tPSA ($Å^2$)	HBD	HBA	R_f[a]	t_R[b] (Min)	m.p.[c] (°C)	Sol.[d] (µM)
61	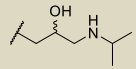	2-Me	316.4	2.364	103.7	2	7	0.08	3.36	244	80
62	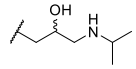	2-Cl	336.8	2.543	103.7	2	7	0.11	3.46	221	80
63	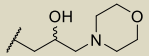	2-Cl	364.8	1.802	104.1	1	8	0.40	3.43	105	160
64	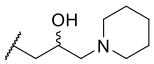	2-Cl	362.8	2.746	94.88	1	7	0.19	3.37	108	80
65	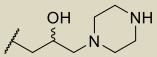	2-Cl	363.8	1.508	106.9	2	8	0.04	3.45	180	160
66	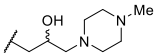	2-Cl	377.8	1.934	98.12	1	8	0.04	3.43	158	>200
67	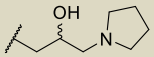	2-Cl	348.8	2.358	94.88	1	7	0.11	3.28	167	>200
68	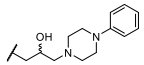	2-Cl	439.9	3.307	98.12	1	8	0.58	4.38	155	80
69	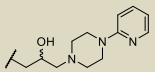	2-Cl	440.9	2.458	111.0	1	9	0.34	4.09	164	80

Table 4.3: Physicochemical properties of the **SAR 1** and **SAR 2** benzoxazole-based oximes.

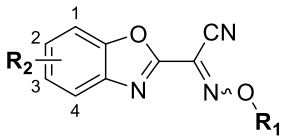

Code	R_1	R_2	Calculated Physicochemical Properties†					Experimental Physicochemical Properties			
			Mwt ($g.mol^{-1}$)	cLogP	tPSA ($Å^2$)	HBD	HBA	R_f[a]	t_R[b] (Min)	m.p.[c] (°C)	Sol.[d] (µM)
70	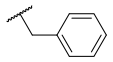	H	277.3	3.51	71.41	0	5	0.80	4.96	133	10
71	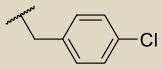	H	311.7	4.123	71.41	0	5	0.80	4.99	122	10
72	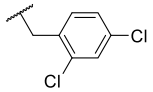	H	346.2	4.682	71.41	0	5	0.78	5.11	117	10
73	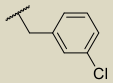	H	311.7	4.123	71.41	0	5	0.80	4.95	140	10
74		H	245.2	1.395	108.7	1	7	0.02	2.98	231	ND

Abbreviations: Mwt = Molecular weight; cLogP = Calculated logarithm of n-octanol/water partition coefficient; tPSA = Topological polar surface area; HBD = Hydrogen bond donors; HBA = Hydrogen bond acceptors; R_f = Retardation factor (TLC); t_R = Retention time (HPLC); m.p. = Melting point; Sol. = Aqueous solubility at pH 7.4; ND = not determined.

†Denotes properties predicted using StarDrop® 6.4; [a]Analytical TLC with 5% methanol in dichloromethane as the mobile phase; [b]HPLC method described in Chapter 6; [c]Average of the melting range; [d]Turbidimetric solubility.

Table 4.4: Physicochemical properties of the **SAR 3** benzoxazole-based analogues.

		Calculated Physicochemical Properties†					Experimental Physicochemical Properties			
Code	**Structure**	**Mwt (g.mol^{-1})**	**cLogP**	**tPSA (Å^2)**	**HBD**	**HBA**	**R_f[a]**	**t_R (Min)[b]**	**m.p. (ºC)[c]**	**Sol. (µM)[d]**
75	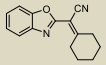	238.3	3.679	49.82	0	3	0.79	4.87	101	10
76	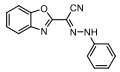	262.3	2.788	74.21	1	5	0.81	5.31	195	5
77	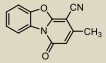	224.2	1.894	58.41	0	4	0.67	3.82	223	20
78		232.3	1.246	55.13	1	4	0.37	3.87	210	40
79	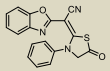	333.4	3.213	70.13	0	5	0.72	4.21	317	5
80	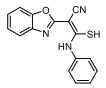	293.3	3.880	61.85	1	4	0.30	4.46	205	5
81	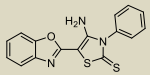	325.4	3.998	56.98	1	4	0.81	4.98	238	10
82	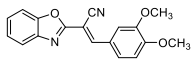	306.3	3.605	68.28	0	5	0.77	4.84	171	5

Abbreviations: Mwt = Molecular weight; cLogP = Calculated logarithm of n-octanol/water partition coefficient; tPSA = Topological polar surface area; HBD = Hydrogen bond donors; HBA = Hydrogen bond acceptors; R_f = Retardation factor (TLC); t_R = Retention time (HPLC); m.p. = Melting point; Sol. = Aqueous solubility at pH 7.4.

†Denotes properties predicted using StarDrop® 6.4; [a]Analytical TLC with 5% methanol in dichloromethane as the mobile phase; [b]HPLC method described in Chapter 6; [c]Average of the melting range; [d]Turbidimetric solubility.

Generally, most of the predicted properties of AQZs and BZOs exhibited normal distribution profiles, most likely due to close similarities among analogues in each class. The conventional anti-TB drugs (TB.Ds) and anti-TB drug candidates (DCs), on the other hand, exhibited non-normal distribution of their physicochemical properties due to the diverse classes of compounds making up each category. For effective statistical comparison, all physicochemical properties were considered to be non-normally distributed. Therefore, the calculated median values were used as the basis of comparison and analysis instead of the calculated mean values. The use of the calculated median, as the more robust variable, was also augmented by the small number of compounds in each class (n < 45). **Table 4.5** below depicts the calculated median values and ranges of each property across the various datasets.

Table 4.5: The calculated median values of the predicted physicochemical parameters.

Property	Calculated Median Values (Range)			
	AQZs [*n* = 43]	**BZOs [*n* = 38]**	**TB.Ds [*n* = 30]**	**DCs [*n* = 11]**
Mwt	414.6 (375.4–544.5)	309.0 (224.2–440.9)	363.4 (102.1–877.0)	456.5 (330.6–1196.0)
cLogP	3.659 (1.98–5.78)	2.361 (1.25–4.68)	0.392 (-3.23–7.59)	2.685 (-0.803–6.33)
tPSA	77.98 (60.91–121.1)	91.72 (49.82–137.5)	85.44 (38.91–358.2)	91.33 (24.06–255.8)
HBD	1 (1–2)	0 (0–2)	3 (0–13)	1 (0–7)
HBA	5 (4–8)	7 (3–10)	7 (2–21)	8 (2–22)

Abbreviations: AQZs = 2-aminoquinazolinones; BZOs = Benzoxazole-based oximes; TB.Ds = Conventional anti-TB drugs; DCs = Anti-TB drug candidates; Mwt = Molecular weight; cLogP = Calculated logarithm of n-octanol/water partition coefficient; tPSA = Topological polar surface area; HBD = Hydrogen bond donors; HBA = Hydrogen bond acceptors. Values in brackets represent range.

The calculated median values indicated full compliance with the Lipinski's RO5 by all the studied compound sets. However, the ranges manifested some degree of deviation from the RO5, particularly in properties associated with TB.Ds and DCs, which further highlighted the structural diversity of compounds in these classes.

Since property distributions were considered non-normal for all compound sets, the non-parametric Mann-Whitney-Wilcoxon statistical comparison

test[9,10] was carried out to establish whether there were any statistical differences between the predicted properties of AQZs and BZOs compared with those of TB.Ds and DCs. In this case, the test was performed by comparing a pair of compound sets for all the predicted properties and determining the *p*-value at the 95% confidence level. The null hypothesis (H_o) for the Mann-Whitney-Wilcoxon comparison was that there is no significant statistical difference in the distribution and the median values of the compared datasets. Since the significance value was 0.05, the null hypothesis was rejected in all cases wherein the *p*-value was less than this cut-off. Conversely, *p*-values greater than 0.05 signified a failure to reject the null hypothesis, and therefore, that there was no statistically significant difference between the compared parameters. **Table 4.6** below shows the results of the Mann-Whitney-Wilcoxon tests between the relevant pairs of compound clusters.

Table 4.6: The Mann-Whitney-Wilcoxon Test (*p*-value) results comparing the differences between the predicted physicochemical properties of AQZs and BZOs versus those of TB.Ds and DCs.

	***p*-values**				
	Mwt	**cLogP**	**tPSA**	**HBD**	**HBA**
AQZs vs TB.Ds	0.075	0.000	0.082	0.000	0.012
AQZs vs DCs	0.388	0.207	0.274	0.474	0.001
BZOs vs TB.Ds	0.061	0.000	0.529	0.000	0.429
BZOs vs DCs	0.000	0.458	0.848	0.017	0.052

Abbreviations: AQZs = 2-aminoquinazolinones; BZOs = Benzoxazole-based oximes; TB.Ds = Conventional anti-TB drugs; DCs = Anti-TB drug candidates; Mwt = Molecular weight; cLogP = Calculated logarithm of n-octanol/water partition coefficient; tPSA = Topological polar surface area; HBD = Hydrogen bond donors; HBA = Hydrogen bond acceptors. Values in red ($p < 0.05$) denote rejection of the null hypothesis at the significance level [that is, there is a difference in the compared datasets].

Consequently, significant differences between AQZs and TB.Ds, with respect to cLogP, HBD, and HBA, were revealed. AQZs and DCs, on the other hand, had similar predicted properties except HBA. BZOs differed from TB.Ds in terms of cLogP and HBD, while when compared to DCs, the differences were mainly in the Mwt and HBD. Frequency distribution histograms were plotted

as shown in **Figure 4.2** and **Figure 4.3** below. As depicted in **Figure 4.2 A**, the molecular weights of AQZs and BZOs ranged from 200 to 550 Da.

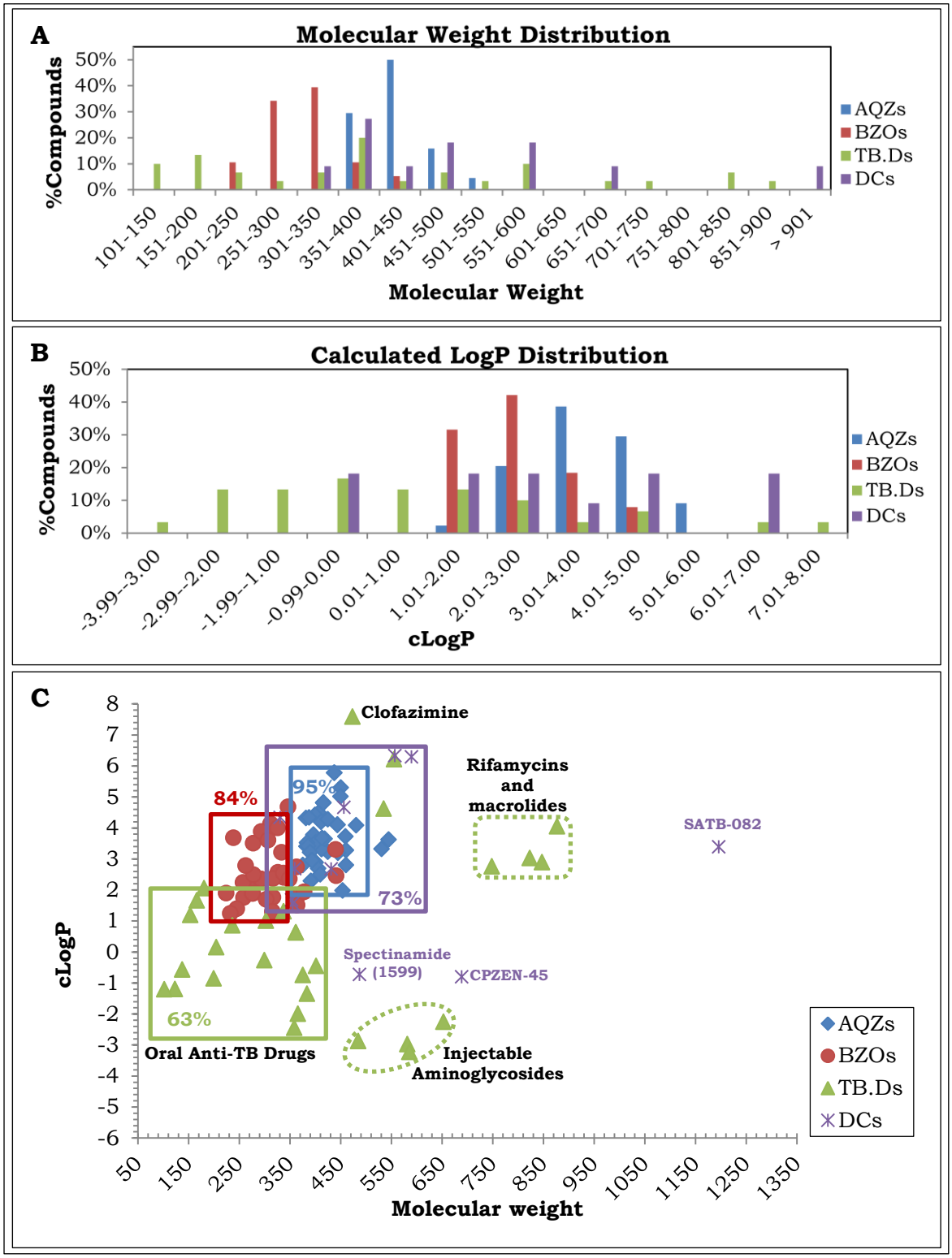

Figure 4.2: Frequency distribution histograms of: **A.** molecular weight; and **B.** cLogP. **C.** Plot showing the chemical space occupied by the studied compound sets with respect to molecular weight and cLogP. Abbreviations: AQZs = 2-aminoquinazolinones; BZOs = Benzoxazole-based oximes; TB.Ds = Conventional anti-TB drugs; DCs = Anti-TB drug candidates.

The Mwt of 95% of AQZs fell between 350 and 450 while 45% of BZOs had Mwt below 300 Da. On the other hand, 60% of TB.Ds and 36% of DCs had Mwt below 400. Moreover, taking into consideration the RO5 violations, 5% AQZs, 30% TB.Ds, and 36% DCs had Mwt > 500, whereas all BZOs had Mwt < 500. Significant differences in cLogP were observed between the compound sets, as illustrated in **Figure 4.2 B** above, and the *p*-values in **Table 4.6** above. As such, while 60% and 18% of TB.Ds and DCs, respectively, had cLogP < 1.0, none of the AQZs and BZOs had cLogP values in this range. TB.Ds, therefore, displayed uniquely lower cLogP values compared to the other clusters. Values of cLogP for 68% of AQZs lay between 3.0 and 5.0, while only 10% of TB.Ds and 30% of DCs exhibited cLogP in this range. In addition, 32% of BZOs had cLogP in the range of 1.0–2.0, while the majority (60%) had values between 2.0 and 4.0. Lipinski's RO5 was violated [cLogP > 5.0] by 9.1%, 6.6%, and 18.2% of AQZs, TB.Ds, and DCs respectively.

In order to visualize the various chemical spaces [with respect to Mwt and cLogP] occupied by the four compound sets, cLogP values were then plotted against Mwt as shown in **Figure 4.2**, plot **C** above. This plot revealed that TB.Ds occupied a unique chemical space compared to the other compound sets. In this case, 63% of TB.Ds had cLogP values < 2 and Mwt < 400 Da. Anti-TB drugs outside this space belong mainly to two classes of compounds: rifamycins and aminoglycosides. Conversely, both AQZs and DCs occupied a chemical space that was distinct from that occupied by TB.Ds. In this regard, 73% of DCs had Mwt ranging from 300 to 600 and cLogP between 1.5 and 6.5. All AQZs fell within this space. BZOs, however, occupied a different chemical space compared to the other categories. This space differed from that occupied by TB.Ds mainly in cLogP values. For instance, 84% of the BZOs had Mwt ranging from 200 to 300 and cLogP values between 1.0 and 4.5. Therefore, this observation implies that for BZOs to occupy a chemical space similar to most TB.Ds, a design strategy leading to lowering of cLogP to values < 1.0 would be most appropriate.

Notably, the most recently approved anti-TB drugs, bedaquiline and delamanid, occupy a chemical space similar to the DCs. This may suggest

utilization of similar approaches and compound libraries in the discovery of small molecule anti-TB drugs during the last few decades.

Generally, the ability of a compound to form hydrogen bonds enhances its aqueous solubility and facilitates drug-target interactions at the sub-cellular active sites. However, it is imperative to strike a balance such that the number of HBD and HBA are not too high to limit permeation of compounds across lipid-rich cell membranes. As such, the Lipinski's RO5 prescribes that in an oral drug-like compound, the ideal number of HBD should be ≤ 5, while HBA should be ≤ 10.[6] The total number of HBA and HBD significantly impact on the tPSA of a compound, which in turn affects the solubility and permeability of a compound. As mentioned earlier, according to Veber *et al.*, the total number of HBD and HBA in a drug-like compound should ideally be ≤ 12, while the tPSA should be ≤ 140 $Å^2$.[7]

In this study, as shown in **Figure 4.3 A** below, most compounds exhibited tPSA values between 50 and 140 $Å^2$, and are therefore in compliance with the Veber *et al.* rule. Notably, injectable TB.Ds [aminoglycosides] as well as the orally administered rifamycins exhibited relatively high tPSA values. It was also observed that all HBD distributions were skewed towards the left, as shown in **Figure 4.3 B** below. For instance, 60% of BZOs had no HBD while 91% of AQZs had one HBD. Similarly, 27% of TB.Ds and DCs had one HBD. In contrast, 13% of TB.Ds and 9% of DCs had > 5 HBD, hence in violation of the RO5. All compound sets exhibited fairly normal distributions of HBA, with values ranging from 2 to 10 as depicted in **Figure 4.3 C** below. About 25% of TB.Ds had > 11 HBA, which was mainly attributable to rifamycins, clarithromycin, and aminoglycosides.

Most compounds in this study occupied a similar chemical space with respect to tPSA [< 140 $Å^2$] and the total number of HBD and HBA [< 12]. This is illustrated in **Figure 4.3 D** below. Also, from this plot, it was evident that a strong linear correlation between the tPSA and the total number of HBD and HBA existed in all the four compound sets, which resulted in linear regression factors (R^2) ranging from 0.88 to 0.99.

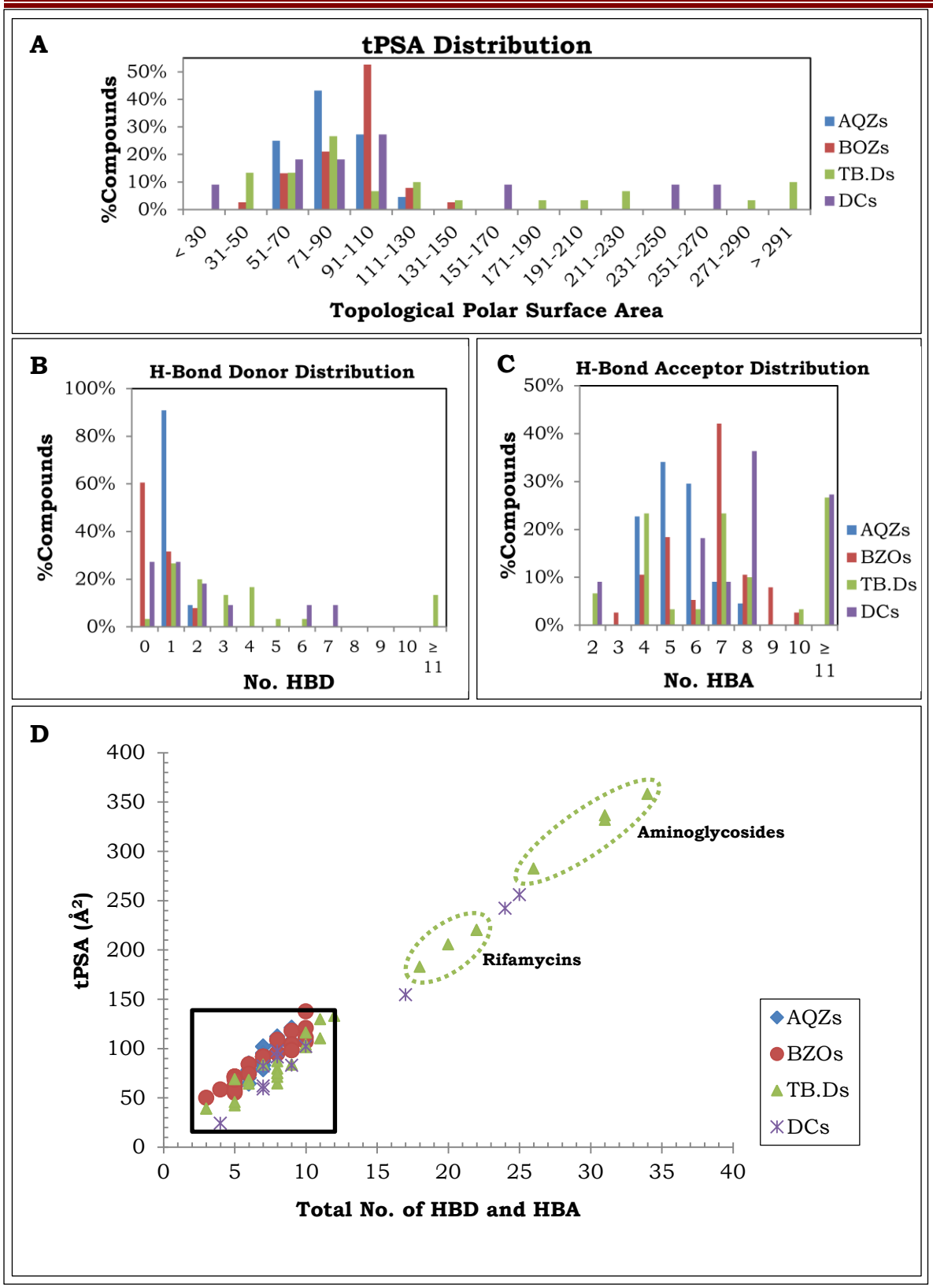

Figure 4.3: Frequency distribution histograms of: **A.** topological polar surface area (tPSA); **B.** hydrogen bond donors (HBD); and **C.** hydrogen bond acceptors (HBA). **D.** Plot showing the chemical space occupied by the studied compound sets with respect to tPSA and the total number of HBD and HBA. Abbreviations: AQZs = 2-aminoquinazolinones; BZOs = Benzoxazole-based oximes; TB.Ds = Conventional anti-TB drugs; DCs = Anti-TB drug candidates.

4.4 Structure-Property Relationships (SPR)

Aqueous solubility is a key compound attribute with tremendous implications during the drug discovery and development process. For instance, solubility influences *in vitro* assays, oral bioavailability as well as formulation processes. In this thesis study, some compounds were designed by taking into consideration strategies that have previously been shown to improve aqueous solubility. These strategies included the classical approaches such as introduction of more hydrophilic polar substituents [increase in HBD]; replacement of phenyl groups with comparable heterocycles such as pyridyl or pyrimidinyl [increase in HBA]; disruption of crystal stacking, for example by introducing chiral center(s) in a molecule to influence crystallinity.

Although majority of compounds studied in this thesis work exhibited low (< 20 µM) and moderate (20−100 µM) aqueous solubility, this section attempts to decipher the factors responsible for any observed solubility improvement. In this regard, factors responsible for improved solubility could be deduced by measuring properties that are inherent and dependent on a compound's structural features. Accordingly, melting points were measured to provide information about crystal packing energies; TLC R_f values and HPLC retention times were determined for all final compounds and used as a measure of relative polarity, while cLogP values were generated *in silico* and used as a measure of lipophilicity. In an effort to establish whether or not any relationship between the aforementioned factors and aqueous solubility existed across a particular class of compounds, correlation graphs of aqueous solubility against the appropriate factor were plotted for each class of compounds, as shown in **Figure 4.4** below.

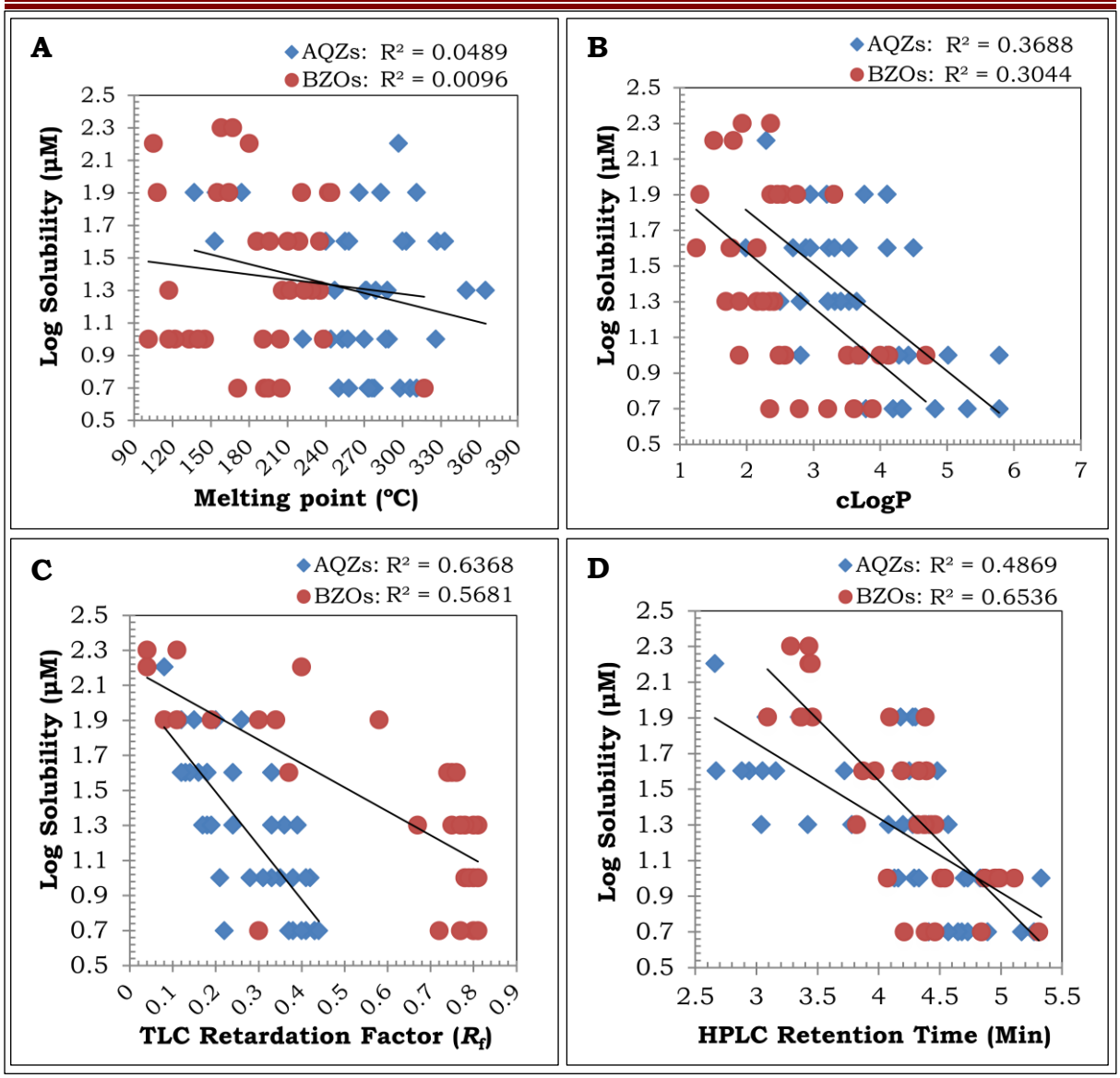

Figure 4.4: Correlation plots of Log solubility [determined by the turbidimetric method using PBS pH 7.4, and expressed in µM] against: **A.** Melting point; **B.** cLogP; **C.** TLC retardation factor; **D.** HPLC retention time. Abbreviations: AQZs = 2-aminoquinazolinones; BZOs = Benzoxazole-based oximes.

These plots revealed that, in both classes of compounds, there was a moderately strong correlation between solubility and TLC R_f values [R^2 = 0.64 for AQZs and 0.57 for BZOs]. A similar pattern was noted with the HPLC retention times [R^2 = 0.45 for AQZs and 0.65 for BZOs]. Therefore, it suffices to conclude at this juncture that, generally, increasing the polarity of both AQZs and BZOs led to improved aqueous solubility.

The two classes of compounds exhibited a relatively weaker correlation between solubility and cLogP (lipophilicity) [R^2 = 0.37 for AQZs and 0.30 for BZOs].

Melting points exhibited no correlation with solubility [R^2 = 0.05 for AQZs and 0.01 for BZOs]. Although compounds with high melting points are generally expected to have lower solubility and vice versa, it is highly likely that the lack of correlation was due to other factors coming into play to reduce the effect of crystal packing energy on solubility.

These correlation studies indicate that many factors simultaneously affect the solubility of compounds across a particular class, and therefore it is important to examine the factors responsible for aqueous solubility on a case by case basis as opposed to examining a whole class of compounds. This is illustrated using examples shown in **Figure 4.5** below. Accordingly, the specific strategies employed in this thesis study were considered. It was observed that the replacement of a methylsulfonyl moiety [SO_2Me: **2**] with a methylsulfinyl [SOMe: **3**] led to improved solubility from 10 to 80 µM. The melting point of **3** [174 °C] was lower than that of **2** [253 °C], therefore signifying a decrease in crystal packing energy and hence the improved solubility. This is most likely due to the chiral sulfur atom in the sulfoxide analogue **3** that affects the crystallinity of the compound leading to less stacking and in turn improved solubility. Notably also, the TLC R_f of **3** was 0.19 compared to 0.33 for **2**. This is an indication that **3** is more polar than **2** and it is thus possible that the increased polarity also has a significant contribution to the enhanced solubility.

Furthermore, it was noted that in instances where a phenyl group in AQZs was replaced with a pyridyl, the resulting compounds exhibited higher melting points despite the observed solubility enhancement, most likely due to increased intermolecular hydrogen bonding. The same general trend was observed whenever more polar hydrophilic substituents were introduced. For example, the carboxamide (−$CONH_2$)-bearing **5** [solubility = 40 µM; R_f = 0.12; m.p. = 300 °C] and the aminosulfonyl (−SO_2NH_2)-containing **6** [solubility = 80 µM; R_f = 0.20; m.p. = 311 °C] had better solubility than **2**. These data revealed that the intended improvement in solubility by addition of polar hydrophilic substituents is inadvertently limited by increased

intermolecular hydrogen bonding, which leads to tighter crystal packing, as supported by the increased melting points.

A similar trend was observed with the BZOs. For instance, replacement of the dimethyl carbamate moiety with β-amino alcohols yielded compounds with improved solubility. This was attributed to reduced crystal stacking, perhaps due to the chiral carbon, as evidenced by the reduced melting points. It could also be due to increased polarity arising from the polar hydroxyl and amino moieties. For instance, the dimethyl carbamate-containing compound **53** had a solubility of 20 µM, melting point of 229 °C, and an R_f value of 0.80 compared to the β-morpholinyl alcohol-bearing **63** with a solubility of 160 µM, melting point of 105 °C, and an R_f value of 0.40.

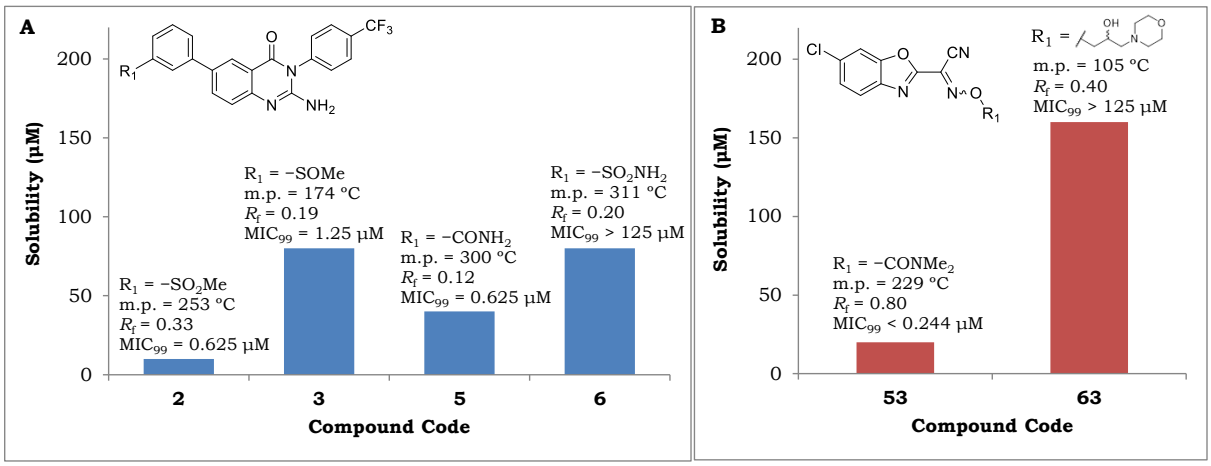

Figure 4.5: Graphical representation of solubility of some selected compounds and the associated experimental factors: **A.** 2-Aminoquinazolinones; **B.** Benzoxazole-based Oximes.

Although the above-mentioned strategies led to relatively improved solubility, albeit modest, structural modification of compounds led to reduced or complete loss of antimycobacterial activity in some instances [**Figure 4.5**]. For example, all the β-amino alcohol-containing BZOs were devoid of antimycobacterial activity, despite their relatively high aqueous solubility. This could be attributable to changes in the pharmacophore necessary for compound-target interaction, or reduced permeability of the compounds across the *Mtb* cell wall. In an effort to investigate whether physical modification of compounds would be a better strategy of improving solubility, compound **3** was selected for supramolecular derivatization studies.

4.5 Supramolecular Derivatization

Compound **3** was subjected to a number of physical derivatization processes aimed at synthesizing cocrystals, salts, and cyclodextrin inclusion complexes, which were largely expected to exhibit improved aqueous solubility. To achieve this, the cascade shown in **Figure 4.6** below was followed.

4.5.1 Single Crystals of 3

Crystal structures provide information on the intrinsic properties of compounds such as molecular geometry, hydrogen bonding interactions, π-π stacking, polymorphism, and solvation profile.[11] These properties in turn influence the solubility profile of a compound as well as facilitate the selection of potential cocrystal co-formers. Therefore, experiments aimed at obtaining single crystals of **3** were initiated for purposes of elucidating its crystal structure. The slow evaporation method was used to crystallize compound **3** in a variety of solvents: ethanol, methanol, acetone, acetonitrile, ethyl acetate, tetrahydrofuran, and chloroform. In all cases, an amount equivalent to about 5 mg of **3** was weighed and dissolved in a minimum amount of the appropriate solvent, aided by heating the mixture to a temperature that was 10 °C below the boiling point of the solvent. After dissolution, a slight excess of the solvent was added, and the mixture filtered through a 0.22 µm nylon filter into a clean vial. The solution was then left to cool to room temperature and evaporate gradually [controlled by using perforated vial stoppers]. Of the seven solvents studied, only ethanol and ethyl acetate produced crystals of adequate size and quality for further characterization.

Single crystal X-ray diffraction (SCXRD) experiments were then conducted on the crystals in order to elucidate the crystal structure of **3**. In addition, the crystals were characterized by thermal methods: thermomicroscopy [hot-stage microscopy (HSM)], thermogravimetric analysis (TGA), and differential scanning calorimetry (DSC).

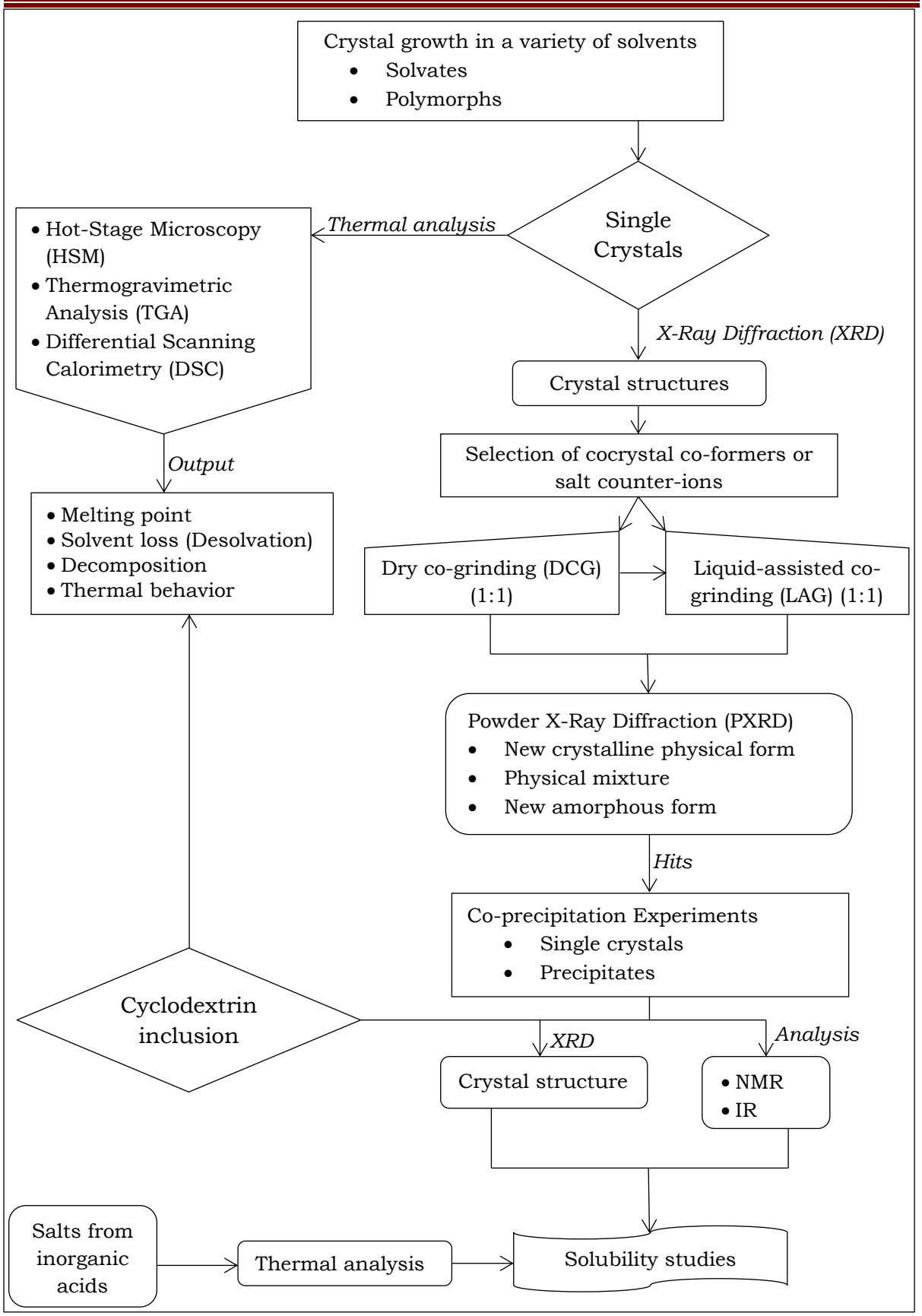

Figure 4.6: The cascade followed in supramolecular derivatization studies.

4.5.2 Thermal Analysis

The results of thermal analysis conducted on the ethyl acetate crystal of **3** immersed in silicone oil are summarized in **Figure 4.7** below.

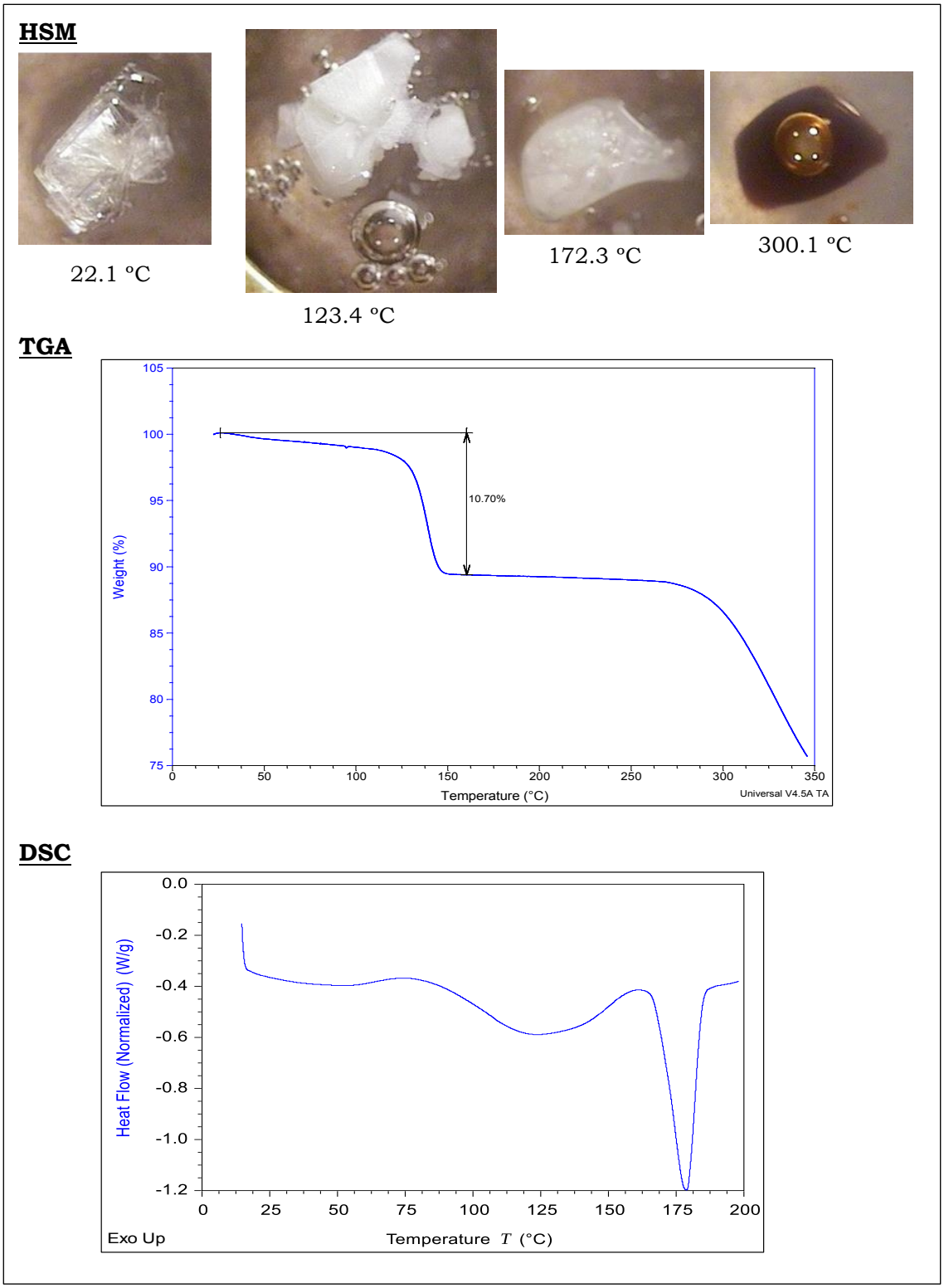

Figure 4.7: Hot-stage microscopy (HSM) micrographs, traces from thermogravimetric analysis (TGA), and differential scanning calorimetry (DSC) of crystals of **3** recrystallized from ethyl acetate.

Thermomicroscopic analysis of a single crystal of **3** was conducted from room temperature (22.1 °C) to 350 °C at a ramp rate of 10 °C min^{-1}. The crystal was mounted on the hot stage and covered with a drop of silicone oil. As shown in **Figure 4.7** above, desolvation was observed in the form of bubbling and cracking that started at ~100 °C and peaked at 123.4 °C. Melting onset temperature was recorded as 170 °C and the endset point at 178.3 °C. The melt darkened at temperatures above 300 °C due to decomposition.

The TGA traces (n = 2) showed a three-step mass loss. The initial average mass loss of 1.3% took place over a wide temperature range, beginning shortly after the start of the experiment from 29.5 to 114 °C. This could be due to loss of surface volatiles or initial loss of a volatile solvent of crystallization. The second average mass loss of 9.3% occurred more drastically, ranging over 115 to 150 °C, and was most likely due to a desolvation process. The total mass loss that could be attributed to desolvation was 10.6 ± 0.1% (n = 2). As discussed in the next section, this loss was confirmed from the crystal structure to be due to loss of 0.5 mole of both water and ethyl acetate per mole of **3** [that is, the crystals existed as a solvate (**3** hemi-ethyl acetate hemihydrate)], which gives a calculated percentage mass of solvent as 10.7%. The third mass loss with an onset of 270 °C was due to decomposition of the desolvated compound.

The DSC traces further reaffirmed the results of HSM and TGA. A small endotherm is noticeable peaking at around 50 °C, perhaps arising from the energy absorbed to release the surface volatiles. However, two distinct endotherms were recorded. The first one corresponded to the desolvation process, meaning that heat was absorbed to eject the solvent molecules from the crystals. This endotherm was broad, occurring over a wide temperature range from 75 °C to 160 °C. The second endotherm with an onset temperature of 168 °C and an endset temperature of 187 °C corresponded to the melting of the anhydrous compound. Notably, the second endotherm is sharper than that attributable to the desolvation process.

4.5.3 Single Crystal XRD Analysis

The single crystal XRD and refinement data for **3** hemi-ethyl acetate hemihydrate are outlined in **Table 4.7** below.

Table 4.7: Data-collection and refinement parameters for **3** hemi-ethyl acetate hemihydrate.

Parameter	**Value**
Molecular Formula	$C_{22}H_{16}F_3N_3O_2S$•0.5($C_4H_8O_2$)•0.5(H_2O)
Formula Weight	496.50
Crystal System	Monoclinic
Space Group	*C*2/c
a (Å)	15.2738(6)
b (Å)	18.2613(8)
c (Å)	16.7701(7)
α (°)	90
β (°)	103.1953(8)
γ (°)	90
V (Å^3)	4554.0(6)
Z	8
D (calc) (g.cm^{-3})	1.445
μ (MoKα) (mm^{-1})	0.202
F (000)	2048
Crystal Size (mm^3)	0.16 × 0.20 × 0.40
Temperature (K)	105(2)
Radiation (Å)	MoKα (0.71073)
θ Min–Max (°)	1.8–28.3
Index ranges ±*h*, ±*k*, ±*l*	-20: 20; -24: 24; -22: 22
Reflections (total)	62842
Reflections (unique)	5675
R (int)	0.041
Reflections with I>2σ(I)	5043
Nref, Npar	5675, 356
R1, w*R*2, S	0.0421, 0.1129, 1.04
Max. and Av. Shift/Error	<0.001, <0.001
$\Delta\rho_{min,\ max}$ (e Å^{-3})	-0.34, 0.59

4.5.3.1 Crystal Structure

Figure 4.8 represents the crystal structure of **3** hemi-ethyl acetate hemihydrate. Full lists of geometrical data (bond lengths, bond angles, torsion angles) for this and other crystal structures were obtained in the form of crystallographic information (CIF) files.

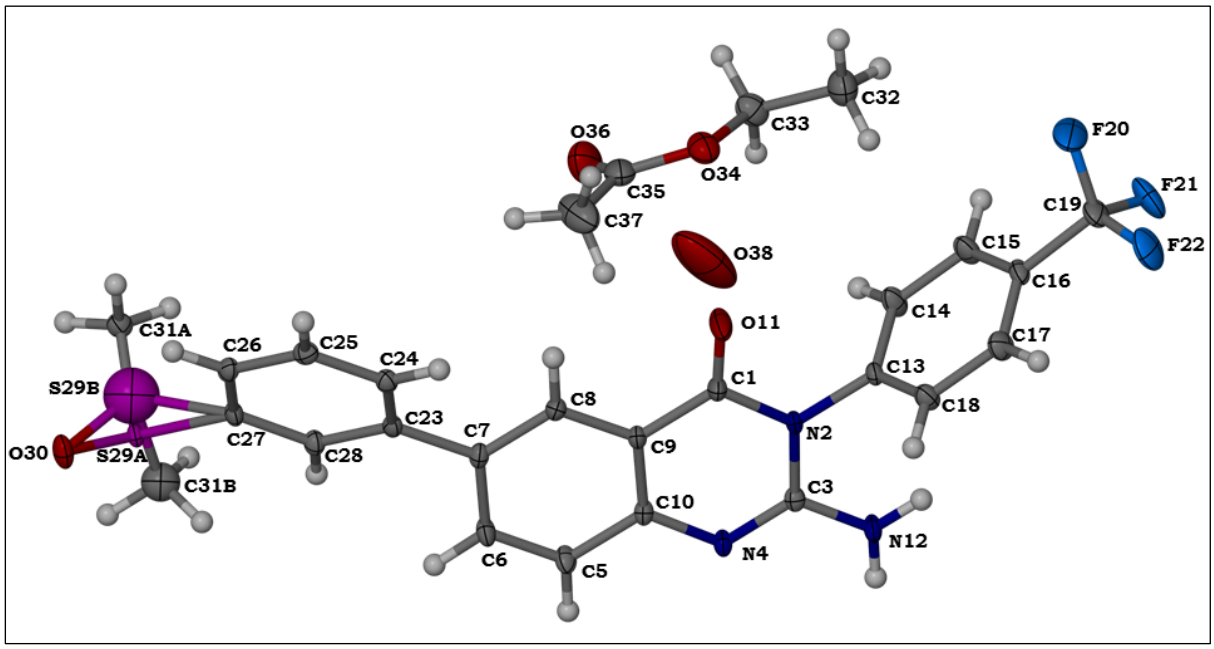

Figure 4.8: The asymmetric unit (ASU) depicting the molecular structure of **3** and the included solvent molecules, with non-H atoms drawn as thermal ellipsoids at the 50% probability level. No H atoms were placed on the disordered water oxygen atom (O38).

The −SOMe group (C31−S29−O30) was found to be disordered over two positions due to high thermal vibrations or the SMe group existing as a pair of rotamers. Nevertheless, S29B and C31B were refined isotropically because the −SOMe group existed with a site-occupancy of 93% at one of the positions. This moiety was found to exhibit a tetrahedral geometry as anticipated. The fused quinazolinone ring system was found to be planar as expected. Similarly, the $-NH_2$ group exhibited a trigonal planar geometry and was coplanar with the fused quinazolinone ring system. The phenyl ring attached to the nitrogen atom N2 was non-coplanar with the quinazolinone ring system [torsion angle C1−N2−C13−C18 = 92.3(2)°], while the phenyl ring attached to C7, on the other hand, had a torsion angle C6−C7−C23−C24 of 149.9(2)°. The ethyl acetate and the oxygen atom of the water molecule (O38) were both included with a site-occupancy factor of 0.5.

4.5.3.2 Hydrogen Bonding Interactions

The principal intermolecular hydrogen bonding interactions are N12–H12A•••N4[a] and N12–H12B•••O30[b]. These bonds appear to be responsible for maintaining the crystal architecture because no significant interactions were recorded between the molecule of **3** and the solvent molecules. These interactions are illustrated in **Figure 4.9** below. The water molecule was found to be hydrogen bonded to atom O34 of the ethyl acetate molecule (O•••O = 2.914(6) Å).

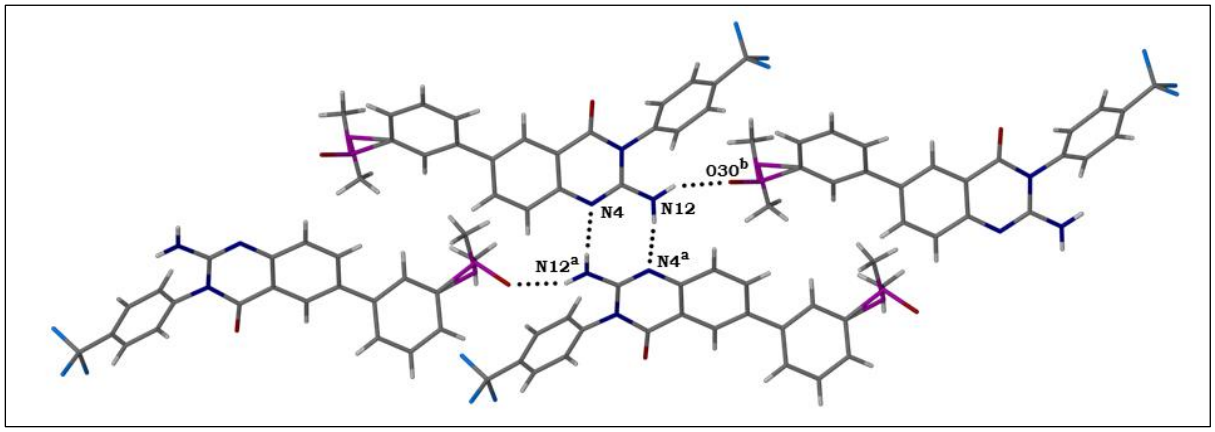

Figure 4.9: Stick diagram showing the principal intermolecular hydrogen bonding interactions in **3**. Molecules of **3** linked by the N-H•••N hydrogen bonds are related by a crystallographic twofold axis parallel to the *b*-axis (normal to the view direction).

Additional hydrogen bonds are outlined in **Table 4.8**.

Table 4.8: Hydrogen bonding interactions for **3** hemi-ethyl acetate hemihydrate.

D–H•••A (Interactions)	d(D–H)	d(H•••A)	d(D•••A)	∠D–H•••A
N12–H12A•••N4[a]	0.88	2.12	2.986(2)	166
N12–H12B•••O30[b]	0.88	2.13	2.925(2)	149
C6–H6•••O38[c]	0.95	2.52	3.352(6)	146
C17–H17•••F22 [Intra]	0.95	2.39	2.716(2)	100
C18–H18•••O30[c]	0.95	2.58	3.279(2)	131

D = Donor; A = Acceptor; d = distance (Å); ∠ = angle (°).
Symmetry codes: [a] 1-x, y, 3/2-z; [b] -1+x, y, z; [c] 3/2-x, 1/2-y, 1-z.

Since there were very weak interactions between the solvent molecules and **3**, their main purpose appears to be that of filling voids in the crystal. This is depicted in the packing diagram shown in **Figure 4.10** below, wherein the

ethyl acetate and water molecules [shown as space-filling models for clarity] appear to be surrounded by the molecules of **3**, and thus tightly embedded within the crystal. This is likely be the reason why the desolvation transition, as recorded by TGA, occurred at temperatures higher than those expected for ethyl acetate and water.

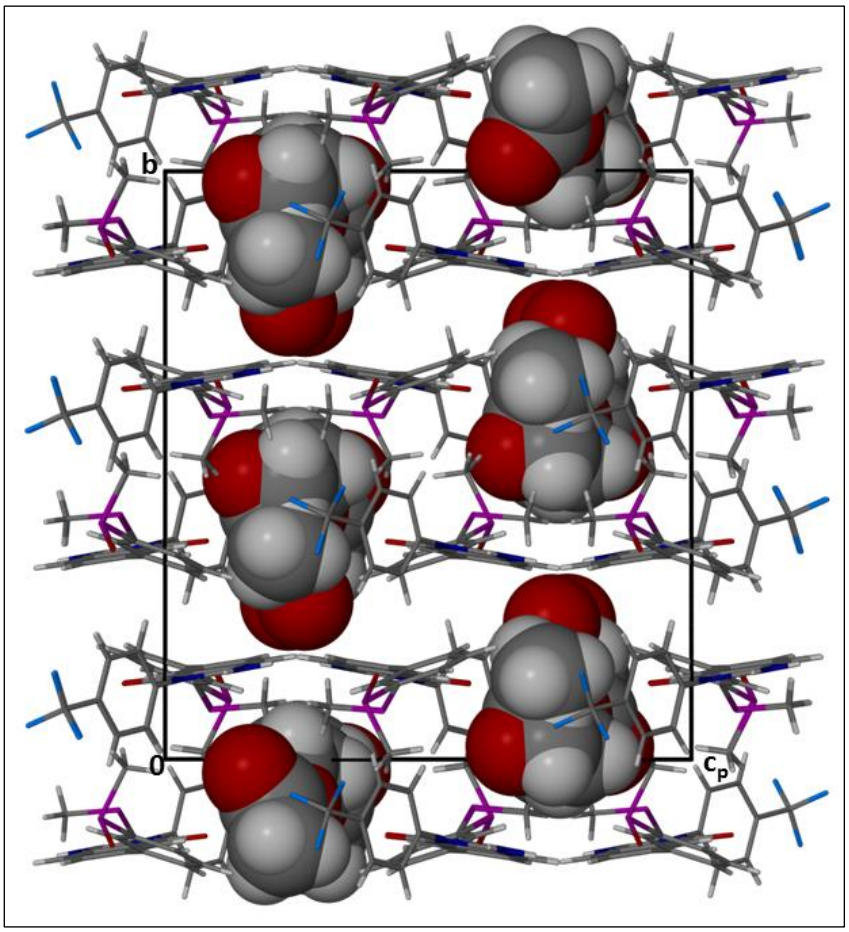

Figure 4.10: Packing characteristics of **3** hemi-ethyl acetate hemihydrate viewed parallel to the *a*-axis.

The crystal structure of an ethanol solvate of **3** was also solved but could not be conclusively refined to an acceptable level because of severe disorder in the trifluoromethyl group and the presence of isolated spurious electron density peaks in the difference Fourier map. Nonetheless, the hydrogen-bonded motif observed for **3** with the hemi-ethyl acetate hemihydrate phase was also observed in this structure. In this case, however, the ASU, as shown in **Figure 4.11** below, contains a dimer of two symmetry-independent molecules of **3** held together by the N12A–H12A•••N4B and N12B–H12B•••N4A hydrogen bonds.

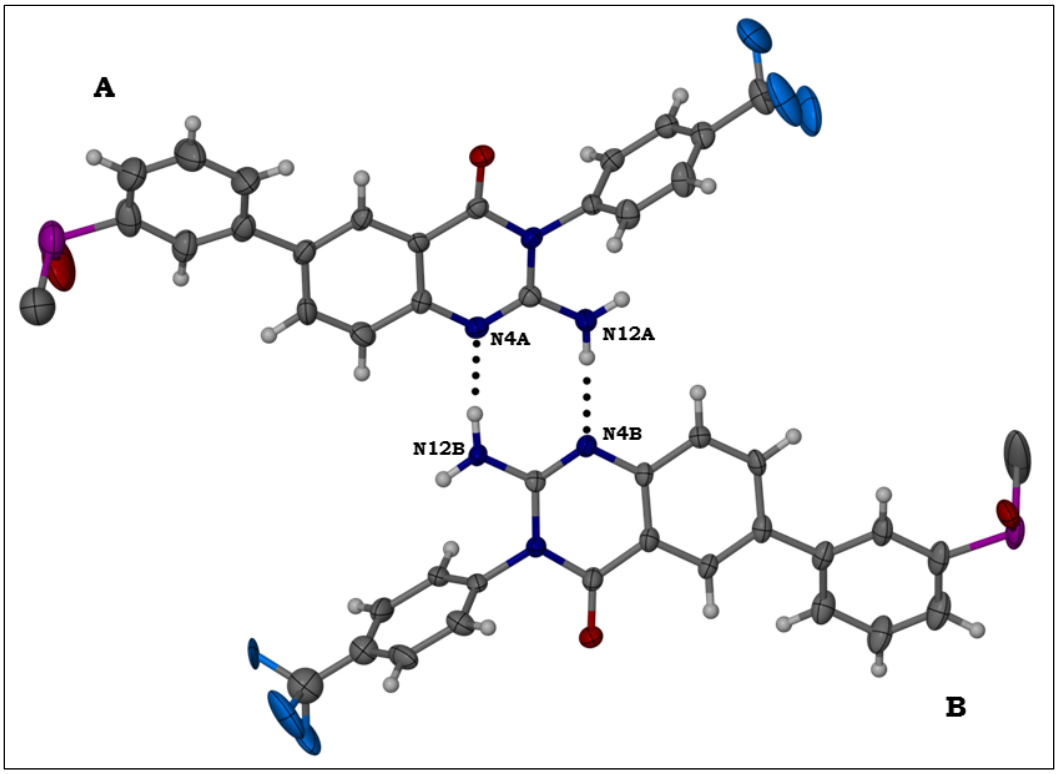

Figure 4.11: The two symmetry-independent molecules of **3** in the ethanol solvate. Solvent molecules are omitted for image clarity.

4.5.4 Cocrystal Screening

Based on the foregoing description of the crystal structure of **3** and its molecular geometry, it was noted that the compound was inclined to form supramolecular structures involving the quinazolinone nitrogen atoms (N4) as the hydrogen bond acceptors and the 2-amino moieties (N12−H12A and N12−H12B) as the hydrogen bond donors. This, therefore, as well as previous work involving compounds with similar functional groups,[12] formed the basis of postulation that co-formers containing a carboxylic acid or an amide functional group were the most suitable candidates for co-crystallization with **3**. The hypothesized supramolecular motifs are shown in **Figure 4.12** below. As such, 11 potential co-formers [urea, nicotinamide, malonic acid, maleic acid, L-tartaric acid, L-proline, L-malic acid, glutaric acid, citric acid, ascorbic acid, and adipic acid] were selected from a list of generally regarded as safe (GRAS) compounds, and prioritized based on their aqueous solubility, since the main aim of these experiments was to physically modify **3** in order to improve its aqueous solubility.

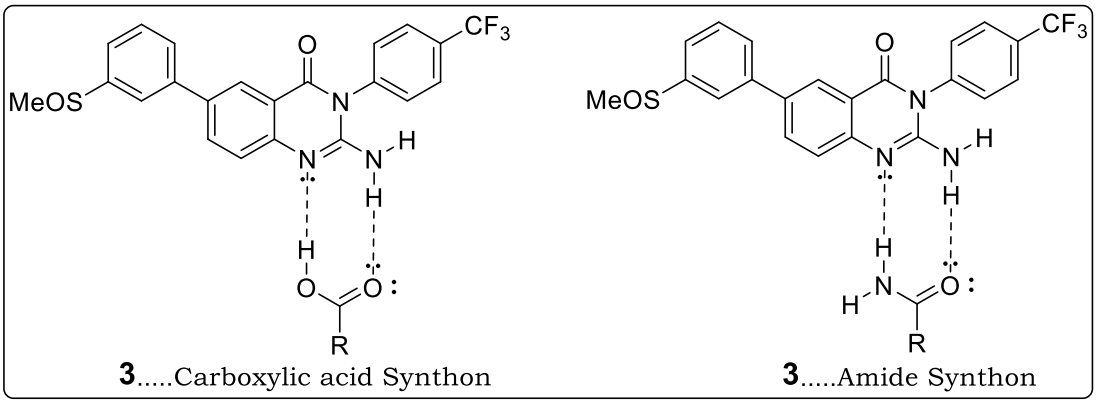

Figure 4.12: Proposed supramolecular synthons involving **3** and a carboxylic acid or an amide functional group.

4.5.4.1 Dry Co-grinding (DCG) Experiments

About 5 mg of compound **3** was accurately weighed and gently pulverized together with an equimolar amount of the appropriate co-former for 15–20 minutes using an agate mortar and pestle. The mixture was then analyzed by powder X-ray diffraction (PXRD) in order to establish whether or not new phases were formed. In all cases, the PXRD trace of a particular mixture was compared with the traces of the separate components. New phases were considered formed in all cases where new peaks could be identified in the PXRD patterns. A physical mixture, on the other hand, was presumed in all instances where the PXRD trace was composed of peaks emanating only from **3** and the appropriate co-former. The results of DCG experiments, as shown in **Figure 4.13** below, indicated that most of the products were physical mixtures. The products from malonic acid and L-malic acid, however, signified formation of new phases, while that of adipic acid was largely an amorphous product.

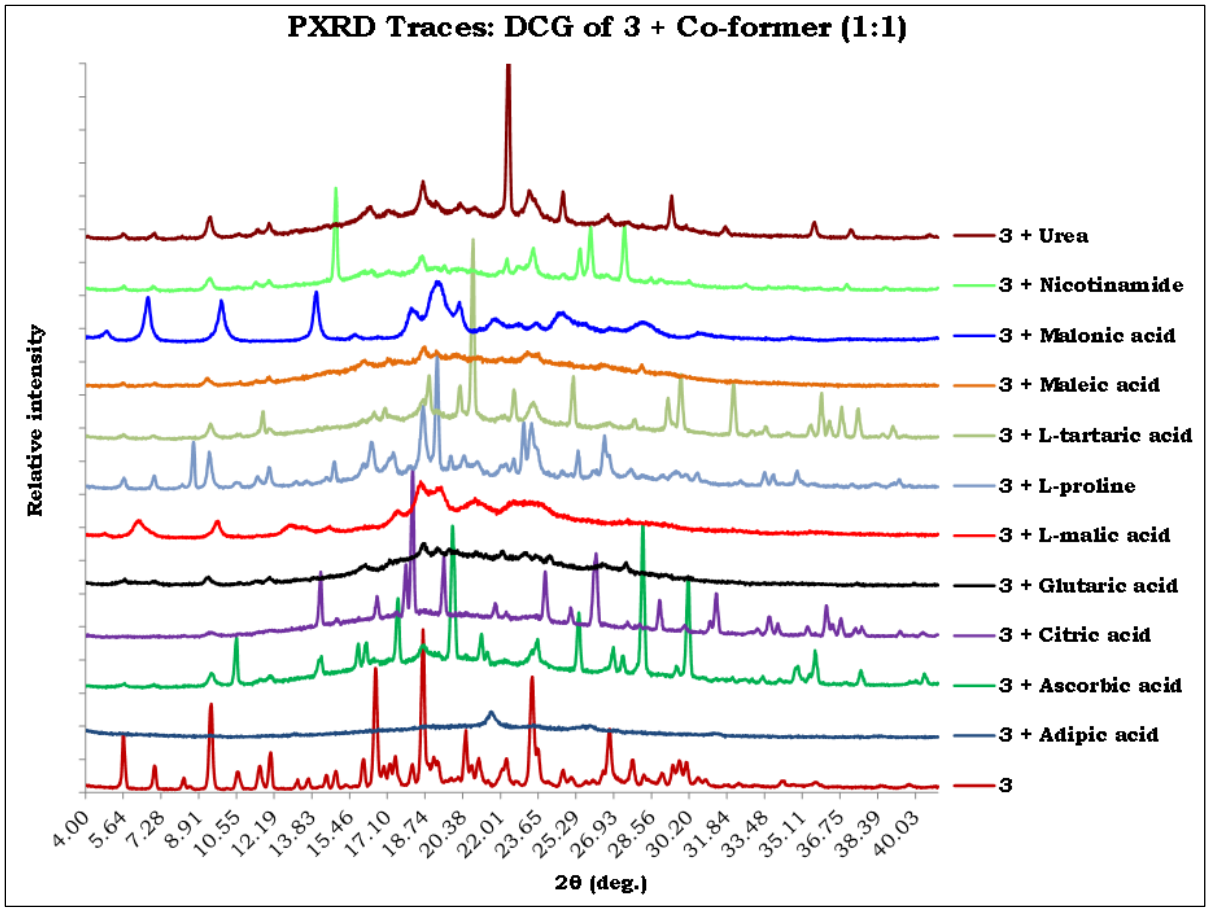

Figure 4.13: PXRD traces of **3** and its products of dry co-grinding with various GRAS potential co-formers.

4.5.4.2 Liquid-assisted Co-grinding (LAG)

The above-mentioned experiments were repeated, but this time, minute amounts of ethanol were added dropwise at intervals during the co-grinding process, which lasted for 15–20 minutes. The resulting PXRD traces for each product are shown in **Figure 4.14** below. Products from the dicarboxylic acids and citric acid produced PXRD traces indicative of the formation of new phases, and were therefore considered hits for co-precipitation and recrystallization experiments. Conversely, products from urea, nicotinamide, L-proline, and ascorbic acid were physical mixtures, and were thus not explored further. Furthermore, the PXRD traces of **3**:malonic acid, **3**:glutaric acid, and **3**:maleic acid were similar, though not identical. The same pattern was observed with those of **3**:L-malic acid and **3**:citric acid. This was interpreted as a pointer to compound **3** being inclined to form isostructural products when combined with these acids.

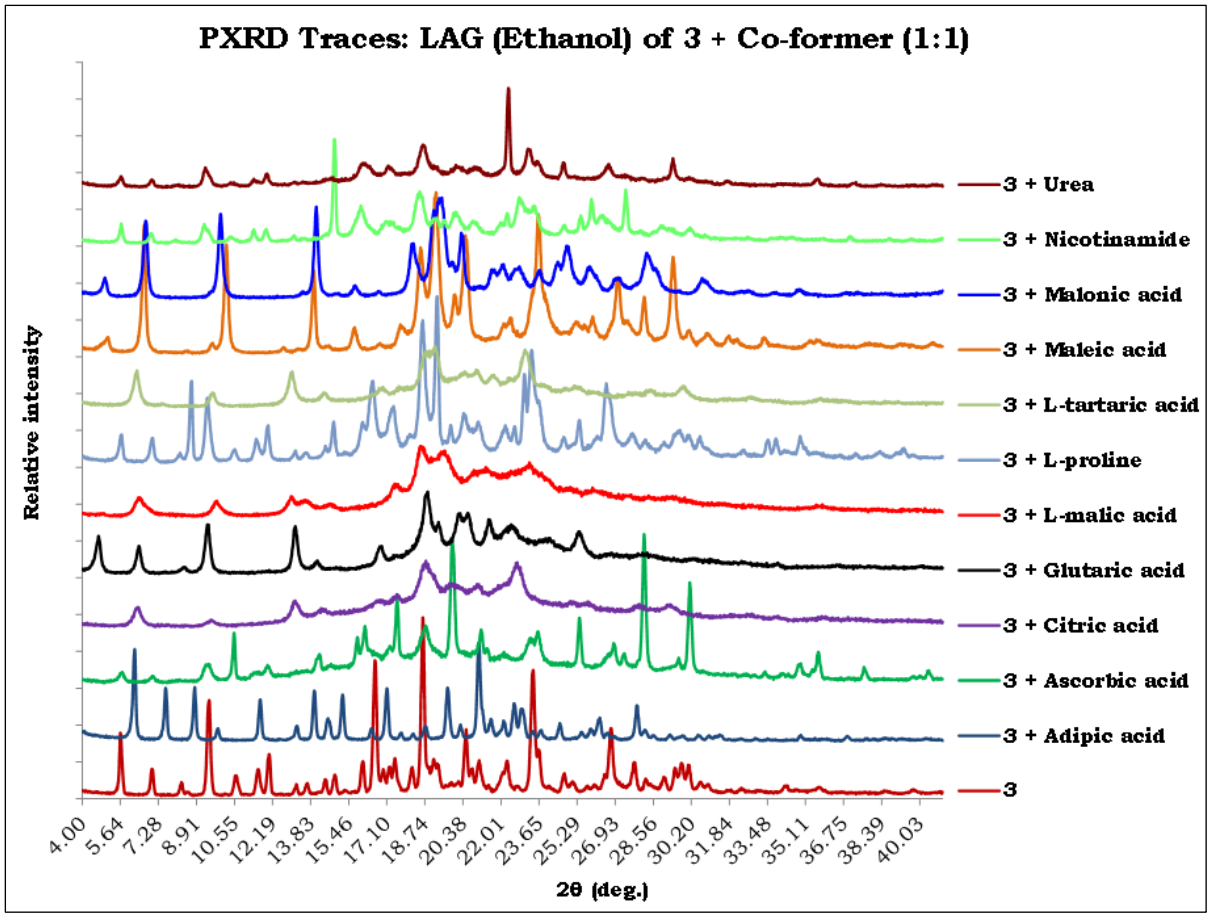

Figure 4.14: PXRD traces of **3** and its products of liquid (ethanol)-assisted co-grinding with various GRAS potential co-formers.

4.5.4.3 Co-precipitation

In order to grow crystals for further characterization experiments such as determination of stoichiometry, products resulting from the LAG experiments, which were new phases, were dissolved in a minimum amount of hot ethanol (50 °C) and left to crystallize by slow evaporation at ambient temperature. None of the mixtures produced crystals of appreciable size and shape. Therefore, crystallization by co-precipitation was explored. Accordingly, in each case, about 10 mg of **3** was accurately weighed, mixed with an equimolar amount of the appropriate co-former, and dissolved in hot ethanol. The mixture of **3** and maleic acid could not dissolve appreciably in any of the attempted solvents: ethanol, methanol, acetone, and acetonitrile.

Within 10 days, all the six solutions had formed crystals. Of these, the citric acid- and the L-malic acid-containing solutions formed crystals of adequate size and quality for SCXRD. On the other hand, the adipic acid- and malonic

acid-containing solutions produced thread-like crystals, which were too small for SCXRD. All attempts to increase their sizes by reducing the rate of evaporation as well as using different solvents were futile. In addition, the L-tartaric acid- and glutaric acid-containing solutions resulted in crystallization of the parent compound **3** only, as established by ^{1}H NMR spectroscopy, and were therefore not explored further.

Products containing L-malic acid, citric acid, malonic acid, and adipic acid were characterized using ^{1}H NMR spectroscopy, thermal analysis, and PXRD. In addition, the single crystals of L-malic acid- and citric acid-containing products were subjected to SCXRD experiments. The main roles of these characterization techniques were to determine the: 1. Stoichiometric ratio of interaction between **3** and the appropriate co-former [^{1}H NMR spectroscopy]; 2. Melting point, presence of solvent/water, and thermal behaviour [thermal analysis]; 3. Formation of a new phase [PXRD]; 4. Molecular geometry, hydrogen bonding interactions, and whether a salt or a cocrystal was formed [SCXRD].

4.5.5 Compound 3:L-malic acid (2:1) Salt

SCXRD studies confirmed that the product of co-precipitation of **3** and L-malic acid was a salt resulting from the transfer of a proton to the nitrogen atom N4. ^{1}H NMR spectroscopy as well as SCXRD confirmed the stoichiometry of **3**:L-malic acid to be 2:1. **Figure 4.15** below depicts the ^{1}H NMR spectrum, TGA and PXRD traces of **3** malate. The TGA trace showed a two-step mass loss. The first mass loss at ~50 °C of 8.2 ± 0.2% (n = 2) was attributed to dehydration that resulted in loss of 2.53 ± 0.06 moles of water per mole of **3** [calculated mass loss of 2.5 moles of water = 8.1%]. The second mass loss at 230 °C coincided with the melting point of **3** malate. This was attributed to decomposition of the malic acid component of the product. The PXRD trace depicted the diffraction pattern resulting from **3** malate crystalline solid.

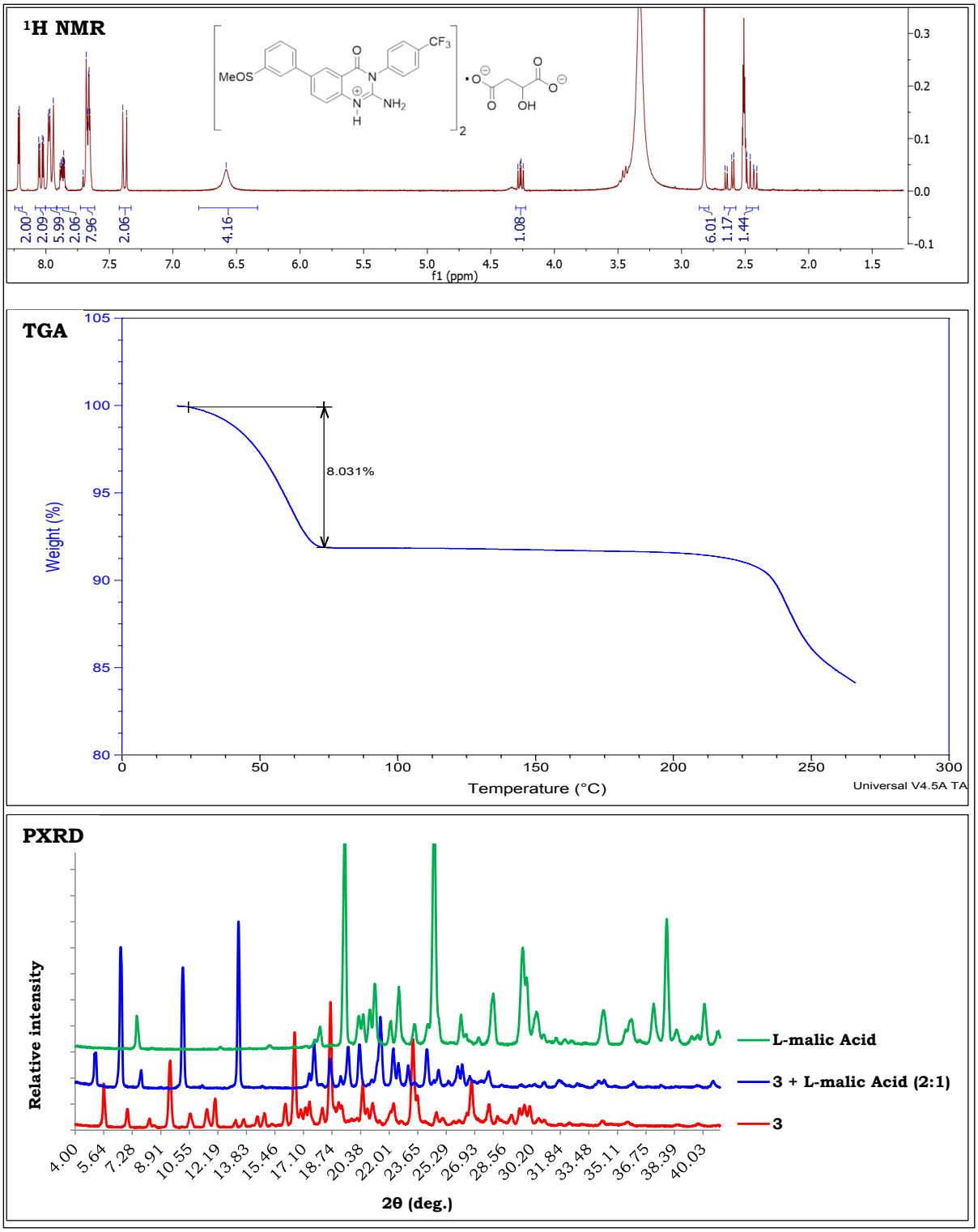

Figure 4.15: [1]H NMR spectrum, TGA and PXRD traces of **3** malate (2:1).

4.5.5.1 Single Crystal X-Ray Analysis of 3 malate.

The single crystal XRD and the refinement data for a hydrated crystal of **3** malate are outlined in **Table 4.9** below.

Table 4.9: Data-collection and refinement parameters for **3** malate.

Parameter	**Value**
Molecular Formula	$2(C_{22}H_{17}N_3O_2S_1F_3)^+ (C_4H_4O_5)^{2-} \bullet 5(H_2O)$
Formula Weight	1111.04
Crystal System	Triclinic
Space Group	$P\bar{1}$
a (Å)	5.1440(8)
b (Å)	13.819(2)
c (Å)	18.262(3)
α (º)	78.836(3)
β (º)	84.768(3)
γ (º)	86.041(3)
V (Å^3)	1266.5(5)
Z	1
D (calc) (g.cm^{-3})	1.431
μ (MoKα) (mm^{-1})	0.200
F (000)	559
Crystal Size (mm^3)	0.13 × 0.17 × 0.52
Temperature (K)	100(2)
Radiation (Å)	MoKα (0.71073)
θ Min–Max (º)	2.1–28.3
Index ranges ±*h*; ±*k*; ±*l*	-6: 6; -18: 18; -24: 24
Reflections (total)	27510
Reflections (unique)	6257
R (int)	0.028
Reflections with I>2σ(I)	5219
Nref, Npar	6257, 342
R1, w*R*2, S	0.1005, 0.2687, 1.10
Max. and Av. Shift/Error	<0.001, <0.001
$\Delta\rho_{min,\ max}$ (e Å^{-3})	-0.67, 1.04

From the above information, the fact that the product crystallised in a centrosymmetric space group ($P\bar{1}$) could have resulted from racemization of L-malic acid after heating during the co-precipitation process. In the crystal, the malate ion is disordered over two overlapping inversion-related positions, a result that has been observed previously when racemic malic acid was employed in co-crystallization.[13] The crystal structure of **3** malate is shown in **Figure 4.16** below. Notably, a proton from the carboxylic acid group of malic acid is transferred to the nitrogen atom N4 of **3**, making the product a salt instead of a cocrystal.

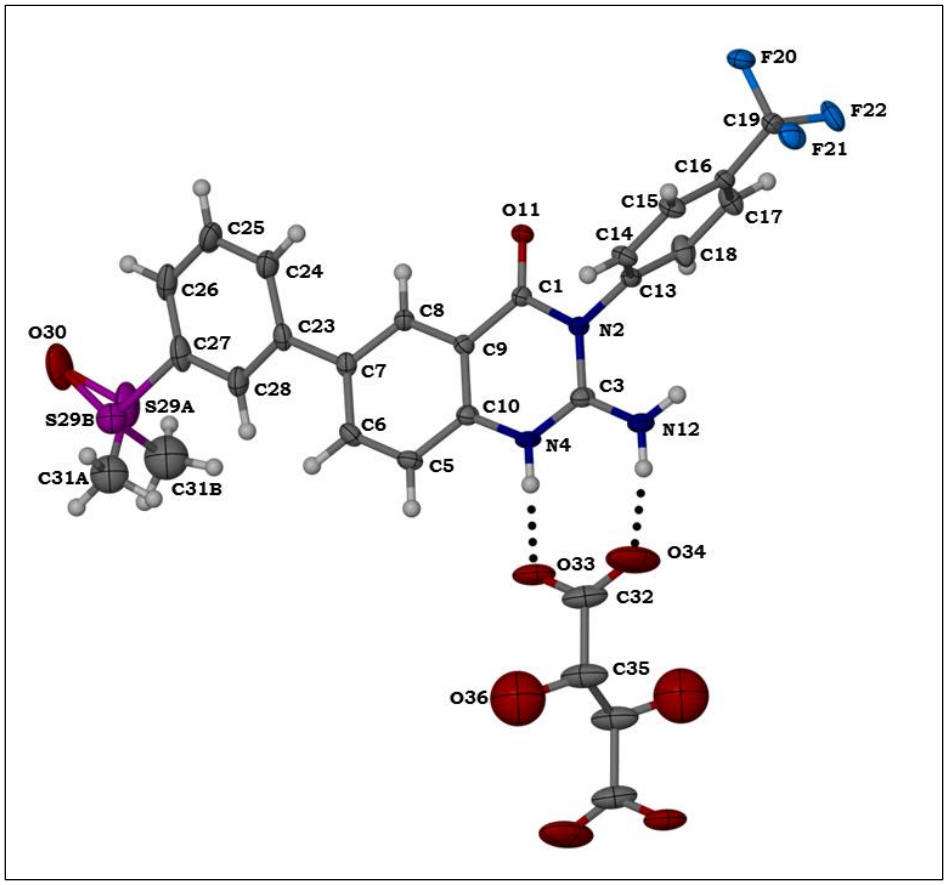

Figure 4.16: The ASU of **3** malate with thermal ellipsoids of non-H atoms drawn at the 50% probability level. The disordered water molecules have been omitted for image clarity.

As observed in the crystal structure of **3** hemi-ethyl acetate hemihydrate, the –SOMe moiety in **3** malate was also disordered over two positions.

As hypothesized, the main hydrogen bonding interactions observed were N4–H4•••O33, N12–H12A•••O34, and N12–H12B•••O30[a]. These, along with other hydrogen bonds are outlined in **Table 4.10** below.

Table 4.10: Hydrogen bonding interactions for **3** malate.

D–H•••A (Interactions)	d(D–H)	d(H•••A)	d(D•••A)	∠D–H•••A
N4–H4•••O33	0.88	1.74	2.619(4)	176
N12–H12A•••O34	0.88	1.87	2.730(6)	167
N12–H12B•••O30[a]	0.88	2.01	2.805(5)	150
C14–H14•••O11[b]	0.95	2.33	3.197(5)	152
C15–H15•••O11[c]	0.95	2.47	3.307(4)	147
C26–H26•••O30 [Intra]	0.95	2.45	2.861(7)	106
C31A–H31B•••O30[b]	0.98	2.57	3.350(10)	136

D = Donor; A = Acceptor; d = distance (Å); ∠ = angle (°)
Symmetry codes: [a] 1+x, 1+y, z; [b] 1+x, y, z; [c] 1-x, 1-y, 1-z

Figure 4.17 below illustrates the aforementioned hydrogen bonding interactions in **3** malate.

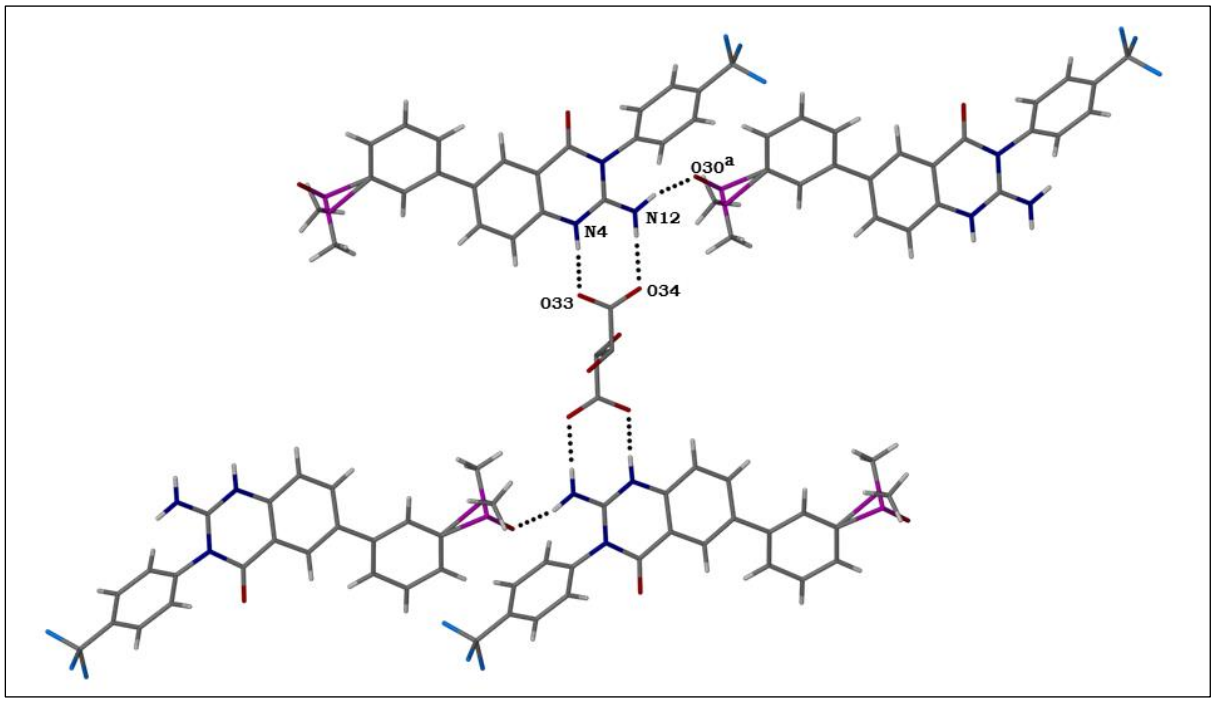

Figure 4.17: Stick diagram depicting the main intermolecular hydrogen bonding interactions in **3** malate.

Although the water molecules are expected to interact with the **3** malate molecules via hydrogen bonding, this was not observed due to the high level of disorder of the water molecules in the crystal structure. The diagram in **Figure 4.18** below shows the packing characteristics of **3** malate counterions. This figure depicts a feature of hydrophilic-hydrophobic alternation in layers parallel to the *b*-direction. The hydrophilic layers contain the malate ions and water molecules whereas the hydrophobic layers are composed of cations of **3**.

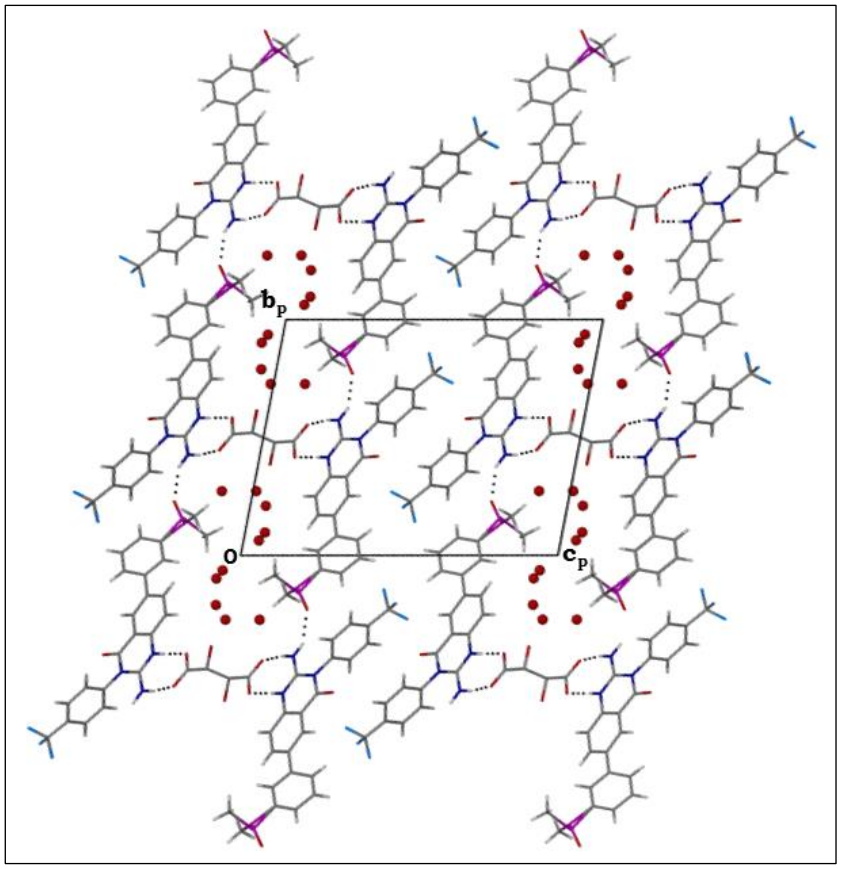

Figure 4.18: Packing characteristics of the **3** malate crystal viewed parallel to the *a*-axis. The red spheres represent the oxygen atoms of the disordered water molecules.

4.5.6 Compound 3:Citric acid (2:1) Salt

Like **3** malate, the crystal structure of **3** citrate was elucidated and found to be a salt. The ^{1}H NMR spectrum, TGA and PXRD traces are shown in appendix A1. The SCXRD and the refinement data for **3** citrate are listed in **Table 4.11** below.

Table 4.11: Data-collection and refinement parameters for **3** citrate.

Parameter	**Value**
Molecular Formula	$2(C_{22}H_{17}N_3O_2S_1F_3)^+ (C_6H_6O_7)^{2-} \bullet 5(H_2O)$
Formula Weight	1169.08
Crystal System	Triclinic
Space Group	$P\bar{1}$
a (Å)	5.1224(7)
b (Å)	13.805(2)
c (Å)	18.581(2)
α (°)	83.284(2)
β (°)	82.780(3)
γ (°)	86.555(2)

Table 4.11: Data-collection and refinement parameters for **3** citrate.

Parameter	**Value**
V (Å^3)	1293.2(5)
Z	1
D (calc) (g.cm^{-3})	1.480
μ (MoKα) (mm^{-1})	0.202
F (000)	590
Crystal Size (mm^3)	0.14 × 0.15 × 0.32
Temperature (K)	173(2)
Radiation (Å)	MoKα (0.71073)
θ Min–Max (º)	1.5–28.4
Index ranges ±*h*; ±*k*; ±*l*	-6: 6; -18: 18; -24: 24
Reflections (total)	27680
Reflections (unique)	6426
R (int)	0.031
Reflections with I>2σ(I)	5009
Nref, Npar	6426, 430
R1, w*R*2, S	0.0579, 0.1713, 1.04
Max. and Av. Shift/Error	<0.001, <0.001
$\Delta\rho_{min,\ max}$ (e Å^{-3})	-0.49, 0.98

The crystal structure of **3** citrate had similar characteristics to those observed with the **3** malate one, as depicted in **Figure 4.19** below. The citrate ion is disordered over a center of inversion and only the labelled half belongs to the asymmetric unit. The water molecules were also disordered and hydrogen atoms could not be placed on them. Also, the –SOMe moiety was disordered over two positions.

Furthermore, comparison of the unit cell data of the two crystals suggested isostructural arrangements of the parent molecules **3** and location of the respective acid anion components in common sites.

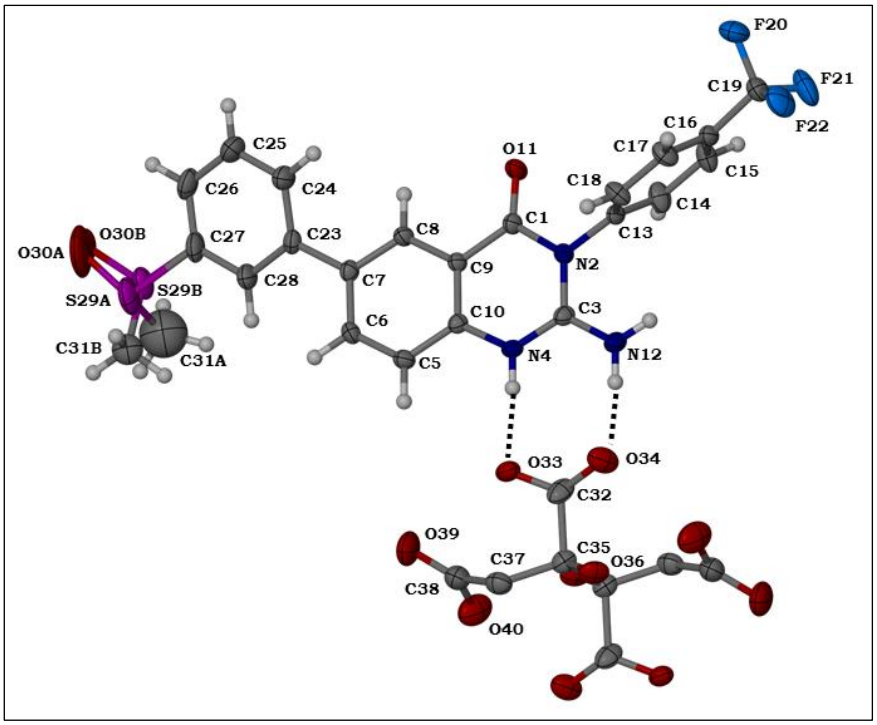

Figure 4.19: The ASU of **3** citrate with thermal ellipsoids represented at the 50% probability level. The disordered water molecules have been omitted for image clarity.

The principal hydrogen bonding interactions are shown in **Table 4.12** below.

Table 4.12: Hydrogen bonding interactions for **3** citrate.

D–H•••A (Interactions)	d(D–H)	d(H•••A)	d(D•••A)	∠D–H•••A
N4–H4•••O33	0.88	1.87	2.754(4)	177
N12–H12A•••O34	0.88	1.89	2.752(2)	165
N12–H12B•••O30[a]	0.88	2.11	2.880(11)	146
C17–H17•••O11[b]	0.95	2.49	3.342(3)	149
C18–H18•••O11[c]	0.95	2.36	3.218(3)	150
C26–H26•••O30 [Intra]	0.95	2.43	2.857(11)	107

D = Donor; A = Acceptor; d = distance (Å); ∠ = angle (°)
Symmetry codes: [a] 1+x, 1+y, z; [b] 1-x, 1-y, 1-z; [c] 1+x, y, z

The above-mentioned interactions and the packing characteristics are illustrated in **Figure 4.20**. As observed with **3** malate, the supramolecular architecture of **3** citrate is characterized by hydrophilic water/citrate ion layers alternating with the hydrophobic layers of **3** cations parallel to the *b*-direction.

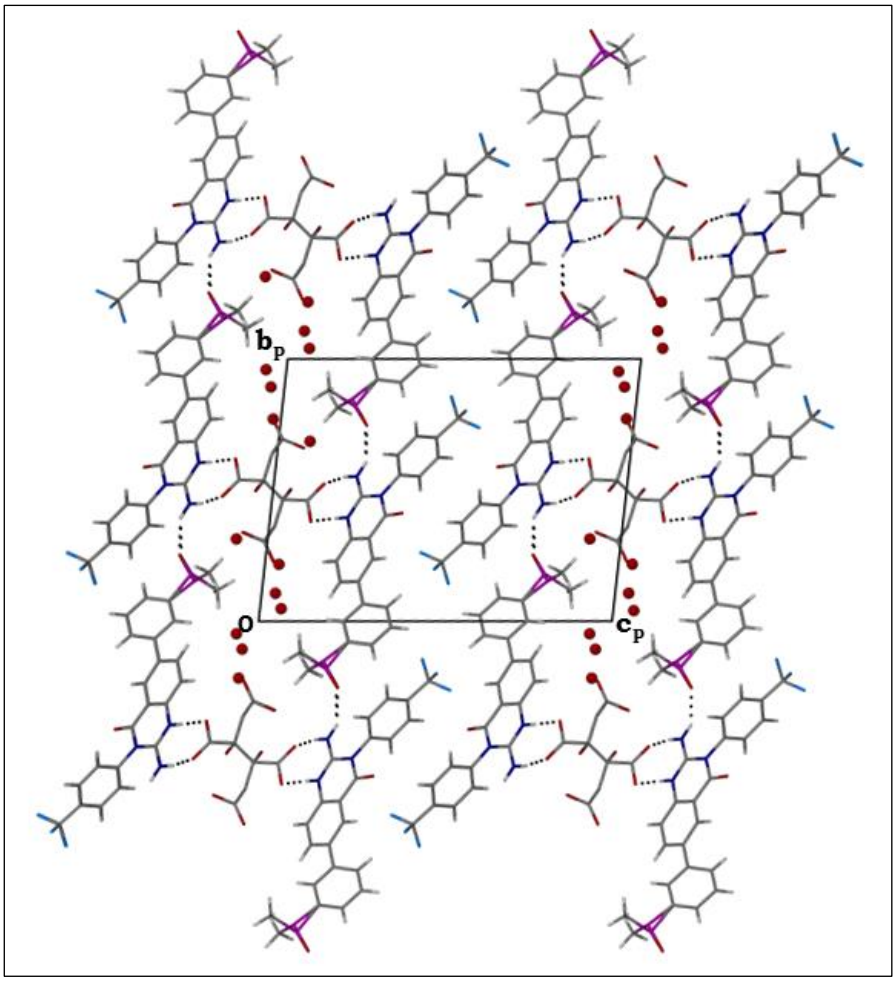

Figure 4.20: Packing characteristics of the **3** citrate crystal viewed parallel to the *a*-axis. The red spheres represent the oxygen atoms of the disordered water molecules.

From the foregoing discussion, it was hypothesized that **3** had the propensity to form isostructural products with dicarboxylic acids. To test this hypothesis, succinic acid, being a symmetrical dicarboxylic acid, was studied. Unfortunately, all attempts to grow single crystals of appreciable size were unsuccessful. However, the product of co-precipitation of **3** and succinic acid (2:1) by slow evaporation in ethanol was characterized by ^{1}H NMR spectroscopy and PXRD. Based on the established isostructurality of **3** malate and **3** citrate, a succinate salt of **3** was assumed in this case. The PXRD traces of the three salts were very similar, as shown in **Figure 4.21** below, proving that indeed the three salts were isostructural and had similar packing characteristics.

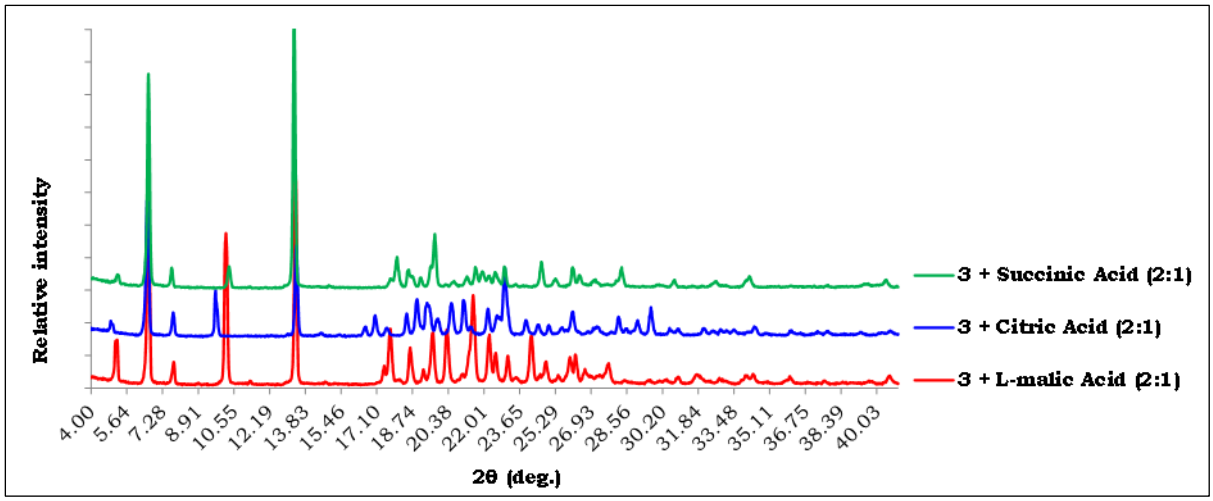

Figure 4.21: PXRD traces of **3** malate, citrate and succinate.

4.5.7 Other Salts of 3

Salt formation is a classical technique usually applied to modify and optimize the physicochemical properties of an ionizable compound. Pharmaceutically acceptable counterions are often used to influence properties such as solubility, dissolution rate, hygroscopicity, thermal stability, impurity profiles, compressibility, and crystal habit.[14–16] Examples of anionic counter-ions commonly used for salt formation with basic active pharmaceutical ingredients (APIs) are summarised in **Figure 4.22** below.

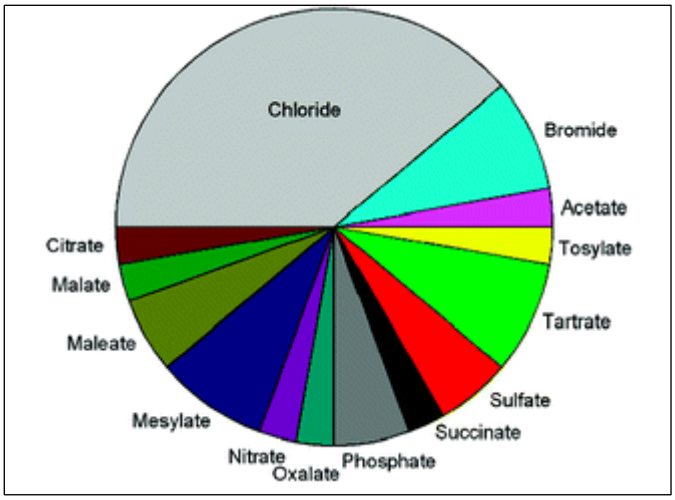

Figure 4.22: Distribution (2002–2006) of anions commonly used with basic APIs containing at least one atom suitable for protonation.[14]

In this thesis work, salts of **3** were prepared by direct acid addition, whereby an equimolar amount of the acid was added to a solution of **3** in chloroform. The precipitate that formed was washed with chloroform and dried *in vacuo*.

These products included the hydrochloride, hydrobromide, sulfate, phosphate, and methanesulfonate (mesylate) salts of **3**. These, together with the salts of **3** with the aforementioned dicarboxylic acids, were then subjected to kinetic solubility studies.

4.5.8 Kinetic Solubility by HPLC

A protocol similar to the turbidimetric assay method was employed to determine the aqueous solubility of the above-mentioned salts. However, instead of taking the concentration at which solids form in PBS solution as the solubility, the exact amount of compound **3** in a 200 µM solution in PBS pH 7.4 (2% DMSO) was determined by a HPLC method. A 9-point calibration curve was prepared using solutions of **3** in DMSO [5, 10, 20, 25, 40, 80, 160, 200, and 250 µM: Appendix A5 (R^2 = 0.9998)]. **Table 4.13** below summarizes the observed solubilities of the studied salts. Notably, the solubility of **3** as determined by HPLC was 21 µM compared to 80 µM observed with the turbidimetric method. This further highlights the fact that the turbidimetric solubility method is less accurate than HPLC, and is thus prone to overestimating solubility values. All the salts, except the malate, had improved solubility, albeit modest, in the range of 1.5- to 2-fold increase. **3** mesylate exhibited the best aqueous solubility of 38 µM.

Table 4.13: Kinetic solubility (HPLC) results and melting points for the various salts of **3**.

Name	Structure	m.p. (°C)	Solubility (µM)
3	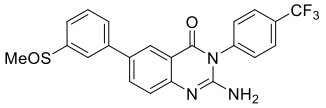	173–175	21
3 malate	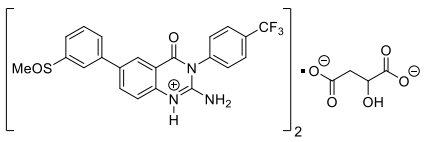	230–235	7
3 citrate	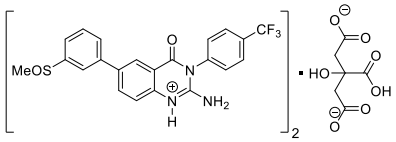	189–192	27
3 succinate	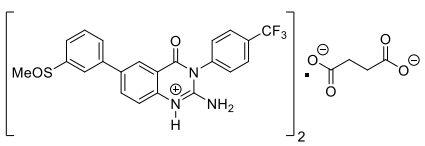	243–246	27

Table 4.13: Kinetic solubility (HPLC) results and melting points for the various salts of **3**.

Name	Structure	m.p. (°C)	Solubility (µM)
3 malonate	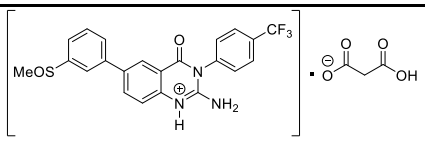	200–201	34
3 adipate	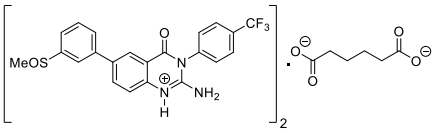	218–220	31
3 hydrochloride	**3**.HCl	299–304	31
3 hydrobromide	**3**.HBr	289–292	36
3 sulfate	**3**.H_2SO_4	228–230	29
3 phosphate	**3**.H_3PO_4	225–226	30
3 mesylate	**3**.CH_3SO_3H	299–302	38

4.6 Conclusion

This chapter described the studies conducted with respect to physicochemical profiling and supramolecular derivatization. Physicochemical profiling revealed that the 2-aminoquinazolinones (AQZs) and benzoxazole-based oximes (BZOs) occupy different chemical spaces [Mwt and cLogP], which are distinct from that occupied by a majority of the conventional anti-TB drugs. Very few violations of the Lipinski's RO5 were observed. In addition, the SPR studies showed that solubility was moderately correlated to HPLC retention time (t_R) [R^2 = 0.49 for AQZs and 0.65 for BZOs] and TLC retardation factor (R_f) [R^2 = 0.64 for AQZs and 0.57 for BZOs], weakly correlated to cLogP [R^2 = 0.37 for AQZs and 0.30 for BZOs], whereas no correlation was observed with melting point [R^2 < 0.05 for both classes].

Formation of cocrystals of **3** with selected potential co-formers was attempted. However, all attempts resulted in salt formation, which was attributed to the transfer of a proton from the acidic co-former to the quinazolinone nitrogen atom N4. All the salts had a moderate improvement in solubility at pH 7.4 in the range of 1.5- to 2-fold that of **3** (21 µM), except **3** malate, which recorded a decline (7 µM). Moreover, the higher melting points of all the salts indicate improved thermal stability. Attempts to complex **3** with the native cyclodextrins [α-, β-, and γ-CD] by co-precipitation using water as the solvent were unsuccessful.

References

(1) Gleeson, P.; Bravi, G.; Modi, S.; Lowe, D. ADMET Rules of Thumb II: A Comparison of the Effects of Common Substituents on a Range of ADMET Parameters. *Bioorg. Med. Chem.* **2009**, *17*, 5906–5919.

(2) Waring, M. J. Lipophilicity in Drug Discovery. *Expert Opin. Drug Discov.* **2010**, *5*, 235–248.

(3) Schuster, D.; Laggner, C.; Langer, T. Why Drugs Fail: A Study on Side Effects in New Chemical Entities. *Curr. Pharm. Des.* **2005**, *11*, 3545–3559.

(4) Hughes, J. D.; Blagg, J.; Price, D. A.; Bailey, S.; Decrescenzo, G. A.; Devraj, R. V; Ellsworth, E.; Fobian, Y. M.; Gibbs, M. E.; Gilles, R. W.; Greene, N.; Huang, E.; Krieger-Burke, T.; Loesel, J.; Wager, T.; Whiteley, L.; Zhang, Y. Physiochemical Drug Properties Associated with *in vivo* Toxicological Outcomes. *Bioorg. Med. Chem. Lett.* **2008**, *18*, 4872–4875.

(5) Leeson, P. Drug Discovery: Chemical Beauty Contest. *Nature* **2012**, *481*, 455–456.

(6) Lipinski, C. A.; Lombardo, F.; Dominy, B. W.; Feeney, P. J. Experimental and Computational Approaches to Estimate Solubility and Permeability in Drug Discovery and Development settings. PII of Original Article: S0169-409X(96)00423-1. The Article Was Originally Published in Advanced Drug Delivery Reviews 23 (1997) 3. *Adv. Drug Deliv. Rev.* **2001**, *46*, 3–26.

(7) Veber, D. F.; Johnson, S. R.; Cheng, H.-Y.; Smith, B. R.; Ward, K. W.; Kopple, K. D. Molecular Properties That Influence the Oral Bioavailability of Drug Candidates. *J. Med. Chem.* **2002**, *45*, 2615–2623.

(8) Bevan, C. D.; Lloyd, R. S. A High-Throughput Screening Method for the Determination of Aqueous Drug Solubility Using Laser Nephelometry in Microtiter Plates. *Anal. Chem.* **2000**, *72*, 1781–1787.

(9) Fay, M. P.; Proschan, M. A. Wilcoxon-Mann-Whitney or T-Test? On Assumptions for Hypothesis Tests and Multiple Interpretations of Decision Rules. *Stat. Surv.* **2010**, *4*, 1–39.

(10) Qu, Y.; Zhao, Y. D.; Rahardja, D. Wilcoxon-Mann-Whitney Test: Stratify or Not? *J. Biopharm. Stat.* **2008**, *18*, 1103–1111.

(11) Aitipamula, S.; Banerjee, R.; Bansal, A. K.; Biradha, K.; Cheney, M. L.; Choudhury, A. R.; Desiraju, G. R.; Dikundwar, A. G.; Dubey, R.; Duggirala, N.; Ghogale, P. P.; Ghosh, S.; Goswami, P. K.; Goud, N. R.; Jetti, R. R. K. R.; Karpinski, P.; Kaushik, P.; Kumar, D.; Kumar, V.;

Moulton, B.; Mukherjee, A.; Mukherjee, G.; Myerson, A. S.; Puri, V.; Ramanan, A.; Rajamannar, T.; Reddy, C. M.; Rodriguez-Hornedo, N.; Rogers, R. D.; Row, T. N. G.; Sanphui, P.; Shan, N.; Shete, G.; Singh, A.; Sun, C. C.; Swift, J. A.; Thaimattam, R.; Thakur, T. S.; Kumar Thaper, R.; Thomas, S. P.; Tothadi, S.; Vangala, V. R.; Variankaval, N.; Vishweshwar, P.; Weyna, D. R.; Zaworotko, M. J. Polymorphs, Salts, and Cocrystals: What's in a Name? *Cryst. Growth Des.* **2012**, *12*, 2147–2152.

(12) Cruickshank, D. L.; Younis, Y.; Njuguna, N. M.; Ongarora, D. S. B.; Chibale, K.; Caira, M. R. Alternative Solid-State Forms of a Potent Antimalarial Aminopyridine: X-Ray Crystallographic, Thermal and Solubility Aspects. *CrystEngComm* **2014**, *16*, 5781–5792.

(13) Smith, G.; Wermuth, U. D. Order and Disorder in the Structures of Two Crystal Polymorphs of the Adduct Bis(Quinolinium-2-Carboxylate) DL-Malic Acid. *J. Chem. Crystallogr.* **2011**, *41*, 241–246.

(14) Paulekuhn, G. S.; Dressman, J. B.; Saal, C. Trends in Active Pharmaceutical Ingredient Salt Selection Based on Analysis of the Orange Book Database. *J. Med. Chem.* **2007**, *50*, 6665–6672.

(15) Berge, S. M.; Bighley, L. D.; Monkhouse, D. C. Pharmaceutical Salts. *J. Pharm. Sci.* **1977**, *66*, 1–19.

(16) Saal, C.; Becker, A. Pharmaceutical Salts: A Summary on Doses of Salt Formers from the Orange Book. *Eur. J. Pharm. Sci.* **2013**, *49*, 614–623.

CHAPTER 5

SUMMARY, CONCLUSIONS AND RECOMMENDATIONS FOR FUTURE WORK

5.1 Summary and Conclusions

This thesis work aimed to optimize previously identified antimycobacterial benzoheterocyclic hit compounds containing either the quinazolin-4(3*H*)-one or the benzoxazole scaffold. Classical hit-to-lead optimization strategies were adapted in order to achieve the overall objective of investigating the antimycobacterial structure-activity relationship (SAR) profiles. An attendant aim was to explore structure-property relationships (SPR) for the target compounds and perform supramolecular derivatization of selected analogues.

The first aim of the study was to design, synthesize, and characterize novel 2-aminoquinazolinone and benzoxazole-based oxime analogues. Several new benzoheterocycles were designed by employing rational medicinal chemistry principles, and thereafter successfully synthesized in accordance with protocols adapted from literature. All the synthesized compounds were fully characterized using spectroscopic techniques such as NMR spectroscopy; chromatographic methods, including TLC and HPLC-MS; along with physicochemical attributes such as appearance, melting point, and aqueous solubility.

The second objective of the study was to biologically evaluate the synthesized compounds for their *in vitro* antimycobacterial potency, cytotoxicity, *in vitro* and *in vivo* DMPK profiles, and *in vivo* efficacy [proof-of-concept studies]. Accordingly, the 2-aminoquinazolinone analogues manifested clear SAR trends (**Figure 5.1** below) following *in vitro* evaluation of their antimycobacterial activity against the drug-susceptible *Mtb* H_{37}Rv strain cultured in GAST-Fe and 7H9/ADC media. In addition, the selected potent compounds exhibited low cytotoxicity against the CHO and HepG2 cell lines, as well as high microsomal metabolic stability in MLM. Besides, the proposed hypothesis behind the design of the sulfoxide-based analogue

3 [**Figure 5.1**: Ar_1 = 3−SOMePh; Ar_2 = 4−CF_3Ph] was supported by experimental findings.

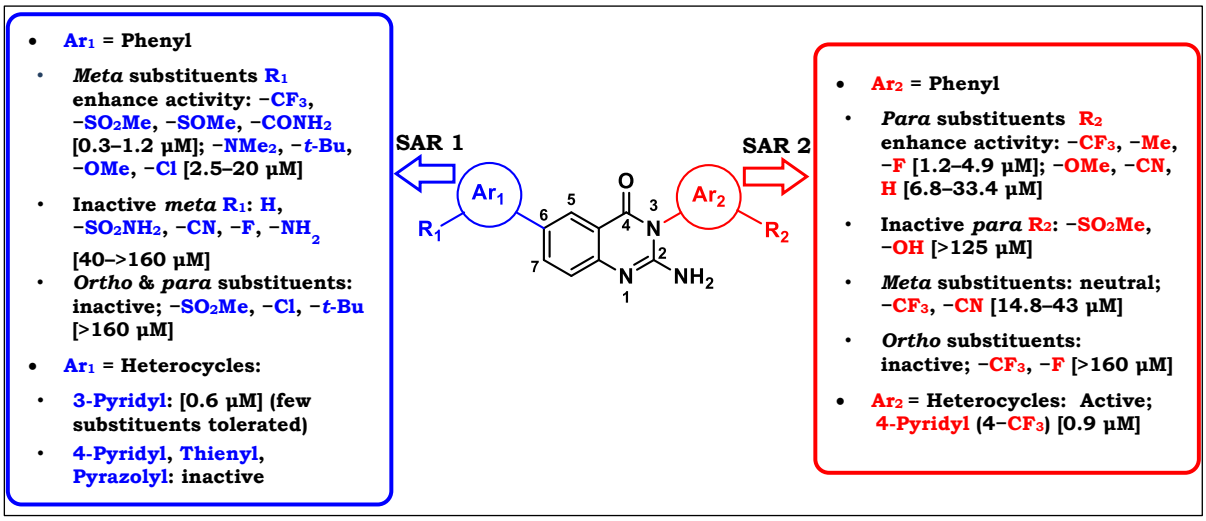

Figure 5.1: Summary of the antimycobacterial SAR for the 2-aminoquinazolinones.

The empirical evidence behind this was provided by the extensive *in vivo* biotransformation of **3** in mice to the equally active but more metabolically stable sulfone-based analogue **2** [**Figure 5.1**: Ar_1 = 3−SO_2MePh; Ar_2 = 4−CF_3Ph]. Both compounds exhibited favourable pharmacokinetic profiles and were well tolerated at the highest administered dose of 300 mg/kg. Despite the good pharmacological profiles exhibited by the 2-aminoquinazolinones, the frontrunner analogue **3** was devoid of *in vivo* efficacy in an acute TB infection mouse model [BALB/c] at 100 and 200 mg/kg doses.

Further studies, including the use of different *in vitro* assay conditions such as glycerol-free media, revealed that the 2-aminoquinazolinones killed *Mtb in vitro* via a glycerol-dependent mechanism of action, hence lacking *in vivo* efficacy. These findings correlated well with the results of studies on generation of spontaneous resistant mutants, whereby all strains resistant to **3** had mutations mapping to the glycerol metabolism genes, which encode for glycerol kinase (*glpK*) and glycerol-3-phosphate dehydrogenase (*glpD2*). Overall, these biological studies highlighted the importance of developing and applying *in vitro* antimycobacterial phenotypic screening conditions, in the early drug discovery stages, which are reflective of the *in vivo* biological

conditions during TB infection.

Benzoxazole-based oximes, on the other hand, exhibited a tight SAR, with only **SAR 2** modifications being tolerated. As such, all attempts to introduce changes at **SAR 1** and **SAR 3** (**Figure 5.2**) yielded inactive compounds.

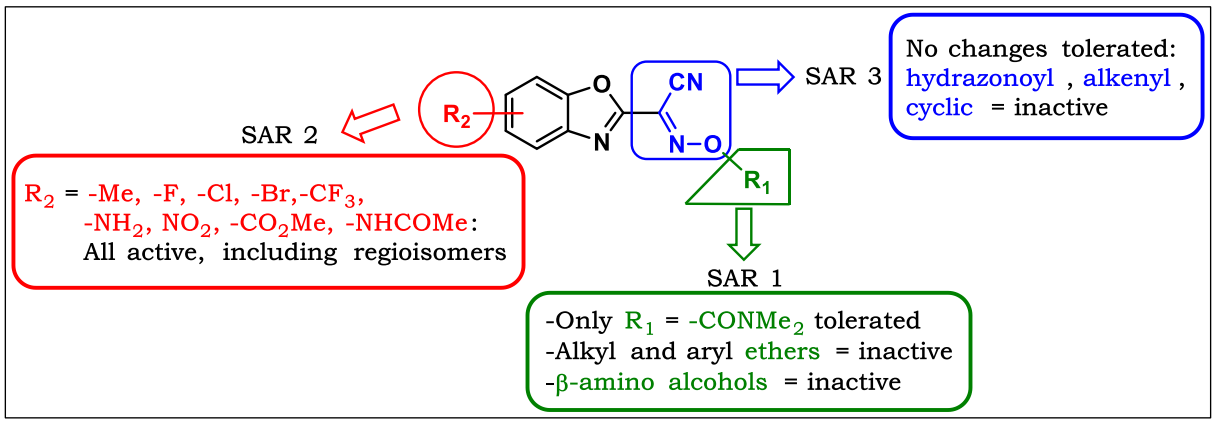

Figure 5.2: Summary of the antimycobacterial SAR for the benzoxazole-based oximes.

To this end, although the active compounds exhibited low *in vitro* cytotoxicity against the CHO cells, the low microsomal metabolic stability exhibited by the representative compound (**46**) [7.3% remaining after 30 minutes in MLM] was the major impediment to advancing the active benzoxazole-based oximes to the other studies in the screening cascade.

The third objective of the study was to profile all final target compounds with respect to physicochemical properties, including aqueous solubility, deduce structure–property relationships (SPR), and carry out supramolecular derivatization of selected potent compounds. Therefore, all target compounds were subjected to aqueous solubility studies, wherein the turbidimetric assay method was employed. The solubility values obtained were then correlated with the experimentally determined melting points, HPLC retention times (t_R), TLC retardation factors (R_f) as well as the virtually predicted physicochemical properties such as cLogP, in order to establish structure-property relationships (SPR). In effect, correlations were deduced, and t_R [R^2 = 0.49 for AQZs and 0.65 for BZOs] and R_f [R^2 = 0.64 for AQZs and 0.57 for BZOs] were found to be the most correlated factors with aqueous solubility, albeit moderate.

Further, compound **3** was selected for supramolecular derivatization studies in an effort to enhance its aqueous solubility [kinetic (HPLC) solubility of **3** = 21 µM], which involved formation of cocrystals, salts, and cyclodextrin inclusion complexes. The crystal structure of **3** revealed the molecular geometry and the main intermolecular interactions, which facilitated the selection of potential co-formers for co-crystallization. All attempts to synthesize cocrystals were, however, unsuccessful, as salts were formed instead. All the new solid states of **3** were characterized by XRD, thermal analysis, NMR spectroscopy, and thereafter subjected to solubility assessment by HPLC. In effect, only a moderate increase in solubility was observed in the salts of **3**, whereby the **3** mesylate exhibited the most improved solubility in the range of 2-fold increase (38 µM).

5.2 Recommendations for Future Work

Based on the good pharmacological profiles exhibited by the 2-aminoquinazolinones, it will be worthwhile to test these compounds in other disease models.

More quinazolinone analogues with improved solubility can be designed by adapting other strategies of solubility enhancement. For instance, a fluoro or a methyl substituent can be introduced at the *ortho*-position of the phenyl ring on the left-hand side (**Figure 5.3** I), in order to increase the dihedral angle and therefore twist the ring out of coplanarity with the fused quinazolinone ring system. This will in turn reduce crystal stacking and thus the potential to improve aqueous solubility. Another viable approach for solubility improvement will be to remove the aromaticity of the phenyl rings in order to reduce the associated π-π stacking (**Figure 5.3** II).

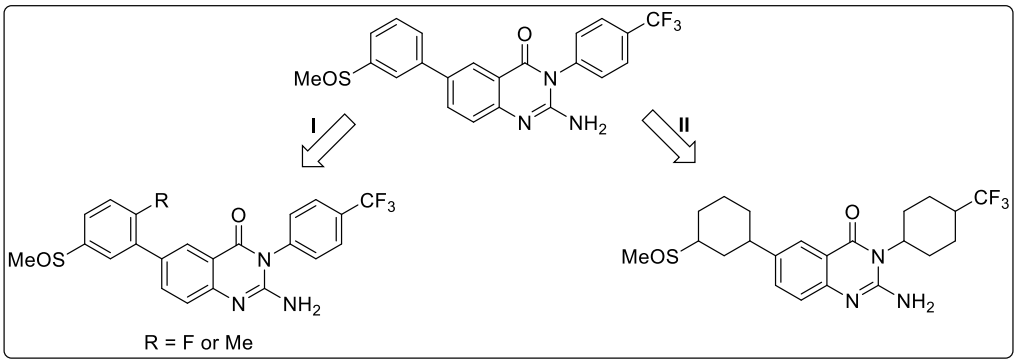

Figure 5.3: Proposed 2-aminoquinazolinone analogues with potential to exhibit improved solubility.

Furthermore, the salts of **3** can be studied for other beneficial effects they may have besides the enhanced solubility and melting point. Indeed, it will be quite informative to investigate how the dissolution rates of these salts would compare to that of the parent compound. In addition, permeability studies can be conducted on selected analogues using the *in vitro* Caco-2 assay or *in silico* permeability prediction. This will provide valuable information regarding whether or not permeability would compensate for the observed low solubility to yield acceptable oral absorption.

As for the benzoxazole-based oximes, the only active compounds were those bearing a dimethyl carbamate-functionalized oxime moiety, while the free oxime-bearing counterparts were not. Given the low metabolic stability of these compounds, it was hypothesized (Chapter 3, **Figure 3.10**) that they could have a prodrug mode of action, wherein they are metabolised intracellularly to the active free oxime-based metabolites by the *Mtb* esterases and amidases. This can be a platform for future prospects towards exploring these hypotheses, which can be two-fold: Firstly, studies regarding permeability into cells can be initiated to test the hypothesis that the free oximes do not penetrate the *Mtb* cells and hence inactive, while the dimethyl carbamate-bearing counterparts permeate the cells. The second stage of investigations would involve studies to monitor the metabolism of the active compounds inside the *Mtb* cells, to prove that indeed the free oximes are the active metabolites. The results of these studies can further be augmented by mechanistic deconvolution of the mode of action(s) involved, which will provide valuable insights into the underlying subcellular compound-target interactions. Moreover, intracellular antimycobacterial assays in macrophages is another possible and viable area for exploration.

Finally, supramolecular derivatization can be applied on the potent benzoxazole-based oximes, which may generate interesting derivatives with better physicochemical attributes. In this regard, the more soluble amorphous cyclodextrin derivatives, such as 2-hydroxypropyl- and sulfobutyl ether-β-CD, can be prioritized due to their potential to significantly improve the solubility of poorly soluble compounds.

CHAPTER 6

EXPERIMENTAL

6.1 Chapter Overview

Chapter 6 supplements the result-oriented Chapters 2, 3, and 4 by describing the experimental protocols involved, particularly those that are not outlined in the main text. In addition, this chapter provides the complete set of characterization information with respect to all the synthesized compounds.

6.2 Chemistry

6.2.1 Reagents and Solvents

All commercially available chemicals and reagents were purchased from either Sigma-Aldrich (South Africa) or Combi-Blocks Limited (USA), and were used without prior purification. Besides, anhydrous solvents such as 1,4-dioxane, acetonitrile, and DMF were purchased as such from Sigma-Aldrich, South Africa. In addition, column chromatography solvents, for example ethyl acetate (EtOAc), dichloromethane (DCM), hexane (Hex), and methanol (MeOH), were purchased as Analytical Reagent (AR grade) solvents from Kimix Chemicals, South Africa, and used directly. HPLC grade acetonitrile and methanol for LC-MS mobile phase preparation were purchased from Romil Ltd (Cambridge, UK).

6.2.2 Physical and Spectroscopic Characterization

Melting points were determined using STUART® SMP 40 automatic melting point apparatus, and are reported as uncorrected values.

NMR spectra were recorded on a Varian Mercury spectrometer [^{1}H: 300 MHz; ^{13}C: 75 MHz], Bruker Ultrashield-Plus spectrometer [^{1}H: 400 MHz; ^{13}C: 101 MHz], or Bruker Ascend™-600 spectrometer [^{1}H: 600 MHz; ^{13}C: 150 MHz]. Samples for NMR spectroscopy were dissolved in deuterated solvents such as dimethylsulfoxide (DMSO-d_6), chloroform ($CDCl_3$), or methanol (Methanol-d_4). Chemical shifts (δ) are reported in parts per million (ppm) and rounded off to two decimal places, while coupling constants (J) are reported

in Hertz (Hz), and rounded off to one decimal place. Abbreviations used to describe ^{1}H-NMR signal multiplicities are: br (broad), d (doublet), dd (doublet of doublets), ddd (doublet of doublet of doublets), dddd (doublet of doublet of doublet of doublets), dt (doublet of triplets), dtd (doublet of triplet of doublets), hept (heptet), m (multiplet), q (quartet), s (singlet), t (triplet), td (triplet of doublets), tdd (triplet of doublet of doublets), and tt (triplet of triplets). ^{13}C-NMR spectra were recorded in the complete proton-decoupled mode, and the chemical shifts are listed without assigning them to the corresponding carbon atoms; a format accepted by most international journals.

6.2.3 Chromatography

Target compound peak purity, retention time, and molecular ion were determined on an Agilent HPLC system, which was equipped with Agilent 1260® Infinity Binary Pump, Agilent 1260® Infinity Diode Array Detector, Agilent 1290® Infinity Column Compartment, Agilent 1260® Infinity Autosampler, low resolution Agilent 6120® Quadrupole mass spectrometer, and Peak Scientific® Genius 1050 Nitrogen Generator. The reverse-phase column used was an X-bridge® C_{18}; 2.5 µm (particle size); 3.0 mm (internal diameter) × 50 mm (length); and maintained at 35 °C. **Table 6.14** below lists the composition, and the gradient conditions of the mobile phase used at a flow rate of 0.9 mL/min. The injection volume was 2 µL while the mass spectra were obtained through the Electron Spray Ionization (ESI) as well as the Atmospheric Pressure Chemical Ionization (APCI), which were set up in either positive or negative mode of ionization. The diode array detector (DAD) was programmed to scan the eluents at absorption wavelengths ranging from 210 to 640 nm. All the reported LC-MS purity values are based on the maximum chromatograms resulting from the DAD [210–640 nm] scans.

Table 6.14: LC-MS Gradient conditions.

Time (min)	% A	% B	Composition	
			A	B
0.00-1.00	90	10	10 mM ammonium acetate buffer (0.4% acetic acid)	10 mM ammonium acetate (0.4% acetic acid) in 90% HPLC grade MeOH in H_2O
1.00-3.00	5	95		
3.00-5.00	5	95		
5.00-6.50	90	10		
6.50-7.00	90	10		

Reactions were monitored by analytical thin layer chromatography (TLC) using Fluka or Merck F_{254} aluminium-backed pre-coated silica gel plates, which were visualized under UV light at a wavelength of 254 or 366 nm, and in some instances, staining was performed to facilitate direct visualization. Gravity column chromatography was performed using Merck Kieselgel® 60 [70–230 mesh] silica gel, while Biotage SNAP® cartridges were packed with 40–65 µm diameter KP-Sil silica gel for flash column chromatography on a Biotage Isolera One® system (Biotage AB, Uppsala, Sweden).

6.2.4 Synthesis and Characterization

6.2.4.1 2-Aminoquinazolinones

Protocols reported in literature were adapted and applied in the synthesis of the target compounds belonging to the 2-aminoquinazolinone series.[1–3]

General procedure 1: Synthesis of intermediates 2.1a–2.1d

A solution of 2-amino-5-iodobenzoic acid (1.0 Eq) and the appropriate aryl isothiocyanate (1.0 Eq) in anhydrous 1,4-dioxane (4 mL/mmol) was treated with triethylamine (1.5 Eq) at ambient room temperature. This solution was then heated under reflux for 6 hours, cooled to room temperature, and the solids that formed filtered, triturated with diethyl ether, and dried *in vacuo* to furnish the desired 2-thioxo-quinazolinone-based intermediate.

***6-Iodo-2-thioxo-3-(4-(trifluoromethyl)phenyl)-2,3-dihydroquinazolin-4(1H)-one,* 2.1a**

White solid (6.85 g, 89%); R_f (EtOAc:Hex, 1:4) 0.33; ^{1}H NMR (400 MHz, DMSO-d_6) δ 13.15 (br s, 1H, **H⁶**), 8.18 (d, J = 2.0 Hz, 1H, **H¹**), 8.08 (dd, J = 8.6, 2.0 Hz, 1H, **H²**), 7.86 (d, J = 8.2 Hz, 2H, **H⁵**), 7.54 (d, J = 8.2 Hz, 2H, **H⁴**), 7.25 (d, J = 8.6 Hz, 1H, **H³**); ^{13}C NMR (101 MHz, DMSO-d_6) δ 175.77, 158.62, 143.84, 142.92, 139.21, 135.32, 130.34 (2C), 128.99, 128.68, 126.22, 126.19, 118.38, 118.12, 87.82; LC-MS (APCI/ESI): Purity > 99%, t_R = 4.69 min, m/z [M-H]$^-$ = 446.9.

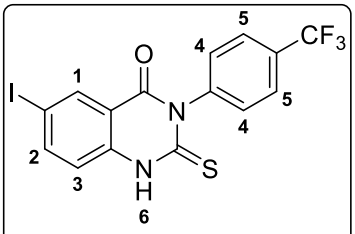

2.1a

$C_{15}H_8F_3IN_2OS$

Exact Mass: 447.9

Mwt: 448.20

6-*Iodo*-3-*phenyl*-2-*thioxo*-2,3-*dihydroquinazolin*-4(1*H*)-*one*, 2.1b

White solid (3.77 g, 87%); R_f (EtOAc:Hex, 2:8) 0.35; ^{1}H NMR (400 MHz, DMSO-d_6) δ 13.07 (br s, 1H, **H^6**), 8.19 (d, J = 2.0 Hz, 1H, **H^1**), 8.08 (dd, J = 8.6, 2.0 Hz, 1H, **H^2**), 7.51–7.45 (m, 2H, **H^5**), 7.44–7.39 (m, 1H, **H^7**), 7.30–7.23 (m, 3H, **H^{3,4}**); ^{13}C NMR (101 MHz, DMSO-d_6) δ 176.58, 159.02, 144.08, 139.59, 135.76, 129.38 (5C), 128.64, 118.72, 118.43, 88.02; LC-MS (APCI/ESI): Purity > 99%, t_R = 4.35 min, m/z $[M+H]^+$ = 380.9.

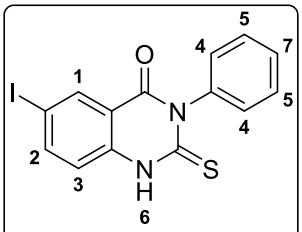

2.1b
$C_{14}H_9IN_2OS$
Exact Mass: 379.9
Mwt: 380.20

6-*Iodo*-2-*thioxo*-3-*(p-tolyl)*-2,3-*dihydroquinazolin*-4(1*H*)-*one*, 2.1c

White solid (4.22 g, 86%); R_f (EtOAc:Hex, 1:4) 0.34; ^{1}H NMR (400 MHz, DMSO-d_6) δ 13.02 (br s, 1H, **H^6**), 8.18 (d, J = 2.0 Hz, 1H, **H^1**), 8.07 (dd, J = 8.6, 2.0 Hz, 1H, **H^2**), 7.28 (d, J = 8.2 Hz, 2H, **H^4**), 7.25 (d, J = 8.6 Hz, 1H, **H^3**), 7.13 (d, J = 8.2 Hz, 2H, **H^5**), 2.38 (s, 3H, **H^7**); ^{13}C NMR (101 MHz, DMSO-d_6) δ 176.70, 159.08, 144.06, 139.50, 137.98, 137.01, 135.78, 129.94 (2C), 129.06 (2C), 118.69, 118.41, 88.05, 21.27; LC-MS (APCI/ESI): Purity > 99%, t_R = 4.48 min, m/z $[M+H]^+$ = 395.0

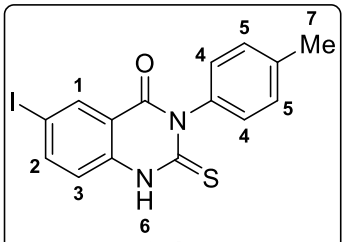

2.1c
$C_{15}H_{11}IN_2OS$
Exact Mass: 394.0
Mwt: 394.23

6-*Iodo*-2-*thioxo*-3-*[3-(trifluoromethyl)phenyl]*-2,3-*dihydroquinazolin*-4(1*H*)-*one*, 2.1d

Off-white solid (4.06 g, 86%); R_f (EtOAc:Hex, 3:7) 0.67; ^{1}H NMR (400 MHz, DMSO-d_6) δ 12.17 (br s, 1H, **H^8**), 8.20 (d, J = 2.0 Hz, 1H, **H^1**), 8.10 (dd, J = 8.6, 2.0 Hz, 1H, **H^2**), 7.83–7.70 (m, 3H, **H^{5,6,7}**), 7.64 (d, J = 7.8 Hz, 1H, **H^5**), 7.29 (d, J = 8.6 Hz, 1H, **H^3**); ^{13}C NMR (101 MHz, DMSO-d_6) δ 176.36, 159.14, 144.18, 140.40, 139.63, 135.71, 134.00, 130.62, 130.41, 130.09, 126.75, 125.57, 118.83, 118.54, 88.18; LC-MS (APCI/ESI): Purity > 99%, t_R = 4.67 min, m/z $[M+H]^+$ = 448.9.

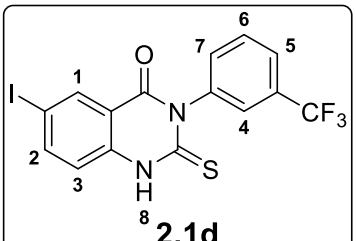

2.1d
$C_{15}H_8F_3IN_2OS$
Exact Mass: 447.9
Mwt: 448.20

General procedure 2: Synthesis of intermediates 2.2a–2.2d

A suspension of intermediate **2.1** (**a**–**d**) (1.0 Eq) in phosphorus oxychloride ($POCl_3$) (23.9 Eq) was treated with phosphorus pentachloride (PCl_5) (1.7 Eq) in one portion, stirred at room temperature for 15 minutes, and then heated at 110 °C for 12–15 hours. The solution was then cooled to room temperature and concentrated to yield a residue that was taken up in ethyl acetate (EtOAc). This mixture was added dropwise into a stirred ice/saturated sodium bicarbonate mixture. The organic layer was then separated, washed with water, brine, dried with anhydrous sodium sulfate, and concentrated under reduced pressure. The residue was then triturated by stirring in diethyl ether, filtered and dried to afford the desired intermediate **2.2** (**a**–**d**), which was used in the subsequent step without further purification.

***2-Chloro-6-iodo-3-(4-(trifluoromethyl)phenyl)quinazolin-4(3H)-one*, 2.2a**

Off-white solid (5.77 g, 85%); R_f (EtOAc:Hex, 1:9) 0.32; ^{1}H NMR (400 MHz, DMSO-d_6) δ 8.38 (d, J = 2.1 Hz, 1H, **H^1**), 8.20 (dd, J = 8.5, 2.1 Hz, 1H, **H^2**), 7.97 (d, J = 8.3 Hz, 2H, **H^5**), 7.79 (d, J = 8.2 Hz, 2H, **H^4**), 7.50 (d, J = 8.5 Hz, 1H, **H^3**); ^{13}C NMR (101 MHz, DMSO-d_6) δ 160.21, 145.82, 143.91, 143.84, 141.16, 135.03, 130.20, 130.04 (2C), 129.87, 128.83, 126.75, 126.71, 122.60, 92.78; LC-MS (APCI/ESI): Purity = 98%, t_R = 4.83 min, m/z $[M+H]^+$ = 450.9.

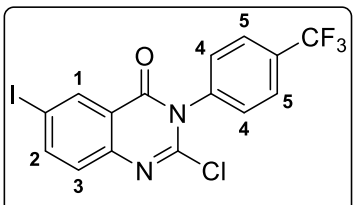

2.2a
$C_{15}H_7ClF_3IN_2O$
Exact Mass: 449.9
Mwt: 450.58

***2-Chloro-6-iodo-3-phenylquinazolin-4(3H)-one*, 2.2b**

White solid (2.91 g, 75%); R_f (EtOAc:Hex, 3:17) 0.51; ^{1}H NMR (400 MHz, DMSO-d_6) δ 8.17 (d, J = 2.1 Hz, 1H, **H^1**), 7.99 (dd, J = 8.6, 2.1 Hz, 1H, **H^2**), 7.50–7.46 (m, 2H, **H^5**), 7.46–7.40 (m, 1H, **H^6**), 7.35–7.29 (m, 2H, **H^4**), 7.07 (d, J = 8.6 Hz, 1H, **H^3**); ^{13}C NMR (101 MHz, DMSO-d_6) δ 161.47, 150.40, 143.63, 139.86, 135.98, 135.89, 129.44 (2C), 129.25 (2C), 128.63, 118.13, 117.00, 85.51; LC-MS

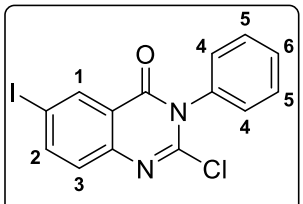

2.2b
$C_{14}H_8ClIN_2O$
Exact Mass: 381.9
Mwt: 382.59

(APCI/ESI): Purity = 97%, t_R = 4.55 min, *m/z* $[M+H]^+$ = 382.9.

2-*Chloro*-6-*iodo*-3-*(p-tolyl)quinazolin*-4*(3H)-one*, 2.2c

White solid (3.0 g, 73%); R_f (EtOAc:Hex, 1:4) 0.58; ^{1}H NMR (400 MHz, DMSO-d_6) δ 8.37 (d, *J* = 2.1 Hz, 1H, **H¹**), 8.19 (dd, *J* = 8.5, 2.1 Hz, 1H, **H²**), 7.49 (d, *J* = 8.5 Hz, 1H, **H³**), 7.36 (s, 4H, **H⁴,⁵**), 2.41 (s, 3H, **H⁶**); ^{13}C NMR (101 MHz, DMSO-d_6) δ 160.69, 146.20, 145.45, 144.03, 139.55, 135.46, 130.37 (2C), 129.77, 129.15, 128.74 (2C), 123.01, 92.99, 21.27; LC-MS (APCI/ESI): Purity = 98%, t_R = 4.74 min, *m/z* $[M+H]^+$ = 397.0

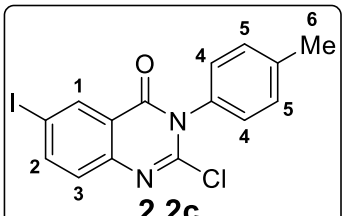

2.2c

$C_{15}H_{10}ClIN_2O$

Exact Mass: 396.0

Mwt: 396.61

2-*Chloro*-6-*iodo*-3-*(3-(trifluoromethyl)phenyl)quinazolin*-4*(3H)-one*, 2.2d

Off-white solid (2.46 g, 63%); R_f (EtOAc:Hex, 1:9) 0.35; ^{1}H NMR (400 MHz, DMSO-d_6) δ 8.40 (d, *J* = 2.1 Hz, 1H, **H¹**), 8.22 (dd, *J* = 8.5, 2.1 Hz, 1H, **H²**), 8.06 (s, 1H, **H⁴**), 7.93 (d, *J* = 7.5 Hz, 1H, **H⁵**), 7.91–7.80 (m, 2H, **H⁶,⁷**), 7.52 (d, *J* = 8.5 Hz, 1H, **H³**); ^{13}C NMR (101 MHz, DMSO-d_6) δ 160.71, 146.19, 144.52, 144.23, 138.72, 135.42, 133.63, 131.25, 130.85, 130.53, 129.21, 126.89, 126.39, 122.99, 93.14; LC-MS (APCI/ESI): Purity = 98%, t_R = 4.83 min, *m/z* $[M+H]^+$ = 450.9.

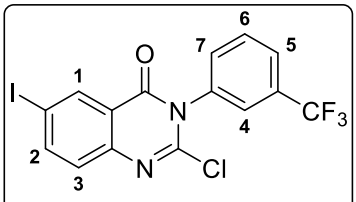

2.2d

$C_{15}H_7ClF_3IN_2O$

Exact Mass: 449.9

Mwt: 450.58

General procedure 3: Synthesis of intermediates 2.3a–2.3d

To a solution of *N,N*-Diisopropylethylamine (DIPEA) (2.0 Eq) and 4-methoxybenzylamine (1.3 Eq) in DMF, the appropriate intermediate **2.2** (**a–d**) (1.0 Eq) was added portionwise. The solution was then heated at 80 °C for 4 h, cooled to room temperature, and diluted with EtOAc. The organic layer was washed with 5% LiCl (×4), brine (×3), dried over anhydrous sodium sulfate, and concentrated to yield a yellow semisolid, which was triturated in diethyl ether, filtered, and dried *in vacuo* to furnish intermediate **2.3 (a–d)**. Where necessary, the product was purified by column chromatography.

***6-Iodo-2-((4-methoxybenzyl)amino)-3-(4-(trifluoromethyl)phenyl)quinazolin-4(3H)-one*, 2.3a**

Yellow solid (6.0 g, 87%); R_f (EtOAc:Hex, 1:4) 0.32; ^{1}H NMR (400 MHz, DMSO-d_6) δ 8.13 (d, J = 2.2 Hz, 1H, **H^1**), 7.95 (d, J = 8.2 Hz, 2H, **H^5**), 7.85 (dd, J = 8.7, 2.2 Hz, 1H, **H^2**), 7.65 (d, J = 8.1 Hz, 2H, **H^4**), 7.22 (d, J = 8.8 Hz, 2H, **H^8**), 7.09 (d, J = 8.7 Hz, 1H, **H^3**), 6.83 (d, J = 8.8 Hz, 2H, **H^9**), 6.65 (d, J = 5.9 Hz, 1H, **H^6**), 4.42 (d, J = 5.9 Hz, 2H, **H^7**), 3.69 (s, 3H, **H^{10}**); ^{13}C NMR (101 MHz, DMSO-d_6) δ 160.62, 158.18, 150.21, 149.20, 142.69, 138.67, 134.57, 131.64, 130.59 (2C), 130.10, 129.79, 128.50 (2C), 127.37, 127.34, 127.21, 119.12, 113.62 (2C), 84.35, 55.11, 43.80; LC-MS (APCI/ESI): Purity = 98%, t_R = 5.20 min, m/z $[M+H]^+$ = 552.0.

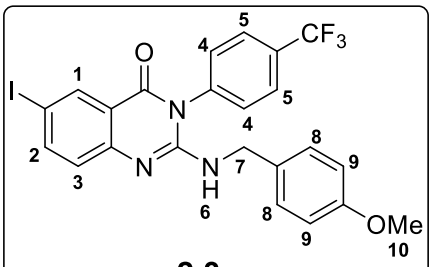

2.3a

$C_{23}H_{17}F_3IN_3O_2$

Exact Mass: 551.0

Mwt: 551.31

6-*Iodo*-2-((4-*methoxybenzyl*)*amino*)-3-*phenylquinazolin*-4(3*H*)-*one*, 2.3b

Off-white solid (2.57 g, 72%); R_f (EtOAc:Hex, 1:4) 0.20; ^{1}H NMR (400 MHz, DMSO-d_6) δ 8.15 (d, J = 2.2 Hz, 1H, **H^1**), 7.86 (dd, J = 8.6, 2.2 Hz, 1H, **H^2**), 7.64–7.58 (m, 2H, **H^5**), 7.58–7.53 (m, 1H, **H^6**), 7.41–7.36 (m, 2H, **H^4**), 7.23 (d, J = 8.8 Hz, 2H, **H^9**), 7.10 (d, J = 8.6 Hz, 1H, **H^3**), 6.84 (d, J = 8.8 Hz, 2H, **H^{10}**), 6.41 (t, J = 5.9 Hz, 1H, **H^7**), 4.44 (d, J = 5.9 Hz, 2H, **H^8**), 3.71 (s, 3H, **H^{11}**); ^{13}C NMR (101 MHz, DMSO-d_6) δ 161.01, 158.57, 150.97, 149.51, 142.92, 135.11, 135.00, 132.06, 130.63 (2C), 129.90, 129.57 (2C), 128.92 (2C), 127.56, 119.64, 114.02 (2C), 84.64, 55.49, 44.26; LC-MS (APCI/ESI): Purity = 98%, t_R = 4.87 min, m/z $[M+H]^+$ = 484.0.

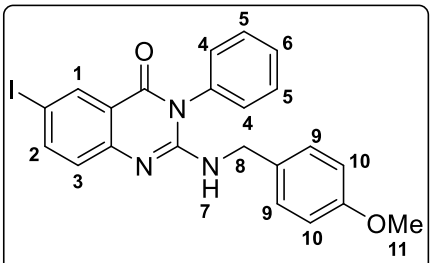

2.3b

$C_{22}H_{18}IN_3O_2$

Exact Mass: 483.0

Mwt: 483.31

6-*Iodo*-2-((4-*methoxybenzyl*)*amino*)-3-(*p-tolyl*)*quinazolin*-4(3*H*)-*one*, 2.3c

Yellow solid (3.0 g, 82%); R_f (EtOAc:Hex, 1:4) 0.31; ^{1}H NMR (400 MHz, DMSO-d_6) δ 8.14 (d, J = 2.2 Hz, 1H, **H^1**), 7.85 (dd, J = 8.6, 2.2 Hz, 1H, **H^2**), 7.40 (d, J = 8.6 Hz, 2H, **H^9**), 7.27–7.21 (m, 4H, **H^{4,5}**), 7.10 (d, J = 8.6 Hz, 1H, **H^3**), 6.84 (d, J = 8.6 Hz, 2H, **H^{10}**), 6.40 (t, J = 5.9 Hz, 1H, **H^7**), 4.43 (d, J = 5.9 Hz, 2H, **H^8**), 3.71 (s, 3H, **H^{11}**), 2.42 (s, 3H, **H^6**); ^{13}C NMR (101 MHz,

DMSO-d_6) δ 161.08, 158.57, 151.11, 149.51, 142.88, 139.34, 135.01, 132.42, 132.11, 131.20 (2C), 129.26 (2C), 128.98 (2C), 127.56, 119.63, 114.01 (2C), 84.61, 55.49, 44.23, 21.34; LC-MS (APCI/ESI): Purity = 99%, t_R = 4.90 min, *m/z* $[M+H]^+$ = 498.1.

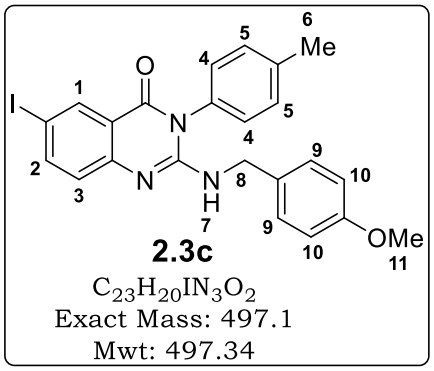

***6-Iodo-2-((4-methoxybenzyl)amino)-3-(3-(trifluoromethyl)phenyl)quinazolin-4(3H)-one*, 2.3d**

Yellow solid (1.67 g, 58%); R_f (EtOAc:Hex, 1:4) 0.33; ^{1}H NMR (400 MHz, DMSO-d_6) δ 8.15 (d, *J* = 2.1 Hz, 1H, **H^{1}**), 7.95–7.79 (m, 4H, **H^{2,4,6,7}**), 7.74 (d, *J* = 8.7 Hz, 1H, **H^{5}**), 7.25 (d, *J* = 8.7 Hz, 2H, **H^{10}**), 7.11 (d, *J* = 8.6 Hz, 1H, **H^{3}**), 6.85 (d, *J* = 8.7 Hz, 2H, **H^{11}**), 6.69 (t, *J* = 5.8 Hz, 1H, **H^{8}**), 4.49 (d, *J* = 5.8 Hz, 2H, **H^{9}**), 3.71 (s, 3H, **H^{12}**); ^{13}C NMR (101 MHz, DMSO-d_6) δ 161.13, 158.58, 150.76, 149.60, 143.03, 136.10, 134.99, 134.14, 132.04, 131.76, 128.88 (2C), 128.75, 127.59, 127.12, 126.84, 125.66, 119.60, 113.99 (2C), 84.67, 55.50, 44.22; LC-MS (APCI/ESI): Purity = 97%, t_R = 5.16 min, *m/z* $[M+H]^+$ = 552.0.

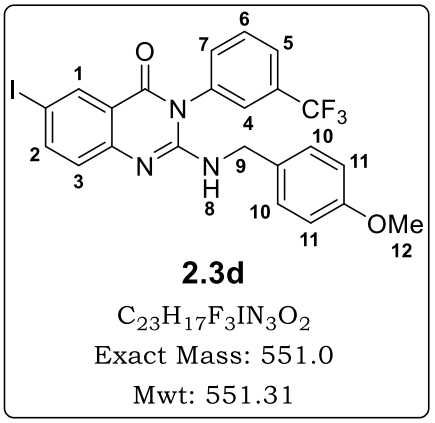

General procedure 4: Synthesis of intermediates 2.4a–2.4d

The appropriate intermediate **2.3** (**a–d**) (1.0 Eq) was dissolved in trifluoroacetic acid (TFA) (63.4 Eq) and heated under reflux at 85 °C for 48 hours, or under microwave conditions at 110 °C for 20 minutes. The solution was then cooled to room temperature, concentrated under reduced pressure, and the residue resuspended in DCM. This suspension was added portionwise to a stirred ice/saturated sodium bicarbonate mixture, and the organic phase was separated together with the solids. Diethyl ether (Et_2O) was added to the DCM suspension in a ratio of DCM:Et_2O (1:1), followed by filtration of the solids, which were then triturated with Et_2O, and dried to afford the desired intermediate **2.4** (**a–d**).

***2-Amino-6-iodo-3-(4-(trifluoromethyl)phenyl)quinazolin-4(3H)-one*, 2.4a**

White solid (3.96 g, 85%); R_f (EtOAc:Hex, 2:3) 0.22; ^{1}H NMR (400 MHz, DMSO-d_6) δ 8.12 (d, J = 2.2 Hz, 1H, **H^1**), 7.91 (d, J = 8.2 Hz, 2H, **H^5**), 7.86 (dd, J = 8.7, 2.2 Hz, 1H, **H^2**), 7.62 (d, J = 8.1 Hz, 2H, **H^4**), 7.06 (d, J = 8.7 Hz, 1H, **H^3**), 6.61 (br s, 2H, **H^6**); ^{13}C NMR (101 MHz, DMSO-d_6) δ 160.63, 151.82, 149.58, 142.69, 139.07, 134.64, 130.21 (2C), 129.97, 129.66, 127.22, 127.18, 126.41, 118.83, 84.06; LC-MS (APCI/ESI): Purity = 99%, t_R = 4.6 min, m/z $[M+H]^+$ = 432.0.

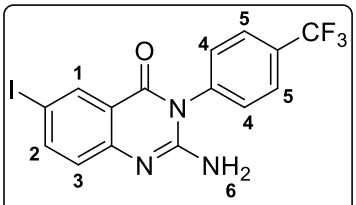

2.4a
$C_{15}H_9F_3IN_3O$
Exact Mass: 431.0
Mwt: 431.16

***2-Amino-6-iodo-3-phenylquinazolin-4(3H)-one*, 2.4b**

Light brown crystals (1.06 g, 69%); R_f (EtOAc:Hex, 4:1) 0.38; ^{1}H NMR (400 MHz, DMSO-d_6) δ 8.14 (d, J = 2.2 Hz, 1H, **H^1**), 7.86 (dd, J = 8.7, 2.2 Hz, 1H, **H^2**), 7.62–7.55 (m, 2H, **H^5**), 7.55–7.49 (m, 1H, **H^6**), 7.41–7.32 (m, 2H, **H^4**), 7.07 (d, J = 8.7 Hz, 1H, **H^3**), 6.39 (s, 2H, **H^7**); ^{13}C NMR (101 MHz, DMSO-d_6) δ 161.07, 152.61, 150.07, 142.89, 135.65, 135.05, 130.46 (2C), 129.75, 129.20 (2C), 126.92, 119.45, 84.31; LC-MS (APCI/ESI): Purity = 97%, t_R = 4.23 min, m/z $[M+H]^+$ = 364.0.

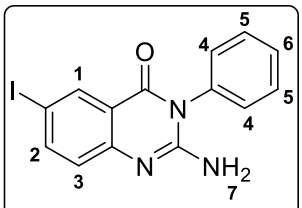

2.4b
$C_{14}H_{10}IN_3O$
Exact Mass: 363.0
Mwt: 363.16

***2-Amino-6-iodo-3-(p-tolyl)quinazolin-4(3H)-one*, 2.4c**

White solid (1.88 g, 86%); R_f (EtOAc:Hex, 1:1) 0.39; ^{1}H NMR (400 MHz, DMSO-d_6) δ 8.13 (d, J = 2.2 Hz, 1H, **H^1**), 7.84 (dd, J = 8.7, 2.2 Hz, 1H, **H^2**), 7.37 (d, J = 8.5 Hz, 2H, **H^4**), 7.22 (d, J = 8.5 Hz, 2H, **H^5**), 7.05 (d, J = 8.7 Hz, 1H, **H^3**), 6.37 (br s, 2H, **H^7**), 2.40 (s, 3H, **H^6**); ^{13}C NMR (101 MHz, DMSO-d_6) δ 161.14, 152.78, 150.07, 142.85, 139.17, 135.06, 133.01, 131.00 (2C), 128.90 (2C), 126.91, 119.43, 84.28, 21.33; LC-MS (APCI/ESI): Purity = 99%, t_R = 4.34 min, m/z $[M+H]^+$ = 378.0.

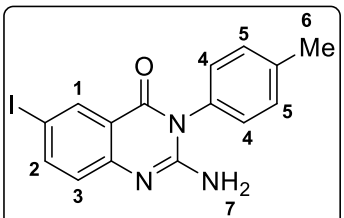

2.4c
$C_{15}H_{12}IN_3O$
Exact Mass: 377.0
Mwt: 377.19

***2-Amino-6-iodo-3-(3-(trifluoromethyl)phenyl)quinazolin-4(3H)-one*, 2.4d**

White solid (0.97 g, 78%); R_f (EtOAc:Hex, 1:1) 0.30; ^{1}H NMR (400 MHz, DMSO-d_6) δ 8.14 (d, J = 2.1 Hz, 1H, **H^1**), 7.91–7.83 (m, 3H, **H^{2,4,5}**), 7.80 (t, J = 7.9 Hz, 1H, **H^6**), 7.70 (d, J = 7.9 Hz, 1H, **H^5**), 7.07 (d, J = 8.7 Hz, 1H, **H^3**), 6.59 (br s, 2H, **H^8**); ^{13}C NMR (101 MHz, DMSO-d_6) δ 161.20, 152.38, 150.21, 142.99, 136.54, 135.03, 133.78, 131.59, 131.31, 130.99, 126.93, 126.71, 122.96, 119.34, 84.28; LC-MS (APCI/ESI): Purity = 98%, t_R = 4.65 min, m/z $[M+H]^+$ = 432.0.

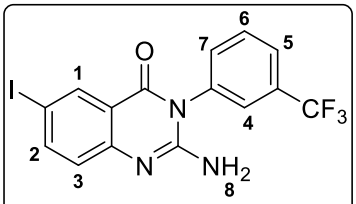

2.4d
$C_{15}H_9F_3IN_3O$
Exact Mass: 431.0
Mwt: 431.16

General procedure 5: Suzuki-Miyaura cross-coupling reaction for the synthesis of SAR 1 2-aminoquinazolinone target compounds 2–31

To a solution of 2-amino-6-iodo-3-(4-(trifluoromethyl)phenyl)quinazolin-4(3*H*)-one [**2.4a**] (0.2 g, 0.46 mmol, 1.0 Eq) and the appropriate arylboronic acid or ester (1.2 Eq) in 1,4-dioxane (1.84 mL), was added a solution of cesium carbonate (3.0 Eq) in water (0.46 mL). This mixture was treated with $PdCl_2$(dppf)-CH_2Cl_2 (0.1 Eq), and heated at 80 °C for 1–3 hours, while monitoring the reaction for completeness using TLC and LC-MS. After cooling to room temperature, the mixture was diluted with EtOAc, then washed with water, brine, dried over anhydrous sodium sulphate, and filtered through a pad of celite. The filtrate was then concentrated under reduced pressure to yield a residue that was purified by flash column chromatography using Biotage Isolera One® machine, SiO_2 (10 g cartridge), and EtOAc/Hexane mixture, with fractions being collected at the λ_{max} (determined by LC-MS) and monitored at 254 nm. Finally, the solvents were rotary evaporated to give a solid that was then triturated with Et_2O or absolute ethanol, filtered, and dried to furnish the desired target analogue.

***2-Amino-6-(3-(methylsulfonyl)phenyl)-3-(4-(trifluoromethyl)phenyl)quinazolin-4(3H)-one*, 2**

Off-white solid (0.164 g, 77%); m.p. 251.1–255.0 °C; R_f (EtOAc:Hex, 1:1) 0.41; ^{1}H NMR (400 MHz, DMSO-d_6) δ 8.22 (d, J = 2.1 Hz, 1H, **H^1**), 8.18 (t, J = 1.7 Hz, 1H, **H^7**), 8.11 (ddd, J = 7.8, 1.8, 1.1 Hz, 1H, **H^{10}**), 8.09 (dd, J = 8.6,

2.4 Hz, 1H, **H²**), 7.94 (d, *J* = 8.3 Hz, 2H, **H⁵**), 7.88 (ddd, *J* = 7.8, 1.8, 1.0 Hz, 1H, **H⁸**), 7.73 (t, *J* = 7.8 Hz, 1H, **H⁹**), 7.65 (d, *J* = 8.1 Hz, 2H, **H⁴**), 7.37 (d, *J* = 8.4 Hz, 1H, **H³**), 6.57 (br s, 2H, **H⁶**), 3.29 (s, 3H, **H¹¹**); ^{13}C NMR (101 MHz, DMSO-d_6) δ 161.87, 151.80, 150.51, 141.85, 140.59, 139.32, 133.28, 131.48, 131.28, 130.27 (3C), 129.92, 129.61, 127.23, 127.20, 125.45, 125.03, 124.59, 124.49, 117.03, 43.57; LC-MS (APCI/ESI): Purity > 98%, t_R = 4.29 min, *m/z* $[M+H]^+$ = 460.1.

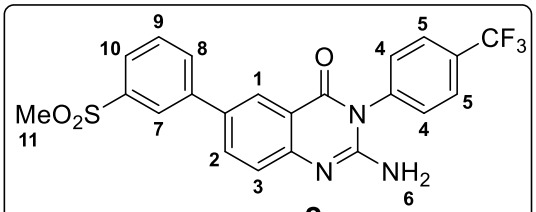

2

$C_{22}H_{16}F_3N_3O_3S$
Exact Mass: 459.1
Mwt: 459.44

***2-Amino-6-(3-(methylsulfinyl)phenyl)-3-(4-(trifluoromethyl)phenyl)quinazolin-4(3H)-one*, 3**

Off-white solid (0.115 g, 57%); m.p. 173.1–175.0 °C; R_f (MeOH:DCM, 1:24) 0.20; ^{1}H NMR (400 MHz, DMSO-d_6) δ 8.20 (d, *J* = 2.2 Hz, 1H, **H¹**), 8.03 (dd, *J* = 8.6, 2.2 Hz, 1H, **H²**), 7.98 (t, *J* = 2.2 Hz, 1H, **H⁷**), 7.95 (d, *J* = 8.2 Hz, 2H, **H⁵**), 7.86 (dt, *J* = 6.6, 2.2 Hz, 1H, **H¹⁰**), 7.70–7.62 (m, 4H, **H⁴,⁸,⁹**), 7.37 (d, *J* = 8.6 Hz, 1H, **H³**), 6.55 (br s, 2H, **H⁶**), 2.81 (s, 3H, **H¹¹**); ^{13}C NMR (101 MHz, DMSO-d_6) δ 162.29, 152.09, 150.69, 147.90, 140.82, 139.74, 133.65, 132.56, 130.67 (2C), 130.46, 130.30, 129.99, 128.87, 127.61, 127.58, 125.35, 124.75, 122.64, 121.50, 117.38, 43.75; LC-MS (APCI/ESI): Purity = 99%, t_R = 4.28 min, *m/z* $[M+H]^+$ = 444.1.

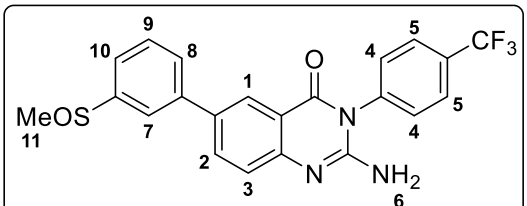

3

$C_{22}H_{16}F_3N_3O_2S$
Exact Mass: 443.1
Mwt: 443.44

***2-Amino-6-phenyl-3-(4-(trifluoromethyl)phenyl)quinazolin-4(3H)-one*, 4**

Off-white solid (0.097 g, 55%); m.p. 294.4–300.6 °C; R_f (EtOAc:Hex, 3:7) 0.30; ^{1}H NMR (300 MHz, DMSO-d_6) δ 8.14 (d, *J* = 2.3 Hz, 1H, **H¹**), 7.97 (dd, *J* = 8.6, 2.4 Hz, 1H, **H²**), 7.95 (d, *J* = 8.3 Hz, 2H, **H⁵**), 7.69 (dd, *J* = 8.6, 2.4 Hz, 2H, **H⁷**), 7.66 (d, *J* = 8.1 Hz, 2H, **H⁴**), 7.48 (t, *J* = 7.5 Hz, 2H, **H⁸**), 7.40–7.32 (m, 2H, **H³,⁹**), 6.52 (br s, 2H, **H⁶**); ^{13}C NMR (101 MHz, DMSO-d_6) δ 162.34, 151.85,

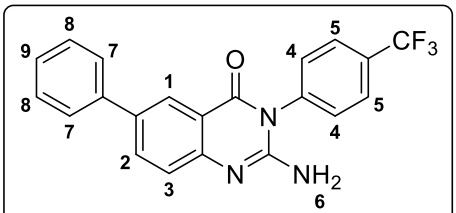

4

$C_{21}H_{14}F_3N_3O$
Exact Mass: 381.1
Mwt: 381.36

150.20, 139.86, 139.78, 133.84, 133.60, 130.68 (2C), 130.28, 129.96, 129.54 (2C), 127.65, 127.58, 127.55, 126.72 (2C), 125.22, 124.33, 117.31; LC-MS (APCI/ESI): Purity = 98%, t_R = 4.68 min, *m/z* $[M+H]^+$ = 382.1.

***3-(2-Amino-4-oxo-3-(4-(trifluoromethyl)phenyl)-3,4-dihydroquinazolin-6-yl)benzamide*, 5**

Off-white solid (0.110 g, 56%); m.p. 299.7–301.2 °C; R_f (MeOH:DCM, 1:24) 0.41; ^{1}H NMR (400 MHz, DMSO-d_6) δ 8.22 (d, *J* = 2.3 Hz, 1H, **H^1**), 8.20 (t, *J* = 1.6 Hz, 1H, **H^7**), 8.13 (br s, 1H, **H^{11a}**), 8.02 (dd, *J* = 8.6, 2.3 Hz, 1H, **H^2**), 7.94 (d, *J* = 8.4 Hz, 2H, **H^5**), 7.88–7.81 (m, 2H, **H^{8,10}**), 7.66 (d, *J* = 8.2 Hz, 2H, **H^4**), 7.54 (t, *J* = 7.7 Hz, 1H, **H^9**), 7.37 (d, *J* = 8.6 Hz, 1H, **H^3**), 7.36 (br s, 1H, **H^{11b}**), 6.53 (br s, 2H, **H^6**); ^{13}C NMR (101 MHz, DMSO-d_6) δ 168.30, 162.34, 151.97, 150.43, 139.82, 135.52, 133.68, 133.19, 130.68 (2C), 130.29, 129.98, 129.52, 129.42, 127.61, 127.58, 126.79, 125.93, 125.70, 125.25, 124.66, 117.37; LC-MS (APCI/ESI): Purity > 99%, t_R = 4.25 min, *m/z* $[M+H]^+$ = 425.1.

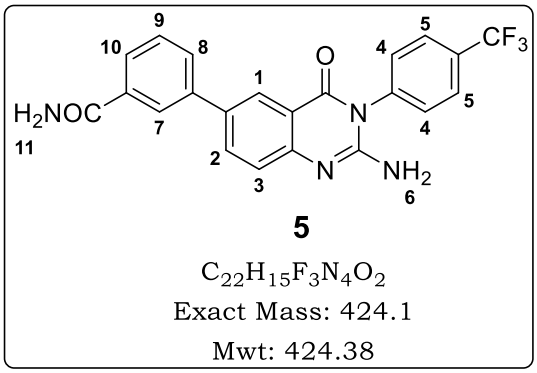

5

$C_{22}H_{15}F_3N_4O_2$

Exact Mass: 424.1

Mwt: 424.38

***3-(2-Amino-4-oxo-3-(4-(trifluoromethyl)phenyl)-3,4-dihydroquinazolin-6-yl)benzenesulfonamide*, 6**

Off-white solid (0.161 g, 71%); m.p. 309.5–313.0 °C; R_f (MeOH:DCM, 1:24) 0.24; ^{1}H NMR (400 MHz, DMSO-d_6) δ 8.21 (d, *J* = 2.1 Hz, 1H, **H^1**), 8.15 (t, *J* = 1.7 Hz, 1H, **H^7**), 8.00 (dd, *J* = 8.6, 2.1 Hz, 1H, **H^2**), 7.95 (d, *J* = 8.3 Hz, 2H, **H^5**), 7.93 (ddd, *J* = 7.7, 1.9, 1.1 Hz, 1H, **H^{10}**), 7.79 (ddd, *J* = 7.8, 1.7, 1.1 Hz, 1H, **H^8**), 7.70–7.63 (m, 3H, **H^{4,9}**), 7.43–7.37 (m, 3H, **H^{3,11}**), 6.57 (br s, 2H, **H^6**); ^{13}C NMR (101 MHz, DMSO-d_6) δ 161.90, 151.76, 150.40, 145.05, 140.12, 139.33, 133.06, 131.82, 130.27 (2C), 129.85, 129.60, 129.48, 127.23, 127.20, 125.53, 125.07, 124.32, 124.14, 123.33, 117.05; LC-MS (APCI/ESI): Purity > 99%, t_R = 4.18 min, *m/z* $[M+H]^+$ = 461.1.

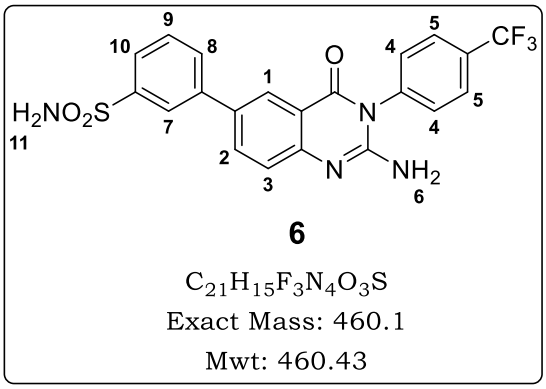

6

$C_{21}H_{15}F_3N_4O_3S$

Exact Mass: 460.1

Mwt: 460.43

3-(2-Amino-4-oxo-3-(4-(trifluoromethyl)phenyl)-3,4-dihydroquinazolin-6-yl)benzonitrile, 7

White solid (0.110 g, 58%); m.p. 300.6–304.7 °C; R_f (EtOAc:Hex, 1:1) 0.4; ^{1}H NMR (400 MHz, DMSO-d_6) δ 8.20 (d, J = 2.0 Hz, 1H, **H^1**), 8.17 (t, J = 1.5 Hz, 1H, **H^7**), 8.04 (ddd, J = 7.5, 1.9, 1.1 Hz, 1H, **H^{10}**), 8.03 (dd, J = 8.6, 2.4 Hz, 1H, **H^2**), 7.95 (d, J = 8.3 Hz, 2H, **H^5**), 7.79 (dt, J = 7.7, 1.3 Hz, 1H, **H^8**), 7.70–7.63 (m, 3H, **H^{4,9}**), 7.37 (d, J = 8.6 Hz, 1H, **H^3**), 6.63 (br s, 2H, **H^6**); ^{13}C NMR (101 MHz, DMSO-d_6) δ 161.76, 151.80, 150.20, 140.59, 139.25, 133.27, 131.24, 131.13, 130.78, 130.31, 130.27 (2C), 129.88, 129.63, 127.24, 127.20, 125.53, 124.79, 124.64, 118.87, 116.97, 112.30; LC-MS (APCI/ESI): Purity > 99%, t_R = 4.48 min, m/z $[M+H]^+$ = 407.1.

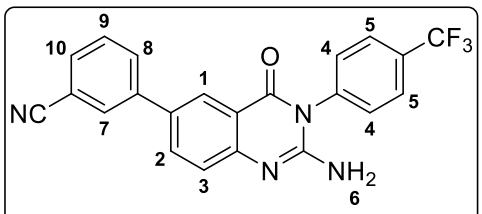

7
$C_{22}H_{13}F_3N_4O$
Exact Mass: 406.1
Mwt: 406.37

2-Amino-6-(3-chlorophenyl)-3-(4-(trifluoromethyl)phenyl)quinazolin-4(3H)-one, 8

White solid (0.128 g, 67%); m.p. 276.1–280.4 °C; R_f (EtOAc:Hex, 1:1) 0.59; ^{1}H NMR (400 MHz, DMSO-d_6) δ 8.13 (d, J = 2.3 Hz, 1H, **H^1**), 7.98 (dd, J = 8.6, 2.4 Hz, 1H, **H^2**), 7.94 (d, J = 8.3 Hz, 2H, **H^5**), 7.72 (t, J = 1.9 Hz, 1H, **H^7**), 7.67 (ddd, J = 7.7, 1.8, 1.1 Hz, 1H, **H^{10}**), 7.65 (d, J = 8.1 Hz, 2H, **H^4**), 7.49 (t, J = 7.9 Hz, 1H, **H^9**), 7.40 (ddd, J = 8.0, 2.1, 1.0 Hz, 1H, **H^8**), 7.35 (d, J = 8.6 Hz, 1H, **H^3**), 6.55 (br s, 2H, **H^6**); ^{13}C NMR (101 MHz, DMSO-d_6) δ 162.25, 152.09, 150.70, 142.07, 139.72, 134.33, 133.62, 132.17, 131.36, 130.67 (2C), 130.30, 129.99, 127.60, 127.57, 127.44, 126.42, 125.45, 125.30, 124.74, 117.33; LC-MS (APCI/ESI): Purity = 98%, t_R = 4.89 min, m/z $[M+H]^+$ = 416.1.

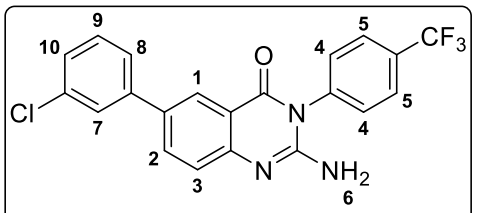

8
$C_{21}H_{13}ClF_3N_3O$
Exact Mass: 415.1
Mwt: 415.80

2-Amino-6-(2-chlorophenyl)-3-(4-(trifluoromethyl)phenyl)quinazolin-4(3H)-one, 9

White solid (0.151 g, 79%); m.p. 247.5–252.7 °C; R_f (EtOAc:Hex, 1:1) 0.49; ^{1}H NMR (400 MHz, DMSO-d_6) δ 7.94 (d, J = 8.4 Hz, 2H, **H^5**), 7.92 (d, J = 2.2 Hz, 1H, **H^1**), 7.70 (dd, J = 8.5, 2.2 Hz, 1H, **H^2**), 7.65 (d, J = 8.2 Hz, 2H, **H^4**), 7.57 (dd, J = 7.5, 1.2 Hz, 1H, **H^{10}**), 7.48–7.37 (m, 3H, **H^{7,8,9}**), 7.34 (d, J = 8.5

Hz, 1H, **H³**), 6.54 (br s, 2H, **H⁶**); ^{13}C NMR (101 MHz, DMSO-d_6) δ 162.21, 152.12, 150.32, 139.74, 139.57, 136.08, 132.26, 131.92, 131.87, 130.68 (2C), 130.39, 130.29, 129.97, 129.62, 128.13, 127.57, 127.54, 127.36, 124.34, 116.74; LC-MS (APCI/ESI): Purity = 97%, t_R = 4.73 min, *m/z* $[M+H]^+$ = 416.1.

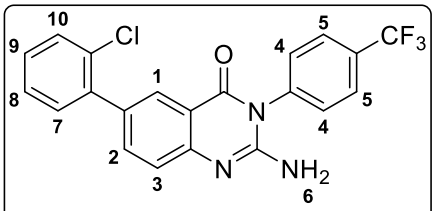

9
$C_{21}H_{13}ClF_3N_3O$
Exact Mass: 415.1
Mwt: 415.80

***2-Amino-6-(4-chlorophenyl)-3-(4-(trifluoromethyl)phenyl)quinazolin-4(3H)-one,* 10**

White solid (0.126 g, 66%); m.p. 303.5–309.1 °C; R_f (EtOAc:Hex, 1:1) 0.58; ^{1}H NMR (400 MHz, DMSO-d_6) δ 8.13 (d, *J* = 2.2 Hz, 1H, **H¹**), 7.95 (dd, *J* = 8.6, 2.4 Hz, 1H, **H²**), 7.94 (d, *J* = 8.2 Hz, 2H, **H⁵**), 7.72 (d, *J* = 8.7 Hz, 2H, **H⁸**), 7.65 (d, *J* = 8.1 Hz, 2H, **H⁴**), 7.51 (d, *J* = 8.7 Hz, 2H, **H⁷**), 7.35 (d, *J* = 8.6 Hz, 1H, **H³**), 6.54 (br s, 2H, **H⁶**); ^{13}C NMR (101 MHz, DMSO-d_6) δ 162.27, 152.00, 150.47, 139.74, 138.67, 133.44, 132.45, 132.40, 130.67 (2C), 130.29, 129.98, 129.46 (2C), 128.47 (2C), 127.59, 127.56, 125.30, 124.41, 117.33; LC-MS (APCI/ESI): Purity = 95%, t_R = 4.89 min, *m/z* $[M+H]^+$ = 416.1.

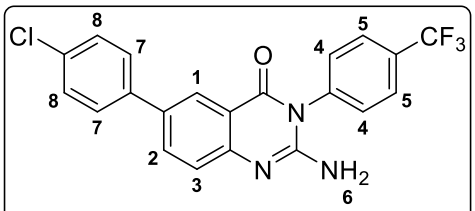

10
$C_{21}H_{13}ClF_3N_3O$
Exact Mass: 415.1
Mwt: 415.80

***2-Amino-6-(3,4-dichlorophenyl)-3-(4-(trifluoromethyl)phenyl)quinazolin-4(3H)-one,* 11**

White solid (0.120 g, 58%); m.p. 270.9–275.1 °C; R_f (EtOAc:Hex, 3:7) 0.45; ^{1}H NMR (400 MHz, DMSO-d_6) δ 8.04 (d, *J* = 2.3 Hz, 1H, **H¹**), 7.88 (dd, *J* = 8.6, 2.4 Hz, 1H, **H²**), 7.85–7.80 (m, 3H, **H⁵,⁷**), 7.59–7.57 (m, 2H, **H⁸,⁹**), 7.54 (d, *J* = 8.2 Hz, 2H, **H⁴**), 7.23 (d, *J* = 8.6 Hz, 1H, **H³**), 6.47 (br s, 2H, **H⁶**); ^{13}C NMR (101 MHz, DMSO-d_6) δ 162.20, 152.19, 150.88, 140.54, 139.69, 133.52, 132.27, 131.55, 131.04, 130.66 (2C), 130.31, 130.24, 130.00, 128.46, 127.62, 127.58, 126.95, 125.33, 124.84, 117.33; LC-MS (APCI/ESI): Purity = 98%, t_R = 5.17 min, *m/z* $[M+H]^+$ = 450.0.

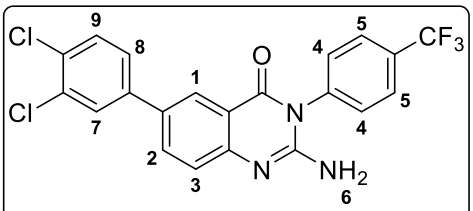

11
$C_{21}H_{12}Cl_2F_3N_3O$
Exact Mass: 449.0
Mwt: 450.24

***2-Amino-6-(3-fluorophenyl)-3-(4-(trifluoromethyl)phenyl)quinazolin-4(3H)-one*, 12**

Off-white solid (0.103 g, 56%); m.p. 286.4–292.2 °C; R_f (EtOAc:Hex, 1:1) 0.47; ^{1}H NMR (400 MHz, DMSO-d_6) δ 8.04 (d, J = 2.1 Hz, 1H, **H^1**), 7.88 (dd, J = 8.6, 2.2 Hz, 1H, **H^2**), 7.83 (d, J = 8.2 Hz, 2H, **H^5**), 7.54 (d, J = 8.1 Hz, 2H, **H^4**), 7.47–7.34 (m, 3H, **H^{7,8,10}**), 7.24 (d, J = 8.6 Hz, 1H, **H^3**), 7.06 (t, J = 8.0 Hz, 1H, **H^9**), 6.44 (br s, 2H, **H^6**); ^{13}C NMR (101 MHz, DMSO-d_6) δ 164.49, 162.26, 152.07, 150.67, 142.40, 139.74, 133.61, 132.35, 131.49, 130.67 (2C), 130.30, 127.57, 125.26, 124.69, 122.78, 117.30, 114.40, 114.19, 113.49, 113.27; LC-MS (APCI/ESI): Purity = 98%, t_R = 4.70 min, m/z $[M+H]^+$ = 400.1.

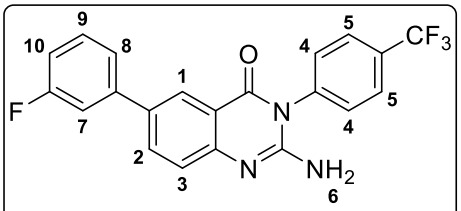

12
$C_{21}H_{13}F_4N_3O$
Exact Mass: 399.1
Mwt: 399.35

***2-amino-6-(3-(trifluoromethyl)phenyl)-3-(4-(trifluoromethyl)phenyl)quinazolin-4(3H)-one*, 13**

As an off-white solid (0.114 g, 55%); m.p. 241.4–246.1 °C; R_f (EtOAc:Hex, 1:1) 0.53; ^{1}H NMR (400 MHz, DMSO-d_6) δ 8.18 (d, J = 2.4 Hz, 1H, **H^1**), 8.03 (dd, J = 8.6, 2.4 Hz, 1H, **H^2**), 8.01–7.98 (m, 1H, **H^{10}**), 7.96 (s, 1H, **H^7**), 7.94 (d, J = 8.2 Hz, 2H, **H^5**), 7.72–7.68 (m, 2H, **H^{8,9}**), 7.66 (d, J = 8.1 Hz, 2H, **H^4**), 7.37 (d, J = 8.6 Hz, 1H, **H^3**), 6.57 (br s, 2H, **H^6**); ^{13}C NMR (101 MHz, DMSO-d_6) δ 162.25, 152.16, 150.81, 140.96, 139.72, 133.71, 132.08, 130.86, 130.66 (2C), 130.52, 130.32, 130.00, 127.61, 127.58, 125.39, 124.92, 124.19, 124.16, 123.06, 123.03, 117.38; LC-MS (APCI/ESI): Purity = 99%, t_R = 4.85 min, m/z $[M+H]^+$ = 450.1.

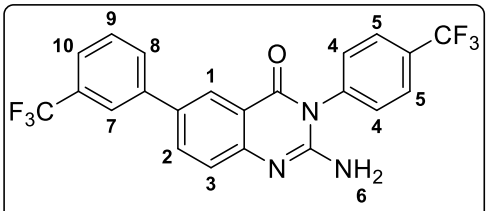

13
$C_{22}H_{13}F_6N_3O$
Exact Mass: 449.1
Mwt: 449.36

***2-amino-6-(3-aminophenyl)-3-(4-(trifluoromethyl)phenyl)quinazolin-4(3H)-one*, 14**

Off-white solid (0.120 g, 66%); m.p. 281.1–284.2 °C; R_f (EtOAc:100%) 0.54; ^{1}H NMR (400 MHz, DMSO-d_6) δ 8.06 (d, J = 2.3 Hz, 1H, **H^1**), 7.94 (d, J = 8.2 Hz, 2H, **H^5**), 7.86 (dd, J = 8.6, 2.3 Hz, 1H, **H^2**), 7.65 (d, J = 8.1 Hz, 2H, **H^4**), 7.32 (d, J = 8.5 Hz, 1H, **H^3**), 7.10 (t, J = 7.8 Hz, 1H, **H^9**), 6.89 (t, J = 1.9 Hz, 1H, **H^7**), 6.80 (ddd, J = 7.6, 1.8, 1.0 Hz, 1H, **H^8**), 6.55 (ddd, J = 8.0, 2.2, 0.9

Hz, 1H, **H10**), 6.46 (br s, 2H, **H6**), 5.14 (br s, 2H, **H11**); ^{13}C NMR (101 MHz, DMSO-d_6) δ 162.39, 151.68, 149.96, 149.71, 140.45, 139.85, 134.67, 133.39, 130.70 (2C), 130.25, 129.99, 129.93, 127.56, 127.53, 124.99, 123.92, 117.20, 114.33, 113.47, 112.08; LC-MS (APCI/ESI): Purity > 99%, t_R = 4.30 min, *m/z* $[M+H]^+$ = 397.1.

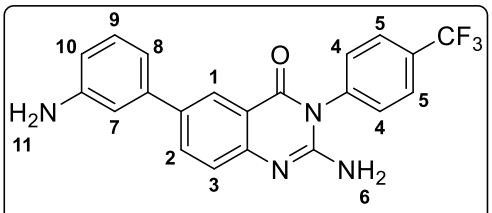

14
$C_{21}H_{15}F_3N_4O$
Exact Mass: 396.1
Mwt: 396.37

***2-amino-6-(3-methoxyphenyl)-3-(4-(trifluoromethyl)phenyl)quinazolin-4(3H)-one*, 15**

Off-white solid (0.125 g, 66%); m.p. 272.9–278.9 °C; R_f (EtOAc:Hex, 3:2) 0.41; ^{1}H NMR (400 MHz, DMSO-d_6) δ 8.12 (d, *J* = 2.3 Hz, 1H, **H1**), 7.96 (dd, *J* = 8.6, 2.4 Hz, 1H, **H2**), 7.94 (d, *J* = 8.3 Hz, 2H, **H5**), 7.65 (d, *J* = 8.1 Hz, 2H, **H4**), 7.38 (t, *J* = 8.0 Hz, 1H, **H9**), 7.34 (d, *J* = 8.6 Hz, 1H, **H3**), 7.24 (ddd, *J* = 7.7, 1.7, 0.9 Hz, 1H, **H8**), 7.18 (t, *J* = 1.8 Hz, 1H, **H7**), 6.93 (ddd, *J* = 8.2, 2.5, 0.9 Hz, 1H, **H10**), 6.51 (br s, 2H, **H6**), 3.83 (s, 3H, **H11**); ^{13}C NMR (101 MHz, DMSO-d_6) δ 161.92, 159.95, 151.47, 149.93, 141.02, 139.39, 133.32, 130.28 (2C), 130.20, 129.88, 129.56, 127.18, 127.14, 124.74, 124.62, 124.06, 118.72, 116.85, 112.87, 111.87, 55.24; LC-MS (APCI/ESI): Purity = 98%, t_R = 4.65 min, *m/z* $[M+H]^+$ = 412.1.

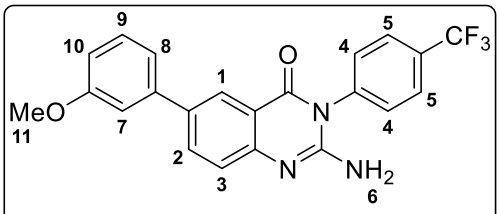

15
$C_{22}H_{16}F_3N_3O_2$
Exact Mass: 411.1
Mwt: 411.38

***2-amino-6-(3-(tert-butyl)phenyl)-3-(4-(trifluoromethyl)phenyl)quinazolin-4(3H)-one*, 16**

As an off-white solid (0.099 g, 49%); m.p. 256.1–258.9 °C; R_f (EtOAc:Hex, 3:7) 0.45; ^{1}H NMR (400 MHz, DMSO-d_6) δ 8.11 (d, *J* = 2.1 Hz, 1H, **H1**), 7.95 (dd, *J* = 8.5, 2.5 Hz, 1H, **H2**), 7.94 (d, *J* = 8.3 Hz, 2H, **H5**), 7.70–7.60 (m, 3H, **H4,7**), 7.51–7.44 (m, 1H, **H8**), 7.41–7.37 (m, 2H, **H9,10**), 7.35 (d, *J* = 8.5 Hz, 1H, **H3**), 6.49 (br s, 2H, **H6**), 1.34 (s, 9H, **H11**); ^{13}C NMR (101 MHz, DMSO-d_6) δ 162.35, 151.89, 151.78, 150.12, 139.80, 139.70, 134.45,

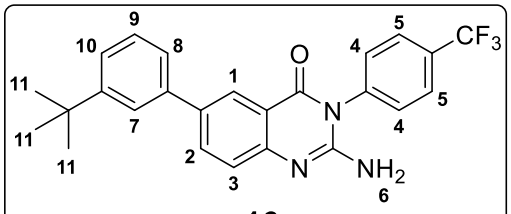

16
$C_{25}H_{22}F_3N_3O$
Exact Mass: 437.2
Mwt: 437.47

133.84, 130.69 (2C), 130.27, 129.95, 129.28, 127.56, 127.53, 125.16, 124.62, 124.35, 124.08, 123.51, 117.27, 35.01, 31.65 (3C); LC-MS (APCI/ESI): Purity = 98%, t_R = 5.27 min, *m/z* $[M+H]^+$ = 438.2.

***2-amino-6-(4-(tert-butyl)phenyl)-3-(4-(trifluoromethyl)phenyl)quinazolin-4(3H)-one*, 17**

Off-white solid (0.123 g, 61%); m.p. 268.1–272.3 °C; R_f (EtOAc:Hex, 3:7) 0.46; ^{1}H NMR (400 MHz, DMSO-d_6) δ 8.11 (d, *J* = 2.3 Hz, 1H, **H^1**), 7.97–7.91 (m, 3H, **H^{2,5}**), 7.65 (d, *J* = 8.1 Hz, 2H, **H^4**), 7.61 (d, *J* = 8.6 Hz, 2H, **H^7**), 7.48 (d, *J* = 8.6 Hz, 2H, **H^8**), 7.34 (d, *J* = 8.5 Hz, 1H, **H^3**), 6.48 (br s, 2H, **H^6**), 1.32 (s, 9H, **H^9**); ^{13}C NMR (101 MHz, DMSO-d_6) δ 162.34, 151.74, 150.12, 150.02, 139.81, 136.99, 133.73, 133.46, 130.69 (2C), 130.26, 129.94, 127.56, 127.53, 126.39 (2C), 126.31 (2C), 125.16, 124.00, 117.31, 34.71, 31.59 (3C); LC-MS (APCI/ESI): Purity > 99%, t_R = 5.33 min, *m/z* $[M+H]^+$ = 438.2.

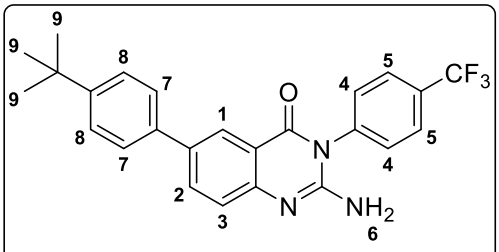

17
$C_{25}H_{22}F_3N_3O$
Exact Mass: 437.2
Mwt: 437.47

***2-amino-6-(3-(dimethylamino)phenyl)-3-(4-(trifluoromethyl)phenyl)quinazolin-4(3H)-one*, 18**

Off-white solid (0.107 g, 55%); m.p. 238.4–242.3 °C; R_f (EtOAc:Hex, 1:1) 0.48; ^{1}H NMR (400 MHz, DMSO-d_6) δ 8.08 (d, *J* = 2.3 Hz, 1H, **H^1**), 7.97–7.88 (m, 3H, **H^{2,5}**), 7.63 (d, *J* = 8.1 Hz, 2H, **H^4**), 7.32 (d, *J* = 8.6 Hz, 1H, **H^3**), 7.25 (t, *J* = 8.0 Hz, 1H, **H^9**), 6.96–6.87 (m, 2H, **H^{7,8}**), 6.71 (ddd, *J* = 8.4, 2.3, 1.0 Hz, 1H, **H^{10}**), 6.47 (br s, 2H, **H^6**), 2.95 (s, 6H, **H^{11}**); ^{13}C NMR (101 MHz, DMSO-d_6) δ 161.97, 151.31, 151.05, 149.66, 140.34, 139.43, 134.59, 133.46, 130.29 (2C), 129.86, 129.62, 129.54, 129.22, 127.12, 124.60, 123.92, 116.78, 114.52, 111.54, 110.24, 40.30 (2C); LC-MS (APCI/ESI): Purity > 99%, t_R = 4.73 min, *m/z* $[M+H]^+$ = 425.2.

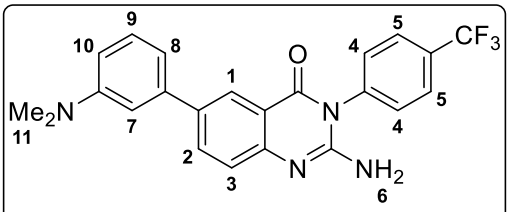

18
$C_{23}H_{19}F_3N_4O$
Exact Mass: 424.2
Mwt: 424.43

***2-amino-6-(3-(morpholinosulfonyl)phenyl)-3-(4-(trifluoromethyl)phenyl)quinazolin-4(3H)-one*, 19**

Off-white solid (0.288 g, 78%); m.p. 278.0–280.1 °C; R_f (100% EtOAc) 0.27; ^{1}H NMR (300 MHz, DMSO-d_6) δ 8.18 (d, J = 2.2 Hz, 1H, **H^1**), 8.08 (dt, J = 7.6, 1.5 Hz, 1H, **H^8**), 8.03 (dd, J = 8.6, 2.4 Hz, 1H, **H^2**), 7.95 (d, J = 8.3 Hz, 2H, **H^5**), 7.92 (t, J = 1.5 Hz, 1H, **H^7**), 7.77 (t, J = 7.7 Hz, 1H, **H^9**), 7.72 (dt, J = 7.8, 1.4 Hz, 1H, **H^{10}**), 7.66 (d, J = 8.1 Hz, 2H, **H^4**), 7.39 (d, J = 8.6 Hz, 1H, **H^3**), 6.61 (br s, 2H, **H^6**), 3.72–3.57 (m, 4H, **H^{12}**), 3.02–2.85 (m, 4H, **H^{11}**); ^{13}C NMR (101 MHz, DMSO-d_6) δ 162.24, 152.20, 150.92, 141.10, 139.68, 135.91, 133.71, 131.80, 131.62, 130.84, 130.65 (2C), 130.32, 130.01, 127.58, 126.61, 125.92, 125.46, 125.20, 124.97, 117.38, 65.80 (2C), 46.42 (2C); LC-MS (APCI/ESI): Purity > 99%, t_R = 4.08 min, m/z $[M+H]^+$ = 531.1.

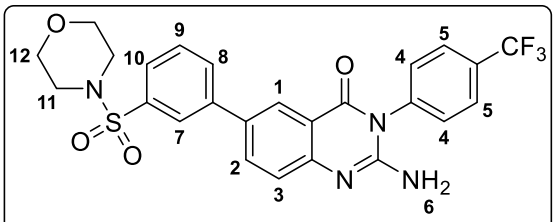

19
$C_{25}H_{21}F_3N_4O_4S$
Exact Mass: 530.1
Mwt: 530.52

***2-amino-6-(2-methyl-5-(morpholinosulfonyl)phenyl)-3-(4-(trifluoromethyl)phenyl)quinazolin-4(3H)-one*, 20**

Off-white solid (0.354 g, 81%); m.p. 219.8–224.8 °C; R_f (EtOAc:Hex, 80:20) 0.16; ^{1}H NMR (400 MHz, $CDCl_3$) δ 8.09 (d, J = 2.0 Hz, 1H, **H^1**), 7.91 (d, J = 8.0 Hz, 2H, **H^5**), 7.75 (d, J = 1.9 Hz, 1H, **H^7**), 7.67 (dd, J = 8.0, 2.0 Hz, 1H, **H^{10}**), 7.62 (dd, J = 8.4, 2.0 Hz, 1H, **H^2**), 7.57 (d, J = 8.0 Hz, 2H, **H^4**), 7.48 (d, J = 8.1 Hz, 1H, **H^9**), 7.42 (d, J = 8.4 Hz, 1H, **H^3**), 3.82–3.71 (m, 4H, **H^{12}**), 3.12–3.01 (m, 4H, **H^{11}**), 2.39 (s, 3H, **H^8**); ^{13}C NMR (101 MHz, $CDCl_3$) δ 161.50, 150.36, 146.98, 141.62, 141.56, 137.72, 136.09, 135.41, 132.83, 132.76, 131.28, 129.43 (2C), 129.09, 127.85, 127.82, 127.65, 126.89, 123.83, 122.04, 117.05, 66.12 (2C), 46.08 (2C), 20.66; HPLC-MS (APCI/ESI): Purity = 99%, t_R = 4.13 min, m/z $[M+H]^+$ = 545.1.

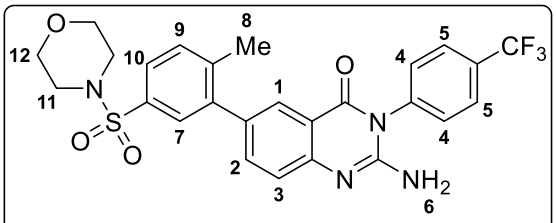

20
$C_{26}H_{23}F_3N_4O_4S$
Exact Mass: 544.1
Mwt: 544.55

***2-amino-6-(pyridin-3-yl)-3-(4-(trifluoromethyl)phenyl)quinazolin-4(3H)-one*, 21**

Off-white solid (0.132 g, 74%); m.p. 286.5–288.9 °C; R_f (100% EtOAc) 0.21; ^{1}H NMR (600 MHz, DMSO-d_6) δ 8.92 (s, 1H, **H⁸**), 8.56 (d, J = 4.7 Hz, 1H, **H⁹**), 8.18 (d, J = 2.3 Hz, 1H, **H¹**), 8.10 (d, J = 8.0 Hz, 1H, **H⁷**), 8.02 (dd, J = 8.6, 2.2 Hz, 1H, **H²**), 7.95 (d, J = 8.4 Hz, 2H, **H⁵**), 7.67 (d, J = 8.3 Hz, 2H, **H⁴**), 7.49 (dd, J = 7.9, 4.7 Hz, 1H, **H¹⁰**), 7.38 (d, J = 8.6 Hz, 1H, **H³**), 6.61 (br s, 2H, **H⁶**); ^{13}C NMR (151 MHz, DMSO-d_6) δ 162.22, 152.12, 150.71, 148.63, 147.74, 139.71, 135.37, 134.16, 133.59, 130.67 (2C), 130.59, 130.24, 130.03, 127.60, 127.58, 125.41, 124.82, 124.41, 117.43; LC-MS (APCI/ESI): Purity = 98%, t_R = 4.28 min, m/z $[M+H]^+$ = 383.1.

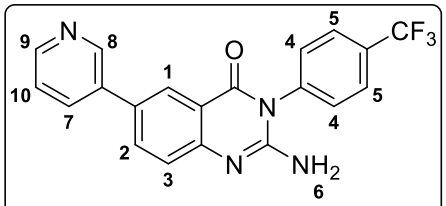

21
$C_{20}H_{13}F_3N_4O$
Exact Mass: 382.1
Mwt: 382.35

***2-amino-6-(5-(methylsulfonyl)pyridin-3-yl)-3-(4-(trifluoromethyl)phenyl)quinazolin-4(3H)-one*, 22**

Off-white solid (0.150 g, 70%); m.p. 323.9–328.5 °C; R_f (100% EtOAc) 0.20; ^{1}H NMR (400 MHz, DMSO-d_6) δ 9.25 (d, J = 2.2 Hz, 1H, **H⁹**), 9.02 (d, J = 2.2 Hz, 1H, **H⁸**), 8.56 (t, J = 2.2 Hz, 1H, **H⁷**), 8.31 (d, J = 2.2 Hz, 1H, **H¹**), 8.13 (dd, J = 8.6, 2.2 Hz, 1H, **H²**), 7.95 (d, J = 8.3 Hz, 2H, **H⁵**), 7.67 (d, J = 8.2 Hz, 2H, **H⁴**), 7.40 (d, J = 8.6 Hz, 1H, **H³**), 6.64 (br s, 2H, **H⁶**), 3.41 (s, 3H, **H¹⁰**); ^{13}C NMR (101 MHz, DMSO-d_6) δ 161.77, 152.04, 151.67, 150.98, 145.83, 139.26, 137.37, 135.38, 133.38, 132.39, 130.25 (2C), 129.95, 129.63, 128.30, 127.25, 127.22, 125.30, 125.15, 117.17, 43.70; LC-MS (APCI/ESI): Purity > 99%, t_R = 4.16 min, m/z $[M+H]^+$ = 461.1.

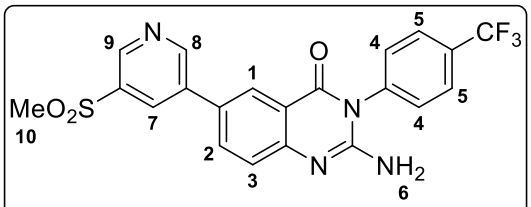

22
$C_{21}H_{15}F_3N_4O_3S$
Exact Mass: 460.1
Mwt: 460.43

***2-amino-6-(5-methylpyridin-3-yl)-3-(4-(trifluoromethyl)phenyl)quinazolin-4(3H)-one*, 23**

Off-white solid (0.113 g, 61%); m.p. 271.9–275.5 °C; R_f (100% EtOAc) 0.20; ^{1}H NMR (400 MHz, DMSO-d_6) δ 8.70 (s, 1H, **H⁸**), 8.39 (s, 1H, **H⁹**), 8.16 (d, J = 2.3 Hz, 1H, **H¹**), 7.99 (dd, J = 8.6, 2.3 Hz, 1H, **H²**), 7.94 (d, J = 8.3 Hz, 2H, **H⁵**), 7.91 (s, 1H, **H⁷**), 7.66 (d, J = 8.1 Hz, 2H, **H⁴**), 7.36 (d, J = 8.6 Hz, 1H, **H³**), 6.56 (br s, 2H, **H⁶**), 2.37 (s, 3H, **H¹⁰**); ^{13}C NMR (101 MHz, DMSO-d_6) δ

161.83, 151.68, 150.25, 148.61, 144.54, 139.34, 134.51, 134.14, 133.21, 130.27 (2C), 129.91, 129.59, 127.21, 127.18, 125.53, 124.97, 124.39, 122.83, 117.05, 17.95; LC-MS (APCI/ESI): Purity = 97%, t_R = 4.41 min, *m/z* $[M+H]^+$ = 397.1.

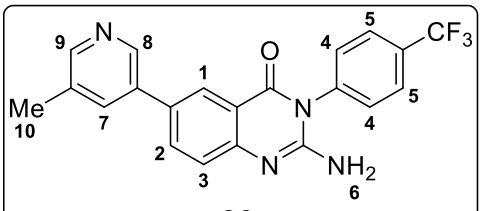

23
$C_{21}H_{15}F_3N_4O$
Exact Mass: 396.1
Mwt: 396.37

2-amino-6-(5-methoxypyridin-3-yl)-3-(4-(trifluoromethyl)phenyl)quinazolin-4(3H)-one, 24

Off-white solid (0.157 g, 82%); m.p. 253.5–256.8 °C; *Rf* (100% EtOAc) 0.24; ^{1}H NMR (400 MHz, DMSO-d_6) δ 8.49 (d, *J* = 1.8 Hz, 1H, **H⁸**), 8.27 (d, *J* = 2.7 Hz, 1H, **H⁹**), 8.18 (d, *J* = 2.3 Hz, 1H, **H¹**), 8.01 (dd, *J* = 8.6, 2.3 Hz, 1H, **H²**), 7.94 (d, *J* = 8.2 Hz, 2H, **H⁵**), 7.66 (d, *J* = 8.1 Hz, 2H, **H⁴**), 7.62 (dd, *J* = 2.7, 1.9 Hz, 1H, **H⁷**), 7.36 (d, *J* = 8.6 Hz, 1H, **H³**), 6.57 (br s, 2H, **H⁶**), 3.92 (s, 3H, **H¹⁰**); ^{13}C NMR (101 MHz, DMSO-d_6) δ 161.82, 155.77, 151.73, 150.40, 139.54, 139.33, 136.27, 135.87, 133.49, 130.27 (2C), 130.08, 129.91, 129.60, 127.21, 127.18, 124.92, 124.68, 117.96, 116.99, 55.74; LC-MS (APCI/ESI): Purity = 99%, t_R = 4.39 min, *m/z* $[M+H]^+$ = 413.1.

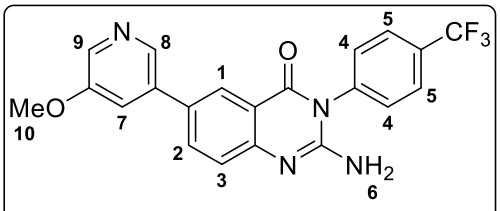

24
$C_{21}H_{15}F_3N_4O_2$
Exact Mass: 412.1
Mwt: 412.37

2-amino-6-(6-methoxy-5-(trifluoromethyl)pyridin-3-yl)-3-(4-(trifluoromethyl)phenyl)quinazolin-4(3H)-one, 25

White solid (0.170 g, 76%); m.p. 254.2–259.6 °C; R_f (EtOAc:Hex, 1:1) 0.26; ^{1}H NMR (400 MHz, DMSO-d_6) δ 8.75 (s, 1H, **H⁷**), 8.29 (d, *J* = 2.2 Hz, 1H, **H¹**), 8.14 (s, 1H, **H⁸**), 7.99 (dd, *J* = 8.6, 2.2 Hz, 1H, **H²**), 7.93 (d, *J* = 8.7 Hz, 2H, **H⁵**), 7.64 (d, *J* = 8.6 Hz, 2H, **H⁴**), 7.34 (d, *J* = 8.6 Hz, 1H, **H³**), 6.55 (br s, 2H, **H⁶**), 4.02 (s, 3H, **H⁹**); ^{13}C NMR (101 MHz, DMSO-d_6) δ 161.78, 159.24, 151.68, 150.20, 148.58, 139.32, 134.98, 134.93, 133.21, 130.25 (2C), 129.91, 129.60, 128.81, 128.77, 127.21, 127.19, 124.97, 124.51, 124.38, 117.02, 54.34; LC-MS (APCI/ESI): Purity > 99%, t_R = 4.83 min, *m/z* $[M+H]^+$ = 481.1.

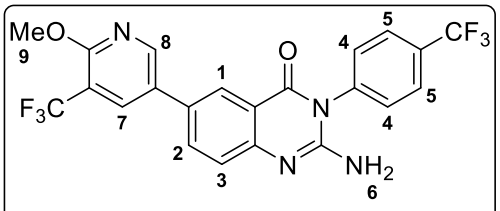

25
$C_{22}H_{14}F_6N_4O_2$
Exact Mass: 480.1
Mwt: 480.37

2-amino-6-(2-fluoropyridin-4-yl)-3-(4-(trifluoromethyl)phenyl)quinazolin-4(3H)-one, 26

White solid (0.100 g, 54%); m.p. 348.1–352.7 °C; R_f (EtOAc:Hex, 3:2) 0.22; ^{1}H NMR (400 MHz, DMSO-d_6) δ 8.30 (d, J = 2.2 Hz, 1H, **H^1**), 8.26 (d, J = 5.3 Hz, 1H, **H^8**), 8.10 (dd, J = 8.7, 2.2 Hz, 1H, **H^2**), 7.93 (d, J = 8.3 Hz, 2H, **H^5**), 7.70 (d, J = 5.3 Hz, 1H, **H^9**), 7.65 (d, J = 8.2 Hz, 2H, **H^4**), 7.51 (s, 1H, **H^7**), 7.35 (d, J = 8.7 Hz, 1H, **H^3**), 6.68 (br s, 2H, **H^6**); ^{13}C NMR (101 MHz, DMSO-d_6) δ 165.48, 161.71, 152.24, 151.70, 148.28, 148.13, 139.19, 133.04, 130.24 (2C), 129.96, 129.64, 128.77, 127.24, 125.23, 125.01, 119.09, 116.94, 106.08, 105.70; LC-MS (APCI/ESI): Purity = 99%, t_R = 4.41 min, m/z $[M+H]^+$ = 401.1.

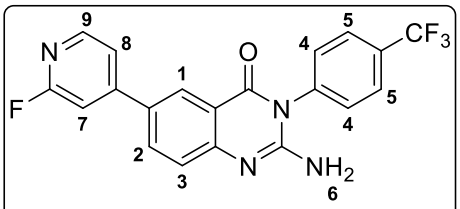

26
$C_{20}H_{12}F_4N_4O$
Exact Mass: 400.1
Mwt: 400.34

2-amino-6-(2,6-difluoropyridin-4-yl)-3-(4-(trifluoromethyl)phenyl)quinazolin-4(3H)-one, 27

White solid (0.116 g, 60%); m.p. 362.9–367.1 °C; R_f (EtOAc:Hex, 1:1) 0.22; ^{1}H NMR (400 MHz, DMSO-d_6) δ 8.34 (d, J = 2.4 Hz, 1H, **H^1**), 8.13 (dd, J = 8.7, 2.4 Hz, 1H, **H^2**), 7.94 (d, J = 8.2 Hz, 2H, **H^5**), 7.65 (d, J = 8.1 Hz, 2H, **H^4**), 7.55 (s, 2H, **H^7**), 7.34 (d, J = 8.7 Hz, 1H, **H^3**), 6.72 (br s, 2H, **H^6**); ^{13}C NMR (101 MHz, DMSO-d_6) δ 163.13, 161.65, 160.73, 160.56, 152.47, 152.19, 139.16, 133.19, 130.24 (2C), 129.98, 129.67, 127.91, 127.27, 127.24, 125.82, 124.96, 116.91, 103.43, 103.03; LC-MS (APCI/ESI): Purity = 97%, t_R = 4.57 min, m/z $[M+H]^+$ = 419.1.

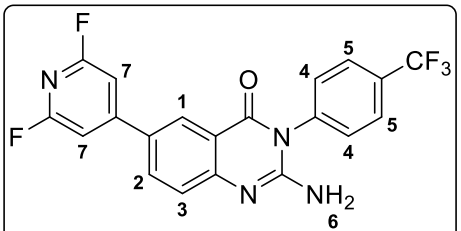

27
$C_{20}H_{11}F_5N_4O$
Exact Mass: 418.1
Mwt: 418.33

2-amino-6-(pyrimidin-5-yl)-3-(4-(trifluoromethyl)phenyl)quinazolin-4(3H)-one, 28

Off-white solid (0.148 g, 83%); m.p. 325.2–328.3 °C; R_f (100% EtOAc) 0.20; ^{1}H NMR (600 MHz, DMSO-d_6) δ 9.16 (s, 1H, **H^8**), 9.14 (s, 2H, **H^7**), 8.26 (d, J = 2.3 Hz, 1H, **H^1**), 8.05 (dd, J = 8.6, 2.3 Hz, 1H, **H^2**), 7.94 (d, J = 8.3 Hz, 2H, **H^5**), 7.66 (d, J = 8.2 Hz, 2H, **H^4**), 7.40 (d, J =

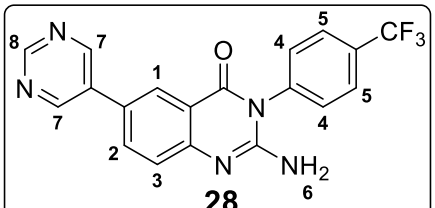

28
$C_{19}H_{12}F_3N_5O$
Exact Mass: 383.1
Mwt: 383.33

8.6 Hz, 1H, **H³**), 6.52 (br s, 2H, **H⁶**); ^{13}C NMR (151 MHz, DMSO-d_6) δ 162.08, 157.32, 154.75 (2C), 152.31, 151.22, 139.66, 133.45, 133.24, 130.63 (2C), 130.36, 130.15, 127.55, 127.53, 127.35, 125.63, 125.25, 117.66; LC-MS (APCI/ESI): Purity > 99%, t_R = 4.18 min, *m/z* $[M+H]^+$ = 384.1.

2-amino-6-(2-methoxypyrimidin-5-yl)-3-(4-(trifluoromethyl)phenyl)quinazolin-4(3H)-one, 29

Off-white solid (0.156 g, 81%); m.p. 284.7–289.4 °C; R_f (100% EtOAc) 0.40; ^{1}H NMR (400 MHz, DMSO-d_6) δ 8.92 (s, 2H, **H⁷**), 8.13 (d, *J* = 2.3 Hz, 1H, **H¹**), 7.96 (dd, *J* = 8.6, 2.3 Hz, 1H, **H²**), 7.93 (d, *J* = 8.5 Hz, 2H, **H⁵**), 7.64 (d, *J* = 8.1 Hz, 2H, **H⁴**), 7.34 (d, *J* = 8.6 Hz, 1H, **H³**), 6.55 (br s, 2H, **H⁶**), 3.96 (s, 3H, **H⁸**); ^{13}C NMR (101 MHz, DMSO-d_6) δ 164.45, 161.75, 157.03 (2C), 151.67, 150.20, 139.32, 132.83, 130.26 (2C), 129.91, 129.59, 127.21, 127.18, 127.12, 127.06, 125.03, 123.99, 117.08, 54.77; LC-MS (APCI/ESI): Purity > 99%, t_R = 4.33 min, *m/z* $[M+H]^+$ = 414.1.

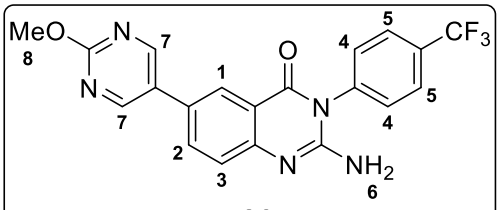

29

$C_{20}H_{14}F_3N_5O_2$

Exact Mass: 413.1

Mwt: 413.36

2-amino-6-(thiophen-3-yl)-3-(4-(trifluoromethyl)phenyl)quinazolin-4(3H)-one, 30

Off-white solid (0.116 g, 64%); m.p. 309.9–312.3 °C; R_f (EtOAc:Hex, 1:1) 0.25; ^{1}H NMR (600 MHz, DMSO-d_6) δ 8.16 (d, *J* = 2.2 Hz, 1H, **H¹**), 8.00 (dd, *J* = 8.6, 2.3 Hz, 1H, **H²**), 7.95 (d, *J* = 8.3 Hz, 2H, **H⁵**), 7.87 (dd, *J* = 2.9, 1.4 Hz, 1H, **H⁷**), 7.68–7.63 (m, 3H, **H⁴,⁸**), 7.57 (dd, *J* = 5.0, 1.4 Hz, 1H, **H⁹**), 7.31 (d, *J* = 8.6 Hz, 1H, **H³**), 6.50 (br s, 2H, **H⁶**); ^{13}C NMR (151 MHz, DMSO-d_6) δ 162.27, 151.71, 149.88, 141.20, 139.81, 133.27, 130.67 (2C), 130.18, 129.97, 129.18, 127.71, 127.57, 127.55, 126.43, 125.07, 123.55, 120.75, 117.21; LC-MS (APCI/ESI): Purity = 98%, t_R = 4.57 min, *m/z* $[M+H]^+$ = 388.1.

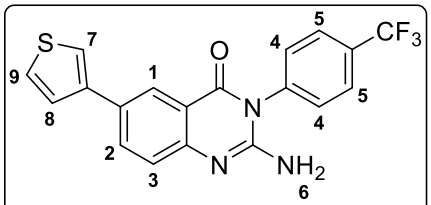

30

$C_{19}H_{12}F_3N_3OS$

Exact Mass: 387.1

Mwt: 387.38

***2-amino-6-(1-methyl-1H-pyrazol-4-yl)-3-(4-(trifluoromethyl)phenyl)quinazolin-4(3H)-one*, 31**

Off-white solid (0.140 g, 78%); m.p. 268.7–272.3 °C; R_f (100% EtOAc) 0.31; ^{1}H NMR (600 MHz, DMSO-d_6) δ 8.12 (s, 1H, **H^8**), 8.02 (d, J = 2.2 Hz, 1H, **H^1**), 7.93 (d, J = 8.3 Hz, 2H, **H^5**), 7.85–7.81 (m, 2H, **H^{2,7}**), 7.64 (d, J = 8.2 Hz, 2H, **H^4**), 7.27 (d, J = 8.6 Hz, 1H, **H^3**), 6.26 (br s, 2H, **H^6**), 3.87 (s, 3H, **H^9**); ^{13}C NMR (151 MHz, DMSO-d_6) δ 162.20, 151.24, 149.00, 139.91, 136.23, 132.51, 130.65 (2C), 130.02, 127.99, 127.47, 127.45, 126.89, 125.46, 125.11, 122.23, 121.95, 117.46, 39.07; LC-MS (APCI/ESI): Purity = 97%, t_R = 4.20 min, m/z $[M+H]^+$ = 386.1.

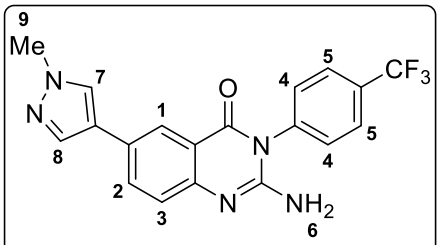

31
$C_{19}H_{14}F_3N_5O$
Exact Mass: 385.1
Mwt: 385.35

Synthesis of *methyl* 5-*bromo*-2-*(3-(ethoxycarbonyl)thioureido)benzoate*, 2.5

To a solution of potassium thiocyanate (3 g, 30.9 mmol, 1.04 Eq) in anhydrous acetonitrile (40 mL), ethyl chloroformate (2.84 mL, 29.7 mmol, 1.0 Eq) was added dropwise while stirring at 25 °C. The solution was then heated at 70 °C for 2 h, cooled to room temperature, solids were filtered and discarded. Methyl 2-amino-5-bromobenzoate (4.55 g, 19.8 mmol, 1.0 Eq) was added to the filtrate [the *in situ* generated ethoxy carbonyl isothiocyanate] portionwise while stirring at 25 °C for 45 minutes. The solids were filtered, washed with acetonitrile, and dried to furnish methyl 5-bromo-2-(3-(ethoxycarbonyl)thioureido) benzoate, **2.5**. In the subsequent scale up reactions, **2.5** was obtained by dissolving Methyl 2-amino-5-bromobenzoate in acetonitrile and treating it with the commercially available ethoxy carbonyl isothiocyanate at 0 °C. In this case, the product formed within ten minutes as a precipitate, which was filtered, washed with acetonitrile, and dried to afford **2.5** as a white solid (6.6 g, 92%); m.p. 155.7–158.9 °C; R_f (EtOAc:Hex, 1:4) 0.35; ^{1}H NMR (400 MHz, $CDCl_3$) δ 12.60 (br s, 1H, **H^5**), 8.47 (d, J = 8.9 Hz, 1H, **H^3**), 8.18 (br s, 1H, **H^6**), 8.16 (d, J = 2.4 Hz, 1H, **H^1**), 7.68 (dd, J = 8.9, 2.4 Hz, 1H, **H^2**), 4.35 (q, J = 7.1 Hz, 2H,

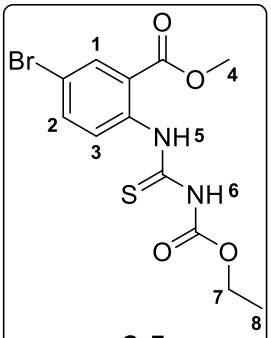

2.5
$C_{12}H_{13}BrN_2O_4S$
Exact Mass: 360.0
Mwt: 361.21

H⁷), 3.97 (s, 3H, **H⁴**), 1.37 (t, *J* = 7.1 Hz, 3H, **H⁸**); ^{13}C NMR (101 MHz, $CDCl_3$) δ 178.12, 165.47, 151.69, 137.96, 135.36, 133.43, 127.87, 123.55, 118.75, 63.07, 52.81, 14.21; LC-MS (APCI/ESI): Purity > 99%, t_R = 4.55 min, *m/z* $[M+H]^+$ = 361.0, 363.0 (1:1).

General procedure 6: Synthesis of intermediates 2.6a–2.6j

The appropriate aniline (1.5 Eq) and *N*-(3-Dimethylaminopropyl)-*N'*-ethylcarbodiimide hydrochloride (EDCI) (2.0 Eq) were successively added to a solution of **2.5** (1.0 Eq) in DCM, and stirred at 25 °C for 6 to 29 hours. After completeness of the reaction, more DCM was added, and washed with 1N HCl/H_2O (2-3%) (20 mL × 2), water (20 mL × 2), brine (20 mL × 2), dried over anhydrous sodium sulfate, and concentrated to yield a residue, which was triturated in diethyl ether, filtered, and dried *in vacuo* to afford the desired intermediate.

***Ethyl (6-bromo-3-(3-cyanophenyl)-4-oxo-3,4-dihydroquinazolin-2-yl)carbamate*, 2.6a**

White solid (0.871 g, 87%); R_f (EtOAc:Hex, 50:50) 0.49; ^{1}H NMR (400 MHz, $CDCl_3$) δ 8.32 (d, *J* = 2.3 Hz, 1H, **H¹**), 7.85 (dd, *J* = 8.6, 2.3 Hz, 1H, **H²**), 7.77 (dt, *J* = 7.8, 1.3 Hz, 1H, **H⁷**), 7.66 (t, *J* = 8.1 Hz, 1H, **H⁶**), 7.58 (t, *J* = 2.0 Hz, 1H, **H⁴**), 7.52 (ddd, *J* = 8.0, 2.1, 1.1 Hz, 1H, **H⁵**), 7.18 (d, *J* = 8.6 Hz, 1H, **H³**), 4.13 (q, *J* = 7.1 Hz, 2H, **H⁹**), 1.27 (t, *J* = 7.1 Hz, 3H, **H¹⁰**); ^{13}C NMR (101 MHz, $CDCl_3$) δ 163.73, 159.63, 154.07, 139.02, 136.44, 135.83, 133.45, 132.66, 132.54, 131.12, 130.36, 118.21, 118.00, 117.75, 117.39, 113.83, 62.40, 14.24; LC-MS (APCI/ESI): Purity > 99%, t_R = 4.27 min, *m/z* $[M+H]^+$ = 413.0, 415.0 (1:1).

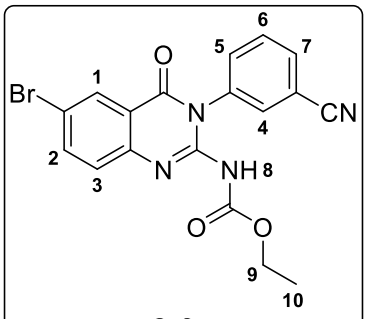

2.6a
$C_{18}H_{13}BrN_4O_3$
Exact Mass: 412.0
Mwt: 413.23

Ethyl (6-bromo-3-(4-(methylsulfonyl)phenyl)-4-oxo-3,4-dihydroquinazolin-2-yl)carbamate, 2.6b

White solid (0.905 g, 81%); m.p. 273.3–278.1 °C; R_f (100% EtOAc) 0.60; ^{1}H NMR (400 MHz, DMSO-d_6) δ 8.09 (d, J = 2.7 Hz, 1H, **H^1**), 8.07 (d, J = 8.7 Hz, 2H, **H^4**), 7.98 (dd, J = 8.8, 2.3 Hz, 1H, **H^2**), 7.77 (d, J = 8.6 Hz, 1H, **H^3**), 7.64 (d, J = 8.7 Hz, 2H, **H^5**), 3.98 (q, J = 7.1 Hz, 2H, **H^8**), 3.32 (s, 3H, **H^6**), 1.11 (t, J = 7.0 Hz, 3H, **H^9**); LC-MS (APCI/ESI): Purity = 96%, t_R = 4.15 min, m/z $[M+H]^+$ = 466.0, 468.0 (1:1).

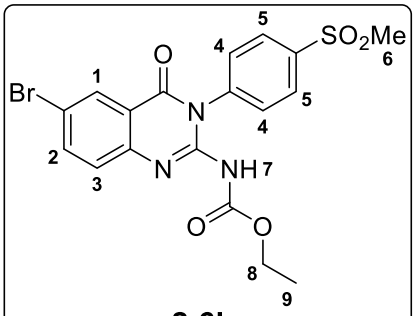

2.6b
$C_{18}H_{16}BrN_3O_5S$
Exact Mass: 465.0
Mwt: 466.31

Ethyl (6-bromo-4-oxo-3-(2-(trifluoromethyl)phenyl)-3,4-dihydroquinazolin-2-yl)carbamate, 2.6c

White solid (0.551 g, 50%); m.p. 201.2–204.3 °C; R_f (EtOAc:Hex, 50:50) 0.47; ^{1}H NMR (400 MHz, $CDCl_3$) δ 8.33 (d, J = 2.3 Hz, 1H, **H^1**), 7.85 (d, J = 8.0, 1H, **H^7**), 7.83 (dd, J = 8.7, 2.3 Hz, 1H, **H^2**), 7.75 (td, J = 7.7, 1.0 Hz, 1H, **H^6**), 7.63 (tt, J = 7.8, 1.0 Hz, 1H, **H^5**), 7.35 (d, J = 7.9 Hz, 1H, **H^4**), 7.18 (d, J = 8.7 Hz, 1H, **H^3**), 4.07 (q, J = 7.1 Hz, 2H, **H^9**), 1.21 (t, J = 7.1 Hz, 3H, **H^{10}**); ^{13}C NMR (101 MHz, $CDCl_3$) δ 163.53, 159.76, 154.15, 138.80, 136.76, 133.25, 133.09, 131.10, 130.99, 129.66, 128.02, 127.77, 127.72, 118.38, 117.82, 117.40, 62.41, 14.25; LC-MS (APCI/ESI): Purity = 90%, t_R = 4.37 min, m/z $[M+H]^+$ = 456.0, 458.0 (1:1).

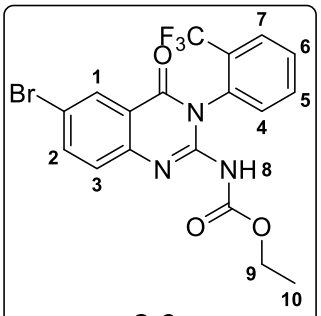

2.6c
$C_{18}H_{13}BrF_3N_3O_3$
Exact Mass: 455.0
Mwt: 456.22

Ethyl (6-bromo-4-oxo-3-(6-(trifluoromethyl)pyridin-3-yl)-3,4-dihydroquinazolin-2-yl)carbamate, 2.6d

White solid (0.645 g, 59%); R_f (EtOAc:Hex, 50:50) 0.49; ^{1}H NMR (400 MHz, $CDCl_3$) δ 8.65 (d, J = 1.9 Hz, 1H, **H^6**), 8.34 (d, J = 2.2 Hz, 1H, **H^1**), 7.90–7.79 (m, 3H, **H^{2,4,5}**), 7.19 (d, J = 8.6 Hz, 1H, **H^3**), 4.13 (q, J = 7.1 Hz, 2H, **H^8**), 1.27 (t, J = 7.1 Hz, 3H, **H^9**); ^{13}C NMR (101 MHz, $CDCl_3$) δ 163.80, 159.54, 154.05, 150.01, 148.14, 147.79, 139.22, 137.97, 136.35, 134.16, 131.21, 122.61, 121.07, 118.11, 117.17, 62.45, 14.21; LC-

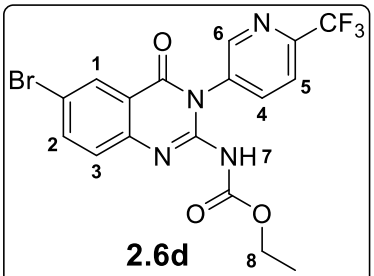

2.6d
$C_{17}H_{12}BrF_3N_4O_3$
Exact Mass: 456.0
Mwt: 457.21

MS (APCI/ESI): Purity = 97%, t_R = 4.42 min, *m/z* $[M+H]^+$ = 457.0, 459.0 (1:1).

***Ethyl (6-bromo-4-oxo-3-(4-(trifluoromethyl)phenyl)-3,4-dihydroquinazolin-2-yl)carbamate*, 2.6e**

White solid (0.960 g, 87%); R_f (EtOAc:Hex, 30:70) 0.30; ^{1}H NMR (400 MHz, $CDCl_3$) δ 8.33 (d, *J* = 2.3 Hz, 1H, **H^1**), 7.84 (dd, *J* = 8.6, 2.3 Hz, 1H, **H^2**), 7.81 (d, *J* = 8.3 Hz, 2H, **H^5**), 7.40 (d, *J* = 8.1 Hz, 2H, **H^4**), 7.18 (d, *J* = 8.7 Hz, 1H, **H^3**), 4.12 (q, *J* = 7.1 Hz, 2H, **H^7**), 1.26 (t, *J* = 7.1 Hz, 3H, **H^8**); ^{13}C NMR (101 MHz, $CDCl_3$) δ 159.74, 154.02, 138.87, 138.14, 136.67, 131.09, 131.00, 129.20 (2C), 126.72, 126.68, 125.11, 122.40, 118.35, 117.91, 117.58, 62.39, 14.24; LC-MS (APCI/ESI): Purity > 99%, t_R = 4.63 min, *m/z* $[M+H]^+$ = 456.0, 458.0 (1:1).

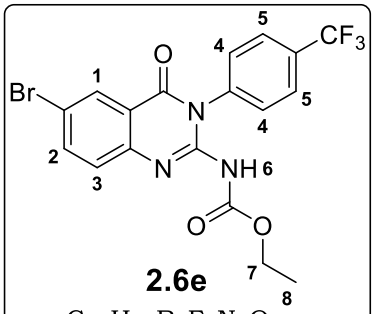

2.6e
$C_{18}H_{13}BrF_3N_3O_3$
Exact Mass: 455.0
Mwt: 456.22

***Ethyl (6-bromo-3-(4-cyanophenyl)-4-oxo-3,4-dihydroquinazolin-2-yl)carbamate*, 2.6f**

White solid (0.781 g, 78%); R_f (EtOAc:Hex, 50:50) 0.46; ^{1}H NMR (400 MHz, $CDCl_3$) δ 8.32 (d, *J* = 2.2 Hz, 1H, **H^1**), 7.84 (dd, *J* = 8.6, 2.3 Hz, 1H, **H^2**), 7.81 (d, *J* = 8.7 Hz, 2H, **H^4**), 7.40 (d, *J* = 8.7 Hz, 2H, **H^5**), 7.18 (d, *J* = 8.6 Hz, 1H, **H^3**), 4.12 (q, *J* = 7.1 Hz, 2H, **H^7**), 1.26 (t, *J* = 7.1 Hz, 3H, **H^8**); ^{13}C NMR (101 MHz, $CDCl_3$) δ 163.76, 159.55, 153.96, 139.06, 139.02, 136.48, 133.33 (2C), 131.11, 129.84 (2C), 118.21, 118.04, 117.99, 117.41, 113.18, 62.39, 14.25; LC-MS (APCI/ESI): Purity = 96%, t_R = 3.90 min, *m/z* $[M+H]^+$ = 413.0, 415.0 (1:1).

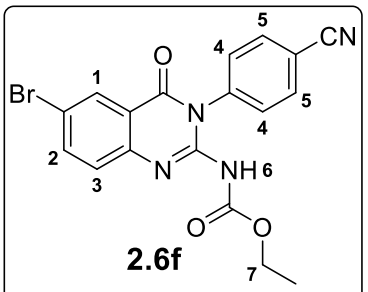

2.6f
$C_{18}H_{13}BrN_4O_3$
Exact Mass: 412.0
Mwt: 413.23

***Ethyl (6-bromo-3-(4-hydroxyphenyl)-4-oxo-3,4-dihydroquinazolin-2-yl)carbamate*, 2.6g**

White solid (0.759 g, 78%); R_f (EtOAc:Hex, 80:20) 0.57; ^{1}H NMR (400 MHz, $CDCl_3$) δ 8.35 (d, *J* = 2.3 Hz, 1H, **H^1**), 7.84 (dd, *J* = 8.7, 2.3 Hz, 1H, **H^2**), 7.25 (d, *J* = 8.6 Hz, 1H, **H^3**), 7.03 (d, *J* = 8.8 Hz, 2H, **H^4**), 6.82 (d, *J* = 8.8 Hz, 2H, **H^5**), 4.19 (q, *J* = 7.1 Hz, 2H, **H^8**), 1.28 (t, *J* = 7.1 Hz, 3H, **H^9**); ^{13}C NMR (101 MHz,

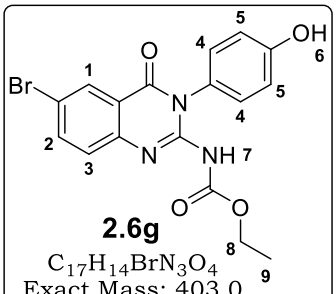

2.6g
$C_{17}H_{14}BrN_3O_4$
Exact Mass: 403.0
Mwt: 404.22

$CDCl_3$) δ 161.20, 160.48, 157.06, 153.20, 138.62, 137.71, 130.92, 129.09 (2C), 126.12, 119.80, 118.13, 117.27, 116.97 (2C), 62.43, 14.22; LC-MS (APCI/ESI): Purity > 99%, t_R = 3.59 min, *m/z* $[M+H]^+$ = 404.0, 406.0 (1:1).

***Ethyl (6-bromo-3-(4-fluorophenyl)-4-oxo-3,4-dihydroquinazolin-2-yl)carbamate*, 2.6h**

Off-white solid (1.030 g, 92%); R_f (EtOAc:Hex, 30:70) 0.30; ^{1}H NMR (300 MHz, $CDCl_3$) δ 8.32 (d, *J* = 2.3 Hz, 1H, **H^1**), 7.82 (dd, *J* = 8.6, 2.3 Hz, 1H, **H^2**), 7.29–7.22 (m, 4H, **H^{4,5}**), 7.20 (d, *J* = 8.6 Hz, 1H, **H^3**), 4.12 (q, *J* = 7.1 Hz, 2H, **H^7**), 1.25 (t, *J* = 7.1 Hz, 3H, **H^8**); ^{13}C NMR (101 MHz, $CDCl_3$) δ 163.88, 162.96, 161.41, 160.05, 153.77, 138.68, 137.09, 131.00, 130.65, 130.26, 130.18, 118.84, 117.88, 116.80, 116.57, 62.38, 14.28; LC-MS (APCI/ESI): Purity = 98%, t_R = 4.08 min, *m/z* $[M+H]^+$ = 406.0, 408.0 (1:1).

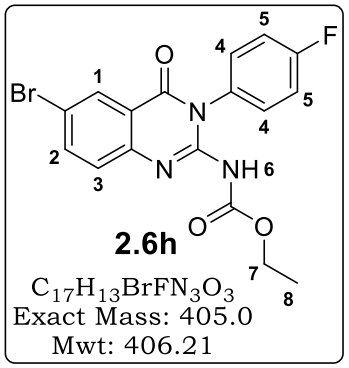

***Ethyl (6-bromo-3-(2-fluorophenyl)-4-oxo-3,4-dihydroquinazolin-2-yl)carbamate*, 2.6i**

White solid (1.050 g, 93%); R_f (EtOAc:Hex, 30:70) 0.26; ^{1}H NMR (300 MHz, $CDCl_3$) δ 8.34 (d, *J* = 2.2 Hz, 1H, **H^1**), 7.83 (dd, *J* = 8.6, 2.3 Hz, 1H, **H^2**), 7.55–7.43 (m, 1H, **H^6**), 7.33–7.23 (m, 3H, **H^{4,5,7}**), 7.19 (d, *J* = 8.6 Hz, 1H, **H^3**), 4.11 (q, *J* = 7.1 Hz, 2H, **H^9**), 1.24 (t, *J* = 7.1 Hz, 3H, **H^{10}**); ^{13}C NMR (101 MHz, $CDCl_3$) δ 163.58, 159.30, 158.92, 156.43, 153.70, 138.72, 136.88, 131.12, 131.01, 130.24, 124.80, 118.46, 117.80, 116.73, 116.54, 62.39, 14.27; LC-MS (APCI/ESI): Purity = 95%, t_R = 4.14 min, *m/z* $[M+H]^+$ = 406.0, 408.0 (1:1).

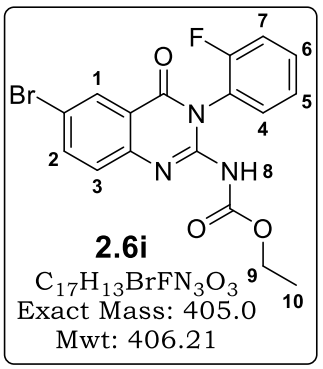

***Ethyl (6-bromo-3-(4-methoxyphenyl)-4-oxo-3,4-dihydroquinazolin-2-yl)carbamate*, 2.6j**

Brown solid (1.099 g, 94%); R_f (EtOAc:Hex, 50:50) 0.49; ^{1}H NMR (400 MHz, $CDCl_3$) δ 8.32 (d, *J* = 2.3 Hz, 1H, **H^1**), 7.80 (dd, *J* = 8.6, 2.3 Hz, 1H, **H^2**), 7.24 (d, *J* = 8.6 Hz, 1H, **H^3**), 7.17 (d, *J* = 9.1 Hz, 2H, **H^4**), 7.05 (d, *J* = 9.1 Hz, 2H, **H^5**), 4.13 (q, *J* = 7.1 Hz, 2H, **H^8**), 3.88 (s, 3H, **H^6**), 1.25 (t, *J* = 7.1

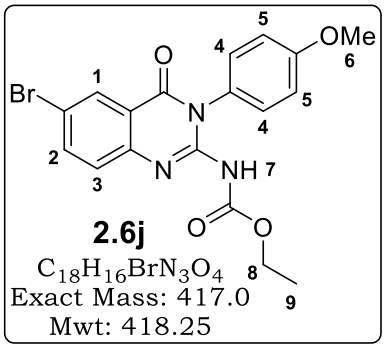

Hz, 3H, **H⁹**); ^{13}C NMR (101 MHz, $CDCl_3$) δ 161.29, 160.37, 159.96, 152.65, 138.42, 138.29, 130.79, 129.35 (2C), 127.16, 120.12, 118.35, 117.88, 115.09 (2C), 62.34, 55.49, 14.29; LC-MS (APCI/ESI): Purity > 99%, t_R = 4.05 min, *m/z* $[M+H]^+$ = 418.0, 420.0 (1:1).

General procedure 7 [Deprotection]: Synthesis of 2-amino-6-bromo-quinazolinone-based intermediates 2.7a–2.7j

The 2-carbamate-based intermediate **2.6 (a–j)** (1.0 Eq) was dissolved in TFA (20.0 Eq). This solution was heated under microwave conditions at 110 °C for 20 min. After cooling to room temperature and evaporating the solvent, the residue was dissolved in DCM/MeOH (1:1). Amberlyst® A21 free base was then added to this solution, stirred at ambient temperature for 45 min, followed by filtration and rinsing of the resin with MeOH. The filtrate was then concentrated under reduced pressure to give a residue that was triturated in Et_2O, filtered, and dried to afford the desired product.

***3-(2-amino-6-bromo-4-oxoquinazolin-3(4H)-yl)benzonitrile*, 2.7a**

Off-white solid (0.360 g, 79%); R_f (100% EtOAc) 0.34; ^{1}H NMR (400 MHz, DMSO-d_6) δ 8.39 (br s, 2H, **H⁸**), 8.10 (d, *J* = 2.1 Hz, 1H, **H¹**), 8.09 (t, *J* = 1.6 Hz, 1H, **H⁴**), 8.06–8.00 (m, 2H, **H²,⁷**), 7.92–7.82 (m, 2H, **H⁵,⁶**), 7.57 (d, *J* = 8.7 Hz, 1H, **H³**); ^{13}C NMR (101 MHz, DMSO-d_6) δ 159.14, 152.29, 139.21, 134.87, 134.82, 134.20, 133.53, 132.24, 130.73, 129.70, 120.61, 118.40, 117.57, 116.75, 113.64; LC-MS (APCI/ESI): Purity = 98%, t_R = 3.32 min, *m/z* $[M+H]^+$ = 341.0, 343.0 (1:1).

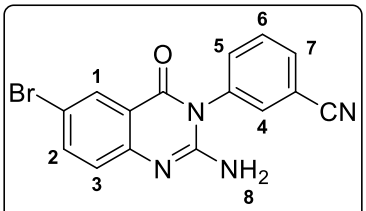

2.7a
$C_{15}H_9BrN_4O$
Exact Mass: 340.0
Mwt: 341.17

***2-amino-6-bromo-3-(4-(methylsulfonyl)phenyl)quinazolin-4(3H)-one*, 2.7b**

White solid (0.571 g, 77%); *Rf* (100% EtOAc) 0.18; ^{1}H NMR (400 MHz, DMSO-d_6) δ 8.15 (d, *J* = 8.7 Hz, 2H, **H⁴**), 8.03 (d, *J* = 2.3 Hz, 1H, **H¹**), 7.88 (dd, *J* = 8.8, 2.4 Hz, 1H, **H²**), 7.74 (d, *J* = 8.7 Hz, 2H, **H⁵**), 7.48 (br s, 2H, **H⁷**), 7.33 (d, *J* = 8.8 Hz, 1H, **H³**), 3.30 (s, 3H, **H⁶**); ^{13}C NMR (101 MHz, DMSO-d_6) δ

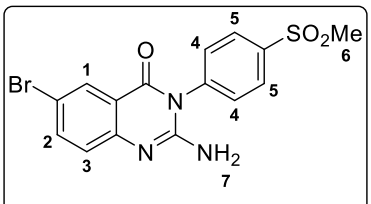

2.7b
$C_{15}H_{12}BrN_3O_3S$
Exact Mass: 393.0
Mwt: 394.24

160.34, 158.80, 152.16, 142.39, 139.19, 138.36, 130.74 (2C), 129.48 (2C), 129.19, 124.11, 118.20, 114.81, 43.97; LC-MS (APCI/ESI): Purity = 99%, t_R = 4.27 min, *m/z* $[M+H]^+$ = 394.0, 396.0 (1:1).

***2-amino-6-bromo-3-(2-(trifluoromethyl)phenyl)quinazolin-4(3H)-one*, 2.7c**

White solid (0.263 g, 71%); R_f (100% EtOAc) 0.37; ^{1}H NMR (400 MHz, DMSO-d_6) δ 7.95 (d, *J* = 2.5 Hz, 1H, **H^1**), 7.95–7.93 (m, 1H, **H^7**), 7.89 (td, *J* = 7.7, 0.9 Hz, 1H, **H^5**), 7.81–7.77 (m, 1H, **H^6**), 7.75 (dd, *J* = 8.8, 2.5 Hz, 1H, **H^2**), 7.63 (d, *J* = 7.8 Hz, 1H, **H^4**), 7.22 (d, *J* = 8.8 Hz, 1H, **H^3**), 6.66 (br s, 2H, **H^8**); ^{13}C NMR (101 MHz, DMSO-d_6) δ 161.37, 152.41, 149.98, 137.83, 135.06, 133.30, 132.30, 130.98, 128.81, 128.39, 128.34, 127.70, 126.95, 118.21, 113.40; LC-MS (APCI/ESI): Purity = 97%, t_R = 3.80 min, *m/z* $[M+H]^+$ = 384.0, 386.0 (1:1).

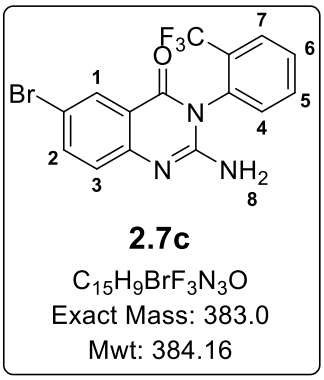

2.7c
$C_{15}H_9BrF_3N_3O$
Exact Mass: 383.0
Mwt: 384.16

***2-amino-6-bromo-3-(6-(trifluoromethyl)pyridin-3-yl)quinazolin-4(3H)-one*, 2.7d**

White solid (0.241 g, 64%); R_f (EtOAc:Hex, 80:20) 0.35; ^{1}H NMR (400 MHz, DMSO-d_6) δ 8.83 (d, *J* = 2.3 Hz, 1H, **H^6**), 8.22 (dd, *J* = 7.7, 2.3 Hz, 1H, **H^4**), 8.13 (d, *J* = 7.6 Hz, 1H, **H^5**), 7.97 (d, *J* = 2.4 Hz, 1H, **H^1**), 7.77 (dd, *J* = 8.8, 2.5 Hz, 1H, **H^2**), 7.23 (d, *J* = 8.7 Hz, 1H, **H^3**), 6.80 (br s, 2H, **H^7**); ^{13}C NMR (101 MHz, DMSO-d_6) δ 161.45, 152.06, 151.03, 149.99, 147.28, 146.94, 139.92, 137.85, 135.80, 128.82, 126.97, 122.72, 118.46, 113.42; LC-MS (APCI/ESI): Purity > 99%, t_R = 3.73 min, *m/z* $[M+H]^+$ = 385.0, 387.0 (1:1).

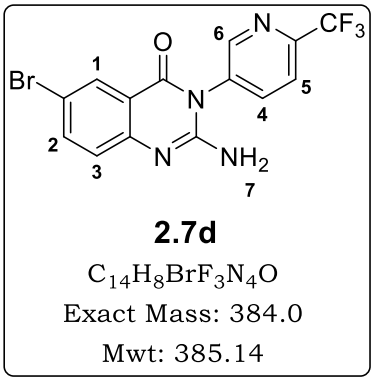

2.7d
$C_{14}H_8BrF_3N_4O$
Exact Mass: 384.0
Mwt: 385.14

***2-amino-6-bromo-3-(4-(trifluoromethyl)phenyl)quinazolin-4(3H)-one*, 2.7e**

White crystalline solid (0.411 g, 57%); R_f (EtOAc:Hex, 70:30) 0.49; ^{1}H NMR (400 MHz, DMSO-d_6) δ 7.96 (d, *J* = 2.4 Hz, 1H, **H^1**), 7.94 (d, *J* = 8.3 Hz, 2H, **H^5**), 7.75 (dd, *J* = 8.8, 2.5 Hz, 1H, **H^2**), 7.65 (d, *J* = 8.1 Hz, 2H, **H^4**), 7.22 (d, *J* = 8.8

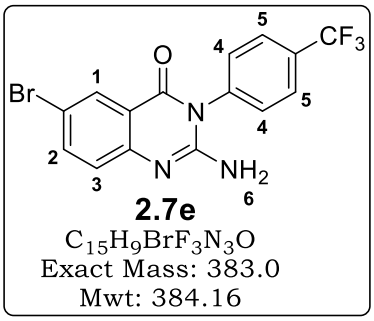

2.7e
$C_{15}H_9BrF_3N_3O$
Exact Mass: 383.0
Mwt: 384.16

Hz, 1H, **H³**), 6.67 (br s, 2H, **H⁶**); ^{13}C NMR (101 MHz, DMSO-d_6) δ 161.19, 152.18, 149.52, 139.40, 137.69, 130.60 (2C), 130.08, 128.85, 127.62, 127.58, 126.68, 123.18, 118.64, 113.43; LC-MS (APCI/ESI): Purity > 99%, t_R = 3.50 min, *m/z* $[M+H]^+$ = 384.0, 386.0 (1:1).

4-*(2-amino-6-bromo-4-oxoquinazolin-3(4H)-yl)benzonitrile*, 2.7f

Off-white solid (0.302 g, 54%); R_f (EtOAc:Hex, 80:20) 0.22; ^{1}H NMR (400 MHz, DMSO-d_6) δ 8.05 (d, *J* = 8.7 Hz, 2H, **H⁴**), 7.95 (d, *J* = 2.5 Hz, 1H, **H¹**), 7.74 (dd, *J* = 8.8, 2.5 Hz, 1H, **H²**), 7.64 (d, *J* = 8.7 Hz, 2H, **H⁵**), 7.21 (d, *J* = 8.8 Hz, 1H, **H³**), 6.59 (br s, 2H, **H⁶**); ^{13}C NMR (101 MHz, DMSO-d_6) δ 161.16, 151.99, 149.90, 140.11, 137.68, 134.62 (2C), 130.91 (2C), 128.80, 126.90, 118.93, 118.65, 113.33, 112.74; LC-MS (APCI/ESI): Purity = 93%, t_R = 3.32 min, *m/z* $[M+H]^+$ = 341.0, 343.0 (1:1).

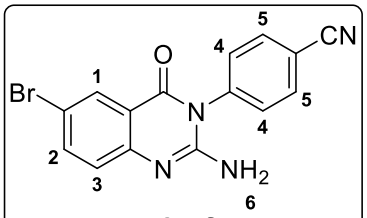

2.7f
$C_{15}H_9BrN_4O$
Exact Mass: 340.0
Mwt: 341.17

2-*amino-6-bromo-3-(4-hydroxyphenyl)quinazolin-4(3H)-one*, 2.7g

White solid (0.320 g, 58%); R_f (100% EtOAc) 0.39; ^{1}H NMR (400 MHz, DMSO-d_6) δ 9.81 (br s, 1H, **H⁶**), 7.94 (d, *J* = 2.5 Hz, 1H, **H¹**), 7.71 (dd, *J* = 8.8, 2.5 Hz, 1H, **H²**), 7.18 (d, *J* = 8.8 Hz, 1H, **H³**), 7.13 (d, *J* = 8.8 Hz, 2H, **H⁴**), 6.91 (d, *J* = 8.8 Hz, 2H, **H⁵**), 6.36 (br s, 2H, **H⁷**); ^{13}C NMR (101 MHz, DMSO-d_6) δ 161.48, 158.46, 153.13, 149.70, 137.39, 130.12 (2C), 128.85, 126.82, 126.39, 118.87, 117.02 (2C), 113.17; LC-MS (APCI/ESI): Purity > 99%, t_R = 3.06 min, *m/z* $[M+H]^+$ = 332.0, 334.0 (1:1).

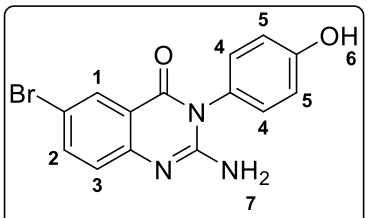

2.7g
$C_{14}H_{10}BrN_3O_2$
Exact Mass: 331.0
Mwt: 332.16

2-*amino-6-bromo-3-(4-fluorophenyl)quinazolin-4(3H)-one*, 2.7h

White solid (0.600 g, 77%); R_f (100% EtOAc) 0.36; ^{1}H NMR (400 MHz, DMSO-d_6) δ 7.95 (d, *J* = 2.4 Hz, 1H, **H¹**), 7.73 (dd, *J* = 8.8, 2.5 Hz, 1H, **H²**), 7.48–7.35 (m, 4H, **H⁴,⁵**), 7.20 (d, *J* = 8.8 Hz, 1H, **H³**), 6.52 (br s, 2H, **H⁶**); ^{13}C NMR (101 MHz, DMSO-d_6) δ 164.03, 161.40,

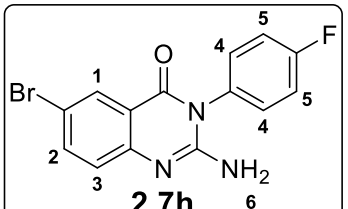

2.7h
$C_{14}H_9BrFN_3O$
Exact Mass: 333.0
Mwt: 334.15

152.70, 149.83, 137.51, 131.85, 131.63, 131.54, 128.84, 126.85, 118.76, 117.49, 117.26, 113.21; LC-MS (APCI/ESI): Purity > 99%, t_R = 3.44 min, *m/z* $[M+H]^+$ = 334.0, 336.0 (1:1).

***2-amino-6-bromo-3-(2-fluorophenyl)quinazolin-4(3H)-one*, 2.7i**

White solid (0.573 g, 73%); R_f (100% EtOAc) 0.33; ^{1}H NMR (400 MHz, DMSO-d_6) δ 7.97 (d, *J* = 2.5 Hz, 1H, **H^1**), 7.76 (dd, *J* = 8.8, 2.5 Hz, 1H, **H^2**), 7.60 (dddd, *J* = 8.4, 7.2, 5.2, 1.8 Hz, 1H, **H^6**), 7.52 (td, *J* = 7.8, 1.7 Hz, 1H, **H^5**), 7.47 (ddd, *J* = 9.8, 8.4, 1.2 Hz, 1H, **H^7**), 7.40 (td, *J* = 7.7, 1.3 Hz, 1H, **H^4**), 7.22 (d, *J* = 8.8 Hz, 1H, **H^3**), 6.73 (br s, 2H, **H^8**); ^{13}C NMR (101 MHz, DMSO-d_6) δ 160.78, 159.39, 156.92, 152.24, 149.83, 137.90, 132.29, 131.42, 128.88, 126.93, 126.29, 118.20, 117.27, 113.57; LC-MS (APCI/ESI): Purity > 99%, t_R = 3.51 min, *m/z* $[M+H]^+$ = 334.0, 336.0 (1:1).

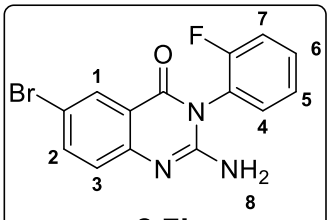

2.7i
$C_{14}H_9BrFN_3O$
Exact Mass: 333.0
Mwt: 334.15

***2-amino-6-bromo-3-(4-methoxyphenyl)quinazolin-4(3H)-one*, 2.7j**

Off-white solid (0.550 g, 80%); R_f (100% EtOAc) 0.24; ^{1}H NMR (400 MHz, DMSO-d_6) δ 7.95 (d, *J* = 2.4 Hz, 1H, **H^1**), 7.72 (dd, *J* = 8.8, 2.5 Hz, 1H, **H^2**), 7.28 (d, *J* = 8.9 Hz, 2H, **H^4**), 7.19 (d, *J* = 8.8 Hz, 1H, **H^3**), 7.11 (d, *J* = 8.9 Hz, 2H, **H^5**), 6.41 (br s, 2H, **H^7**), 3.84 (s, 3H, **H^6**); ^{13}C NMR (101 MHz, DMSO-d_6) δ 161.47, 160.10, 153.02, 149.76, 137.42, 130.31 (2C), 128.86, 128.02, 126.84, 118.85, 115.72 (2C), 113.18, 55.88; LC-MS (APCI/ESI): Purity = 99%, t_R = 3.57 min, *m/z* $[M+H]^+$ = 346.0, 348.0 (1:1).

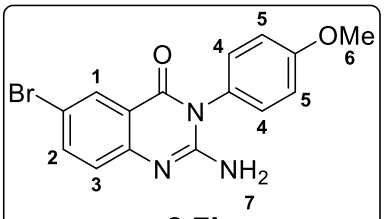

2.7j
$C_{15}H_{12}BrN_3O_2$
Exact Mass: 345.0
Mwt: 346.18

General procedure 8: Synthesis of SAR 2 2-aminoquinazolinone-based target compounds 32–44 [Suzuki-Miyaura cross-coupling reaction]

The appropriate arylboronic acid [in most cases, 3-(methylsulfinyl)phenyl) boronic acid] (1.2 Eq) and the corresponding 2-amino-6-bromo-quinazolinone-based intermediate **2.7** (**a–j**) (1.0 Eq) were dissolved in DMF (5 mL). The mixture was flushed with nitrogen gas for about 10 min at room

temperature, after which $Pd(PPh_3)_2Cl_2$ (0.05 Eq) and K_2CO_3 (3 Eq) were added successively, and the mixture heated at 100 °C for 1 to 4 h. After cooling to room temperature, the mixture was diluted with EtOAc (10 mL) and water (30 mL), and the extracted with EtOAc (20 mL × 3). The combined organic fractions were filtered through a pad of celite, washed with 5% LiCl (30 mL × 3), brine (30 mL × 2), and dried over anhydrous $MgSO_4$. The solvents were then removed *in vacuo* to yield a residue that was purified by column chromatography using Biotage Isolera One® machine, SiO_2 (10 g cartridge), DCM/MeOH, with fractions being collected at the λ_{max} and monitored at 254 nm. Finally, the solvents were rotary evaporated to give a solid that was then triturated with Et_2O, filtered, or recrystallized in an appropriate solvent [ethanol was used in most cases], and dried to furnish the desired final target compound.

***2-amino-6-(3-(methylsulfinyl)phenyl)-3-phenylquinazolin-4(3H)-one*, 32**

White solid (0.170 g, 55%); m.p. 229.6–232.8 ºC; R_f (MeOH:DCM, 8:92) 0.32; ^{1}H NMR (400 MHz, DMSO-d_6) δ 8.22 (d, J = 1.8 Hz, 1H, **H^1**), 8.03 (dd, J = 8.5, 1.8 Hz, 1H, **H^2**), 7.98 (s, 1H, **H^8**), 7.90–7.82 (m, 1H, **H^9**), 7.73–7.51 (m, 5H, **H^{4,5,6}**), 7.46–7.31 (m, 3H, **H^{3,10,11}**), 6.39 (br s, 2H, **H^7**), 2.82 (s, 3H, **H^{12}**); ^{13}C NMR (101 MHz, DMSO-d_6) δ 162.29, 152.50, 150.48, 147.89, 140.86, 135.86, 133.50, 132.53, 130.49 (2C), 129.74, 129.29 (2C), 128.86, 125.25, 124.79, 122.61, 122.38, 121.49, 117.56, 43.75; LC-MS (APCI/ESI): Purity = 95%, t_R = 3.78 min, m/z $[M+H]^+$ = 376.1.

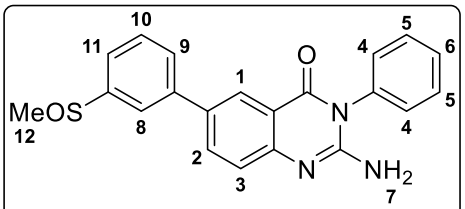

32
$C_{21}H_{17}N_3O_2S$
Exact Mass: 375.1
Mwt: 375.45

***2-amino-6-(3-(methylsulfinyl)phenyl)-3-(p-tolyl)quinazolin-4(3H)-one*, 33**

Off-white solid (0.100 g, 32%); m.p. 243.9–250.8 ºC; R_f (MeOH:DCM, 8:92) 0.42; ^{1}H NMR (400 MHz, DMSO-d_6) δ 8.21 (d, J = 2.3 Hz, 1H, **H^1**), 8.02 (dd, J = 8.6, 2.4 Hz, 1H, **H^2**), 7.98 (dd, J = 2.2, 1.3 Hz, 1H, **H^8**), 7.87 (dt, J = 6.6, 2.2 Hz, 1H, **H^9**), 7.70–

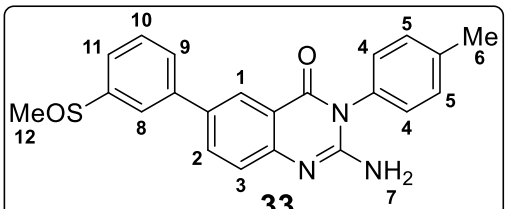

33
$C_{22}H_{19}N_3O_2S$
Exact Mass: 389.1
Mwt: 389.47

7.63 (m, 2H, **H^{10,11}**), 7.40 (d, *J* = 8.5 Hz, 2H, **H^{4}**), 7.37 (d, *J* = 8.8 Hz, 1H, **H^{3}**), 7.26 (d, *J* = 8.3 Hz, 2H, **H^{5}**), 6.36 (br s, 2H, **H^{7}**), 2.82 (s, 3H, **H^{12}**), 2.42 (s, 3H, **H^{6}**); ^{13}C NMR (101 MHz, DMSO-d_6) δ 162.34, 152.65, 150.50, 147.88, 140.87, 139.13, 133.44, 133.22, 132.47, 131.02 (2C), 130.44, 128.97 (2C), 128.85, 125.25, 124.79, 122.59, 121.48, 117.56, 43.74, 21.34; LC-MS (APCI/ESI): Purity = 97%, t_R = 3.42 min, *m/z* $[M+H]^+$ = 390.1.

***2-amino-6-(3-(methylsulfinyl)phenyl)-3-(3-(trifluoromethyl)phenyl)quinazolin-4(3H)-one*, 34**

Off-white solid (0.169 g, 55%); m.p. 152.1–153.9 °C; R_f (MeOH:DCM, 8:92) 0.36; ^{1}H NMR (400 MHz, DMSO-d_6) δ 8.21 (d, *J* = 2.3 Hz, 1H, **H^{1}**), 8.03 (dd, *J* = 8.6, 2.4 Hz, 1H, **H^{2}**), 7.98 (s, 1H, **H^{4}**), 7.90 (d, *J* = 8.3 Hz, 1H, **H^{7}**), 7.88–7.84 (m, 2H, **H^{5,12}**), 7.82 (t, *J* = 7.8 Hz, 1H, **H^{11}**), 7.73 (d, *J* = 8.0 Hz, 1H, **H^{10}**), 7.68 (t, *J* = 6.1 Hz, 1H, **H^{6}**), 7.67 (s, 1H, **H^{9}**), 7.38 (d, *J* = 8.6 Hz, 1H, **H^{3}**), 6.57 (br s, 2H, **H^{8}**), 2.82 (s, 3H, **H^{13}**); ^{13}C NMR (101 MHz, DMSO-d_6) δ 162.41, 152.24, 150.69, 147.90, 140.85, 136.75, 133.84, 133.59, 132.50, 131.60, 131.32, 131.00, 130.46, 128.84, 126.80, 126.64, 125.31, 124.76, 122.63, 121.47, 117.45, 43.74; LC-MS (APCI/ESI): Purity = 96%, t_R = 3.72 min, *m/z* $[M+H]^+$ = 444.1.

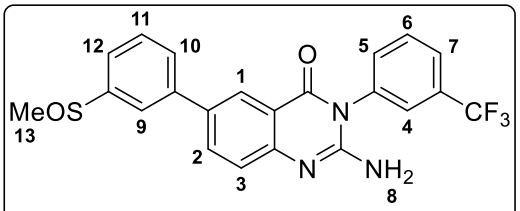

34
$C_{22}H_{16}F_3N_3O_2S$
Exact Mass: 443.1
Mwt: 443.44

***2-amino-6-(3-(methylsulfinyl)phenyl)-3-(2-(trifluoromethyl)phenyl)quinazolin-4(3H)-one*, 35**

Off-white solid (0.080 g, 33%); m.p. 135.7–138.3 °C; R_f (MeOH:DCM, 6:94) 0.26; ^{1}H NMR (400 MHz, DMSO-d_6) δ 8.20 (d, *J* = 2.4 Hz, 1H, **H^{1}**), 8.04 (dd, *J* = 8.6, 2.4 Hz, 1H, **H^{2}**), 8.00–7.94 (m, 2H, **H^{9,10}**), 7.91 (dd, *J* = 7.7, 0.9 Hz, 1H, **H^{7}**), 7.89–7.86 (m, 1H, **H^{12}**), 7.82–7.75 (m, 1H, **H^{11}**), 7.69–7.62 (m, 3H, **H^{4,5,6}**), 7.38 (d, *J* = 8.6 Hz, 1H, **H^{3}**), 6.61 (br s, 2H, **H^{8}**), 2.82 (s, 3H, **H^{13}**); ^{13}C NMR (101 MHz, DMSO-d_6) δ 162.38, 152.32, 150.76, 147.88, 140.75, 135.04, 133.78, 133.59, 132.62, 132.36, 130.91, 130.43, 128.89, 128.40, 127.80,

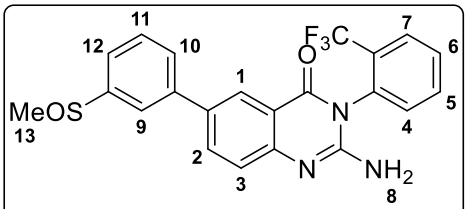

35
$C_{22}H_{16}F_3N_3O_2S$
Exact Mass: 443.1
Mwt: 443.44

127.50, 125.37, 124.75, 122.62, 121.55, 116.99, 43.76; LC-MS (APCI/ESI): Purity = 97%, t_R = 3.35 min, *m/z* $[M+H]^+$ = 444.1.

2-amino-6-(3-(methylsulfinyl)phenyl)-3-(6-(trifluoromethyl)pyridin-3-yl)quinazolin-4(3H)-one, 36

Off-white solid (0.130 g, 56%); m.p. 153.0–155.8 °C; R_f (MeOH:DCM, 6:94) 0.16; ^{1}H NMR (400 MHz, DMSO-d_6) δ 8.86 (d, *J* = 2.3 Hz, 1H, **H^6**), 8.25 (dd, *J* = 8.3, 2.3 Hz, 1H, **H^4**), 8.22 (d, *J* = 2.3 Hz, 1H, **H^1**), 8.14 (d, *J* = 8.3 Hz, 1H, **H^5**), 8.05 (dd, *J* = 8.6, 2.4 Hz, 1H, **H^2**), 7.98 (dd, *J* = 2.2, 1.2 Hz, 1H, **H^8**), 7.91–7.84 (m, 1H, **H^9**), 7.71–7.64 (m, 2H, **H^{10,11}**), 7.39 (d, *J* = 8.6 Hz, 1H, **H^3**), 6.78 (br s, 2H, **H^7**), 2.82 (s, 3H, **H^{12}**); ^{13}C NMR (101 MHz, DMSO-d_6) δ 162.46, 151.95, 151.09, 150.74, 147.90, 147.22, 146.88, 140.73, 139.95, 136.01, 133.83, 132.67, 130.46, 128.87, 125.41, 124.74, 123.42, 122.68, 121.50, 117.15, 43.74; LC-MS (APCI/ESI): Purity = 99%, t_R = 3.38 min, *m/z* $[M+H]^+$ = 445.1.

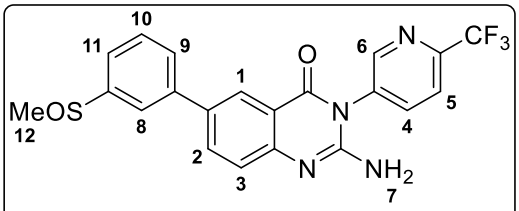

36
$C_{21}H_{15}F_3N_4O_2S$
Exact Mass: 444.1
Mwt: 444.43

4-(2-amino-6-(3-(methylsulfinyl)phenyl)-4-oxoquinazolin-3(4H)-yl)benzonitrile, 37

Off-white solid (0.070 g, 32%); m.p. 331.7–334.5 °C; R_f (MeOH:DCM, 6:94) 0.19; ^{1}H NMR (400 MHz, DMSO-d_6) δ 8.21 (d, *J* = 2.2 Hz, 1H, **H^1**), 8.07 (d, *J* = 8.6 Hz, 2H, **H^4**), 8.03 (dd, *J* = 8.6, 2.4 Hz, 1H, **H^2**), 7.98 (s, 1H, **H^7**), 7.86 (dt, *J* = 6.7, 2.1 Hz, 1H, **H^8**), 7.71–7.63 (m, 4H, **H^{5,9,10}**), 7.37 (d, *J* = 8.6 Hz, 1H, **H^3**), 6.57 (br s, 2H, **H^6**), 2.82 (s, 3H, **H^{11}**); ^{13}C NMR (101 MHz, DMSO-d_6) δ 162.17, 151.89, 150.67, 147.86, 140.79, 140.35, 134.63 (2C), 133.67, 132.57, 130.98 (2C), 130.46, 128.86, 125.34, 124.73, 122.66, 121.47, 118.96, 117.35, 112.70, 43.73; LC-MS (APCI/ESI): Purity = 98%, t_R = 2.94 min, *m/z* $[M+H]^+$ = 401.1.

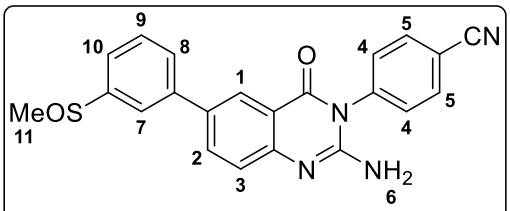

37
$C_{22}H_{16}N_4O_2S$
Exact Mass: 400.1
Mwt: 400.46

***3-(2-amino-6-(3-(methylsulfinyl)phenyl)-4-oxoquinazolin-3(4H)-yl)benzonitrile*, 38**

Off-white solid (0.113 g, 38%); m.p. 255.6–259.5 °C; R_f (MeOH:DCM, 6:94) 0.19; ^{1}H NMR (400 MHz, DMSO-d_6) δ 8.21 (d, J = 2.2 Hz, 1H, **H^1**), 8.07–7.99 (m, 3H, **H^{2,7,9}**), 7.98 (s, 1H, **H^4**), 7.87 (dt, J = 6.6, 2.1 Hz, 1H, **H^{10}**), 7.81–7.75 (m, 2H, **H^{5,11}**), 7.71–7.63 (m, 2H, **H^{6,12}**), 7.38 (d, J = 8.6 Hz, 1H, **H^3**), 6.60 (br s, 2H, **H^8**), 2.82 (s, 3H, **H^{13}**); ^{13}C NMR (101 MHz, DMSO-d_6) δ 162.31, 152.12, 150.67, 147.90, 140.80, 136.89, 134.90, 133.67 (3C), 132.56, 131.74, 130.46, 128.86, 125.34, 124.74, 122.65, 121.48, 118.69, 117.37, 113.47, 43.74; LC-MS (APCI/ESI): Purity > 99%, t_R = 2.88 min, *m/z* $[M+H]^+$ = 401.1.

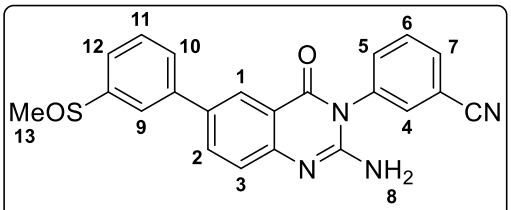

38
$C_{22}H_{16}N_4O_2S$
Exact Mass: 400.1
Mwt: 400.46

***2-amino-6-(3-(methylsulfinyl)phenyl)-3-(4-(methylsulfonyl)phenyl)quinazolin-4(3H)-one*, 39**

Off-white solid (0.070 g, 20%); m.p. 298.3–301.9 °C; R_f (MeOH:DCM, 6:94) 0.15; ^{1}H NMR (400 MHz, DMSO-d_6) δ 8.21 (d, J = 2.2 Hz, 1H, **H^1**), 8.13 (d, J = 8.5 Hz, 2H, **H^4**), 8.04 (dd, J = 8.6, 2.3 Hz, 1H, **H^2**), 7.98 (s, 1H, **H^8**), 7.87 (dt, J = 7.4, 1.9 Hz, 1H, **H^9**), 7.71 (d, J = 8.4 Hz, 2H, **H^5**), 7.69–7.63 (m, 2H, **H^{10,11}**), 7.39 (d, J = 8.6 Hz, 1H, **H^3**), 6.57 (br s, 2H, **H^7**), 3.31 (s, 3H, **H^6**), 2.82 (s, 3H, **H^{12}**); ^{13}C NMR (101 MHz, DMSO-d_6) δ 162.25, 151.99, 150.65, 147.85, 141.87, 140.80, 140.53, 133.70, 132.60, 130.76 (2C), 130.47, 129.33 (2C), 128.89, 125.35, 124.73, 122.67, 121.48, 117.34, 44.02, 43.73; LC-MS (APCI/ESI): Purity > 99%, t_R = 2.67 min, *m/z* $[M+H]^+$ = 454.1.

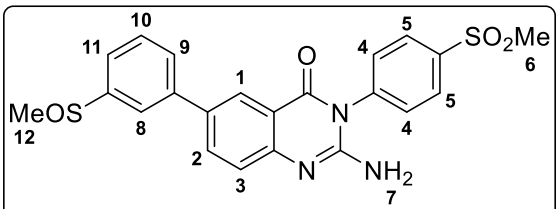

39
$C_{22}H_{19}N_3O_4S_2$
Exact Mass: 453.1
Mwt: 453.53

***2-amino-3-(4-methoxyphenyl)-6-(3-(methylsulfinyl)phenyl)quinazolin-4(3H)-one*, 40**

Off-white solid (0.172 g, 81%); m.p. 237.7–241.7 °C; R_f (MeOH:DCM, 5:95) 0.14; ^{1}H NMR (400 MHz, DMSO-d_6) δ 8.21 (d, J = 2.3 Hz, 1H, **H^1**), 8.01 (dd, J = 8.6, 2.3 Hz, 1H, **H^2**), 7.98 (s, 1H, **H^8**), 7.87 (dt, J = 6.7, 2.0 Hz, 1H, **H^9**), 7.71–7.63 (m, 2H, **H^{10,11}**), 7.36 (d, J = 8.6 Hz, 1H, **H^3**), 7.30 (d, J = 8.9 Hz,

2H, **H⁴**), 7.12 (d, *J* = 8.9 Hz, 2H, **H⁵**), 6.38 (br s, 2H, **H⁷**), 3.85 (s, 3H, **H⁶**), 2.82 (s, 3H, **H¹²**); ^{13}C NMR (101 MHz, DMS-*d*$_6$) δ 162.48, 160.06, 152.92, 150.51, 147.87, 140.89, 133.40, 132.41, 130.44, 130.37 (2C), 128.84, 128.25, 125.23, 124.80, 122.58, 121.46, 117.56, 115.73 (2C), 55.88, 43.74; LC-MS (APCI/ESI): Purity = 97%, t_R = 3.16 min, *m/z* $[M+H]^+$ = 406.1.

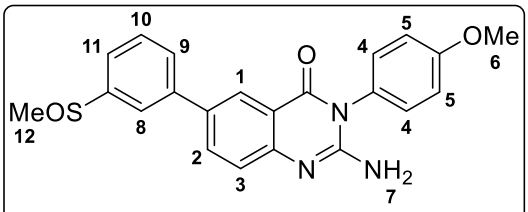

40
$C_{22}H_{19}N_3O_3S$
Exact Mass: 405.1
Mwt: 405.47

***2-amino-3-(4-hydroxyphenyl)-6-(3-(methylsulfinyl)phenyl)quinazolin-4(3H)-one*, 41**

White solid (0.110 g, 40%); m.p. 294.4–300.1 °C; R_f (MeOH:DCM, 10:90) 0.32; ^{1}H NMR (400 MHz, DMSO-*d*$_6$) δ 9.80 (br s, 1H, **H⁶**), 8.20 (d, *J* = 2.2 Hz, 1H, **H¹**), 8.01 (dd, *J* = 8.6, 2.3 Hz, 1H, **H²**), 7.97 (s, 1H, **H⁸**), 7.86 (dt, *J* = 6.8, 2.0 Hz, 1H, **H⁹**), 7.72–7.62 (m, 2H, **H¹⁰,¹¹**), 7.35 (d, *J* = 8.6 Hz, 1H, **H³**), 7.15 (d, *J* = 8.8 Hz, 2H, **H⁴**), 6.93 (d, *J* = 8.8 Hz, 2H, **H⁵**), 6.33 (br s, 2H, **H⁷**), 2.82 (s, 3H, **H¹²**); ^{13}C NMR (101 MHz, DMSO-*d*$_6$) δ 162.50, 158.41, 153.05, 150.52, 147.87, 140.91, 133.36, 132.38, 130.44, 130.19 (2C), 128.84, 126.65, 125.24, 124.81, 122.57, 121.47, 117.60, 117.03 (2C), 43.74; LC-MS (APCI/ESI): Purity > 99%, t_R = 2.66 min, *m/z* $[M+H]^+$ = 392.1.

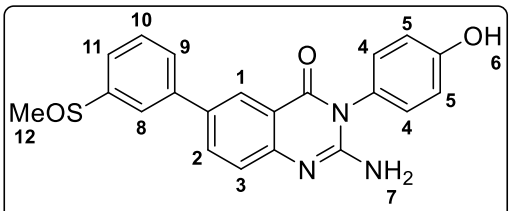

41
$C_{21}H_{17}N_3O_3S$
Exact Mass: 391.1
Mwt: 391.45

***2-amino-3-(4-fluorophenyl)-6-(3-(methylsulfinyl)phenyl)quinazolin-4(3H)-one*, 42**

White solid (0.188 g, 71%); m.p. 232.6–238.1 °C; R_f (MeOH:DCM, 6:94) 0.22; ^{1}H NMR (400 MHz, DMSO-*d*$_6$) δ 8.21 (d, *J* = 2.2 Hz, 1H, **H¹**), 8.02 (dd, *J* = 8.6, 2.4 Hz, 1H, **H²**), 7.98 (s, 1H, **H⁷**), 7.86 (dt, *J* = 6.7, 2.1 Hz, 1H, **H⁸**), 7.71–7.63 (m, 2H, **H⁹,¹⁰**), 7.50–7.38 (m, 4H, **H⁴,⁵**), 7.37 (d, *J* = 8.6 Hz, 1H, **H³**), 6.49 (br s, 2H, **H⁶**), 2.82 (s, 3H, **H¹¹**); ^{13}C NMR (101 MHz, DMSO-*d*$_6$) δ 164.00, 162.41, 161.56, 152.61, 150.62, 147.89, 140.86, 133.49, 132.44,

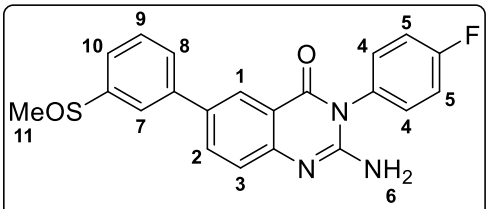

42
$C_{21}H_{16}FN_3O_2S$
Exact Mass: 393.1
Mwt: 393.44

132.09, 131.68, 131.59, 130.44, 128.83, 125.27, 124.77, 122.60, 121.46, 117.48, 117.26, 43.74; LC-MS (APCI/ESI): Purity = 98%, t_R = 3.05 min, *m/z* $[M+H]^+$ = 394.1.

***2-amino-3-(2-fluorophenyl)-6-(3-(methylsulfinyl)phenyl)quinazolin-4(3H)-one*, 43**

White solid (0.234 g, 66%); m.p. 263.1–268.4 °C; R_f (MeOH:DCM, 6:94) 0.20; ^{1}H NMR (400 MHz, DMSO-d_6) δ 8.22 (d, *J* = 2.3 Hz, 1H, **H^1**), 8.05 (dd, *J* = 8.6, 2.4 Hz, 1H, **H^2**), 7.99 (s, 1H, **H^9**), 7.88 (ddd, *J* = 6.4, 2.6, 2.0 Hz, 1H, **H^{10}**), 7.71–7.65 (m, 2H, **H^{11,12}**), 7.64–7.58 (m, 1H, **H^6**), 7.54 (td, *J* = 7.8, 1.7 Hz, 1H, **H^5**), 7.48 (ddd, *J* = 9.8, 8.4, 1.2 Hz, 1H, **H^7**), 7.44–7.37 (m, 2H, **H^{3,4}**), 6.68 (br s, 2H, **H^8**), 2.82 (s, 3H, **H^{13}**); ^{13}C NMR (101 MHz, DMSO-d_6) δ 161.81, 159.48, 157.00, 152.16, 150.67, 147.90, 140.76, 133.85, 132.76, 132.28, 131.49, 130.45, 128.90, 126.28, 125.38, 124.82, 122.66, 121.56, 117.46, 116.98, 43.74; LC-MS (APCI/ESI): Purity > 99%, t_R = 3.08 min, *m/z* $[M+H]^+$ = 394.1.

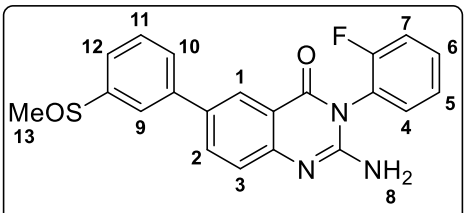

43
$C_{21}H_{16}FN_3O_2S$
Exact Mass: 393.1
Mwt: 393.44

***2-amino-3-(2-fluorophenyl)-6-(3-(methylsulfonyl)phenyl)quinazolin-4(3H)-one*, 44**

White solid (0.200 g, 76%); m.p. 270.0–273.9 °C; R_f (MeOH:DCM, 6:94) 0.35; ^{1}H NMR (400 MHz, DMSO-d_6) δ 8.25 (d, *J* = 2.2 Hz, 1H, **H^1**), 8.21 (t, *J* = 1.7 Hz, 1H, **H^9**), 8.11–8.04 (m, 2H, **H^{2,12}**), 7.91 (ddd, *J* = 7.8, 1.7, 1.0 Hz, 1H, **H^{10}**), 7.75 (t, *J* = 7.8 Hz, 1H, **H^{11}**), 7.65–7.58 (m, 1H, **H^6**), 7.55 (td, *J* = 7.8, 1.7 Hz, 1H, **H^5**), 7.49 (ddd, *J* = 9.8, 8.4, 1.2 Hz, 1H, **H^7**), 7.45–7.37 (m, 2H, **H^{3,4}**), 6.71 (br s, 2H, **H^8**), 3.31 (s, 3H, **H^{13}**); ^{13}C NMR (101 MHz, DMSO-d_6) δ 162.77, 161.79, 159.48, 157.00, 152.27, 150.87, 142.23, 140.94, 133.88, 132.09, 131.71, 131.48, 130.67, 126.27, 125.86, 125.47, 125.06, 124.95, 117.47, 117.02, 43.95; LC-MS (APCI/ESI): Purity = 98%, t_R = 3.04 min, *m/z* $[M+H]^+$ = 410.1.

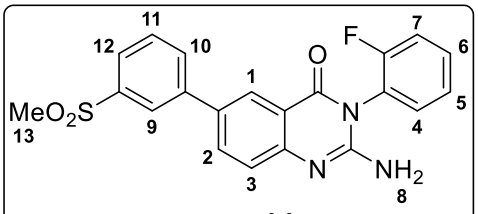

44
$C_{21}H_{16}FN_3O_3S$
Exact Mass: 409.1
Mwt: 409.44

6.2.4.2 Benzoxazole-Based Oxime Series

The synthetic protocols followed in the synthesis of benzoxazole-based oxime analogues were based on various methods reported in literature, which were appropriately modified to generate the relevant synthetic schemes.[4–9]

***2-cyanoacetimidic acid ethyl ester hydrochloride*, 2.8**

Ethanol (13.3 mL, 228 mmol, 2.0 Eq), TMSCl (14.5 mL, 114 mmol, 1.0 Eq), and malononitrile (7.5 g, 114 mmol, 1.0 Eq) were sequentially added to a dry round bottom flask (100 mL) at 0 °C, and stirred at this temperature for 17 h under nitrogen atmosphere. The solids in the mixture were then filtered, washed thoroughly with dry Et_2O, and dried *in vacuo* to furnish **2.8** as an off-white crystalline solid (14.1 g, 83%); ^{1}H NMR (300 MHz, DMSO-d_6) δ 4.16 (q, J = 7.1 Hz, 2H, **H³**), 4.00 (s, 2H, **H¹**), 3.87 (br s, 2H, **H²**), 1.21 (t, J = 7.1 Hz, 3H, **H⁴**); ^{13}C NMR (101 MHz, DMSO-d_6) δ 164.75, 115.51, 62.37, 24.98, 14.33.

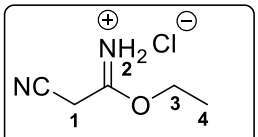

2.8
$C_5H_9ClN_2O$
Exact Mass: 148.0
Mwt: 148.59

General procedure 9: Synthesis of Benzoxazole-2-acetonitrile-based intermediates 2.9a–2.9o

An appropriately substituted 2-aminophenol (1.0 Eq) was added to a stirred suspension of **2.8** (1.2 Eq) in dry DCM and stirred at 25 °C for 10 min. The mixture was then heated to reflux at 50 °C for 20 h, cooled to room temperature, filtered, and the solids discarded. This was followed by concentration of the filtrate under reduced pressure to yield a crude residue, which was washed with water, dried, and recrystallized in EtOAc:Hex mixture to afford the desired product.

***2-(benzo[d]oxazol-2-yl)acetonitrile*, 2.9a**

Off-white solid (6.800 g, 69%); R_f (EtOAc:Hex, 3:7) 0.30; ^{1}H NMR (300 MHz, DMSO-d_6) δ 7.81–7.71 (m, 1H, **H⁴**), 7.62–7.52 (m, 1H, **H¹**), 7.48–7.33 (m, 2H, **H²,³**), 4.13 (s, 2H, **H⁵**); LC-MS (APCI/ESI): Purity > 99%, t_R = 2.81 min, m/z $[M-H]^-$ = 157.1.

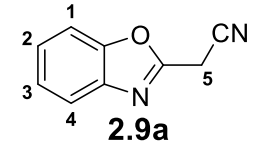

2.9a
$C_9H_6N_2O$
Exact Mass: 158.1
Mwt: 158.16

2-*(6-methylbenzo[d]oxazol-2-yl)acetonitrile*, 2.9b

Brown crystalline solid (0.860 g, 73%); R_f (EtOAc:Hex, 20:80) 0.22; ^{1}H NMR (300 MHz, DMSO-d_6) δ 7.63 (d, J = 8.1 Hz, 1H, **H³**), 7.56 (dt, J = 1.5, 0.7 Hz, 1H, **H¹**), 7.23 (ddd, J = 8.1, 1.5, 0.6 Hz, 1H, **H²**), 4.66 (s, 2H, **H⁴**), 2.45 (s, 3H, **H⁵**); ^{13}C NMR (101 MHz, DMSO-d_6) δ 157.37, 151.31, 138.68, 136.16, 126.45, 119.61, 115.58, 111.29, 21.65, 18.78; LC-MS (APCI/ESI): Purity > 99%, t_R = 2.43 min, m/z [M-H]$^-$ = 171.1.

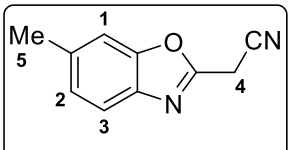

2.9b
$C_{10}H_8N_2O$
Exact Mass: 172.1
Mwt: 172.19

2-*(4-methylbenzo[d]oxazol-2-yl)acetonitrile*, 2.9c

Yellow solid (0.501 g, 43%); R_f (EtOAc:Hex, 50:50) 0.51; ^{1}H NMR (300 MHz, DMSO-d_6) δ 7.55 (d, J = 8.1 Hz, 1H, **H¹**), 7.32 (t, J = 7.8 Hz, 1H, **H²**), 7.22 (d, J = 7.5 Hz, 1H, **H³**), 4.68 (s, 2H, **H⁴**), 2.54 (s, 3H, **H⁵**); LC-MS (APCI/ESI): Purity > 99%, t_R = 2.30 min, m/z [M-H]$^-$ = 171.1.

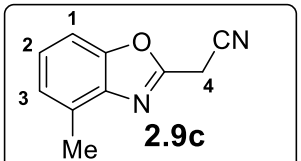

2.9c
$C_{10}H_8N_2O$
Exact Mass: 172.1
Mwt: 172.19

2-*(5-methylbenzo[d]oxazol-2-yl)acetonitrile*, 2.9d

Yellow solid (1.010 g, 86%); R_f (EtOAc:Hex, 50:50) 0.53; ^{1}H NMR (300 MHz, $CDCl_3$) δ 7.54 (d, J = 1.6 Hz, 1H, **H³**), 7.43 (d, J = 8.4 Hz, 1H, **H¹**), 7.22 (dd, J = 8.4, 1.2 Hz, 1H, **H²**), 4.10 (s, 2H, **H⁴**), 2.49 (s, 3H, **H⁵**); LC-MS (APCI/ESI): Purity > 99%, t_R = 2.25 min, m/z [M−H]$^-$ = 171.1.

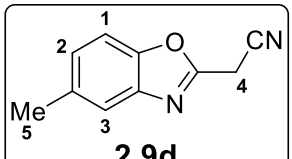

2.9d
$C_{10}H_8N_2O$
Exact Mass: 172.1
Mwt: 172.19

2-*(5-bromobenzo[d]oxazol-2-yl)acetonitrile*, 2.9e

Orange crystalline solid (1.13 g, 71%); R_f (EtOAc:Hex, 30:70) 0.26; ^{1}H NMR (300 MHz, DMSO-d_6) δ 8.04 (d, J = 1.8 Hz, 1H, **H³**), 7.77 (d, J = 8.7 Hz, 1H, **H¹**), 7.61 (dd, J = 8.7, 1.9 Hz, 1H, **H²**), 4.71 (s, 2H, **H⁴**); ^{13}C NMR (101 MHz, DMSO-d_6) δ 159.68, 150.21, 142.60, 128.92, 122.99, 117.31, 115.32, 113.26, 18.98; LC-MS (APCI/ESI): Purity = 97%, t_R = 2.82 min, m/z [M-H]$^-$ = 235.0, 237.0 (1:1).

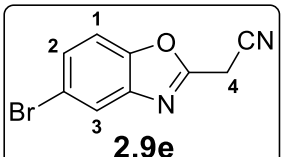

2.9e
$C_9H_5BrN_2O$
Exact Mass: 236.0
Mwt: 237.06

2-(6-bromobenzo[d]oxazol-2-yl)acetonitrile, 2.9f

Brown solid (0.854 g, 54%); R_f (EtOAc:Hex, 50:50) 0.50; ^{1}H NMR (400 MHz, DMSO-d_6) δ 8.12 (d, J = 1.8 Hz, 1H, **H^1**), 7.74 (d, J = 8.5 Hz, 1H, **H^3**), 7.59 (dd, J = 8.5, 1.8 Hz, 1H, **H^2**), 4.69 (s, 2H, **H^4**); ^{13}C NMR (101 MHz, DMSO-d_6) δ 158.95, 151.62, 140.27, 128.59, 121.72, 118.17, 115.32, 114.80, 18.91; LC-MS (APCI/ESI): Purity > 99%, t_R = 2.69 min, m/z [M-H]$^-$ = 235.0, 237.0 (1:1).

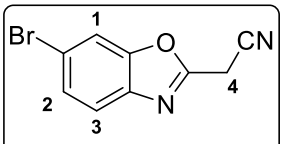

2.9f
$C_9H_5BrN_2O$
Exact Mass: 236.0
Mwt: 237.06

Methyl 2-(cyanomethyl)benzo[d]oxazole-6-carboxylate, 2.9g

Yellow solid (1.16 g, 80%); R_f (EtOAc:Hex, 30:70) 0.15; ^{1}H NMR (400 MHz, DMSO-d_6) δ 8.29 (d, J = 1.1 Hz, 1H, **H^1**), 8.03 (dd, J = 8.4, 1.5 Hz, 1H, **H^2**), 7.90 (d, J = 8.4 Hz, 1H, **H^3**), 4.76 (s, 2H, **H^4**), 3.91 (s, 3H, **H^5**); ^{13}C NMR (101 MHz, DMSO-d_6) δ 166.17, 161.26, 150.79, 144.79, 127.54, 126.60, 120.31, 115.26, 112.47, 52.93, 19.19; LC-MS (APCI/ESI): Purity = 97%, t_R = 2.16 min, m/z [M-H]$^-$ = 215.1.

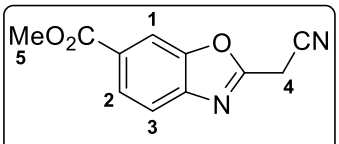

2.9g
$C_{11}H_8N_2O_3$
Exact Mass: 216.1
Mwt: 216.20

2-(6-(trifluoromethyl)benzo[d]oxazol-2-yl)acetonitrile, 2.9h

Yellow solid (1.080 g, 71%); R_f (EtOAc:Hex, 50:50) 0.49; ^{1}H NMR (300 MHz, DMSO-d_6) δ 8.30 (s, 1H, **H^1**), 8.00 (d, J = 8.4 Hz, 1H, **H^3**), 7.78 (dd, J = 8.4, 1.0 Hz, 1H, **H^2**), 4.78 (s, 2H, **H^4**); LC-MS (APCI/ESI): Purity = 92%, t_R = 2.96 min, m/z [M-H]$^-$ = 225.0.

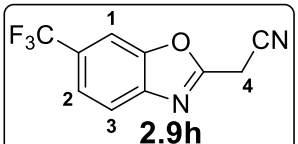

2.9h
$C_{10}H_5F_3N_2O$
Exact Mass: 226.0
Mwt: 226.16

2-(6-chlorobenzo[d]oxazol-2-yl)acetonitrile, 2.9i

Dark brown solid (0.950 g, 73%); R_f (EtOAc:Hex, 50:50) 0.53; ^{1}H NMR (300 MHz, $CDCl_3$) δ 7.68 (d, J = 8.5 Hz, 1H, **H^3**), 7.59 (d, J = 1.7 Hz, 1H, **H^1**), 7.39 (dd, J = 8.5, 1.9 Hz, 1H, **H^2**), 4.12 (s, 2H, **H^4**); LC-MS (APCI/ESI): Purity = 98%, t_R = 2.64 min, m/z [M-H]$^-$ = 191.0.

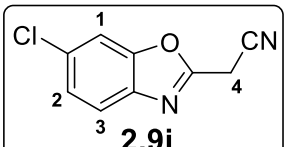

2.9i
$C_9H_5ClN_2O$
Exact Mass: 192.0
Mwt: 192.60

2-(5-*chlorobenzo[d]oxazol-2-yl)acetonitrile*, 2.9j

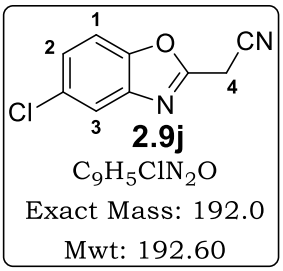

Yellow solid (0.570 g, 44%); R_f (EtOAc:Hex, 50:50) 0.53; ^{1}H NMR (300 MHz, $CDCl_3$) δ 7.75 (d, *J* = 2.0 Hz, 1H, **H³**), 7.50 (d, *J* = 8.7 Hz, 1H, **H¹**), 7.39 (dd, *J* = 8.7, 2.1 Hz, 1H, **H²**), 4.13 (s, 2H, **H⁴**); LC-MS (APCI/ESI): Purity > 99 %, t_R = 2.36 min, *m/z* $[M-H]^-$ = 191.0.

2-(6-*fluorobenzo[d]oxazol-2-yl)acetonitrile*, 2.9k

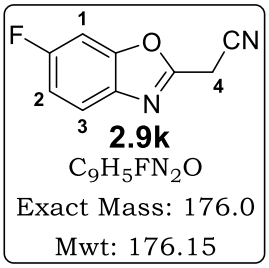

Dark brown solid (0.750 g, 63%); R_f (EtOAc:Hex, 50:50) 0.49; ^{1}H NMR (300 MHz, $CDCl_3$) δ 7.70 (dd, *J* = 8.8, 4.8 Hz, 1H, **H³**), 7.30 (dd, *J* = 7.7, 2.2 Hz, 1H, **H¹**), 7.15 (ddd, *J* = 9.5, 8.8, 2.4 Hz, 1H, **H²**), 4.12 (s, 2H, **H⁴**); LC-MS (APCI/ESI): Purity = 95%, t_R = 1.09 min, *m/z* $[M-H]^-$ = 175.0.

2-(5-*fluorobenzo[d]oxazol-2-yl)acetonitrile*, 2.9l

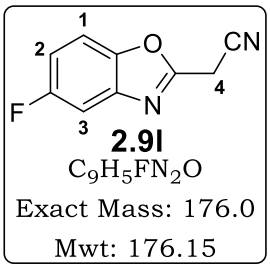

Yellow solid (1.050 g, 87%); R_f (EtOAc:Hex, 50:50) 0.50; ^{1}H NMR (300 MHz, $CDCl_3$) δ 7.51 (dd, *J* = 9.0, 4.2 Hz, 1H, **H¹**), 7.44 (dd, *J* = 8.1, 2.5 Hz, 1H, **H³**), 7.16 (td, *J* = 9.1, 2.6 Hz, 1H, **H²**), 4.13 (s, 2H, **H⁴**); LC-MS (APCI/ESI): Purity = 95%, t_R = 1.07 min, *m/z* $[M-H]^-$ = 175.0.

2-(6-*nitrobenzo[d]oxazol-2-yl)acetonitrile*, 2.9m

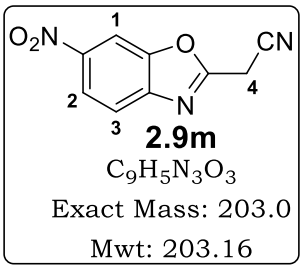

Brown solid (1.400 g, 90%); R_f (100% DCM) 0.31; ^{1}H NMR (300 MHz, DMSO-d_6) δ 8.77 (d, *J* = 2.1 Hz, 1H, **H¹**), 8.33 (dd, *J* = 8.8, 2.2 Hz, 1H, **H²**), 8.02 (d, *J* = 8.8 Hz, 1H, **H³**), 4.81 (s, 2H, **H⁴**); LC-MS (APCI/ESI): Purity > 99%, t_R = 0.67 min, *m/z* $[M-H]^-$ = 202.0.

2-(6-*aminobenzo[d]oxazol-2-yl)acetonitrile*, 2.9n

To a solution of 2-(6-nitrobenzo[*d*]oxazol-2-yl)acetonitrile, **2.9m** (1.300 g, 6.40 mmol, 1.0 Eq) in methanol (25 mL), 10% palladium on carbon catalyst [Pd/C] (0.390 g) was added. The reaction flask was then sealed, evacuated twice, filled with H_2 gas, and stirred at 25 °C for 15 h. The reaction mixture was then filtered through a pad of celite and concentrated. A black oily

substance was obtained, which was then purified by column chromatography (SiO_2, 100% DCM) to furnish **2.9n** as a yellow solid (0.620 g, 56%); R_f (MeOH:DCM, 2:98) 0.31; ^{1}H NMR (300 MHz, DMSO-d_6) δ 7.36 (d, J = 8.5 Hz, 1H, **H³**), 6.77 (d, J = 2.0 Hz, 1H, **H¹**), 6.63 (dd, J = 8.5, 2.0 Hz, 1H, **H²**), 5.38 (br s, 2H, **H⁵**), 4.52 (s, 2H, **H⁴**); ^{13}C NMR (101 MHz, DMSO-d_6) δ 153.91, 152.65, 148.41, 130.98, 119.99, 115.83, 112.82, 94.73, 18.48; LC-MS (APCI/ESI): Purity = 97%, t_R = 0.95 min, m/z $[M-H]^-$ = 172.1.

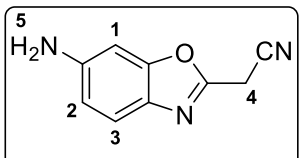

2.9n
$C_9H_7N_3O$
Exact Mass: 173.1
Mwt: 173.18

***N*-(2-(cyanomethyl)benzo[*d*]oxazol-6-yl)acetamide, 2.9o**

To a mixture of **2.9n** (0.25 g, 1.44 mmol, 1.0 Eq) and K_2CO_3 (3.0 Eq) in acetonitrile at 40 °C, acetyl chloride (2.0 Eq) was added, and the mixture stirred at this temperature for 30 minutes. Upon removal of acetonitrile, the residue was suspended in water and extracted with DCM (×3). The combined organic extracts were then rinsed with brine, dried over anhydrous $MgSO_4$, concentrated, and the residue purified by column chromatography (SiO_2, 100% DCM) to afford **2.9o** as a brown solid (0.208 g, 67%); R_f (100% DCM) 0.39; ^{1}H NMR (400 MHz, DMSO-d_6) δ 10.21 (br s, 1H, **H⁵**), 8.18 (d, J = 1.8 Hz, 1H, **H¹**), 7.68 (d, J = 8.7 Hz, 1H, **H³**), 7.41 (dd, J = 8.6, 1.9 Hz, 1H, **H²**), 4.64 (s, 2H, **H⁴**), 2.09 (s, 3H, **H⁶**); ^{13}C NMR (101 MHz, DMSO-d_6) δ 169.00, 157.39, 151.15, 137.86, 136.18, 119.94, 116.98, 115.52, 101.66, 24.48, 18.77; LC-MS (APCI/ESI): Purity > 99%, t_R = 1.27 min, m/z $[M-H]^-$ = 214.1.

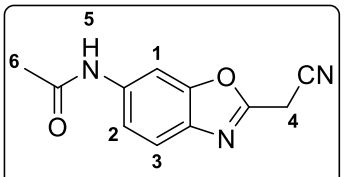

2.9o
$C_{11}H_9N_3O_2$
Exact Mass: 215.1
Mwt: 215.21

General procedure 10: Synthesis of oxime intermediates 2.10a–2.10o

The appropriate benzoxazole-2-acetonitrile intermediate [**2.9 (a–o)**] (1.0 Eq) was dissolved in glacial acetic acid (10 mL) at ambient temperature. This solution was then cooled to 0 °C resulting in a frozen mixture, after which sodium nitrite (2.0 Eq) was added at once. The reaction mixture was allowed to thaw slowly and then stirred at 25 °C for 12 hours. Water (50 mL) was then added into the reaction mixture leading to a rapid precipitation of

solids, which were filtered, washed thoroughly with water, and dried in a desiccator charged with sodium hydroxide pellets. In instances whereby further purification was necessary, the solid was recrystallized in an appropriate solvent [absolute ethanol was used in most cases], or column chromatographed (SiO_2, MeOH-DCM) to afford the desired product.

***N*-hydroxybenzo[*d*]oxazole-2-carbimidoyl cyanide, 2.10a**

Yellow crystalline solid (2.456 g, 83%); R_f (MeOH:DCM, 5:95) 0.37; ^{1}H NMR (400 MHz, DMSO-d_6) δ 15.04 (br s, 1H, **H^5**), 7.89 (ddd, J = 7.7, 1.4, 0.7 Hz, 1H, **H^4**), 7.82 (ddd, J = 8.2, 1.2, 0.7 Hz, 1H, **H^1**), 7.56–7.51 (m, 1H, **H^2**), 7.48 (td, J = 7.7, 1.2 Hz, 1H, **H^3**); ^{13}C NMR (101 MHz, DMSO-d_6) δ 155.57, 150.51, 140.87, 127.65, 126.04, 123.14, 121.09, 111.77, 108.82; LC-MS (APCI/ESI): Purity = 98%, t_R = 3.63 min, m/z [M-H]$^-$ = 186.1.

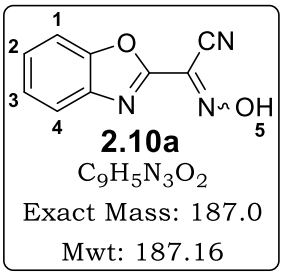

2.10a
$C_9H_5N_3O_2$
Exact Mass: 187.0
Mwt: 187.16

***N*-hydroxy-6-methylbenzo[*d*]oxazole-2-carbimidoyl cyanide, 2.10b**

Yellow solid (1.050 g, 90%); m.p. 229.2–231.4 °C; R_f (MeOH:DCM, 5:95) 0.47; ^{1}H NMR (300 MHz, DMSO-d_6) δ 14.93 (br s, 1H, **H^4**), 7.76 (d, J = 8.2 Hz, 1H, **H^3**), 7.63 (s, 1H, **H^1**), 7.30 (dd, J = 8.2, 0.9 Hz, 1H, **H^2**), 2.48 (s, 3H, **H^5**); ^{13}C NMR (101 MHz, DMSO-d_6) δ 155.13, 150.82, 138.79, 138.08, 127.29, 123.14, 120.47, 111.63, 108.90, 21.84; LC-MS (APCI/ESI): Purity = 99%, t_R = 4.08 min, m/z [M-H]$^-$ = 200.1.

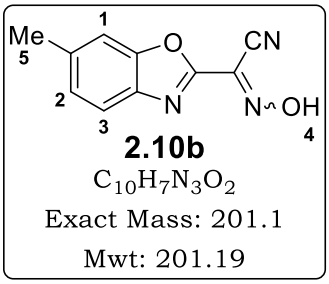

2.10b
$C_{10}H_7N_3O_2$
Exact Mass: 201.1
Mwt: 201.19

***N*-hydroxy-4-methylbenzo[*d*]oxazole-2-carbimidoyl cyanide, 2.10c**

Off-white solid (0.401 g, 84%); m.p. 234.4–236.8 °C; R_f (MeOH:DCM, 5:95) 0.45; ^{1}H NMR (300 MHz, DMSO-d_6) δ 14.98 (br s, 1H, **H^4**), 7.61 (d, J = 8.1 Hz, 1H, **H^1**), 7.41 (t, J = 7.9 Hz, 1H, **H^2**), 7.28 (d, J = 7.5 Hz, 1H, **H^3**), 2.58 (s, 3H, **H^5**); ^{13}C NMR (101 MHz, DMSO-d_6) δ 154.85, 150.31, 140.21, 131.31, 127.40, 126.32, 123.17, 108.99, 108.91, 16.55; LC-MS (APCI/ESI): Purity > 99%, t_R = 3.36 min, m/z [M-H]$^-$ = 200.1.

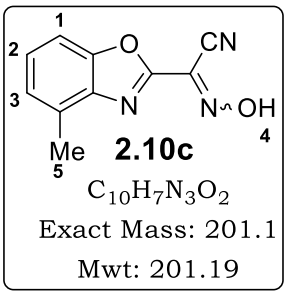

2.10c
$C_{10}H_7N_3O_2$
Exact Mass: 201.1
Mwt: 201.19

***N-hydroxy*-5-*methylbenzo[d]oxazole*-2-*carbimidoyl cyanide*, 2.10d**

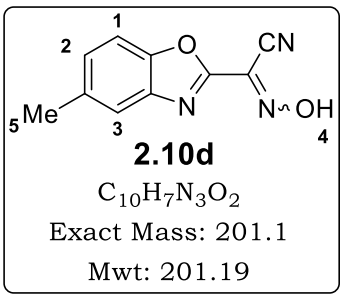

2.10d
$C_{10}H_7N_3O_2$
Exact Mass: 201.1
Mwt: 201.19

Yellow solid (0.950 g, 92%); m.p. 207.5–209.0 °C; R_f (MeOH:DCM, 5:95) 0.39; ^{1}H NMR (300 MHz, DMSO-d_6) δ 14.97 (br s, 1H, **H⁴**), 7.72–7.64 (m, 2H, **H¹,³**), 7.34 (dd, J = 8.5, 1.1 Hz, 1H, **H²**), 2.46 (s, 3H, **H⁵**); ^{13}C NMR (101 MHz, DMSO-d_6) δ 155.60, 148.79, 141.09, 135.66, 128.74, 123.17, 120.74, 111.18, 108.86, 21.40; LC-MS (APCI/ESI): Purity > 99%, t_R = 3.28 min, m/z $[M-H]^-$ = 200.0.

5-*bromo*-*N*-*hydroxybenzo[d]oxazole*-2-*carbimidoyl cyanide*, 2.10e

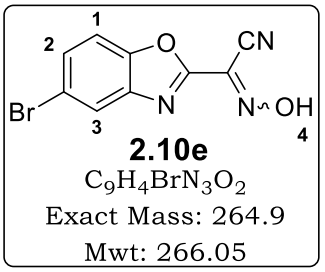

2.10e
$C_9H_4BrN_3O_2$
Exact Mass: 264.9
Mwt: 266.05

Brown solid (0.800 g, 75%); m.p. 229.0–231.8 °C; R_f (MeOH:DCM, 5:95) 0.37; ^{1}H NMR (300 MHz, DMSO-d_6) δ 15.13 (br s, 1H, **H⁴**), 8.16 (d, J = 1.9 Hz, 1H, **H³**), 7.83 (d, J = 8.7 Hz, 1H, **H¹**), 7.69 (dd, J = 8.7, 2.0 Hz, 1H, **H²**); ^{13}C NMR (101 MHz, DMSO-d_6) δ 156.81, 149.73, 142.58, 130.35, 123.72, 123.00, 117.95, 113.69, 108.75; LC-MS (APCI/ESI): Purity > 99%, t_R = 3.57 min, m/z $[M-H]^-$ = 263.9, 265.9 (1:1).

6-*bromo*-*N*-*hydroxybenzo[d]oxazole*-2-*carbimidoyl cyanide*, 2.10f

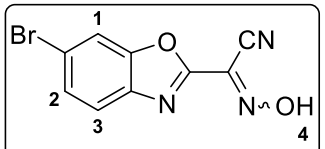

2.10f
$C_9H_4BrN_3O_2$
Exact Mass: 264.9
Mwt: 266.05

Yellow solid (0.680 g, 71%); m.p. 224.3–226.9 °C; R_f (MeOH:DCM, 5:95) 0.37; ^{1}H NMR (300 MHz, DMSO-d_6) δ 15.13 (br s, 1H, **H⁴**), 8.19 (d, J = 1.5 Hz, 1H, **H¹**), 7.86 (d, J = 8.5 Hz, 1H, **H³**), 7.65 (dd, J = 8.5, 1.8 Hz, 1H, **H²**); ^{13}C NMR (101 MHz, DMSO-d_6) δ 156.21, 151.10, 140.30, 129.31, 123.00, 122.50, 119.75, 115.21, 108.74; LC-MS (APCI/ESI): Purity = 98%, t_R = 3.54 min, m/z $[M-H]^-$ = 263.9, 265.9 (1:1).

***Methyl* 2-(*cyano*(*hydroxyimino*)*methyl*)*benzo[d]oxazole*-6-*carboxylate*, 2.10g**

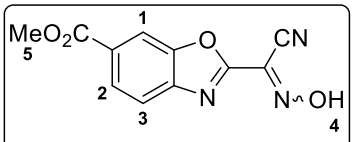

2.10g
$C_{11}H_7N_3O_4$
Exact Mass: 245.0
Mwt: 245.19

Yellow solid (0.850 g, 81%); m.p. 236.1–240.7 °C; R_f (MeOH:DCM, 5:95) 0.34; ^{1}H NMR (300 MHz, DMSO-d_6) δ 15.23 (br s, 1H, **H⁴**), 8.33 (dd, J = 1.5, 0.6 Hz, 1H, **H¹**), 8.06 (dd, J = 8.4, 1.5 Hz, 1H, **H²**), 7.99 (dd, J = 8.4, 0.6 Hz, 1H, **H³**), 3.91 (s, 3H, **H⁵**); ^{13}C NMR

(101 MHz, DMSO-d_6) δ 166.01, 158.14, 150.28, 144.63, 128.65, 127.04, 123.05, 121.10, 112.87, 108.72, 53.02; LC-MS (APCI/ESI): Purity > 99%, t_R = 2.99 min, *m/z* $[M-H]^-$ = 244.0.

***N*-hydroxy-6-(trifluoromethyl)benzo[*d*]oxazole-2-carbimidoyl cyanide, 2.10h**

Yellow solid (0.536 g, 65%); m.p. 180.0–184.8 °C; R_f (MeOH:DCM, 5:95) 0.34; ^{1}H NMR (300 MHz, DMSO-d_6) δ 15.12 (br s, 1H, **H⁴**), 8.27 (s, 1H, **H¹**), 8.00 (d, *J* = 8.4 Hz, 1H, **H³**), 7.77 (dd, *J* = 8.4, 1.1 Hz, 1H, **H²**); ^{13}C NMR (101 MHz, DMSO-d_6) δ 161.01, 150.00, 144.57, 126.55, 126.23, 123.08, 122.65, 120.93, 110.63, 109.30; LC-MS (APCI/ESI): Purity = 99%, t_R = 3.66 min, *m/z* $[M-H]^-$ = 254.0.

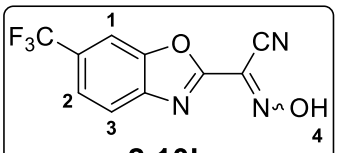

2.10h
$C_{10}H_4F_3N_3O_2$
Exact Mass: 255.0
Mwt: 255.16

6-*chloro*-*N*-hydroxybenzo[*d*]oxazole-2-carbimidoyl cyanide, 2.10i

Pink solid (0.700 g, 77%); m.p. 221.8–224.6 °C; R_f (MeOH:DCM, 5:95) 0.39; ^{1}H NMR (300 MHz, DMSO-d_6) δ 15.11 (br s, 1H, **H⁴**), 8.06 (d, *J* = 1.7 Hz, 1H, **H¹**), 7.91 (d, *J* = 8.6 Hz, 1H, **H³**), 7.53 (dd, *J* = 8.6, 2.0 Hz, 1H, **H²**); ^{13}C NMR (101 MHz, DMSO-d_6) δ 156.40, 150.84, 139.96, 131.88, 126.59, 122.99, 122.10, 112.43, 108.73; LC-MS (APCI/ESI): Purity > 99%, t_R = 3.40 min, *m/z* $[M-H]^-$ = 220.0.

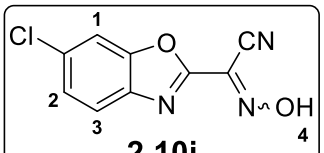

2.10i
$C_9H_4ClN_3O_2$
Exact Mass: 221.0
Mwt: 221.60

5-*chloro*-*N*-hydroxybenzo[*d*]oxazole-2-carbimidoyl cyanide, 2.10j

Yellow solid (0.501 g, 92%); m.p. 222.3–225.8 °C; R_f (MeOH:DCM, 5:95) 0.37; ^{1}H NMR (300 MHz, DMSO-d_6) δ 15.15 (br s, 1H, **H⁴**), 8.03 (d, *J* = 1.8 Hz, 1H, **H³**), 7.88 (d, *J* = 8.8 Hz, 1H, **H¹**), 7.57 (dd, *J* = 8.8, 2.1 Hz, 1H, **H²**); ^{13}C NMR (101 MHz, DMSO-d_6) δ 157.00, 149.35, 142.11, 130.25, 127.66, 123.02, 120.79, 113.24, 108.73; LC-MS (APCI/ESI): Purity > 99%, t_R = 3.38 min, *m/z* $[M-H]^-$ = 220.0.

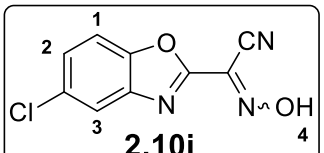

2.10j
$C_9H_4ClN_3O_2$
Exact Mass: 221.0
Mwt: 221.60

6-*fluoro*-*N*-hydroxybenzo[*d*]oxazole-2-carbimidoyl cyanide, 2.10k

Brown solid (0.400 g, 57%); m.p. 183.5–187.4 °C; R_f (MeOH:DCM, 5:95) 0.45; ^{1}H NMR (300 MHz, DMSO-d_6) δ 15.11 (br s, 1H, **H⁴**), 7.90 (dd, *J* = 8.8,

5.0 Hz, 1H, **H³**), 7.83 (dd, *J* = 8.4, 2.4 Hz, 1H, **H¹**), 7.35 (ddd, *J* = 9.9, 8.9, 2.5 Hz, 1H, **H²**); ^{13}C NMR (101 MHz, DMSO-d_6) δ 162.48, 160.06, 156.96, 150.72, 137.65, 121.77, 114.07, 109.22, 100.12; LC-MS (APCI/ESI): Purity > 99%, t_R = 2.76 min, *m/z* $[M-H]^-$ = 204.0.

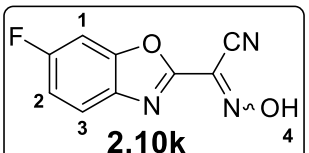

2.10k
$C_9H_4FN_3O_2$
Exact Mass: 205.0
Mwt: 205.15

***5-fluoro-N-hydroxybenzo[d]oxazole-2-carbimidoyl cyanide*, 2.10l**

Yellow solid (0.984 g, 92%); m.p. 143.1–148.0 °C; R_f (MeOH:DCM, 5:95) 0.39; ^{1}H NMR (300 MHz, DMSO-d_6) δ 15.11 (br s, 1H, **H⁴**), 7.88 (dd, *J* = 9.1, 4.1 Hz, 1H, **H¹**), 7.80 (dd, *J* = 8.6, 2.4 Hz, 1H, **H³**), 7.40 (ddd, *J* = 9.6, 9.1, 2.7 Hz, 1H, **H²**); ^{13}C NMR (101 MHz, DMSO-d_6) δ 161.48, 159.10, 157.30, 147.10, 141.67, 123.06, 115.43, 112.76, 107.55; LC-MS (APCI/ESI): Purity > 99%, t_R = 2.75 min, *m/z* $[M-H]^-$ = 204.0.

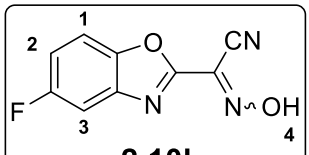

2.10l
$C_9H_4FN_3O_2$
Exact Mass: 205.0
Mwt: 205.15

***N-hydroxy-6-nitrobenzo[d]oxazole-2-carbimidoyl cyanide*, 2.10m**

Yellow solid (1.003 g, 74%); m.p. 186.5–190.4 °C; R_f (MeOH:DCM, 5:95) 0.26; ^{1}H NMR (300 MHz, DMSO-d_6) δ 15.40 (br s, 1H, **H⁴**), 8.83 (d, *J* = 1.9 Hz, 1H, **H¹**), 8.37 (dd, *J* = 8.8, 2.2 Hz, 1H, **H²**), 8.13 (d, *J* = 8.8 Hz, 1H, **H³**); ^{13}C NMR (101 MHz, DMSO-d_6) δ 161.35, 149.82, 146.40, 145.81, 123.17, 121.70, 120.83, 109.55, 108.33; LC-MS (APCI/ESI): Purity = 96%, t_R = 3.59 min, *m/z* $[M-H]^-$ = 231.0.

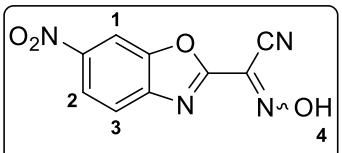

2.10m
$C_9H_4N_4O_4$
Exact Mass: 232.0
Mwt: 232.16

***6-amino-N-hydroxybenzo[d]oxazole-2-carbimidoyl cyanide*, 2.10n**

Brown solid (0.340 g, 44%); R_f (MeOH:DCM, 5:95) 0.19; ^{1}H NMR (300 MHz, DMSO-d_6) δ 13.54 (br s, 1H, **H⁴**), 7.31 (d, *J* = 8.2 Hz, 1H, **H³**), 6.65 (d, *J* = 2.0 Hz, 1H, **H¹**), 6.61 (dd, *J* = 8.2, 2.0 Hz, 1H, **H²**), 4.95 (br s, 2H, **H⁵**); LC-MS (APCI/ESI): Purity = 95%, t_R = 1.95 min, *m/z* $[M-H]^-$ = 201.0.

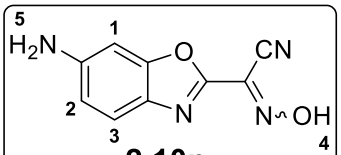

2.10n
$C_9H_6N_4O_2$
Exact Mass: 202.0
Mwt: 202.17

***6-acetamido-N-hydroxybenzo[d]oxazole-2-carbimidoyl cyanide*, 2.10o**

Brown solid (0.161 g, 71%); R_f (MeOH:DCM, 5:95) 0.37; ^{1}H NMR (400 MHz, DMSO-d_6) δ 14.92 (br s, 1H, **H^4**), 10.32 (s, 1H, **H^5**), 8.26 (d, J = 1.7 Hz, 1H, **H^1**), 7.81 (d, J = 8.7 Hz, 1H, **H^3**), 7.46 (dd, J = 8.7, 1.9 Hz, 1H, **H^2**), 2.10 (s, 3H, **H^6**); ^{13}C NMR (101 MHz, DMSO-d_6) δ 169.18, 155.12, 150.87, 139.29, 136.27, 123.01, 120.96, 117.77, 108.82, 101.54, 24.54; LC-MS (APCI/ESI): Purity = 98%, t_R = 2.94 min, m/z $[M-H]^-$ = 243.1.

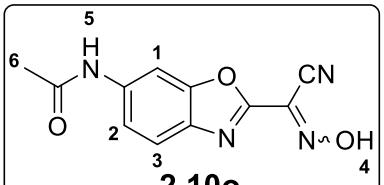

2.10o
$C_{11}H_8N_4O_3$
Exact Mass: 244.1
Mwt: 244.21

General procedure 11: Synthesis of SAR 2 benzoxazole-based target compounds 45–58

Triethylamine (5.0 Eq) and dimethylcarbamoyl chloride (3.0 Eq) were successively added to a suspension of the appropriate oxime intermediate **2.10** (**a–o**) (1.0 Eq) in anhydrous DCM at room temperature. This solution was purged with nitrogen gas for 10 minutes, heated to reflux at 50 ºC for 15 h, then cooled to room temperature, and water (20 mL) was added. The mixture was extracted with DCM (20 mL × 3) and the combined organic phases rinsed with brine (50 mL × 2), dried over anhydrous $MgSO_4$, and concentrated to give a residue, which was column chromatographed (SiO_2, EtOAc-hexane) to give the desired product. Alternatively, the general procedure 12 described below was also successful, whereby dimethylcarbamoyl chloride was used in place of epichlorohydrin.

***N*-((dimethylcarbamoyl)oxy)benzo[d]oxazole-2-carbimidoyl cyanide, 45**

Yellow solid (0.252 g, 79%); m.p. 217.2–220.7 ºC; R_f (EtOAc:Hex, 1:1) 0.39; ^{1}H NMR (400 MHz, $CDCl_3$) δ 7.92 (ddd, J = 7.9, 1.3, 0.7 Hz, 1H, **H^4**), 7.67 (d, J = 8.27 Hz, 1H, **H^1**), 7.57–7.52 (m, 1H, **H^3**), 7.51–7.45 (m, 1H, **H^2**), 3.19 (s, 3H, **H^{5a}**), 3.14 (s, 3H, **H^{5b}**); ^{13}C NMR (101 MHz, $CDCl_3$) δ 153.36, 151.24, 151.00, 141.04, 128.40, 126.88, 125.95, 121.70, 111.61, 106.99, 37.53, 36.20; LC-MS (APCI/ESI): Purity > 99%, t_R = 3.97 min, m/z $[M+46]^+$ = 304.1.

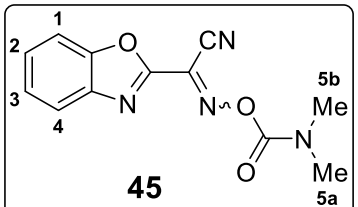

45
$C_{12}H_{10}N_4O_3$
Exact Mass: 258.1
Mwt: 258.24

***N*-((dimethylcarbamoyl)oxy)-6-methylbenzo[*d*]oxazole-2-carbimidoyl cyanide, 46**

Off-white fluffy solid (0.312 g, 77%); m.p. 203.4–209.2 °C; R_f (EtOAc:Hex, 1:1) 0.41; ^{1}H NMR (300 MHz, $CDCl_3$) δ 7.77 (d, *J* = 8.3 Hz, 1H, **H^3**), 7.44 (d, *J* = 0.7 Hz, 1H, **H^1**), 7.29 (dd, *J* = 8.3, 1.0 Hz, 1H, **H^2**), 3.18 (s, 3H, **H^{4a}**), 3.13 (s, 3H, **H^{4b}**), 2.55 (s, 3H, **H^5**); ^{13}C NMR (101 MHz, $CDCl_3$) δ 153.55, 152.89, 151.38, 139.61, 139.04, 127.47, 127.00, 121.01, 111.51, 107.07, 37.51, 36.19, 22.06; LC-MS (APCI/ESI): Purity > 99%, t_R = 4.43 min, *m/z* $[M+46]^+$ = 318.1.

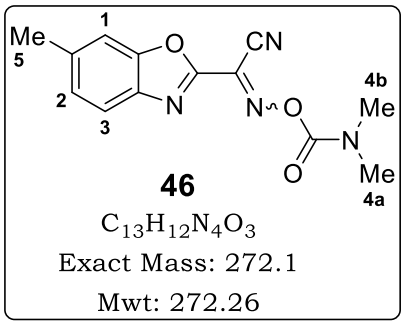

46
$C_{13}H_{12}N_4O_3$
Exact Mass: 272.1
Mwt: 272.26

***N*-((dimethylcarbamoyl)oxy)-4-methylbenzo[*d*]oxazole-2-carbimidoyl cyanide, 47**

Yellow solid (0.233 g, 69%); m.p. 184.4–187.3 °C; R_f (EtOAc:Hex, 1:1) 0.42; ^{1}H NMR (400 MHz, $CDCl_3$) δ 7.46 (d, *J* = 7.7 Hz, 1H, **H^1**), 7.44–7.38 (m, 1H, **H^2**), 7.26 (dt, *J* = 7.2, 1.0 Hz, 1H, **H^3**), 3.19 (s, 3H, **H^{4a}**), 3.14 (s, 3H, **H^{4b}**), 2.70 (s, 3H, **H^5**); ^{13}C NMR (101 MHz, $CDCl_3$) δ 152.51, 151.34, 150.86, 140.64, 132.68, 128.12, 127.05, 126.23, 108.72, 107.08, 37.51, 36.19, 16.40; LC-MS (APCI/ESI): Purity > 99%, t_R = 4.39 min, *m/z* $[M+46]^+$ = 318.1.

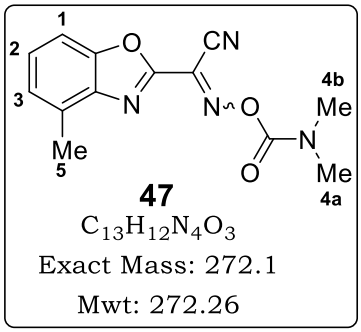

47
$C_{13}H_{12}N_4O_3$
Exact Mass: 272.1
Mwt: 272.26

***N*-((dimethylcarbamoyl)oxy)-5-methylbenzo[*d*]oxazole-2-carbimidoyl cyanide, 48**

Yellow solid (0.288 g, 71%); m.p. 193.1–198.9 °C; R_f (EtOAc:Hex, 1:1) 0.41; ^{1}H NMR (400 MHz, $CDCl_3$) δ 7.68 (dt, *J* = 1.6, 0.8 Hz, 1H, **H^3**), 7.53 (d, *J* = 8.5 Hz, 1H, **H^1**), 7.35 (ddd, *J* = 8.5, 1.7, 0.6 Hz, 1H, **H^2**), 3.19 (s, 3H, **H^{4a}**), 3.14 (s, 3H, **H^{4b}**), 2.53 (s, 3H, **H^5**); ^{13}C NMR (101 MHz, $CDCl_3$) δ 153.35, 151.29, 149.32, 141.29, 136.10, 129.77, 126.97, 121.30, 110.94, 107.05, 37.52, 36.19, 21.48; LC-MS (APCI/ESI): Purity > 99%, t_R = 4.33 min, *m/z* $[M+46]^+$ = 318.1.

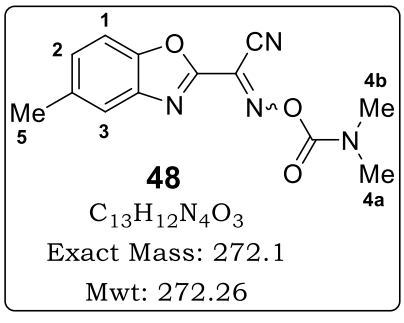

48
$C_{13}H_{12}N_4O_3$
Exact Mass: 272.1
Mwt: 272.26

***5-bromo-N-((dimethylcarbamoyl)oxy)benzo[d]oxazole-2-carbimidoyl cyanide*, 49**

Yellow solid (0.105 g, 56%); m.p. 231.1–232.7 °C; R_f (EtOAc:Hex, 1:1) 0.46; ^{1}H NMR (400 MHz, $CDCl_3$) δ 8.09 (d, J = 2.0 Hz, 1H, **H^3**), 7.81 (d, J = 8.5 Hz, 1H, **H^1**), 7.67 (dd, J = 8.5, 2.1 Hz, 1H, **H^2**), 3.13 (s, 3H, **H^{4a}**), 3.09 (s, 3H, **H^{4b}**); ^{13}C NMR (101 MHz, $CDCl_3$) δ 157.21, 152.77, 141.98, 130.12, 126.53, 122.86, 122.71, 117.74, 112.87, 107.65, 37.41, 36.28; LC-MS (APCI/ESI): Purity > 99%, t_R = 4.45 min, m/z $[M+46]^+$ = 382.0, 384.0 (1:1).

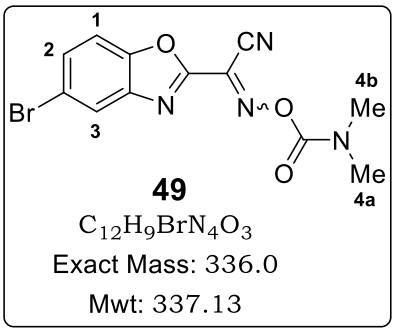

49
$C_{12}H_9BrN_4O_3$
Exact Mass: 336.0
Mwt: 337.13

***6-bromo-N-((dimethylcarbamoyl)oxy)benzo[d]oxazole-2-carbimidoyl cyanide*, 50**

Brown solid (0.187 g, 49%); m.p. 232.9–236.6 °C; R_f (EtOAc:Hex, 1:1) 0.47; ^{1}H NMR (400 MHz, $CDCl_3$) δ 7.84 (d, J = 1.9 Hz, 1H, **H^1**), 7.77 (d, J = 8.5, 1H, **H^3**), 7.63 (dd, J = 8.5, 1.9 Hz, 1H, **H^2**), 3.19 (s, 3H, **H^{4a}**), 3.14 (s, 3H, **H^{4b}**); ^{13}C NMR (101 MHz, $CDCl_3$) δ 153.75, 151.33, 151.13, 140.15, 129.73, 126.54, 122.58, 121.89, 115.15, 106.82, 37.57, 36.21; LC-MS (APCI/ESI): Purity > 99%, t_R = 4.46 min, m/z $[M+46]^+$ = 382.0, 384.0 (1:1).

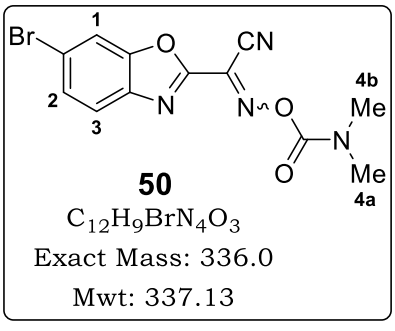

50
$C_{12}H_9BrN_4O_3$
Exact Mass: 336.0
Mwt: 337.13

***Methyl 2-(cyano(((dimethylcarbamoyl)oxy)imino)methyl)benzo[d]oxazole-6-carboxylate*, 51**

Off-white solid (0.282 g, 73%); m.p. 233.7–237.1 °C; R_f (EtOAc:Hex, 1:1) 0.38; ^{1}H NMR (400 MHz, $CDCl_3$) δ 8.33 (d, J = 1.1 Hz, 1H, **H^1**), 8.20 (dd, J = 8.5, 1.4 Hz, 1H, **H^2**), 7.95 (d, J = 8.4 Hz, 1H, **H^3**), 4.00 (s, 3H, **H^5**), 3.20 (s, 3H, **H^{4a}**), 3.15 (s, 3H, **H^{4b}**); ^{13}C NMR (101 MHz, $CDCl_3$) δ 165.83, 155.52, 151.05, 150.65, 144.32, 130.28, 127.39, 126.56, 121.38, 113.24, 106.79, 52.66, 37.60, 36.23; LC-MS (APCI/ESI): Purity > 99%, t_R = 4.19 min, m/z $[M+46]^+$ = 362.1.

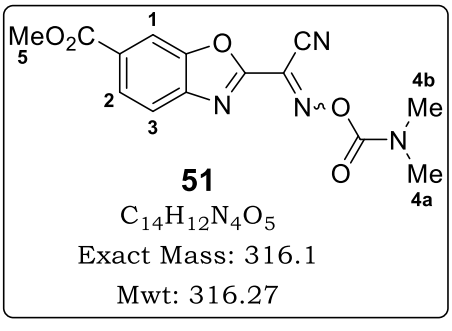

51
$C_{14}H_{12}N_4O_5$
Exact Mass: 316.1
Mwt: 316.27

***N-((dimethylcarbamoyl)oxy)-6-(trifluoromethyl)benzo[d]oxazole-2-carbimidoyl cyanide*, 52**

Off-white solid (0.105 g, 59%); m.p. 189.0–192.4 °C; R_f (EtOAc:Hex, 1:1) 0.48; ^{1}H NMR (400 MHz, $CDCl_3$) δ 8.03 (d, J = 8.5, 1H, **H^3**), 7.95 (d, J = 2.0,

1H, **H[1]**), 7.79 (dd, *J* = 8.5, 2.0 Hz, 1H, **H[2]**), 3.20 (s, 3H, **H[4a]**), 3.15 (s, 3H, **H[4b]**); ^{13}C NMR (101 MHz, $CDCl_3$) δ 155.48, 150.99, 150.36, 143.38, 130.39 (q), 126.37, 124.89, 123.19, 122.31, 109.49, 106.72, 37.61, 36.22; LC-MS (APCI/ESI): Purity > 99%, t_R = 4.51 min, *m/z* $[M+46]^+$ = 372.1.

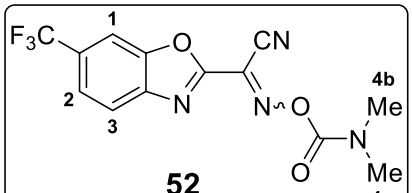

52
$C_{13}H_9F_3N_4O_3$
Exact Mass: 326.1
Mwt: 326.24

***6-chloro-N-((dimethylcarbamoyl)oxy)benzo[d]oxazole-2-carbimidoyl cyanide*, 53**

Brown solid (0.160 g, 81%); m.p. 227.9–230.8 °C; R_f (EtOAc:Hex, 1:1) 0.45; ^{1}H NMR (400 MHz, $CDCl_3$) δ 7.83 (dd, *J* = 8.6, 0.5 Hz, 1H, **H[3]**), 7.67 (dd, *J* = 1.9, 0.5 Hz, 1H, **H[1]**), 7.47 (dd, *J* = 8.6, 1.9 Hz, 1H, **H[2]**), 3.19 (s, 3H, **H[4a]**), 3.14 (s, 3H, **H[4b]**); ^{13}C NMR (101 MHz, $CDCl_3$) δ 153.92, 151.11 (2C), 139.74, 134.43, 126.98, 126.51, 122.20, 112.17, 106.81, 37.56, 36.20; LC-MS (APCI/ESI): Purity > 99%, t_R = 4.38 min, *m/z* $[M+46]^+$ = 338.1.

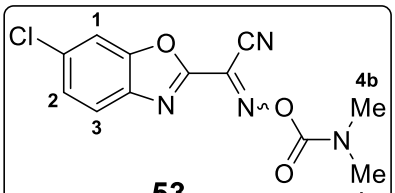

53
$C_{12}H_9ClN_4O_3$
Exact Mass: 292.0
Mwt: 292.68

***5-chloro-N-((dimethylcarbamoyl)oxy)benzo[d]oxazole-2-carbimidoyl cyanide*, 54**

Yellow solid (0.207 g, 72%); m.p. 191.0–193.1 °C; R_f (EtOAc:Hex, 1:1) 0.44; ^{1}H NMR (400 MHz, $CDCl_3$) δ 7.90 (dd, *J* = 2.1, 0.5 Hz, 1H, **H[3]**), 7.60 (dd, *J* = 8.8, 0.5 Hz, 1H, **H[1]**), 7.52 (dd, *J* = 8.8, 2.0 Hz, 1H, **H[1]**), 3.19 (s, 3H, **H[4a]**), 3.14 (s, 3H, **H[4b]**); ^{13}C NMR (101 MHz, $CDCl_3$) δ 154.49, 151.08, 149.52, 141.95, 131.71, 128.82, 126.51, 121.49, 112.41, 106.79, 37.57, 36.21; LC-MS (APCI/ESI): Purity > 99%, t_R = 4.38 min, *m/z* $[M+46]^+$ = 338.1.

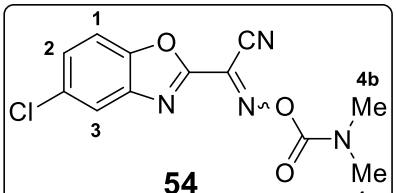

54
$C_{12}H_9ClN_4O_3$
Exact Mass: 292.0
Mwt: 292.68

***N-((dimethylcarbamoyl)oxy)-6-fluorobenzo[d]oxazole-2-carbimidoyl cyanide*, 55**

Brown solid (0.225 g, 67%); m.p. 202.5–205.9 °C; R_f (EtOAc:Hex, 1:1) 0.39; ^{1}H NMR (400 MHz, $CDCl_3$) δ 7.87 (dd, *J* = 8.8, 5.0 Hz, 1H, **H[3]**), 7.83 (dd, *J* = 8.5, 2.3 Hz, 1H, **H[1]**), 7.35 (ddd, *J* = 9.8, 8.8, 2.3 Hz, 1H, **H[2]**), 3.19 (s, 3H, **H[4a]**), 3.14 (s, 3H,

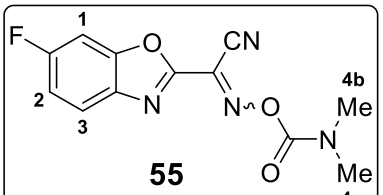

55
$C_{12}H_9FN_4O_3$
Exact Mass: 276.1
Mwt: 276.23

H^{4b}); ^{13}C NMR (101 MHz, $CDCl_3$) δ 163.77, 161.28, 153.97, 151.09, 137.47, 126.50, 122.44, 114.77, 106.85, 99.70, 37.55, 36.19; LC-MS (APCI/ESI): Purity > 99%, t_R = 4.07 min, *m/z* $[M+46]^+$ = 322.1.

***N*-((dimethylcarbamoyl)oxy)-5-fluorobenzo[*d*]oxazole-2-carbimidoyl cyanide, 56**

Yellow solid (0.167 g, 62%); m.p. 196.5–197.7 ºC; R_f (EtOAc:Hex, 1:1) 0.40; ^{1}H NMR (400 MHz, DMSO-d_6) δ 7.83 (dd, *J* = 8.9, 4.0 Hz, 1H, **H^1**), 7.78 (dd, *J* = 8.5, 2.6 Hz, 1H, **H^3**), 7.40 (ddd, *J* = 9.6, 8.9, 2.7 Hz, 1H, **H^2**), 3.20 (s, 3H, **H^{4a}**), 3.16 (s, 3H, **H^{4b}**); ^{13}C NMR (101 MHz, DMSO-d_6) δ 164.08, 160.23, 155.98, 148.31, 142.20, 126.57, 122.91, 114.57, 112.81, 107.49, 37.53, 36.21; LC-MS (APCI/ESI): Purity > 99%, t_R = 4.14 min, *m/z* $[M+46]^+$ = 322.1.

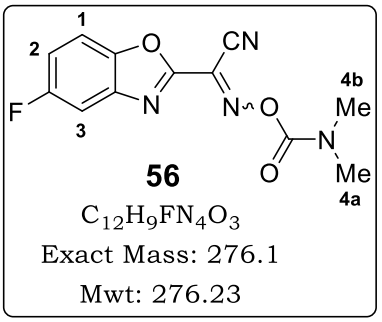

56
$C_{12}H_9FN_4O_3$
Exact Mass: 276.1
Mwt: 276.23

***N*-((dimethylcarbamoyl)oxy)-6-nitrobenzo[*d*]oxazole-2-carbimidoyl cyanide, 57**

Brown solid (0.114 g, 55%); m.p. 210.4–212.8 ºC; R_f (EtOAc:Hex, 1:1) 0.36; ^{1}H NMR (400 MHz, DMSO-d_6) δ 8.57 (d, *J* = 2.0 Hz, 1H, **H^1**), 8.45 (dd, *J* = 8.8, 2.0 Hz, 1H, **H^2**), 8.05 (d, *J* = 8.8 Hz, 1H, **H^3**), 3.21 (s, 3H, **H^{4a}**), 3.16 (s, 3H, **H^{4b}**); ^{13}C NMR (101 MHz, DMSO-d_6) δ 157.18, 150.82, 150.13, 147.29, 145.41, 126.05, 121.96, 121.74, 108.31, 106.54, 37.66, 36.25; LC-MS (APCI/ESI): Purity = 96%, t_R = 4.37 min, *m/z* $[M+46]^+$ = 349.1.

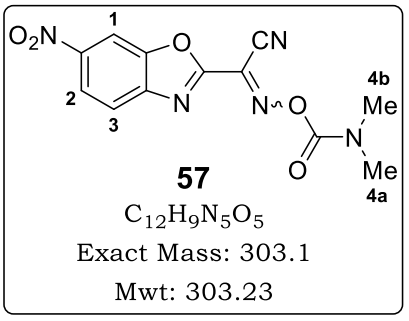

57
$C_{12}H_9N_5O_5$
Exact Mass: 303.1
Mwt: 303.23

***6*-acetamido-*N*-((dimethylcarbamoyl)oxy)benzo[*d*]oxazole-2-carbimidoyl cyanide, 58**

Yellow solid (0.071 g, 47%); m.p. 240.6–243.7 ºC; R_f (EtOAc:Hex, 1:1) 0.37; ^{1}H NMR (400 MHz, DMSO-d_6) δ 10.41 (br s, 1H, **H^5**), 8.27 (d, *J* = 2.1 Hz, 1H, **H^1**), 7.86 (d, *J* = 8.9 Hz, 1H, **H^3**), 7.55 (dd, *J* = 8.9, 2.1 Hz, 1H, **H^2**), 3.09 (s, 3H, **H^{4a}**), 3.05 (s, 3H, **H^{4b}**), 2.12 (s, IH, **H^6**); ^{13}C NMR (101 MHz, DMSO-d_6) δ 169.13, 153.97, 151.59, 151.42, 140.03, 136.04, 127.62, 121.59, 118.41, 108.41, 101.59, 37.62,

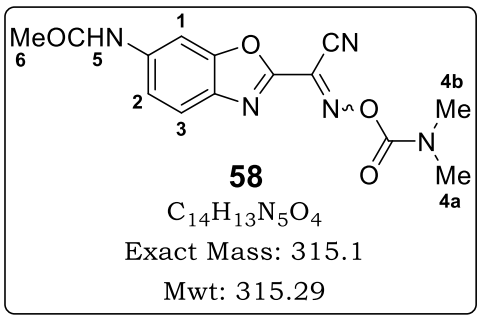

58
$C_{14}H_{13}N_5O_4$
Exact Mass: 315.1
Mwt: 315.29

36.03, 24.76; LC-MS (APCI/ESI): Purity > 99%, t_R = 3.09 min, *m/z* $[M+46]^+$ = 361.1.

General procedure 12: Synthesis of epoxide-based compounds 59 and 60

To a stirred solution of **2.10b** or **2.10i** (1.0 Eq) in anhydrous acetonitrile, K_2CO_3 (3.0 Eq) was added, and the mixture was heated to reflux at 90 °C for 30 minutes under N_2 atmosphere. Epichlorohydrin (5.0 Eq) was then added to this mixture and refluxed for 18 h. Upon removal of acetonitrile under reduced pressure, a black solid was obtained, which was then resuspended in water and extracted with DCM (×3). The combined organic extracts were then rinsed with brine, dried over anhydrous $MgSO_4$, concentrated, and the residue was purified by column chromatography (SiO_2, 100% DCM) to afford compound **59** or **60**.

***6-methyl-N-(oxiran-2-ylmethoxy)benzo[d]oxazole-2-carbimidoyl cyanide*, 59**

Yellowish green solid (0.320 g, 45%); m.p. 116.0–118.9 °C; R_f (EtOAc:Hex, 1:1) 0.45; ^{1}H NMR (400 MHz, $CDCl_3$) δ 7.74 (d, *J* = 8.2 Hz, 1H, **H^3**), 7.42 (dt, *J* = 1.5, 0.7 Hz, 1H, **H^1**), 7.27 (dd, *J* = 8.2, 1.5 Hz, 1H, **H^2**), 4.78 (dd, *J* = 12.3, 3.4 Hz, 1H, **H^{4a}**), 4.54 (dd, *J* = 12.3, 6.1 Hz, 1H, **H^{4b}**), 3.42 (dddd, *J* = 6.0, 4.1, 3.4, 2.6 Hz, 1H, **H^5**), 2.96 (dd, *J* = 4.8, 4.2 Hz, 1H, **H^{6a}**), 2.79 (dd, *J* = 4.8, 2.6 Hz, 1H, **H^{6b}**), 2.54 (s, 3H, **H^7**); ^{13}C NMR (101 MHz, $CDCl_3$) δ 153.37, 151.12, 138.90, 138.70, 127.22, 123.41, 120.79, 111.17, 107.25, 78.90, 49.13, 44.54, 22.00; LC-MS (APCI/ESI): Purity > 99%, t_R = 4.32 min, *m/z* $[M+H]^+$ = 258.1.

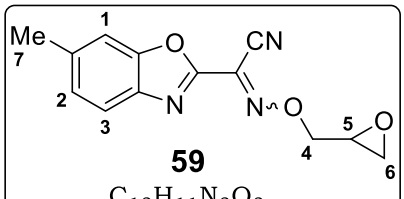

59
$C_{13}H_{11}N_3O_3$
Exact Mass: 257.1
Mwt: 257.25

***6-chloro-N-(oxiran-2-ylmethoxy)benzo[d]oxazole-2-carbimidoyl cyanide*, 60**

Yellow solid (3.15 g, 46%); m.p. 143.2–147.7 °C; R_f (100% DCM) 0.42; ^{1}H NMR (400 MHz, $CDCl_3$) δ 7.80 (d, *J* = 8.6 Hz, 1H, **H^3**), 7.65 (d, *J* = 1.9 Hz, 1H, **H^1**), 7.45 (dd, *J* = 8.6, 1.9 Hz, 1H, **H^2**), 4.81 (dd, *J* = 12.3, 3.3 Hz, 1H, **H^{4a}**), 4.55 (dd, *J* = 12.3, 6.1 Hz, 1H, **H^{4b}**), 3.43 (dddd, *J* = 5.9, 3.9, 3.3, 2.8

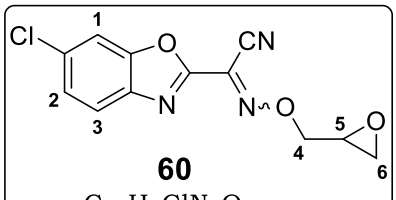

60
$C_{12}H_8ClN_3O_3$
Exact Mass: 277.0
Mwt: 277.66

Hz, 1H, **H[5]**), 3.01–2.92 (m, 1H, **H[6a]**), 2.79 (dd, *J* = 4.8, 2.6 Hz, 1H, **H[6b]**); ^{13}C NMR (101 MHz, $CDCl_3$) δ 154.46, 150.90, 139.72, 133.64, 126.75, 123.03, 121.99, 111.85, 107.02, 79.21, 49.09, 44.50; HRMS (EI) *m/z*, 276.9896 (M^+ $C_{12}H_8ClN_3O_3$ requires 277.0254); LC-MS: Purity > 99%, t_R = 4.54 min.

General procedure 13: Synthesis of β-amino alcohol-based target compounds 61–69

To a stirred solution of the epoxide-based **59** or **60** (1.0 Eq) and lithium perchlorate (2.0 Eq) in anhydrous acetonitrile, the appropriate alkyl amine (4.0 Eq) was added, and this mixture was stirred at 25 °C for 2 to 24 h. After completion of the reaction, acetonitrile was removed *in vacuo*, and the resulting crude residue was treated with water and then extracted with DCM (×4). The organic extracts were combined, rinsed with brine, dried over anhydrous $MgSO_4$, followed by removal of DCM. The residue was then purified by column chromatography (SiO_2, MeOH-DCM) to furnish the desired target compound.

***N*-(2-hydroxy-3-(isopropylamino)propoxy)-6-methylbenzo[*d*]oxazole-2-carbimidoyl cyanide, 61**

Off-white solid (0.231 g, 94%); m.p. 241.5–245.8 °C; R_f (MeOH:DCM, 1:9) 0.26; ^{1}H NMR (400 MHz, Methanol-d_4) δ 7.72 (d, *J* = 8.3 Hz, 1H, **H[3]**), 7.52 (dt, *J* = 1.9, 0.7 Hz, 1H, **H[1]**), 7.34 (dd, *J* = 8.2, 1.9 Hz, 1H, **H[2]**), 4.63 (dd, *J* = 5.3, 2.8 Hz, 2H, **H[4]**), 4.33 (dtd, *J* = 10.5, 5.3, 3.2 Hz, 1H, **H[5]**), 3.46 (hept, *J* = 6.6 Hz, 1H, **H[9]**), 3.28 (dd, *J* = 12.7, 3.1 Hz, 1H, **H[6a]**), 3.12 (dd, *J* = 12.7, 9.8 Hz, 1H, **H[6b]**), 2.54 (s, 3H, **H[11]**), 1.38 (dd, *J* = 6.5, 2.7 Hz, 6H, **H[10]**); ^{13}C NMR (101 MHz, Methanol-d_4) δ 153.88, 151.06, 138.94, 138.56, 126.98, 123.24, 119.97, 110.71, 106.99, 79.53, 65.33, 50.67, 46.62, 20.47, 18.16, 17.60; LC-MS (APCI/ESI): Purity = 98%, t_R = 3.36 min, *m/z* $[M+H]^+$ = 317.1.

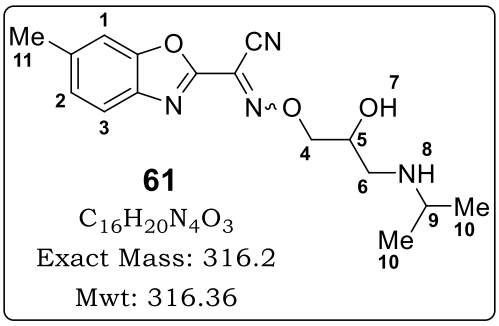

***6*-chloro-*N*-(2-hydroxy-3-(isopropylamino)propoxy)benzo[*d*]oxazole-2-carbimidoyl cyanide, 62**

Yellow solid (0.390 g, 92%); m.p. 218.5–223.9 °C; R_f (MeOH:DCM, 1:9) 0.34; ^{1}H NMR (400 MHz, DMSO-d_6) δ 8.30 (s, 1H, **H[8]**), 8.13 (d, *J* = 2.0 Hz, 1H, **H[1]**),

7.98 (d, *J* = 8.6 Hz, 1H, **H³**), 7.59 (dd, *J* = 8.6, 2.0 Hz, 1H, **H²**), 5.94 (s, 1H, **H⁷**), 4.62 (dd, *J* = 11.6, 4.5 Hz, 1H, **H⁴ᵃ**), 4.56 (dd, *J* = 11.7, 6.3 Hz, 1H, **H⁴ᵇ**), 4.27–4.16 (m, 1H, **H⁵**), 3.39–3.32 (m, 1H, **H⁹**), 3.14 (dd, *J* = 12.7, 3.0 Hz, 1H, **H⁶ᵃ**), 2.96 (dd, *J* = 12.7, 9.6 Hz, 1H, **H⁶ᵇ**), 1.25 (dd, *J* = 6.5, 3.7 Hz, 6H, **H¹⁰**); ^{13}C NMR (101 MHz, DMSO-d_6) δ 155.42, 150.86, 139.86, 132.55, 126.98, 123.40, 122.47, 112.53, 108.30, 80.30, 65.64, 50.43, 46.37, 19.35, 18.71; LC-MS (APCI/ESI): Purity = 96%, t_R = 3.46 min, *m/z* $[M+H]^+$ = 337.1.

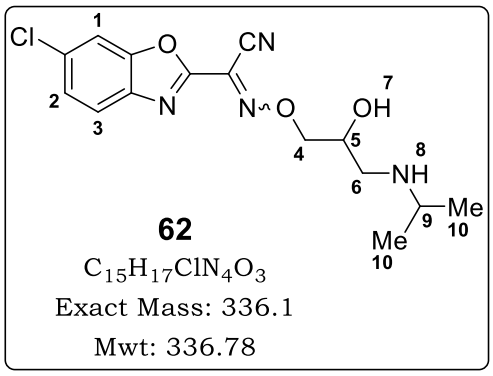

62
$C_{15}H_{17}ClN_4O_3$
Exact Mass: 336.1
Mwt: 336.78

***6-chloro-N-(2-hydroxy-3-morpholinopropoxy)benzo[d]oxazole-2-carbimidoyl cyanide*, 63**

Off-white solid (0.220 g, 56%); m.p. 102.4–108.3 °C; R_f (MeOH:DCM, 5:95) 0.36; ^{1}H NMR (400 MHz, DMSO-d_6) δ 8.12 (d, *J* = 1.9 Hz, 1H, **H¹**), 7.95 (d, *J* = 8.6 Hz, 1H, **H³**), 7.57 (dd, *J* = 8.6, 2.0 Hz, 1H, **H²**), 5.04 (d, *J* = 5.1 Hz, 1H, **H⁷**), 4.62 (dd, *J* = 11.3, 3.7 Hz, 1H, **H⁴ᵃ**), 4.51 (dd, *J* = 11.3, 6.7 Hz, 1H, **H⁴ᵇ**), 4.10–3.99 (m, 1H, **H⁵**), 3.58 (t, *J* = 4.7 Hz, 4H, **H⁹**), 2.49–2.36 (m, 6H, **H⁶,⁸**); ^{13}C NMR (101 MHz, DMSO-d_6) δ 155.61, 150.89, 139.91, 132.31, 126.82, 122.59, 122.34, 112.56, 108.37, 82.29, 66.72 (2C), 66.60, 61.44, 54.49 (2C); LC-MS (APCI/ESI): Purity > 99%, t_R = 3.43 min, *m/z* $[M+H]^+$ = 365.1.

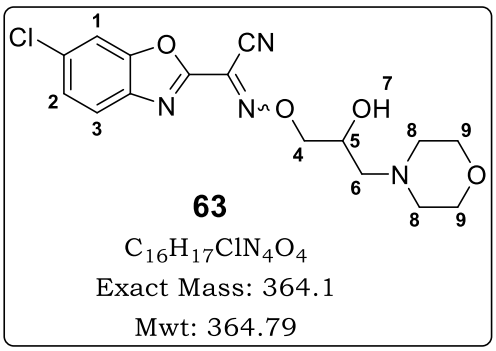

63
$C_{16}H_{17}ClN_4O_4$
Exact Mass: 364.1
Mwt: 364.79

***6-chloro-N-(2-hydroxy-3-(piperidin-1-yl)propoxy)benzo[d]oxazole-2-carbimidoyl cyanide*, 64**

Light brown solid (0.178 g, 55%); m.p. 106.7–110.0 °C; R_f (MeOH:DCM, 1:9) 0.27; ^{1}H NMR (400 MHz, DMSO-d_6) δ 8.12 (d, *J* = 1.9 Hz, 1H, **H¹**), 7.95 (d, *J* = 8.6 Hz, 1H, **H³**), 7.57 (dd, *J* = 8.6, 2.0 Hz, 1H, **H²**), 4.96 (s, 1H, **H⁷**), 4.61 (dd, *J* = 11.3, 3.5 Hz, 1H, **H⁴ᵃ**), 4.48 (dd, *J* = 11.3, 6.8 Hz, 1H, **H⁴ᵇ**), 4.09–3.93 (m, 1H, **H⁵**), 2.48–2.29 (m, 6H, **H⁶,⁸**), 1.57–1.43 (m, 4H, **H⁹**), 1.43–1.31 (m, 2H, **H¹⁰**); ^{13}C NMR (101

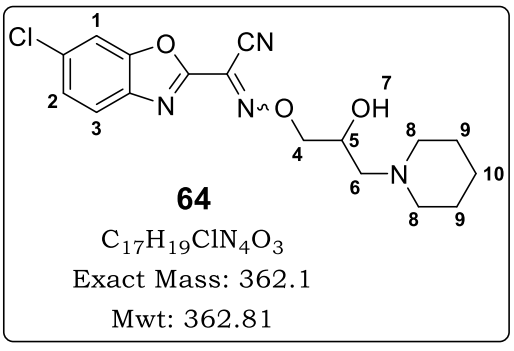

64
$C_{17}H_{19}ClN_4O_3$
Exact Mass: 362.1
Mwt: 362.81

MHz, DMSO-d_6) δ 155.62, 150.89, 139.91, 132.30, 126.82, 122.53, 122.33, 112.57, 108.37, 82.49, 66.74, 61.80, 55.27 (2C), 26.12 (2C), 24.40; LC-MS (APCI/ESI): Purity > 99%, t_R = 3.37 min, *m/z* $[M+H]^+$ = 363.1.

6-chloro-N(2-hydroxy-3-(piperazin-1-yl)propoxy)benzo[d]oxazole-2-carbimidoyl cyanide, 65

Yellow solid (0.118 g, 36%); m.p. 178.2–181.3 °C; R_f (DCM:MeOH:7N NH_3-MeOH), 9:1:0.2) 0.11; ^{1}H NMR (400 MHz, DMSO-d_6) δ 8.40 (s, 1H, **H^{10}**), 8.11 (d, *J* = 2.0 Hz, 1H, **H^1**), 7.96 (d, *J* = 8.6 Hz, 1H, **H^3**), 7.58 (dd, *J* = 8.6, 2.0 Hz, 1H, **H^2**), 5.12 (d, *J* = 4.9 Hz, 1H, **H^7**), 4.62 (dd, *J* = 11.3, 3.9 Hz, 1H, **H^{4a}**), 4.52 (dd, *J* = 11.3, 6.5 Hz, 1H, **H^{4b}**), 4.11–3.97 (m, 1H, **H^5**), 3.16–3.03 (m, 4H, **H^8**), 2.75–2.60 (m, 4H, **H^9**), 2.51–2.42 (m, 2H, **H^6**); ^{13}C NMR (101 MHz, DMSO-d_6) δ 155.58, 150.87, 139.90, 132.36, 126.88, 122.70, 122.37, 112.54, 108.38, 81.98, 66.94, 60.31, 50.53 (2C), 43.64 (2C); LC-MS (APCI/ESI): Purity = 97%, t_R = 3.45 min, *m/z* $[M+H]^+$ = 364.1.

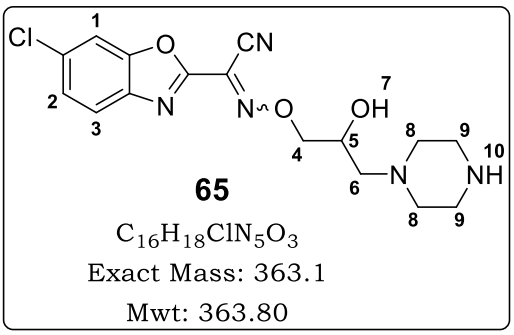

6-chloro-N(2-hydroxy-3-(4-methylpiperazin-1-yl)propoxy)benzo[d]oxazole-2-carbimidoyl cyanide, 66

Yellow solid (0.155 g, 41%); m.p. 154.4–161.4 °C; R_f (DCM:MeOH:7N NH_3-MeOH), 9:1:0.2) 0.43; ^{1}H NMR (400 MHz, Methanol-d_4) δ 7.85–7.80 (m, 2H, **H^{1,3}**), 7.52 (dd, *J* = 8.5, 2.0 Hz, 1H, **H^2**), 4.69 (dd, *J* = 11.5, 4.0 Hz, 1H, **H^{4a}**), 4.61 (dd, *J* = 11.5, 6.2 Hz, 1H, **H^{4b}**), 4.29–4.16 (m, 1H, **H^5**), 3.30–3.19 (m, 4H, **H^8**), 3.05–2.94 (m, 4H, **H^9**), 2.88 (s, 3H, **H^{10}**), 2.73–2.65 (m, 2H, **H^6**); ^{13}C NMR (101 MHz, Methanol-d_4) δ 155.31, 150.95, 139.66, 133.02, 126.27, 122.42, 121.39, 111.47, 106.96, 80.94, 66.72, 58.99, 53.51 (2C), 50.59 (2C), 42.36; LC-MS (APCI/ESI): Purity = 97%, t_R = 3.43 min, *m/z* $[M+H]^+$ = 378.1.

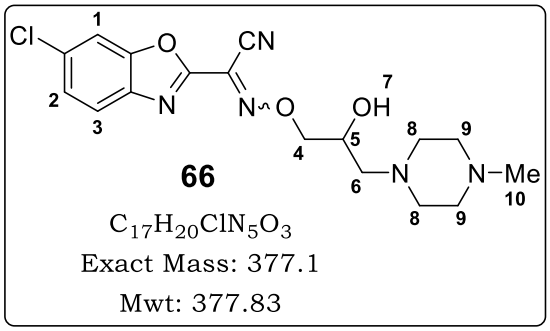

6-chloro-N'-(2-hydroxy-3-(pyrrolidin-1-yl)propoxy)benzo[d]oxazole-2-carbimidoyl cyanide, 67

Off-white solid (0.151 g, 48%); m.p. 165.7–167.5 °C; R_f (MeOH:DCM, 1:9) 0.24; ^{1}H NMR (400 MHz, Methanol-d_4) δ 7.84 (d, J = 8.6 Hz, 1H, **H^3**), 7.81 (d, J = 2.0 Hz, 1H, **H^1**), 7.52 (dd, J = 8.6, 2.0 Hz, 1H, **H^2**), 4.65 (dd, J = 11.3, 4.3 Hz, 1H, **H^{4a}**), 4.61 (dd, J = 11.3, 5.1 Hz, 1H, **H^{4b}**), 4.41 (tdd, J = 7.0, 5.5, 4.8 Hz, 1H, **H^5**), 3.57–3.42 (m, 4H, **H^8**), 3.40 (d, J = 7.0 Hz, 2H, **H^6**), 2.21–2.07 (m, 4H, **H^9**); ^{13}C NMR (101 MHz, Methanol-d_4) δ 155.14, 150.97, 139.64, 133.14, 126.32, 123.09, 121.45, 111.49, 106.85, 79.79, 64.76, 56.50, 54.20 (2C), 22.52 (2C); LC-MS (APCI/ESI): Purity > 99%, t_R = 3.28 min, m/z $[M+H]^+$ = 349.1.

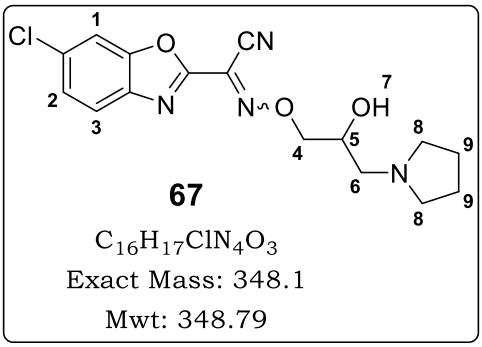

67

$C_{16}H_{17}ClN_4O_3$

Exact Mass: 348.1

Mwt: 348.79

6-chloro-N'-(2-hydroxy-3-(4-phenylpiperazin-1-yl)propoxy)benzo[d]oxazole-2-carbimidoyl cyanide, 68

Yellow solid (0.209 g, 53%); m.p. 152.8–158.0 °C; R_f (MeOH:DCM, 5:95) 0.59; ^{1}H NMR (400 MHz, $CDCl_3$) δ 7.80 (d, J = 8.6 Hz, 1H, **H^3**), 7.65 (d, J = 1.9 Hz, 1H, **H^1**), 7.45 (dd, J = 8.6, 1.9 Hz, 1H, **H^2**), 7.30 (dd, J = 8.8, 7.3 Hz, 2H, **H^{11}**), 6.95 (dd, J = 8.8, 1.0 Hz, 2H, **H^{10}**), 6.94–6.88 (m, 1H, **H^{12}**), 4.67 (d, J = 5.0 Hz, 2H, **H^4**), 4.38–3.29 (m, 1H, **H^5**), 3.39–3.26 (m, 4H, **H^9**), 3.04–2.94 (m, 2H, **H^6**), 2.84–2.68 (m, 4H, **H^8**); ^{13}C NMR (101 MHz, $CDCl_3$) δ 154.53, 150.89, 150.81, 139.73, 133.60, 129.22, 126.74, 125.81, 122.77, 121.95, 120.32, 120.24, 116.39, 111.84, 107.16, 80.68, 65.01, 60.20, 53.41 (2C), 48.93 (2C); LC-MS (APCI/ESI): Purity > 99%, t_R = 4.38 min, m/z $[M+H]^+$ = 440.1.

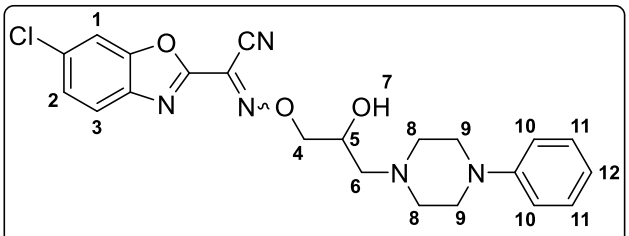

68

$C_{22}H_{22}ClN_5O_3$

Exact Mass: 439.1

Mwt: 439.90

6-chloro-N'-(2-hydroxy-3-(4-(pyridin-2-yl)piperazin-1-yl)propoxy)benzo[d]oxazole-2-carbimidoyl cyanide, 69

Light brown solid (0.364 g, 92%); m.p. 161.7–166.1 °C; R_f (MeOH:DCM, 5:95) 0.44; ^{1}H NMR (400 MHz, $CDCl_3$) δ 8.26–8.18 (m, 1H, **H^{13}**), 7.80 (d, J = 8.6 Hz, 1H, **H^3**), 7.65 (d, J = 1.9 Hz, 1H, **H^1**), 7.52 (ddd, J = 8.6, 7.3, 2.0 Hz, 1H, **H^{11}**), 7.45 (dd, J = 8.6, 1.9 Hz, 1H, **H^2**), 6.71–6.65 (m, 2H, **H^{10,12}**), 4.66 (d, J = 5.0 Hz, 2H, **H^4**), 4.39–4.28 (m, 1H, **H^5**), 3.76–3.59 (m, 4H, **H^9**), 3.02–2.85

(m, 2H, **H⁶**), 2.83–2.62 (m, 4H, **H⁸**); ^{13}C NMR (101 MHz, $CDCl_3$) δ 159.06, 154.52, 150.89, 147.95, 139.72, 137.66, 133.59, 126.73, 122.76, 121.95, 113.82, 111.85, 107.23, 107.15, 80.68, 65.02, 60.32, 53.18 (2C), 44.93 (2C); LC-MS (APCI/ESI): Purity = 99%, t_R = 4.09 min, *m/z* $[M+H]^+$ = 441.1.

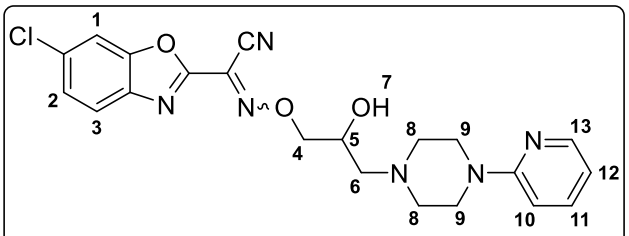

69

$C_{21}H_{21}ClN_6O_3$

Exact Mass: 440.1

Mwt: 440.89

Synthesis of oxime ether-based target compounds 70–74

General procedure 12 was adapted, wherein the appropriate halide (2.0 Eq) was used in place of epichlorohydrin and reacted with the free oxime intermediate **2.10a** (1.0 Eq).

***N*-(benzyloxy)benzo[*d*]oxazole-2-carbimidoyl cyanide, 70**

White solid (0.269 g, 71%); m.p. 130.9–135.1 °C; R_f (EtOAc:Hex, 50:50) 0.52; ^{1}H NMR (400 MHz, $CDCl_3$) δ 7.90–7.86 (m, 1H, **H⁴**), 7.66–7.62 (m, 1H, **H¹**), 7.54–7.39 (m, 7H, **H²,³,⁶,⁷,⁸**), 5.60 (s, 2H, **H⁵**); ^{13}C NMR (101 MHz, $CDCl_3$) δ 154.12, 150.75, 141.01, 134.64, 129.10, 128.81 (4C), 127.51, 125.70, 122.82, 121.42, 111.17, 107.43, 80.70; LC-MS (APCI/ESI): Purity = 98%, t_R = 4.96 min, *m/z* $[M+H]^+$ = 278.1.

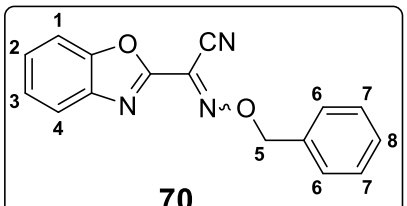

70

$C_{16}H_{11}N_3O_2$

Exact Mass: 277.1

Mwt: 277.28

***N*-((4-chlorobenzyl)oxy)benzo[*d*]oxazole-2-carbimidoyl cyanide, 71**

White solid (0.270 g, 66%); m.p. 120.7–123.5 °C; R_f (EtOAc:Hex, 50:50) 0.59; ^{1}H NMR (400 MHz, $CDCl_3$) δ 7.88 (ddd, *J* = 7.7, 1.5, 0.7 Hz, 1H, **H⁴**), 7.65–7.62 (m, 1H, **H¹**), 7.53–7.48 (m, 1H, **H²**), 7.48–7.43 (m, 1H, **H³**), 7.42 (s, 4H, **H⁶,⁷**), 5.56 (s, 2H, **H⁵**); ^{13}C NMR (101 MHz, $CDCl_3$) δ 153.95, 150.75, 140.98, 135.20, 133.12, 130.19 (2C), 129.06 (2C), 127.61, 125.75, 123.13, 121.46, 111.18, 107.33, 79.65; LC-MS (APCI/ESI): Purity = 97%, t_R = 4.99 min, *m/z* $[M+H]^+$ = 312.1.

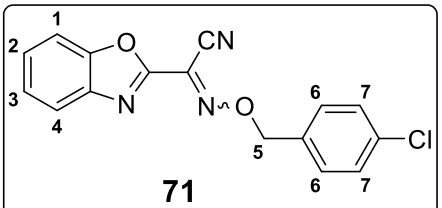

71

$C_{16}H_{10}ClN_3O_2$

Exact Mass: 311.1

Mwt: 311.73

***N-((2,4-dichlorobenzyl)oxy)benzo[d]oxazole-2-carbimidoyl cyanide*, 72**

Yellow solid (0.204 g, 74%); m.p. 115.9–118.3 °C; R_f (EtOAc:Hex, 1:4) 0.40; ^{1}H NMR (400 MHz, $CDCl_3$) δ 7.89 (ddd, J = 7.7, 1.5, 0.7 Hz, 1H, **H^4**), 7.64 (ddd, J = 8.2, 1.3, 0.7 Hz, 1H, **H^1**), 7.54–7.49 (m, 2H, **H^{2,3}**), 7.49–7.44 (m, 2H, **H^{6,8}**), 7.34 (dd, J = 8.3, 2.1 Hz, 1H, **H^7**), 5.69 (s, 2H, **H^5**); ^{13}C NMR (101 MHz, $CDCl_3$) δ 153.85, 150.77, 140.98, 135.71, 134.69, 131.18, 131.12, 129.74, 127.69, 127.49, 125.79, 123.41, 121.50, 111.20, 107.21, 76.85; LC-MS (APCI/ESI): Purity > 99%, t_R = 5.11 min, m/z $[M+H]^+$ = 346.0.

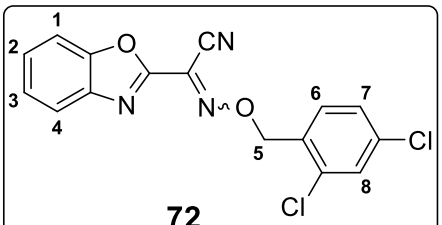

72
$C_{16}H_9Cl_2N_3O_2$
Exact Mass: 345.0
Mwt: 346.17

***N-((3-chlorobenzyl)oxy)benzo[d]oxazole-2-carbimidoyl cyanide*, 73**

White solid (0.270 g, 81%); m.p. 138.0–141.2 °C; R_f (EtOAc:Hex, 1:4) 0.31; ^{1}H NMR (400 MHz, $CDCl_3$) δ 7.89 (ddd, J = 7.7, 1.5, 0.7 Hz, 1H, **H^4**), 7.64 (ddd, J = 8.2, 1.3, 0.7 Hz, 1H, **H^1**), 7.51 (ddd, J = 8.2, 7.4, 1.5 Hz, 1H, **H^2**), 7.48–7.43 (m, 2H, **H^{3,9}**), 7.41–7.36 (m, 3H, **H^{6,7,8}**), 5.56 (s, 2H, **H^5**); ^{13}C NMR (101 MHz, $CDCl_3$) δ 153.92, 150.76, 140.98, 136.60, 134.74, 130.14, 129.27, 128.75, 127.64, 126.76, 125.76, 123.25, 121.47, 111.20, 107.30, 79.56; LC-MS (APCI/ESI): Purity > 99%, t_R = 4.95 min, m/z $[M+H]^+$ = 312.1.

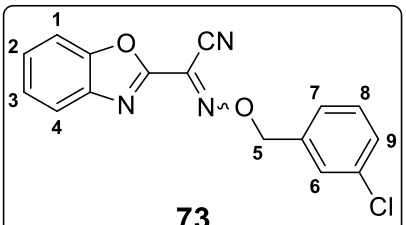

73
$C_{16}H_{10}ClN_3O_2$
Exact Mass: 311.1
Mwt: 311.73

***2-(((benzo[d]oxazol-2-yl(cyano)methylene)amino)oxy)acetic acid*, 74**

Off-white solid (0.043 g, 19%); m.p. 228.9–233.4 °C; R_f (DCM:MeOH:7N NH_3-MeOH) 0.27; ^{1}H NMR (400 MHz, DMSO-d_6) δ 7.91 (d, J = 7.8 Hz, 1H, **H^4**), 7.83 (d, J = 8.2 Hz, 1H, **H^1**), 7.56 (td, J = 7.8, 1.4 Hz, 1H, **H^2**), 7.50 (td, J = 7.7, 1.2 Hz, 1H, **H^3**), 4.72 (s, 2H, **H^5**); LC-MS (APCI/ESI): Purity > 99%, t_R = 2.98 min, m/z $[M+H]^+$ = 246.0.

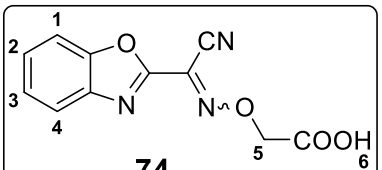

74
$C_{11}H_7N_3O_4$
Exact Mass: 245.0
Mwt: 245.19

Synthesis of SAR 3 benzoxazole-based target compounds 75–82

2-(benzo[d]oxazol-2-yl)-2-cyclohexylideneacetonitrile, 75

To a solution of 2-(benzo[*d*]oxazol-2-yl)acetonitrile, **2.9a** (0.200 g, 1.26 mmol) in absolute ethanol (4 mL), ammonium acetate (0.77 g, 10 mmol) and cyclopentanone or cyclohexanone (10 mmol) were added. The reaction mixture was heated under reflux for 2 h and left to cool to room temperature. The separated crystalline product was filtered, dried and recrystallized from ethanol. White solid (0.276 g, 92%); m.p. 99.5–102.8 °C; R_f (EtOAc:Hex, 1:1) 0.60; ^{1}H NMR (400 MHz, $CDCl_3$) δ 7.79–7.76 (m, 1H, **H^4**), 7.61–7.58 (m, 1H, **H^1**), 7.43–7.36 (m, 2H, **H^{2,3}**), 3.23–3.15 (m, 2H, **H^5**), 2.87–2.80 (m, 2H, **H^9**), 1.93–1.86 (m, 2H, **H^6**), 1.85–1.80 (m, 2H, **H^8**), 1.78–1.71 (m, 2H, **H^7**); ^{13}C NMR (101 MHz, $CDCl_3$) δ 174.31, 157.50, 149.84, 141.29, 125.82, 124.91, 120.28, 115.32, 110.81, 97.67, 36.63, 32.41, 28.52, 28.08, 25.65; LC-MS (APCI/ESI): Purity > 99%, t_R = 4.87 min, *m/z* $[M+H]^+$ = 239.1.

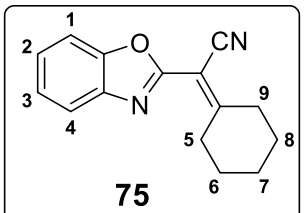

75
$C_{15}H_{14}N_2O$
Exact Mass: 238.1
Mwt: 238.29

N-phenylbenzo[d]oxazole-2-carbohydrazonoyl cyanide, 76

Orange solid (0.201 g, 61%); m.p. 192.8–197.7 °C; R_f (EtOAc:Hex, 2:3) 0.55; ^{1}H NMR (400 MHz, $CDCl_3$) δ 13.59 (s, 1H, **H^5**), 7.84–7.81 (m, 1H, **H^4**), 7.70–7.66 (m, 1H, **H^1**), 7.54–7.42 (m, 6H, **H^{2,6,7}**), 7.23 (tt, *J* = 7.4, 1.4 Hz, 1H, **H^8**); ^{13}C NMR (101 MHz, $CDCl_3$) δ 155.72, 148.20, 141.42, 140.16, 129.64 (2C), 127.07, 125.67, 125.53, 119.85, 115.85 (2C), 114.94, 111.41, 101.44; LC-MS (APCI/ESI): Purity > 99%, t_R = 5.31 min, *m/z* $[M+H]^+$ = 263.1.

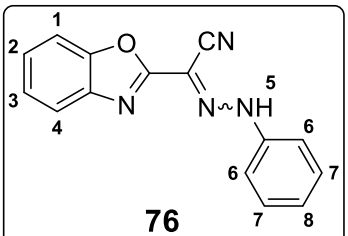

76
$C_{15}H_{10}N_4O$
Exact Mass: 262.1
Mwt: 262.27

***3-methyl-1-oxo-1H-benzo[4,5]oxazolo[3,2-a]pyridine-4-carbonitrile*, 77**

White solid (0.220 g, 69%); m.p. 221.1–225.8 °C; R_f (EtOAc:Hex, 1:1) 0.35; ^{1}H NMR (400 MHz, $CDCl_3$) δ 8.56–8.52 (m, 1H, **H^4**), 7.65–7.61 (m, 1H, **H^1**), 7.59–7.54 (m, 1H, **H^2**), 7.54–7.49 (m, 1H, **H^3**), 6.30 (q, *J* = 0.9 Hz, 1H, **H^5**), 2.52 (d, *J* = 1.0 Hz, 3H, **H^6**); ^{13}C NMR (101 MHz, $CDCl_3$) δ 157.58, 156.87, 151.59, 146.67, 127.58, 126.87, 125.96, 117.10, 112.97, 111.50, 111.11, 73.68, 20.96; LC-MS (APCI/ESI): Purity > 99%, t_R = 3.82 min, *m/z* $[M+H]^+$ = 225.1.

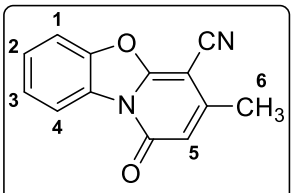

77

$C_{13}H_8N_2O_2$

Exact Mass: 224.1

Mwt: 224.22

***2-(benzo[d]oxazol-2-ylmethylene)thiazolidin-4-one*, 78**

Brown solid (0.099 g, 34%); m.p. 209.3–211.6 °C; R_f (EtOAc:Hex, 1:1) 0.43; ^{1}H NMR (400 MHz, DMSO-d_6) δ 11.59 (br s, 1H, **H^6**), 7.64–7.60 (m, 1H, **H^4**), 7.60–7.57 (m, 1H, **H^1**), 7.33–7.24 (m, 2H, **H^{2,3}**), 6.05 (s, 1H, **H^5**), 3.94 (s, 2H, **H^7**); ^{13}C NMR (101 MHz, DMSO-d_6) δ 174.18, 163.07, 153.32, 149.39, 142.52, 124.76, 124.18, 118.69, 110.43, 85.49, 33.82; LC-MS (APCI/ESI): Purity = 84% (*E*/*Z*), 14% (*E*/*Z*), t_R = 3.87 (*E*/*Z*), 4.44 (*E*/*Z*) min, *m/z* $[M+H]^+$ = 233.0.

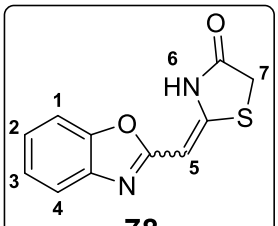

78

$C_{11}H_8N_2O_2S$

Exact Mass: 232.0

Mwt: 232.26

***2-(benzo[d]oxazol-2-yl)-2-(5-oxo-3-phenylthiazolidin-2-ylidene)acetonitrile*, 79**

Brown solid (0.280 g, 67%); m.p. 315.2–317.9 °C; R_f (EtOAc:Hex, 1:1) 0.49; ^{1}H NMR (400 MHz, DMSO-d_6) δ 7.76–7.72 (m, 1H, **H^4**), 7.72–7.69 (m, 1H, **H^1**), 7.60–7.54 (m, 3H, **H^{7,8}**), 7.53–7.48 (m, 2H, **H^6**), 7.42–7.34 (m, 2H, **H^{2,3}**), 4.22 (s, 2H, **H^5**); ^{13}C NMR (101 MHz, DMSO-d_6) δ 173.60, 167.59, 160.17, 149.20, 141.53, 135.30, 131.09, 130.00 (2C), 129.89 (2C), 125.44 (2C), 119.30, 112.20, 111.04, 73.00, 33.50; LC-MS (APCI/ESI): Purity > 99%, t_R = 4.21 min, *m/z* $[M+H]^+$ = 334.1.

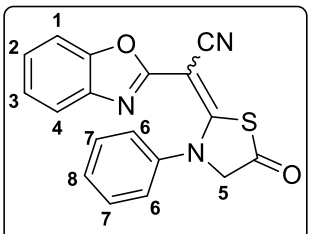

79

$C_{18}H_{11}N_3O_2S$

Exact Mass: 333.1

Mwt: 333.37

2-*(benzo[d]oxazol-2-yl)*-3-*mercapto*-3-*(phenylamino)acrylonitrile*, 80

Yellow solid (0.199 g, 54%); m.p. 203.2–206.6 °C; R_f (EtOAc:Hex, 1:1) 0.61; ^{1}H NMR (300 MHz, DMSO-d_6) δ 10.80 (s, 1H, **H^5**), 7.69–7.52 (m, 4H, **H^{1,4,8}**), 7.45–7.38 (m, 1H, **H^2**), 7.36 (d, J = 8.0 Hz, 2H, **H^7**), 7.33–7.23 (m, 1H, **H^3**), 7.23–7.15 (m, 1H, **H^9**); LC-MS (APCI/ESI): Purity = 95%, t_R = 4.46 min, m/z $[M+H]^+$ = 294.1.

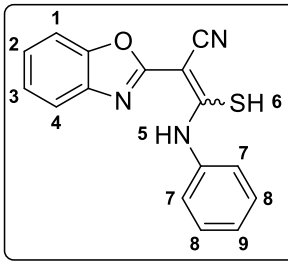

80
$C_{16}H_{11}N_3OS$
Exact Mass: 293.1
Mwt: 293.34

4-*amino*-5-*(benzo[d]oxazol-2-yl)*-3-*phenylthiazole*-2*(3H)*-*thione*, 81

Yellowish green solid (0.110 g, 27%); m.p. 236.5–239.5 °C; R_f (EtOAc:Hex, 1:1) 0.47; ^{1}H NMR (400 MHz, $CDCl_3$) δ 7.72–7.62 (m, 4H, **H^{6,7}**), 7.53 (ddd, J = 7.7, 1.4, 0.6 Hz, 1H, **H^4**), 7.44–7.40 (m, 2H, **H^{1,8}**), 7.37 (td, J = 7.6, 1.4 Hz, 1H, **H^2**), 7.34–7.29 (m, 1H, **H^3**), 6.36 (br s, 2H, **H^5**); ^{13}C NMR (101 MHz, $CDCl_3$) δ 187.54, 157.01, 148.83, 148.48, 139.48, 134.52, 131.02, 130.78 (2C), 128.64 (2C), 125.20, 124.34, 117.62, 110.34; LC-MS (APCI/ESI): Purity > 99%, t_R = 4.98 min, m/z $[M+H]^+$ = 326.0.

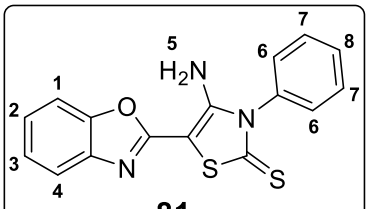

81
$C_{16}H_{11}N_3OS_2$
Exact Mass: 325.0
Mwt: 325.40

2-*(benzo[d]oxazol-2-yl)*-3-*(3,4-dimethoxyphenyl)acrylonitrile*, 82

Yellow solid (0.321 g, 83%); m.p. 169.0–173.3 °C; R_f (EtOAc:Hex, 1:1) 0.40; ^{1}H NMR (400 MHz, $CDCl_3$) δ 8.26 (s, 1H, **H^5**), 7.90 (d, J = 2.2 Hz, 1H, **H^6**), 7.82–7.78 (m, 1H, **H^4**), 7.60–7.57 (m, 1H, **H^1**), 7.53 (ddd, J = 8.4, 2.2, 0.5 Hz, 1H, **H^7**), 7.43–7.37 (m, 2H, **H^{2,3}**), 6.99 (d, J = 8.5 Hz, 1H, **H^8**), 4.01 (s, 3H, **H^9**), 4.00 (s, 3H, **H^{10}**); ^{13}C NMR (101 MHz, $CDCl_3$) δ 159.51, 153.34, 150.69, 149.46, 148.81, 141.67, 127.14, 125.81, 125.36, 125.14, 120.31, 115.68, 111.27, 111.12, 110.59, 95.95, 56.15, 56.11; LC-MS (APCI/ESI): Purity > 99%, t_R = 4.84 min, m/z $[M+H]^+$ = 307.1.

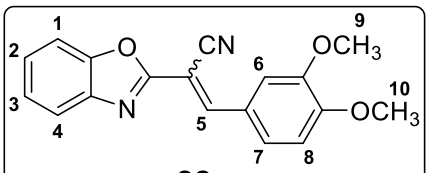

82
$C_{18}H_{14}N_2O_3$
Exact Mass: 306.1
Mwt: 306.32

6.3 Biological Evaluation

6.3.1 *In vitro* Antimycobacterial Assay

Minimum inhibitory concentrations (MIC) were determined using the standard broth micro dilution method. In this case, a 12.8 mM stock solution of the test compound was prepared in DMSO, and then diluted using the appropriate growth medium (GAST-Fe or 7H9/ADC) to a concentration of 640 µM. 100 µL of this solution was added into wells in row 1 in duplicate, while 50 µL of the appropriate growth medium was added into wells in rows 2–12. This was followed by a two-fold serial dilution, which was attained by transferring 50 µL of a solution from row 1 to a subsequent row until row 12 was reached, from which 50 µL was discarded so as to bring the final volume in all wells to 50 µL, and concentrations ranging from 320–0.3125 µM in rows 2–12, respectively. At the same time, a 10 mL culture of *Mtb* ($H_{37}Rv$) was grown until they reached an optical density of 0.6–0.7 at 600 nm (OD600). This culture was then diluted 1:100 using the appropriate medium as the diluent. Thereafter, 50 µL of the diluted *Mtb* culture was added to all wells in rows 2-12. As such, cells were not added to wells in row 1 because they served as contamination controls. Other controls included the neat medium, 5% DMSO, rifampicin, and kanamycin. The microplate was then placed in a secondary container and incubated at 37 °C, in the presence of a humidifier to minimize liquid evaporation. Finally, the lowest concentration of the test compound that inhibited the growth of more than 99% of the *Mtb* population [Minimum Inhibitory Concentration (MIC_{99})] was scored visually at Day 7 and day 14 post inoculation. MIC_{99} scoring was facilitated by the use of Alamar blue dye in a technique commonly referred to as Microplate Alamar Blue Assay (MABA), which is paramount in the visual, or fluorimetric cell-growth reading. In some instances, the green fluorescent protein (GFP)-tagged *Mtb* $H_{37}Rv$ (pMSP12::GFP) was used in the assays. In this case, the MICs were determined using a dose-response curve analysis of the relative fluorescence (excitation wavelength at 485 nm, and emission wavelength at 520 nm) measured on the FLUOstar OPTIMA microplate reader. Data was normalized to the minimum and maximum inhibition controls to generate a dose

response curve (% inhibition) using the Levenberg-Marquardt algorithm (damped least-squares) method, from which the MIC_{90} and MIC_{99} were calculated.

6.3.2 *In vitro* Cytotoxicity Assay

In vitro cytotoxicity of potent target compounds against the Chinese Hamster Ovarian (CHO) cells was performed using the 3-(4,5-dimethylthiazol-2-yl)-2,5-diphenyltetrazolium bromide (MTT)-assay, which determines cellular growth and survival. For each test compound, a stock solution (2 mg/mL) was prepared in 10% DMSO, and then diluted with the assay medium to yield a starting concentration of a 100 µg/mL. This was then serially 10-fold diluted to give six assay concentrations ranging from 100–0.001 µg/mL. Emetine was subjected to similar dilutions and used as the positive assay control. In all cases, triplicate samples were prepared. Negative control was the highest concentration of DMSO used, which had to be demonstrated that it had no measurable effect on the viability and survival of CHO cells.

A solution of MTT was then added after 44 hours of exposure of the cells to the test compound. This was followed by a further 4 hours of incubation at 37 °C, after which the supernatant was separated from the cells by suction. Crystals of the reduced dye were then dissolved by addition of DMSO to each well. The amount of formazan in each well was determined by measuring the absorbance at 540 nm, which was then used to prepare dose-response curves. A non-linear dose-response curve analysis, using GraphPad Prism software, generated the 50% inhibitory concentration (IC_{50}) values.

6.4 Turbidimetric Solubility Assay

Turbidimetric method described by Bevan and Lloyd was adapted to provide an estimate of aqueous solubility of each target compound at pH 7.4. A 10 mM stock solution of the appropriate test and control compound [reserpine and hydrocortisone] was prepared in DMSO, and 50 µL was placed in triplicate in row H of a 96-well microtiter plate. An 8 mM (100 µL) solution in DMSO was prepared in row G and then serially diluted by transferring 50 µL to the wells above it [containing 50 µL DMSO] up to row B. This yielded

eight pre-dilution solutions with concentrations of 0.00, 0.25, 0.50, 1.00, 2.00, 4.00, 8.00, and 10.00 mM in rows A, B, C, D, E, F, G, and H respectively. Secondary dilutions, in triplicate, of the pre-dilution solutions were prepared in DMSO (wells in columns 1–6) and 0.01M pH 7.4 phosphate buffered saline (PBS) (wells in columns 7–12) in a second 96-well microtiter plate, which thus meant that only two test compounds could be accommodated per plate. This was accomplished by pipetting 4 µL of each pre-dilution solution to the corresponding well of the second plate containing 196 µL of the appropriate diluent (DMSO or PBS). Therefore, the final concentration of DMSO in the PBS preparations was 2% v/v. The final 200 µL assay solutions had concentrations of 0.0, 5.0, 10.0, 20.0, 40.0, 80.0, 160.0, and 200.0 µM.

Subsequently, the plates were covered and left to equilibrate for 2 hours at ambient room temperature. This was followed by reading the UV-VIS absorbances at 620 nm using a SpectraMax 340PC^{384} microplate reader (Molecular Devices, Sunnydale, CA). For each compound, a line graph of corrected absorbance [that is; absorbance of PBS solution minus the absorbance of the corresponding DMSO solution] against concentration was plotted. Solubility of each test compound was then taken as that concentration at which the line graph raised from the zero absorbance (DMSO) line. For instance, compound **3** had an estimated solubility of 80 µM as depicted in **Figure 6.1** below.

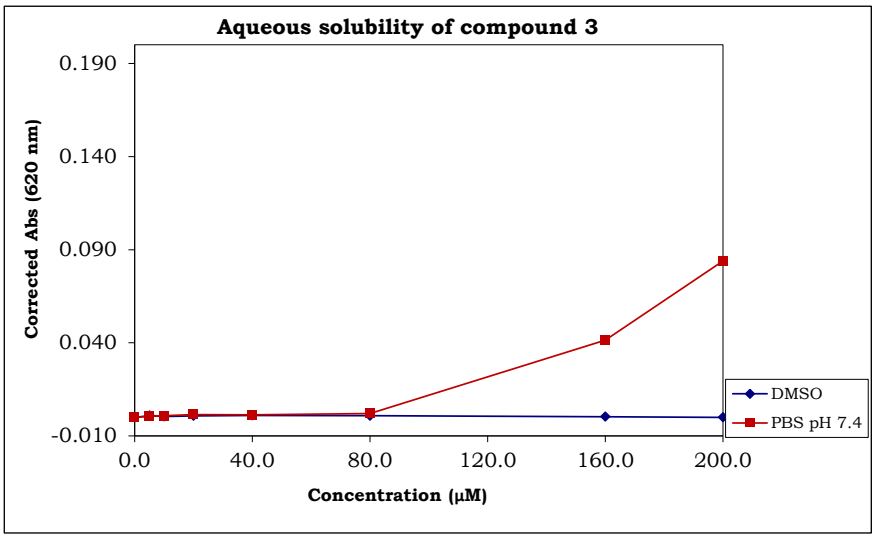

Figure 6.1: Aqueous solubility of compound **3** estimated by turbidimetric method.

6.5 Supramolecular Derivatization Studies

6.5.1 Powder X-ray Diffraction (PXRD)

Powder X-ray diffraction patterns were recorded on a BRUKER D8 Advance X-ray diffractometer using CuKα_1 radiation (λ = 1.5406 Å). Approximately 5 mg of a manually ground test sample was placed on a zero background sample holder and scanned over a 2θ range of 4–40° at a rate of 0.03° per second. The X-ray generator was set at 30 kV and 40 mA.

6.5.2 Elucidation of Crystal Structure

Single crystal intensity data were collected on a Bruker KAPPA APEX II DUO X-ray diffractometer using graphite-monochromated MoKα radiation (λ = 0.71073 Å), which was generated by a Bruker K780 generator operating at 50 kV and 30 mA. A Cryostream cooler (Oxford Cryostreams, UK), with N_2 gas flowing at 20 cm^3 min^{-1}, was used to facilitate low-temperature data collections. The Bruker SAINT Software[10] was used for unit cell refinement and data reduction. All intensity data were corrected for Lorentz-polarisation effects and the multi-scan method (SADABS)[11] was employed to correct data for absorption effects.

The observed Laue symmetry of the diffraction pattern was used to establish the crystal system while the space group was determined by examining systematic absences and matching the observed conditions to a known space group. The input files for structure solution were prepared using the program XPREP.[12] Programs SHELXS, SHELXL, and SHELXH were employed for structure solution and refinement.[13,14] All these programs were operated within the X-SEED interface.[15] Intramolecular and intermolecular geometrical parameters were calculated using the program PLATON.[16,17] POV-Ray[15] was used to create crystal structure images whereas the program LAYER[15] was used for the graphic display of intensity data.

6.5.3 Hot-Stage Microscopy (HSM)

Test samples were placed on a cover slip with silicone oil and placed on a Linkam TH MS600 hot stage coupled to a Linkam TP92 temperature control unit. The hot stage was fitted with a Nikon SMZ-10 stereoscopic microscope for sample monitoring and the images were captured using a real-time Sony

Digital Hyper HAD color video camera operating on Soft Imaging System [analySIS] software.

6.5.4 Thermogravimetric Analysis (TGA)

A TA-Q500 Thermogravimetric Analyzer (TA instruments) with Universal Analysis 2000 Software (v4.5A, TA Instruments-Waters LLC) was used. The instrument was operated with a dry nitrogen purge gas flowing at 60 cm^3 min^{-1}. All test samples (2–3 mg) were heated at a rate of 10 °C min^{-1} in an open aluminium crucible.

6.5.5 Differential Scanning Calorimetry (DSC)

Data were recorded on a pre-calibrated TA DSC-25 (Discovery Series) Differential Scanning Calorimeter (TA instruments) operated with TRIOS Software v4.2.1. Sample masses, scanning rates, purge gas flow rates were in the same ranges as those employed in TGA. An aluminium standard mass was used as the reference.

References

(1) Leivers, A. L.; Tallant, M.; Shotwell, J. B.; Dickerson, S.; Leivers, M. R.; McDonald, O. B.; Gobel, J.; Creech, K. L.; Strum, S. L.; Mathis, A.; Rogers, S.; Moore, C. B.; Botyanszki, J. Discovery of Selective Small Molecule Type III Phosphatidylinositol 4-Kinase Alpha (PI4KIIIα) Inhibitors as Anti Hepatitis C (HCV) Agents. *J. Med. Chem.* **2014**, *57*, 2091–2106.

(2) Lecoutey, C.; Fossey, C.; Rault, S.; Fabis, F. Efficient Room-Temperature One-Pot Synthesis of 2-Amino-3-alkyl(3-Aryl)quinazolin-4(3*H*)-Ones. *European J. Org. Chem.* **2011**, *2011*, 2785–2788.

(3) Ishimoto, K.; Fukuda, N.; Nagata, T.; Sawai, Y.; Ikemoto, T. Development of a Scalable Synthesis of a Vascular Endothelial Growth Factor Receptor-2 Kinase Inhibitor: Efficient Construction of a 6-Etherified [1,2,4]Triazolo[1,5-a]Pyridine-2-Amine Core. *Org. Process Res. Dev.* **2014**, *18*, 122–134.

(4) Das, J.; Rao, C. V. L.; Sastry, T. V. R. S.; Roshaiah, M.; Sankar, P. G.; Khadeer, A.; Kumar, M. S.; Mallik, A.; Selvakumar, N.; Iqbal, J.; Trehan, S. Effects of Positional and Geometrical Isomerism on the Biological Activity of Some Novel Oxazolidinones. *Bioorg. Med. Chem. Lett.* **2005**, *15*, 337–343.

(5) Ilkun, O. T.; Archibald, S. J.; Barnes, C. L.; Gerasimchuk, N.; Biagioni, R.; Silchenko, S.; Gerasimchuk, O. A.; Nemykin, V. N. Benz(2-Heteroaryl)cyanoximes and Their Tl(I) Complexes: New Room Temperature Blue Emitters. *Dalton Trans.* **2008**, 5715–5729.

(6) Tseng, C.-H.; Tzeng, C.-C.; Chiu, C.-C.; Yang, C.-L.; Lu, P.-J.; Chou, C.-K.; Liu, C.-Y.; Chen, Y.-L. Synthesis and Antiproliferative Evaluation of 9-Methoxy-6-(Piperazin-1-yl)-11*H*-indeno[1,2-C]quinoline-11-One Derivatives. Part 4. *Med. Chem. Commun.* **2014**, *5*, 937–948.

(7) Saccomanni, G.; Badawneh, M.; Adinolfi, B.; Calderone, V.; Cavallini, T.; Ferrarini, P. L.; Greco, R.; Manera, C.; Testai, L. Synthesis and β-Blocking Activity of (R, S)-(*E*)-Oximeethers of 2,3-Dihydro-1,8-Naphthyridine and 2,3-dihydrothiopyrano[2,3-b]pyridine: Identification of β-3 Antagonists. *Bioorg. Med. Chem.* **2003**, *11*, 4921–4931.

(8) Ferrarini, P. L.; Mori, C.; Badawneh, M.; Calderone, V.; Greco, R.; Manera, C.; Martinelli, A.; Nieri, P.; Saccomanni, G. Synthesis and Beta-Blocking Activity of (R,S)-(*E*)-Oximeethers of 2, 3-Dihydro-1,8-Naphthyridine and 2,3-dihydrothiopyrano[2,3-b]pyridine:potential Antihypertensive Agents - Part IX. *Eur. J. Med. Chem.* **2000**, *35*, 815–826.

(9) Rida, S.; Ashour, F.; Elhawash, S.; Elsemary, M.; Badr, M.; Shalaby, M. Synthesis of Some Novel Benzoxazole Derivatives as Anticancer, Anti-HIV-1 and Antimicrobial Agents. *Eur. J. Med. Chem.* **2005**, *40*, 949–959.

(10) Bruker AXS Inc. Program SAINT, Version 7.60a, Madison,Wisconsin, USA, 2008.

(11) Sheldrick, G. M. SADABS, Program for Empirical Absorption Correction of Area Detector Data. Göttingen, Germany: University of Göttingen, 1997.

(12) Bruker AXS Inc. XPREP, Release 5.1/NT; X-Ray Data Preparation and Reciprocal Space Exploration Program, Madison,Wisconsin, USA, 1997.

(13) Sheldrick, G. M. A Short History of SHELX. *Acta Crystallogr. A.* **2008**, *64*, 112–122.

(14) Sheldrick, G. M. Crystal Structure Refinement with SHELXL. *Acta Crystallogr. Sect. C Struct. Chem.* **2015**, *71*, 3–8.

(15) Barbour, L. J. X-Seed — A Software Tool for Supramolecular Crystallography. *J. Supramol. Chem.* **2001**, *1*, 189–191.

(16) Spek, A. L. Structure Validation in Chemical Crystallography. *Acta Crystallogr. Sect. D Biol. Crystallogr.* **2009**, *65*, 148–155.

(17) Spek, A. L. Single-Crystal Structure Validation with the Program PLATON. *J. Appl. Crystallogr.* **2003**, *36*, 7–13.

APPENDICES

Appendix A1: ^{1}H NMR spectrum {in DMSO-d_6 at 300 MHz}, TGA and PXRD traces of **3** citrate (2:1).

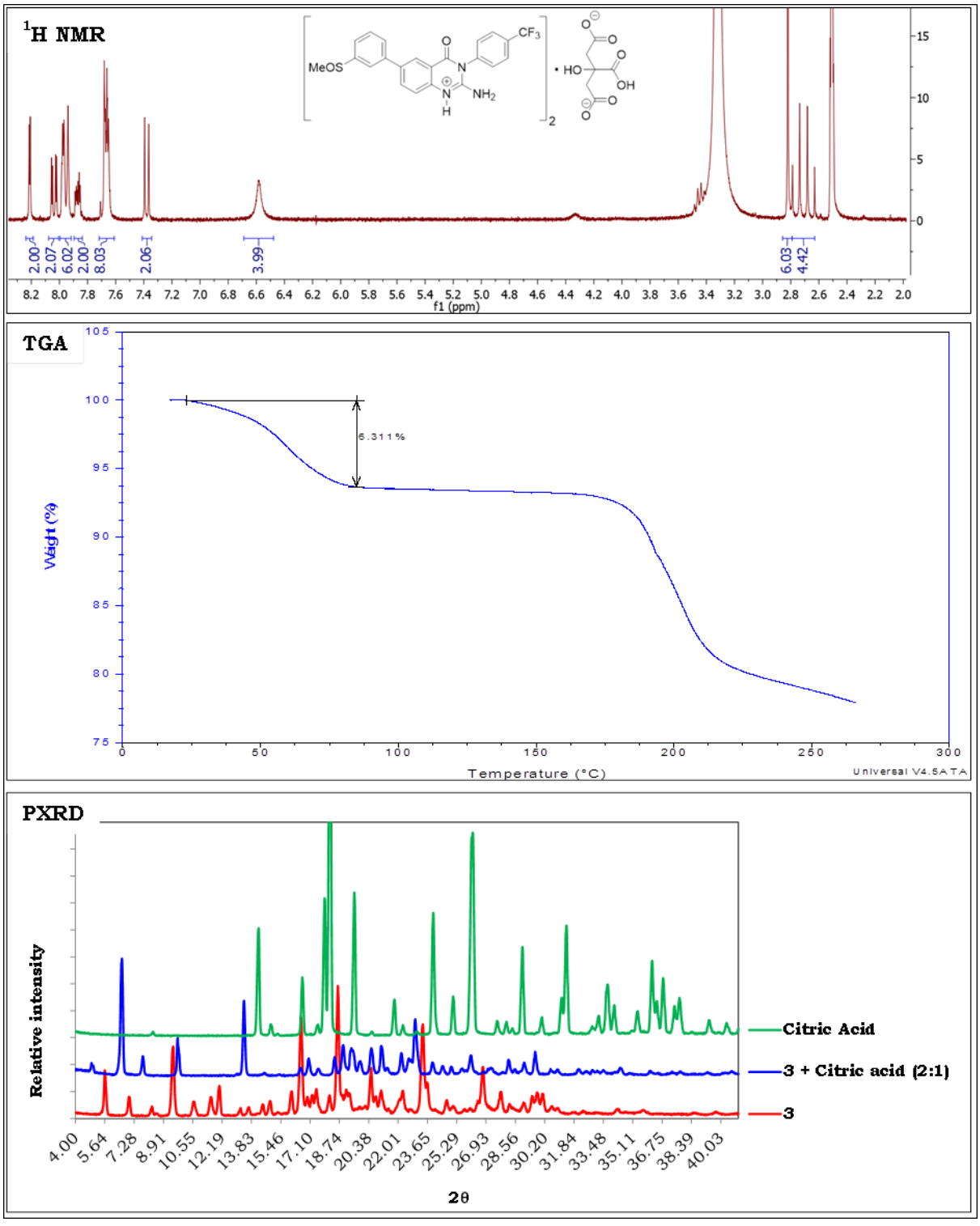

Appendix A2: ^{1}H NMR spectrum {in DMSO-d_6 at 300 MHz}, TGA and PXRD traces of **3** malonate (1:1).

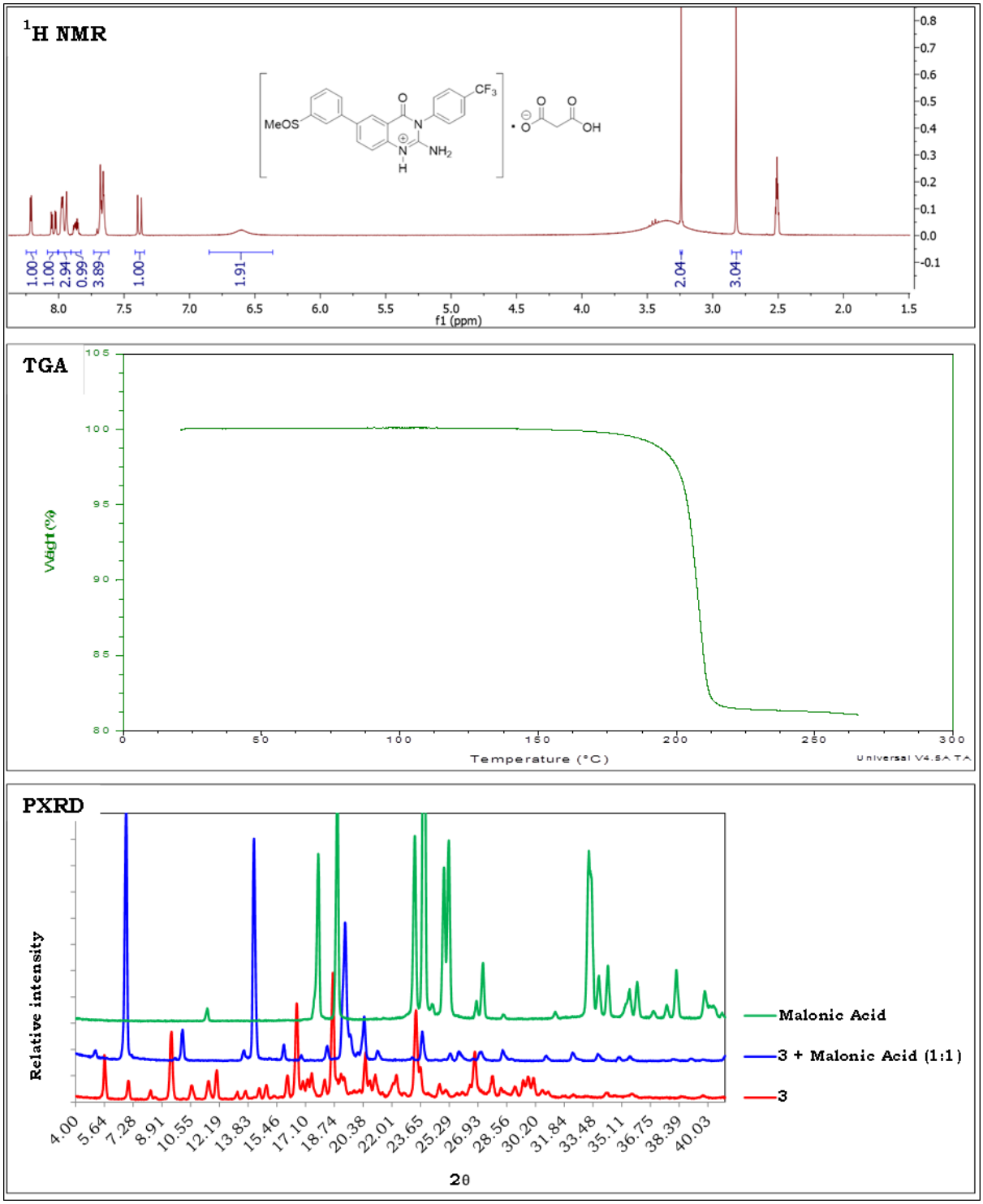

Appendix A3: ^{1}H NMR spectrum {in DMSO-d_6 at 300 MHz}, TGA and PXRD traces of **3** succinate (2:1).

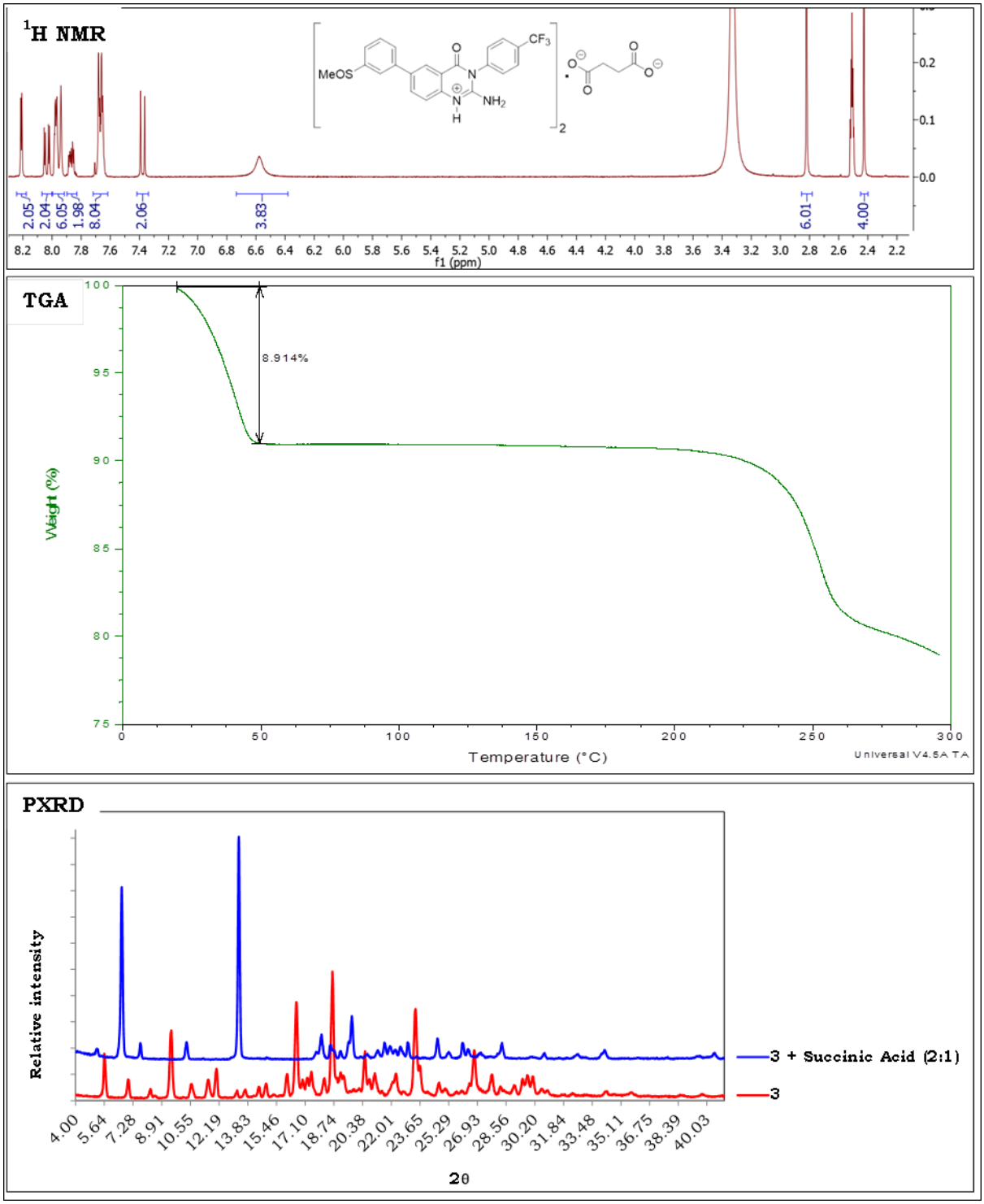

Appendix A4: ^{1}H NMR spectrum {in DMSO-d_6 at 300 MHz}, TGA and PXRD traces of **3** adipate (2:1).

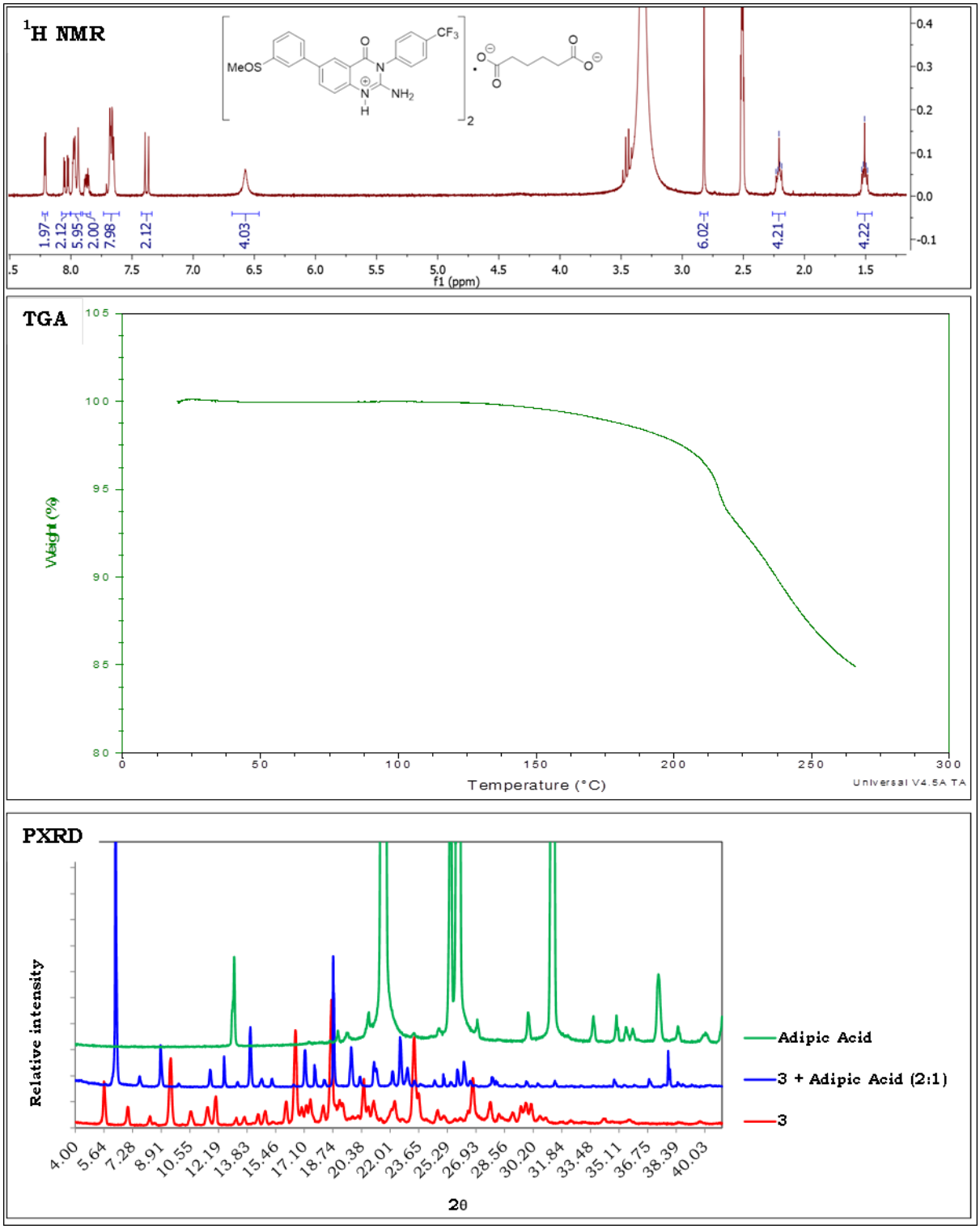

Appendix A5: Summary of HPLC solubility (PBS pH 7.4) determination. HPLC method = that described in the experimental section with a flow rate of 0.7 mL/min.

Calibration Curve Peak Areas [3]				
Sample 1	Sample 2	Sample 3	Conc. (µM)	Av. Peak Area
5050.5	5036.5	5074.6	250	5054
4070.2	4100.5	4119.4	200	4097
3326.0	3294.9	3356.3	160	3326
1662.0	1669.8	1673.7	80	1669
820.3	817.8	817.6	40	819
529.3	527.6	527.8	25	528
425.2	424.8	423.4	20	424
212.6	219.9	212.4	10	215
109.5	112.5	112.5	5	112

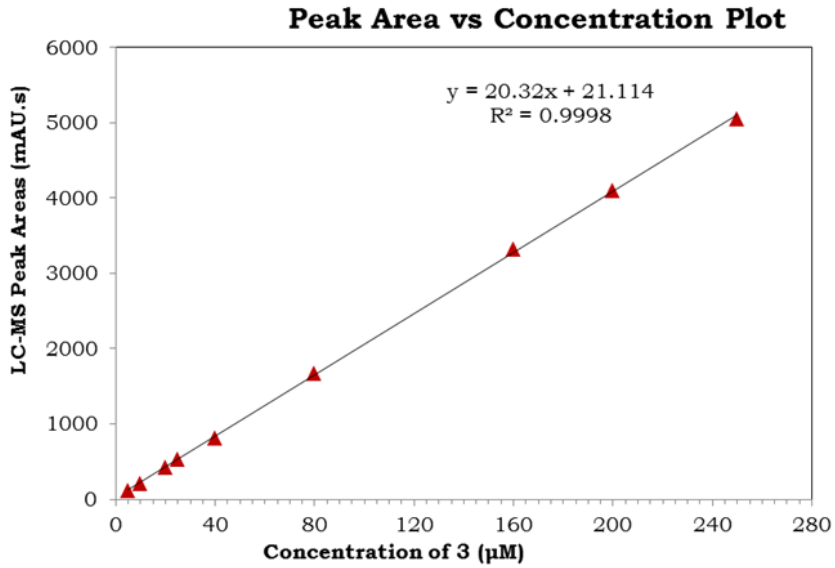

	Peak areas of 200 µM solutions in PBS pH 7.4 (2% v/v DMSO)				
Compound	Sample 1	Sample 2	Sample 3	Average	Solubility (µM)
3	458.6	453.7	457.6	456.6	21
3 + L-Malic Acid (2:1)	166.5	167.1	165.4	166.3	7
3 + Adipic Acid (2:1)	655.5	647.9	668.5	657.3	31
3 + Malonic Acid (1:1)	702.8	693.7	723.9	706.8	34
3 + Citric Acid (2:1)	565.0	562.3	570.6	566.0	27
3 + Succinic Acid (2:1)	569.8	565.8	575.8	570.5	27
3 + HCl (1:1)	649.0	641.2	655.0	648.4	31
3 + HBr (1:1)	752.7	728.3	781.7	754.2	36
3 + H_2SO_4 (1:1)	615.6	607.9	637.1	620.2	29
3 + H_3PO_4 (1:1)	630.9	618.5	670.0	639.8	30
3 + CH_3SO_3H (1:1)	777.2	744.3	873.4	798.3	38